# BIOINSPIRED NANOCARRIERS FOR THERAPEUTIC NUCLEIC ACID DELIVERY

Giulia Della Pelle

**Doctoral Dissertation**
**Jožef Stefan International Postgraduate School**
**Ljubljana, Slovenia**

**Supervisor:** Assist. Prof. Nina Kostevšek, IPS and Jožef Stefan Institute, Jamova Cesta 39, Ljubljana 1000, Slovenija

**Evaluation Board:**

Prof. Dr. Toni Petan, Chair, IPS and Jožef Stefan Institute, Ljubljana, Slovenia

Prof. Dr. Petra Kocbek, Member, Faculty of Pharmacy, University of Ljubljana, Slovenia

Prof. Dr. Mauro Comes Franchini, Member, Department of Industrial Chemistry »Toso Montanari«, University of Bologna, Italy

MEDNARODNA PODIPLOMSKA ŠOLA JOŽEFA STEFANA
JOŽEF STEFAN INTERNATIONAL POSTGRADUATE SCHOOL




Giulia Della Pelle

# BIO-INSPIRED NANOCARRIERS FOR THERAPEUTIC NUCLEIC ACID DELIVERY

**Doctoral Dissertation**

# BIOMIMETSKI NANONOSILCI ZA TERAPEVTSKO DOSTAVO NUKLEINSKIH KISLIN

**Doktorska disertacija**

**Supervisor:** Assist. Prof. Nina Kostevšek

Ljubljana, Slovenia, June 2025

*To my cats*

# Acknowledgments

Writing the acknowledgement of this thesis, now that I'm doing it, it's proving to be the most challenging part of it all. The actual work was not difficult; it was not challenging *per se*. It was a long journey, that now, in hindsight, is already tinted with mist – it has the shade of a long run, the kind that doesn't allow the runner to stop and take a breath. I was not yet 28 when I move to Slovenija. Now I'm almost 33, and this long run is not over yet. What no one tells you, at the beginning of this long, sandy, sweaty, run, is that in order to keep on learning – for those little, angry neurons to keep on firing in your brain –, you have to be patient. That, despite not having the time to take a deep breath, you'll feel the force of time itself passing through you – with all its burden of tragicomical, useless, sometimes happy and meaningful, events. Wars started and ended during my PhD. The human world changed into a ugly, bitter, remorseful thing. Young enough to keep on running, too old – just like a desperate horse – to know how to stop. A world where someone may dream of solar sails bring us to Proxima, where cancer and genetic diseases are becoming just a memory of the past.

To my old self, that 27-year-old girl that was crying while passing through the Fernetti border control, I'd just say: Be patient. Everything will be alright.

During this run, I met some amazing people. I met my best friend, Surur Semsari. I met my partner, Ennio Visconti, and I thank both greatly for the everlasting support even during the hardest moments, when, I'm aware, - I was being myself an ugly, remorseful and bitter thing. I met my supervisor, Nina Kostevsek, whom I've never seen in person before, a passionate and curious scientist, who was always ready to listen to my, sometimes, bad ideas and be proud of them. Who trusted me enough with this huge project, that finally came to light. Among many, I'm extremely thankful to Urša Čerček for her precious contribution in the final paper of this thesis (Chapter 7) and for her kind friendship.

I thank K7 youngsters for making bad days look more bearable: Abhilash Krishnamurthy, for his caustic judgement over everything; Belisa Alcantara, for bringing a light of joy even during the most tedious moments; Katarina Tomic, for her everlasting yearn for knowledge. My office mates, Ipeknaz Ozden and Nikhil Boothpur, for the random laughs and the very deep, equally random, discussions that we had. My affection and gratitude go also to Jernej Sribar, whose humanity and friendship have enriched my days.

My little family, down there in Italy, never understood what I was working on, being composed of lawyers and linguists: but they all supported me, even when I announced that I was moving away from the country. Thank you, Mum, for your unconditional support and love. And for taking good care of the cats as a single parent.

For the realization of this thesis, I sincerely thank Slovenian Research and Innovation Agency ARIS (program numbers P1-0207, P2-0084, P3-0003, P3-0108, project numbers PR-10482, J3-14531 and J4-50150).

# Abstract

The development of efficient, biocompatible drug delivery systems is a major challenge in modern medicine, particularly for nucleic acid-based therapies. This doctoral dissertation explores bioinspired and biomimetic nanocarriers designed for the delivery of small-interfering RNA (siRNA), offering novel approaches to address pharmacokinetic limitations, immune recognition, and delivery efficiency. The work focuses on the synthesis, characterization, and therapeutic evaluation of nanocarriers inspired by natural systems such as erythrocytes and natural crosslinkers. The thesis integrates principles of nanotechnology, gene therapy, pharmacology, and materials science to present a multidisciplinary strategy for enhancing siRNA delivery via nanomedicine.

The first part of the thesis provides a comprehensive review of nanomedicine, outlining its historical development, key innovations in drug delivery systems, approved nanodrugs (including gene therapy) and the emerging field of theranostics—where therapeutic and diagnostic functions are combined in a single nanosystem. Nanodrugs offer several advantages over conventional therapies, including prolonged circulation time, reduced toxicity, improved biodistribution, and the ability to cross biological barriers. However, challenges such as immune system recognition and activation, clearance by the reticuloendothelial system (RES), and endosomal trapping remain significant obstacles.

To overcome these, we researched erythrocyte membrane vesicles (EMVs) as natural, stealth carriers that retain immune-evasive markers such as CD47, enabling prolonged systemic circulation and passive tumor targeting via enhanced permeation and retention effect. Genipin-crosslinked polyamine nanoparticles (GxS5) are also developed for their ability to complex siRNA and their inherent fluorescence properties, which facilitate real-time tracking. The work further explores the combination of these two approaches through a hybrid system in which GxS5 nanoparticles are coated with erythrocyte membranes, merging the advantages of both carriers. The EMV formulation also show promise in terms of stability, controlled release, and imaging capabilities using indocyanine green (ICG) dyes for photothermal therapy. Several hypotheses are addressed, including the impact of zwitterionic surface modifications, membrane fusion mechanisms, and the Enhanced Permeability and Retention (EPR) effect in tumor tissue.

Through a series of in experiments, we demonstrated the effectiveness of these nanocarriers in delivering siRNA to melanoma-derived tumors *in vivo* and *in vitro*, and lymphoblastoid cell lines, achieving significant gene knockdown with minimal cytotoxicity.

This research contributes to the ongoing evolution of non-viral gene therapy methods and underscores the potential of bioinspired materials in next-generation nanomedicine. By tailoring carriers to evade immune responses, promote targeted delivery, and integrate diagnostic functions, this thesis presents a comprehensive platform for the treatment of genetic and oncological diseases. The findings support the feasibility of multifunctional nanocarriers and provide a foundation for future clinical translation. The dissertation concludes with a critical assessment of the limitations and prospects of RNAi-based

treatments, highlighting the importance of rational design, biocompatibility, and adaptability in therapeutic development.

# Povzetek

Razvoj učinkovitih, biokompatibilnih dostavnih sistemov za zdravila je velik izziv v sodobni medicini, zlasti za terapije na osnovi nukleinskih kislin. Ta doktorska disertacija raziskuje biomimetične nanonosilce za dostavo malih interferenčnih RNK (siRNK). Naša zasnova ponuja nove pristope za farmakokinetičnih omejitev, imunskega odziva in učinkovitosti dostave. Delo se osredotoča na sintezo, karakterizacijo in terapevtsko vrednotenje nanonosilcev, ki jih navdihujejo naravni sistemi, kot so eritrociti in naravni zamreževalci. Teza združuje načela nanotehnologije, genske terapije, farmakologije in znanosti o materialih, da bi predstavila multidisciplinarno strategijo za izboljšano dostavo siRNK s pomočjo nanomedicine.

Prvi del teze ponuja celovit pregled nanomedicine, v katerem je opisan njen zgodovinski razvoj, ključne inovacije dostavnih sistemov, odobrena nanozdravila (vključno z gensko terapijo) in nastajajoče področje teranostike – kjer so terapevtske in diagnostične funkcije združene v enem samem nanosistemu. Nanozdravila ponujajo več prednosti pred konvencionalnimi terapijami, vključno s podaljšanim časom cirkulacije, zmanjšano toksičnostjo, izboljšano biodistribucijo in sposobnostjo premostitve bioloških ovir. Vendar pa izzivi, kot so prepoznavanje in aktivacija imunskega sistema, odstranjevanje s strani retikuloendotelijskega sistema (RES) in endosomski pobeg, ostajajo ključne ovire.

Da bi te izzive premostili, smo raziskali vezikle na osnovi eritrocitnih membran (EMV) kot naravne, neimunogene nosilce, ki vsebujejo imunske markerje za izogib imunskemu sistemu, kot je CD47, kar omogoča podaljšan sistemski krvni obtok in pasivno ciljanje tumorja z izboljšanim učinkom prepustnosti in zadrževanja. Z genipinom zamreženi poliaminski nanodelci (GxS5) so bili razviti zaradi svoje sposobnosti kompleksiranja siRNK in zaradi svojih inherentnih fluorescenčnih lastnosti, ki omogočajo sledenje v realnem času. Delo nadalje raziskuje kombinacijo teh dveh pristopov s hibridnim sistemom, v katerem so nanodelci GxS5 prevlečeni z eritrocitnimi membranami, kar združuje prednosti obeh nosilcev. Formulacija EMV je obetavna tudi glede stabilnosti, nadzorovanega sproščanja in uporabe v diagnostiki z uporabo barvila indocianin zeleno (ICG) za fototermično terapijo. Obravnavanih je več hipotez, vključno z vplivom modifikacij zwitterionske površine, mehanizmi membranske fuzije in učinkom izboljšane prepustnosti in zadrževanja (EPR) v tumorskem tkivu.

Z vrsto in vivo ter in vitro poskusov smo dokazali učinkovitost teh nanonosilcev pri dostavi siRNK v melanomske tumorje, ter v limfoblastoidne celične linije, s čimer smo dosegli znatno zmanjšanje genske aktivnosti z minimalno citotoksičnostjo.

Ta raziskava ključno prispeva k razvoju metod nevirusne genske terapije in poudarja potencial bio-navdahnjenih materialov v nanomedicini naslednje generacije. S prilagajanjem nosilcev za izogibanje imunskemu odzivu, spodbujanje ciljne dostave in integracijo diagnostičnih funkcij ta teza predstavlja celovito platformo za zdravljenje genetskih in onkoloških bolezni. Rezultati in ugotovitve podpirajo možnost priprave večfunkcionalnih nanonosilcev in zagotavljajo osnovo za prihodnjo klinično translacijo.

Disertacija se zaključi s kritično oceno omejitev in obetov zdravljenja na osnovi RNAi, pri čemer poudarja pomen racionalne zasnove, biokompatibilnosti in prilagodljivosti pri terapevtskem razvoju.

# Contents

**List of Figures** **xvii**

**List of Tables** **xix**

**Abbreviations** **xx**

**1. Introduction** **1**

1.1 The (Yet) Short and Intense Story of Nanomedicine ... 1

1.2 The Pharmacokinetic of Nanodrugs ... 2

1.2.1 Liberation ... 2

1.2.2 Absorption ... 3

1.2.3 Distribution ... 3

1.2.4 Metabolism ... 3

1.2.5 Excretion ... 3

1.3 Advantages of Nanodrugs ... 6

1.4 The "Nano-Bio" Interface ... 10

1.4.1 How to avoid nanoparticle immune system recognition: PEGylation ... 12

1.5 Gene Therapy: General Overview ... 14

1.5.1 RNA interference overview and mechanism ... 17

1.5.2 What are the biological barriers for a siRNA to exert its action? ... 21

1.5.3 Overview of approved interference drugs ... 23

1.5.4 Nanostructured approaches in theranostics and "precision medicine" ... 24

1.5.5 Drawbacks of RNA interference as a therapeutic approach ... 25

1.6 Bio-Inspired Therapeutic Nucleic Acids Carriers ... 28

1.6.1 Nature-engineered nanocarriers: exosomes and viral particles ... 28

1.6.2 Whole-cell approach: the case of erythrocytes ... 29

1.6.3 Cell membrane-drug interaction: pharmacological features ... 31

1.6.4 Erythrocytes membrane vesicles or nanoerythrosomes, EMVs ... 32

1.7 Polymeric Nanoparticles: Principles, Advantages and Drawbacks ... 34

1.7.1 Biomedical applications of genipin and reaction mechanism ..... 34
1.7.2 Polyamines: natural polycations ..... 35
1.7.3 Genipin-polyamine-glycine nanoparticles ..... 36

**2. Aims and Hypotheses** **37**

2.1 Aims and Rationale ..... 38
2.2 Hypothesis 1: Prolonging Nanodrug Circulation Time via "Don't Eat Me" CD47 Marker41
2.3 Hypothesis 2: Taking Advantage of Extracellular Vesicles Machinery for Successful Internalization and Cargo Release ..... 41
2.4 Hypothesis 3: Exploiting Enhanced Permeation and Retention Effect for Tumor Tissue Penetration ..... 42
2.5 Hypothesis 4: Stabilizing Cyanine Dyes Monomeric Forms to Reduce Light-induced Degradation and Improve Photothermal Properties ..... 43
2.6 Hypothesis 5: Tailoring the Cationic Charge of Transfecting Agents Towards a Zwitterionic Character ..... 44
2.7 Hypothesis 6: Coating Zwitterionic Polymers with Erythrocyte Membranes would lead to Novel Material with Properties Belonging to Both Models ..... 46
2.8 Hypothesis 7: The Self-Fluorescence, in Green and Red, of GxS5 Polymers, would make it possible to follow their Internalization Route in Real Time ..... 47

**3. Materials and Methods** **49**

3.1 Materials ..... 49
3.1.1 Cell culture-related chemicals ..... 50
3.2 Small interfering RNAs and RT-qPCR primers ..... 50
3.3 Blood sourcing and ethical approvals ..... 51
3.4 Nanoparticles preparation and basic characterization and storage ..... 51
3.4.1 Erythrocytes membrane vesicles (EMVs) preparation ..... 51
3.4.1.1 Density-changing centrifugation (DCC) ..... 51
3.4.2 Liposomes preparation ..... 52
3.4.3 Labeling with lipophilic trackers ..... 53
3.4.4 GXS5 (Genipin-polyamine-glycine) polymers preparation and siRNA complexation ..... 53
3.4.4.1 Size exclusion purification (GxS5 polymers and ICG/IR-820 EMVs) ..... 53
3.4.5 Freeze drying of DCC-siRNA-EMVs and GxS5 polymers ..... 54
3.4.6 UV/Vis and fluorescence readings ..... 54

3.4.7 Superresolution Fluorescence Microscopy ..... 54
3.4.8 Quantification of siRNA via Quantifluor assay ..... 54
3.4.9 Quantification of lipids and proteins in EMVs/ghosts ..... 54
3.4.10 Quantification of primary and secondary amines in GxS5 polymers ..... 55
3.4.11 Laser irradiation on ICG/IR820 EMVs/liposomes for photostability/photothermal effect ..... 55
3.4.12 Dynamic light scattering (DLS) and Zeta-potential measurements ..... 55
3.5 Microscopy techniques used in Chapter 6 and 7 ..... 56
3.5.1 Negative-stain transmission electron microscopy (TEM) ..... 56
3.5.2 Cryo-TEM and freeze fracture microscopies ..... 56
3.5.3 Atomic Force Microscopy, used in Chapter 7 ..... 57
3.6 Cell biology methods used in Chapter 5, 6, 7 ..... 57
3.6.1 Cell culture condition ..... 57
3.6.2 Cytotoxicity test ..... 58
3.6.3 B16F10 in vitro transfection with EMVs, GxS5 and Hybrid-G10S5 ..... 58
3.6.4 Lymphoblastoid cells in vitro transfection with G10S5 and Hybrid-G10S5 ..... 58
3.6.5 Hemotoxicity study ..... 59
3.7 Molecular biology methods used in Chapter 5, 6, 7 ..... 59
3.7.1 Agarose gel assays: RNAse A resistance, dye exclusion assay heparin displacement ..... 59
3.7.2 Quantitative Reverse Transcriptase Polymerase chain reaction of tdTomato mRNA ..... 60
3.7.3 Protein knockdown quantification in lymphoblastoid cells ..... 60
3.8 In vivo assays in Chapter 6 ..... 60
3.8.1 DCC-siRNA-EMVs administration to tumor-affected mice: biodistribution ..... 60
3.8.2 DCC-siRNA-EMVs administration to tumor-affected mice: RNA interference quantification and tdTomato fluorescence ..... 61
3.9 Stem-loop PCR for quantification of siRNA guide-strand in tissues and plasma 61
3.10 Fluorescence microscopy in Chapter 6 ..... 62
3.10.1 Internalization of DCC-siRNA-EMVs in B16F10, CT26 and NHLF ..... 62
3.10.2 Fluorescence-aided tissue biodistribution of DCC-siRNA-EMVs ..... 62
3.11 Statistical analysis ..... 62

**4. Cyanine dyes for Photo-Thermal Therapy: A Comparison of Synthetic Liposomes and Natural Erythrocytes-Based Carriers 63**

**5. Efficient siRNA delivery to murine melanoma cells via a novel genipin-based nano-polymer 81**

**6. Red Blood Cell Membrane Vesicles for siRNA Delivery: A Biocompatible Carrier with Passive Tumor Targeting and Prolonged Plasma Residency 103**

**7. Novel Vector for Efficient siRNA Delivery to Lymphoblasts and Melanoma based on Genipin-Spermine Nanocarriers Protected with Hybrid Erythrocyte Membrane Coating 139**

**8. Conclusions 165**

**9. Appendix A 169**

**10. Appendix B 171**

**11. Appendix C 185**

**12. Appendix D 196**

**13. References 205**

**14. Bibliography 231**

**15. Biography 235**

# List of Figures

Figure 1: Schematic representation of LADME phases and of the main pharmacokinetic parameters that can be inferred from the Area Under the Curve.....5

Figure 2 Example of a theranostic nanoparticle in nanomedicine for therapeutic nucleic acids (TNA) delivery .....10

Figure 3 Schematic representation of opsonization ("bio-corona" formation) on a NP in hematic flux. .....11

Figure 4 Summary of RNA interference mechanism main actors.....21

Figure 5 The main barriers that are a naked siRNA must overcome to exert its function. .....23

Figure 6 Schematic representation of the generation of erythrocytes membrane vesicles from whole erythrocytes. EMVs still retain CD47, sialic acids glycocalyx forest, and the antigen system AB0. .....33

Figure 7 Schematic representation of the building block for the synthesis of genipin-polyamines-glycine polymers.....36

Figure 8 Overview of the hypothesis and the results thesis.. .....37

Figure 9 Summary of the hypotheses on which this Thesis is based. Each of them is addressed more in depth in the body of text. .....40

Figure 10 Summary of the main steps of endosomal escape mechanism by cationic/ionizable nanoparticles. . .....46

Figure 11 Summary of Hypothesis 7. Hybrid membranes, composed of erythrocyte ghost membranes and external phospholipids, will be employed to coat G10S5-siRNA polyplexes, resulting in nanoparticles sporting the advantages of both systems.....48

Figure 12 Graphical Abstract for Chapter 5. Reprinted from [330]. .....82

Figure 13 Graphical Abstract of Chapter 6, reprinted from [208]. .....105

Figure 14 Graphical Abstract of Chapter 7.....141

# List of Tables

Table 1: General overview of the most common approaches for nanoparticle synthesis for biomedical applications. ....8

Table 2: Mechanism of action, molecular agent, application, approved drugs and nanocarrier for the main gene therapy approaches currently used. ....16

Table 3: Overview of the main bioactive RNA classes. ....18

Table 4: Overview o of advantages and disadvantages of RNAi agents' delivery systems. ....27

Table 5: Summary Table with the rejection, acceptance of partial acceptance of the formulated hypotheses. ....166

# Abbreviations

| | | |
|---|---|---|
| AFM | ... | Atomic force microscopy |
| DDS | ... | Drug Delivery System |
| DNA | ... | Deoxyribonucleic acids |
| DSPE | ... | 1,2-distearoyl-sn-glycero-3-phosphoethanolamine |
| DPPC | ... | Diplamitoylphosphatodyl-choline |
| FDA | ... | Good and Drug Administration |
| EMA | ... | European Medicine Agency |
| EMV | ... | Erythrocyte membrane particle |
| EPR | ... | Enhanced Permeation and Retention effect |
| EV | ... | Extracellular vesicle |
| LADME | ... | Liberation, absorption, distribution, metabolism, excretion |
| MRI | ... | Magnetic resonance imaging |
| JSI | ... | Jožef Stefan Institute |
| IPS | ... | International Postgraduate School |
| PEG | ... | Polyethylen-glycole |
| PEI | ... | polyethyleneimine |
| POPC | ... | Palmitoyl-oleyl-glycero-phosphocholine |
| RISC | ... | RNA-induced silencing complex |
| RES | ... | Reticuloendothelial system |
| ROS | ... | Reactive oxygen species |
| RNA | ... | Ribonucleic acid |
| SPION | ... | Superparamagnetic iron oxide nanoparticle |
| TEM | ... | Transmission Electron Microscopy |
| VLP | ... | Virus like particles |

# Chapter 1

# Introduction

The research work presented in this thesis was published in three scientific papers. The focus of the PhD was on the development of biocompatible, biomimetic small-interfering RNA carriers with added properties, such as indocyanine green fluorescence. The following introduction serves as a broad audience review about nanomedicine, its basis, where I further delve into the hurdles and advantages of drug miniaturization and engineering.

The chapters presenting the research work are presented as four first-author papers. Each one has a focused and detailed literature review of the problem and the aim of the research. Together, they concur with creating a story about the development and optimization of bioinspired and biomimetic nanodrug carriers, based on liposomal-like particles and polymeric nanoparticles.

## 1.1 The (Yet) Short and Intense Story of Nanomedicine

According to Britannica Encyclopedia, the definition of nanomedicine is as follows: a *branch of medicine that seeks to apply nanotechnology—that is, the manipulation and manufacture of materials and devices that are approximately 1 to 100 nanometers (nm; 1 nm = 0.0000001 cm) in size—to the prevention of disease and to imaging, diagnosis, monitoring, treatment, repair, and regeneration of biological systems.*

Life has already discovered and evolved the advantages of miniaturization, with enzymes, ribozymes, exo/endosomes and lysosomes, for signaling, degradation, reactive oxygen species resistance, and many other functions. For example, while a typical folded monomer of hemoglobin or Rubisco is approximately 5 nm, multiprotein complexes such as human v-SNARE, which are associated with a t-SNARE—an adhesion ring-like complex for membrane fusion—can reach up to 300 nm in size according to atomic force microscopy (AFM) measurements [1]; bacterial virus capsids, bacteriophages, which are usually within the range of 100–200 nm, are the same as the photosystems in plant cells [2], whereas the infamous SARS-CoV-2 virion is approximately 100 nm and comprises a lipidic–glucidic envelope [3]; furthermore, extracellular vesicles—lipidic and protein nanoparticles naturally secreted by cells for various reasons—usually account for a size of 100 nm [4].

As an official beginning of nanotechnology, the legendary speech by Richard Feyman in *1959—there is plenty of room at the bottom* [5]—can be identified. On the other hand, the properties of colloidal suspensions of copper, gold and silver nanoparticles have been exploited in glass art crafts, although they are not understood, since the Bronze Age—Lycurgus cup—is the most famous example. During the Renaissance, the famous alchemist Paracelsus (whose birth name is Philippus Aureolus Theophrastus Bombastus von Hohenheim) claimed to have synthesized the elixir for eternal life: Aurum Potabile, i.e., drinkable gold. Currently, the oral administration of heavy metal nanoparticles has no

health benefits; if anything, prolonged ingestion can cause kidney failure, liver stenosis and cirrhosis. Despite the myth surrounding drinkable gold, physicians of the Paracelsus era noted a correlation between certain symptoms and the habit of drinking colloidal gold: they called it auric fever, and its manifestation is that of typical heavy metal intoxication. Nevertheless, colloidal gold and, lately, colloidal silver were used for treating a wide range of conditions, mostly of bacterial origin, such as tuberculosis, in the late 19$^{th}$ century [6].

As a codified science, nanomedicine is still a young field. Like nanotechnology, it evolved together with analysis tools capable of visualizing such small objects: in 1928, the team of Adolf Matthias from the Technische Hochschule in Charlottenburg, and, mainly, Max Knoll and Ernst Ruska, managed to optimize an almost century-old design of a cathode–ray oscilloscope adapted for lens-focused magnetic fields. In 1933, the first electron beam-generated pictures were acquired. In the fourties, transmission electron microscopy (TEM) methods were already commercially available. After the Second World War, simultaneous advancements in biology (with the elucidation of DNA structure in 1959, for instance), nanotechnology, pharmaceutics, and computing power all concurred with rapid improvements in drug delivery science. During those years, the LADME basics (liberation, absorption, distribution, metabolism, and excretion) and the kinetics of release (zero-, first-, and second-order, retarded/sustained/controlled release) were first developed [7]. Of tremendous importance was the work of Professor Peter Paul Speiser, from ETH Zurich: polyacrylic beads, microcapsules, and micellized drugs were first introduced [8]. Moreover, the knowledge of clearance systems and organs has increased: the function of the reticuloendothelial system (RES) was investigated via album microspheres in the early 1970s [9] by the same group. In addition, more: liposomes. The first mention of "lipid spontaneous aggregates" was in 1964, in a work from the lab of Alec D. Bangham [10], where lecithin double layers were characterized via first-ever negative staining with phosphotungstic acid; the first attempt to use liposomes as a delivery system for therapeutic purposes was in 1973 [11], with the loading, by G. Gregoriadis, of actinomycin D in DPPC (1,2-dipalmitoyl-sn-glycero-3-phosphocholine) liposomes doped with cholesterol. Currently, as of 2024, more than 10,000 peer-reviewed papers containing the keyword "nanomedicine" have been published, and an ever-growing number of nanodrugs are being approved throughout the world [12].

## 1.2 The Pharmacokinetic of Nanodrugs

Pharmacokinetics is the study of how the body interacts with administered substances for the entire duration of exposure. The encapsulation of a molecule, or a complex inside a nanodrug, will alter its pharmacokinetic parameters; therefore, knowledge of the pharmacokinetic steps is instrumental for optimizing a nanodrug. Conventionally, pharmacokinetic steps are collectively referred to as ADME (adsorption, distribution, metabolism, excretion), rules, or, more recently, LADME, including the liberation phase, where the drug is liberated from the dosage form (capsule, nanodispersion, or crystalline drug) [13]. The steps are briefly described and schematically illustrated in **Figure 1**.

### 1.2.1 Liberation

The liberation stage refers to the first step of the release of the active pharmaceutical ingredient (API) of a drug. It is highly relevant for orally administered drugs, such as

tablets, and involves the dissolution of excipients within the gastroenteric tract, making the API available for absorption.

### 1.2.2 Absorption

The absorption stage describes how a drug enters the bloodstream after administration (oral, parenteral, etc.). A drug can be broken away by enzymes in the gastrointestinal tract or even in the bloodstream; the final amount that will be capable of exerting an effect is defined by the term bioavailability. A drug that will not be broken down by bloodstream enzymes and that is intravenously administered will, conventionally, have 100% **bioavailability**, while this dramatically decreases for drugs that are orally administered, since they will encounter the liver. Factors such as drug solubility, pH, and the presence of food can affect absorption.

### 1.2.3 Distribution

Once absorbed, drugs are distributed throughout the body via the bloodstream to reach their target tissues or organs. The efficiency of this distribution depends on factors such as blood flow, tissue permeability, and the drug's ability to bind to plasma proteins (such as albumin). Plasma protein complexation is a key factor in nanodrug delivery since it can either improve biodistribution or hinder it. Briefly, objects not recognized as "self" by innate immune system phagocytic cells are rapidly cleared from the bloodstream by kidney filtration; this process is enhanced by the surface binding of opsonizing molecules (complement proteins, IgG) in the form of a "bocorona" [14]. Drugs tend to be distributed more easily to tissues with heavily perfused tissues, such as the brain, liver, and kidneys, whereas tissues with lower blood flow, such as muscle and fat, receive the drug more slowly. At this stage, the **volume of distribution ($V_d$)** is the key parameter, representing the apparent volume in which a drug is dispersed throughout the body. A higher $V_d$ suggests extensive tissue distribution, whereas a lower $V_d$ indicates that the drug stays more within the bloodstream. This parameter is not strictly related to the actual efficacy of the drug or to the clearance speed since it does not include the **effective dose** of the drug.

### 1.2.4 Metabolism

Metabolism involves the chemical alteration of a drug, primarily by liver enzymes, to transform it into metabolites, which are more easily excreted. The cytochrome P450 enzyme system in the liver plays a critical role in drug metabolism, often converting drugs into inactive or less active forms. In some cases, metabolism may activate a drug (as with prodrugs) or convert it into toxic metabolites. **First-pass metabolism** occurs when a drug is metabolized significantly before it reaches systemic circulation, reducing its bioavailability. Metabolic reactions are categorized into two phases [15]:

- **Phase I**: Chemical modification of the drug (oxidation, reduction, or hydrolysis).
- **Phase II**: Conjugation reactions, where the drug is linked with another compound to increase its water solubility for excretion.

### 1.2.5 Excretion

Excretion is the removal of drugs and their metabolites from the body, primarily through the kidneys in urine, although drugs can also be excreted in bile, sweat, and breath subsequently to accumulate in the lungs or feces. Renal excretion involves processes such as glomerular filtration, tubular secretion, and reabsorption. This process, for nanodrugs,

is heavily dependent on the size of the nanoparticles and is related to the pore size of the blood vessel endothelium of the main clearance organ. For example, nanoparticles smaller than 5 nm are directly filtered by kidneys without participating in metabolic activity; those with sizes up to 400 nm are mostly cleared by the spleen and kidneys; an unquantifiable but large portion, 50–200 nm, ends in liver Kupffer cells [16] (**Paragraph 0**).

A drug's **half-life** (t½) is the time it takes for the concentration of the drug in the blood to decrease by half, and it plays a significant role in determining the administered dose and the frequency of treatment. **Clearance (Cl)** is the rate at which a drug is eliminated from the body and is determined by both metabolism and excretion. The **mean residence time** is another key pharmacokinetic parameter: it indicates the time spent by a drug within the bloodstream [17], depending on the absorption time and administered dose. Conventionally, these parameters can be inferred from the integral of the **area under the curve** (AUC) in a plot of the plasma concentration of the drug (mg/l, g/l, UI/l and so on) vs. time. Its integral, therefore, represents the whole exposure to the drug of the organism [18].

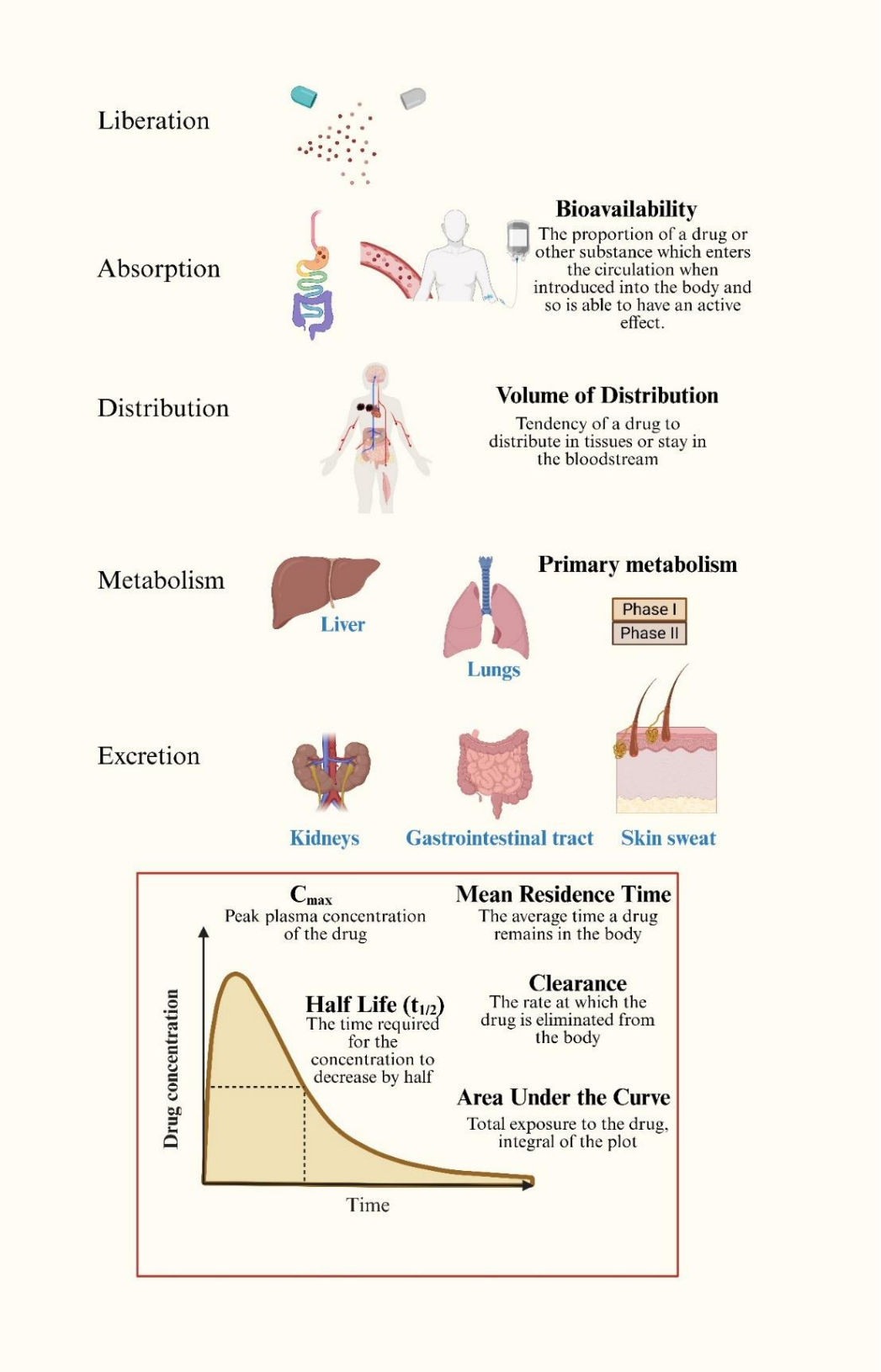



Figure 1: Schematic representation of LADME phases and of the main pharmacokinetic parameters that can be inferred from the Area Under the Curve.

## 1.3 Advantages of Nanodrugs

In the last two decades, the most important aim of nanomedicine has been to positively alter the pharmacokinetic parameters of the loaded active ingredient and improve its **therapeutic index,** defined as the ratio between the median lethal dose and median effective dose. For the sake of simplicity, the forthcoming paragraph refers only to intravenously administered drugs.

Loading the active ingredient (AI) in a small, controlled-release box, indeed, would ideally have the following advantages [19]:

- *Protection* of the drug from natural body clearance, exerted by the reticuloendothelial system (RES), spleen, liver, kidneys, and, in minor, by bone marrow and lungs [16], [20], will extend the circulation *half-life* of the drug; in this case, particular attention must be given to the size of the nanoparticles, since each organ has a slightly different optimum *clearance* in terms of diameter.
- Achieving *sustained or controlled release*, resulting in a more favorable pharmacokinetic profile [21];
- Shielding the drug from the immune system so that, in the case of protein- or nucleic acid-based drugs, it can avoid recognition as *nonself* by innate immune system cells (*stealth effect*) without activating inflammatory pathways [22];
- Improvement of the *uptake* and *internalization* rates in the case of targeted delivery by surface charge (i.e., zeta potential), curvature radius, and drug solubility in aqueous or lipid phases (for example, crossing the cell membrane via the *endosomal pathway and subsequent escape* in siRNA delivery);
- *Active delivery*, with the use of a targeting agent (antibody, aptamer, peptide, or receptor);
- In the case of a nanoparticle coated with a drug monomer, the high surface/volume ratio due to miniaturization would allow it to host a high quantity of active molecule (*nanosponge*) and, at the same time, its synergistic drug [23] or its targeting agent (i.e., an aptamer, an antibody);
- Extension and improvement of the imaging properties of encapsulated or adsorbed agents, such as superparamagnetic iron oxide nanoparticles (SPIONs) or cyanine dyes [24], [25], [26], and a reduction in toxicity;
- In the case of anticancer drugs, nanoparticles could take advantage of the *enhanced permeation and retention effects* [27] due to the leakiness of newly formed blood vessels in tumor tissues.

All the above improvements in design would ultimately improve the therapeutic index of the drug. For example, Abraxane, an FDA-approved nanodrug of paclitaxel conjugated with albumin, eliminates the need for toxic solvents (e.g., Cremophor EL) used in conventional paclitaxel formulations, reducing hypersensitivity reactions and improving the drug's therapeutic index. The nanoparticle formulation also enhances drug delivery to tumors [28]. Similarly, the liposomal formulation of cytarabine, DepoCyt, has a prolonged **release** phase, allowing for less frequent dosing and improved therapeutic effects with reduced neurotoxicity related to free cytarabine. Last, Doxil (nanoformulated doxorubicin,

in liposomes) causes little to no cardiotoxicity and is conventionally bound to free dexamethasone; increased compliance from patients, due to reduced side effects, has led to successful approval of the drug, despite not having definitively greater anticancer potency than the free form does [27].

Moreover, nanoparticles themselves are currently used as antibiotic agents: commonly called, collectively, "nanoantibiotics", they are usually some units to hundreds of nm-sized nanoparticles of metal oxides (Zn, Ag, Cu, and Ti) [29], [30]. Therefore, nanoparticles could be both inert and safe carriers (such as mesoporous materials)[31]) or play an active role in the pharmacological effect of the drug, enhancing its therapeutic effect as a main aim. With respect to contrast agents, the case of approved (even if withdrawn later) SPIONs, which are used to reduce the T2 relaxation time in magnetic resonance imaging (MRI) applications [24], is remarkable: iron oxide gains a superparamagnetic character only if it is in the nanoparticle phase [25].

### 1.3.1 Synthesis of nanodrugs

Nanodrugs can be synthesized via 1) a top-down approach, as in nanocrystals, bioderived materials such as extracellular vesicles, or 2) a bottom-up approach, as in liposomes [32], lipid and polymeric nanoparticles, which are drug conjugated. Many different typologies of nanostructures have been developed for drug delivery, as shown in Table 1, ranging from one borrowed from another field of application (quantum dots, carbon allotropes) to traditional ones, such as nanocrystalline drugs and liposomes.

Table 1: General overview of the most common approaches for nanoparticle synthesis for biomedical applications.

| **Synthesis modality** | **Name of nanoparticle typology** | **Description** | **Reference** |
|---|---|---|---|
| **Self-assembly** | Liposomes | A double layered vesicle composed of lipids, or lipid mimicking molecules, with a hollow space of various diameter; characterized as colloidal matter | [33], [34], [35] |
| **Self-assembly** | Dendrimers | Branched "tree like" polymers entrapping the drug | [36] |
| **Self-assembly** | Micelles | Lipidic/polymeric micelles entrapping the drug in the hydrophobic core, usually termed as *lipoplex* | [37], [38] |
| **Chemical conjugation** | Drug conjugate | Around the drug, that is in crystalline phase (if a small molecule) or monomeric state (if an enzyme), a massive polymer (i.e. PEG, PGLA, HPMA) or a protein (i.e. albumin) is built | [39] |
| **Self-assembly/catalytic polymerization** | Polymeric nanogels | Cross-linked material entrapping the drug | [34], [40] |
| **Shear stress processes** | Cell-membrane based | Cell membrane is processed to give birth to a liposomal-like *suspension*; used as *coating* for nanoparticles; for physical adsorption of the drug (*nanosponge*) | [41] |
| **Milling, high-pressure homogenization** | Nanocrystalline drug | A single crystal of the drug. It can be covered or not in a lipidic or polysaccharide envelope | [32] |
| **Chemical conjugation, layer-by-layer deposition** | Quantum dots and nanocrystals | Surface decorated with the drug of interest, often via a spacer directly bound to the surface. Possible applications in imaging | [23], [42] |
| **Chemical conjugation, layer-by-layer deposition** | Metal nanoparticles | Single crystal of transition metals, that can be surface functionalized for carrying the drug. Applications also in thermal therapy and imaging | [12] |
| **Adsorption** | Mesoporous materials | Usually $SiO_2$, high surface to volume ratio able to adsorb and host large quantity of drug. They can be coated or not in lipids and polysaccharides | [31], [34] |
| **Chemical conjugation + supramolecular hierarchical assemble** | Carbon nanotubes, fullerenes, Carbon dots | Carbon allotropes conjugated with drug of interest | [43], [44] |

### 1.3.2 Theranostics concept within nanomedicine

The steady increase in the market of nanodrugs has led to the birth of the concept of "theranostics", therapeutic *and* diagnostic, all in one formulation [45]. An ideal envelope will thus contain an actual drug (i.e., a chemotherapy agent, an antibiotic, a nucleic acid, a protein, or a photothermal agent) and one or more diagnostic agents (an MRI or ultrasound contrast agent or a fluorescence imaging fluorochrome) [46], as shown in **Figure 2**. Therefore, they do not interact with each other (if this hinders their activity), do not create aggregates, disturb their solubility, or destructively interact with the chosen drug delivery system (DDS). A synergistic effect between the drug and the diagnostic agent is strongly desirable [47]. Additionally, active targeting (i.e., the delivery of the formulation directly to the tissue of interest and easy entry into the cell, if the desired action has to take place intracellularly) is a highly desirable feature via conjugation with antibodies, aptamers, and cell-penetrating peptides; controlled release of the payload could also be exploited in particular cases by embedding in pH-, ultrasound- or temperature-sensitive lipids and polymers or upon binding of the target, triggering a cascade of events [48], [49], [50]. The concept of theranostics is not new to nuclear medicine since nuclear isotopes have long been used both as therapeutic and contrast agents [51] for MRI or positron emission tomography (PET) and single-photon emission computed tomography (SPECT). The encapsulation of contrast and imaging agents is a reality [25], as in the case of dextran-coated maghemite and magnetite nanoparticles. Contrast and imaging properties are usually improved by encapsulation [52], [53], [54], as in the case of indocyanine green.

There are, anyway, some features to consider. While dealing, for example, with solid nanoparticles entrapped within a matrix and with the therapeutic active ingredient, efflux from the matrix must be carefully controlled because the contrast/imaging agent could have different kinetics of activity than the drug, leading to unwanted effects, such as bioaccumulation off-target [55]. Furthermore, the steric hindrance of the nanoparticle must be assessed to optimize the amount of drug that can be loaded. Such an evaluation must be performed not only in the case of self-assembled nanocarriers, such as liposomes but also in the solid phase while dealing with mesoporous materials.

Theranostics are bound not only to imaging but also to what technique can be used to monitor the progression of the illness in real time [56] (the so-called *companion diagnostics*) and pharmacokinetic and pharmacodynamic studies [57], [58].

## 1.4 The "Nano-Bio" Interface

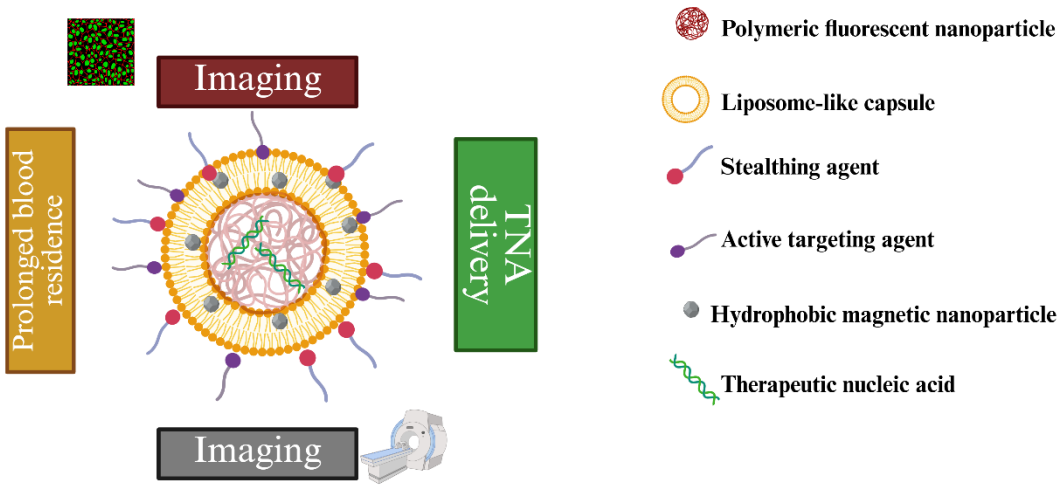



Figure 2: Example of a theranostic nanoparticle in nanomedicine for therapeutic nucleic acid (TNA) delivery, with dual imaging: a core composed of a fluorescent nanoparticle and, embedded in a liposomal-like coating, magnetic nanoparticles for MRI contrast. Furthermore, the surface of liposomes can be tailored with active targeting and stealthing agents (PEG, heparin, etc.).

What changes with miniaturization in terms of physical behavior has important consequences from a pharmacokinetic point of view. Drug delivery is a complex phenomenon arising from the interplay of surface potential (due to defects, vacancies, electron holes in crystalline solid nanoparticles, or simply ionization in lipid vesicles), curvature, the presence of pores, and hydrophobicity—in addition to the latter, all arising from the much higher surface free energy in nanoparticles than in the bulk [59], [60]. At the macroscopic level, size and shape dominate: usually, shapes with extreme aspect ratios are less prone to phagocytosis by macrophages but also to less internalization by target cells [61], [62]. Additionally, the crystalline structure of nanodrugs is important since amorphous drugs have different bioavailabilities [63], as in the case of nanocrystalline drugs such as Emend [64]. Applying these properties to the overall behavior of a single nanoparticle inside the human body, important implications are evident: how the particle joins the serum suspension in blood flow; if it tends to stick and fuse with nanoparticles of the same nature [60], [65] according to the **DLVO (Derjaguin–Landau–Verwey–Overbeek)** theory; if it will end up being coated—opsonized—with a "biocorona" [66] (**Figure 3**); its behavior in the case of laminar flow [67]; and how its shape, surface charge, and geometry allow it to interact with cell receptors, thus passively targeting a certain tissue [56]. Observations of these properties led to the birth of the concept of the " nanobio interface" by a groundbreaking paper by Nel et al. [68]. This topic is the subject of extensive

research, both from the synthetic side and from the biological side: liposomes, dendrimers, crystalline drugs, metallic nanoparticles (oxides or not), or even biocompatible nanostructures can impair their supposed pharmacodynamic properties through opsonization and subsequent recognition by the immune system.

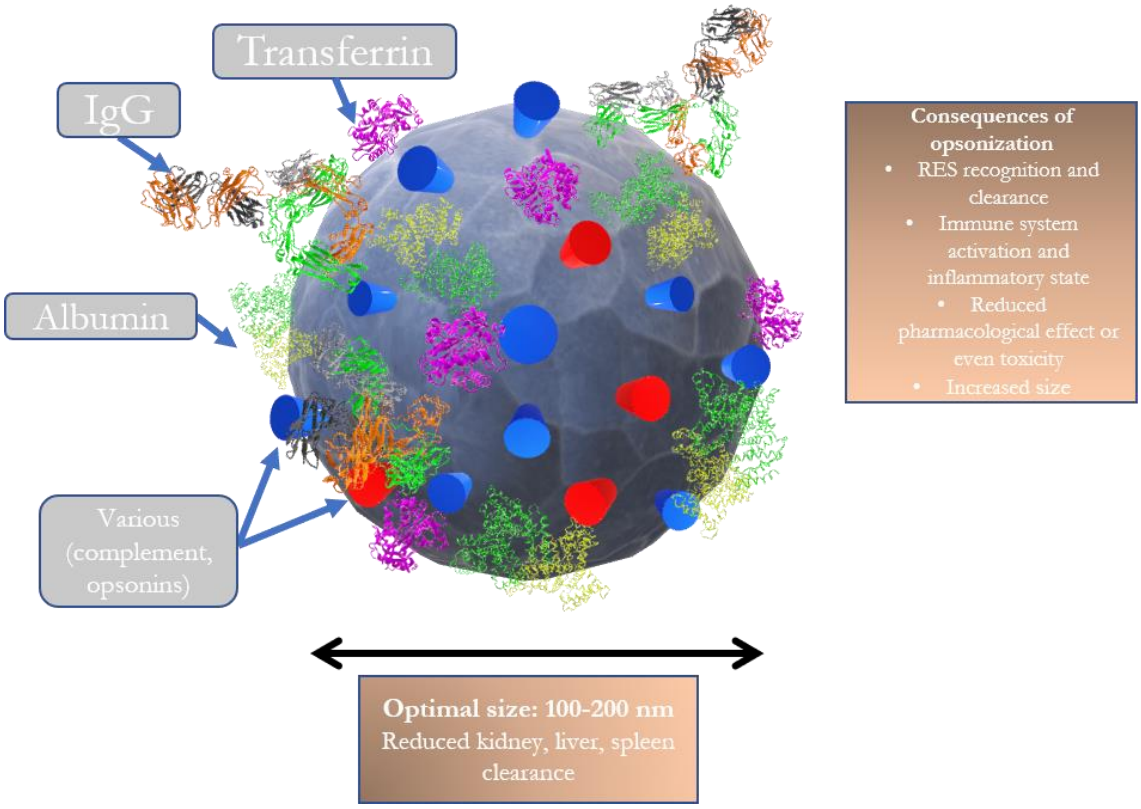



Figure 3: Schematic representation of opsonization ("bio-corona" formation) on a NP in hematic flux. The proteins and glycoproteins represented are the most common to opsonize foreign nanoparticles. Protein Data Bank entries: IgG (1igy); transferrin (1a8e); Albumin (1ao6). Immunoglobulins (IgG) in soluble form can adhere to the surface of nanoparticles in transient binding (together with HDL/LDL proteins, not shown), while albumin usually forms an “heavy corona” with complement proteins and opsonins [14].

As stated, body clearance is strictly related to size and geometry, so, while developing a nanodrug, its fate must be considered. For blood-administered nanoparticles, the quickest clearance systems are the spleen and reticuloendothelial system (RES), while the most efficient systems involve Kupffer cells in the liver [69], [70]. RES not only physically removes all *nonself* nanoparticles from blood and tissues via macrophage phagocytosis but also opsonizes them to be degraded and excreted. Under normal conditions with no surface functionalization, 60-80 nm-sized nanoparticles are cleared by the spleen in the red pulp, whereas the impact of a nanoparticle (entities such as liposomes or colloidal nanoparticles of 100–200 nm) on the spleen is essentially on the white pulp, which is colonized mainly by B lymphocytes and marginal-zone macrophages [69]. For larger hydrodynamic radii (up to 400 nm), filtration occurs mainly on the red pulp, accounting for nearly the total

administered dose in a few hours [67]. To avoid RES opsonization [71], albumin, or HDL/LDL deposition in the blood [14], [67], and IgM binding [72] and to minimize splenic, hepatic, and renal clearance [71], [73], the perfect size would therefore be 100–200 nm. Indeed, it is the most common size for approved nanodrugs, such as Doxil, Ambisome, or Eligard.

Circulation time is a key pharmacokinetic parameter for drugs **(Paragraph 1.2**). According to the classic definition of pharmacology, it is the time that a drug spends in the blood during the distribution phase (according to the LADME theory). Indeed, the distribution phase is, in terms of drug efficiency, opposed to the clearance (or elimination) phase: even though the drug will exert its effect in the target tissue, a portion of it will always be lost owing to accumulation in off-target sites, biotransformation by the liver, kidney filtration and so on. Within drug distribution, the drug is transported in plasma, i.e., the noncorpuscolar portion of the blood, and can bind plasma proteins (albumins, transferrins, circulating IgG, α-glycoproteins, coagulation factors, fibrinogen, and complement proteins) [13]. This phenomenon usually hampers the biodistribution of a small-molecule drug due to the steric hindrance of the complex (up to a few tens of nanometers) and modified lipophilicity. In the case of nanodrugs, a common way to describe this complex is with the term "biocorona" [74], [75], which is divided into soft and hard coronas, where the hard corona represents the first layer of proteins directly in contact with the surface of the nanoparticle. This occurrence must not be imagined as a rigid structure but rather as a dynamic, ever-changing equilibrium: Vroman, in 1962, postulated that the continuous association and disassociation of plasma proteins from the surface of a (nano)drug can be described with a classic kinetic law [76]. Opsonization by circulating IgG, present in the "soft corona", leads to enhanced clearance from the blood [77]. The main mechanisms responsible for the clearance of nanoparticles from an organism are either direct clearance organs (kidneys, spleen, containing red and white pulp macrophages, liver, with Kupffer cells) or, systemically, the mononuclear phagocyte system (MPS), i.e., the totality of circulating macrophages, astrocytes, dendritic cells, alveolar macrophages in the lungs, Langerhans cells in the skin, and other small populations in exocrine glands and organs such as the placenta [78]. Nanoparticle opsonization by serum proteins enhances recognition by phagocytic cells due to the increased bulk size of the nanoparticle [79], complement activation and complement-mediated clearance in the liver [70], and signaling from the Fc portion of the coronal IgG [16].

### 1.4.1 How to avoid nanoparticle immune system recognition: PEGylation

The most commonly used approach to avoid opsonization is the use of polyethylene glycol (PEG) [73], whose heavy, negatively charged, hydrophilic chain physically impairs opsonization and prolongs nanoparticle plasma circulation; the occurring hydrated cloud precludes the interaction of the nanoparticles with each other and with proteins; furthermore, recent findings suggest the capacity of "stealth" nanocarriers to bind only "neutral", not opsonizing, plasma protein markers (mainly apolipoproteins, where the coating with IgG, albumin, vitronectin and fibrinogen is of minor importance) effectively masking them from macrophages and dendritic cells [80]. Despite being almost not degraded in the human body [81], PEG is generally regarded as safe and widely used in cosmetic products. Many FDA-approved nanodrugs contain PEGylated lipids [82], to a certain degree, with individual branched monomers usually in the range of 2–10,000 Da

(light/medium chains of PEG), resulting in a final 5–15% molar ratio of PEGylated lipids to other lipids; a PEG side chain of 2 kDa is considered the gold standard [83]. Despite effectively prolonging the circulation time of the drug (Doxil circulation time is 5--6 hours, unlike the few minutes of unencapsulated doxorubicin)[84]), PEGylation has many drawbacks: it impairs endosomal escape (**paragraph 2.6**), cell uptake, and the activation of apoptosis cascades necessary for effective cancer-targeted therapy and is not suitable for prolonged therapies and frequent administration. Indeed, the so-called ABC effect (Accelerated Blood Clearance) was discovered in the early 2000s, i.e., the fast opsonization and clearance of PEGylated liposomes upon subsequent infusions, purportedly caused by preexisting or freshly developed adaptive immunity-related circulating IgMs, with splenic B lymphocytes having a determining role. Upon IgM binding, complement activation and opsonization occur, leading to fast recognition by liver Kupffer cells and clearance. Furthermore, the presence of anti-PEG antibodies can lead to anaphylactic reactions in patients [85], collectively known as CARPA (complement-mediated pseudoallergy), which can be avoided by increasing the time between PEGylated drug infusions [86]. Furthermore, the body of evidence suggesting preexisting, common immunity due to the ubiquitous presence of PEG in daily cosmetic products continues to grow [82]; PEG works as a T-cell-independent antigen and, most importantly, behaves as a hapten for the conjugated nanodrug, eliciting a strong immune response toward its cargo. A few alternatives to PEG have been proposed, such as heparin [87], polysorbate, and polyglutamic acid, which are heavy, hydrophilic, slightly negatively charged at neutral pH, and block copolymers [88]. However, in the case of therapies requiring multiple administrations, an alternative to PEG is needed.

## 1.5 Gene Therapy: General Overview

The US FDA (United States Food and Drug Administration) official definition of gene therapy is as follows: "Gene therapy is a technique that modifies a person's genes to treat or cure a disease. It can work by several mechanisms: replacing a disease-causing gene with a healthy copy; inactivating a disease-causing gene that is not functioning properly; and introducing a new or modified gene into the body to help treat a disease". Despite plasmid technology, in bacteria, has been known for nearly sixty years [89], other attempts to introduce foreign genetic material into living organisms occurred only in the 1980s, owing to the work of Martin Cline. Quite early, it appeared evident that a gene could not be introduced *per se* as a coding sequence for a specific protein but needed a "vector", i.e., either other genetic material to coadjuvate its insertion or any other technology capable of entering the nucleus and interacting with the recipient DNA. Bacteria and some yeasts have evolved plasmids as a physiological mechanism of horizontal gene transfer, but the success of infection by many retroviruses indeed relies on insertion within the host's genome: an increase in efforts toward basic research on recombinant DNA led to the establishment of many **genetic engineering** protocols over the course of the 1990s and early '00 [90]. Standard, proprietary transfection plasmids were developed by biotech companies for the purpose of research and treatment; transposons, such as *Sleeping Beauty* or *piggiBAC,* were engineered and adapted for gene transfer; adenoviruses were deprived of their perilous genes and forcefully evolved to retain infectivity but be harmless; adeno-associated viruses were optimized as episomal viruses; and lentiviruses were developed from HIV. Enzymes such as zinc fingers and TALEN nucleases have become well-known genome editing tools. Nanomedicine came into play in the last quarter of the XX century, therefore developing the thriving field of nonviral gene transfer. Electroporation, gene guns, magnetofection and derived methods have become well-established techniques worldwide [91]. The definition of gene therapy was broad in 1993, including any treatment that would "modify or manipulate the expression of genetic material or to alter the biological properties of living cells", thus including epigenetic mutations, newly discovered RNA interference, and yet-to-come mRNA vaccines. In 2018, it was narrowed again to "genetic elements that mediate their effects by transcription or translation of transferred genetic material or by specifically altering host genetic sequences". Finally, the discovery of CRISPR-Cas9 opened a new world for precision medicine, which includes the permanent excision of a desired gene; currently, prime editing (a mechanism involving a fusion protein between the nickase Cas9 and a reverse transcriptase) has become the gold standard for genome editing [92]. The main gene therapy approaches are shown in Table 2.

Currently, gene therapy can be roughly divided into the following:

- **Gene augmentation:** the addition of a gene for the purpose of expressing a new protein or for correcting a nonfunctional one (gene replacement).
- **Gene silencing**: the loss-of-function of a desired protein, which can be either persistent, such as in the case of CRISPR-Cas9, TALEN, and Zing finger knockdown, or transient, such as RNA interference knockdown. The latter acts on transcribed genes, blocking their translation and therefore not requiring entry into the nucleus.

Both approaches can be used either in vivo, on the whole organism, or *ex vivo*, i.e., in cells collected from the organism and externally transfected (as in CAR-T-cell therapy);

at the same time, either on somatic cells or on the germline, the latter can exhibit heritable traits.

RNA interference therapy has various advantages over conventional gene therapy. First, the transience of its effect, which is usually limited to a few months in vivo, allows rapid changes in therapeutic approaches. The advantages and disadvantages of this therapeutic approach are discussed in the next section.

Table 2: Mechanism of action, molecular agent, application, approved drugs and nanocarrier for the main gene therapy approaches currently used.

| **Mechanism of action** | **Agent** | **Main medical applications** | **FDA or EMA approved drugs/Trials** | **Preferred nanocarrier** |
|---|---|---|---|---|
| **Gene knockout or gene repair via homologous directed repair** | CRISPR-Cas9 and variants [93], either in plasmid or mRNA forms | Treatment of gene-linked diseases and tumors, transformation ex vivo of lymphocytes for CAR-T generation), transformation ex vivo of hematopoietic cells for bone marrow diseases | Casgevy (sickle cell disorder) | Viruses, Lipid nanoparticles, Liposomes, Nanopolymers |
| **Prime editing (direct genomic DNA re-write from a scaffold)** | CRISPR-Cas9 and prime editing guide RNA | Treatment of gene-linked diseases and tumors, transformation ex vivo of lymphocytes for CAR-T generation), transformation ex vivo of hematopoietic cells for bone marrow diseases | PM3259 (Trial I) for chronic granulomatous disease | Viruses, lipid nanoparticles |
| **RNA interference** | siRNA, miRNA, short-hairpin RNA [94] | Treatment of hereditary genetic illnesses, cancer therapy | Onpattro (hATTR amyloidosis) | Lipid nanoparticles, polymers, dendrimers, liposomes, extracellular vesicles |

| | | | | |
|---|---|---|---|---|
| **Block of translation due to heteroduplex formation and subsequent RNAse H cleavage; steric hindrance on ribosome binding; uncomplete maturation of mRNA** | Antisense-oligonucleotides (DNA), modified [95] | Treatment of hereditary genetic illnesses, cancer therapy | Fomivirsen (hampers cytomegalovirus replication in retinopathy-affected patiens) | Naked, or with the same carriers as siRNA/miRNAs |
| **Transient expression of a protein** | mRNA | mRNA based vaccines and protein replacement therapy | Spikevax (Sars-Cov-2 vaccine) | Lipid nanoparticles, cationic polymers, dendrimers |
| **mRNA transcription and long-term translation of protein product** | Plasmid DNA | Infective illnesses, protein-replacement therapy, cancer therapy | JVS 100 (Clinical Trial II for chronic limb-threatening ischemia; heart failure; peripheral arterial disorders) | Naked, lipid nanoparticles, cationic polymers |

### 1.5.1 RNA interference overview and mechanism

RNA interference is a phenomenon common to all eukaryotic species; its evolutionary relationship with the CRISPR-Cas9 system in Prokaryota is yet unclear [96]. To elucidate the underlying molecular mechanisms, Andrew Fire and Craig C. Mello obtained the Nobel Prize for Physiology or Medicine in 2006. First characterized in *Caenorhabditis elegans*, it was later discovered that RNA interference is ubiquitous in Eukaryota and that some protein components can be tracked back to Archea. In 2024, Victor Ambros and Gary Ruvkun received the Nobel Prize for Physiology or Medicine for this discovery in the late 1990s and early 20 s [97]. The RNA interference mechanism of action involves repressing the expression of a specific gene in a physiological way (from gene-encoded micro interfering RNAs), either by repressing protein translation (i.e., the synthesis of proteins from messenger RNA scaffolds occurring in ribosomes) via degradation of the mRNA or by proteolysis of the final protein The main classes of natural and synthetic RNA are listed in **Table 3**.

Table 3: Overview of the main bioactive RNA classes.

| Type | Size | Origin | Function |
|---|---|---|---|
| Messenger RNA (mRNA) | ~500 to >10,000 nt (usually single stranded) | Endogenous, gene encoded, translated | Encoding of a protein, to be translated by ribosomes |
| Short hairpin RNA (shRNA) | ~ 50-70 bp (usually double stranded) | Exogenous or endogenous if recombinantly introduced the relative DNA in the host genome | Forms a stem-loop, processed by Dicer into siRNA; silences specific gene |
| Micro RNA (miRNA) | ~ 21-23 bp (usually double stranded) | Endogenous, gene encoded, untranslated | Gene silencing by mRNA degradation or translational repression; transposon silencing, antiviral resistance. |
| Small interfering RNA (siRNA) | ~ 21-23 bp (usually double stranded) | Exogenous | Gene silencing via mRNA cleavage (perfect match), translational repression |
| Piwi-RNA (PIWI-interactin RNA) | ~24-31 bp (usually single stranded) | Germline cells | Genome stability, suppression of transposons |

A central enzymatic and binding multiprotein system, the RNA-induced silencing complex (RISC), is the core of this process since it binds the lead strand of the siRNA and uses it as a template to cleave other foreign or unwanted dsRNAs. RNAi plays an important role in viral resistance and gene expression modulation; micro RNAs are short, double-stranded RNAs that originate from longer transcripts called pri-miRNAs. After its elucidation in 1998 [54] and characterization of the specific features needed by an RNA to be bound by Dicer first and Argonaute then, RNAi technology gained the attention of the pharmaceutical world as a good alternative to DNA antisense oligonucleotides and DNA plasmids. This is mostly due to the greater robustness of siRNA target delivery: siRNAs do not require extensive modifications and generally show greater knockdown potency [98].

When a physiological mechanism, RNA interference in mammals has less antiviral importance than in plants, and it is mostly devoted to silence regulatory short RNAs, which are genome encoded, and generally called microRNAs. Of lesser importance are P-element-induced wimpy testes (PIWI)-interacting RNAs, which are conventionally bound to repress transposable elements [99]. The pri-microRNA, which is directly transcribed from the genome in the nucleus by RNA polymerase III, results in a double-stranded stem loop that is subsequently processed by an RNAse, Drosha, and is subsequently available

to be exported in the cytoplasm and further processed by another nuclease, Dicer. Indeed, Dicer is a cytosolic protein. The resulting miRNA, and its synthetic counterpart siRNA, possess overhangs at the 3' and 5' termini, the latter being a monophosphate nucleotide. The selection between the passenger strand and the guide strand is based on thermodynamic stability: the strand whose 5' is a less stable base pair—adenine or uracyl bases—will probably be selected as a guide strand [99] by the RISC complex. In Figure 4, the RNA interference mechanism and the main differences between miRNA and siRNA sequences are summarized.

Therefore, the protein actors involved in RNA interference are as follows:

- **Dicer**, a nuclease responsible for cleaving a pre-miRNA and obtaining a mature, fully functional microRNA. It has a nuclease, a helicase and a PAZ (Piwi/Argonaute/Zwille) domain of yet unknown function [100]. It cleaves the pre-miRNA into 21--23 dsRNA fragments.
- **(TAR) RNA-binding protein (TRBP)**, a dsRNA-binding protein usually associated with Dicer in the case of miRNA, is responsible for recruiting Ago2.
- **Argonaute 2 (Ago2)** is the main character**:** a protein responsible for binding either an already processed miRNA or a small-interfering RNA, a synthetic analog already sporting the posttranscriptional modifications that lead to a miRNA. The Ago2 subunit first disassembles the dsRNA, degrading the passenger strand, 5'-3', and incorporating the guide strand. This stage is called pre-RISC. This complexation leads to the recruitment of other proteins to give rise to RISCs.
- The **RNA-induced silencing complex (RISC)** is a massive ribonucleoprotein complex composed of the guide strand, Ago2, SND1, AEG1, FMR1, VIG, R2D2, another argonaute-like protein and, finally, an RNA helicase domain. Its assembly has been extensively studied and dramatically differs from that of humans to that of plants and insects [101]. In the RISC, the role of the guide strand is to scan the cytoplasm for complementary mRNAs with mi/siRNAs. Usually, gene-encoded miRNAs are directed toward the 3'UTR of mRNAs and require further machinery for mRNA degradation, while siRNAs are perfectly complementary to an exon region in the target, and the Ago2 PIWI domain itself catalytically cleaves it.
- **Chaperons**, such as Hsp40, 90 and 70, protect the RISC from proteasome degradation. Furthermore, their ATP-lytic domain seems to be instrumental for effective dsRNA loading into Argonaute 2 but not for cleavage activity [101].
- **GW182**, a regulatory protein that interacts with Ago2, which is rich in glycine–tryptophan repeats, is present in suborganelles in the cytoplasm and is named glycine–tryptophan bodies. It is involved in repressing post-RISC translation of target mRNAs. The removal of GW bodies in humans impairs RNA interference, while transfection with exogenous siRNA significantly increases their number and size [102].
- **Regulatory kinases** cycle-phosphorylating Ago2 [103] and increase its RNA-binding activity.

Small RNAs in the RISC are divided into 4 domains, which are 21-23 bp in length: the guide strand, which is a seed of 6 nucleotides (2-8); the central region, which is 3-4 nucleotides and is conventionally the area of cleavage in the complementary mRNA; the supplementary region, which ensures stability in complementarity with the target; and the tail region, which initiates complexing with the RISC and whose optimization improves the turnover of cleavage and final knockdown. RNA interference does not exert its activity by simply cleaving the target mRNA. In physiological regulatory miRNAs, as mentioned, even imperfect pairing in the seed region can lead to the recruitment of other regulatory

proteins to target the mRNA, causing deadenylation of the polyA tail and degradation of the corresponding mRNA, RISC directly decapping the mRNA, or blocking the translation of the final protein via GW182 activity. Indeed, translation inhibition appears to be the greatest outcome of physiological RNA interference, where miRNAs are usually more prone to mismatch with the target than are siRNAs: in insects, the GW182 protein binds PABS, which, in turn, does not complex eukaryotic initiation factor 4 complex (elF4G) assembly to begin translation; in mammals, a similar mechanism is followed, probably involving a paralog of the insect elF4G [104]. In the case of siRNAs, which therefore possess a perfect match with their target mRNAs, the main knockdown source appears to be the PIWI-mediated cleavage of mRNAs within the RISC rather than protein translation blockage [105]. Finally, the fate of the leftover parts of the sliced mRNA is still somewhat unknown: in *Arabidopsis thaliana*, secondary protein machinery degrades them and prevents such fragments from being intercepted by Ago1 and working as "secondary" siRNA[106]; in mammals, these fragments might still be translated into truncated, nonfunctional proteins, which are highly likely to be concurring, in the end, with cytotoxicity [107]. The problem of the intrinsic toxicity of interference drugs is elucidated in **Paragraph 1.5.5** "Drawbacks of RNA interference as a therapeutic approach".

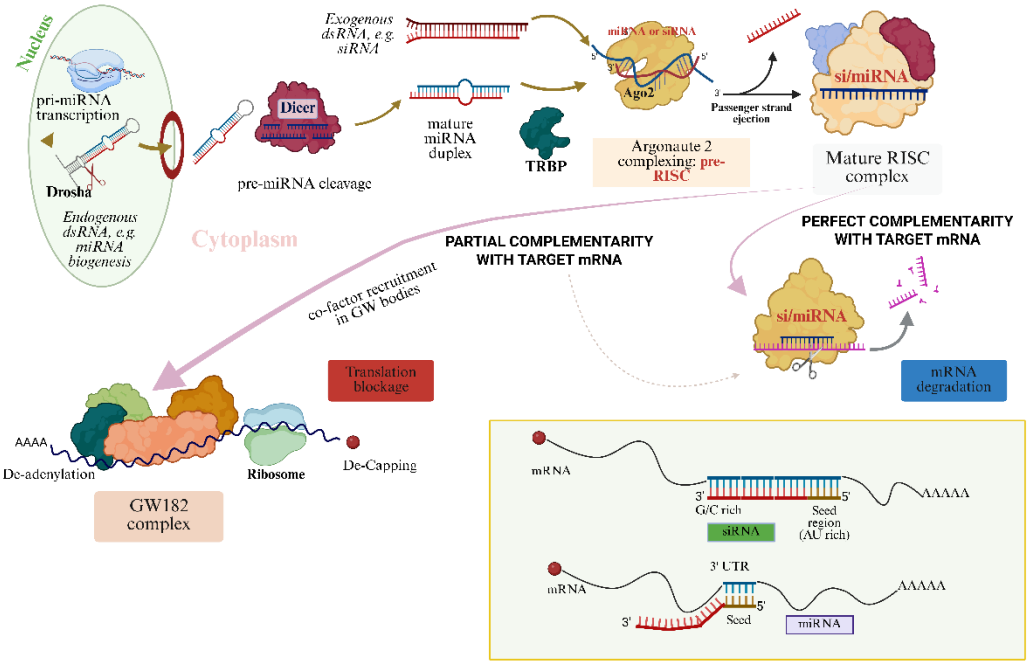



Figure 4 Summary of the main actors of the RNA interference mechanism. A pri-miRNA is a gene encoded and transcribed in the nucleus, processed by Drosha and then exported as a pre-miRNA in the cytoplasm; it is further processed by Dicer into 21–22 bp doublestranded oligonucleotides. At this point, the fate of a physiological miRNA is shared with that of an exogenous siRNA: while miRNA requires a further co-factor to be loaded with Ago2 (TRBP), a siRNA is directly loaded in the active site. This complex is pre-RISC. The passenger strand is subsequently ejected from the complex, and more cofactors bind RISC, leading to a mature RISC complex. Then, according to the complementarity ratio with the target mRNA, two different pathways can be followed: for perfectly complementary siRNAs, the main outcome would be direct cleavage of the target mRNA, whereas for miRNAs, there would be further recruitment of cofactors, shuttling to GW bodies, and complexing with the GW182 complex for translation blockage.

### 1.5.2 What are the biological barriers for a siRNA to exert its action?

siRNAs are double-stranded RNA molecules. For immunity studies, polyinosine polycytidylic acid (poly I:C) is used to mimic dsRNA. Conventionally, dsRNA molecules are inherently troublesome for eukaryotes because of their connection with negative-strand RNA viruses, such as NDV, Sendai, seasonal influenza virus or hepatitis C virus. In innate immune cells (macrophage and dendritic cells), these byproducts of viral replication behave as PAMPs (pathogen-associated molecular patterns); they activate an antiviral cascade via toll-like receptor 3 recognition, including dsRNA-activated protein kinase R (PKR), which inhibits mRNA translation by phosphorylating elF2a, even though the occurrence of such

effects in mammals in vivo is the subject of debate [108]. Moreover, in mammals, Type-I interferons, which are activated by the presence of dsRNA, further activate a cascade of approximately 2000 genes, including those involved in signal transducer and activator of transcription (STAT) metabolism. Finally, mitochondrial apoptosis is initiated via dsRNA-dependent caspase-binding domains in important RNA helicases and transducers such as MDA5 and RIG-I [109]. Caspase-1 inflammasomes are formed during this stage, with final activation by a protein belonging to the NOD-like receptor superfamily, Nlrp3 [110]. "Infected" cells undergo programmed cell death and release inflammatory cytokines, such as IL-1β, that are directly activated by Caspase 1.

The discovery of miRNAs has complicated our understanding of anti-dsRNA immunity. Precursors of miRNAs, long noncoding RNAs, indeed have double-stranded portions, and even pre-miRNAs possess a stem loop. The selectivity toward RNAi-activating dsRNA resides in their sequence: the helicase domains of RIG-I are not activated by siRNAs or miRNAs, not just owing to their length but also due to the presence of 3' overhangs and a 5' monophosphate group and, in pre-miRNAs, the stem–loop structure [108].

The challenges to overcome for an external siRNA/miRNA to exert its effects are summarized in **Figure 5**. Apart from immunogenicity, a major hurdle that a miRNA or a siRNA must overcome to exert its activity is its insolubility in cell membranes owing to its hydrophilicity and bulk size. In general, humans do not possess SID-1, an Arthropoda-specific dsRNA transporter [111], which is often used for pest control trials [112]; double-stranded RNA is rapidly cleared when intravenously injected, ends up in the kidneys or is degraded by hepatocytes in the liver [113]. Additionally, in human blood, there are circulating RNases such as RNase 4 [114], which rapidly cleave any "naked" molecules together with phosphatases.

Even if internalized by cells, a macromolecule such as a siRNA is likely trapped in an endosome, a membrane invagination involved in the internalization of solutes, molecules and nanoparticles. There are many different proposed mechanisms for endocytosis, such as caveolar- and clathrin-mediated endocytosis, potocytosis, pinocytosis, and patocytosis [115]. A small interfering RNA, when not rapidly cleared (10 minutes) by kidney filtration, extravasates due to its small size (approximately 4 Angstroms), and from the interstitial space, it reaches organ tissues; if internalized by cells, it is trapped in endosomes and then matures into lysosomes; therefore, the molecule needs to find a way out of the lysosome/endosome via endosomal escape. The chances of this happening spontaneously are reported to be 0.2% [116]. The acidic enzymes within lysosomes are involved in degrading the dsRNA. This barrier can be overcome by 1) using a cationic, buffering polymeric nanoparticle capable of complexing the nucleic acid; 2) avoiding this limiting step by aiming to direct cell membrane fusion, taking advantage of the extracellular vesicle machinery; and 3) incorporating the siRNA in nanocarriers that are endocytosed but capable of endosomal escape via membrane fusion and, finally, liberating the content in the cytoplasm [117]. In **Paragraph 2.3,** we explore the last two approaches, while the first approach is explained in 2.6 and 2.7.

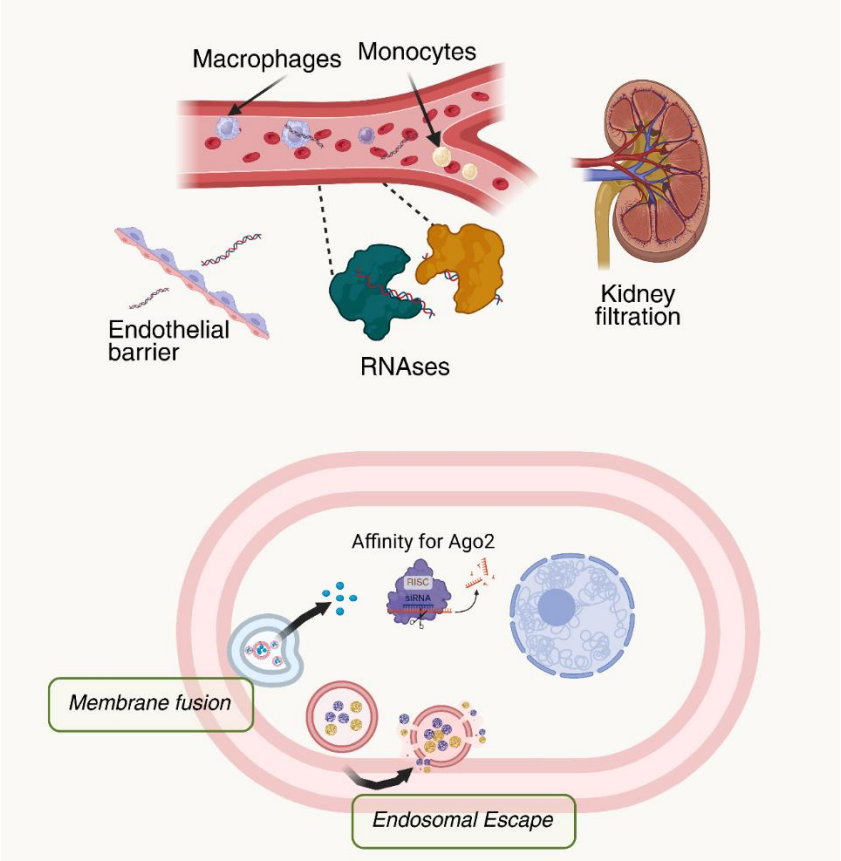



Figure 5: The main barriers that a naked siRNA must overcome to exert its function. Within the blood, circulating RNAses quickly degrade them, and the kidney filters them out; hardly ever would it be possible to surpass the blood vessel endothelium. On the other hand, when a carrier is used, cytoplasmic delivery can be achieved both by direct membrane fusion with the endosome and endosomal escape via rupture. Finally, even in the cytoplasm, the sequence could have a low affinity for Ago2; therefore, the molecules would be incorporated at a low rate in the RISC complex..

### 1.5.3 Overview of approved interference drugs

The pioneering intuition of Friedman and Roblin, in 1972 [118], paved the way for the development of a revolution in medicine—gene therapy. For the first time, a nucleic acid was meant to be a drug; thus far, we can define all the approved plasmid DNAs, antisense oligonucleotides, siRNA-lipid complexes, viruses, and genetically engineered cellular therapy products under the umbrella term “gene therapy”.

In November 2012, the European Commission granted marketing authorization for the first gene therapy medicine, Glybera, in all 27 European Union member states; it was developed by UniQure (formerly Amsterdam Molecular Therapeutics) for the treatment of patients with familial lipoprotein lipase deficiency; unfortunately, its authorization was not renewed in 2016 owing to excessive cost. Glybera is an adeno-associated virus whose genome encodes a lipoprotein-lipase substitute. Fomivirsen, on the other hand, was the first oligonucleotide phosphorothiolate to be approved; in 1998, it was withdrawn because of negligible market sales [119]. However, other than orphan diseases, the most promising field of application of gene therapy is oncology, a field suffering from multiple issues: lack

of specificity in medications, severe countereffects, frequent emergence of drug resistance in aggressive tumor cases [120], and, finally, only temporary resolutive treatment. The potency of gene therapy resides in the fact that, virtually, it is possible to modulate, suppress, enhance, or activate the expression of whatever gene—even if not present at all in the recipient, introducing it—with no or mild side effects—the so-called precision medicine. Two main events pushed even forward the research with this approach: the discovery of RNA interference and of the CRISPR–Cas9 system (and analogous) [121] in bacteria, the latter becoming a powerful biomedical research tool. Most approved gene therapy drugs are enclosed within a viral vector, such as an adenovirus, an adeno-associated virus, or a lentivirus capsule [119], [122], but such an approach is cause of some concern [123]. Furthermore, most Cas9 gene therapy treatments involve at least one *ex vivo* step, with the harvesting of hematopoietic stem cells, their editing, and reinjection in an immunosuppressed patient. Finally, DNA plasmids, as gene therapy agents, usually do not require an additional DDS and, therefore, are administered "naked" [124].

The first RNAi-based drug was Onpattro, approved by the EMA (European Medicine Agency) and FDA (Food and Drug Administration) in 2018, for polyneuropathy caused by hereditary transthyretin amyloidosis (hATTR); its RNA oligonucleotide is enclosed in liposomes made up of DLin-MC3-DMA ((6Z,9Z,28Z,31Z)-Heptatriaconta-6,9,28,31-tetraen-19-yl 4-(dimethylamino)butanoate), $PEG_{2000}$-C-DMG ( 1,2-dimyristoyl-rac-glycero-3-methoxypolyethylene glycol-2000), DSPC (distearoylphosphatidylcholine), and cholesterol [125].

Notably, the development of nonviral vectors—while viral vectors often lead to an inflammatory state, unwanted sites of insertion, and allergic responses—has markedly increased the number of gene therapy drug approvals and publications [126]. As of 2022, five siRNA drugs have been approved by the US FDA and, later, by the European Medicine Agency (EMA): the already mentioned Patisiran (Onpattro), Givosiran (Givlaari), Lumasiran (Oxlumo), Inclisiran (Leqvio), and Vutrisiran (Amvutta), all of which are directed to the liver. Apart from Onpattro, which exploits a lipid nanoparticle, all the others are N-acetylgalactosamine conjugated; indeed, this moiety has a high affinity for the asialoglycoprotein receptor, whose expression is concentrated almost exclusively in parenchymal hepatocytes. Therefore, nanocarriers capable of targeting other organs rather than the liver are urgently needed for systemic delivery. Another route of administration involves the eyes and the eye cavity: as an immune-privileged sector, any adverse reaction is concentrated at such a site and allows local treatment. Indeed, as of 2024, many formulations in clinical trials are against glaucoma, macular eye degeneration and Leber congenital amaurosis [127]; cosdosiran and tivanisiran are examples that are currently in the third phase of clinical trials under the FDA.

### 1.5.4 Nanostructured approaches in theranostics and "precision medicine"

As the concept of theranostics has already been defined, a great advantage is the ability to deliver, simultaneously, an interference drug and a reporting/imaging agent. Multiple examples of coadministration of gene therapy agents, for example, siRNAs and imaging or contrast agents, include mixed siRNA/chitosan/poly-L-arginine and PEGylated SPION [128]; nonionic surfactant nanoparticles loaded with indocyanine green for infrared imaging

and si/miRNA [129]; rod-like radiolabeled nano-objects with a hydrophilic shell electrostatically binding siRNAs [44]; PDMA-b-PCL (poly(dimethylacrylamide)/polycaprolactone) micelles loaded with an irinotecan-like molecule, a PEGylated siRNA and ultrasmall-SPIONs [38]; and quantum dots encapsulated in aptamer-liposomes together with a siRNA for fluorescence in vivo imaging [130]. Finally, erythrocyte membranes have shown excellent properties as carriers for indocyanine green imaging and MRI contrast agents [131], [132]; additionally, as gold-nanoparticle carriers, they have been employed for dynamic X-ray imaging of blood flow [133].

As stated before, the main advantages of such an approach are the simultaneous: 1) evaluation of delivery in the tissue of interest; 2) eventual bioaccumulation; 3) precise enhanced imaging (regardless of the technique of interest) of the target tissue; and 4) synergistic effects. The latter consists of an imaging agent that can also act as a photothermal agent: this is the case for gold nanoparticles, which, owing to their unique local surface plasmon resonance effect, can generate heat upon laser irradiation, cause payload release and act as a photoacoustic agent [134]; cyanine dyes have the same effect. All these features are of utmost importance in the case of cancer therapy via chemotherapy: the targeting agent must be robust enough to ensure good internalization of the drug and good, and less toxic, uptake of the imaging agent [46].

### 1.5.5 Drawbacks of RNA interference as a therapeutic approach

RNA interference is a powerful tool. One siRNA, once loaded into the RISC, can cleave several mRNAs before its turnover; it is highly specific but temporary, providing the chance to adjust the therapy in a timely manner. As of 2024, many nanoparticle-siRNA formulations (such as CALAA-01 and ARC-520) fail in clinical translation due to off-site accumulation and knockdown of off-target mRNAs, insufficient gene knockdown in target tissues, and hepatic or kidney toxicity. At the microscopic and cellular levels, several mechanisms have been reported to lead to siRNA-induced cytotoxicity; among those mechanisms, RISC saturation seems to be particularly common. Indeed, synthetic siRNAs are bound to compete with physiological miRNAs, therefore hindering certain cell pathways that are RNA interference dependent [135]. The toxic effect of externally induced RNA interference was reported very early in the history of this phenomenon, in 2006, when Mello and Fire received the Nobel prize for its discovery: upon adeno-associated virus delivery (and stable integration and expression in hepatocytes) of short hairpin RNAs, many hAAT (hereditary transthyretin-mediated amyloidosis)-phenotype rats showed signs of hepatotoxicity, even with a scramble, not targeted short hairpin RNA. Interestingly, the study did not show that the activation of double-stranded RNA elicited antiviral pathways. During this seminal study, the most suitable way to repress a gene without causing cytotoxicity was to use (either via stable expression or temporary delivery) a short, targeted 19–21 RNA dimer at the lowest dose possible capable of eliciting any RNAi effect. Furthermore, the root cause of such fatal effects has been confirmed to be, indeed, the inability of the cell to carry out the physiological functions of RNAi, such as the cell cycle (e.g., miR-122)[136]. The toxicity of an excess dose of an interfering drug in the liver is ultimately related to nuclear karyopherin exportin-5, a double-stranded RNA-binding protein transporter involved in RISC activation and Dicer turnover [137].

Apart from RISC oversaturation, another intrinsic drawback of the use of RNAi drugs is the possibility of off-target effects in terms of sequence, resulting in the targeting of undesirable mRNAs. With respect to this, computational biology has aided in the development of more efficient algorithms for siRNA/shRNA sequence prediction[135], [138]. In addition to sequence optimization, chemical modifications, such as phosphorothioate linkages, methylation of the 2-OH group of ribose [139], and the presence of DNA overhangs [140], appear to improve the specificity of the target. The enormous corpus of research within this approach led, finally, to the approval of Onpattro, against hereditary transthyretin-mediated amyloidosis, which has 2'-O-methyl (2'-OMe) and 2'-fluoro (2'-F) modifications to increase stability and reduce immunogenicity; more recently, Vutrisiran (Ammvuttra), approved in 2022, was conjugated with N-acetylgalactosamine (GalNAc), and its sequence includes six PS linkages, 35 2'-OMe, and nine 2'-F modifications, offering extended metabolic stability and infrequent dosing schedules. For a comprehensive review of the existing (and most successful) nucleic acid modification techniques, the reader is encouraged to read them [141]. Another reason to optimize the sequence of an RNAi drug is the potential translation of truncated/not completely cleaved mRNAs, leading to aberrant, nonfunctional, incorrectly folded or toxic enzymes and proteins: a gain-of-function temporary mutation that can cause an undesirable phenotype in cases where the P-bodies GW182 suborganelles are not efficient enough to block the translation of the defective mRNA [142].

Finally, another source of potential toxicity in the case of RNAi drugs is off-site delivery in terms of the target tissue/organ. Since most of the currently approved RNAi formulations are lipid nanoparticle-based (**Table 4**), whose natural tropism would be in the liver, research has focused on the use of this tropism to cure liver-affecting diseases, such as hepatitis B (Heplisav), TTR (TEGSEDI, an ASO; ONPATTRO, a siRNA), and hypercholesterolemia familial (LEQVIO, a GalNac siRNA), and, alternatively, the use of immune-privileged sites of the eye, therefore leading to the development of Vitravene (ASO), against CMV retinitis. Interestingly, naked nucleic acid drugs can be directly injected into the ocular site, eliminating the need for a capsule, such as QPI-1007, an orphan drug used to treat glaucoma that is currently in Clinical Trial III. Actively targeted nanomedicines can aid in changing the tropism and pharmacodynamics/pharmacokinetics of nucleic acid-based drugs, such as the use of aptamers, peptides, and antibody-conjugated nanoparticles, with additional properties (e.g., endosomal escape routes, the “proton-sponge effect”, and direct membrane fusion). Furthermore, in addition to increasing uptake in target tissues, nanomedicine can also minimize circulation in nontarget tissues by adjusting the nanoparticle size, surface charge and shape (i.e., minimizing kidney and liver clearance, avoiding the blood–brain barrier)[143].

Table 4: Overview o of advantages and disadvantages of RNAi agents' delivery systems.

| **Carrier** | **Example** | **Advantages** | **Drawbacks** |
|---|---|---|---|
| Lipid nanoparticles (cationic lipids and nucleic acid core covered by phospholipids) | Ionizable lipids (SpikeVax, Patisaran) | -Efficient encapsulation<br>-Efficient endosomal escape<br>-clinically validated | -May trigger immune responses<br>-Need optimization for tissue targeting<br>-Fast clearance |
| Polymeric nanoparticles | Polyethylenimine (PEI), PLGA | - Versatile and modifiable<br>- Biodegradable (e.g., PLGA)<br>- Protects siRNA from degradation | -Cationic charge-induced toxicity<br>-Variable release kinetic |
| Liposomes[144] | DPPC-DSPE-PEG2000 liposomes | -Easy to prepare<br>-Tunable surface chemistry<br>-Biocompatibility | -Unstable encapsulation<br>-Fast clearance |
| Viruses[145] | Adeno-associated virus (AAVs) | -Good transfection efficiency<br>-natural tropism | Hepatotoxicity<br>-May trigger immuno response |
| Cell penetrating peptides | TAT peptide, penetratin | -Direct cell entry<br>-Chemical conjugation with siRNA | -Fast degradation<br>-Lack of tropism |
| EV-like particles | Engineered exosomes vesicles | -Biocompatible<br>-Natural tropism according to membrane receptors<br>-Absent immunogenicity | -Challenging isolation and low yields<br>-Labour intensive loading<br>-Presence of endogenous miRNA |
| Antibody-conjugated | Interchain/lysine/Asparagine conjugates with siRNA on 3' terminus | -Biocompatible<br>-Excellent targeting activity | -Expensive<br>-Fast clearance |

## 1.6 Bio-Inspired Therapeutic Nucleic Acids Carriers

Despite the many therapeutic successes and approvals of synthetic nanoparticles, such as liposomes and lipid nanoparticles, some concerns regarding their safety and the development of adverse immune reactions remain. An improved biocompatibility would enhance cell uptake, prolong circulation time, and avoid bioaccumulation in the liver; biotechnology techniques came into play with the discovery of extracellular vesicles and virus-like particles (VLPs), conjugation with massive proteins (antibodies, albumin–paclitaxel), and the use of the whole cell membrane as a starting material for a drug delivery system. The premise of these biocompatible nanocarriers is to minimize adverse reactions and/or to target a specific tissue by exploiting natural tropism, i.e., mimicking the natural function of the original material. Hereby, the most important examples are briefly treated

### 1.6.1 Nature-engineered nanocarriers: exosomes and viral particles

Since the discovery of liposomal-like, cell-derived objects, in the Seventies, the number of studies on extracellular vesicles (EVs) has increased. Despite representing a wide range of cell-secreted particles with diverse biogenesis, the collectively accepted term refers to 50–200 nm liposomal-like particles with tissue-specific receptors, coreceptors and fusogenic proteins on their membrane (tetraspanins, ALIX, flotillins, TSG101, etc.); such proteins are currently being investigated as markers. They are naturally equipped with delivery machinery [115], [146] and often follow a direct-internalization pathway or exhibit a fusion-mediated endosomal escape mechanism. Notably, "extracellular vesicle" is an umbrella term for membrane-bound particles released by cells, which carry proteins, lipids, signal nucleic acids, and are involved in cell-to-cell communication. Exosomes are the most characterized ones, ranging from 30--150 nm in size, and are formed inside endosomal compartments in the multivesicular bodies within the cell membrane and released via exocytosis. Other EV objects are microsomes and apoptotic bodies [147].

Despite the evident advantages (natural tropism, total biocompatibility), several drawbacks of exosomes/EVs can be noted: their purification from cell culture medium is tedious and laborious, with a yield restricted to a few micrograms per milliliter of medium [148]. Interestingly, red blood cells appear to be among the cells which releases the most EVs in the human body [149]. Despite countless attempts [147], [150], [151], no RNAi/gene therapy drug encapsulated within an exosome/EV has ever been approved.

Other nano-objects engineered by nature and evolution include virus capsids, which, when depleted of their internal content and virulence capacity, are called virus-like particles (VLPs). The clear advantages of using VLPs are their extreme resistance to unsuitable environments (GI tract, mature lysosomes); their ability to penetrate stiff matrices such as the extracellular matrix, blood–brain barrier, and blood endothelium; and facilitated uptake from host cells [152]. For decades, viruses have been used in vaccines [153], which is different from viral infection because of the absence of a genome; therefore, they are capable of infection: only the capsid and its natural tropism are responsible for delivery. Indeed, capsid proteins are usually self-assembled [154] into nanosized (20–250 nm) virions that are icosahedral, spherical, helicoidal, or rod shaped and have slightly variable numbers of building blocks; the act of assembling itself is responsible for entrapping the cargo in a shell-pearl fashion. In the case of lentiviruses, the only required protein is indeed Gag. In other viruses, up to three different proteins are required for self-assembly; for example,

influenza virus requires both hemoagglutinin and neuraminidase [155]. The greater the number of proteins, the more complex the virus. Conventionally, VLPs are generated in vitro via cells encoding a plasmid containing the few genes encoding proteins required for assembly and are subsequently purified from the cell culture medium after being released. Depending on the nature of the original virus, the VLP can be enveloped by the plasma membrane; furthermore, if enveloped, the outer shell can be organized into one or two layers of the "stolen" plasma membrane. VLPs, therefore, still retain their function as PAMPs (pathogen-associated molecular patterns), i.e., they are easily recognized by the immune system. VLPs can be easily engineered. A common approach is to substitute an unnecessary infective protein within an operon with an agent with a desired function, i.e., an antibody for active targeting or any other surface antigen—a fusion protein. This surface display method is currently used in nanovaccines, such as hepatitis B and malaria [156]. More recently, the AstraZeneca SARS-CoV-2 vaccine employs an adenovirus capsid to deliver spike protein mRNA. Indeed, many attempts have been made to load VLPs with therapeutic nucleic acid/RNAi drugs: plant-infecting viruses, such as cowpea chlorotic mottle virus [157] and brome-mosaic virus [158], appear to generate the highest yield, most diverse, and least immunogenic VLPs for this purpose. Despite being widely used for vaccines, no approved RNAi/gene therapy formulation uses the VLP platform.

### 1.6.2 Whole-cell approach: the case of erythrocytes

Compared with other immune-masking technologies, the use of the whole membrane of cells has many advantages. In addition to masking from immune system recognition, cell-membrane-coated nanoparticles mimic the surface properties of the source cells: biocompatibility, inherent tropism toward certain tissues, and a relatively high rate of endocytosis. To date, various cell lines have been used as coating materials for solid (i.e., metal nanoparticles, mesoporous silica) and soft nanoparticles (e.g., polymers, dendrimers), including stem cells, neutrophils, cancer cells, platelets, and, finally, erythrocytes [159], [160]. Erythrocytes have a long history of attempts in terms of clinical translation and some success. In the 1970s, Ihler et al. succeeded in loading erythrocyte ghosts (i.e., those depleted of hemoglobin) with B-glucocerebrosidase [161]. Currently, a few erythrocyte-based therapies are undergoing advanced stages of clinical trials: RTX-224 (NCT05219578, Rubius Pharmaceuticals), which uses engineered allogenic erythrocytes with interleukin 12 and costimulatory molecule 4-1BB ligands on their surface for hyperactivation of natural killer cells in the case of solid tumors; an ex EU, now the United Kingdom, which is a trial for using erythrocytes as carriers for thymidine phosphorylase replacement therapy for the treatment of mitochondrial neurogastrointestinal encephalomyopathy [162]; the Italian company Erydel, which has developed an automated method to load autologous erythrocytes; the patented "red cell loader" for dexamethasone; and its EryDex kit, which is currently in phase III clinical trials against Ataxia telangiectasia [163]. Erytech, a French company, has developed eryaspase, which encapsulates L-asparaginase inside erythrocytes to treat cancers such as pancreatic cancer and leukemia. Kan101, which is based on modified, sporting gluten moieties on its surface, apoptotic erythrocytes, and liver targeted, in phase 2 as of 2024. Unfortunately, RTX-134, again from Rubius Therapeutics, which uses allogenic erythrocytes loaded with phenylalanine hydroxylase against phenylketonuria, was discontinued in 2021.

While the history of taking advantage of the erythrocyte membrane as a drug delivery system (DDS) is long and tortuous, other cell-membrane-based DDSs have been developed: for example, stem cells have natural tumor-tropism and can be used as "Trojan horses" [164] to deliver nanoparticles to the target tissue; moreover, the same approach has been

used for macrophages (immune system cells), which naturally tend to accumulate in tumor tissues, loaded with doxorubicin [165] and iron oxide therapeutic particles [166]; to target inflamed blood vessels, neutrophil-derived vesicles have been employed in vivo to take advantage of integrin $\beta_2$, which binds to endothelial cells via ICAM-1 molecules [167]. To date, none of these attempts have been translated into preclinical or clinical trials. Erythrocytes are not only hemoglobin containers; their interactome is vast and diverse. This process includes the transfer of opsonized particles to macrophages via the CR1 protein, cytokine storm clearance, ROS protection, and, of course, the initiation of blood clotting via phosphatidylserine (usually confined on the inner leaflet) exposure via a prothrombin pathway [168].

As this thesis focuses on the use of erythrocyte membranes as a starting material, the following advantages in the use of erythrocytes can be identified:

- Erythrocytes are easy-to-collect and abundant. In human blood, there are $5\times10^9$ cells/mL; indeed, patient blood could be used in therapeutic applications to avoid allergic reactions to allogenic blood (due to Rh antigens and AB0 incompatibility).
- They express, on their membrane, some coreceptors, such as CD47 and TER 119 [169], that make them naturally "stealth" to the immune system;
- Their membrane is somewhat unique because of the elastic properties of the spectrin-actin-ankyrin cytoskeleton [170].
- They possess an aspecific RNAse inhibitor of 31 kDa that, in vitro, removes any RNAse activity in erythrocyte lysates [171].
- Owing to the accelerated blood clearance phenomenon, erythrocytes circulate for a few hours--three days [73], [172], [173], and the average life of erythrocytes before spleen clearance is approximately 3 months.
- They can be easily depleted of hemoglobin via various methods [174], thus recovering what is called a *red blood cell ghost*: this membrane, which still retains integral proteins (with stealth effects), can be used for more refined purposes than whole-cell loading [175]. We can consider, for example, its use as a coating agent for underlying nanoparticles [176], [177] and its extrusion and sonication (shear stress-related processes) to produce nanoerythrosomes.

There are several procedures that can be carried out to load erythrocytes with external agents, such as dialysis, hypotonic swelling (on which EryDel technology is based), and electroporation. For a thorough review on this topic, the reader can consult [168].

Unfortunately, there are several disadvantages to the use of erythrocytes as drug delivery systems or as sources of nanoparticles. Indeed, upon aging, they are subjected to spleen clearance, while the blood rate in the human spleen is 150–200 ml/min [178]. Furthermore, if ATP is depleted, since lipid composition imbalance between the two leaflets is an energy-consuming process, phosphatidylserine could flip-flop to the outer leaflet; the imbalance is maintained by the enzymes flippase and floppase. This leads to rapid clearance [179] and, further, degradation by calpain (an enzyme hydrolyzing protein membrane anchorages to actin) and gelsolin (which severes actin filaments). All these enzymes are activated by the presence of calcium ions. Indeed, flippase inactivation leads to membrane budding, leading to the formation of natural extracellular vesicles [180], [181]. Additionally, the use of allogeneic erythrocytes for therapeutic purposes is inherently difficult because of the presence of AB0 and Rhesus antigens; the first are various sets of sugars exposed on the outer leaflet of the erythrocyte membrane, whereas RhD is a massive transmembrane protein. While the absence of AB0 markers leads to functional erythrocytes, RhD has a pivotal role in maintaining their discoidal shape. The Kell antigen system is based on the Kell protein, which is encoded by a highly polymorphic locus: some alleles are linked to

degenerative, genetic diseases such as muscle dystrophy [182], [183]. Recently, Zhao et al. managed to remove the RhD antigen by engineering an RBC membrane via an immobilized horseradish peroxidase shielded by a tyramine-polysialic acid 3D hydrogel structure. Therefore, the safe administration of the subsequently modified erythrocytes in the bloodstream is recommended [184]. Furthermore, band-3 membrane integral proteins can behave as antigens in senescent erythrocytes; their aging process is related to the loss of a segment of the band-3 protein, which is lacking only in senescent cells. This has long been known as the "senescent antigen". To date, it is the only known autoimmunogenic feature of these cells in the absence of illnesses [185].

The cytoskeleton of erythrocytes is an intricate scaffold of spectrin, ankyrin and actin underneath the cell membrane and is anchored to integral proteins, such as glycophorin A, band 4.1 and band 3 proteins. It is composed of spectrin tetramers connected to an actin network; band 3 protein, an integral protein, then bridges spectrin and actin via ankyrin. The degradation of the band 3 protein is connected to spherocytosis and erythrocyte aging [186]. All the metabolic activities of erythrocytes are somewhat anchored to the cytoskeleton. Erythrocytes also possess an unusual number of large proteasomes [187], 19S and 26S, of which only 19S is active and complex, detoxifying byproducts of glycolysis. Therefore, the structural integrity and shape of erythrocytes are strictly connected to the cytoskeleton, and this structure must be preserved if they are used as drug delivery systems.

### 1.6.3 Cell membrane-drug interaction: pharmacological features

The eukaryotic cell membrane is a complex structure, as it is also that of erythrocytes. It acts as an ion and molecule filter from the outer environment, as it is channeled by proteins; it hosts enzymes; it shows unique lipid-driven biochemistry, with a combination of many different phospholipids and cholesterol; it drives cell differentiation and specialization via the exposure of markers on its surface during cell signaling processes; it takes part in cell migration—for example, in macrophages [188], [189]; and it can be decorated by a forest of polysaccharides of various natures. Therefore, when a cell is depleted of its cytoplasm and used as a drug carrier, regardless of whether processing is necessary, the interaction of the drug with it must be considered. The main issues to address are as follows:

1) Semipermeability and drug release kinetics must be fully characterized for each different drug to encapsulate due to the heterogeneity of the membrane. ;

2) Solubility in the lipid phase, i.e., if it tends to be embedded in the double layer or if it *partitions* within the latter;

3) eventual interaction with integral proteins (inner and outer) and the glycocalyx;

4) Zeta potential of the lipid surface;

5) Microfluidity of the double layer. A thorough characterization of the double layer/drug interaction is lacking in the current literature, whereas it has been well reviewed in model membranes [190], [191], [192].

Therefore, the "topological" arrangement of a drug, when loaded in a cell-based nanodrug, must be analyzed since there is no coherent theory for predicting behavior. This could be accomplished via techniques such as fluorescence spectroscopy or immunogold labeling for electron microscopy [193]. These features dramatically influence the *encapsulation efficiency* of a drug and, consequently, the scaling-up of the process.

### 1.6.4 Erythrocytes membrane vesicles or nanoerythrosomes, EMVs

The idea of taking advantage of erythrocyte membrane properties is not new. Small objects derived from erythrocyte membranes, termed nanoerythrosomes, were developed by Lejeune in the 1990s [194]. Shear stress methods, including sonication, followed by the extrusion of filters with a 200 nm pore size, are used to prepare nanoerythrosomes [176]. The Deàk group [195], [196] compared the structure of nanoerythrosomes with that of erythrocyte ghosts and reported that no considerable protein degradation occurred after extrusion/sonication. The bilayer thickness, including the glycocalyx, was estimated to be 11 nm after small-angle X-ray scattering (SAXS) analysis, which is significantly greater than the 50 nm thickness of native erythrocytes and the 20--25 nm thickness of compressed cells at $10^3$ Pascals [195], [197]. Recently, the nanoerythrosome membrane was reported to be approximately 65% stiffer than that of parental erythrocytes [198]; however, the reasons behind this phenomenon have yet to be investigated.

Some sample inhomogeneity is present in the samples analyzed in Lejeune papers [199], [200] with respect to their hydrodynamic radii. The thickness of the bilayer is 4 nm; the remainder is a cytoskeleton and glycocalyx forest that is slightly modified by shear stress. Most peripheral proteins are removed during hemoglobin removal and subsequently undergo osmotic shock, but proteins contributing to the stealth effect, such as CD47 and [201], are untouched. The Lejeune group did not describe in vivo toxicity [202]. In addition, hypotonic swelling, sonication and extrusion essentially do not change the content of the marker membrane proteins CD47 and TER119 [203]. To date, nanoerythrosomes have been used as antigen carriers in spleen-targeting immune vaccines [204], for the delivery of daunorubicin [205], for encapsulation with fasudil [206], for the delivery of indocyanine green [132], [207], for the systemic delivery of siRNAs [208] and as carriers for iron oxide nanoparticles as MRI contrast agents [209].

The generation of nanoerythrosomes/EMVs is depicted in **Figure 6**. A nanoerythrosome suspension may also be characterized in terms of its colloidal properties, which are akin to those of other drug delivery nanoparticles. Zeta potential is slightly negative (around – 20 mV) given the ability of sialyl groups to mimic native erythrocytes whole glycocalix [207]. Different biophysical techniques used to study nanoerythrosomes include DLS, SAXS, SANS (small-angle X-ray scattering), freeze-fracture or cryo/conventional TEM, and 2D/1D NMR, FT-IR and Raman spectroscopy. Notably, nanoerythrosomes mostly maintain the biconcave shape of parental erythrocytes, according to the Canham-Helfrich effect [210], since the cytoskeleton is not destroyed during shear stress processing. In Figure 6, the potential issues associated with the use of erythrocytes as a starting material are summarized: they are all closely intertwined with erythrocyte aging, which is accelerated by processing. Phosphatidylserine exposure to the outer leaflet might lead to immune system recognition, similar to Band 3 unfolding [211]; furthermore, the erythrocyte membrane will continue budding during storage, generating defective extracellular vesicles and causing early release of the payload.

Nanoerythrocytes have also been extensively used as coating materials for solid nanoparticles, as in the case of cationic bovine serum albumin [212], for polymeric nanoparticles [213], [214]. The superiority of EMVs over PEGylated nanoparticles for prolonging drug residence time is outlined in **Hypothesis 1**; the use of the already present,

naturally occurring in erythrocyte membranes, exosome/EV protein machinery for achieving a high delivery rate and biocompatibility is described in **Hypothesis 2**. The advantages, in terms of passive targeting to solid tumors, given the smaller size of EMVs, are treated in **Hypothesis 3**. In **Hypothesis 4**, the improvement in indocyanine green photothermal properties when encapsulated in EMVs was explored. In the present thesis, EMVs are investigated as small-interfering RNA carriers[208] in **Chapter 6** and in **4** for cyanine photothermal dyes [54]. Last, in **Chapter 7**, EMVs are investigated as camouflaging materials for genipin-spermine-glycine-based nanoparticles.

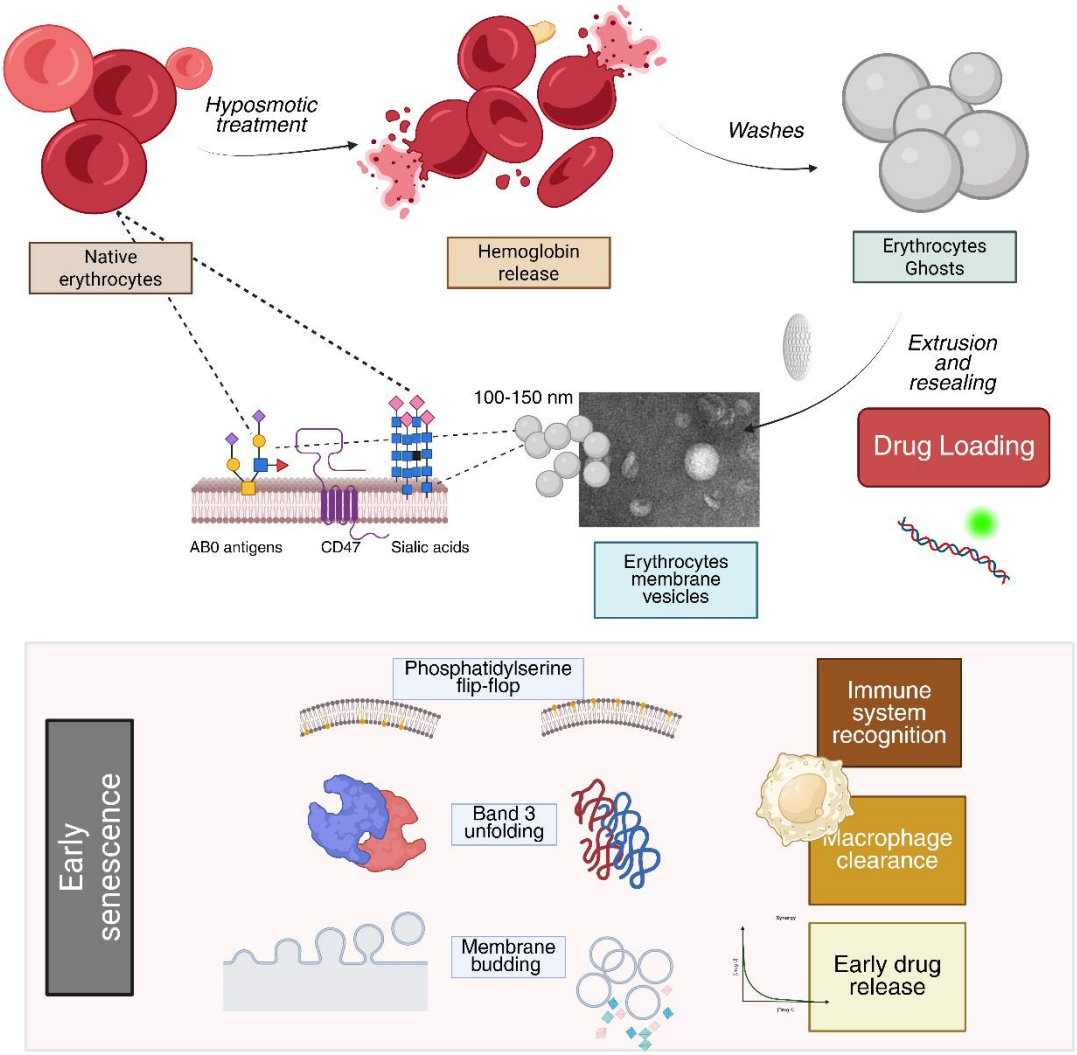



Figure 6: Schematic representation of the generation of erythrocytes membrane vesicles from whole erythrocytes. EMVs still retain CD47, sialic acids glycocalyx forest, and the antigen system AB0. Furthermore, the risks associated with the use of erythrocytes as starting material are mostly connected to early senescence: phosphatidylserine exposure, a phagocytic signal; similarly, unfolding of Band-3 protein. Lastly, aging erythrocytes are big producers of extracellular vesicles: membrane budding is a common mechanism that will cause early release of the encapsulated drug.

## 1.7 Polymeric Nanoparticles: Principles, Advantages and Drawbacks

Like lipid nanoparticles (LNPs) nanocomplexes, the rationale of delivery via polymeric nanoparticles relies on electrostatic interactions, i.e., a cationic nanosized polymer capable of complexing negatively charged nucleic acids. A specific group of polymeric nanoparticles is represented by dendrimers, i.e., heavily branched polymers stemming from a central core [215]. Many commercially available, well-established, positively charged polymers, such as Lipofectamine, have been used to complex nucleic acids. The commonly used polymers include polyethylenetanolamine (PEI), which is commercially available with different branches and molecular weights, polylysine (PL), polyaspartate with modified side chains, and crosslinked chitosan [216]. However, polymeric transfection relies on an intrinsically cytotoxic mechanism for transfection: endosomal escape via endosomal rupture [217]. Therefore, a heavy cationic charge and an excessively strong buffering ability can lead to cytotoxic effects [218].

DNA and RNA are negatively charged; therefore, a cationic or ionizable polymeric net is theoretically suitable for electrostatic interaction: such a nanoparticle is termed a *polyplex*. Cationic polymers, or a polymerized mixture of cationic lipids, are usually employed for in vitro transfection for basic research applications: gold standards such as Lipofectamine are easy to use, relatively cheap and well-established products. In this case, complexes of nucleic acids and cationic lipids are called lipoplexes and conventionally form the nucleus of lipid nanoparticles [219] in a core–shell fashion. Typically, a positive charge is provided by amine groups (primary, secondary, tertiary, and quaternary). The molecular weight, branching, charge, and composition can vary, making polymeric nanoparticles highly tunable drug delivery systems. The most common polymers include polylysine, polyethyleneimine, and polyornithine, but the application of natural polysaccharides as scaffolds offers a wide variety of arrangements. Conventionally, chitosan, dextran, alginate, and gelatin monomers are employed in polymeric hybrid nanoparticles. The mechanism of action of polymeric nanoparticles is explained in **Hypothesis 5**.

In the present study, the potential of genipin as a crosslinking agent to generate zwitterionic nanoparticles capable of complexing small-interfering RNAs was explored. Genipin can crosslink unprotonated amines (refer to section **1.7.1 Biomedical applications of genipin and mechanism of action**), and naturally occurring polyamines serve as excellent scaffolds. Genipin can bridge only two polymerized chains; therefore, a size tuning agent is needed. For this reason, glycine, a simple amino acid with a carboxylic and an amine moiety, was used to block the polymerization chain.

### 1.7.1 Biomedical applications of genipin and reaction mechanism

Genipin is a secoiridoid extracted from the fruit of *Gardenia jasminoides*, where it acts as a crosslinker to generate a pigment called blue gardenia. Additionally, it is present in relatively high concentrations in *Genipia americana* [220]. Recently, it has gained attention as a natural, nontoxic, amine crosslinker and as a replacement for glutaraldehyde [221]. Colorless by itself, it is mildly soluble in water (up to 5 mg/ml) and completely soluble in ethanol. Its mechanism of action has been partially elucidated, but it is still somewhat elusive: genipin reacts with nonprotonated amines—its reaction is, therefore, heavily

dependent on pH—and crosslinking involves at least two steps. The first is the opening of the iridoid ring, with the formation of a heterocycle and simultaneous release of methanol, followed by final crosslinking on the overhanging amidic moiety [222], [223]. Additionally, genipin can react with both aliphatic and aromatic amines [224], with the final product color varying according to the length of the substrate. Given the multiple steps involved in the reaction, its reaction orders appear to be fractional [222], [225]. In every case, the final crosslinked product will possess faint fluorescence (1–2% fluorescein isothyocyanate and rhodamine B) in the green and red regions, whose excitation peaks depend heavily on the structure of the product [226].

Genipin toxicity appears to be several thousand times lower than that of glutaraldehyde for fibroblasts [227]; in Caco2 and MCR5 cells, the viability was greater than 75% at 3 mM and 60% at 5 mM [228]. Additionally, free genipin is involved in many apoptotic and antiproliferative pathways: it activates the Cas3 cascade in the MDA-MB-231 breast cancer cell line [229], and it actively inhibits the Hedgehog pathway [230]. Owing to its anti-inflammatory properties and preventive action against ischemic brain injury, atherosclerosis, platelet aggregation, hyperglycemia, hyperlipidemia, and hypertension, it has been used for centuries in traditional medicine [231].

Owing to its interesting properties and mild reaction conditions (RT, aqueous solution), genipin has attracted interest as a crosslinker for biomedical matrices: collagen, as a support hydrogel scaffold for cell differentiation and growth [232], [233]; chitosan, a polysaccharide composed of D-glucosamine and N-acetylglucosamine, for almost unlimited biomedical applications [234]; wearable patches for wound healing [235]; and even siRNA delivery among those [236] and nanoparticles for the sustained delivery of α1-antitrypsin [237]. Finally, even the extracellular matrix derived from the human umbilical cord, where genipin has greater biocompatibility than another conventional crosslinker, EDC [238]. Owing to its safety and wide range of applications, genipin is reported to be present in many cosmetic formulations from L'Oreal and Estèe Lauder.

### 1.7.2 Polyamines: natural polycations

Naturally occurring polyamines, particularly putrescine, spermine and spermidine, are small, organic cationic molecules found in all living cells. They are involved in a wide range of cellular processes, including DNA stabilization, gene expression, cell growth, ROS protection and aging [239], [240]. In mammals[241], they also play a role in hair growth and wound healing. Two naturally occurring polyamines, spermine and spermidine, are bound to RNA in the cytoplasm of all living beings on Earth [242]. Spermidine appears to be involved in autophagy, and its concentration is directly intertwined with longevity [243]. On the other hand, spermine regulates cell proliferation, apoptosis, and differentiation and has an impact on mitochondrial function [244]. Furthermore, spermine and spermidine (**Figure 7**) also possess interesting properties in terms of the ionizability of their amine groups. At physiological pH (7.4), spermine has a charge of +4, whereas spermidine has a charge of +3, both with full protonation of the amino groups. The short length of the aliphatic chain (with spermine being approximately a rod with a length of 4.4 Angstroms) and the heavily concentrated charge make them extremely prone to interact with nucleic acids: in the cytoplasm, one to four spermines are found for each 100 bp mRNA, stabilizing (but not condensing) the double-stranded portions[245]. Spermine and spermidine are safe molecules, with LD50 values (in mice, administered intravenously) of 600 mg/kg circa and 50–100 mg/kg, respectively [246]. They have been widely used for complexing nucleic acids in nanomedicine: spermine has been used to modify dendrimers, liposomes or polymers, facilitating endosomal escape as well [247], [248], [249], whereas spermidine has been used

to functionalize nanoporous nanosilica beads [250]. Owing to their biocompatibility, safety and interesting chemical properties, spermidine and spermine were chosen as building blocks to explore genipin-polyamine-based nanosized polymers (**Paragraph 1.7.3**).

### 1.7.3 Genipin-polyamine-glycine nanoparticles

As previously mentioned, genipin reacts with nonprotonated amine groups. To generate crosslinked polyamines, genipin can be allowed to react with a molar excess of spermine and spermidine , naturally occurring polyamines. The success of such reaction, with similar occurring natural polyamines has been already reported elsewhere[251]. Given the stoichiometry of the mechanism of action of genipin, it is possible to tune the properties of nano-sized polymers based on it.

In **Hypothesis 5,** the feasibility, in terms of siRNA transfection efficiency, from a tailored and tuned particle size, zeta potential and ionizability are explored; the possibility of following the intracellular fate and cell uptake using GxS5 own fluorescence is outlined in **Hypothesis 6**. The experimental results regarding the ultrastructure, reaction kinetics, cytotoxicity and transfection efficiency of siRNA have been reported [252] and are described in **Chapter 7.** Finally, in **Hypothesis 7**, the favorable properties arising from camouflaging genipin-spermine-glycine nanoparticles with EMVs are described. Lastly, in **Chapter 8,** the relative results are reported as in [253]

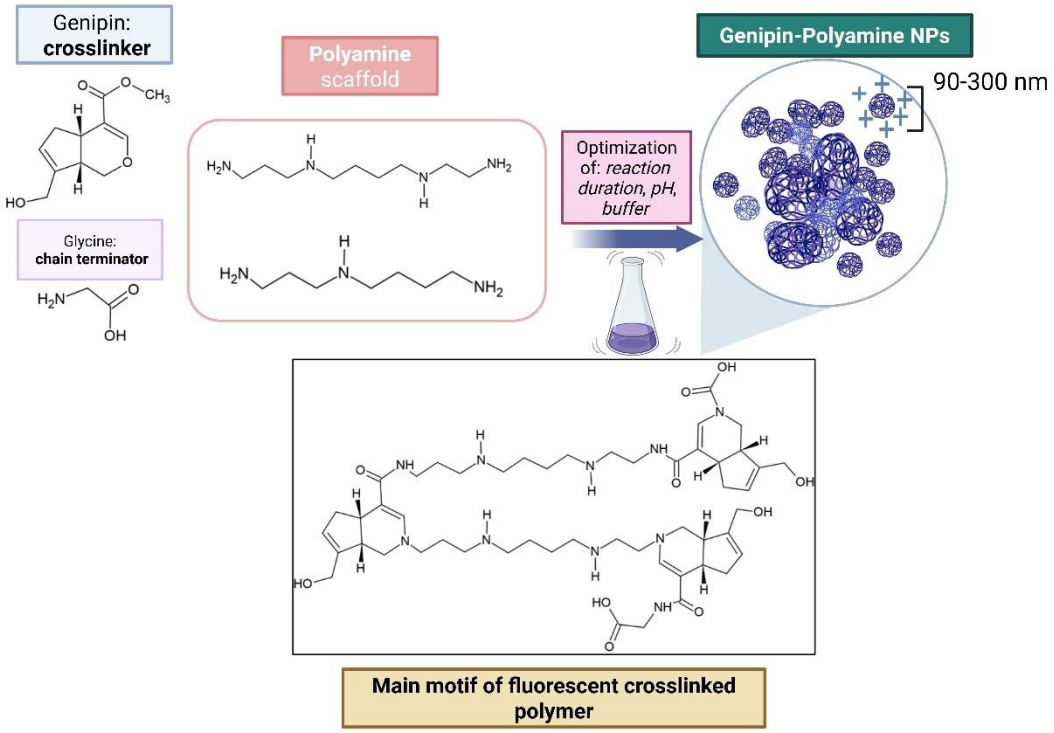



Figure 7 Schematic representation of the building block for the synthesis of genipin-polyamines-glycine polymers.

# Chapter 2

# Aims and Hypotheses

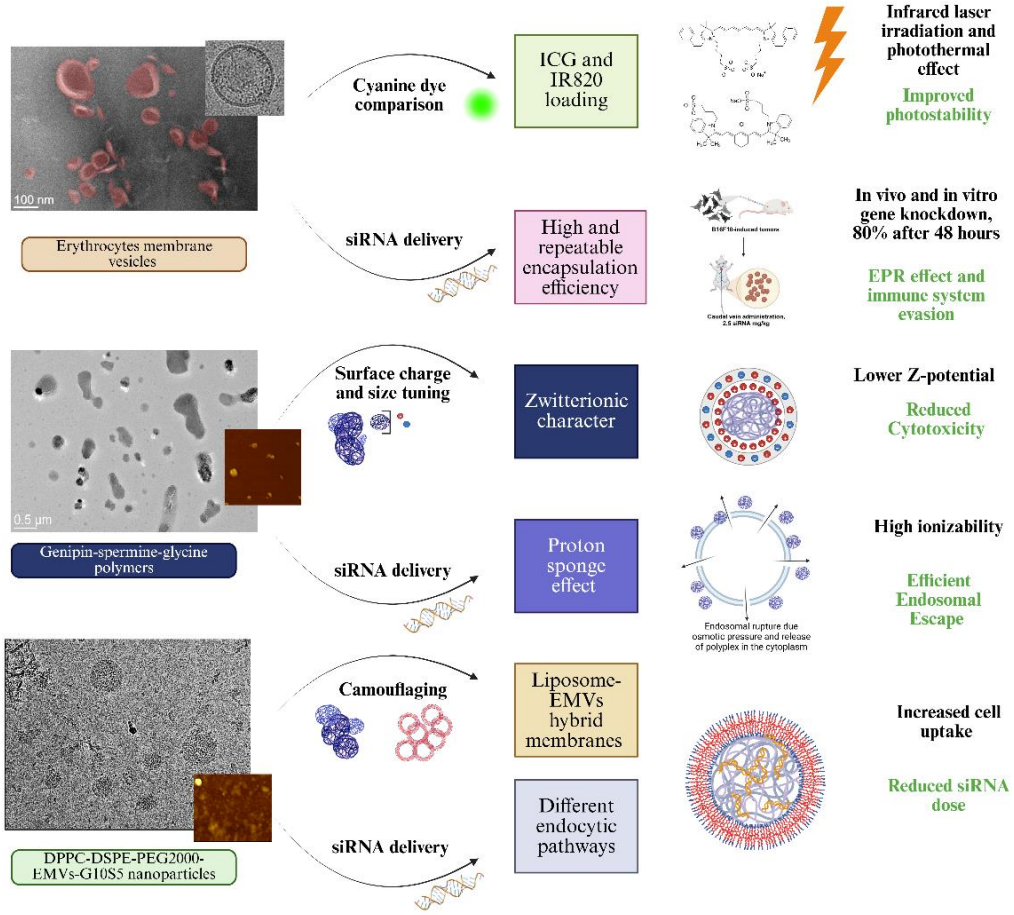



Figure 8: Overview of the hypotheses and the results of the thesis. Briefly, three nanocarriers were developed, the last starting from the first two. EMVs are derived from erythrocyte ghost membranes, as outlined in **Paragraph 1.6.4**. They are meant to be used to 1) compare two cyanine dyes, IR820 and the well-known indocyanine green, and 2) serve as novel small-interfering RNA carriers for in vivo delivery. Second, GXS5 nanoparticles, described in **Paragraph 1.7.3**, are also meant for siRNA delivery, but their development also includes physiochemical property tuning to exert more efficient action. Finally, the most efficient GxS5 nanoparticle is chosen because of its superior biocompatibility and ability to be camouflaged with hybrid membranes composed of EMVs and DPPC-DSPE-PEG2000 phospholipids (**Chapter 7**).

## 2.1 Aims and Rationale

The main aim of this dissertation is the development of safe, biocompatible therapeutic nucleic acid carriers on the basis of

a) **erythrocyte membranes** and
b) **on zwitterionic nanosized polymers**.
The application and main outcomes are described in Figure 8.

These will serve as alternatives to toxic, commercially available transfection agents with added functionalities, as follows:

- Photothermal/photodynamic properties;
- In vivo tracking and imaging for diagnostic purposes;
- Biocompatibility (as a lack of immunogenicity) due to the use of the patient's own blood as the starting material;
- A lower cationic charge in the case of polymeric transfection agents, due to the introduction of carboxylic groups in the net, reduces the eventual cytotoxicity;
- The successful camouflaging of polymeric nanoparticles using erythrocyte membranes improved cell uptake and therefore dose reduction.

These carriers are based on nanoerythrosomes, as described in section 1.6.4, and on genipin-based cationic polymers, as described in section 1.7.3.

Furthermore, this study aimed to establish a reliable, well-characterized protocol for loading siRNAs with good encapsulation efficiency (>50%) within EMVs (erythrocyte membrane vesicles). The protocol will serve as the basis for a future scale-up program and will include the removal of unloaded siRNA to obtain a ready-to-go formulation. Indeed, purification from unloaded siRNA appears to be lacking in the literature regarding noncationic (neutral) transfection agent preparation, despite the inherently toxic nature of the molecule (**Paragraph 1.5.5**). This study aimed to determine whether EMVs are suitable carriers for cyanine dyes with photothermal properties and whether encapsulation can help stabilize them and reduce potential cytotoxicity, together with stabilizing them. Moreover, it aims not only to develop a novel class of genipin-spermine-based zwitterionic transfection agents but also to optimize their size and shape by tuning the glycine concentration in the reaction batch and thoroughly characterizing their spectroscopic properties. Finally, we explored the possibility of using EMVs to camouflage genipin-spermine-glycine complexes with siRNA and demonstrated how the coating improved the transfection efficiency of the carrier.

The results in these arose from confirmation, partial confirmation or rejection of seven different hypotheses, hereby briefly summarized and in Figure 9:

1) *To prolong the nanodrug circulation time thanks to the presence of the "don't eat me" CD47 marker.* The erythrocyte membrane contains a phagocytosis inhibitor that is active on phagocytic cells (mainly macrophages), whose presence on a nanoparticle might increase its circulation time.

2) *The internalization efficiency and the cargo release of the nanodrug can be increased by the presence of extracellular vesicle machinery on erythrocytes membrane.* Erythrocytes are the largest producers of extracellular vesicles (EVs) in the body and already serve as typical EV markers in their proteome. Such protein armories can be used to achieve transfection efficiencies like those of naturally occurring EVs.

3) *Exploiting the enhanced permeation and retention effect (EPR) for tumor tissue penetration.* The EPR effect is a well-known mechanism by which nanoparticles of a certain size extravasate from leaky, heavily fenestrated neoplastic blood vessels and accumulate in solid tumors. It has a minor role in humans than it does in rodents; therefore, careful tailoring of the nanoparticle shape and maximization of the circulation time are needed.

4) *Stabilizing cyanine dye monomeric forms to reduce light-induced degradation and improve the photothermal properties.* ICG is generally regarded as a safe, approved molecule for imaging purposes. The encapsulation within erythrocyte membrane vesicles might stabilize their photoinduced degradation and prolong the lifetime of the fluorophore.

5) *Improving endosomal escape and biocompatibility via tailoring the cationic charge of transfecting agents toward a zwitterionic character.* In a mildly acidic environment, ionizability is instrumental for successful proton-sponge effects and endosomal escape in the case of cationic polymers used for nucleic acid transfection. Optimizing the amount of tertiary, ionizable amines would improve the endosomal escape ratio.

6) *Camouflaging the genipin-polyamine nanoparticles with erythrocyte-derived membranes to generate a novel vector with properties of both.* Such an approach would create a new nanoparticle with the advantages of both systems, i.e., biocompatibility and enhanced endosomal escape.

7) *The self-fluorescence, both green and red, of GxS5 polymers makes it possible to follow their internalization route in real time.* Genipin polymerization products are self-fluorescent over a wide range, and despite having a low quantum yield, their cell internalization can be used to investigate their mechanism and cytoplasmic localization. The use of self-fluorescence, together with endocytosis inhibitors, would help elucidate the mechanism of internalization by cells by tracking uptake.

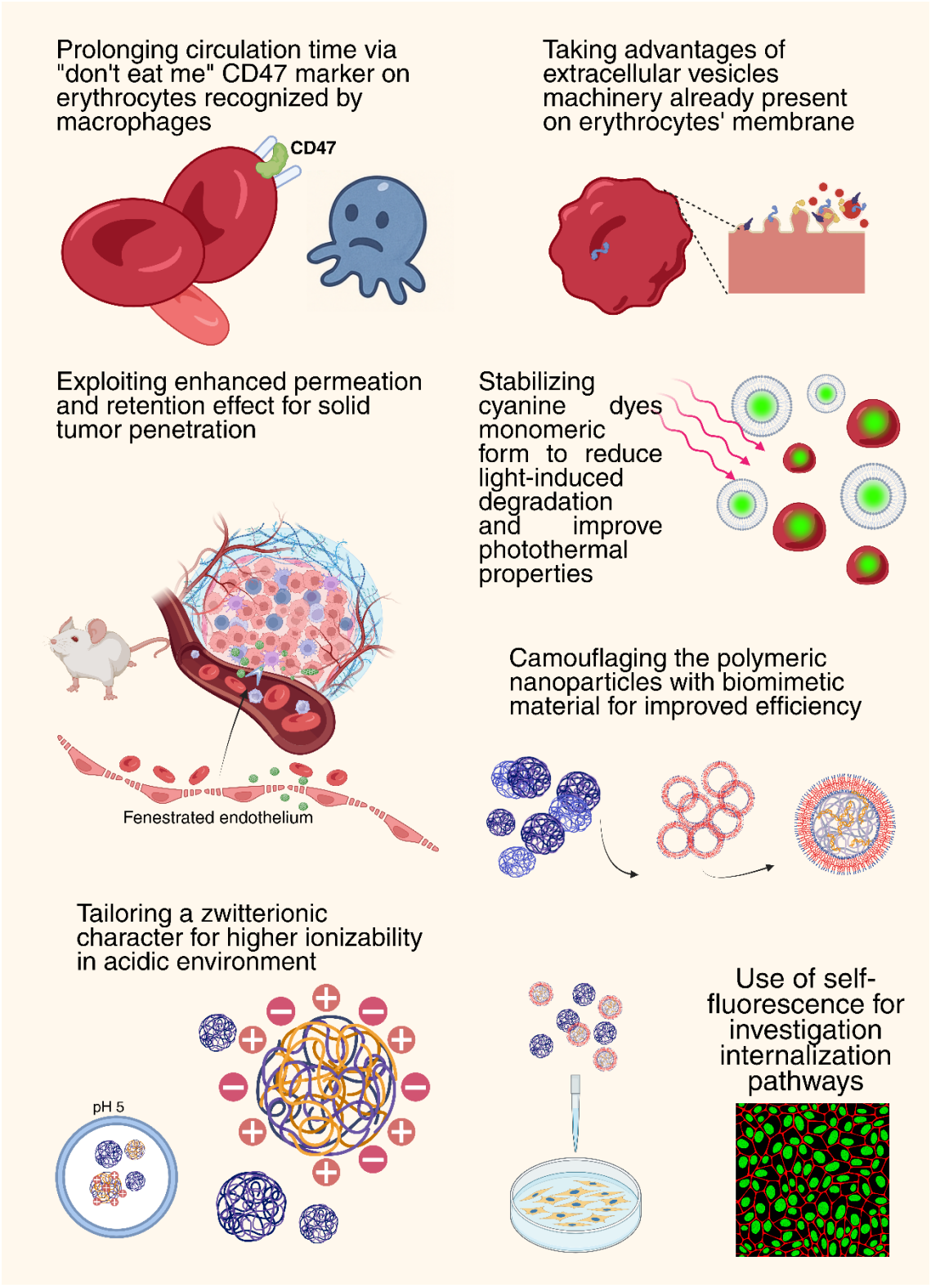



Figure 9 Summary of the hypotheses on which this Thesis is based. Each of them is addressed more in depth in the body of text.

## 2.2 Hypothesis 1: Prolonging Nanodrug Circulation Time via “Don’t Eat Me” CD47 Marker

As stated in Paragraphs 1.4. and 1.4.1, the circulation time is a key parameter for the performance of a nanodrug. Circulation time is strictly connected to clearance, which, in turn, is affected by immune system recognition and the deposition of opsonizing molecules (antibodies, albumin, transferrin, complement proteins, and plasma components). An important feature of erythrocytes is the presence of the CD47 coreceptor on their membrane: it can mask the surroundings from phagocytosis by macrophages [254]. The relationship between macrophages (and phagocytic cells in general) and red blood cells is complicated and intertwined with other parties. Macrophages are involved in erythroid differentiation and erythrocyte maturation, but in the spleen, within sinusoids, they are responsible for checking their loss of deformability due to aging, the presence of oxidized hemoglobin inclusions (Heinz bodies) and other defects; the presence of phosphatidylserine in the outer membrane leaflet, due to senescence, elicits strong clearance [189]. Erythrocytes naturally avoid opsonization under physiological conditions and are embedded in their membrane, and CD47, a coreceptor that acts as a “don’t eat me!” marker for macrophages [12]. CD47 is a well-characterized phagocytosis inhibition marker for macrophages since it binds Sirpα, an inhibitory membrane receptor present on macrophages [255].

As stated in Paragraph1.6.4, this protein is also retained in erythrocyte membrane vesicles (somewhere else termed nanoerythrosomes). A chronic issue in delivering siRNAs is their fast clearance (Paragraph 1.5.5): a few hours of blood residence is not enough to exert any significant therapeutic effect. To date, the issue of a short residence time has been addressed via the use of lipid nanoparticles (or other kinds of artificial nanoparticles) conjugated with polyethylene glycoles of various molecular weights (Paragraph 1.4.1). This approach has many drawbacks, such as an accelerated blood clearance effect and IgM arising against the nanoparticle itself, which is enhanced by PEG itself. Therefore, PEGylated formulations are not suitable for multiple administrations, such as RNAi therapies. Erythrocyte membrane vesicles (EMVs), which retain CD47 on their membrane, can serve as alternatives to PEGylated nanoparticles for longer circulation times and efficacious delivery of the siRNA payload to the target site. We aim to take advantage of this property and prepare vehicles that are not recognized by the immune system as nonself and, consequently, have long circulation times in blood. This approach has been used multiple times for hybrid nanoparticles and liposomes [255]. A technique for loading high quantities of siRNA inside EMVs will be optimized, together with the removal of unloaded siRNA.

## 2.3 Hypothesis 2: The Internalization Efficiency and the Cargo Release of the Nanodrug Can Be Increased by the Presence of Extracellular Vesicle Machinery on Erythrocytes Membrane

Erythrocytes are the most abundant cells in mammals, and they continuously release extracellular vesicles (EVs). EVs directly bud from the cell membrane since erythrocytes do not possess a Golgi apparatus [256]. Erythrocytes release EVs containing regulatory miRNAs, such as miR-125b-5p, which are capable of inhibiting the inflammatory

TRAF6/MAPKs/NF-κB pathway in chondrocytes [257]. The exact endocytic mechanism followed by erythrocyte-derived EVs is still unclear, but it is mediated by the interaction between a cell receptor and a signaling protein on the EV surface; an important role of lipid rafts and their embedded proteins cannot be ruled out. Among the most important contributors to membrane fusion are tetraspanins, a wide class of membrane-spanning proteins that play a role in protein adhesion and phagocytosis initiation, and they organize themselves within tetraspanin-enriched microdomains. Despite being of low abundance, human erythrocytes possess CD82 and CD151 [258]. Another class of important EV markers is integrins, and CIB1 is well represented in erythrocytes and erythrocyte ghosts; CIB1 appears to play a role in adhesion (by binding FAK, focal adhesion kinase)[259]), spreading, calcium flux regulation, and, overall, integrin biology by binding the αIIb cytoplasmic domain [260]. In addition to tetraspanins and integrins, erythrocytes contain other typical EV proteins, such as ALIX and TSG101, which are involved in the packing of miRNAs and other short RNAs in exosomes [261]. Overwhelming evidence suggests that EVs and exosomes are usually internalized by recipient cells via caveolae- or clathrin-mediated endocytosis, aided by the above-described classes of proteins [115].

Finally, a well-represented protein pair in erythrocytes is flotillin 1 and 2 [186], [262]: these two proteins are capable of inducing membrane microdomains that result in a caveolae/clathrin-independent endocytosis mechanism. This protein machinery is involved in direct membrane fusion and endosomal escape. Therefore, we postulate that EMVs are successfully internalized in cells via a membrane fusion mechanism and later escape endosomes and release siRNA at the target site.

## 2.4 Hypothesis 3: Exploiting Enhanced Permeation and Retention Effect for Tumor Tissue Penetration

The term enhanced permeation and retention effect (EPR effect), which has been known since the beginning of the last century regarding solid tumors, was coined by Hiroshi Maeda from Kumamoto University School of Medicine in 1986. It refers to the extravasation and accumulation of macromolecular complexes, or nanoparticles, in solid tumors and metastases, whose newly formed blood vessels possess leaky and heavily fenestrated endothelium [263]. It has been described in model mammals (rodents, monkeys) and humans and exploited by approved nanodrugs such as Doxil [84] to passively deliver doxorubicin to the target tissue. The nanoparticles extravasated not only because of fenestration but also because of the increased permeability of the endothelium itself, which is physiological for fast-growing tissues such as solid tumors. Furthermore, the substantial lack of infiltrated lymphatic cells in solid tumors reduces clearance by the reticuloendothelial system. At the same time, delicate equilibrium within the tumor microenvironment is at play: owing to rapid and uncontrollable growth, the interstitial fluid pressure pushes toward the marginal zone of the tumor, compressing the blood vessels and causing a theoretical impediment to the diffusion of macromolecules [264]. For this reason, nanoparticles and macromolecules tend to accumulate in peritumoral areas; at the same time, interstitial fluid pressure causes hypoxia in the central area of the tumor, leading to necrosis. The unorganized extracellular matrix, which is composed of unaligned collagen fibers present in solid tumors, further hinders tissue penetration by nanoparticles [265].

Unfortunately, after many years of elusive research, the EPR effect has been much more effective in rodents and small animals than in humans [27]; this discrepancy is due to the much stronger blood flow rate—and, therefore, greater shear force—in humans than in

mice [266]. For this reason, careful optimization of a tentative nanodrug must be carried out, together with coupling for adjuvant therapies. For example, the application of angiotensin II improved, both in rodents and humans, the perfusion rate in solid tumors but did not affect the blood pressure in healthy vessels; increasing the tumor perfusion rate can lead to optimal penetration of the nanodrug farther from capillaries [267].

There are few strategies that can be used to improve tissue penetration, owing to the EPR effect, of nanoparticles: 1) tailoring the particle size, shape, and charge; 2) engineering the nanoparticles to have tissue-penetrating activity, such as conjugating them with metalloproteases or using an external stimulus to trigger ultrastructure modification and enhance tissue penetration [268]; and 3) exploiting the acidity of the tumor microenvironment (6, 6.5 pH) for a tropism-optimized nanoparticle [264]. In terms of optimal size, many studies have confirmed that a diameter of 100–200 nm is optimal both for avoiding kidney clearance and enhancing extravasation and retention within tumor tissue [269]; ellipsoidal shapes appear to penetrate better than spherical or extreme aspect ratio shapes [61]. In this context, we aim to exploit the small size of EMVs (100–170 nm), their slightly negative zeta potential, and their biconcave disk-like shape to achieve an efficient EPR effect and good solid tumor penetration.

## 2.5 Hypothesis 4: Stabilizing Cyanine Dyes Monomeric Forms to Reduce Light-induced Degradation and Improve Photothermal Properties

Indocyanine green (ICG), also known as Cardiogreen, is generally regarded as a safe (GRAS) dye. It is widely used for blood vessel tracking because of its strong infrared emission, widely approved, and common use in ophthalmology. It has a high affinity for plasma proteins, especially human globulins [270], and a very short plasma residence, on the order of minutes, without any known liver metabolites [271]. However, it is a relatively unstable molecule in aqueous solution [272] and undergoes fast degradation even in the absence of light [54]. Furthermore, it is capable of releasing heat during IR-laser irradiation, making it suitable for photothermal therapy (PTT) [273], a novel approach used to sensitize cancer cells to more favorable uptake of anticancer drugs or, when the local temperature increases, trigger a cell death cascade [274]. The limitations of its clinical translation as a PTT agent are, indeed, its scarce accumulation in tissues, its short lifetime, and, importantly, the presence of degradation products after IR irradiation [271].

The mechanism of ICG degradation in aqueous suspensions involves radical oxygen and ion mediation; therefore, human tissues and plasma are suitable environments for the accumulation of leucoforms during light-induced degradation[272]. Therefore, as ICG is not a good source of singlet oxygen upon photoinduced degradation, these degradation products are indeed the source of intrinsic cytotoxicity [275]. ICG spontaneously inserts within a phospholipid double layer, and its fluorescence is greatly enhanced without the need for binding to plasma proteins [276], as is the case for nanoerythrosome membranes [54], [273].

The steps of the degradation mechanism are as follows:

- ICG, in water, is either in monomeric form or in H-dimer aggregates: the two forms have distinct absorbance spectra, and the preference for one form or the other is dependent on the concentration of the substance [277], with the fully

monomeric form present in water until 0.5 mM; in the presence of salts and at millimolar concentrations, J-type oligomers also appear [278], a rather stable form if stored in the dark. Within double layers at a suitable lipid/ICG ratio [276], the fully monomeric form is predominant.

- Upon laser irradiation at IR wavelengths, singlet oxygen is formed from atmospheric oxygen due to energy transfer from the triplet ICG excited state (due to the intersystem crossing mechanism); the radical ignites a degradation reaction with the concurrent emission of heat [279].
- In the presence of H and J aggregates, the triplet state half-life appears to be longer; therefore, the formation of singlet oxygen radicals is more likely, leading to overall faster photooxidation and subsequent degradation [271], [280], [281]. The spatial proximity of ICG molecules further increases the reaction speed.
- The monomeric form of ICG, on the other hand, consists of well-spaced, unorganized molecules—the excitation lifetime is shorter, leading to less ROS production [278]; furthermore, superoxide radical diffusion is hampered within double layers, slowing the chain reaction [271] and ultimately leading to complete photobleaching.

There is a growing amount of evidence regarding the stabilization of monomeric forms within micellar/liposomal objects: within erythrocyte-derived vesicles [54], [273], PEGylated liposomes [276], [282], and even block copolymers [283]. Therefore, encapsulation with a nanocarrier would be beneficial for ICG properties for many reasons: enhancing the fluorescence properties, stabilizing the monomeric form (leading to lower photodegradation), and, overall, reducing the formation of potentially toxic leucoforms. Finally, all the known advantages of biocompatible nanocarriers, such as EMVs, have been added in addition to what has just been elucidated: these advantages include the generation of a theranostic nanoparticle (**Paragraph 1.3.2** and **Paragraph 1.5.4**), an all-in-one formulation capable of delivering both siRNA and a safe, approved, imaging agent such as ICG. Within the scope of this hypothesis, alternative IR-820 materials will be evaluated in terms of their photothermal efficiency and the protection that EMVs will exert against photoinduced degradation. Indeed, IR-820 has a more stable absorbance spectrum and is less influenced by the chemical environment [284], [285], making its spectroscopic properties easier to investigate. Additionally, it has a lower degradation rate upon infrared irradiation and simply upon light exposure [284]. The evaluation of the properties of IR-820 when encapsulated in EMVs will provide a theoretical basis for research on theranostics capable of photothermal degradation, such as nanodrugs.

## 2.6 Hypothesis 5: Improving Endosomal Escape and Biocompatibility via Tailoring the Cationic Charge of Transfecting Agents toward a Zwitterionic Character

Nucleic acid transfection via cationic or ionizable lipids is the gold standard for in vitro transfection [286], but the intrinsic cytotoxicity of the mechanism of action hampers its clinical translation, i.e., the **proton sponge effect**. Cationic nanoparticles are taken up

by cells predominantly through endocytosis, becoming encapsulated within endosomes for several hours postinternalization [287]. As the endosome matures into a lysosome, its internal pH decreases due to proton influx. The presence of ionizable tertiary or quaternary amine groups within the LNPs contributes to the "proton sponge effect," which remains debated. Briefly, the nanoparticles buffer the increasing proton concentration, which drives the cotransport of chloride ions (Cl-) into the endosome. This ion accumulation increases osmotic pressure, ultimately causing endosomal rupture and the release of the nanoparticles into the cytosol [288]. The mechanism is explained in Figure 10.

A dense and highly cationic charge in transfecting agents has been connected to increased cytotoxicity and the activation of multiple apoptotic cascades [289]. The lower net surface charge of genipin-spermine-glycine polymers (**paragraph 1.7.3**, **GxS5)** improves the overall biocompatibility, and a neutral-to-negative charge, due to complexation with siRNA, increases the cell uptake efficiency.

The presence of ionizable tertiary amines is instrumental for the successful cationic delivery of therapeutic nucleic acids [290]. The increasing glycine ratio in the GxS5 reaction batch increased the pKa of the nanoparticles due to the presence of tertiary amines in the iridoid ring of genipin. This further protonation occurs at mildly acidic pH values, such as those of endosomes [291], at approximately 5–5.5, whereas the overall charge of the nanoparticle is milder at neutral pH. This approach, which involves ionizable polymers or ionizable lipids, is extremely successful and has led to the approval of many nanodrugs, such as the Covid Pfizer/BioNtech vaccines. We aimed to ameliorate the cationic charge of a genipin-polyamine-based scaffold by tailoring the amount of glycine, a small amino acid containing only one amine moiety, in the initial reaction batch. Glycine not only stops the reaction chain (as explained in **Paragraph 1.7.3**) but also confers a zwitterionic character due to the presence of carboxylic moieties in the nanoparticles [292]. This milder cationic charge can effectively improve the biocompatibility, reduce the cytotoxicity of the nanoparticles and enhance their uptake by target cells.

.

.

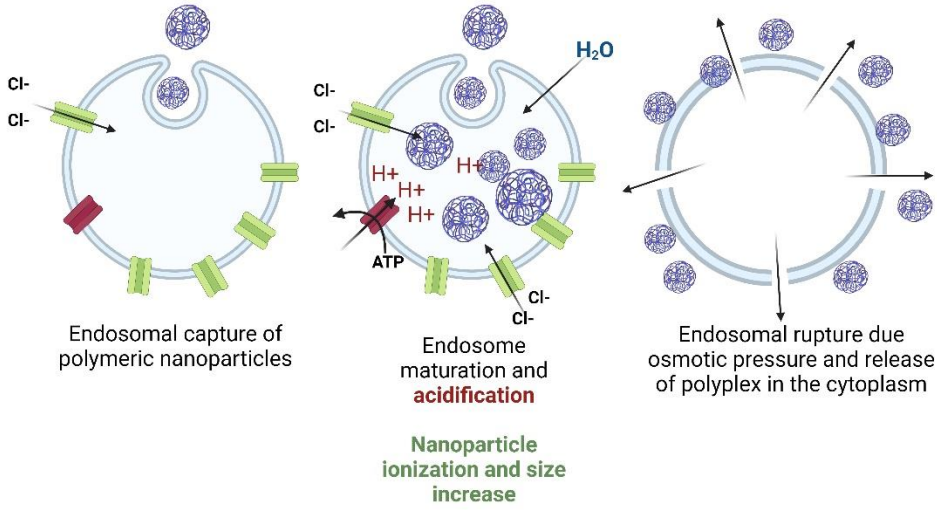



Figure 10 Summary of the main steps of endosomal escape mechanism by cationic/ionizable nanoparticles. Upon maturation, endosomes, containing the nanoparticles, acidify, with influx of chlorine ion as co-substrate of protons. Ionizable moieties of the nanoparticles act as buffer, therefore allowing the influx of even more protons and chlorine ions. After a certain threshold, the endosome will undergo rupture and release its content.

## 2.7 Hypothesis 6: Coating Zwitterionic Polymers with Erythrocyte Membranes would lead to Novel Material with Properties Belonging to Both Models

Camouflaging (i.e., coating) nanoparticles via a biomimetic agent, which is usually derived from naturally occurring cell membranes [293], has become a thriving field of research to confer interesting properties to parental nanoparticles. For these purposes, we aimed to select the genipin-spermine-glycine polymer with the best properties in terms of biocompatibility and transfection efficiency. A commonly used source of camouflaging material is indeed erythrocytes [294], [295], which are frequently used to coat polymeric nanoparticles (such as polylacticglycolic acid, PLGA)[296], or solid, mesoporous silica nanoparticles[297], [298]. While G10S5 (genipin-to-glycine molar ratio, in the reaction batch, 1:10, and 1:5 with respect to spermine) showed the lowest cytotoxicity and the most efficient siRNA complexation and transfection, it suffered from insufficient cell uptake at low concentrations, which hindered its activity. We therefore hypothesize that by coating G10S5-siRNA polyplexes with internalization activity, which can be followed by self-fluorescence of the polymer (Hypothesis 6), the siRNA dose, which is effective in exerting significant knockdown of a reporter gene, can be reduced. Furthermore, if the erythrocyte

membrane alone is not able to efficiently cloak G10S5 polyplexes, the addition and tailoring of the concentration of external phospholipids, such as dipalmytoilphosphatidylcholine (DPPC) and 1,2-distearoyl-sn-glycero-3-phosphoethanolamine-N-[amino(polyethylene glycol)-2000] (DSPE-PEG-2000), would confer new mechanical properties to the resulting hybrid membranes. Shear stress processes (such as extrusion and sonication) can be adapted to generate stable, repeatable, fully coated polyplexes. The final nanoparticles (Figure 10) therefore possess both erythrocyte endocytosis-favorable membrane characteristics (outlined in **Hypothesis 2**) and the ionizability of tertiary amines when in a mildly acidic environment, i.e., efficient endosomal escape, of G10S5 (**Hypothesis 5**).

## 2.8 Hypothesis 7: The Self-Fluorescence, in Green and Red, of GxS5 Polymers, would make it possible to follow their Internalization Route in Real Time

It has long been known that genipin products, once crosslinked, exhibit fluorescence [299], [300], [301]. This effect arises from the long, π-conjugated double bonds in the crosslinked matrix, and it is highly dependent on the reaction conditions. Indeed, in [302], continuous emission from 500 to 800 nm was reported for excitation at 488 nm; in this case, genipin was used to crosslink collagen matrices, as already established for soluble collagen [303]. Conversely, a peak at 615 nm was reported for genipin-conjugated PEI/globin [304]. For hydrogels composed of chitosan and polyvinylpyrrolidone (PVP) crosslinked with genipin, an excitation of 485 nm was used, and the peak was identified at 520 nm; a faster increase in the total fluorescence was evident when the reaction was carried out at pH 10, followed by a faster decrease over the course of 24 hours, suggesting crosslinking degradation and the establishment of thermodynamic equilibrium. Furthermore, such fluorescence intensity is strong enough to allow quantification of the uptake efficiency. To date, no in vivo studies of the biodistribution of genipin products in vivo have been reported, but the biocompatibility, cost-effectiveness and low cytotoxicity of such entities make them suitable for in vivo imaging and as potential theranostic agents.

Owing to their intrinsic fluorescent properties, we hypothesize that these NPs can be used for following the internalization route used by cells and how camouflaging (**Hypothesis 6**) affects the endocytosis mechanism. Indeed, the preferential route of internalization followed by various classes of nanoparticles is still a matter of debate [305], and it strongly depends on the surface chemistry of the nanoparticle and/or the presence of biomimetic agents [306]. The fluorescence of GXS5 was used to prove 1) its successful internalization and, if so, at which rate, how the uptake efficiency is affected by the zwitterionic character according to **Hypothesis 5**) to investigate the preferential mechanism (caveolae, clathrin-coated vesicles, pinocytosis, etc.) by which cells internalize the above-described fluorescent particles.

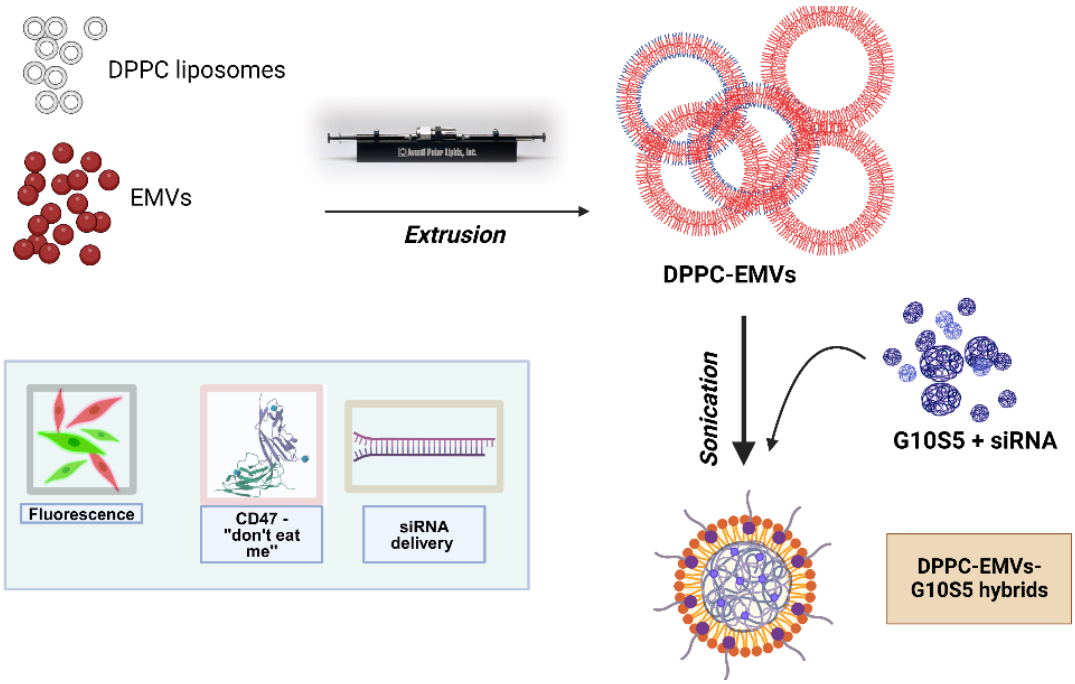



Figure 11 Summary of Hypothesis 7. Hybrid membranes, composed of erythrocyte ghost membranes and external phospholipids, will be employed to coat G10S5-siRNA polyplexes, resulting in nanoparticles sporting the advantages of both systems.

# Chapter 3

# Materials and Methods

This doctoral thesis has two main cores: the preparation of erythrocyte-based nanocarriers, termed erythrocyte membrane vesicles (EMVs), and the preparation of genipin-polyamine-based nanocarriers. The characterization techniques are mostly superimposable, apart from where specifically stated. **Paragraph 3.1** pools all the materials used in the thesis.

## 3.1 Materials

Indocyanine green (ICG, laser grade) was purchased from Acros Organic (Thermo Fisher Scientific Company, Morris Plains, NJ, USA), and IR820 (dye content 80%) and CHCl3 (>99%) were purchased from Sigma–Aldrich (Sigma–Aldrich, Munich, Germany). Liposomes were prepared using 1,2-dipalmitoyl-sn-glycero-3-phosphatidylcholine (DPPC), 1-myristoyl-2-stearoyl-sn-glycero-3-phosphocholine (MSPC), and N-[carbonyl methoxy(polyethylene glycol)-2000]-1,2-distearoyl-sn-glycero-3-phosphoethanolamine, a sodium salt (DSPE-PEG2000) purchased from Lipoid GmbH (Ludwigshafen, Germany).

For all preparations, the following chemicals were used: phosphate-buffered saline buffer (PBS, tablets; Sigma Aldrich), Alsever's medium (TCS Biosciences Ltd., UK), and NaCl (Sigma–Aldrich, >99.5%). For purposes involving siRNA, diethylpirocarbonate (DEPC)-treated water and buffers were used. -HCl (306-67-2), spermidine (124-20-9), glycine (56-40-6), heparin sodium salt (porcine intestinal mucosa, 9041-08-1), and genipin (6902-77-8) were purchased from Sigma–Aldrich. The latter stereoisomer was reported to be 1S, 2R, 6S (PubChem SID 329799931, Figure 1). The buffer of choice was PBS (cat. number P4417), which was dissolved from tablets in DEPC Milli-Q water at a final concentration of 10 mM phosphate buffer, 137 mM sodium chloride, and 2.7 mM potassium chloride (from now on, 1× PBS). RNase A from bovine pancreas (EN0531) was purchased from Thermo Fisher. Ninhydrin (485-47-02, amino acid detection grade) was purchased from Sigma Aldrich, and TNBS (2,4,6-trinitrobenzene sulfonic acid) was purchased from Pierce Protease Assay (Thermo Scientific catalog, 23263). All the disposables were certified to be pyrogenase-, DNase- and RNase-free, and the glassware used was autoclaved before use. Sephadex G25 PD10 columns were purchased from Cytiva, UK, and each column was used up to ten times and regenerated with a 20× excess of elution volume after every purification round and kept under sterile conditions in DEPC water/PBS. Trisodium citrate dihydrate, RNase A (catalog number 10109142001) and Amicon centrifugal devices (30, 10 and 4 kDa NMWL, EMD Millipore), as well as fluorescent dyes (CM-DiI, C7000, and Vybrant DiO, V22886), were purchased from Sigma Aldrich. For the Stewart assay, ferric chloric hexahydrate (F2877) and ammonium thiocyanate (A7149) were obtained from Sigma Aldrich, whereas the heart lipid extract (171201), which was used as a standard, was obtained from Avanti Polar lipids. The Bradford reagent was prepared according to the traditional recipe (Coomassie Brilliant Blue R-250, B7920, ethanol and phosphoric acid

were obtained from Sigma Aldrich), and bovine serum albumin (A9418, Sigma Aldrich) at a stock concentration of 1 mg/mL was used as a standard.

For agarose gel assays, low-melting-point agarose (Promega) and custom-made Tris-acetic acid-EDTA buffer were used (all reagents were purchased from Sigma Aldrich). Midori Green was purchased from Nippon Genetics.

For extrusion, the polycarbonate membranes were 19 mm wide, 800 nm wide (610009), and 200 nm wide (610006), and the support filters (610014) were all purchased from Avanti Polar and installed on an Avanti Polar mini extruder.

The Presto Blue reagent (A13261) and Hoechst 33342 solution (62249) were purchased from Thermo Fisher Scientific, and the MemBrite® Fix 488/515 Cell Surface Staining Kit from Biotium (#30093-T, Fremont, CA, USA) were used.

### 3.1.1 Cell culture-related chemicals

Advanced Dulbecco's modified MEM (ADMEM), Advanced Roswell Park Memorial Institute 1640 medium (RPMI-1640), and MCDB 131 media were purchased from Gibco (Thermo Fisher Scientific, VA, US), and FGM™-2 fibroblast growth medium-2 BulletKit™ was purchased from Lonza (Basel, CH). All media except FGM™-2 were supplemented with GlutaMAX (100x, Gibco) and penicillin–streptomycin (100x, Sigma–Aldrich, Merck, Darmstadt, Germany). ADMEM and ARPMI were supplemented with 5% fetal bovine serum (FBS; Gibco). MCDB 131 was supplemented with 10% FBS (Gibco), 10 ng/mL epidermal growth factor (EGF; Gibco), 1 µg/mL hydrocortisone (Sigma–Aldrich) and 10 mm glutamine (GlutaMAX; Gibco). The MycoAlertTM PLUS Mycoplasma Detection Kit was purchased from Lonza (Basel, CH). The B16F10 (CRL-6475), CT26 (CRL-2638), 4T1 (CRL-2539), and Hulec-5a (CRL-3244) cell lines were purchased from ATCC (VA, US), the NHLF cell line was purchased from Lonza (Basel, CH), and the B16F10-tdTomato line was a kind gift from Dr. Muriel Golzio (The Institute of Pharmacology and Structural Biology, IPBS-Toulouse). HaCat cells (ATCC PCS-200-011) were also purchased from ATCC. Lymphoblastoid cells were isolated as reported previously [307]. The cells were cultured in RPMI 1640 (Gibco, Thermo Fisher Scientific, Waltham, Massachusetts, USA) with endocytosis inhibitors (chlorpromazine, imipramine and genistein). The endocytosis inhibitors used for the experiments described in **Chapter 7** were purchased from Sigma Aldrich, dissolved in DMSO at a final concentration of 30 mg/ml and stored at 4°C.

## 3.2 Small interfering RNAs and RT-qPCR primers

Anti-TdTomato siRNA was purchased from IDT Genomics from Custom Silencer™ ThermoFisher design; its sequence is 5'rGrCrC rArCrC rArCrC rUrGrU rUrCrC rUrGrU rATT- 3′; 3′rUrArC rArGrG rArArC rArGrG rUrGrGrUrGrG rCGG-5′; "r" stands for ribonucleotide to distinguish it from DNA overhangs). For in vivo tracking, as in **Paragraph 3.8**, the Cy-5 fluorophore is conjugated at the 5' end of the passenger strand. In **Appendix A** of this thesis, the tdTomato cDNA sequence is reported with highlighted primer positions and siRNA guide strand complementary sequences. Cy-5 conjugated siRNA had the same sequence, but the fluorophore was conjugated at the 5′

end of the anti-tdTomato passenger strand.

| Primer | Sequence |
|---|---|

| | |
|---|---|
| TdTomato - Forward | 5'-GACAACAACATGGCCGTC-3' |
| TdTomato - Reverse | 5'-GGTCTGGGTGCCCTCGTA-3' |
| β-actin - Forward | 5'- GAAGTGTGACGTTGACATCC -3' |
| β-actin – Reverse | 5'- ACTCATCGTACTCCTGCTTG -3' |

## 3.3 Blood sourcing and ethical approvals

The whole blood of the sheep used for EV preparation described in **Chapter 6** was supplied by the Veterinary Faculty (University of Ljubljana, Slovenia) in homemade Alsever's medium (pH 6.1) and used within 1 week. Red blood cells for the preparation of DCC-siRNA-EMVs (**Chapter 6**) and EMV-hybrid coatings (**Chapter 7**) were obtained from the Transfusion Center of Ljubljana (ethical approval number 0120-592/2020/7) and belonged to two young anonymous males, a RhD+ blood type supplemented with CPD-SAGM preservative, 70% v/v hematocrit, accounting for 4 × 109 RBCs per ml. The experiments involving live animals were approved by the Ministry of Agriculture, Forestry and Food of the Republic of Slovenia (permissionno. U34401-35/2020/8).

## 3.4 Nanoparticles preparation and basic characterization and storage

### 3.4.1 Erythrocytes membrane vesicles (EMVs) preparation

EMVs are prepared from erythrocytes (fresh, stored at -80°C in Alsever's solution, human or sheep) via the hypotonic lysis method [208]. Briefly, 1 ml of erythrocytes is dispersed in 40 ml of 0.1x PBS (where the composition of 1x PBS is 10 mM phosphate buffer, 137 mM sodium chloride, and 2.7 mM potassium chloride) and incubated at 4°C for one hour or overnight. Afterwards, the suspension was centrifuged multiple times to remove excess hemoglobin. The incubation with a hypotonic buffer causes the opening of transient pores in the cell membrane, and the hemoglobin can subsequently flow outside toward the gradient [308]. After 4 rounds of washing, the pellet was rehydrated with 1x PBS containing the molecule of interest to be loaded (indocyanine green, IR-820, or siRNA). Afterwards, the suspension was sonicated in a sonicating finger (Vibra Cell) for 10 s (1 second on, 1 second off) and extruded at 37°C at 800 nm five times and via 200 nm membranes 15 times in an Avanti Polar Mini extruder. Sonication and extrusion confer the shear force necessary to break down and reduce the size of self-assembled, multilamellar liposomal suspensions, and it is also applicable to whole cells, such as in the case of erythrocyte ghosts [309]. During the photostability assays in [54], extrusion was avoided to keep the ICG/IR820 concentration constant

#### 3.4.1.1 Density-changing centrifugation (DCC)

To select only the most dense siRNA-packed EMVs, a protocol was adapted [310]. This allows selection on the basis of the mixed effects of changed solubility and density rather than time-consuming sucrose gradient ultracentrifugation. Heavier and denser EMVs will be found in the upper layer of the tube with decreasing siRNA concentration while approaching the bottom, where protein and other cellular debris, together with

unloaded siRNA, will be pelleted. A solution of 20% trisodium citrate (w/v) in PBS was added to an ultracentrifuge tube, and the siRNA-EMV suspension was carefully pipetted on top of it. The final volume ratio of the TC solution to the siRNA-EMVs was 1:1. The tubes were subsequently centrifuged in a Beckman Coulter Optima XPN-90 ultracentrifuge equipped with an SW 60 Ti swinging bucket rotor for 40 minutes at 4°C and 100.000 × g (27.200 rpm). Eight 0.25 mL fractions were then collected and subjected to analysis. The six top fractions were determined to contain siRNA via a Quantifluor RNA assay. The TC was removed with an Amicon centrifugal device, 10 kDa NMWL (EMD Millipore, UFC8010). Finally, the DCC-siRNA-EMVs were resuspended in PBS and stored at 4°C until further use. The prepared DCC-siRNA-EMVs were used for all further in vitro and in vivo experiments without any further addition.

The rationale behind DCC exploits density deltas among the colloidal suspension. The heaviest particles, but capable of floating—a tightly closed liposome-like suspension—accumulated toward the top of the tube after centrifugation; the particles incapable of floating, i.e., cell debris or unloaded siRNA—pelleated at the bottom of the tube.

### 3.4.2 Liposomes preparation

Liposomes are prepared via the conventional thin film method. In the case of [54], a mixture of phospholipids composed of DPPC (1,2-dipalmitoyl-sn-glycero-3-phosphatidylcholine), DSPE-PEG2000 (N-[carbonyl-methoxy(polyethylene glycol)-2000]-1,2-distearoyl-sn-glycero-3-phosphoethanolamine) and MSPC (1-myristoyl-2-stearoyl-sn-glycero-3-phosphocholine) was used. This formulation is clinically approved (DPPC/MSPC/DSPE- mPEG2000 = 90:10:4 molar ratio, i.e., low-temperature-sensitive formulation, ThermoDox®). MSPC is a lysolipid, i.e., sporting only one acyl tail, and, upon mild heating (approximately 41°C, as the DPPC transition temperature to liquid-crystalline from the gel ordered phase), tends to leave the double layer, effectively releasing the internal content. Above a certain temperature, a lysolipid tends to reside in the solution rather than in the double layer, reaching its critical micelle concentration and effectively creating pores in the liposomes [311]. For **Hypothesis 6** and **Chapter 7** formulation preparation, the addition of a lysolipid was avoided.

In the thin-film method, the lipids are mixed from chloroform/methanol at a precise molar ratio; the organic solvent is then evaporated under continuous rotation in Rotavapor equipment (R-100 equipped with a heating bath, Interface I-100, and vacuum pump V-100; Bunchi, Switzerland) and allowed to dry completely. This mixture is subsequently rehydrated at temperatures higher than the melting point of the main lipid with an appropriate water-based buffer containing the molecule that it is intended to encapsulate; at this point, any phospholipid suspension spontaneously forms multilamellar liposomes [309]. For the encapsulation of cyanine dyes, the thin film was rehydrated with PBS containing 30 µg/ml ICG or IR-820. Multilamellarity is reduced, and the size of liposomes is equal when shear stress- and pressure-based techniques, such as ultrasonic sonication and extrusion, are used. More specifically, for Thermodox-based liposomes (excluding the Doxil drug, therefore only the DPPC-DSPE-PEG2000-MSPC phospholipid formulation), we allowed the thin film to rehydrate at 60°C while extruding it 5 times via the 800 nm pore membrane, 10 via the 200 nm membrane, and 20 via the 100 nm membrane. During the photostability assays described in **Chapter 5**, extrusion was avoided to keep the ICG/IR820 concentration constant.

To summarize how liposomes are employed in the present thesis, compared with the EMVs used for cyanine dye experiments in **Chapter 4** and without MSPC, additional phospholipids are used to generate the coating material in **Chapter 7**.

### 3.4.3 Labeling with lipophilic trackers

EMVs and liposomes (as described in **Chapters 6** and **7**) were labeled with lipophilic trackers, such as DiI, DiO, and DiD, according to the manufacturer's specifications. Erythrocyte ghosts were incubated in PBS with 1 µM dye for any experiment, while thin films were rehydrated with buffer containing the same concentration. Erythrocyte ghosts and rehydrated thin films were incubated with the dye for 15 minutes at 37°C, then incubated for 15 minutes at 4°C, and then briefly washed by centrifugation.

### 3.4.4 GXS5 (Genipin-polyamine-glycine) polymers preparation and siRNA complexation

GXS5 nanoparticles are composed of a mixture of genipin crosslinked with spermine/spermidine polyamines, whose polymerization chain is blocked by the addition of glycine, a small amino acid with only one amino group. The reaction kinetics and mechanism of action are explained in **Paragraph 1.7.1** "Biomedical applications of genipin and mechanism of action". In a buffered solution (pH 7, 10 mM phosphate buffer, 137 mM sodium chloride, and 2.7 mM potassium chloride), genipin, spermine and glycine were added at a molar ratio (relative to genipin) of 1:5:1/5/10, with a variable concentration of glycine. Notably, genipin reacts only with unprotonated amines, requires oxygen and has extremely long reaction times at neutral pH in the presence of biomolecules [312]; therefore, the obtained suspension was incubated for 36 hours with vigorous shaking in the presence of air. The nanoparticles were subsequently purified via size exclusion purification.

In the present thesis, GxS5 polymers are employed in the confirmation of **Hypotheses 6** and **7** and in **Chapters 7** and **8**.

#### 3.4.4.1 Size exclusion purification (GxS5 polymers and ICG/IR-820 EMVs)

For ICG/IR820-loaded EMVs, an easy table-top, scaled-down, size exclusion chromatography protocol was applied to remove the unloaded cyanine dye particles [54]. Commercially available, Sepharose-packed columns are commonly employed for either buffer exchange or solute removal for nanoparticulate suspensions. Sepharose (a portmanteau of *separation-pharmacia-agarose*) is the tradename for a crosslinked, beaded form of agarose and therefore a porous, gel-like matrix with a lattice of various areas; it is registered by Cytiva (formerly GE Healthcare). The rationale of this technique relies on the differential ability of a nanoparticle suspension, depending on the bulk size of the particles, to enter the lattice of the packed column: incapable of entering the lattice, the largest particles are promptly eluted upon addition of the buffer; the smallest particles will enter the lattice and will be eluted last. Therefore, in [54], from a sample volume of 1 ml, the ICG/IR820-loaded EMVs are eluted after the addition of 5/6 ml, for a total wash volume of 20 ml of the column (PD-10 column, GE-Healthcare). Similarly, in the case of GxS5 polymers [252], the almost spherical, larger, and dispersed nanoparticles are eluted after the addition of 6/7 ml of DEPC water, whereas the unreacted spermine and glycine are eluted last.

### 3.4.5 Freeze drying of DCC-siRNA-EMVs and GxS5 polymers

Long-term storage was optimized for both DCC-siRNA-EMVs and GxS5 polymers. First, various cryoprotectants were tested (50 mM sucrose/trehalose, presence and absence of 2.5% PVP40). Briefly, DCC-siRNA-EMVs were concentrated, dispersed in a PBS solution containing the cryoprotoprotectant, flash-frozen in liquid nitrogen and subsequently freeze-dried in a Martin Christ table-top freeze-drier. After rehydration, the loss of siRNA content (in the eluted volume of ultrafiltration with Amicon 30 kDa centrifugal devices), together with the ultrastructure of the siRNA, was checked via transmission electron microscopy (TEM), as in negative-stain transmission electron microscopy (TEM). On the other hand, for the GxS5 polymers, after size exclusion purification and elution with DEPC water, no cryoprotectants were added, and lyophilization was carried out on the same Martin Christ table-top freeze-drier. The polymers were rehydrated to 20 mg/ml in 1× PBS after storage at RT.

### 3.4.6 UV/Vis and fluorescence readings

The total UV/Vis spectra presented in this thesis were acquired either on a Lambda950 UV/VIS/NIR spectrometer (PerkinElmer, Waltham, MA, USA) or on a Synergy Microplate Reader (Biotek). The latter was also used for fluorescence spectra.

### 3.4.7 Superresolution Fluorescence Microscopy

The total UV/Vis spectra presented in this thesis were acquired either on a Lambda950 UV/VIS/NIR spectrometer (PerkinElmer, Waltham, MA, USA) or on a Synergy Microplate Reader (Biotek). The latter was also used for fluorescence spectra.

### 3.4.8 Quantification of siRNA via Quantifluor assay

The most common quantification method for nucleic acids is the use of an intercalating dye whose fluorescence emission is stronger when intercalated in the double strand [313]. This effect has been used to develop multiple proprietary assays and molecules, in addition to the well-established but cancerogenic ethidium bromide [314]. In our case, we chose the QuantiFluor RNA System assay developed by Promega, which can be used either with the proprietary Quantus™ Fluorometer or in a microplate-based assay. The fluorophore dye therefore inserts within double-stranded sections of the RNA, those accessible to the solvent. It can be used for absolute quantification via a calibration curve using a reference RNA of known concentration. The following equation was used to quantify the efficiency of siRNA encapsulation in [208], [252] (**Equation (1)**):

$$EE\ \% = \frac{\mu g\ of\ siRNA\ in\ DCC{-}EMVs}{\mu g\ of\ added\ siRNA} \times 100 \quad \text{(Equation 1)}$$

### 3.4.9 Quantification of lipids and proteins in EMVs/ghosts

For the quantification of proteins in erythrocyte ghosts and EMVs, the widely used Bradford assay was used, with bovine serum albumin used as a standard (2 mg/ml standard). An in-house assay was prepared according to the conventional recipe [315] with a final 1:30 v/v ratio of sample to assay. Moreover, for lipid quantification, a Stewart assay, another colorimetric assay based on ferric chloric hexahydrate and ammonium thiocyanate in a chloroform solution, which uses a heart lipid extract (Avanti Polar) as a standard, was used [316]. While the Bradford assay was carried out in microplates (96 wells) and

visualized on a Synergy Microplate (Biotek) reader, for the Stewart assay, a quartz cuvette and a UV/Vis spectrophotometer were used because of the presence of chloroform.

### 3.4.10 Quantification of primary and secondary amines in GxS5 polymers

For the quantification of the primary and secondary amines present in the GXS5 polymers, the ninhydrin assay was used. Ninhydrin is a compound capable of forming a purple complex with primary and secondary amines. The final assay conditions were a 2 mg/ml concentration of ninhydrin in absolute ethanol at a 1:5 volume ratio with the assayed suspension/standard. As a standard reference, spermine in aqueous solution was used [317]. The reaction was carried out in Eppendorf tubes, heated at 85°C for five minutes and allowed to cool at room temperature for one hour. The final absorbances of both the samples and standards were recorded at 290, 350, 400 and 570 nm. The obtained amount of amines was then termed the "*total nitrogen concentration*".

### 3.4.11 Laser irradiation on ICG/IR820 EMVs/liposomes for photostability/photothermal effect

To test the photostability of cyanine-carrying nanoparticles in [54], an n FC-808 Fiber Coupled Laser System (CNI Optoelectronics Tech, Changchun, China) configured for continuous-wave operation at 808 nm with different powers was used. This experiment mimics real-life conditions for cyanine dyes to exert their photothermal activity [318]. The laser light was focused on a quartz cuvette (size $1 \times 1 \times 3$ $cm^3$) via an optical lens with a spot size of approximately 8 mm. PBS was used as a control. The employed laser power was P = 0.5, 1, or 3 $W/cm^2$ for 5 min. The temperature of the liquid samples (volume of 1 mL) was measured with a J-type Teflon thermocouple that was immersed in the cuvette and connected to a computer to collect the data in real time. The UV/Vis spectra of the irradiated samples were subsequently visualized in triplicate on a microplate.

### 3.4.12 Dynamic light scattering (DLS) and Zeta-potential measurements

DLS is a widely used technique, useful to characterize the size, size distribution and surface charge (termed Z-potential) of nanoparticles distribution. It is based on the Brownian motion of the particles, i.e. the random movement of small objects in aqueous solution; when hit by a laser beam, smaller particles move faster, bigger particles move slower. According to an autocorrelation function, the diffusion coefficient is calculated by the built-in software of the equipment; the Stokes-Einstein equation then allows the calculation of the hydrodynamic diameter ($d_h$, Equation 2). Additional proprietary algorithms, such as Antoon Paar's Kallyope, permit to weight the recorded events according to their refractive indexes, obtaining different information according to the nature of the nanoparticles. Moreover, more advanced algorithms are also able to calculate the surface, number or volume weighted size of the nanoparticles.

$$d_{h=} \frac{k_b T}{3\pi\eta D} \quad \text{(Equation 2)}$$

where:

- $K_b$ = Boltzmann constant

- T = Temperature (Kelvin)
- $\eta$ = Viscosity of the medium
- T = Diffusion coefficient

Also, DLS calculated the polydispersity index (PDI) of the suspension, ranging from 0 to 1, where a 0 value corresponds to hypothetically size uniform particles. DLS assumes particles to be spherical and Anton Paar Litesizer 501 allows three angles of measurement (i.e. the angle in which the laser beam impacts with the cuvette), 15° (*forward scatter*), 90° (*side scatter*) and 175° (*back scatter*). Within [54], [208], backscattering was used, as more reliable for heavily concentrated suspension, with volume-weighted algorithm; in [252], for GXS5 polymers, forward scatter settings were used, due to their low refractivity and high PDI. Litesizer by Anton Paar allows also for Zeta potential measurement, given in millivolt units: in this case, the zeta potential is measured on the counter-ions on the particle surface, defined as electro-chemical double layer. Reusable Omega Cuvettes from Anton Paar were used for all measurements.

## 3.5 Microscopy techniques used in Chapter 6 and 7

### 3.5.1 Negative-stain transmission electron microscopy (TEM)

Liposomes and EMVs are composed of phospholipoids that have low electron density and cannot be visualized under regular transmission electron microscopy (TEM) conditions. Therefore, to enhance the contrast, a negative stain is used. The name describes how the dye acts: electron-dense compounds that surround the sample and that appear bright against a dark or dark gray background. Usually, heavy metal salts and weak acids with high lipophilicity, such as osmium tetroxide, uranyl acetate, phosphotungstic acid, yttrium salts, and ammonium molybdate, are used. The technique requires a formvar or collodion-coated TEM grid, nickel-copper, to better adhere the sample to the substrate. Unfortunately, the salts need to be dissolved in a percentage of ethanol (up to 10% v/v) that can harm particularly susceptible samples; moreover, yttrium salts and phosphotungstic acid are susceptible to mildly acidic pH, collapsing into crystals rather than entering the phospholipid double layer. Overall, negative staining is a fast and easy technique that can lead to artifacts and misinterpretations. In the case of EMVs, a drop of 7–10 µl is blotted onto the Co grid and allowed to adhere for 15 minutes, after which the excess water is removed; prefixation with paraformaldehyde can help preserve the sample on the grid for longer periods. Afterwards, the grid was placed on a drop of negative stain (UA Zero from Agar Scientific) for 30 s, allowed to dry and imaged on a Jeol JEM-2100.

### 3.5.2 Cryo-TEM and freeze fracture microscopies

Cryo-TEM is a nondestructive technique that allows reliable imaging of low-contrast biological samples, eliminating the chance of possible dye-related artifacts. The EMV suspension (DCC with and without siRNA) was subjected to flash freezing via Vitrobot Mark IV and imaged on Quantifoil® R 2/2, 200 mesh holey carbon grids via a 200 kV Glacios microscope. On the other hand, freeze fracture microscopy provides insight into the internal side of the assayed nanoparticles: the same set of samples used for cryo-TEM was also prepared for freeze fracture TEM. The samples were mixed 1:1 with 60% glycerol, frozen in liquid nitrogen, transferred to a freeze-fracture device (BALZERS, BAF200),

fractured (knife temperature of −150°C), shadowed with carbon-platinum (nominal angle of 45°) and further strengthened with carbon (nominal angle of 90°). The obtained replicas were cleaned overnight in a sodium hypochlorite solution, subsequently collected on copper microscopic grids and examined with a CM100 transmission electron microscope (Philips, Netherlands) running at 80 kV. CryoTEM was used in Chapter 6 to characterize EMVs and DCC-EMVs and in Chapter 7 to investigate the ultrastructures of DPPC-DSPE-PEG2000/EMV hybrids and hybrid-camouflaged G10S5.

### 3.5.3 Atomic Force Microscopy, used in Chapter 7

Atomic force microscopy is a nondestructive technique that is useful for investigating the surface properties of soft and stiff samples at the nanometer scale. It works by scanning a sharp tip attached to a flexible cantilever across a sample's surface. As the tip interacts with the surface (via weak interactions), it deflects, according to Hooke's law. A laser beam reflected off the cantilever measures these deflections, and a computer uses that data to construct a 3D image of the surface. It can work in two main modes: contact and tapping. In contact mode, the tip is kept close to the surface, and it scans it via cantilever deflection; in this case, the spring constant of the cantilever is instrumental for the sensitivity and resolution of the scans (the less rigid the spring constant is, the better the signal). In tapping mode, the AFM cantilever oscillates up and down near its resonance frequency, typically using a piezoelectric element. Contact with the surface is therefore fast, and in this technique, the cantilever can be worn out less at the end of the measurement.

Furthermore, AFM can image nonconductive and biological samples in both settings. The following operating conditions can be adapted to a sample: air, vacuum, or liquid.

For the experiments in Chapter 7, an AFM Digital Instruments Dimension 3100 was operated in contact mode, and the cantilever (ContGD-G-10, gold contact mode AFM probe; spring constant of 0.2 N/m, frequency of 13 kHz, beam shape) was obtained from Nanoandmore GMBH. The samples (EMVs, G10S5, hybrid membranes, liposomes, and camouflaged G10S5) were mounted on polylysine-coated glass (Sigma–Aldrich, P0425), allowed to adhere, gently washed with 0.2 µm filtered water to remove salts and allowed to dry.

## 3.6 Cell biology methods used in Chapter 5, 6, 7

### 3.6.1 Cell culture condition

Cell tests were carried out at the Oncology Institute of Ljubljana, at the K9 Advanced Materials Department of Institute Jozef Stefan and at the B3 Department of Biotechnology of Institute Jozef Stefan. All media (RPMI, DMEM and GMEM) were supplemented with GlutaMAX (100x, Gibco), 5% fetal bovine serum (FBS, Gibco), and penicillin–streptomycin (100x, Sigma–Aldrich, Merck, Darmstadt, Germany). The cells were routinely tested for mycoplasma infection via the MycoAlertTM PLUS Mycoplasma Detection Kit (Lonza, Basel, Switzerland) and were mycoplasma free. While all the other cell lines were grown in DMEM (Advanced Dulbecco's modified MEM) or GMEM (Glasgow's MEM), the CT26 and 4T1 cells were cultured in Advanced Roswell Park Memorial Institute 1640 medium (RPMI-1640, Gibco, Thermo Fisher Scientific, VA, US). Lymphoblastoid cells were cultured in RPMI 1640 (Gibco, Thermo Fisher Scientific, Waltham, Massachusetts, USA) supplemented with 15% FBS and 100 U/mL penicillin/streptomycin. The conditions were, in all cases, a 5% $CO_2$ atmosphere at 37°C.

### 3.6.2 Cytotoxicity test

GxS5 polymer cytotoxicity was tested in murine melanoma B16F10 (CRL-6475), kidney epithelium-like 293T (CRL-3216), undifferentiated colon carcinoma CT26 (CRL-2638), and human stage IV breast cancer 4T1 (CRL-2539) cells at various concentrations. A total of 1500 cells were seeded on a 96-well plate and incubated with the polymers for 72 hours. The Presto Blue assay was subsequently employed to determine cell growth (fluorescence/emission at 590/560 nm measured after 1 hour of incubation, read on a Cytation 1 system by BioTek Instruments). Furthermore, HaCat cells (PCS-200-011, 20,000 cells in a 24-well plate) were incubated with GXS5 polymers for 72 hours at various concentrations, and the Presto Blue assay was used to determine cell viability. For EMV cytotoxicity, the same protocol used for GxS5 was followed, with the addition of Hulec-5a (CRL-3244) and NHLF cell lines. To assess the cytotoxicity of DPPC-DSPE-PEG2000/EMVs camouflaged with G10S5 (Chapter 7), B16F10 and NHLF were employed, and a Presto Blue assay was similarly used. For determination of lymphoblastoid cell viability, 200,000 cells per well in a 24-well plate were seeded the day prior to the addition of the carriers. After incubation with DPPC-DSPE-PEG2000/EMVs camouflaged with G10S5 (hybrid-G10S5), 4% trypan blue in water was added to the cells, and the cells were allowed to grow. was determined via a Countess 3 automated cell counter. The same settings (focus = 65 and light = 37) were used to estimate the percentage of dead cells. The experiment was repeated three times with two technical replicates. [319].

### 3.6.3 B16F10 in vitro transfection with EMVs, GxS5 and Hybrid-G10S5

B16F10 (ATCC number CRL-6475) is a well characterized, immortalized murine melanoma cell line. TdTomato expressing B16F10 were chosen as the model cell line for both the nanoparticles examined in this thesis, i.e. GxS5 polymers and EMVs. A custom small-interfering RNA was purchased from ThermoFisher, generated via Silencer ™ algorithm. As positive control, RNAiMAX was used. In both [208], [252], 50.000 cells, seeded in a 24-well plate, were transfected with 30 picomoles of siRNA, contained either in RNAiMAX, GxS5 polymers or DCC-siRNA-EMVs. After 48 hours of incubation, RNA extraction was carried out as in "Quantitative Reverse Transcriptase Polymerase chain reaction of tdTomato mRNA". The experimental setting was similar, for DPPC-DSPE-PEG2000/EMVs camouflaged G10S5 (Hybrid-G10S5), but doses of 5 and 10 picomoles were used.

### 3.6.4 Lymphoblastoid cells in vitro transfection with G10S5 and Hybrid-G10S5

Small interfering RNA (siRNA) targeting FARSA (phenylalanyl-tRNA synthetase alpha chain; UniProt ID: Q9Y285) was used as part of an ongoing characterization of lymphoblastoid cells (Malnar Črnigoj et al., 2023). Two hundred thousand cells per well in 24-well plates were seeded the day prior to transfection. Protein knockdown was assessed by Western blotting of the FARSA protein 72 hours posttransfection with siRNA-loaded carriers (20 and 30 pmol). Flow Cytometry

To quantify B16F10 uptake by GxS5 polymers in complex with or without siRNA, flow cytometry (BD FACSymphony™ A3 Cell Analyzer) was used. After being trypsinized and

washed, the cells were stained with DAPI (3 µg/ml) after coincubation for 72 hours with GxS5 polymers, and the intrinsic orange fluorescence of the polymers was used to quantify the internalization in the PE channel. The data are reported as the median fluorescence intensity.

### 3.6.5 Hemotoxicity study

To evaluate the hemotoxicity of ICG/IR820 EMVs/liposomes and GxS5 polymers, fresh red blood cells were employed, and their hemoglobin release at 541 nm was checked. In the case of cyanine dye-containing EMVs, sheep red blood cells (from the Veterinary Faculty of Ljubljana) were washed and stored in 1× PBS and subsequently incubated with the carriers for 3 h at 37°C under gentle shaking; 1× PBS and water were used as negative and positive controls, respectively. After incubation, the cells were pelleted (1500 rpm, 4 minutes), and the supernatant was analyzed in triplicate in a 96-well plate. The following equation was used for quantification: hemolysis (%)=$100\cdot(A_{\text{sample}} - A_{\text{control}})/(A_{100\%\ \text{dead}} - A_{\text{control}})$.

## 3.7 Molecular biology methods used in Chapter 5, 6, 7

### 3.7.1 Agarose gel assays: RNAse A resistance, dye exclusion assay heparin displacement

As electrophoresis agarose gels have long been used for basic purposes in molecular biology and, in lesser part, proteomics, their nucleic acid resolving capability can also be applied to nanoparticles. Gels can be prestained with UV-excited fluorescent intercalating dyes, e.g., Midori Green and Sybr Gold. Resolved nucleic acids are therefore visualized owing to the fluorescence emitted by the intercalated dye upon UV excitation in a transilluminator. The "molecular sieve" ability of agarose gels was exploited in [208], [252] to test the ability of the carriers (EMVs and GxS5 polymers) to exclude the siRNA from the buffer, which contained a commonly used RNase, Rnase A, from bovine pancreas, for 4 and 24 hours of incubation, 5–50 µg/ml of enzyme. The running buffer of choice, which was also used for gel preparation, was TAE buffer (pH 8.5, 40 mM Tris, 20 mM acetic acid, and 1 mM EDTA sodium salt) diluted 1:10000 with Midori Green dye. In the case of GxS5 polymers, two prerequisite tests were performed: to test the exclusion of siRNA from the buffer due to the electrostatic interaction with GxS5 positively charged nanoparticles, a dye exclusion assay was performed. Briefly, various siRNA backbone phosphate-to-nitrogen ratios (quantified as in **Paragraph 3.4.10** "Quantification of primary and secondary amines in GXS5 polymers") were allowed to run on a 2% w/v agarose gel and then visualized: the stronger the band, the fainter the interaction. A heparin displacement assay was subsequently performed to decomplex the polyplex (polymer/siRNA complex), exploiting the ability of heparin to sequester positively charged nanoparticles. After incubation at various P/N ratios, with the RNase A enzyme, the polyplexes were disassembled via incubation with 2 mg/ml heparin before being subjected to a normal electrophoresis run and visualization on a transilluminator (ChemiDoc gel imager).

### 3.7.2 Quantitative Reverse Transcriptase Polymerase chain reaction of tdTomato mRNA

The gene of choice to be silenced was tdTomato (tandem-dimer tomato), an orange-emitting fluorescent protein derived from Coral *Discosoma* sp. [320], expressed by tdTomato + B16F10 murine melanoma cells. The primers were generated from the mRNA sequence via Primer-BLAST. After the cells were transfected as described in **Paragraph 3.5.3** "B16F10 in vitro transfection with EMVs and GxS5", the mRNA was extracted with PEQgold total RNA (VWR), retrotranscribed via a Scriptase II kit (Nippon genetics, according to the manufacturer's specifications), and subsequently used as a template for qRT–PCR. PowerSybr Green (Applied Biosystems) master mix was used, with 2 ng/µl template. TdTomato mRNA was quantified via the ddCT method, and murine β-actin was used as a calibrator for both EMVs and GxS5-mediated transfection. The primers used are listed in Table 1 and Table 5 of [208], [252].

### 3.7.3 Protein knockdown quantification in lymphoblastoid cells

Lymphoblastoid cells were transfected as described in **Paragraph 3.6.4**. Total protein lysates were prepared via RIPA buffer (50 mM Tris-HCl, pH 8.0; 150 mM NaCl; 0.5 mM sodium deoxycholate; 0.1% SDS; 1% Triton X-100) supplemented with protease inhibitors. The lysates were mixed with 2× SDS loading buffer containing 200 mM dithiothreitol (DTT) and denatured at 95 °C for 5 minutes. Equal amounts of protein were resolved on 12% stain-free SDS–PAGE gels (Bio–Rad, Hercules, CA, USA) at 125 V and transferred to nitrocellulose membranes (GE Healthcare, Chicago, IL, USA) via a semidry transfer system (Bio–Rad). The gels were imaged via the GelDoc System and ImageLab software (Bio-Rad) to assess the total protein load via stain-free technology. Blocking was performed for 1 hour at room temperature with 5% (w/v) skim milk in TBS. The membranes were incubated overnight at 4°C with an anti-FARS-A primary antibody (Proteintech, USA) at a 1:1000 dilution, followed by a 2-hour incubation at 4°C with a StarBright 520-conjugated anti-rabbit secondary antibody (Bio-Rad) according to the manufacturer's protocols. Fluorescent signal detection and imaging were conducted via the GelDoc System and ImageLab software. Densitometric analysis was performed via ImageJ (NIH, Bethesda, MD, USA). FARSA protein levels were normalized to total protein per lane, as quantified via stain-free images.

## 3.8 In vivo assays in Chapter 6

### 3.8.1 DCC-siRNA-EMVs administration to tumor-affected mice: biodistribution

Vybrant-DiO and Cy-5-siRNA containing DCC-EMVs were intravenously injected at a dose of 1.5 mg of siRNA/kg of mouse weight into B16F10 (tdTomato +)-tumor-induced mice (6–8-week-old C57BL/6NCrl, Charles River, Lecco, Italy). The mice were randomly divided into four groups: the control group (n=4), 2 hours after injection (n=5), 24 hours after injection (n=5) and 48 hours after injection (n=5). A more thorough description of the experiment is reported in [208]. Ten minutes after the injection, 100 µl of blood was collected from the retro-orbital blood vessel and used for quantification. At the time of mouse sacrifice, the spleen, lungs, brain, kidneys, tumor, heart and liver were collected and

weighed, and one half of each organ was flash frozen. Additionally, blood was extracted, and plasma was separated from red blood cells and leucocytes via BD Microtainer SST Blood Collection Tubes. The resulting powder was collected and stored at −80°C until further use. The other half of each organ/tumor was fixed in 4% PFA overnight at 4°C and dehydrated in 30% sucrose overnight at 4°C before being embedded in Tissue-Tek O.C.T. compound (Sakura Finetek, VWR) and stored at −80°C for further use.

### 3.8.2 DCC-siRNA-EMVs administration to tumor-affected mice: RNA interference quantification and tdTomato fluorescence

Similarly, for Cy-5/DiO EMVs, a single dose of unlabeled DCC-siRNA-EMVs was injected into 6 tumor-induced mice, which were sacrificed after 48 hours. As negative controls, a similar amount of naked siRNA and a similar volume of 1× PBS were injected into n=5 and n=4 mice, respectively. The fluorescence of the tdTomato-B16F10-induced tumors was monitored via a SteREO Lumar V12 fluorescence microscope (Zeiss) at 2, 24 and 48 hours. Images were processed via ImageJ, which was also used for the quantification of tdTomato fluorescence. Furthermore, after 48 hours and for controls, the tumors were processed for RNA extraction with a mirVANA MagMax kit (Thermo Fisher), and tdTomato mRNA was quantified as described in **Paragraph 3.6.2** "Quantitative reverse transcriptase polymerase chain reaction of tdTomato mRNA".

## 3.9 Stem-loop PCR for quantification of siRNA guide-strand in tissues and plasma

The other half of each organ (spleen, lungs, brain, kidneys, tumor, heart and liver) was processed for RNA extraction with liquid nitrogen and a mortar and pestle. The weight of each powdered organ subsequently used for RNA extraction was noted (≤ 15 mg), and for RNA extraction, a mirVANA MagMax kit (Thermo Fisher) was used. A TaqMan assay, specifically for anti-tdTomato siRNA, was purchased from Applied Biosystems and contained a proprietary reverse transcriptase primer (5 ng of initial total RNA/reaction, with a MicroRNA Reverse Transcription Kit). The resulting cDNA was subsequently used as a template for stem–loop PCR via a TaqMan real-time PCR kit. A standard curve was generated from naked siRNA, where 5 nanograms were subjected to serial dilutions, retrotranscripted and used as a template for qPCR. For the quantification of siRNA quantities in the tissues, the following equation was used (Equation 3):

$$\frac{\frac{ng\ of\ duplex}{grams\ of\ processed\ tissue}}{} = ng\ in\ PCR\ reaction \times \frac{RNA\ stock\ concentration}{DF_{cDNA-qPCR} \times DF_{RNA\ stock-cDNA} \times Elution\ volume \times amount\ of\ processed\ tissue\ (g)}$$

(Equation 3)

A similar approach was used for quantification of siRNA in plasma; these data were then used to calculate pharmacokinetic parameters of DCC-siRNA-EMVs with the help of PKSolver Excell add-in [321]. Stem Loop PCR is a technology developed for quantification of short RNAs, such as miRNAs, since regular qPCR requires a template at least 200 nt long; therefore, during retrotranscription, a special primer, containing a stem-loop

structure, is added. Such primer has a specificity at the 3' end of the siRNA sequence, preventing non-specific binding due to steric hindrance. This primer is also retrotranscribed during the regular RT stage. During qPCR, the forward primer is specific for the siRNA sequence, while the reverse prime targets the stem-loop sequence; a TaqMan fluorescent probe is also added to the master mix, and it binds specifically to the amplified siRNA cDNA, emitting fluorescence proportionally to the initial siRNA template quantity [322].

## 3.10 Fluorescence microscopy in Chapter 6

### 3.10.1 Internalization of DCC-siRNA-EMVs in B16F10, CT26 and NHLF

To determine whether and how the DCC-siRNA-EMVs were internalized by the abovementioned cell lines, they were incubated with CM-DiO-labeled carriers containing Cy-5-labeled siRNA. The cells were incubated with DCC-siRNA-EMVs for 24, 48 and 72 hours, washed, labeled with the MemBrite® Fix 488/515 Cell Surface Staining Kit (Biotium) and Hoechst 33342, following the manufacturer's instructions, fixed with 4% PFA, mounted with Prolong Glass Antifade Mount (Thermo Fisher Scientific) for 24 h at RT, and then sealed with nail polish. Finally, the samples were imaged with an LSM 800 confocal microscope (Carl Zeiss, Oberkochen, Germany). This experiment allows precise estimation and theorization of EV internalization pathways.

### 3.10.2 Fluorescence-aided tissue biodistribution of DCC-siRNA-EMVs

As stated, half of each organ (spleen, lungs, brain, kidneys, tumor, heart and liver) was saved and prepared for fluorescence microscopy. From each organ, 14 µm thick slices were cut with a Leica CM1850 cryostat and collected on SuperFrost Plus slides; nuclei were labeled with 3 µg/mL Hoechst 33342 nuclear stain, the sections were mounted with ProLong Glass Antifade Mountant and the coverslip 1.5# was sealed with nail polish. The slides were subsequently imaged on an Axio Observer 7. tdTomato fluorescence intensity in tumors was quantified using ImageJ suite. With this approach, the fine distribution of EMVs within tissues can be appreciated.

## 3.11 Statistical analysis

In all cases, Graphpad 9.0 or 10.0 (Prism) was used for statistical analysis. For q-RT PCR, tdTomato and β-actin gene expression, CTs data were trimmed with built-in Graphpad 10 outlier recognition algorithm. Dall datasets were tested for normality or lognormality before any stat test. ANOVA, two or one way, were used for normally distributed data, while non-parametric Kruskall-Wallis was used for lognormal data. For all purposes and in all papers, significance was determined as $p \leq 0.05$ *, $p \leq 0.01$ **, $p \leq 0.001$ ***, $p \leq 0.0001$ ****

63

# Chapter 4

# Cyanine dyes for Photo-Thermal Therapy: A Comparison of Synthetic Liposomes and Natural Erythrocytes-Based Carriers

In this work, we aimed to compare the properties of an approved liposomal formulation Thermodox, used for Doxil delivery, with those of a nanocarrier derived from an erythrocyte membrane, hereby named erythrocyte membrane vesicles (EMVs). Indocyanine green (commercially known as cardiogreen) is an approved infrared dye for imaging cardiac and eye blood vessels and is generally regarded as safe [323]. It binds quickly to plasma protein upon intravenous injection [324] but has a short circulation time (3–4 minutes). Furthermore, indocyanine green and a related dye (IR-820) are capable, upon IR-laser irradiation, of photothermal effects coupled with a singlet oxygen-based radical degradation pathway [325]. This moderate and local increase in temperature paves the way for in vivo mild photodynamic therapy and photothermal therapy [326]. It has been shown that cyanine degradation products upon laser irradiation have potentially mitochondria-bound toxic effects [325], [327]. Finally, the degradation of NIR dyes seems to be related to the proximity of monomers and/or their aggregation in dimers and trimers and, therefore, a more favorable diffusion of singlet oxygen that would lead to decomposition [328]. Loading into nanocarriers to stabilize the monomeric form of the dyes would improve their photothermal properties while reducing the amount of cytotoxic degradation products, i.e., the leucoforms arising from the decomposition of parental cyanine dyes. Moreover, erythrocytes have been proven to be suitable starting materials for biomimetic nanocarriers. Finally, a suitable alternative to ICG is IR-820, a similar, but more stable, cyanine dye [284].

With these bases, we aimed to compare either a) a thermally sensitive liposomal formulation containing a lysolipid (MSPC) or b) erythrocyte membrane vesicles, which are ICG and IR-820 carriers. c) Photothermal performance and degradation of ICG and IR-820. Thermodox-based liposomes decomplex once their lipid transition temperature is reached, and for this reason, they are widely used for photodynamic therapy. Our findings revealed that loading ICG in EMVs not only stabilizes their monomeric form, as measured by the decrease in absorbance after IR-laser irradiation but also does not affect the hemolytic activity of Thermodox-ICG formulations. ICG and IR-820 are highly likely localized within the phospholipid double layer. Therefore, EMVs exhibit great potential as near-infrared dye carriers. Finally, we confirmed the superiority of ICG as a photothermal agent with respect to IR-820, since, under our experimental conditions, it showed the same degradation rate but a lower heat generation.

In this paper, **Hypothesis 4 was assayed and confirmed**.

International Journal of *Molecular Sciences*

MDPI

*Article*

# Cyanine Dyes for Photo-Thermal Therapy: A Comparison of Synthetic Liposomes and Natural Erythrocyte-Based Carriers

**Giulia Della Pelle [1,2,*], Andrea Delgado López [3], Marina Salord Fiol [3] and Nina Kostevšek [1,*]**

[1] Department for Nanostructured Materials, Jožef Stefan Institute, 1000 Ljubljana, Slovenia
[2] Jožef Stefan International Postgraduate School, 1000 Ljubljana, Slovenia
[3] Faculty of Pharmacy and Food Science, University of Barcelona, 08028 Barcelona, Spain; andrea.delgadolopez98@gmail.com (A.D.L.); marina1325@hotmail.es (M.S.F.)
* Correspondence: giulia.della.pelle@ijs.si (G.D.P.); nina.kostevsek@ijs.si (N.K.)

**Abstract:** Cyanine fluorescent dyes are attractive diagnostic or therapeutic agents due to their excellent optical properties. However, in free form, their use in biological applications is limited due to the short circulation time, instability, and toxicity. Therefore, their encapsulation into nano-carriers might help overcome the above-mentioned issues. In addition to indocyanine green (ICG), which is clinically approved and therefore the most widely used fluorescent dye, we tested the structurally similar and cheaper alternative called IR-820. Both dyes were encapsulated into liposomes. However, due to the synthetic origin of liposomes, they can induce an immunogenic response. To address this challenge, we proposed to use erythrocyte membrane vesicles (EMVs) as "new era" nano-carriers for cyanine dyes. The optical properties of both dyes were investigated in different biological relevant media. Then, the temperature stability and photo-stability of dyes in free form and encapsulated into liposomes and EMVs were evaluated. Nano-carriers efficiently protected dyes from thermal degradation, as well as from photo-induced degradation. Finally, a hemotoxicity study revealed that EMVs seem less hemotoxic dye carriers than clinically approved liposomes. Herein, we showed that EMVs exhibit great potential as nano-carriers for dyes with improved stability and hemocompatibility without losing excellent optical properties.

**Keywords:** indocyanine green; IR-820; liposomes; erythrocyte membrane vesicles; photo-thermal therapy

check for updates

**Citation:** Della Pelle, G.; Delgado López, A.; Salord Fiol, M.; Kostevšek, N. Cyanine Dyes for Photo-Thermal Therapy: A Comparison of Synthetic Liposomes and Natural Erythrocyte-Based Carriers. *Int. J. Mol. Sci.* **2021**, *22*, 6914. https://doi.org/10.3390/ijms22136914

Academic Editors: Agnes Csiszár and Bernd Hoffmann

Received: 18 May 2021
Accepted: 25 June 2021
Published: 27 June 2021

**Publisher's Note:** MDPI stays neutral with regard to jurisdictional claims in published maps and institutional affiliations.

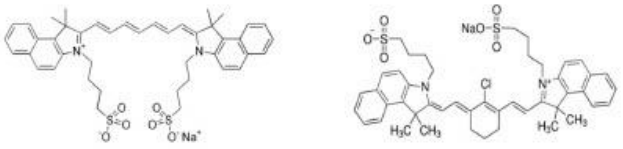
**Copyright:** © 2021 by the authors. Licensee MDPI, Basel, Switzerland. This article is an open access article distributed under the terms and conditions of the Creative Commons Attribution (CC BY) license (https://creativecommons.org/licenses/by/4.0/).

## 1. Introduction

Cyanine fluorescent dyes are widely used as diagnostic or therapeutic agents. Indocyanine green (ICG) is a tricarbocyanine dye that absorbs and emits in the near-infrared (NIR) region of the spectrum (peak spectral absorption at about 800 nm) and has small absorption in the visible range [1]. The absorbed light is then emitted in the form of fluorescence and heat [2]. Due to its optical properties, ICG is a contrast agent commonly used for in vivo cardiovascular fluorescence imaging and NIR optical imaging for intervention in cases of lymphatic abnormalities [3,4]. It was clinically approved in 1959 by the Food and Drug Administration but was widely used during the Second World War for fluorescence-aided surgery [5,6]. It has been investigated as a photo-thermal agent and photo-sensitizer as well [7]. Not being a good source of singlet oxygen, its possible applications in photodynamic therapy are limited [8]. Despite its excellent optical properties, ICG has some disadvantages for biological applications because of its short plasma residence time (2–4 min), instability in aqueous solutions, and concentration-dependent peak emission location [9]. Despite excellent imaging and clearance properties (ICG follows an almost entirely bile juice route for clearance and has no known metabolites [10]), there are some concerns about its safety in limited applications. The latter is the case of retinal toxicity [11] arising from decreased mitochondrial activity while exposed to a light source, while increasing DNA synthesis. It has been earlier demonstrated that ICG toxicity upon

light irradiation is mainly due to the presence of dissolved photo-degradation products in the cell cytoplasm rather than the generation of singlet oxygen [8,12].

A similar cyanine dye, IR-820, has optical and thermal generation properties similar to those of ICG but with higher solubility and improved in vitro and in vivo stability [9,13]. An additional chlorobenzene ring in the IR-820 structure is expected to increase molecular stability [9]. This indicates that IR-820 could be an alternative to ICG in clinical use. The chemical structures of ICG and IR-820 are shown in Figure 1.



(a) ICG (indocyanine green), $M$ = 774.96 g/mol (b) IR-820, $M$ = 849.47 g/mol

**Figure 1.** Chemical structure and molecular weight of (**a**) indocyanine green (ICG) and (**b**) IR-820.

To overcome the issues with stability and degradation, encapsulation into nano-carriers, such as liposomes, might help reduce the plasma degradation of ICG, extend the circulation time, and reduce toxicity [3,14]. However, due to the synthetic nature of liposomes, they can be recognized and eliminated as a foreign substance by the immune system [15]. Efforts to extend nanoparticle residence time in vivo have inspired many strategies of particle surface modifications to bypass macrophage uptake and systemic clearance. Using the body's own cells for the preparation of a safer delivery system is the most recent and advanced approach in the field of nanomedicine and represents an elegant, safe, and effective solution. Disguised with cell membranes, dyes can act as autogenous cells and thus ensure inherent biocompatibility. Among different circulatory cells, erythrocytes are the most abundant and thus can be isolated in sufficiently large quantities to decrease the complexity and cost of the treatment [16]. Erythrocytes have cell markers (CD47) on their surface that provide them with the ability to escape immune system attack [17,18]. For example, a biodistribution study on erythrocyte-coated iron oxide nanoparticles showed a longer circulation time than polyethylene-glycol-coated ones and lower accumulation in the liver and spleen, two major organs of the reticuloendothelial system (RES) [13]. To date, only a few reports can be found on the encapsulation of ICG into erythrocyte-membrane-based carriers, hereinafter referred to as erythrocyte membrane vesicles (EMVs). Bahmani et al. [19] reported the preparation of ICG-loaded EMVs, and high-energy laser irradiation (19.7 W/cm$^2$) showed heating due to photo-thermal conversion (investigated only single concentration and single laser power). Interestingly, free ICG heated more than ICG EMVs, which also showed stronger photo-degradation. In later research, they demonstrated diagnostic (fluorescence imaging) and therapeutic capabilities (photo-destruction of SKBR3 breast cancer cells) of ICG-EMVs in vivo [20]. These reports clearly show the high potential of fluorescent-dye-encapsulated EMVs for theranostic purposes (a portmanteau for therapeutic + diagnostic) [21]. However, more research to elucidate the basic physicochemical properties of such nanostructures is warranted, which will help optimize the protocols for the development of safe cell-based nano-carriers with superior theranostic properties compared with free dyes.

Therefore, this article represents the first systematic, comparative study where both types of nano-carriers, EMVs and clinically more established liposomes, loaded with either ICG or IR-820 as an alternative, were compared to free dyes in terms of thermal stability, photo-stability, and hemotoxicity. The aim of this study is to answer the following questions: (a) whether encapsulation into EMVs can improve thermal stability and photo-stability of free dyes, both of which are important to achieve the maximum-possible photo-thermal effect in cancer therapy; (b) how this compares to liposomal formulation; and (c) whether IR-

820, as a structurally similar fluorescent dye to ICG, has similar optical properties, stability, and safety and thus can be used as a cheaper alternative to ICG in medical applications.

## 2. Results and Discussion

### *2.1. Light Absorption Properties of ICG and IR-820 in Different Solvents*

The absorption spectra of ICG solutions in water, PBS buffer, 0.9% NaCl(aq), and blood plasma are shown in Figure 2a. ICG solution in ultrapure water showed two distinctive peaks: ICG monomers (λ = 780 nm) and H-type dimers (λ = 718 nm) [22–24]. In this concentration range, the monomeric form is predominant [23,25]. With the addition of salts (NaCl) and consequently increased ionic strength of the media, dimerization becomes more significant [22]. Therefore, saline and PBS solutions have a similar position of absorption peaks than pure water solutions but a significantly lower absorbance value (especially for the monomeric peak) and broader peaks. Additionally, the peak for the J-type dimer (λ > 840 nm) appeared. H-type dimers (λ = 718 nm) absorb at a shorter wavelength than monomers due to side-to-side arrangement of two ICG molecules, and the J-type oligomer absorbs at a longer wavelength than monomers due to the head-to-tail arrangement of ICG molecules [2]. These significant changes in the absorption properties indicate that the selection of solvent plays an important role and can modify the dye's optical and photo-thermal properties. To test biologically relevant conditions, the absorption spectrum for ICG in blood plasma was recorded as well. Interestingly, when dissolved in plasma, ICG showed higher absorption and red shift of absorption peaks compared to the aqueous solution. The peak for H-type dimers shifted from 718 to 768 nm, and the monomeric peak shifted from 780 to 840 nm. Additionally, the monomeric peak increased compared to the ICG solution in pure water, indicating that plasma proteins stabilize the monomeric form of ICG [23]. ICG therefore is supposed to be adsorbed by plasma proteins, such as albumin, as already demonstrated through human serum albumin titration.

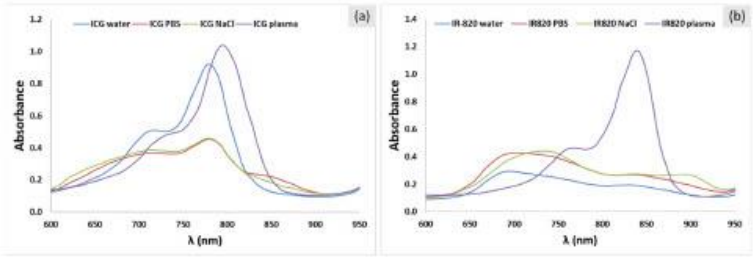



**Figure 2.** Absorption spectra of (**a**) ICG and (**b**) IR-820 in water, PBS buffer, 0.9% NaCl(aq), and blood plasma. The dye concentration is 10 μg/mL in all cases.

Despite the structural similarity, the absorption spectra of IR-820 solutions (Figure 2b) differed significantly from ICG solutions (Figure 2a). IR-820 in pure water had two absorption peaks at 690 and 813 nm [9]. At the same concentration (10 μg/mL), ICG had significantly higher absorption than IR-820, which could make ICG a more efficient photothermal agent [9]. In contrast to ICG, the addition of salts to IR-820 (solution in PBS and saline) led to absorption increase and the occurrence of three less distinctive peaks, indicating the presence of dimerization and the formation of higher oligomers. Interestingly, in the case of 0.9% NaCl(aq), absorption peaks red-shifted compared to IR820 in water. Similar to ICG, the IR-820 solution in plasma had significantly higher absorption than other IR-820 solutions, with two distinctive peaks at 768 and 840 nm. Plasma proteins interact with dyes in a similar manner, making monomers the most stable form. The monomer peak position for ICG and IR-820 in plasma was 794 and 840 nm, respectively.

### 2.2. Temperature-Stability Study of ICG and IR-820 in Different Solvents

Despite the broad use of ICG for different medical applications, no systematic study on its temperature stability in different biologically relevant solvents can be found. Only stability studies in aqueous solutions have been reported [9,25–27]. To fill this gap, we investigated solutions of both dyes (ICG and IR-820) in water, PBS buffer, 0.9% NaCl(aq), and blood plasma. All samples contained 10 µg/mL of the dye and were incubated for 24 h at 4, 25, and 37 °C in the dark. This concentration was chosen since it has been proved that the monomeric form is still predominant without signs of aggregation [25,26]. Single-wavelength absorbance was measured every hour at the absorption maximum determined for each sample from the spectra shown in Figure 2. The calculated percentage absorbance decrease after 24 h incubation at 25 and 37 °C for all tested solutions is presented in Figure 3. At 25 °C, ICG solutions in water, 0.9% NaCl(aq), and PBS showed evidence of degradation, with 24.8%, 21.6%, and 17.8% absorbance decrease, respectively, consistently with literature data [2]. In aqueous solutions, ICG degrades to leucoforms due to the saturation of double bonds. Leucoforms can further fragment into smaller molecules with intact aromatic end groups [26]. Interestingly, the ICG solution in plasma exhibited excellent stability with only 1.2% degradation after 24 h. At higher temperature (37 °C), the degradation rate even increased in all cases, reaching up to 37% in water and PBS. Importantly, the percentage degradation in plasma remained low, indicating possible stabilization of ICG by plasma proteins, avoiding the formation of J or H aggregates [19,24], the latter being responsible, at higher temperatures, for facilitating the exchange of single oxygen radicals known to trigger ICG degradation, as it happens in light-induced degradation [2,8,26].

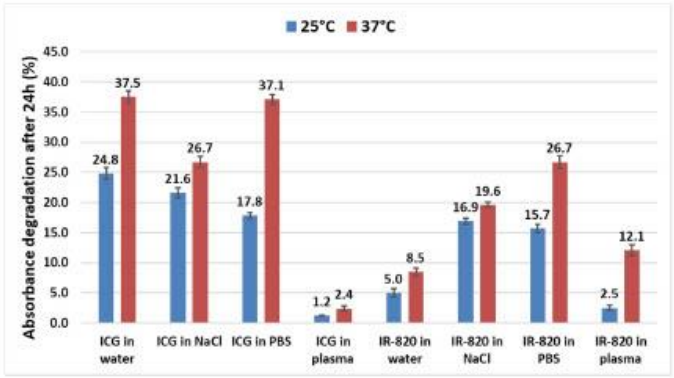



**Figure 3.** Temperature stability study of ICG and IR-820 solutions in different solvents at 25 and 37 °C. Absorbance decrease (%) after 24 h incubation in the dark was calculated from the absorbance peak values measured before and after incubation. Measurements were performed in triplicate. Statistical analysis confirmed that the means of each data pair (sample at 25 and 37 °C) are not equal, and therefore, the absorbance values differ significantly ($p < 0.05$).

Interestingly, at both 25 and 37 °C, IR-820 solutions in water, NaCl, and PBS degraded less than ICG solutions, with the highest detected degradation in PBS at 37 °C (26.7%). On the contrary, in plasma, degradation of IR-820 was more pronounced (12.1% at 37 °C) than for ICG (2.4% at 37 °C). From these results, we concluded that IR-820 seems to be more stable in water compared with ICG, while the opposite is valid in plasma, indicating ICG stability superiority in a biologically relevant medium. Stability in NaCl and PBS was slightly in favor of IR-820.

Finally, all solutions were incubated for 24 h at 4 °C in the dark. No drop in absorbance was detected in all cases (graphs not shown), indicating that temperature plays a crucial

role in dye degradation, with a higher degradation rate at higher temperature. This has to be considered when planning dye stock solution storage (ideally at 4 °C in the dark) and in vitro and in vivo experiments that are conducted at 37 °C. Fernandez-Fernandez et al. [9] tested the stability of ICG and IR-820 aqueous solutions (0.625 µg/mL) at 4, 22, and 42 °C in the dark and observed a significant fluorescence decrease after 24 h. The most intensive degradation was observed for ICG at 42 °C (>80% signal decrease), and the least degraded sample was IR-820 at 4 and 22 °C (approx. 35% signal decrease). Further, Mindt et al. [27] observed a fluorescence intensity decrease for an ICG aqueous solution (50 µg/mL) of only about 6.3% after 24 h at room temperature and slightly less at 4 °C. Our results, i.e., ICG aqueous solution degradation (10 µg/mL) after 24 h at 25 and 37 °C, fall between the results of these two reports. Deviations can be attributed to the different testing conditions, such as different dye concentrations (higher degradation at lower tested concentration [9]) and measurements of fluorescence [9,27] and, in our case, absorbance.

### *2.3. Photo-Stability Study of ICG and IR-820 Solutions in PBS*

To study photo-stability, ICG and IR-820 solutions in PBS with three different concentrations (5, 25, and 50 µg/mL) were irradiated with three different laser powers (P = 0.5, 1, and 3 W/cm$^2$). PBS was selected as a biologically relevant medium since most of the tested samples from the literature are dispersed in PBS or similar buffers. Heating profiles for ICG solutions are shown in Figure 4. The calculated absorbance decrease after laser irradiation for all solutions is listed in Table 1. As expected, from the calculated $\Delta T$ (difference between final and initial temperatures after 5 min irradiation), it is evident that higher laser power and higher ICG concentration lead to higher $\Delta T$. At laser power P = 3 W/cm$^2$, temperature saturates at 76 and 54 °C for an ICG concentration of 50 and 25 µg/mL, respectively. Saturation is a result of the dye-intensive decomposition at higher light irradiance, which is visible as a color change from green to yellow and detected as an absorption decrease.

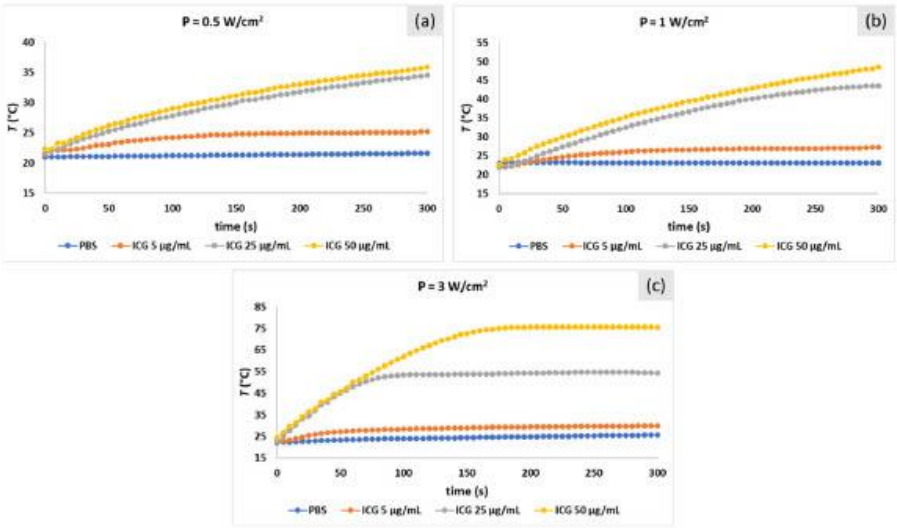



**Figure 4.** Temperature profiles of ICG solutions (5, 25, and 50 µg/mL) in PBS irradiated with 808 nm laser at laser power (a) P = 0.5 W/cm$^2$, (b) P = 1 W/cm$^2$, and (c) P = 3 W/cm$^2$. PBS solution was irradiated as a control.

**Table 1.** Calculated absorbance decrease after irradiation with 808 nm laser (P = 0.5, 1, and 3 W/cm$^2$) of ICG solutions in PBS. An increase in temperature ($\Delta T$) was calculated by subtracting the initial temperature ($t$ = 0 s) from the maximum temperature reached.

| Concentration (μg/mL) | P (W/cm$^2$) | Absorbance before Irradiation | Absorbance after Irradiation | % Degradation | $\Delta T$ (°C) |
|---|---|---|---|---|---|
| 5 | 0.5 | 0.748 | 0.295 | 60.5 | 3.8 |
| 5 | 1.0 | 0.748 | 0.237 | 68.3 | 5.1 |
| 5 | 3.0 | 0.748 | 0.145 | 80.6 | 7.5 |
| 25 | 0.5 | 2.326 | 1.884 | 19.0 | 13.2 |
| 25 | 1.0 | 2.326 | 1.398 | 39.9 | 21.8 |
| 25 | 3.0 | 2.326 | 0.375 | 83.9 | 31.1 |
| 50 | 0.5 | 3.678 | 3.567 | 3.0 | 12.8 |
| 50 | 1.0 | 3.678 | 3.197 | 13.1 | 24.2 |
| 50 | 3.0 | 3.678 | 1.182 | 67.9 | 50.7 |

Heating profiles of IR-820 solutions are shown in Figure 5. The calculated absorbance decrease after laser irradiation for all solutions is listed in Table 2. Similar to ICG solutions, $\Delta T$ is a function of laser power and dye concentration. The highest $T$ (52 °C) was achieved at the highest laser power P = 3 W/cm$^2$ and IR-820 concentration = 50 μg/mL (Figure 5c). Interestingly, due to the dye decomposition, in this extreme case, the temperature did not saturate at the maximum value but slowly decreased.

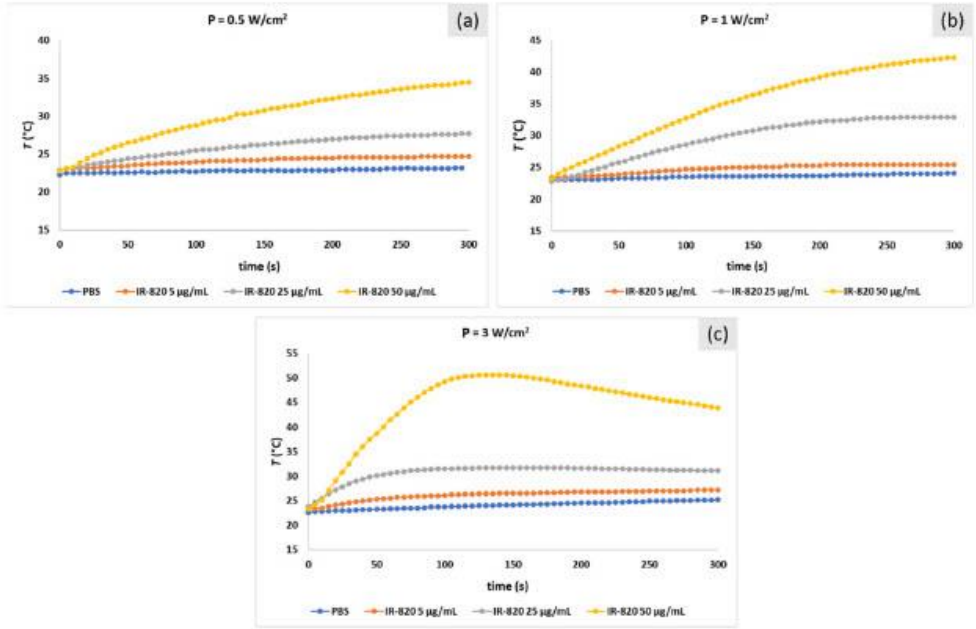



**Figure 5.** Temperature profiles of IR-820 solutions with three different concentrations (5, 25, and 50 μg/mL) in PBS irradiated with 808 nm laser at laser power (a) P = 0.5 W/cm$^2$, (b) P = 1 W/cm$^2$, and (c) P = 3 W/cm$^2$. PBS solution was irradiated as a control.

**Table 2.** Calculated absorbance decrease after irradiation with 808 nm laser (P = 0.5, 1, and 3 W/cm$^2$) of IR-820 solutions in PBS. An increase in temperature ($\Delta T$) was calculated by subtracting the initial temperature ($t$ = 0 s) from the maximum temperature reached.

| Concentration (μg/mL) | P (W/cm$^2$) | Absorbance before Irradiation | Absorbance after Irradiation | % Degradation | $\Delta T$ (°C) |
|---|---|---|---|---|---|
| 5 | 0.5 | 0.160 | 0.070 | 56.3 | 1.8 |
| 5 | 1.0 | 0.160 | 0.056 | 64.8 | 2.0 |
| 5 | 3.0 | 0.160 | 0.036 | 77.4 | 3.4 |
| 25 | 0.5 | 0.491 | 0.150 | 69.5 | 4.8 |
| 25 | 1.0 | 0.491 | 0.117 | 76.1 | 10.0 |
| 25 | 3.0 | 0.491 | 0.095 | 80.7 | 8.0 |
| 50 | 0.5 | 1.410 | 0.655 | 53.5 | 11.7 |
| 50 | 1.0 | 1.410 | 0.271 | 80.8 | 19.0 |
| 50 | 3.0 | 1.410 | 0.093 | 93.4 | 27.3 |

Absorption spectra before and after laser irradiation for ICG and IR-820 solutions (50 μg/mL) in PBS are shown in Figures 6a and 6b, respectively. Results clearly indicate that higher laser power leads to a stronger absorption decrease after the same irradiation time (5 min). For example, for the 50 μg/mL ICG solution in PBS, absorbance decreased after 5 min of irradiation by 3%, 13%, and 68% at 0.5, 1, and 3 W/cm$^2$, respectively (Table 1 and Figure 6a). For the 50 μg/mL IR-820 solution, the percentage decrease was 53%, 81%, and 93% at 0.5, 1, and 3 W/cm$^2$, respectively (Table 2 and Figure 6b). The same trend was observed for ICG and IR-820 solutions with concentrations of 5 and 25 μg/mL in PBS but with lower absorbance values (Tables 1 and 2). In summary, a higher laser power leads to a higher temperature increase but with more severe dye degradation. In agreement with our results, Saxena et al. [26] showed faster ICG degradation in aqueous solutions when exposed to laser light (λ = 786 nm, P = 70 mW) than ambient light. Degradation half-times were calculated to be 2.3 and 14.4 h, respectively. Acceleration in ICG degradation with a stronger light source was attributed to the increase in the production of photo-excited ICG molecules, which tend to form radicals, which further lead to faster degradation toward leucoforms. ICG and IR820 degradation products (Figure 6) did not show absorbance in the same range of parental molecules, thus confirming previously reported data for one decomposition compound analyzed by Engel et al. [8].

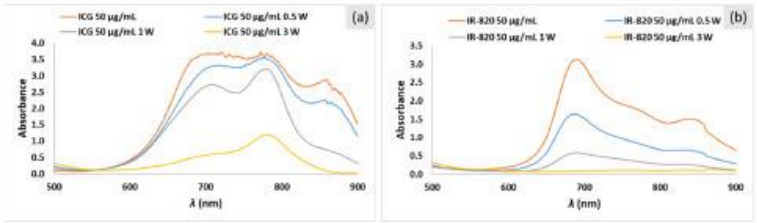



**Figure 6.** Absorption spectra of (a) ICG and (b) IR-820 solutions in PBS (50 μg/mL) before and after laser irradiation with P = 0.5, 1, and 3 W/cm$^2$ for 5 min.

In clinical photo-thermal applications, the required temperature increase is in the range of 5 °C (e.g., mild hyperthermia region, 41–43 °C), which can be easily achieved with low laser power to reduce dye degradation and low dye concentration to reduce the risk of toxicity. For example, heating for approx. 5 °C can be observed with 5 μg/mL and P = 1 W/cm$^2$ for ICG and 25 μg/mL and P = 0.5 W/cm$^2$ for IR-820. As already expected from higher absorbance, under the same conditions, ICG showed a higher photo-thermal effect than IR-820. Importantly, not only heat generation (photo-thermal therapy) but also light-

induced degradation products (photo-dynamic therapy) should be carefully considered as an additional toxic event in the exposed cells. Namely, ICG photo-degrades via oxidative C–C cleavage of the polymethine chain, where several different degradation products are formed, depending on the environmental conditions (e.g., oxygen concentration, presence of $^1O_2$ quenchers) [28]. To enhance dye stability, in our study, ICG and IR-820 were encapsulated into liposomes and erythrocyte membrane vesicles (EMVs).

### 2.4. Preparation of ICG- and IR-820-Loaded Carriers

A comparison, in terms of size and zeta potential, of free carriers (liposomes and EMVs) and loaded ones was carried out, and the encapsulation efficiency (EE) was in parallel estimated. As listed in Table 3, encapsulation of ICG or IR-820, at a working concentration, did not influence liposome size compared to empty liposomes (115 nm). However, the polydispersity index increased, indicating broader size distribution due to uneven dye encapsulation. This could arise from uneven encapsulation among carriers of quantity of dyes, since ICG is known to locate within the double layer and increase the size accordingly [3]. No statistically significant difference in the EE between ICG (45%) and IR-820 (46%) was observed (Table 3). The same parameters were measured for EMVs. Both size and the PDI of EMVs were found to be larger than for liposomes due to the more complex membrane structure (presence of proteins, lipid rafts, and other molecules that contribute to the hydrodynamic diameter) and extrusion process. The EE of IR-820- and ICG-loaded EMVs was determined to be 57% and 53%, respectively. From the comparison of the results obtained for dye-loaded liposomes and EMVs, we can conclude that on average, the EE for both dyes is around 50%.

**Table 3.** Particle size, polydispersity index (PDI), and dye encapsulation efficacy (EE) of empty, ICG-, and IR-820-loaded liposomes and EMVs ($n = 3$).

| Sample | Size (nm) | PDI | EE (%) |
|---|---|---|---|
| Empty LPS | 115 ± 1 | 0.087 ± 0.050 | - |
| Empty EMVs | 234 ± 4 | 0.238 ± 0.011 | - |
| ICG LPS | 126 ± 3 | 0.171 ± 0.083 | 45 ± 3 |
| ICG-EMVs | 215 ± 5 | 0.198 ± 0.075 | 57 ± 2 |
| IR-820 LPS | 116 ± 2 | 0.142 ± 0.091 | 46 ± 4 |
| IR-820 EMVs | 260 ± 4 | 0.229 ± 0.081 | 53 ± 3 |

The absorbance spectra of ICG- and IR-820-loaded carriers are shown in Figures 7a and 7b, respectively. The shape of the spectra for dye-loaded liposomes and EMVs was similar. However, they strongly differed from the spectra of free dyes in PBS. Interestingly, spectra for dye-loaded liposomes and EMVs resembled more the spectra obtained in plasma (Figure 2), indicating stabilization of the monomeric form by lipid components of the carriers.

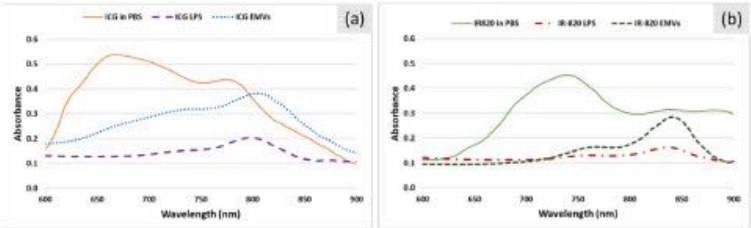



**Figure 7.** Characterization of purified ICG- and IR-820-loaded liposomes and EMVs. (a) Absorption spectra of ICG samples: ICG in PBS, ICG-loaded liposomes (LPS), and ICG-loaded EMVs. (b) Absorption spectra of IR-820 samples: IR-820 in PBS, IR-820-loaded liposomes (LPS), and IR-820-loaded EMVs. Liposomes and EMVs are dispersed in PBS buffer.

### 2.5. Temperature Stability of Dye-Loaded Liposomes and EMVs

To evaluate the temperature stability of dye-loaded carriers, samples were incubated at 25 and 37 °C for 24 h. Interestingly, liposomes and EMVs significantly improved the dye stability compared to the stability of free dyes in PBS, even at higher temperature (37 °C) (Figure 8). The highest detected percentage degradation of ICG in EMVs was 6.2%, which is a 6-fold improvement compared to the free dye in PBS (37%). Similarly, IR-820 in EMVs degraded by about 10% compared to a 3.5-fold higher degradation in PBS at 37 °C. These data confirm for EMVs, too, what has been already observed in the case of polymeric nanostructure encapsulation [29] and PGLA [30]. Importantly, it seems that liposomes and EMVs equally protect dyes from degradation at 25 and 37 °C. The observed percentage degradation was similar to free dyes in plasma but with other added functionalities that nano-carriers can offer, i.e., preparation of theranostic nanostructures and a prolonged circulation time. This protective effect from temperature degradation is due to supposedly reduced vibrational, rotational, and translation motions among ICG molecules, causing less pronounced radical formation and subsequent degradation [2], as observed in the case of plasma (Section 2.2).

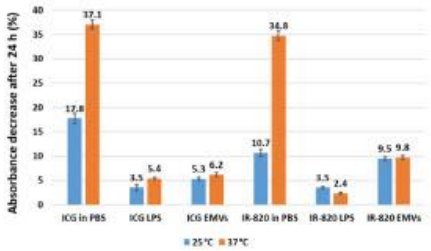



**Figure 8.** Temperature stability study of ICG- and IR-820-loaded carriers at 25 and 37 °C. Absorbance decrease (%) after 24 h incubation in the dark was calculated from the absorbance peak values measured before and after incubation. Measurements were performed in triplicate. Statistical analysis confirmed that the means of each data pair (sample at 25 and 37 °C) are not equal, and therefore, the absorbance values differ significantly ($p < 0.05$), except for IR-820-loaded EMVs at 25 and 37 °C, where no statistically significant difference could be observed.

### 2.6. Photo-Thermal Effect of ICG- and IR-820-Loaded Liposomes and EMVs

Photo-stability and laser-induced heating capability of dye-loaded nano-carriers was studied by irradiating samples with different laser powers (P = 0.5 and 3 W/cm$^2$) for 5 min. Heating profiles for ICG and IR-820 samples are shown in Figures 9a and 9b, respectively. Calculated $\Delta T$ values obtained after 5 min laser irradiation for all solutions are presented in Figure 9c. Expectedly, a higher laser power led to a higher temperature increase ($\Delta T$). Empty carriers showed minimal heating (for liposomes, up to 3.3 °C at P = 3 W/cm$^2$). For example, for ICG- and IR-820-loaded liposomes, at laser power P = 3 W/cm$^2$, the temperature increased by 41.6 and 5.8 °C, respectively. At a lower laser power, P = 0.5 W/cm$^2$, all ICG samples reached a similar $\Delta T$ (approx. 10 °C). Interestingly, at a higher laser power, ICG-loaded EMVs showed a lower $\Delta T$ (31.6 °C) than ICG in PBS and ICG-loaded liposomes (39.3 and 41.6 °C, respectively). This is in accordance with the observation of Bahmani et al. [19], where ICG-loaded EMVs exhibited a lower $\Delta T$ than free ICG. However, they observed strong photo-degradation and a temperature decrease during irradiation, which was not the case in our experiment. Even though experiments were carefully designed to have the same dye concentration in all cases (10 µg/mL), this discrepancy for ICG-loaded EMVs at P = 3 W/cm$^2$ might be attributed to a small deviation in the actual ICG concentration due to extrusion processes, which we avoided to use in this experimental design. On the contrary, IR-820-loaded EMVs showed a similar heating

effect to IR-820-loaded liposomes at both laser powers (and both nano-carriers exhibited a similar $\Delta T$ than free IR-820). These results indicate that the photo-thermal efficacy of dyes is not hindered at all by the encapsulation of dyes into liposomes or EMVs.

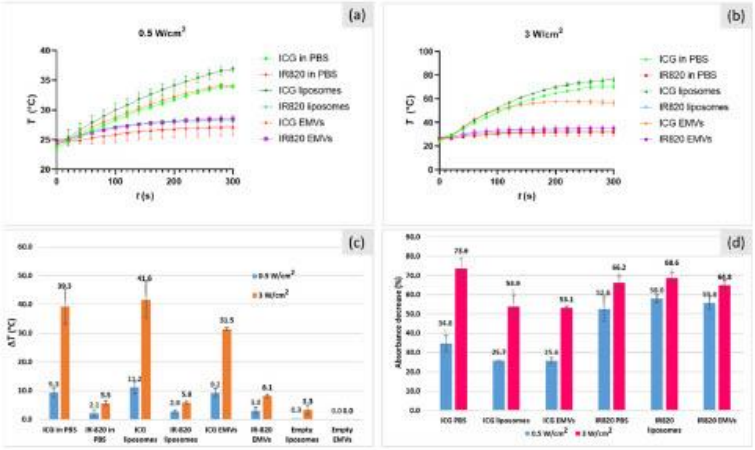



**Figure 9.** Photo-thermal experiments on dye-loaded nano-carriers. Heating profiles after 5 min irradiation with laser power (**a**) 0.5 and (**b**) 3 W/cm$^2$. Data were reported as the mean ± SD. (**c**) Calculated temperature increase after 5 min laser irradiation. An increase in temperature ($\Delta T$) was calculated by subtracting the initial temperature ($t$ = 0 s) from the maximum temperature reached. Three measurements were performed for each sample. (**d**) Absorbance decrease (%) as an indicator of dye decomposition was calculated from the absorbance peak values measured before and after irradiation. Three measurements were performed for each sample. Observed lower degradation for ICG-loaded carriers, at both laser powers, was proven to be statistically significant with Brown–Forsyth ANOVA ($p < 0,05$). No statistically relevant differences were confirmed for IR820-loaded carriers.

Finally, dye stability after laser irradiation was evaluated by comparing absorbance peak values before and after irradiation. The calculated absorbance decrease (%) for all samples is shown in Figure 9d. Laser power again proved to have an influence on free ICG in PBS, with a lower degradation rate at P = 0.5 W/cm$^2$ (34.8%) than at P = 3 W/cm$^2$ (73.6%). These results (ICG 10 µg/mL) coincide well with ICG solutions in PBS tested previously (Table 1, ICG concentrations 5, 25, and 50 µg/mL). Interestingly, ICG nano-carriers degraded similarly (around 50% for 3 W/cm$^2$ and 25% at 0.5 W/cm$^2$) at both laser powers. Such a decrease in peak absorbance (measured at 800 nm, i.e., peak for the monomeric form) was remarkably lower in the carrier rather than as free ICG (significant, with significance set at $p > 0.05$, according to Brown–Forsythe corrected ANOVA) in the case of both 0.5 and 3 W/cm$^2$. This behavior can be explained by the stabilization effect of the monomeric form of ICG due to interaction with lipids and proteins; degradation is slowed down since the dye does not form H or J aggregates; therefore, diffusion of singlet oxygen, mainly responsible of ICG degradation, is reduced, too [8]. In particular, singlet oxygen diffusion in carriers can be decreased by the presence of PEG2000 in liposomes and unsaturated fatty acids and proteins in EMVs [31,32]. Such phenomenon has been already observed for dextran mesocapsules [33], in PEG-poly(ε-caprolactone) micelles [34], and in DSPE-PEG micelles as well [35]. In addition, all IR-820 samples had a similar degradation profile, no matter whether in free or encapsulated form (52% at P = 0.5 W/cm$^2$ and 68% at P = 3 W/cm$^2$), again showing that in the case of IR820, encapsulation does not protect the dye from photo-degradation. While for ICG, localization and degradation mechanisms are well known, the same cannot be said for IR820, as already proven that embedding

within a carrier (PGLA) does not improve photostability [36]. However, as mentioned before, encapsulation in nano-carriers can offer a prolonged circulation time at the same photo-thermal efficacy (same achieved temperature increase as in the case of free dyes).

### 2.7. Hemolysis Study

To evaluate the possible hemotoxicity of dyes, ICG and IR-820 solutions in PBS (1–30 µg/mL) were incubated with red blood cells (RBCs, 5 vol.%) for 3 h (Figure 10a). Hemolysis was found negligible (0.1%) up to 10 µg/mL for both dyes, with a slight increase at the highest tested concentrations (0.33% and 0.26% at 30 µg/mL of ICG and IR-820, respectively). Then, the hemolysis after incubation with dye-loaded nano-carriers was evaluated (Figure 9b, dye concentration 10 µg/mL). All EMV-based samples showed minimal hemolysis, while, strikingly, liposomes induced severe hemolysis. Since this was observed for empty liposomes, too, we further investigated the origin of the hemotoxicity. Reducing the liposome concentration by 5 and 10 times resulted in drastic hemolysis reduction (Figure 10), indicating hemotoxicity as a consequence of high phospholipid concentration (5 mM in initial samples). This formulation is clinically approved (DPPC/MSPC/DSPE-mPEG2000 = 90:10:4 molar ratio, i.e., low-temperature-sensitive formulation, ThermoDox®; Celsion Corporation, USA). However, it apparently induces hemotoxicity, which could be originating from the lysolipid component (MSPC). It was demonstrated [37] that under ideal conditions (absence of plasma proteins, other double layers than liposomes), the lysolipid is kept in the lipid double layer below the phase transition temperature (approx. 41 °C for this formulation). Instead, under real-life conditions, MSPC can be released from the liposomes and fuse with other bilayers [38], such as RBCs in our case. It was observed [37] that after injection in mice, the concentration of marked MSPC kept on decreasing in hematic flux. Unfortunately, hemotoxicity was not assessed. The authors, instead, incubated the Thermodox formulation with whole blood, discovering that over 4 h, a small but important loss of lysolipid occurs, enough to dramatically reduce the concentration of the drug within the liposomes, which indicates a disturbance in both double layers. On the contrary, we assayed in a quantitative way only from the erythrocytes' point of view. To confirm this assumption, we then tested formulations without MSPC (DPPC:DSPE-mPEG2000) and observed a drastic decrease in hemolysis down to 8.1% at 5 mM (compared to 37.3 % for the full formulation). Further dilution (5 and 10 times) resulted in the measured hemolysis at a level of control samples (<0.1%). In conclusion, from the hemolytic point of view, EMVs prove to be less hemotoxic dye carriers than clinically approved lipid formulations.

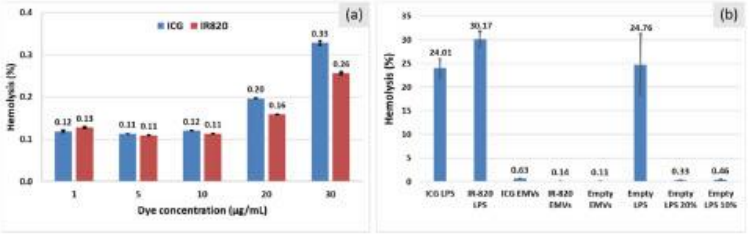



**Figure 10.** Influence of ICG and IR-820 dyes on red blood cells toxicity. All measurements were performed in triplicate. (**a**) Hemolysis determination of PBS solutions of dyes in the concentration range from 1 to 30 µg/mL after 3 h incubation at 37 °C. Data analysis revealed no statistically significant difference in the cell viability values between tested groups (ICG and IR-820 at a given concentration, $p > 0.05$) up to 10 µg/mL. At a higher concentration (20 and 30 µg/mL), hemolysis values become significantly different between tested groups ($p < 0.05$). (**b**) Hemolysis determination of dye-containing liposomes (LPS) and EMVs after 3 h incubation at 37 °C. Empty carriers were tested as control groups. Liposomal samples (without dilution) showed a statistically significant difference between hemolysis values (ANOVA test, F > F critical = 20.09 > 5.14, $p < 0.005$). Hemolysis values for all EMV samples differed significantly (ANOVA test, F > F critical = 34.89 > 5.14, $p < 0.001$).

## 3. Materials and Methods

### 3.1. Chemicals

Indocyanine green (ICG, laser grade) was purchased from Acros Organic (a Thermo Fisher Scientific company, Morris Plains, NJ, USA), and IR820 (dye content 80%) and $CHCl_3$ (>99%) were purchased form Sigma-Aldrich (Sigma-Aldrich, Munich, Germany ). Liposomes were prepared using 1,2-dipalmitoyl-sn-glycero-3-phosphatidylcholine (DPPC), 1-myristoyl-2-stearoyl-sn-glycero-3-phosphocholine (MSPC), and N-[carbonyl-methoxy(polyethylene glycol)-2000]-1,2-distearoyl-sn-glycero-3-phosphoethanolamine, a sodium salt (DSPE-PEG2000) purchased from Lipoid GmbH (Ludwigshafen, Germany). For EMV preparation, the following chemicals were used: phosphate-buffered saline buffer (PBS, tablets; Sigma Aldrich), Alsever's medium (TCS Biosciences Ltd., UK), and NaCl (Sigma-Aldrich, >99.5%).

### 3.2. Preparation of Dye-Loaded Liposomes

Liposomes were prepared by a thin-film hydration method followed by extrusion [39]. Briefly, 8.6 µmol of DPPC (10 mg/mL), 1 µmol of MSPC (5 mg/mL), and 0.4 µmol of DSPE-PEG2000 (10 mg/mL) were dissolved in $CHCl_3$. The organic mixture was transferred to a round-bottom flask (25 mL), and then $CHCl_3$ was removed at 40 °C using a rotary evaporator (Rotavapor R-100 equipped with a heating bath, Interface I-100, and vacuum pump V-100; Bunchi, Switzerland). Once a lipid film was formed, the pressure in the flask was reduced to 10 mbar for 1 h. The dried lipid film was then hydrated with 2 mL of 30 µg/mL of ICG or IR-820 dye in 0.1× PBS in a circulating flask at 60 °C for 30 min. Particle size was reduced using a mini-extruder (Avanti Polar lipid, USA). Samples were extruded at 60 °C through 800 nm (5 cycles), 200 nm (15 cycles) and lastly through 100 nm membranes (25 times, PC membrane filters; Avanti Polar lipid, USA), left to anneal for 2 h at room temperature and stored at 4 °C for further experiments.

### 3.3. Preparation of Dye-Loaded EMVs

Whole blood of sheep was supplied by the Veterinary Faculty (University of Ljubljana, Slovenia) in Alsever's medium (pH 6.1) and used within 1 week. Erythrocytes were isolated via centrifugation (2500 rpm/10 min) and washed 3 times with PBS buffer. Plasma was used for stability study purposes. For the preparation of empty EMVs, 3 mL of 20 vol.% of erythrocytes in PBS buffer was centrifuged (model 5804 Eppendorf) at 8000 rpm for 10 min. The supernatant was discarded, and the pellet was redispersed with 0.1× PBS, incubated for 20 min at 4 °C to release the hemoglobin and centrifuged at 8000 rpm. The supernatant was discarded. The incubation–centrifugation step was repeated until the supernatant was clear and only a white pellet of cell membranes remained. As prepared, empty EMVs were then redispersed in 1 mL of 30 µg/mL dye in 1× PBS and incubated at room temperature for 15 min. Afterward, the samples were homogenized using an ultrasound finger (ultrasonic processor Sonics Vibra cell VC-505; pulses: 1 s on, 1 s off; 20% amplitude). To reduce the particle size, samples were extruded at 37 °C through 800 nm (5 cycles) and 200 nm (15 cycles) membrane filters. EMVs were left to anneal for 2 h at room temperature and stored at 4 °C for further experiments.

### 3.4. Purification of Dye-Loaded EMVs/Liposomes and Encapsulation Efficiency

The purification step involved removal of the non-encapsulated dye from liposomes and EMVs by gel filtration using a PD-10 column (GE Healthcare, UK) equilibrated with 1× PBS. Briefly, 1 mL of the extruded sample was inserted into the column, and seven fractions (1 mL each) were collected. The presence of liposomes/EMVs was proved via particle size and absorbance measurements of each fraction. Only in fractions 3 and 4, liposomes with a size of around 115 nm and a considerable count rate were detected, which was further supported with absorbance measurements using 96-well transparent F-bottom microplates and a Synergy H4 Hybrid microplate reader (BioTek, Winooski, VT, USA). A 2× dilution factor was considered when calculating the encapsulation efficiency (EE%).

The same procedure was applied for EMVs. Fractions 4 and 5 were collected, having a considerable count rate and a particle size of 220–230 nm on average.

### 3.5. Hydrodynamic Diameter and Zeta Potential Measurements

The hydrodynamic diameter, polydispersity index (PDI), and zeta potential (ζ-potential) of empty and dye-containing liposomes and EMVs were determined using a zeta potential and particle size analyzer ZetaPALS (Brookhaven Instruments Corporation, New York, NY, USA) at 25 °C. Disposable polystyrene cells (Q-Vettes; Ratiolab, Germany) were used for particle size and zeta potential measurement.

### 3.6. Absorption Spectra of IR-820 and ICG Solutions

Due to the limited solubility of dyes in phosphate-buffered saline (PBS), 0.9% saline, and blood plasma, ICG and IR-820 were first dissolved in ultrapure water to obtain a dye concentration pf 0.5 mg/mL and then diluted further with PBS, 0.9% saline, or blood plasma to reach working solutions in the concentration range of 1–50 µg/mL. Measurements were performed using a Lambda950 UV/VIS/NIR spectrometer (PerkinElmer, Waltham, MA, USA), quartz cuvettes, and a microplate reader with 96-well plates. Absorption spectra were recorded in the wavelength range from 500 to 900 nm.

### 3.7. Temperature Stability of IR-820 and ICG Solutions

ICG and IR-820 solutions (10 µg/mL) in water, PBS, 0.9% NaCl(aq), and blood plasma were incubated for 24 h at 4, 25, and 37 °C using a microplate reader. Absorbance peak values were recorded every hour. Final and initial values were used for calculation of the percentage absorbance decrease, which served as an indicator of dye degradation. Similarly, temperature stability of ICG- and IR-820-loaded liposomes and EMVs (all with dye concentration 10 µg/mL) was determined via 24 h incubation at 25 and 37 °C using a microplate reader, following the above-described protocol. A concentration of 10 µg/mL was chosen since it is diluted enough to have monomeric forms of ICG and IR820 to be predominant. The reaction volume was 1 mL, and the thermal expansion of water was negligible. All samples were allowed to cool at room temperature before final spectra measurement, the latter being used as an indicator of dye degradation, to avoid water thermal expansion concentration bias.

One-way ANOVA and unpaired Student's *t*-test was used for our statistical analysis, assuming normal distribution of data. The differences were considered significant at $p < 0.05$. Data were shown as the mean ± SD ($n = 3$).

### 3.8. Photo-Stability of IR-820 and ICG Solutions

Photo-thermal experiments were performed using an FC-808 Fiber Coupled Laser System (CNI Optoelectronics Tech, Changchun, China) configured for continuous-wave operation at 808 nm with different powers. Laser light was focused on a quartz cuvette (size 1 × 1 × 3 $cm^3$) using an optical lens with a spot size of about 8 mm. Control (PBS buffer) and dye-containing solutions were irradiated at laser power P = 0.5, 1, and 3 $W/cm^2$ for 5 min. Such duration was chosen to mimic an in vivo photo-thermal experiment [7,40]. The temperature of the liquid samples (volume 1 mL) was measured with a J-type Teflon thermocouple that was immersed in the cuvette and connected to a computer to collect the data in real time. To evaluate photo-induced degradation, absorbance spectra in the range of 500–900 nm were recorded before and after laser irradiation. In the case of absorbance spectra recorded after irradiation, the impact of the degradation products of dyes, influencing the ionic strength of samples, was assumed to be negligible and to not influence the shape and reliability of the remaining ICG molecules' spectrum [8]. Loaded carriers were prepared, as described in Sections 3.2 and 3.3, avoiding the extrusion process and only sonicating the samples in order to keep the initial concentration of the dye constant and to ensure no experimental bias due to differential encapsulation efficiency. Brown–Forsythe ANOVA was employed to evaluate

the consistency of observed data. Differences were considered relevant at $p < 0.05$. Data were shown as the mean ± SD ($n = 3$).

### 3.9. Hemotoxicity Study

To assert the hemolytic activity of liposomes and EMVs, a hemoglobin leakage assay was used [41]. Briefly, erythrocytes were isolated from the whole blood of sheep, as described in the section for the preparation of EMVs. Control (PBS only), dyes in PBS (1–50 µg/mL), empty liposomes, empty EMVs, and dye-loaded liposomes and EMVs were incubated with 5 vol.% of erythrocytes in PBS (pH 7.4) for 3 h at 37 °C with constant orbital shaking in 1.5 mL tubes (Eppendorf, Germany; volume of samples 1 mL; all samples in triplicate). After incubation, tubes were centrifuged (1500 rpm/4 min) to sediment cells, and the supernatant was analyzed in triplicate. Hemolysis was evaluated by measuring the released hemoglobin absorbance ($A$) at 541 nm using a plate reader. Samples representing "100% dead" were prepared by lysing control samples with deionized water via hypotonic osmotic shock. The percentage hemolysis was then calculated as follows:

$$\text{Hemolysis}\ (\%) = 100 \times \frac{\left(A_{\text{sample}} - A_{\text{control}}\right)}{\left(A_{100\%\ \text{dead}} - A_{\text{control}}\right)} \quad (1)$$

One-way ANOVA and Student's $t$-test were used for our statistical analysis. Data were presented as the mean ± SD for all experiments.

## 4. Conclusions

This study provided enough experimental evidence to answer the burning questions that were raised in the Introduction section. First, we found that encapsulation of dyes in liposomes and EMVs can improve the dyes' thermal stability. In addition, specific carrier encapsulation can prevent quick photo-degradation, due to stabilization of the monomeric form, in the case of ICG, known to locate within double layers; a carrier then has to be carefully engineered to reduce the singlet oxygen diffusion rate. Second, IR-820 exhibits similar stability but a lower photo-thermal conversion efficacy than ICG at the same dye concentration and is thus a less appropriate photo-thermal agent than ICG, and carriers are not proven to be able to protect it from photo-degradation, giving hints of its localization within them. More studies are needed to better characterize IR820 localization and interaction with biological matter. Finally, DPPC/DSPE-PEG2000/MSPC liposomes themselves were found to be hemotoxic at as high concentrations as 5 mM, which highlight the superiority of EMVs regarding the hemocompatibility profile. In conclusion, the use of the body's own cells as nano-carriers for dyes and other active components is a highly attractive strategy that might help overcome the challenges current nanomedicine is facing.

**Author Contributions:** Conceptualization, N.K.; methodology, N.K.; formal analysis, G.D.P., A.D.L., M.S.F., and N.K.; investigation, G.D.P., A.D.L., M.S.F., and N.K.; writing—original draft preparation, N.K.; writing—review and editing, G.D.P. and N.K.; supervision, N.K.; project administration, N.K.; funding acquisition, N.K. All authors have read and agreed to the published version of the manuscript.

**Funding:** This research was funded by the Slovenian Research Agency ARRS (project nos. Z2-9218 and P2-0084).

**Institutional Review Board Statement:** Not applicable.

**Informed Consent Statement:** Not applicable.

**Data Availability Statement:** Not applicable.

**Conflicts of Interest:** The authors declare no conflict of interest.

## References


1. Herrmann, J.; Bodmeier, R. Degradation Kinetics of Somatostatin in Aqueous Solution. *Drug Dev. Ind. Pharm.* **2003**, *29*, 1027–1033. [CrossRef] [PubMed]
2. Holzer, W.; Mauerer, M.; Penzkofer, A.; Szeimies, R.M.; Abels, C.; Landthaler, M.; Bäumler, W. Photostability and thermal stability of indocyanine green. *J. Photochem. Photobiol. B Biol.* **1998**, *47*, 155–164. [CrossRef]
3. Kraft, J.C.; Ho, R.J.Y. Interactions of indocyanine green and lipid in enhancing near-infrared fluorescence properties: The basis for near-infrared imaging in vivo. *Biochemistry* **2014**, *53*, 1275–1283. [CrossRef]
4. Alander, J.T.; Kaartinen, I.; Laakso, A.; Pätilä, T.; Spillmann, T.; Tuchin, V.V.; Venermo, M.; Välisuo, P. A Review of indocyanine green fluorescent imaging in surgery. *Int. J. Biomed. Imaging* **2012**, *2012*, 940585. [CrossRef] [PubMed]
5. Zhou, J.; Yang, F.; Jiang, G.; Wang, J. Applications of indocyanine green based near-infrared fluorescence imaging in thoracic surgery. *J. Thorac. Dis.* **2016**, *8*, S738–S743. [CrossRef] [PubMed]
6. Qi, C.; Zhang, H.; Chen, Y.; Su, S.; Wang, X.F.; Huang, X.Q.; Fang, C.; Li, B.; Xia, X.M.; He, P. Effectiveness and safety of indocyanine green fluorescence imaging-guided hepatectomy for liver tumors: A systematic review and first meta-analysis. *Photodiagn. Photodyn. Ther.* **2019**, *28*, 346–353. [CrossRef]
7. Shirata, C.; Kaneko, J.; Inagaki, Y.; Kokudo, T.; Sato, M.; Kiritani, S.; Akamatsu, N.; Arita, J.; Sakamoto, Y.; Hasegawa, K.; et al. Near-infrared photothermal/photodynamic therapy with indocyanine green induces apoptosis of hepatocellular carcinoma cells through oxidative stress. *Sci. Rep.* **2017**, *7*, 13958. [CrossRef]
8. Engel, E.; Schraml, R.; Maisch, T.; Kobuch, K.; Konig, B.; Szeimies, R.M.; Hillenkamp, J.; Baümler, W.; Vasold, R. Light-induced decomposition of indocyanine green. *Investig. Ophthalmol. Vis. Sci.* **2008**, *49*, 1777–1783. [CrossRef] [PubMed]
9. Fernandez-Fernandez, A.; Manchanda, R.; Lei, T.; Carvajal, D.A.; Tang, Y.; Kazmi, S.Z.R.; McGoron, A.J. Comparative study of the optical and heat generation properties of IR820 and indocyanine green. *Mol. Imaging* **2012**, *11*, 99–113. [CrossRef]
10. Food and Drug Administration Product Insert: Indocyanine Green (IC-GreenTM). Available online: https://www.accessdata.fda.gov/drugsatfda_docs/label/2006/011525s017lbl.pdf (accessed on 7 June 2021).
11. Narayanan, R.; Kenney, M.C.; Kamjoo, S.; Trinh, T.H.T.; Seigel, G.M.; Resende, G.P.; Kuppermann, B.D. Toxicity of indocyanine green (ICG) in combination with light on retinal pigment epithelial cells and neurosensory retinal cells. *Curr. Eye Res.* **2005**, *30*, 471–478. [CrossRef]
12. Bäumler, W.; Abels, C.; Karrer, S.; Weiß, T.; Messmann, H.; Landthaler, M.; Szeimies, R.-M. Photo-oxidative killing of human colonic cancer cells using indocyanine green and infrared light. *Br. J. Cancer* **1999**, *80*, 360–363. [CrossRef]
13. Conceição, D.S.; Ferreira, D.P.; Vieira Ferreira, L.F. Photochemistry and cytotoxicity evaluation of heptamethinecyanine near infrared (NIR) dyes. *Int. J. Mol. Sci.* **2013**, *14*, 18557–18571. [CrossRef]
14. Yoon, H.J.; Lee, H.S.; Lim, J.Y.; Park, J.H. Liposomal Indocyanine Green for Enhanced Photothermal Therapy. *ACS Appl. Mater. Interfaces* **2017**, *9*, 5683–5691. [CrossRef] [PubMed]
15. Su, W.; He, M.; Xing, J.; Zhong, Y.; Li, Z. Facile synthesis of porous bifunctional $Fe_3O_4$@$Y_2O_3$:Ln nanocomposites using carbonized ferrocene as templates. *RSC Adv.* **2013**, *3*, 25970. [CrossRef]
16. Phua, K.K.L.; Boczkowski, D.; Dannull, J.; Pruitt, S.; Leong, K.W.; Nair, S.K. Whole Blood Cells Loaded with Messenger RNA as an Anti-Tumor Vaccine. *Adv. Healthc. Mater.* **2014**, *3*, 837–842. [CrossRef]
17. D'Alessandro, A.; Righetti, P.G.; Zolla, L. The red blood cell proteome and interactome: An update. *J. Proteome Res.* **2010**, *9*, 144–163. [CrossRef] [PubMed]
18. Oldenborg, P.A.; Zheleznyak, A.; Fang, Y.F.; Lagenaur, C.F.; Gresham, H.D.; Lindberg, F.P. Role of CD47 as a marker of self on red blood cells. *Science* **2000**, *288*, 2051–2054. [CrossRef] [PubMed]
19. Bahmani, B.; Bacon, D.; Anvari, B. Erythrocyte-derived photo-theranostic agents: Hybrid nano-vesicles containing indocyanine green for near infrared imaging and therapeutic applications. *Sci. Rep.* **2013**, *3*, 2180. [CrossRef] [PubMed]
20. Burns, J.M.; Vankayala, R.; Mac, J.T.; Anvari, B. Erythrocyte-Derived Theranostic Nanoplatforms for Near Infrared Fluorescence Imaging and Photodestruction of Tumors. *ACS Appl. Mater. Interfaces* **2018**, *10*, 27621–27630. [CrossRef]
21. Ryu, J.H.; Lee, S.; Son, S.; Kim, S.H.; Leary, J.F.; Choi, K.; Kwon, I.C. Theranostic nanoparticles for future personalized medicine. *J. Control. Release* **2014**, *190*, 477–484. [CrossRef]
22. Weigand, R.; Rotermund, F.; Penzkofer, A. Aggregation dependent absorption reduction of indocyanine green. *J. Phys. Chem. A* **1997**, *101*, 7729–7734. [CrossRef]
23. Jung, B.; Vullev, V.I.; Anvari, B. Revisiting indocyanine green: Effects of serum and physiological temperature on absorption and fluorescence characteristics. *IEEE J. Sel. Top. Quantum Electron.* **2014**, *20*, 7000409. [CrossRef]
24. Emerson, E.S. The geometrical structure and absorption spectrum of a cyanine dye aggregate. *J. Phys. Chem.* **1967**, *71*, 2396–2403. [CrossRef]
25. Zhou, J.F.; Chin, M.P.; Schafer, S.A. Aggregation and Degradation of Indocyanine Green. In *Proceedings SPIE 2128, Laser Surgery: Advanced Characterization, Therapeutics, and Systems IV*; SPIE Society of Photo-Optical Instrumentation Engineers: Bellingham, WA, USA, 1994; Volume 2128, pp. 495–505. [CrossRef]
26. Saxena, V.; Sadoqi, M.; Shao, J. Degradation kinetics of indocyanine green in aqueous solution. *J. Pharm. Sci.* **2003**, *92*, 2090–2097. [CrossRef] [PubMed]
27. Mindt, S.; Karampinis, I.; John, M.; Neumaier, M.; Nowak, K. Stability and degradation of indocyanine green in plasma, aqueous solution and whole blood. *Photochem. Photobiol. Sci.* **2018**, *17*, 1189–1196. [CrossRef]

28. Gorka, A.P.; Nani, R.R.; Schnermann, M.J. Cyanine polyene reactivity: Scope and biomedical applications. *Org. Biomol. Chem.* **2015**, *13*, 7584–7598. [CrossRef]
29. Saxena, V.; Sadoqi, M.; Shao, J. Enhanced photo-stability, thermal-stability and aqueous-stability of indocyanine green in polymeric nanoparticulate systems. *J. Photochem. Photobiol. B Biol.* **2004**, *74*, 29–38. [CrossRef]
30. Lee, Y.-H.; Lai, Y.-H. Synthesis, Characterization, and Biological Evaluation of Anti-HER2 Indocyanine Green-Encapsulated PEG-Coated PLGA Nanoparticles for Targeted Phototherapy of Breast Cancer Cells. *PLoS ONE* **2016**, *11*, e0168192. [CrossRef] [PubMed]
31. Ehrenberg, B.; Anderson, J.L.; Foote, C.S. Kinetics and Yield of Singlet Oxygen Photosensitized by Hypericin in Organic and Biological Media. *Photochem. Photobiol.* **1998**, *68*, 135–140. [CrossRef] [PubMed]
32. Hackbarth, S.; Pfitzner, S.; Guo, L.; Ge, J.; Wang, P.; Röder, B. Singlet Oxygen Kinetics in Polymeric Photosensitizers. *J. Phys. Chem. C* **2018**, *122*, 12071–12076. [CrossRef]
33. Yaseen, M.A.; Yu, J.; Wong, M.S.; Anvari, B. Stability assessment of indocyanine green within dextran-coated mesocapsules by absorbance spectroscopy. *J. Biomed. Opt.* **2007**, *12*, 064031. [CrossRef]
34. Yeroslavsky, G.; Umezawa, M.; Okubo, K.; Nigoghossian, K.; Thi Kim Dung, D.; Miyata, K.; Kamimura, M.; Soga, K. Stabilization of indocyanine green dye in polymeric micelles for NIR-II fluorescence imaging and cancer treatment. *Biomater. Sci.* **2020**, *8*, 2245–2254. [CrossRef]
35. Yeroslavsky, G.; Umezawa, M.; Okubo, K.; Nigoghossian, K.; Dung, D.T.K.; Kamimura, M.; Soga, K. Photostabilization of indocyanine green dye by energy transfer in phospholipid-peg micelles. *J. Photopolym. Sci. Technol.* **2019**, *32*, 115–121. [CrossRef]
36. Valcourt, D.M.; Dang, M.N.; Day, E.S. IR820-loaded PLGA nanoparticles for photothermal therapy of triple-negative breast cancer. *J. Biomed. Mater. Res. Part A* **2019**, *107*, 1702–1712. [CrossRef] [PubMed]
37. Banno, B.; Ickenstein, L.M.; Chiu, G.N.C.; Bally, M.B.; Thewalt, J.; Brief, E.; Wasan, E.K. The functional roles of poly(ethylene glycol)-lipid and lysolipid in the drug retention and release from lysolipid-containing thermosensitive liposomes in vitro and in vivo. *J. Pharm. Sci.* **2010**, *99*, 2295–2308. [CrossRef]
38. Needham, D.; Zhelev, D.V. Lysolipid exchange with lipid vesicle membranes. *Ann. Biomed. Eng.* **1995**, *23*, 287–298. [CrossRef] [PubMed]
39. Kostevšek, N.; Cheung, C.C.L.L.; Serša, I.; Kreft, M.E.; Monaco, I.; Franchini, M.C.; Vidmar, J.; Al-Jamal, W.T.; Comes Franchini, M.; Vidmar, J.; et al. Magneto-liposomes as MRI contrast agents: A systematic study of different liposomal formulations. *Nanomaterials* **2020**, *10*, 889. [CrossRef]
40. Chen, W.R.; Adams, R.L.; Higgins, A.K.; Bartels, K.E.; Nordquist, R.E. Photothermal effects on murine mammary tumors using indocyanine green and an 808-nm diode laser: An in vivo efficacy study. *Cancer Lett.* **1996**, *98*, 169–173. [CrossRef]
41. Su, F.Y.; Chen, J.; Son, H.N.; Kelly, A.M.; Convertine, A.J.; West, T.E.; Skerrett, S.J.; Ratner, D.M.; Stayton, P.S. Polymer-augmented liposomes enhancing antibiotic delivery against intracellular infections. *Biomater. Sci.* **2018**, *6*, 1976–1985. [CrossRef]

# Chapter 5

# Efficient siRNA delivery to murine melanoma cells via a novel genipin-based nano-polymer

Genipin is known to be a safe amine-group crosslinker that is used as an alternative to glutaraldehyde. It has been used to crosslink chitosan, collagen, and other naturally occurring amine-containing polymers. In its 2-step mechanism of reaction, a monomer of genipin can spontaneously include an unprotonated amine group in its iridoid ring; as a second step, or finally crosslinking, two amined genipin moieties can crosslink on the overhanging carboxylic group via a substitution reaction and finally produce methanol [223]. The reaction is strongly pH dependent and can therefore be tuned by changing the acidity of the solution. The products of the polymerization of genipin are green–blue-purple according to the length of the amine-donor aliphatic chain [224].

Polyamines are a wide group of short, aliphatic carbon- and nitrogen-based molecules; both spermine and spermidine are ubiquitous in life on Earth and are necessary for many cell functions, such as RNA and DNA stabilization, mitochondrial metabolism, and differentiation, and they are strongly linked to mammal fertility [329]. They both have a highly cationic charge at neutral pH, +3 and +4 for spermidine and spermine, respectively, which is derived from their high pKas values for all amine groups (>9.5).

We therefore speculated that it would be possible to obtain polymeric nanoparticles by carefully tuning the molar ratios of genipin and polyamines, while the polymerization chain can be blocked by the addition of a small amino acid, glycine, containing only one amino group. The addition of a carboxylic moiety can also contribute to reducing potential cytotoxicity by tuning the "zwitterionic character" of nanosized polymers. As stated in the introduction, an excessive cationic charge can elicit an apoptotic cascade in eukaryotic cells and, thus, high cytotoxicity. Polymeric nanoparticles represent a growing field of study in terms of transfecting agents, both for RNA and DNA agents [40], owing to their concentrated positive charge, which makes them capable of complexing with the phosphate backbone of nucleic acids .

The synthesis of genipin-polyamines-glycine polymers is outlined in **Figure 12**. During this study, while the pH (7.4) and the genipin to spermine molar ratio (1:5) were held constant, the final amount of glycine in the reaction batch was varied. We finally selected G1S5, G5S5 and G10S5 (collectively termed GxS5), with 1:1, 1:5 and 1:10 glycine-to-genipin ratios, respectively, in the reaction batch. All three of these polymers presented strong short-RNA complexing ability, which was the initial hypothesis. Furthermore, the GxS5 polymers showed continuous fluorescence emission from light orange to far red, despite having a low quantum yield (approximately 1% with respect to Rhodamine B and

Fluorescein), but they were strong enough to quantify the internalization efficiency via FACS. Indeed, as a transfection model, B16F10 murine melanoma was used as a fast-growing and well-known cancer model. Interestingly, the polymers appeared to have little toxicity to various cell lines – normal and cancerous—with G10S5 being the least toxic polymer. Additionally, G10S5 was the most efficient transfection agent among the set, capable of eliciting 60% gene knockdown at a 30 nM dose in various complexes combined with siRNAs. Taken together, our data suggest that the genipin-polyamine scaffold represents a promising starting point for a novel class of safe and self-fluorescent polymeric transfection agents. Finally, the supplementary material from this chapter is presented in **Appendix B**.

In this paper, **Hypothesis 5 and Hypothesis 7 were assayed and confirmed**.

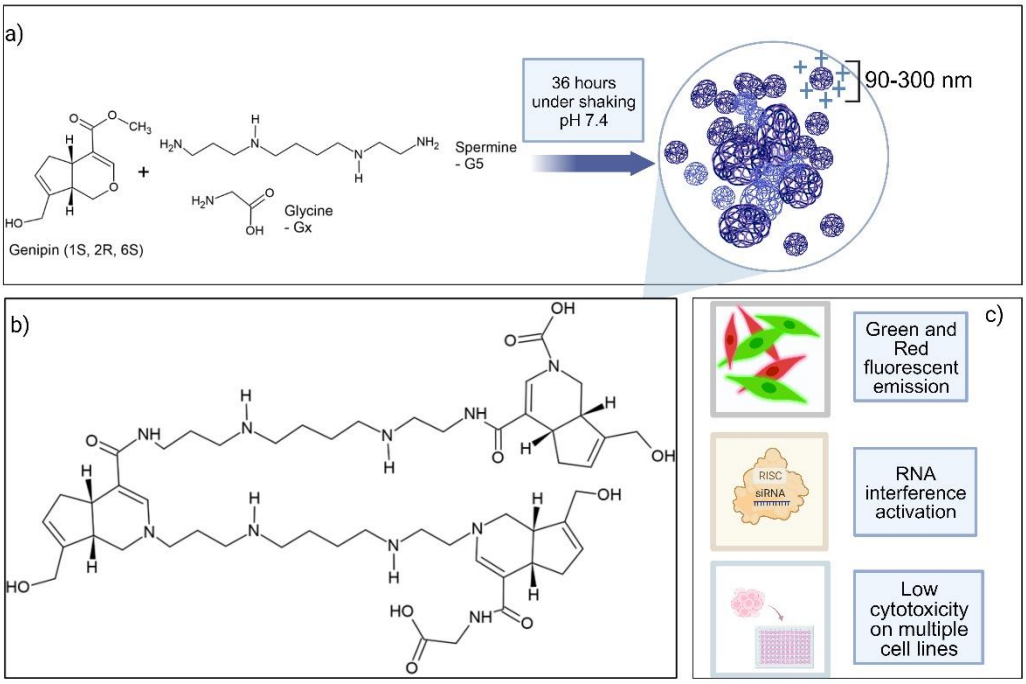



Figure 12 Graphical Abstract for Chapter 5. Reprinted from [330].

Nanoscale Advances

ROYAL SOCIETY OF CHEMISTRY

PAPER

View Article Online
View Journal | View Issue

Check for updates

Cite this: *Nanoscale Adv.*, 2024, **6**, 4704

# Efficient siRNA delivery to murine melanoma cells *via* a novel genipin-based nano-polymer†

Giulia Della Pelle, *[ab] Tim Bozic, [c] Marija Vukomanović, [d] Gregor Sersa, [ce] Bostjan Markelc [c] and Nina Kostevšek [ab]

Small-interfering RNAs (siRNAs) are therapeutic nucleic acids, often delivered *via* cationic polymers, liposomes, or extracellular vesicles, each method with its limitations. Genipin, a natural crosslinker for primary amines, was explored for siRNA delivery scaffolds. Spermine/genipin-based GxS5 polymers were synthesized, showing slightly positive $\zeta$ potential at neutral pH and intrinsic fluorescence. We then tuned their polymerization adding glycine to the reaction batch, from 1 to 10 molar ratio with genipin, therefore conferring them a "zwitterionic" character. GxS5 efficiently internalized into B16F10 murine melanoma cells, and exhibited strong siRNA-complexing ability and they were able to elicit up to 60% of gene knock-down without any toxicity. This highlights GxS5's potential as a safe, replicable, and tunable platform for therapeutic nucleic acid delivery, suggesting broader applications. This innovative approach not only sheds light on the intricate genipin reaction mechanism but also underscores the importance of fine-tuning nanoparticle properties for effective siRNA delivery. GxS5's success in mitigating cytotoxicity while maintaining delivery efficacy signifies a promising step towards safer and more efficient nucleic acid therapeutics.

Received 2nd May 2024
Accepted 15th July 2024

DOI: 10.1039/d4na00363b

rsc.li/nanoscale-advances

Open Access Article. Published on 19 July 2024. Downloaded on 5/15/2025 12:59:42 PM.
This article is licensed under a Creative Commons Attribution 3.0 Unported Licence.

## 1 Introduction

The story of the clinical translation of small-interfering RNA (siRNA) began in 2018, with the approval of Patisaran.[1] Due to their 3′ overhangs, small-interfering RNAs can elicit RNA interference upon RISC-complex binding, taking advantage of the pre-existing machinery originally destined for micro RNAs (miRNAs).[2] Quantitatively speaking, the exact number of siRNA molecules per cell necessary to elicit a strong response varies according to a variety of factors: membrane permeability, internalization efficiency, and endosomal escape rate.[3] Quantitatively speaking, the number of siRNA molecules per cell, for lipofectamine-siRNA complexes, was reported to be as low as few thousands of molecule per cell necessary to elicit a detectable knock-down, with a strict dependence on the sequence potency.[4] Lipofectamine, although very effective, is known to be toxic.[4,5] Therefore, the development of a safer alternative is of great interest. Endosomal escape still represents the major bottleneck to overcome in non-viral siRNA transfection:[6] mammals do not possess any specific RNA transporter, in contrast to Nematoda species, such as *Caenorhabditis elegans*.[7,8] Whereas single-stranded antisense oligonucleotides can be easily modified to be RNAse-resistant and are promptly endocytosed by cells, only 1% of the injected dose in mice, in the absence of coating or nano-encapsulation, spontaneously escapes the endosomes.[9]

In contrast, double-stranded, small-interfering RNAs cannot be chemically modified to a great extent. They are, therefore, readily degraded by circulating RNAses and by anti-viral machinery. A carrier is required to ensure a longer circulation time and an effective transfection.[10,11] Most common approaches to siRNA delivery, such as lipofection or the use of polycations, take advantage of the well-established proton-sponge effect, and subsequent "endosomal escape".[12] For very positively charged carriers, though, it is safer to speak about "endosomal rupture" rather than "endosomal escape". The lumen of an endosome, while maturing into a late endosome (pH 5–5.5), and, later, turning into a lysosome, is subjected to acidification by ATPase proton pumps. During the occurrence of this phenomenon, the presence of any ionizable conjugate or small molecule with H-buffering capability leads to an increase in the accumulation of $Cl^-$ ions within the lumen (as a co-substrate of $H^+$). Later, lysis of the membrane can occur, with the simultaneous release in the cytoplasm of an ionizable conjugate acting as a transfection agent – although resulting, briefly, in a certain degree of cytotoxicity.[13,14] Therefore, the so-called, yet debated, proton-sponge effect,[15] is connected to the buffering capability of the transfection agent, as N-quaternized

[a]Department for Nanostructured Materials, Jožef Stefan Institute, 1000 Ljubljana, Slovenia. E-mail: giulia.della.pelle@ijs.si
[b]Jožef Stefan International Postgraduate School, 1000 Ljubljana, Slovenia
[c]Department of Experimental Oncology, Institute of Oncology Ljubljana, 1000 Ljubljana, Slovenia
[d]Advanced Materials Department, Jožef Stefan Institute, 1000 Ljubljana, Slovenia
[e]Faculty of Health Sciences, University of Ljubljana, Zdravstvena pot 5, SI-1000 Ljubljana, Slovenia

† Electronic supplementary information (ESI) available. See DOI: https://doi.org/10.1039/d4na00363b



© 2024 The Author(s). Published by the Royal Society of Chemistry

Open Access Article. Published on 19 July 2024. Downloaded on 5/15/2025 12:59:42 PM.
This article is licensed under a Creative Commons Attribution 3.0 Unported Licence.

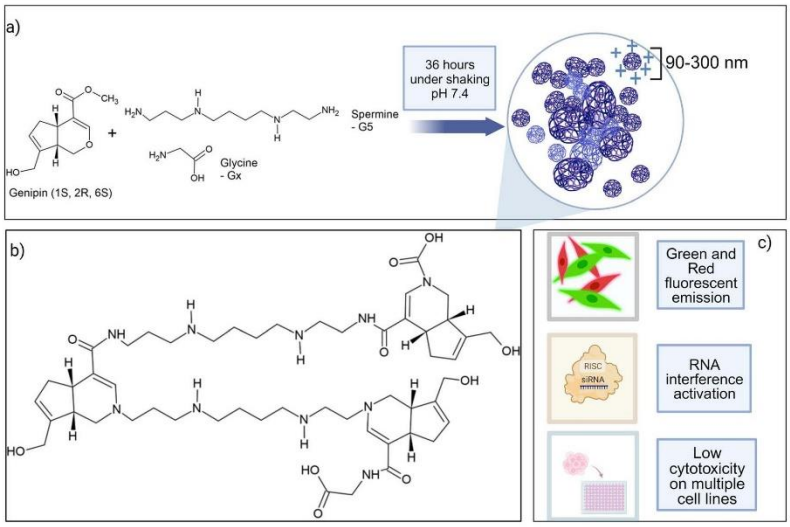



Fig. 1 (a) Components of GxS5 polymers and overview of the synthesis process; (b) general structure of GxS5 polymers; (c) main properties of GxS5 polymers. For the sake of simplicity, some chemical bonds have been elongated and the image is not representative of the structural arrangement of the polymer in water or a buffer.

PEI shows a reduced transfection ability.[16] Now, an ideal cationic transfection agent should be able to escape the endosomes, causing a limited rupture. It must possess a moderate buffering capability to balance the delicate interplay among (a) a nucleic acid complexing ability, (b) cytotoxicity due to endosomal rupture, (c) active or passive internalization, (d) a residency time in the cytoplasm, and (e) an ability in the case of siRNAs to release the cargo for RISC-complex uptake. Apart from buffering capabilities, another essential characteristic of a polymeric transfection agent should be intrinsic in its spatial arrangement in aqueous medium. Upon the total protonation of amine groups, the monomer size should increase slightly due to the electrostatic repulsions,[17,18] leading to an easier decomplexation of the payload.

A wide range of nanomaterials is currently available for small-interfering RNA transfection, mostly relying on artificial polycationic polymers such as PEI, PAMAM, block-copolymers or surface-engineered liposomes.[19–22] Conventional dendrimer approaches suffer from a high-to-moderate cytotoxicity due to the concentrated positive charge, rapid clearance or kidney/liver bioaccumulation, lack of biodegradability *in vivo* and scarce solubility. Extreme cationic charge, indeed, despite representing the easiest route for a nanoparticle to enter a cell membrane, leads to a cascade of events, including $Ca^{2+}$-induced apoptosis.[23,24] Therefore, due to an increasing interest in nucleic acid delivery for gene therapy, the development of novel, safer and highly efficient transfection agents is vital to overcome the limitations of the current delivery systems. To reach that goal, a good balance among a number of factors must be achieved, *i.e.*, the ability to form complex therapeutic nucleic acids *via* either ionic bridges and hydrophobic interactions,[25] the ionizability of amine groups within the maturing endosome compartment,[13] and, finally, an adequate endosome-escape ratio without significantly impacting the cell viability by activating apoptotic pathways.

Here, we introduce novel, genipin-based, cationic polymer nanoparticles (NPs) as a safe and efficient RNA transfection agent of natural origin, which also has inherent fluorescence that can be used for imaging purposes. Our polymers are composed of polyamines, genipin and glycine. To the best our knowledge, this is the first time that such a combination has been used for the preparation of well-characterized and stable nanoparticles for the delivery of a nucleic acid.

Polyamines, *i.e.*, spermine and spermidine, were chosen because they are naturally complexed with mRNAs and other cytosolic RNAs.[26–28] More specifically, spermine in solution inserts itself within the minor groove of double-stranded RNA,[27] and it locks it in a relatively stable configuration that prevents aggregation. Then, genipin was applied to crosslink the polyamines. Genipin, a naturally occurring iridoid (belonging to the family of cyclic monoterpene secondary metabolites),[29] has a relatively low cytotoxicity compared to other common crosslinkers and it can react with unprotonated amines, yielding products of various colours according to the amine moiety's chemical environment.[30] Genipin-crosslinked polymers also exhibit red fluorescence,[31,32] which can be exploited for intracellular tracking and the investigation of degradation pathways.

© 2024 The Author(s). Published by the Royal Society of Chemistry

Open Access Article. Published on 19 July 2024. Downloaded on 5/15/2025 12:59:42 PM. This article is licensed under a Creative Commons Attribution 3.0 Unported Licence.

The genipin was allowed to react with different molar ratios of naturally occurring polyamines, spermine and spermidine. Glycine, a small amino acid with only one reactive amino group was chosen to terminate the polymerization chain of the genipin and spermine moieties. Finally, a 1 : 5 molar ratio of genipin-to-spermine was chosen, while the glycine molar ratio was kept variable. Polymers were therefore called G*x*S5, where "G" stands for glycine, "*x*" for the different molar ratios of glycine-to-genipin, "S" stands for spermine, whereas "5" stands for its molar ratio with regard to genipin (Fig. 1). We first characterized the genipin reaction mechanism and kinetics in the presence of spermine and spermidine in terms of the reaction rate and reaction order. Next, the fluorescence of the products and their anti-oxidant activity were quantitatively investigated. Their small-interfering RNA complexing ability, complex stability, cytotoxicity and behaviour under endosome-mimicking conditions were investigated for gene-silencing applications. Finally, the capability to transfect murine melanoma cells with an anti-reporter gene siRNA was demonstrated. The presence and the molar ratio of glycine was found to be instrumental with regard to the particle size, cytotoxicity, siRNA complexing ability, and transfection efficiency.

## 2 Results

### 2.1 UV/vis analysis of genipin–spermine-based polymers

Genipin is known to react with unprotonated primary amines,[33] but its reaction kinetics with naturally occurring spermine and spermidine, each one of them possessing two primary amines, is yet to be fully investigated. First, the spectra of genipin–polyamine-based polymers showed the typical features of a crosslinked genipin matrix[34,35] (Fig. 2a, and b). Due to the iridoid ring opening, genipin's peculiar peak at 240 nm evolves into three different signals at 290, 375 and 580 nm. Subsequently, the final polymerization product, with an absorbance peak at 580 nm, will be termed P580. Four tested molar ratios of genipin-to-glycine, defined as G*x*S5 (Materials and methods), gave rise to remarkably similar spectra, with maxima at 290 and 580 nm (Fig. 2a), and a weak hump at 375 nm. Then, to ascertain whether there was any significant difference in terms of reaction kinetics between the spermine and spermidine, different molar ratios of polyamines to genipin (as in Table 1) were incubated for 48 hours at room temperature, at pH 7.4, in the absence of glycine. Genipin concentration was kept constant at 0.000168 M. The absorbances at 240 nm, 280 nm, 375 nm and 580 nm were continuously monitored (Fig. 2b). The reaction was over after 36 hours of incubation (data not shown). The decrease, over time, of unreacted genipin was derived from a calibration curve (Fig. S1†). The increase in the absorbance of the intermediates at 280 nm and 375 nm is due to genipin consumption (240 nm) as well as the formation of the final product absorbing at 580 nm. The genipin consumption, monitored at 240 nm, and the formation of the final product at 580 nm were chosen to investigate the final kinetics law to shed light on its reaction mechanism, and allow us to optimize subsequent steps for our polymer's synthesis.

Furthermore, to ascertain the reaction order relative to the two reagents, *i.e.*, genipin and the primary amine-group donors

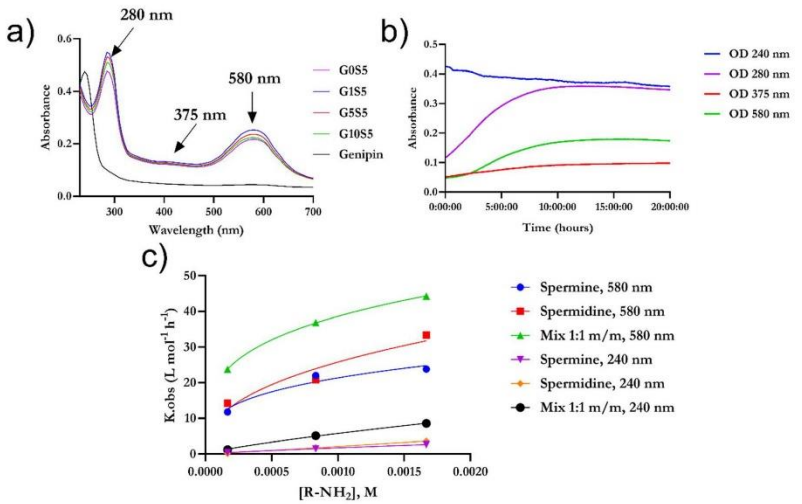



Fig. 2 (a) Fig. 3 UV/vis spectra of genipin–polyamines–glycine polymers. The initial genipin concentration was set at 0.167 mM and it was consistent for the four samples. Final P580 concentration is 0.38 ± 2.5 $10^{-4}$ and does not differ significantly among the formulations ($n = 6$ for each kind of sample). (b) Example of evolution in terms of absorbance of a genipin-polymerization reaction in the presence of spermine. For experiments regarding the nature of the mechanism and reaction kinetics of genipin, glycine was omitted. (c) $K_{obs}$ calculated with genipin consumption monitored at 240 nm and 580 nm *vs.* amine concentration. Fitting was determined according to eqn (11) using data from Table 1.

 © 2024 The Author(s). Published by the Royal Society of Chemistry

Open Access Article. Published on 19 July 2024. Downloaded on 5/15/2025 12:59:42 PM.
This article is licensed under a Creative Commons Attribution 3.0 Unported Licence.

Table 1 Values obtained for $k_{obs}$ for each concentration of polyamines and amine sources. Data were then used in the plot in Fig. 2c and fitted in eqn (11)

| Amine source | [R–$NH_2$] (M) | $K_{obs}$ ($M^{-1}$ $h^{-1}$) | Monitored parameter (M) |
|---|---|---|---|
| Spermine | 0.000167 | 11.78 | [P580] |
| Spermidine | 0.000167 | 14.22 | [P580] |
| Spermine/spermidine 1 : 1 | 0.000167 | 23.76 | [P580] |
| Spermine | 0.00083 | 22.02 | [P580] |
| Spermidine | 0.00083 | 20.86 | [P580] |
| Spermine/spermidine 1 : 1 | 0.00083 | 36.88 | [P580] |
| Spermine | 0.00167 | 23.80 | [P580] |
| Spermidine | 0.00167 | 33.44 | [P580] |
| Spermine/spermidine 1 : 1 | 0.00167 | 44.28 | [P580] |
| Spermine | 0.000167 | 0.41 | [Genipin] |
| Spermidine | 0.000167 | 0.2 | [Genipin] |
| Spermine/spermidine 1 : 1 | 0.000167 | 1.23 | [Genipin] |
| Spermine | 0.00083 | 1.46 | [Genipin] |
| Spermidine | 0.00083 | 1.82 | [Genipin] |
| Spermine/spermidine 1 : 1 | 0.00083 | 5.12 | [Genipin] |
| Spermine | 0.00167 | 2.65 | [Genipin] |
| Spermidine | 0.00167 | 3.60 | [Genipin] |
| Spermine/spermidine 1 : 1 | 0.00167 | 8.55 | [Genipin] |

(the polyamines spermine and spermidine), we first evaluated the apparent consumption speed $\vartheta_n$ (M $h^{-1}$) at 240 nm in terms of the genipin consumption (eqn (1)), where $n$ stands for different genipin concentrations ($n_1$–$n_4$, see Table S1†).

$$\vartheta_n = -\frac{d[G]}{dt} = k_n[G]^{a_1}[R-NH_2]^{b_1} \quad (1)$$

[G] and [R–$NH_2$] are the concentrations of genipin and polyamine, respectively, with [R–$NH_2$] being a constant (0.00083 M). $a_1$ and $b_1$ are the reaction orders and $k$ is the kinetic constant. The isolation method was used to determine the reaction order $a_1$ for genipin consumption. In the isolation method, one reagent is kept constant while the others are varied over a known range, and the initial reaction speeds $\vartheta_n$, defined as the slope of the linear area of the absorbance plot, are compared.[36] Thus, different $\frac{\vartheta_{n+1}}{\vartheta_n}$ ratios of the initial [G] concentrations were used, as shown in eqn (2). Finally, the Van't Hoff differential method[37] was applied to derive $a_1$ (eqn (3)). The reaction order for the consumption of genipin monitored at 240 nm was found to be $a_1 = 1.57 \pm 0.25$.

$$\frac{\vartheta_{n+1}}{\vartheta_n} = \frac{k[G]_{n+1}^{a_1}[R-NH_2]_0^{b_1}}{k[G]_n^{a_1}[R-NH_2]_0^{b_1}}, [R-NH_2]_0 = \text{constant} \quad (2)$$

$$a_1 = \frac{\ln\frac{\vartheta_{n+1}}{\vartheta_n}}{\ln\frac{[G]_{n+1}}{[G]_n}} \quad (3)$$

Then, the same protocol was applied to determine $b_1$ for the three amine sources. Again, different $\frac{\vartheta_{m+1}}{\vartheta_m}$ ratio combinations of the initial [R–$NH_2$] concentrations were used (see Table S2†) and [G] was kept constant at (0.000168 M) to derive eqn (4), which allows the calculation of $b_1$. The three amine sources [R–$NH_2$] (spermine, spermidine, and 1 : 1 m m$^{-1}$ mix of them) were mathematically treated separately (see Table S2†). The reaction order was calculated to be $b_1 = 1.16 \pm 0.32$. For further analysis, we approximate $a_1$ and $b_1$ to be 1.5 and 1, respectively.

$$b_1 = \frac{\ln\frac{\vartheta_{m+1}}{\vartheta_m}}{\ln\frac{[R-NH_2]_{m+1}}{[R-NH_2]_m}} \quad (4)$$

The same protocol was applied to determine the reaction orders $a_2$ and $b_2$ for the formation of the product absorbing at 580 nm, termed P580 (Tables S3 and S4†), expressed as eqn (5):

$$\vartheta_m = \frac{d[P580]}{dt} = k_m[G]^{a_2}[R-NH_2]^{b_2} \quad (5)$$

For the formation of the product, reaction orders $a_2$ and $b_2$ were found to be $1.51 \pm 0.8$, with respect to genipin, and $0.53 \pm 0.17$, with respect to the concentration of the amine groups. We approximate their values to be $a_1 = a_2 \approx 1.5$ and $b_2 \approx 0.5$.

Using different initial concentrations of genipin also allowed us to calculate the molar extinction coefficient $\varepsilon$ of P580 ($\varepsilon_{P580} = 8.5\ 10^3$ mol$^{-1}$ L$^{-1}$), the product appearing at 580 nm, as the slope of the plot in Fig. S2a,† and a path-length correction protocol was used. $\varepsilon$ was used to estimate the P580 concentration (Fig. S2b†) in later experiments.

At this stage of the analysis, the reaction laws, for the consumption of genipin and the production of P580, respectively, can be approximated as:

$$-\frac{d[G]}{dt} = k_n[G]^{1.5}[R-NH_2]^1 \quad (6)$$

© 2024 The Author(s). Published by the Royal Society of Chemistry

Open Access Article. Published on 19 July 2024. Downloaded on 5/15/2025 12:59:42 PM. This article is licensed under a Creative Commons Attribution 3.0 Unported Licence.

$$\frac{d[P580]}{dt} = k_m[G]^{1.5}[R - NH_2]^{0.5} \quad (7)$$

To determine the rate-limiting step of the genipin polymerization and shed more light on its reactivity within our system, the reaction-rate constants $k$ must be determined. The values can be obtained by solving the following equation:

$$K_{obs_{m,n}} = k_{n,m}[R\text{–}NH_2]^{b_{1,2}}$$

where $k_{obs}$ is generally defined as the observed experimental rate constant, dependent on the initial concentration of the unisolated reactant, *i.e.*, primary amines, the reaction step, and the monitored parameter. Therefore, pseudo-order reactions as mathematical treatments must be introduced, using the integration method described by Upadhyay.[36] To calculate the observed reaction-rate constant ($k_{obs}$) we used the methodology presented in ref. 36 for the fractional reaction orders $b_2 = 0.5$ and $a_1 = 1.5$ (Fig. S3†). By integrating eqn (6) and (7) over time, respectively, for all concentrations of [G] and [P580], we obtained the following, as generalized forms:

$$k_{obs_n} = \frac{2}{t}\left(\frac{1}{[A]^{0.5}} - \frac{1}{[A]_0^{0.5}}\right) \text{ for } a_1 = 1.5 \quad (8)$$

$$k_{obs_m} = \frac{2}{t}\left([A]^{0.5} - [A]_0^{0.5}\right) \text{ for } b_2 = 0.5 \quad (9)$$

where [A] is the concentration of genipin or P580 at any given time, and $[A]_0$ is the initial concentration.

Again, as formalized by Upadhyay, to obtain the value of the observed experimental reaction constants $k_{obs}$, from eqn (8) and (9) we can extract and plot $1/[G]^{0.5}$ or $1/[P580]^{0.5}$ against time (Fig. S3a and S3b,† respectively, expressed in hours). As a derivation from eqn (8) and (9), the values of $k_{obs}$ are equal to twice the slopes (eqn (10)). Each amine group source (spermine, spermidine, and 1 : 1 mix of them) was mathematically treated separately (Table 1 and Fig. 1c). The slopes of the plots were calculated and the $k_{obs}$ values were obtained with the $r^2 > 0.97$.

$$k_{obs} = 2 \times \text{slope} \quad (10)$$

For the genipin consumption monitored at 240 nm, the experimental reaction order of $b_1$, 1.16 ± 0.32 was confirmed to be approximately 1, from the least-squares fitting of eqn (11) (0.81 ± 0.06, 1.054 ± 0.02, and 0.79 ± 0.09 for spermine, spermidine, and 1 : 1 molar mix), and the rate constant $k$, L mol$^{-2}$ h$^{-2}$ was subsequently derived using the already-introduced relationship (Fig. 2c):

$$K_{obs_{n,m}} = k_{n,m}[R\text{–}NH_2]^{b_{1,2}} \quad (11)$$

where $k_{obs_{n,m}}$ are the observed experimental reaction constants, $k_{n,m}$ are the reaction constants for the genipin consumption and P580 formation, and $b_{1,2}$ are the reaction orders obtained with the exponential fitting ($r > 0.95$). The reaction constants $k_n$ for the consumption of genipin under our conditions are 153.3 ± 9.12, 968.7 ± 12.64, and 507.5 ± 34.12 L mol$^{-2}$ h$^{-2}$ for the three amine sources: spermine, spermidine, and 1 : 1 molar mix, respectively. The 1 : 1 mix's kinetic reaction constant was found to be between those of spermine and spermidine. Applying the same procedure for the formation of P580, the experimental reaction order $b_2$ with regard to the amines for the formation of the P580 (0.53 ± 0.17, Table S3†) was confirmed *via* the fitting of eqn (6) ($r^2 > 0.97$), obtaining a value of $b_2$ equal to 0.43 ± 0.04, 0.51 ± 0.09, and 0.49 ± 0.07 for spermine, spermidine, and the 1 : 1 molar mix, respectively (Fig. 2c). The reaction-rate constants $k_m$ for the formation of P580 were found to be 105.8 ± 7.34, 275.5 ± 63.9, and 204.8 ± 46.5 L mol$^{-2}$ h$^{-2}$ for spermine, spermidine, and the 1 : 1 molar mix, respectively, fitting eqn (11). Therefore, the final crosslinking of the genipin moieties, represented by the formation of P580, is the limiting step of the reaction, as reported in ref. 33 and 38, *i.e.*, that dictating the actual reaction speed.

The final kinetic law of genipin polymerization in the presence of the amine sources is therefore:

$$-\frac{d[G]}{dt} = k[G]^{3/2}[R - NH_2]^{1/2} \quad (12)$$

The values of the rate constants arise from the charge distribution within the polyamine molecule. Indeed, the p$K_a$ of the two external amines of spermine are respectively 10.9 and 10.1, while those of spermidine 10.1 and 9.9,[39] thus increasing slightly (0.11% of spermine *vs.* 0.25% of spermidine) the chances of a primary amine not being protonated and therefore available for reaction.

Despite this finding, we decided to choose spermine as the primary amine source for the synthesis of our polymer due to its longer aliphatic chain and higher net-positive charge.

### 2.2 Size, zeta potential and ultrastructure characterization of genipin–polyamine-based polymers: optimization of molar ratios of the polyamines

The dynamic light-scattering technique was used to investigate the size and ζ potential of our polymers. We first determined which polyamine, *i.e.*, spermine and spermidine, was more suitable as a scaffold (Table S5†). The spermidine-based polymers had a lower ζ-potential (5–12 mV) than the spermine-based polymers (12–18 mV), likely due to the protonation of the only remaining amine in the aliphatic chain not occupied in crosslinking with genipin, in place of spermine having two amines that can sport a positive charge. Within the same molar ratio range for genipin (1–10), no improvement in this parameter for the genipin/spermine molar ratios higher than five was observed. Spermine's extra internal amine group therefore provided a higher surface positive charge and, probably, a higher nucleic-acid-complexing ability. For this reason, we decided to keep genipin/spermine 1 : 5 as the molar ratio for all future synthesis (Table 2), while changing the glycine molar ratio. Since glycine possesses only one amine group, such an amino acid was chosen to end the polymerization chain, tentatively reducing the size of the nanoparticles and conferring on them a zwitterionic character. Since genipin is only able to

 © 2024 The Author(s). Published by the Royal Society of Chemistry

Open Access Article. Published on 19 July 2024. Downloaded on 5/15/2025 12:59:42 PM.
This article is licensed under a Creative Commons Attribution 3.0 Unported Licence.

react with unprotonated amine groups,[40] and the glycine amine group p$K_a$ is 9.8 at 25 °C, roughly only about 1% of all the groups would be available for a reaction at pH 7.4 at any moment. For all the spermine/glycine combinations the ζ potential was found to be positive (from +18.1 to +12.53 mV, Table 2), and the glycine molar ratio had a moderate effect on the value, decreasing it from G1S5 to G10S5. Furthermore, the increasing glycine concentration influenced the nanoparticles' size. At a 1 : 10 molar ratio with genipin, the particle size was found to be less than 200 nm for most of the recorded events. All three polymers showed a majority, in terms of the percentage of recorded events, of small nanoparticles (100–300 nm) and a minority of aggregates ranging from 800 nm to a micron. The two main particle populations were, respectively, termed "Population 1" (P1) and "Population 2" (P2). To characterize the polymers' ultrastructure, we conducted an aspect-ratio analysis using TEM images (Fig. S4,† $n$ of images = 10). Confirming the DLS data, several larger clots can be observed among an overwhelming majority of smaller particles. For the sake of simplicity, we focused on smaller particles (Population 1). The polymers appeared as dark, mostly regular, ellipsoidal clots that rapidly disintegrated under the TEM's electron beam (Fig. 3, 50.000 magnification). The glycine's increasing molar ratio proved to be instrumental in the formation and stabilization of individual nanoparticles, since no well-dispersed particle can be noted in the case of G0S5 (Fig. S4†). Surprisingly, the aspect ratio of G10S5 was higher than for G5S5 and G1S5(Fig. S4†). While G1S5 and G5S5 were found to follow a lognormal distribution, the G10S5 aspect-ratio frequency distribution was ambiguous, with only a Kolmogorov–Smirnov test considering it ($p = 0.035$) lognormal. Moreover, while the G1S5 and G5S5 aspect-ratio distributions are not significantly different, a Kruskall–Wallis test proved that the G10S5 nanoparticles' dimensions statistically diverge from the others ($p = 0.005$ with regard to G5S5 and $p = 0.0007$ with regard to G1S5). The apparent radius of a circle with the same area as the ellipse was used to compare the P1's and P2's relative abundancies in the TEM images. The latter yielded similar results to that already obtained with the DLS, confirming the reliability of this technique for such an object. As already known,[41] DLS overestimates the particle size by around 1.5 to 2 times due to the hydration-shell disturbance. Finally, we found a linear relationship between the mass concentration of the GxS5 polymers and the OD at 580 nm, which was used in all the subsequent experiments to calculate the mass concentration of the samples. The protocol and calibration curve are shown in the ESI (Fig. S5).†

### 2.3 Fluorescence investigation of genipin–spermine–glycine-based polymers

Although the fluorescence properties of genipin products are already known,[32,40] they were never investigated in a quantitative manner and in the presence of aliphatic amine sources such as spermine and spermidine. Two excitation/emission peaks were identified (Fig. 4a) when the polymers were dissolved in PBS, one with a near-UV excitation maximum at 375 nm, and emitting in the green region, and another in the blue area (561 nm), while emitting in the near red. Then, we monitored the evolution of the two fluorescence peaks over 6 hours at 375/460 nm em/ex and 561/620 em/ex (Fig. 4b, and 4c). Such timing was chosen to investigate the earlier, rate-determining hours of the reaction (Fig. 4b).

Interestingly, the evolution kinetics in terms of the A.U./h of the peak recorded in the red at 620 nm (Fig. 4c, and e) was found to be related (correlation matrix, $p < 0.001$) to the formation of the product at 580 nm (see Section 2.1), hinting that such a fluorescence emission is due to the final crosslinked genipin moieties, previously termed P580. On the other hand (Fig. 4b, and d), the nature of the peak being excited in the near-UV (375/460 ex/em) and emitting in green looks to be correlated (correlation matrix, $p = 0.002$) with the formation of an intermediate, weakly absorbing at 375 nm (Fig. 2a, and b). The fluorescence intensity of such an intermediate appears to rapidly reach a peak and then start to steeply decrease during the first two hours of reaction as already observed in ref. 38, therefore purportedly originating from an amine-substituted genipin. Such an intermediate disappears over time due to its final crosslinking.

We also tested whether the fluorescence emission was concentration-dependent and if any self-quenching effect was noticeable in the P580 molar-concentration range between 0.2 mM and 5 μM. We monitored the signal at em/ex 375/460 and 560/620 nm. The plots of [P580] against fluorescence

Table 2 Comparison of ζ-potential, DLS (number-weighted) and TEM particle size for different spermine-based polymer formulations, ±SD. The ratio between the two populations (see text for definition) is reported as %. DLS data arise from five independent measurements for each formulation of three different technical replicates. TEM particle size measurements were obtained with the ImageJ built-in measuring tool, on the basis of $n = 10$ micrographies for each formulation, three technical replicates of each GxS5, at 15.000× magnification

| Sample, molar ratio with genipin | ζ potential, mV | DLS particle size (nm) | Ratio P1/P2% in DLS | PDI (×100) | TEM diameter, nm | Ratio P1/P2% in TEM |
|---|---|---|---|---|---|---|
| Genipin: glycine: spermine = 1 : 1 : 5 (G1S5) | 18.1 ± 2.6 | 271.3 ± 49.5<br>832.4 ± 275.5 | 1.23 ± 0.67 | 15.23<br>11.17 | 160 ± 20<br>948 ± 12 | 5.02 ± 1.78 |
| Genipin: glycine: spermine = 1 : 5 : 5 (G1S5) | 12.5 ± 1.5 | 190.04 ± 72.7<br>1187.4 ± 683 | 3.86 ± 0.69 | 2.76<br>6.06 | 125 ± 16<br>1065 ± 50 | 9.47 ± 2.36 |
| Genipin: glycine: spermine = 1 : 10 : 5 (G10S5) | 12.3 ± 0.7 | 120.6 ± 10.7<br>997.8 ± 23.5 | 5.93 ± 1.54 | 7.94<br>5.33 | 98 ± 28<br>576 ± 73 | 14.36 ± 3.61 |
| Genipin: glycine: spermine = 1 : 0 : 5 (G0S5) | 18.9 ± 1.1 | 1014.3 ± 400 | ~0 | 15.46 | Not recognizable individual nanoparticles | |

Open Access Article. Published on 19 July 2024. Downloaded on 5/15/2025 12:59:42 PM.
This article is licensed under a Creative Commons Attribution 3.0 Unported Licence.

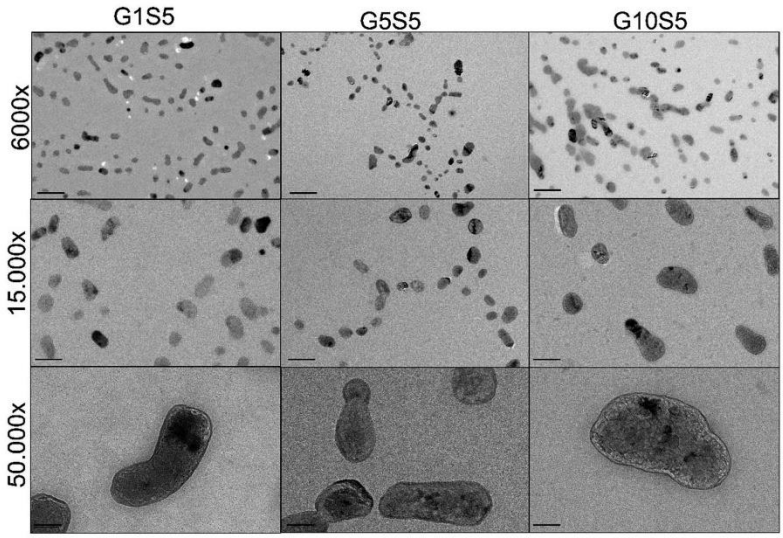



Fig. 3 TEM pictures of genipin-based polymers. From top to bottom, the scalebar is, respectively, 500, 200 and 50 nm. The magnification is reported on the left side.

emission were found to be linearly correlated for both maxima (Fig. S6†), with $r^2 > 0.90$ in all cases. Nevertheless, deviations from linearity appear evident from [P580] > 0.00012 M, hinting at a self-quenching at high concentrations (Fig. S6†).

**2.3.1 Quantum-yield (QY) determination in water and human plasma.** We then calculated the fluorescence quantum yield of both peaks ($\Phi_f$) of the GxS5 polymers using the gradient method.[42,43] Fluorescein isothiocyanate (FITC) was used as a reference dye for the green emission maximum, and rhodamine B was used for the red. Optical data for both dyes were obtained from ref. 44. Quantum yields $\Phi$ were calculated according to the equation:

$$\Phi_{460,620\text{nm}} = \Phi_{\text{FITC,rhodamine B}} \frac{\text{slope, polymer}}{\text{slope FITC, rhodamine B}} \times \left(\frac{n_{\text{polymer}}}{n_{\text{FITC,rhodamine B}}}\right) \quad (13)$$

Meanwhile, the "slope" is defined as the slope of the linear plot for the OD at the excitation wavelength *vs.* the integral of the emission spectrum of the dye excited at that wavelength, and $n$ is the refractive index of the solvent. ODs between 0.01 and 0.1 were used for the reference dyes, while P580 molar concentration was kept below 0.00012 M to avoid self-quenching effects and therefore variations from linearity. Slopes of reference dyes did not significantly differ from PBS to plasma 25% v/v (ANCOVA test, $p = 0.59$ for FITC and $p = 0.29$ for rhodamine B, Fig. S7b†). Both peaks of the polymers reflected a relatively low QY compared to rhodamine B (36%)[45] and FITC (90%),[46] as reported in Table 3, in an aqueous environment, while moderately increasing in the presence of plasma proteins. When mixed with plasma, the emission peak of all the polymers (Fig. S7†) was superimposed to that of the NADH ring: indeed, in plasma, two prominent peaks can be seen (see Fig. S7†), around 445 nm and the other one at 485 nm, belonging to the nicotinamide ring[47] present in NADH, one of the main fluorescence emitters in plasma. In the presence of plasma proteins, the QY slightly increased in all three polymers both in the red and green regions, but not in a statistically significant fashion ($p > 0.2$ for all buffer *vs.* plasma comparisons). The slopes of GxS5 appear substantially parallel, with no significant variations due to glycine concentration in the reaction batch (Fig. 4e, and f). The calculated blueshift in 25% plasma *vs.* water of the emission peak accounted for 15 nm with all three polymers.

### 2.4 Reaction with ninhydrin for amine-group determination

The number of amine groups available for nucleic acid complexation is a crucial parameter for the successful transfection of therapeutic nucleic acids. A ninhydrin assay is a widely used test for determining the concentration of amine groups,[48] and, although it has been extensively used for such a determination in chitosan,[49] extracellular matrix[50] and collagen[51] crosslinked substrates, to the best of our knowledge, this is the first reported use of such an assay for genipin–polyamine-based polymeric nanoparticles. It is known that the ninhydrin absorbance spectrum shows different peaks

 © 2024 The Author(s). Published by the Royal Society of Chemistry

Open Access Article. Published on 19 July 2024. Downloaded on 5/15/2025 12:59:42 PM.
This article is licensed under a Creative Commons Attribution 3.0 Unported Licence.

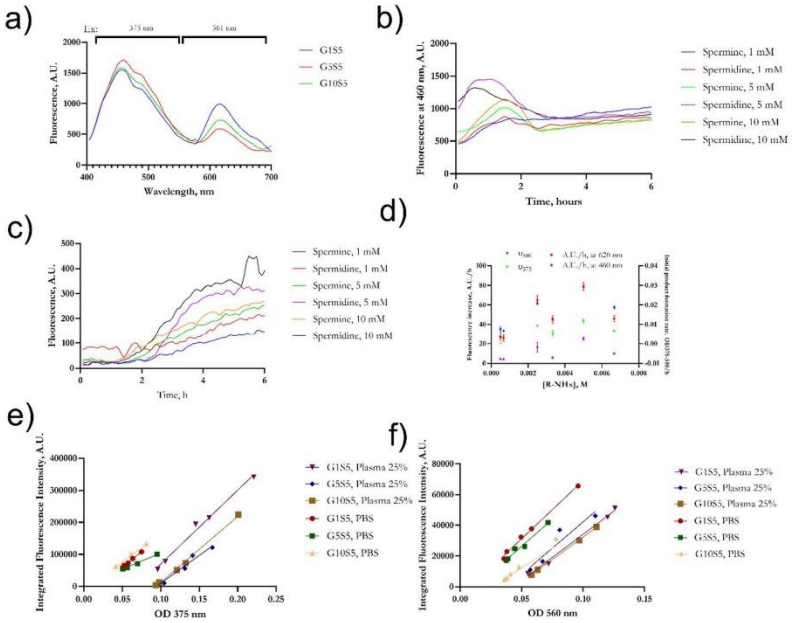



Fig. 4 (a) Merged emission spectra of column-purified polymers recorded at two different excitation wavelengths. (b) Kinetics of fluorescence emission for 375/460 nm ex/em; (c) for 561/615 nm ex/em. For the kinetic studies, no glycine was added, and the chosen amine source was spermine. (d) Rate of increase of fluorescence/hour, within 4 hours – linear range, compared with P580 formation rate and 375 nm product formation. (e) Plots of OD at 375 m *vs.* the integrated fluorescence intensity between 425 and 600 nm. (f) Plots of OD at 375 m *vs.* the integrated fluorescence intensity between 580 and 700 nm. Data (±SD) in (b–d) refer to the same experiment, $n = 3$ technical replicates.

according to the various amine sources the molecule is complexed with.[52] In our case, the main ninhydrin peak at 570 nm, conventionally used for quantification, overlaps with the P580 broad absorbance peak of the polymers (Fig. S8a†), and the signal at 400 nm was absent, whereas it was present when spermine is used as the amine source for a standard curve. Therefore, we checked the reliability of the signal present at 345 nm, while the concentration of [R–NH*x*], with a signal at 570 nm, was calculated by subtracting the polymer background. We used spermine as the source of amines for the calibration curve, determined at 345 nm ($r^2$ 0.97) and 570 nm ($r^2$ 0.92). Due to the low molar absorptivity at 570 nm of the complex formed by ninhydrin and polymer, we also used the signal at 345 nm for amine-group determination. The final molar concentrations of the amine groups for 100 mg $ml^{-1}$ polymers are reported in Table 4.

To ascertain the reliability of the ninhydrin assay in quantifying the secondary amines, we also carried out a TNBS assay (Table 4), which is widely reported as being able to form absorbing complexes only with primary amines,[53] using glycine as the standard reference (Fig. S8b†). Indeed, the ninhydrin assay was capable of detecting almost four times the amount of amines of TNBS.

Subsequently, concentrations obtained from the ninhydrin assay were used to calculate the total amine concentration, and it will be referred to as total nitrogen amount, *N*, from now on.

Table 3 Quantum yield of GxS5 polymers relative to reference dyes, expressed in %

| Polymer | $H_2O$, 375 ex/460 em | Plasma 25%, 375 ex/460 em ($M^{-1}$) | $H_2O$, 561 ex/620 em | Plasma, 25% v/v, 561 ex/620 em |
|---|---|---|---|---|
| G1S5 | 0.55 ± 0.004 | 2.01 ± 0.011 | 0.76 ± 0.025 | 0.98 ± 0.007 |
| G5S5 | 0.52 ± 0.002 | 1.50 ± 0.010 | 0.62 ± 0.023 | 1.01 ± 0.011 |
| G10S5 | 0.67 ± 0.009 | 0.95 ± 0.012 | 0.47 ± 0.036 | 0.89 ± 0.007 |

© 2024 The Author(s). Published by the Royal Society of Chemistry

Table 4 Concentration of amine groups in G*x*S5 polymers rehydrated at 100 mg ml$^{-1}$ according to ninhydrin and TNBS assays. The ratio of amines detected with TNBS assay *vs.* ninhydrin assay is reported

| Sample | [R–NH*x*] at 345 nm, ninhydrin assay, M | [R–NH*x*], at 570 nm | [R–NH$_2$], TNBS assay, M | TNBS/ninhydrin assay detected [R–NH*x*] |
|---|---|---|---|---|
| G1S5 | 0.123 ± 0.002 | 0.148 ± 0.054 | 0.029 ± 0.002 | 0.21 |
| G5S5 | 0.155 ± 0.003 | 0.163 ± 0.033 | 0.038 ± 0.002 | 0.24 |
| G10S5 | 0.182 ± 0.006 | 0.181 ± 0.011 | 0.048 ± 0.002 | 0.26 |

Open Access Article. Published on 19 July 2024. Downloaded on 5/15/2025 12:59:42 PM. This article is licensed under a Creative Commons Attribution 3.0 Unported Licence.

As reported in ref. 52, only proline and hydroxyproline have a signal maximum at 350 nm, followed by a faint hump at 400 nm, indicating the presence of *cis*-oriented secondary amines. The ninhydrin assay is therefore a valid assay to determine the concentration of the secondary and primary amine groups in this novel class of polymeric nanoparticles.

### 2.5 Genipin-based polymers and their ability to complex with small-interfering RNA in polyplexes: optimization of siRNA phosphate/total nitrogen (P/N) ratio for tdTomato knock-down

**2.5.1 ζ Potential and particle size investigation.** Due to their polymeric nature and positive charge, the G*x*S5 materials were expected to be able to complex nucleic acids. We titrated a fixed amount of polymer with increasing concentrations of small-interfering RNA (siRNA) against tdTomato fluorescent protein, thereby slowly increasing the molar phosphate-to-nitrogen (P/N) ratio, to simulate actual experimental conditions and avoiding sequence-related unexpected results. Upon addition of the siRNA, at neutral pH, the ζ potential drops until a negative plateau (Fig. 5a), −15, ≈ 0, and −2.5 mV mV for G1S5, G5S5, G10S5, respectively. We then aimed to optimize the phosphate-to-nitrogen ratios to be used in the knock-down experiment, in terms of particle size and nanoparticle aggregation upon siRNA titration (Fig. 5b). The response varies according to the glycine-to-genipin molar ratio in the initial reaction batch. In all three samples, a bimodal particle size distribution can be noted, which is due to the aggregation of smaller particles in response to the complexation with siRNA, with the population composed of larger aggregates ranging from 300 nm to 1 micron in diameter (termed "Population 2", as in Ultrastructure and particle size of G*x*S5 polymers) increasing in size according to the siRNA concentration, whereas the population composed of smaller than 300 nm nanoparticles shows a less dramatic size increase (Population 1, Fig. S10†). These aggregates are stable over time in PBS 7.4 (data not shown). Although the presence of two particle size populations was already established *via* TEM on free polymers (Table 2), this increase in particle size can be directly addressed to a complexation with siRNA phosphate groups. The transition to Population 2 can be attributed to aggregation/flocculation due to the neutralization of repulsive charges and the complexation with siRNA, which increases the total bulk size (refer to Fig. S10† for size evolution). However, the ratio of the frequency of events relative to Population 1 or Population 2 does not follow a linear trend upon siRNA titration (Fig. 5b), but some areas of dramatic prevalence for Population 1 events can be noted. At a 1 : 25 P/N (0.04) ratio, polyplexes arising from the three G*x*S5 show a small and monodisperse particle size distribution. Interestingly, the higher the glycine molar ratio, the more significant the contribution by carboxylic groups belonging to genipin: electrostatic repulsions with phosphate groups probably cause an internal rearrangement within the genipin–spermine net, exposing more charged amine groups on the outside shell of the nanoparticle and thus increasing the surface available for siRNA complexing.

**2.5.2 Protection against RNase A degradation and intercalating dye exclusion.** To ascertain the intercalating dye-exclusion ability of the three polymers, different P/N ratios (1 : 500 to 1 : 1) were diluted in PBS with a pH of 7.4 and incubated with 1 μM of anti-tdTomato siRNA in 10 μl of PBS. Subsequently, polyplex samples were run on a 1.5% agarose gel pre-stained with Midori Green. No signal could be detected in the lanes containing the siRNA/G*x*S5 complexes up to a 1 : 1 ratio, suggesting the impossibility of Midori Green being able to bind to nucleic acid due to highly tight complexation (Fig. 5c) with the polymers, and, subsequently, the lack of fluorescence. Although present at a 1 : 1 P/N ratio, the band belonging to the complexes appears to be delayed in migration, as reported already elsewhere.[22,54,55]

Furthermore, the protection ability against RNAse A degradation was also assayed. Briefly, siRNA polyplexes of 1 : 25 and 1 : 50 P/N ratios of G*x*S5 polymers were incubated with 5 μg ml$^{-1}$ of RNase A for 4 and 24 hours (Fig. 5d). Subsequently, the polyplexes were de-complexed with heparin. All three polymers offered excellent protection against siRNA degradation, while lanes containing free siRNA incubated with the enzyme showed no band, even after 4 hours.

**2.5.3 G*x*S5 behaviour in an endosomal-mimicking environment and potentiometric back-titration.** Endosomal pH being mildly acidic,[17,56] amine groups are expected to be fully protonated, with unforeseeable consequences regarding polyplex de/stabilization. Therefore, we first tested the avidity of the G*x*S5 polymer in complexing with siRNA, pre-incubated with Quantus dye, detected as the decrease of fluorescence due to dye exclusion. Subsequently, we monitored the eventual spontaneous release of the siRNA from polyplexes, G1S5, G5S5 and G10S5 at 1 : 2, 1 : 25 and 1 : 50 P/N ratios, at pH 7.4 and pH 5, during 3 hours of incubation and 37 °C. Finally, we assayed the relative complexation strength, by de-complexing siRNA–G*x*S5 polymers by increasing the amounts of heparin, measured as the increase in the baseline fluorescence, due to the re-

 © 2024 The Author(s). Published by the Royal Society of Chemistry

Open Access Article. Published on 19 July 2024. Downloaded on 5/15/2025 12:59:42 PM.
This article is licensed under a Creative Commons Attribution 3.0 Unported Licence.

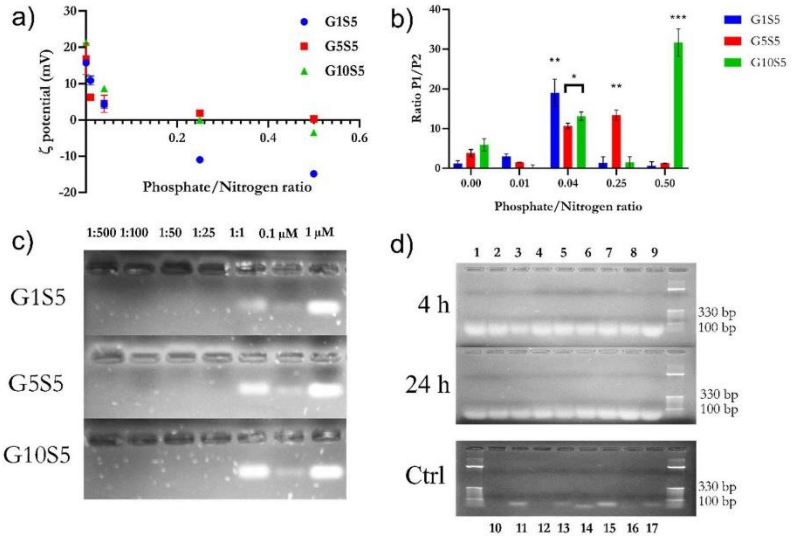



Fig. 5 (a) Evolution of ζ potential ±SD in mV according to the P/N ratio for the three polymers. Data refer to 3 independent technical replicates for each GxS5, coming from the same synthesis batch. at pH 7.4. (b) Ratio of number of recorded events as "Population 1" and "Population 2", whereas P2 is assumed to be resulting from the aggregation of nanoparticles from P1, against siRNA backbone phosphates/polymer nitrogen ratio. The relative abundance of P1 was assessed to be statistically different from the titration starting point (in the absence of phosphate backbone groups) with ANOVA two-ways. Data refer to 3 independent technical replicates, each one composed of 10 measurements. GxS5 came from the same synthesis batch. (c) Agarose gel migration of different P/N ratios of polymers and siRNA. For comparison, two different concentrations of free siRNA were added (0.1 and 1 μM) (d) RNase A (5 μg $ml^{-1}$) and heparin displacement assay. Lanes are as follows: (1) G1S5, P/N 1 : 2; (2) G1S5, P/N 1 : 25; (3) G1S5, P/N 1 : 50; (4) G5S5, P/N 1 : 2; (5) G5S5, P/N 1 : 25; (6) G5S5, P/N 1 : 50; (7) G10S5, P/N 1 : 2; (8) G1S5, P/N 1 : 25; (9) G10S5, P/N 1 : 50; (10) naked siRNA 1 μM, RNase A+, 24 h; (11) naked siRNA 1 μM, RNase A−, 24 h; (12) naked siRNA 0.1 μM, RNase A+, 24 h; (13) naked siRNA 0.1 μM, RNase A−, 24 h; (14) naked siRNA 1 μM, RNase A+, 4 h; (15) naked siRNA 1 μM, RNase A−, 4 h; (16) naked siRNA 0.1 μM, RNase A+, 4 h; (17) naked siRNA 0.1 μM, RNase A−, 4 h.

accessibility of the dye to the substrate. G10S5 exhibited the highest dye exclusion of the three polymers at both pH values compared to G1S5 and G5S5 (Fig. 6a, $p = 0.0037$). The behaviour of the polymers at mildly acidic pH, *i.e.*, the slightly increased complexation with siRNA, suggests further protonation, with G1S5 being the polymer with the highest further complexation at pH 5, at 1 : 25 P/N ($p = 0.021$). In the presence of heparin, G1S5 at 1 : 25 P/N had already released roughly 50% of siRNA at 5 μg $ml^{-1}$, while G10S5 released a similar amount at only 2 mg $ml^{-1}$ of heparin (Fig. 6b). Overall, G10S5 showed the highest siRNA retention and the most stable complexes, while, intuitively, the higher the P/N ratio, the lower the complexation strength. The ζ-potential data confirmed that G10S5 has the highest increase in protonation among the three polymers, with a 64% increase in surface charge at lower pH (Fig. 6c, ANOVA one-way). Interestingly, upon acidification, the ratios between Population 1 and Population 2 of the nanoparticles rose significantly, with a dramatic shift towards Population 1 (assumed to be composed of monomers of the polymer, 100–300 nm, Table S6†), with a substantial percentage increase in the monomer particle size. While the first effect can be related to stronger electrostatic repulsions due to further amino-group protonation, surprisingly, the highest growth in particle size was shown by G10S5: from a roughly 2.25-fold increase in terms of diameter, the volume of the monomers increased more than eleven times, suggesting an additional endosomal evasion mechanism (Table S6†).

To further investigate the re-protonation phenomenon in GxS5, we performed a back titration (Fig. 6d) with NaOH from pH 2 to 10. G1S5 showed a lower buffering capability than G5S5 and G10S5. The latter showed a more extended buffering ability due to the larger number of carboxylic acid moieties belonging to glycine. At the same time, the tertiary amines' $pK_a$ were found to be, respectively, for G1S5, G5S5, and G10S5, 7.16, 7.09 and 6.57. Therefore, the lower $pK_a$ in the case of G10S5 explains the higher degree of further complexation with siRNA at lower pH and eventually a more substantial proton-sponge effect.

### 2.6 Cytotoxicity of GxS5 polymers on different cell lines

To evaluate the toxicity of the polymeric nanoparticles, several cell lines were incubated with different concentrations of GxS5 (Fig. 7a). Regarding the non-malignant cell lines, on kidney

© 2024 The Author(s). Published by the Royal Society of Chemistry

Open Access Article. Published on 19 July 2024. Downloaded on 5/15/2025 12:59:42 PM. This article is licensed under a Creative Commons Attribution 3.0 Unported Licence.

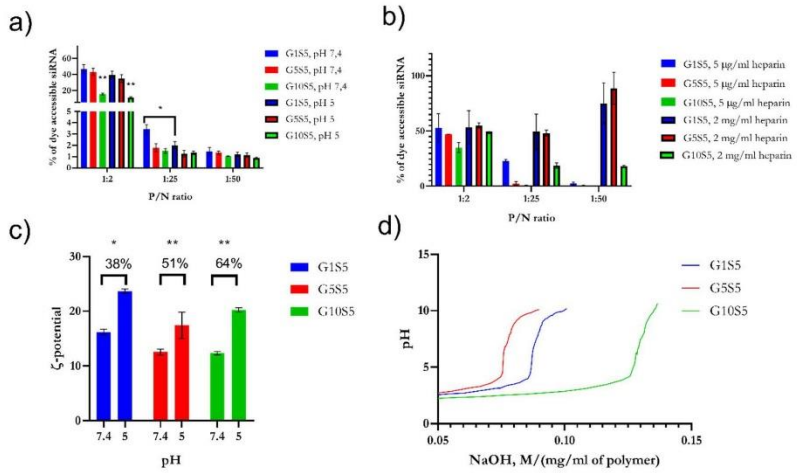



Fig. 6 (a) Spontaneous release at pH 5 and pH 7.4 of siRNA from GxS5 polymers. siRNA de-complexation, measured as an increase or decrease of Quantus dye fluorescence, after incubation at pH 5 and pH 7.4. (b) To assess the relative strength of the complexation, samples were treated with heparin at increasing concentrations of heparin for pH 5 and pH 7.4. (c) Change in ζ potential of GxS5 from pH 7.4 to 5; data were collected over 5 replicates for each pH/polymer combination. (d) Back-titration of GxS5 with NaOH 0.1 N, normalized for the dilution of the polymer. $p \leq 0.05$*, $p \leq 0.01$**, $p \leq 0.001$***, $p \leq 0.0001$****.

epithelial cells (HEK 293T) and murine connective-tissue cells (L-929), G10S5 was the least toxic polymer at 0.08 mg ml$^{-1}$, even though, at varying degrees, all the GxS5 were cytotoxic at 0.8 mg ml$^{-1}$. Interestingly, G10S5 had a significant stimulating effect ($p < 0.0001$) on the growth of the HEK 293T cells.

G10S5 proved to be the least toxic polymer on the CT26 cells, while on the 4T1 breast-cancer model, at 0.08 mg ml$^{-1}$, no polymer showed significant cytotoxicity. Furthermore, we tested the biocompatibility of our polymers on human immortalized keratinocytes (HaCaT). Even after 72 hours, the GxS5 polymers showed little-to-no toxicity on HaCaT cells (Fig. S12†). We therefore decided to wash the cells and replace the medium, and prolong the experiment for another 72 hours. After a total of 6 days of co-incubation, the resulting cytotoxicity followed the already-described trend, decreasing with the higher glycine molar ratio. Finally, on our cell line of choice for the knock-down experiments, B16F10, a wider range of concentrations was tested. Again, at the highest concentration (0.8 mg ml$^{-1}$), only cells treated with G10S5 retained 20% of viability, following the already-described trend. Also, all the GxS5 polymers showed little-to-no hemolytic activity over fresh human red-blood cells (Fig. S11†), up to 0.02 mg ml$^{-1}$, while lipofectamine 2000 was reported to have 20% of hemolytic activity at similar concentrations.[57]

### 2.7 Internalization of polymers and polymer/siRNA complexes in B16F10 cells and knock-down ability

To assess the internalization ratio of the GxS5 we took advantage of the intrinsic polymer fluorescence and measured it in the PE channel (ex: 560 nm, em: 585/15 nm) of the flow cytometer to detect their presence in B16F10 cells. The normalized median fluorescence intensity (MFI) of the live-cell population is related to the tested polymer concentration (Fig. 8d). Furthermore, the determined MFI did not change significantly when the cells were incubated with polymer/siRNA polyplexes, indicating that the complexation with siRNA, and, therefore, the lower ζ potential, did not significantly affect the internalization efficiency (Fig. 8d, and 5a for ζ-potential values). Also, despite their relatively low quantum yield, it was possible to visualize the internalization of the GxS5 in the FITC channel by B16F10 cells (Fig. 8a–c).

### 2.8 Efficacy as siRNA carrier for RNA interference

The three GxS5 polymers, complexed with siRNA at different phosphate-to-nitrogen (P/N) ratios (1 : 2, 1 : 25 and 1 : 50) were tested for their ability to deliver siRNA targeting tdTomato to B16F10 cytoplasm and elicit RNA interfering towards the target gene (Fig. 8b–d). In all cases the polymer concentration in the wells was below the cytotoxicity threshold (Table S7† and Fig. 7e). As a preliminary study we used flow cytometry to determine the tdTomato fluorescence intensity at 72 hours after transfection with the polymer/siRNA complexes at a 1 : 25 P/N ratio (Fig. S13†). This ratio was chosen (Fig. 6b) due to the polymers showing an overwhelming majority of mono-dispersed, small, unclustered nanoparticles. All three tested polymer/siRNA polyplexes reduced the tdTomato MFI in the transfected cells compared to the control cells; however, their silencing efficacy was lower than RNAiMAX, which served as

 © 2024 The Author(s). Published by the Royal Society of Chemistry

Open Access Article. Published on 19 July 2024. Downloaded on 5/15/2025 12:59:42 PM.
This article is licensed under a Creative Commons Attribution 3.0 Unported Licence.

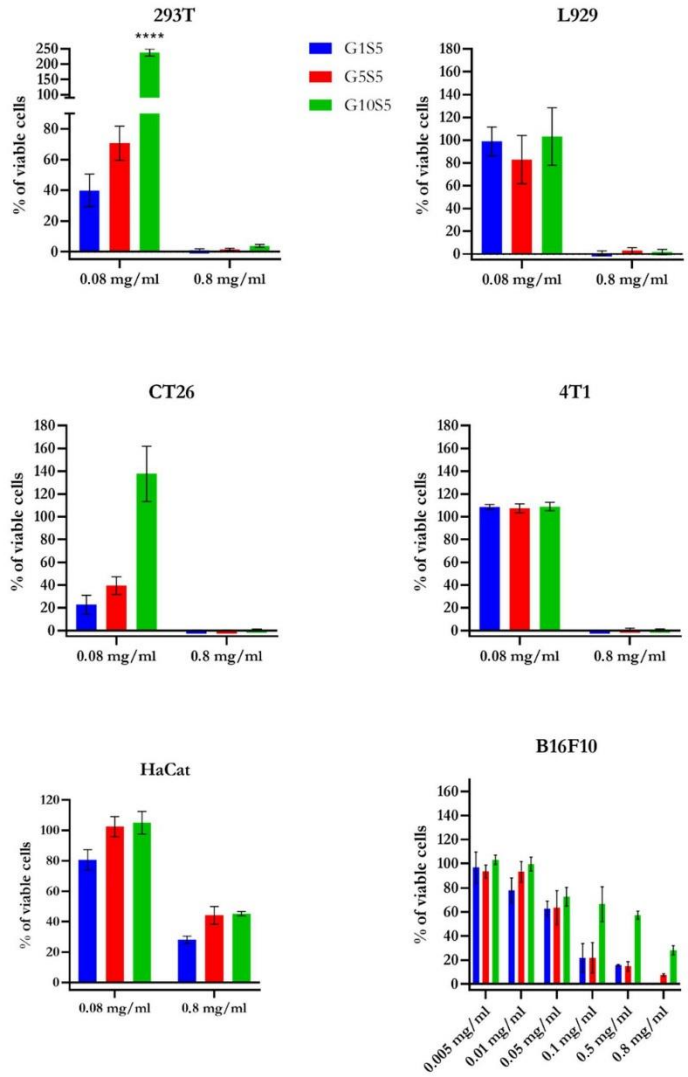



Fig. 7 Presto Blue detected cytotoxicity at increasing concentrations of GxS5. HaCat data are relative to 6 days of co-incubation. For all cell lines except for HaCaT, the incubation time was 72 hours. Data ($n = 6$ for every concentration/cell line) are ±SD. $p \leq 0.0001$****.

a positive control (Fig. S13†). As a proof of concept, within the same experiment, we also checked the capability of G0S5 – a polymer composed only of genipin and spermine – to transfect the B16F10 cells with siRNA targeting tdTomato (Fig. S13†). Interestingly, no silencing of the tdTomato was observed in the presence of the G0S5/siRNA complexes, indicating that the nanoparticulate and well-disperse nature of the GxS5 polymers is key to a successful transfection. Due to the overlapping of the tdTomato emission peak with the emission peak of our polymers, we used qRT-PCR to determine the tdTomato silencing

© 2024 The Author(s). Published by the Royal Society of Chemistry

Open Access Article. Published on 19 July 2024. Downloaded on 5/15/2025 12:59:42 PM.
This article is licensed under a Creative Commons Attribution 3.0 Unported Licence.

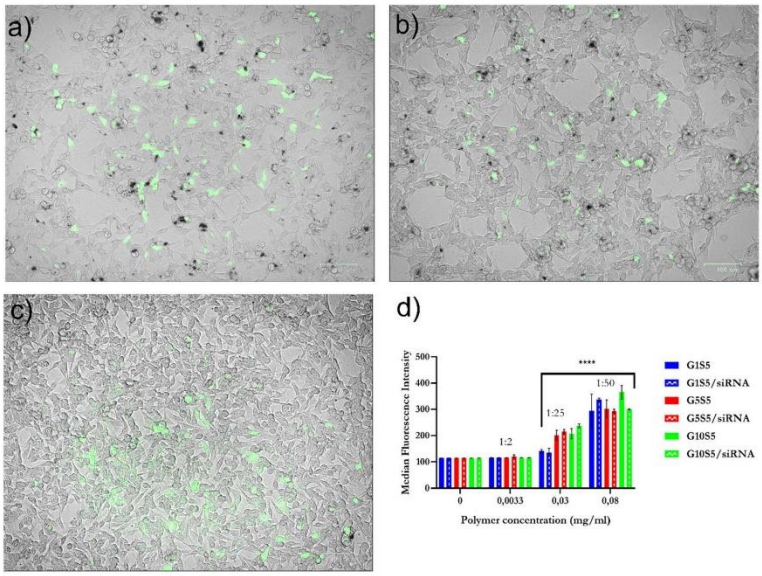



Fig. 8 (a) B16F10 incubated with 0.08 mg ml$^{-1}$ of G1S5, after 48 hours; (b) with G5S5; (c) with G10S5. Brightfield pictures are superimposed with FITC-channel acquisition. (d) Median Fluorescence Intensity of GxS5, complexed or not with siRNA, as detected with FACS in the PE channel (±SD, $n = 3$), $p \leq 0.0001$****. The P/N ratio of polyplexes is reported above the plot.

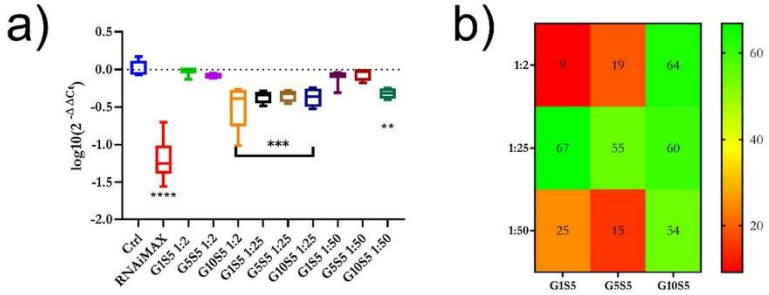



Fig. 9 (a) Log 10 of tdTomato gene expression fold change, after transfection with 30 nanomoles of siRNA complexed with GxS5. Anova One-Way was used to assess the statistical consistency of the data. $p \leq 0.05$*, $p \leq 0.01$**, $p \leq 0.001$***, $p \leq 0.0001$****. (b) Heatmap with % of gene knockdown, according to polymer identity and P/N ratio.

efficacy of the polymer/siRNA complexes. We also tested two other P/N ratios, *i.e.*, 1 : 2 and 1 : 50, to investigate the effects of different nanoparticles' ζ potentials, from neutral to negative, on the transfection efficiency. All the polymers at a 1 : 25 P/N ratio showed around 60% of gene knockdown (Fig. 9a and b), while only G10S5 was effective at 1 : 2 and 1 : 50 P/N as well exhibiting 63% and 54% tdTomato knock-down, respectively. Empty polymers, at the same concentration of polymer/siRNA

Table 5 Primer sequence used for quantification of knockdown

| Primer | Sequence |
|---|---|
| TdTomato – forward | 5′-GACAACAACATGGCCGTC-3′ |
| TdTomato – reverse | 5′-GGTCTGGGTGCCCTCGTA-3′ |
| β-actin – forward | 5′-GAAGTGTGACGTTGACATCC-3′ |
| β-actin – reverse | 5′-ACTCATCGTACTCCTGCTTG-3′ |


© 2024 The Author(s). Published by the Royal Society of Chemistry

Open Access Article. Published on 19 July 2024. Downloaded on 5/15/2025 12:59:42 PM.
This article is licensed under a Creative Commons Attribution 3.0 Unported Licence.

complex per well, did not significantly affect either the β-actin or the tdTomato gene expression (Fig. S14†).

## 3 Discussion

Genipin has been widely used as an ingredient in novel, nanoparticle-based delivery systems, but, to the best of our knowledge, this is the first reported therapeutic nucleic acid application. So far, genipin-based nanoparticulate delivery systems involved mostly topical applications: a 2003 breakthrough paper by Liang *et al.*[58] demonstrated how genipin-crosslinked gelatin microspheres induce an inflammatory response in skeletal rat muscle, dramatically lower than glutaraldehyde, and, thus, are safer for *in vivo* application. A poloxamer–genipin-based hydrogel was also proven safe for intra-ocular quercetin delivery,[59] while a lysine–folic-acid, genipin-based particulate dispersion was an efficient dyeing and doxorubicin-carrying agent for glioma cells.[60]

We thoroughly investigated with UV/vis and fluorescence spectroscopies the reaction kinetics of genipin incubated at pH 7.4 and in an excess of molecular oxygen with spermidine, spermine, and a 1 : 1 molar mix of both. Genipin reacts with overhanging primary amines of polyamines, very much depending on the pH, with a complex reaction mechanism involving at least two steps, *i.e.*, iridoid ring opening and heterocyclic ring formation, together with the simultaneous release of methanol and slow, rate-determining final cross-linking on an amidic moiety. The reaction orders are reported to be fractionary, and our findings therefore confirm the literature.[33,38,61] According to ref. 33, genipin follows a second-order reaction in the presence of a primary amine source (*i.e.*, ethylendiamine), while we found it to follow instead an order of 1.5 for genipin consumption, with the final product appearing at 580 nm, and a square-root dependence on the amine groups' concentration, better reflecting the intricate mechanism of the reaction of genipin. Although already described,[32,40] the fluorescence of genipin products was never thoroughly investigated and compared with well-known dyes. Our G*x*S5 polymers show fluorescence in the red area, as already well-established for genipin products,[62] but the wider, green emitting maximum has never been investigated before. As reported in ref. 63, despite their excitation maximum being set at 480 nm and so only partially overlapping with our green signal, a net decrease follows an initial steep increase, also consistent with the kinetics of the peak appearing at 375 nm in our case. Such a signal is due to the heterocyclic pyridine ring of genipin.[38] This result is consistent with the use of a single stereo-isomer source, as we did, and not with a racemic mixture. Pizzolitto *et al.*[38] reported the computed UV/vis intermediate spectra of all three stereo-isomers of genipin and our results are consistent with the optical behaviour of *S*,*R*,*S* stereo-isomers. The green fluorescence emission of a racemic genipin mixture, if existing, is yet to be determined. Despite being relatively low, the fluorescence quantum yield in red G*x*S5 showed a slight improvement in the presence of serum proteins and it was strong enough to be detected for FACS, making it possible to follow, in further experiments, the route of the nanoparticles within the cells.

Since, in our case, tertiary amines are formed during iridoid-ring reactions with spermine and with the only amine of glycine, the higher the molar fraction of the latter, the higher the amount of tertiary amines in the polymer net, together with carboxylic moieties (Fig. 1). It has been widely demonstrated[17,64,65] that the presence of ionizable tertiary amines is of crucial importance for successful and harmless gene delivery, since highly branched polymers sporting tertiary amines undergo, during endosome maturation and a subsequent decrease in pH, complete protonation and a net charge increase, ultimately leading to rupture of the endosome. For this reason, similar to our G*x*S5, histidine, due to its ionizable tertiary amine present in the imidazole ring, is a promising substituent in bio-compatible transfection agents.[66] Our results in an endosomal mimicking environment confirmed the ionization of tertiary amine present on the indole ring of genipin, a destabilization of the nanoplex structure, as already reported,[17] with a moderate but detectable increase in size due to electrostatic repulsions among the positively charged groups. G10S5 proved to be the polymer with the higher re-ionizability, the higher volume increase at acidic pH (instrumental, according to "the umbrella hypothesis"[67]), but, counterintuitively, also the faintest release in the presence of heparin (a negatively charged displacing agent), whereas G5S5 and G1S5 allowed the complete recovery of the siRNA at all the P/N ratios (Fig. 6a and b). On the other hand, at neutral pH, polymers, at any phosphate-to-nitrogen ratio, equally protected the siRNA from RNase A degradation and excluded siRNA-intercalating dyes in agarose gel up to a 1 : 1 P/N ratio. It must be pointed out that the condensation strength in polyplexes is the key to successful transfection: a too densely packed polyplex would be incapable of releasing the payload in the cytoplasm[68] (or, if ever, it would happen after very long incubation times), it will cause excess cytotoxicity due to cationic charges.[69,70] For instance, a reported threshold value for PEI is N/P > 3, since a certain number of free cationic chains is instrumental for plasmid transfection efficiency.[71] In contrast, a too laxly packed one will release the payload in the culture medium, or it will not fully protect it from endosomal RNase/DNase degradation.[70] The growing volumetric expansion from G1S5 to G10S5 upon acidification hints at an internal rearrangement, where the yet-unprotonated imidazole ring, upon protonation, comes into contact with the particle surface; the more pronounced this effect is, the purportedly higher is the transfection efficiency.

We then decided to focus on an often-overlooked parameter in therapeutic nucleic acid (TNA) transfection, such as the phosphate-to-nitrogen (P/N) ratio. The complexation between a cationic nanoparticle and TNA predictably changes the spatial arrangement of the nanoparticles, and such folding is connected to copies of the TNA per nanoparticle. In our case, this affected both the particle size and the ζ potential of the G*x*S5 nanosized polymers (Fig. 6c and S10†). At a 1 : 50 P/N ratio, or 0.08 mg ml$^{-1}$ of concentration, G1S5 and G5S5 yielded little-to-no gene knockdown despite showing a high internalization efficiency *via* FACS and 80–90% of cell viability. This can be

© 2024 The Author(s). Published by the Royal Society of Chemistry

Open Access Article. Published on 19 July 2024. Downloaded on 5/15/2025 12:59:42 PM. This article is licensed under a Creative Commons Attribution 3.0 Unported Licence.

explained with the extremely tight complexation of the polymer and siRNA in high excess of unshielded cationic charges; the polyplexes, despite being effectively internalized, will not release their cargo for Argonaute uptake within the 48 hours of our experiment. All three polymer monomers at 1 : 50 P/N were less than 200 nm in diameter (Fig. S10†), with the average size of the G10S5 being 95 nm. G10S5, indeed, at a 1 : 50 P/N ratio, yielded an almost 60% of tdTomato knockdown: therefore, either the internalization mechanism followed by the latter must differ from the others due to a smaller size (*via* clathrin-mediated endocytosis, for instance), or the polymer shedding from siRNA, due to the shorter length of the genipin–spermine backbone and the presence of carboxylic groups, is more likely to happen.[72]

At a 1 : 25 P/N ratio, all the GxS5 showed a comparable, sustained gene knockdown and similar uptake efficiency in FACS: the behaviour of the polymers within endosomal mimicking experiments is consistent with such an outcome since all the polyplexes showed a well-monodispersed size distribution, a moderately positive ($\approx$10 mV) $\zeta$ potential, a total dye exclusion in agarose gel and a 20–50% payload release upon the addition of 2 mg ml$^{-1}$ of heparin, confirming every existing model about cationic-assisted transfection.[73,74]

Interestingly, only G10S5 showed a good knock-down effect at a 1 : 2 ratio (or 0.003 mg ml$^{-1}$), as well: the siRNA/G10S5 complex possesses a neutral-to-negative surface charge and the highest, among the set, complexation strength (lowest release upon heparin incubation). Mott *et al.*[75,76] recently demonstrated that, in HeLa and 293T cells, negatively charged polyplexes mostly co-localize with clathrin-coated vesicles, suggesting a different internalization pathway for G10S5 at a 1 : 2 P/N ratio in B16F10. We can, therefore, speculate that each polymer monomer can carry more than one copy of the siRNA since even at low concentrations, G10S5 can effectively deliver its payload to the cytoplasm. With only such a low amount required, there is room to scale up the concentration of polyplexes, while remaining within the high cell-viability window. The presence of a carboxylic group is instrumental to balancing good endosomal escape/direct internalization ratio with an effective condensation of siRNA: in the GxS5 polymers the supposed presence of ionic bonds between the carboxylic and amine groups within the polymer net helps create a tridimensional structure with better transfection-efficiency ability. Our overall data confirm that a transfection polymer's "zwitterionic" character plays a significant role in cell uptake, endosomal escape, and eventually successful transfection.[77,78] Finally, a substantial role for GxS5 aggregates in successful transfection ("Population 2" in DLS and TEM, 0.3–0.9 μm of diameter) cannot be ruled out: as macropinocytosis was determined to be inducible in B16F10 cells,[79] and, although the authors did not state the average molecular weight of the biopolymer, characteristic membrane ruffles were observed in confocal laser scanning microscopy. The latter are believed to form macro-pinosomes, intracellular vesicles exploited by several viruses to enter the cells,[80] but their fate, whether they fuse with mature lysosomes or whether they are driven back to the plasma membrane, therefore releasing their cargo intracellularly, is yet to be determined, despite having been successfully exploited for nucleic acid delivery.[81] It is also interesting how the zwitterionic character impacted the cytotoxicity on different cell lines. Our data overwhelmingly suggest that the lower, and more distributed, positive net charge significantly reduced the cytotoxicity. For comparison, Grecka *et al.*[82] reported 80% B16F10 mortality in the presence of 0.01 mg ml$^{-1}$ of PEI. Finally, as established by our results on fresh human erythrocytes, with little-to-absent lysis (Fig. S11†), while a nanoparticle–membrane interaction cannot be ruled out, any toxicity must be attributed to intracellular metabolic activity rather than simple membrane disruption.[83]

## 4 Conclusions

We developed a set of self-fluorescent, genipin–spermine-based polymers with a nucleic acid complexing ability and mild cationic charge. We succeeded in tailoring their size by changing the glycine molar ratio in the initial reaction batch, conferring on them a "zwitterionic" character, and improving their biocompatibility. Our data, taken together, suggest that genipin-based cationic polymers are a novel class of transfection agents. Their low cytotoxicity, mild reaction conditions, high tunability, good transfection efficiencies, and self-fluorescence properties make these polymers a platform suitable for the development of theranostic agents. In the future, we aim to elucidate their 3D-spatial arrangements *via* nuclear magnetic resonance, their *in vivo* and *in vitro* biodegradability, bioactivity, and clearance routes, and we aim to improve their transfection efficiencies *via* stealth coating or further conjugation.

## 5 Materials and methods

### 5.1 Reagents

For all purposes, DEPC Milli-Q water was used. Spermine–HCl (306-67-2), spermidine (124-20-9), glycine (56-40-6), heparin sodium salt (porcine intestinal mucosa, 9041-08-1), and genipin (6902-77-8) were purchased from Sigma-Aldrich. The latter stereoisomer was reported to be 1*S*,2*R*,6*S* (PubChem SID 329799931, Fig. 1). The buffer of choice was PBS (cat. number P4417), dissolved from tablets in DEPC milliQ water at a final concentration of 10 mM phosphate buffer, 137 mM sodium chloride, and 2.7 mM potassium chloride (from now on, PBS 1×). RNase A from bovine pancreas (EN0531) was purchased from Thermo Fisher. Ninhydrin (485-47-02, amino acid detection grade) was purchased from Sigma-Aldrich and TNBS (2,4,6-trinitrobenzene sulfonic acid) came from Pierce protease assay (Thermoscientific, 23 263). All disposables were certified pyrogenase, DNase and RNase free, and glassware was autoclaved before use. Sephadex G25 PD10 columns were purchased from GE Healthcare, UK, and each column was used up to ten times and regenerated with a 20× excess of elution volume after every purification round, and kept under sterile conditions. Anti-TdTomato siRNA was purchased from IDT Genomics from a Custom Silencer™ ThermoFisher design. For agarose gel assays, agarose low-melting-point (Promega) and home-made

 © 2024 The Author(s). Published by the Royal Society of Chemistry

Open Access Article. Published on 19 July 2024. Downloaded on 5/15/2025 12:59:42 PM.
This article is licensed under a Creative Commons Attribution 3.0 Unported Licence.

TRIS-acetic acid-EDTA buffer were used (all reagents were purchased from Sigma-Aldrich).

### 5.2 Preparation of genipin-based polymers

Different concentrations (from 1 to 10 mM) of polyamines and glycine (from 1 to 10 molar ratio with genipin) were used to prepare different formulations of the polymer. Briefly, glycine and polyamines were first mixed in 300 μl of 1× PBS, pH 7.4, and finally genipin was added. The reaction was carried on in an excess of oxygen, in 24-well plates, under continuous shaking for a minimum of 20 hours to a maximum of 48 hours, at 25 °C. The reaction time was finally standardized to 36 hours. To avoid excessive evaporation of the solution, neighbouring wells were filled with water. The whole reaction was carried on in a sterile environment. To remove excess polyamines and glycine, the final suspension was eluted, 1 ml at a time, with water with a Sephadex PD10 G50 column, the nanoparticles eluting at fraction 6 and 7. The suspension was subsequently freeze-dried in a Martin Christ freeze drier and powders were rehydrated at 20 mg $ml^{-1}$ in PBS 1× and energetically vortexed after rehydration to allow complete solubilization of the clumps. To avoid spontaneous oxidation of the spermine and spermidine moieties, final suspensions were stored under an argon atmosphere at 4°. According to experimental necessities, the procedure above was upscaled or downscaled. Polymers were named G*x*S5, whereas *x* is the molar ratio of glycine-to-genipin, *i.e.*, 1, 5 and 10.

### 5.3 Quantification of free amine groups

For quantification of free amine groups in G*x*S5 samples, ninhydrin assay was used. Powdered ninhydrin (Sigma-Aldrich) was resuspended at a final concentration of 2 mg $ml^{-1}$ in absolute ethanol, and added in a 1 : 5 volume/ratio with the sample, to sample/standard containing tubes. Tubes were heated up at 85° for five minutes and allowed to cool at room temperature for one hour. The final absorbance was recorded at 290, 350, 400 and 570 nm. Spermine from a 0.50 M water stock was used as the standard for calibration curve determination, within a range of 0.08–15 mM. Each sample was prepared in triplicate and normalized for intrinsic polymer absorbance at the corresponding wavelength. The nitrogen amount was defined as the quantity of ninhydrin-reacted amine groups in polymers, quantified at 350 and 570 nm. For TNBS (2,4,6-trinitrobenzene sulfonic acid), a stock in methanol (5% w/v) was stored at 4°, and diluted up to 0.1 w/v % for the assay procedure. All experiments for the TNBS assay were performed in 0.1 M sodium bicarbonate as the working buffer, pH 8.5. Glycine, from a water stock of 0.50 M, was used as the standard to build a calibration curve. Briefly, the solution and glycine standard were diluted in 1.5 ml Eppendorf tubes in a working buffer up to 0.25 ml of volume, and 0.125 ml of 0.1% TNBS was added. Tubes were incubated at 37° for two hours, until the development of a strong orange colour. Absorbance was recorded at 335 nm, measuring therefore picric acid formation. All samples were run in triplicate. The conventional use of sodium dodecyl sulphate was avoided to maximize the sensitivity.[53]

### 5.4 Complexation of siRNA–G*x*S5

TdTomato siRNA was mixed at various nitrogen-to-siRNA phosphate (N/P) molar ratios with G*x*S5 polymers, vortexed for 10 seconds, and incubated for at least half an hour at room temperature, in sterile-filtered, autoclaved DEPC-PBS 1× (pH 7.4). Samples were used without further purification. For the sake of clarity, where complexed with siRNA, G*x*S5 are referred to as "polyplexes".

### 5.5 Dynamic light scattering and ζ-potential measurements

Particle size, polydispersity and ζ-potential measurements were all carried out in an Anton Paar Litesizer within 1 week from the rehydration of samples. A total of 1000–650 μl was added in an Omega Cuvette and repeated measurements ($n > 5$) were carried on to ensure statistical repeatability. A number-weighted, built-in algorithm was used for all particle size measurements.

### 5.6 Determination of P580 molar absorptivity

For the determination of the molar absorptivity of the product forming at 580 nm (P580) different concentrations of genipin (from 0.168 mM to 0.5 mM) were allowed to react with 5 mM spermine and the final OD at 580 nm was plotted against the initial genipin concentration and the absorbance was recorded, on a Greiner Bio-One UV-Star™ 96-well Microplates, on a Synergy Microplate (Biotek) reader. After 36 hours of reaction, final absorbance values at 580 nm and 375 nm were used to build a calibration curve, whereas the slope represents the molar absorptivity $\varepsilon$ of P580 and at P375. The following pathlength-correction protocol was applied in order to correct the absorbance for the volume present in the microwell and standardize all the OD values to a virtual 1 cm quartz cuvette.

$$\text{OD corrected to 1 cm cuvette} = \frac{\text{OD}_{\text{sample,buffer}} \times 0.18}{\text{OD}_{977,\ \text{sample}} - \text{OD}_{900,\text{sample}}} \quad (14)$$

### 5.7 Agarose gel assays

To assess the stability of the complexation of the polymers with TdTomato siRNA, complexes at different P/N ratios were loaded in a 2.5% agarose gel, pre-stained with Midori Green (Nippon Genetics), and allowed to run for 20 minutes at 70 V in TAE buffer 1× (pH 8.5, TRIS 40 mM, acetic acid 20 mM, EDTA sodium salt 1 mM). Briefly, 10 μl, in PBS, contained 1 μM of siRNA, which was kept constant for each P/N polyplex, while the amount of polymers was varied accordingly. The whole volume for each P/N was then loaded in the agarose gel. Subsequently, bands were visualized in a ChemiDoc gel imager. Heparin sodium salt was used to de-complex the siRNA from polymers at a final concentration of 5 mg $ml^{-1}$. A similar procedure was followed after incubation of polymers at 1 : 25 and 1 : 50 P/N ratios with RNAse A for 4 and 24 hours. The DNA ruler is 10 bp DNA ladder (Thermo Fisher Scientific, Waltham, MA, USA; cat. 10 821–015).

### 5.8 TEM imaging conditions and image analysis

An unfixed sample was dropcast onto a copper-nickel 200-mesh TEM grid (Agar Scientific, AGS138) and characterized using

Open Access Article. Published on 19 July 2024. Downloaded on 5/15/2025 12:59:42 PM. This article is licensed under a Creative Commons Attribution 3.0 Unported Licence.

a transmission electron microscope (TEM Jeol JEM-2010F), operated at 200 k eV. For image analysis, ImageJ software was used on a $n > 10$ micrographs.

### 5.9 Potentiometric pH titration

Freeze-dried suspensions of polymers were rehydrated with water at a final concentration of 5 mg $ml^{-1}$. Subsequently, the pH was adjusted at around pH 2 with 0.5 M HCl and suspensions were back-titrated with 0.1 M NaOH to pH 10. Final back-titration profiles were normalized for the dilution of the polymer.

### 5.10 Spontaneous release assay

To assay the eventual spontaneous de-complexation of siRNA from GxS5 polymers, a Quantifluor dye-based assay was established. A total of 0.1 μM of siRNA was allowed to complex with RNA Quantifluor dye (from RNA Quantifluor kit, Promega E3310) in PBS 7.4 for 20 minutes, and baseline fluorescence was recorded. Subsequently, an amount corresponding to a final 1 : 2, 1 : 25 and 1 : 50 phosphate/nitrogen ratio amounts of G1S5, G5S5, and G10S5 was added to siRNA, and incubated for an additional 20 minutes before recording the fluorescence. To assess the de-complexation under conditions mimicking the endosomal environment, 1 M HCl was added to the wells dropwise until pH 5 was reached, carefully measuring the pH with a microprobe. The evolution of fluorescence was recorded during 1 hour of incubation and fluorescence values were normalized for a free-siRNA control for pH-related hypochromic shifts. To assess the complete release of siRNA from nanoplexes, 5 μg $ml^{-1}$ and 2 mg $ml^{-1}$ of heparin (from porcine pancreas, Sigma-Aldrich) were added to the samples and consequent fluorescence spikes were recorded. The final de-complexation is expressed as the increase of fluorescence occurring upon freeing of siRNA by the change in pH or heparin addition.

### 5.11 Characterization of FT-IR polymers

Roughly 2 mg of GxS5 polymers were freeze-dried in the absence of salts and argon-flushed before analysis. A GX Fourier-transform IR spectrometer (PerkinElmer) equipped with a Model 300 photoacoustic detector (MTEC) was used and spectra were transformed in absorbance units and normalized for the strong absorbance peak at 542 $cm^{-1}$. Spectra were recorded from 450 $cm^{-1}$ to 4000 $cm^{-1}$.

### 5.12 Cell culture conditions and cytotoxicity evaluation

Cell lines B16F10 (CRL-6475) 293T (CRL-3216), CT26 (CRL-2638), and 4T1 (CRL-2539) were originally purchased from ATCC (VA, US) and the B16F10-tdTomato cells were a kind gift from Dr Muriel Golzio (The Institute of Pharmacology and Structural Biology, IPBS-Toulouse). L929 cells were originally purchased from Merck (NJ, USA). B16F10, 293T, B16F10-tdTomato and L929 cells were cultured in Advanced Dulbecco's modified MEM medium (DMEM, Gibco, Thermo Fisher Scientific, VA, US). CT26 and 4T1 cells were cultured in Advanced Roswell Park Memorial Institute 1640 medium (RPMI-1640, Gibco, Thermo Fisher Scientific, VA, US). All media were supplemented with GlutaMAX (100×, Gibco), 5% foetal bovine serum (FBS, Gibco), and penicillin–streptomycin (100×, Sigma-Aldrich, Merck, Darmstadt, Germany). The cells were routinely tested for mycoplasma infection by MycoAlert™ PLUS Mycoplasma Detection Kit (Lonza, Basel, Switzerland) and were mycoplasma free. Cells (1500/well) were seeded in a 96 well plate (VWR, PA, US), allowed to grow overnight, and later incubated for 48 hours with increasing concentrations of polymers. Next, 10 μl per well of Presto Blue reagent (A13261) was added to cells and incubated at 37° for 1 hour. Finally, the emitted fluorescence was read with a Cytation 1 system (BioTek Instruments), VT, USA. HaCaT human keratinocyte cells (ATCC PCS-200-011) were confluently grown from a frozen low passage in a T25 flask with 10 ml of full medium containing DMEM supplemented with 10% FBS and 1% penicillin streptomycin. The diluted HaCaT cells were seeded (at 20 000 cells per well) onto a tissue-culture treated 24-well plate until 80% confluency. At this point 10 vol% of Presto Blue Cell Viability (fluorescence/emission at 590/560 nm measured after 1 hour of incubation) was used to measure cellular growth before treatment. After removing the dye (2× washing with PBS) a fresh full DMEM medium with different concentrations of tested polymers were added to the cells. Cells were incubated with polymers (humidified 5% $CO_2$ atmosphere at 37 °C (in MCO-19AIC(UV)-PE incubator, Panasonic)) for 3 days. After that, DMEM medium with the tested polymer was removed (2× washed in DPBS), replaced with fresh full DMEM medium and cell proliferation was further monitored for the next three days. Presto Blue Cell Viability Reagent was used to detect viability of cells after 3 days incubation with polymers as well as during the following 3 days incubation without the polymer. The test was performed at least in two independent experiments, each time using three parallels for each sample. References were tested compounds in supplemented DMEM without cells, pure dye in DMEM, cells without tested compounds (as a negative control), and cells with Triton 100 (as a positive control).

### 5.13 Hemolysis test

Red blood cells were obtained from the Transfusion Center of Ljubljana (Ethical approval number 0120-592/2020/7), and belonged to two young anonymous males, A RhD+ blood type, supplemented with CPD-SAGM preservative, 70% v/v hematocrit, accounting for $4 \times 10^9$ RBCs per ml. Plasma from whole blood purification was also obtained and used for fluorescence studies. The cells were used within three days, at final 5% haematocrit, and incubated with 0.0035–0.02 mg $ml^{-1}$ of GxS5 polymers for 4 hours at 37%, $n = 3$ for each concentration. Red blood cells incubated only with PBS were used as the negative control. After incubation, cells were pelleted and the absorbance of the surnatant was measured at 541 nm.

### 5.14 Flow cytometry

To ascertain any differences in B16F10 cells' uptake among siRNA-complexed and empty polymers their internalization was

 © 2024 The Author(s). Published by the Royal Society of Chemistry

Open Access Article. Published on 19 July 2024. Downloaded on 5/15/2025 12:59:42 PM.
This article is licensed under a Creative Commons Attribution 3.0 Unported Licence.

determined with flow cytometry using a BD FACSymphony™ A3 Cell Analyzer. The cells were incubated for 48 hours with 1 : 2, 1 : 25 and 1 : 50 P/N GxS5 polymers and the corresponding concentration of uncomplexed polymers. After 48 hours, cells were trypsinized and resuspended in phenol-free-DMEM, incubated with 3 μg $ml^{-1}$ of DAPI to exclude dead cells. From the live cell population the percentage of fluorescent positive cells, indicating the uptake of polymers, was determined. Additionally, the median fluorescence intensity (MFI) in the PE channel of the live-cell population was determined. Similarly, the silencing efficacy of polyplexes was determined with flow cytometry. Briefly, 50 000 cells were seeded on a 24 well plate, and let to grow overnight. Transfection was carried out with a total amount of 10 picomoles of siRNA per well. Free polymers, with the same final concentration, were used as the negative control. After 72 h hours of growth, the cells were trypsinized, washed in 1× PBS and stained with DAPI to label dead cells. From the live cell population, the percentage of tdTomato positive cells and their MFI was determined. The MFI of treated groups was then normalized to the negative control group.

### 5.15 Determination of silencing efficacy with q-RT PCR

At 1 : 2, 1 : 25 and 1 : 50 siRNA backbone phosphate/total nitrogen content ratios, polyplexes were used to transfect B16F10 murine melanoma cells, expressing tdTomato fluorescent protein. Before transfection, polyplexes were mixed with the same volume of OPTImem medium. Polyplexes were dropped in each well without mixing. RNAiMAX, a state of the art polymer for lipofection, was used as the positive control. Briefly, 50 000 cells were seeded on a 24-well plate, and let to grow overnight. Transfection was carried out with a total amount of 30 picomoles of siRNA per well, on $n = 3$ biological replicates. Free polymers, with the same final concentration, were used as the reference for tdTomato and β-actin gene fluctuations. After 48 hours of incubation, total RNA was extracted with a VWR pGold Total RNA kit and quantified on a Take3 plate on a Cytation 1 (BioTek Instruments, VT, USA). A Scriptase II kit (Nippon Genetics, LS53) was used to synthesize cDNA at a final concentration of 50 ng $\mu l^{-1}$. Finally, a Power Sybr Green master mix (Applied Biosystem, 4 367 659) was used for qPCR on a Quantstudio 3 apparatus and the $2\Delta\Delta C_T$ method was used for relative quantification (Table 5 for primer sequence). $N = 6$ technical replicates were used for $C_T$ quantification.

### 5.16 Statistical analysis

All statistical analysis were run in Graphpad 10. For tdTomato and β-actin gene expression, CT data were trimmed with a built-in Graphpad 10 outlier recognition algorithm. All datasets were tested for normality or lognormality before any stat test. ANOVA, two or one way, was used for normally distributed data, while non-parametric Kruskall–Wallis was used for lognormal. ANOVA-One Way was used to assess the statistical significance of the data on the log10 of fold changes against the control ($n \geq 6$). For all purposes, significance was determined as $p \leq 0.05$*, $p \leq 0.01$**, $p \leq 0.001$***, and $p \leq 0.0001$****.

## Ethical approval

For the hemolysis test, human red blood cells were used, and obtained from the Transfusion Center of Ljubljana, as per Ethical approval number 0120-592/2020/7 (National Medical Ethics Committee of Slovenian Republic).

## Consent for publication

All authors have read the manuscript and expressed their consent for publication.

## Author contributions

All authors approved the submitted version. G. D. P. made the major contribution in conceptualization, experimental part, data analysis, figure preparation and writing of the manuscript. T. B. and B. M. provided help in cell culture and manuscript revision. M. V. contributed to Fig. 7 and ESI Fig. S12.† G. S. contributed during revision and funding acquisition. N. K. provided all TEM pictures and played a major role in mentoring, conceptualization, revision and funding acquisition.

## Conflicts of interest

The authors declare that they have no competing interests.

## Acknowledgements

The study was supported by the Slovenian Research Agency ARIS (program numbers P2-0084, P3-0003, project numbers PR-10482, J3-14531 and J4-50150).

## References

1 R. R. Nikam and K. R. Gore, *Nucleic Acid Ther.*, 2018, **28**, 209–224.
2 N. Agrawal, P. V. N. Dasaradhi, A. Mohmmed, P. Malhotra, R. K. Bhatnagar and S. K. Mukherjee, *Microbiol. Mol. Biol. Rev.*, 2003, **67**, 657–685.
3 B. R. Meade and S. F. Dowdy, *Adv. Drug Delivery Rev.*, 2008, **60**, 530–536.
4 T. G. Park, J. H. Jeong and S. W. Kim, *Adv. Drug Delivery Rev.*, 2006, **58**, 467–486.
5 T. Wang, L. M. Larcher, L. Ma and R. N. Veedu, *Molecules*, 2018, DOI: **10.3390/MOLECULES23102564**.
6 S. F. Dowdy, *Rna*, 2023, **29**, 396–401.
7 J. D. Shih and C. P. Hunter, *RNA*, 2011, **17**, 1057.
8 F. Braukmann, D. Jordan, B. Jenkins, A. Koulman and E. A. Miska, *RNA Biol.*, 2021, **18**, 888–899.
9 C. He, M. T. Migawa, K. Chen, T. A. Weston, M. Tanowitz, W. Song, P. Guagliardo, K. S. Iyer, C. F. Bennett, L. G. Fong, P. P. Seth, S. G. Young and H. Jiang, *Nucleic Acids Res.*, 2021, **49**, 1.
10 B. Hu, L. Zhong, Y. Weng, L. Peng, Y. Huang, Y. Zhao and X. J. Liang, *Signal Transduction Targeted Ther.*, 2020, **5**, 1–25.
11 S. F. Dowdy, *Nat. Biotechnol.*, 2017, **35**(3), 222–229.

© 2024 The Author(s). Published by the Royal Society of Chemistry

Open Access Article. Published on 19 July 2024. Downloaded on 5/15/2025 12:59:42 PM. This article is licensed under a Creative Commons Attribution 3.0 Unported Licence.

12 Y. Sakurai, H. Hatakeyama, Y. Sato, H. Akita, K. Takayama, S. Kobayashi, S. Futaki and H. Harashima, *Biomaterials*, 2011, **32**, 5733–5742.
13 R. V. Benjaminsen, M. A. Mattebjerg, J. R. Henriksen, S. M. Moghimi and T. L. Andresen, *Mol. Ther.*, 2013, **21**, 149–157.
14 D. U. Lee, J. Y. Park, S. Kwon, J. Y. Park, Y. H. Kim, D. Khang and J. H. Hong, *Nanoscale*, 2019, **11**, 19980–19993.
15 L. M. P. Vermeulen, S. C. De Smedt, K. Remaut and K. Braeckmans, *Eur. J. Pharm. Biopharm.*, 2018, **129**, 184–190.
16 A. Akinc, M. Thomas, A. M. Klibanov and R. Langer, *J. Gene Med.*, 2005, **7**, 657–663.
17 D. Dhumal, W. Lan, L. Ding, Y. Jiang, Z. Lyu, E. Laurini, D. Marson, A. Tintaru, N. Dusetti, S. Giorgio, J. L. Iovanna, S. Pricl and L. Peng, *Nano Res.*, 2021, **14**, 2247–2254.
18 C. Qiu, F. Xia, J. Zhang, Q. Shi, Y. Meng, C. Wang, H. Pang, L. Gu, C. Xu, Q. Guo and J. Wang, *Research*, 2023, **6**, DOI: **10.34133/research.0148**.
19 X. X. Zhang, T. J. McIntosh and M. W. Grinstaff, *Biochimie*, 2012, **94**, 42–58.
20 S. Biswas and V. P. Torchilin, *Pharmaceuticals*, 2013, **6**, 161–183.
21 T. T. Hoang Thi, E. H. Pilkington, D. H. Nguyen, J. S. Lee, K. D. Park and N. P. Truong, *Polymers*, 2020, **12**, 298.
22 D. Zhang, Q. Song, W. Wang, Q. Li, Z. Zhao, Y. Jiang and Y. Luan, *Adv. Funct. Mater.*, 2024, **2315447**, 1–14.
23 C. M. Beddoes, C. P. Case and W. H. Briscoe, *Adv. Colloid Interface Sci.*, 2015, **218**, 48–68.
24 S. M. Moghimi, P. Symonds, J. C. Murray, A. C. Hunter, G. Debska and A. Szewczyk, *Mol. Ther.*, 2005, **11**, 990–995.
25 S. Thalmayr, M. Grau, L. Peng, J. Pöhmerer, U. Wilk, P. Folda, M. Yazdi, E. Weidinger, T. Burghardt, M. Höhn, E. Wagner and S. Berger, *Adv. Mater.*, 2023, **2211105**, 1–22.
26 L. Frydman, P. C. Rossomando, V. Frydman, C. O. Fernandez, B. Frydman and K. Samejima, *Proc. Natl. Acad. Sci. U. S. A.*, 1992, **89**, 9186–9190.
27 A. M. Katz, I. S. Tolokh, S. A. Pabit, N. Baker, A. V. Onufriev and L. Pollack, *Biophys. J.*, 2017, **112**, 22–30.
28 H. Sanayama, K. Ito, S. Ookawara, T. Uemura, Y. Sakiyama, H. Sugawara, K. Tabei, K. Igarashi and K. Soda, *Biomedicines*, 2023, 1403.
29 A. M. Ramos-de-la-Peña, C. M. G. C. Renard, J. Montañez, M. de la Luz Reyes-Vega and J. C. Contreras-Esquivel, *Phytochem. Rev.*, 2016, **15**, 37–49.
30 N. M. Bonanno, F. Jeeva, A. Bhattacharjee, C. N. Garrard, J. LeBlanc, H. N. Hunter and C. B. Caputo, *Pigment.*, 2023, **220**, 111681.
31 S. L. Reay, E. L. Jackson, A. M. Ferreira, C. M. U. Hilkens and K. Novakovic, *Mater. Adv.*, 2022, **3**, 7946–7959.
32 Y. Zhang, L. Mao, J. Liu and T. Liu, *Mater. Sci. Eng., C*, 2017, **71**, 17–24.
33 C. Ninh, A. Iftikhar, M. Cramer and C. J. Bettinger, *J. Mater. Chem. B*, 2015, **3**, 4607–4615.
34 M. Arteche Pujana, L. Pérez-Álvarez, L. C. Cesteros Iturbe and I. Katime, *Carbohydr. Polym.*, 2013, **94**, 836–842.
35 F.-L. Mi, S.-S. Shyu and C.-K. Peng, *J. Polym. Sci., Part A: Polym. Chem.*, 2005, **43**, 1985–2000.
36 S. K. Upadhyay, *Chemical Kinetics and Reaction Dynamics*, Springer, Netherlands, Dordrecht, 2006.
37 K. J. Laidler, *Arch. Hist. Exact Sci.*, 1985, **32**, 43–75.
38 C. Pizzolitto, M. Cok, F. Asaro, F. Scognamiglio, E. Marsich, F. Lopez, I. Donati and P. Sacco, *Int. J. Mol. Sci.*, 2020, **21**, 1–17.
39 I. S. Blagbrough, A. A. Metwally and A. J. Geall, in *Methods in molecular biology*, Clifton, N. J., 2011, vol. 720, pp. 493–503.
40 H. Chen, W. Ouyang, B. Lawuyi, C. Martoni and S. Prakash, *J. Biomed. Mater. Res., Part A*, 2005, **75**, 917–927.
41 B. K. Wilson and R. K. Prud'homme, *J. Colloid Interface Sci.*, 2021, **604**, 208–220.
42 K. Rurack, *Fluorescence Quantum Yields: Methods of Determination and Standards*, 2008.
43 A. L. Antaris, H. Chen, S. Diao, Z. Ma, Z. Zhang, S. Zhu, J. Wang, A. X. Lozano, Q. Fan, L. Chew, M. Zhu, K. Cheng, X. Hong and H. Dai, *Nat. Commun.*, 2017, **8**, 1–11.
44 L. Wang, A. K. Gaigalas, J. Blasic and M. J. Holden, *Spectrochim. Acta, Part A*, 2004, **60**, 2741–2750.
45 X. F. Zhang, Y. Zhang and L. Liu, *J. Lumin.*, 2014, **145**, 448–453.
46 K. A. Kang, J. Wang, J. B. Jasinski and S. Achilefu, *J. Nanobiotechnol.*, 2011, DOI: **10.1186/1477-3155-9-16**.
47 L. Ramishvili, I. Bochorishvili, N. Gabunia, Z. Kuchukashvili, M. Gordeziani, T. Chigogidze, A. Khazaradze, Z. Melikishvili and N. Kotrikadze, *J. Cancer Ther.*, 2014, **05**, 1021–1030.
48 C. B. Bottom, S. S. Hanna and D. J. Siehr, *Biochem. Educ.*, 1978, **6**, 4–5.
49 F. A. Whitehead, S. A. Young and S. Kasapis, *Int. J. Biol. Macromol.*, 2020, **164**, 3075–3083.
50 B. Nyambat, Y. B. Manga, C.-H. Chen, U. Gankhuyag, A. Pratomo WP, M. Kumar Satapathy and E.-Y. Chuang, *Int. J. Mol. Sci.*, 2020, **21**, 4864.
51 L. Yan, Y. Wang, L. Ren, G. Wu, S. G. Caridade, J. Fan, L. Wang, P. Ji, J. T. J. M. Oliveira, J. T. J. M. Oliveira, J. F. Mano and R. L. Reis, *J. Biomed. Mater. Res., Part A*, 2010, **95A**, 465–475.
52 D. I. Seracu, *Anal. Lett.*, 1987, **20**, 1417–1428.
53 P. Cayot and G. Tainturier, *Anal. Biochem.*, 1997, **249**, 184–200.
54 X. Liu, C. Liu, J. Zhou, C. Chen, F. Qu, J. J. Rossi, P. Rocchi and L. Peng, *Nanoscale*, 2015, **7**, 3867–3875.
55 S. Plianwong, P. Opanasopit, T. Ngawhirunpat and T. Rojanarata, *BioMed Res. Int.*, 2013, **2013**, 1–9.
56 Y. B. Hu, E. B. Dammer, R. J. Ren and G. Wang, *Transl. Neurodegener.*, 2015, **4**, 1–10.
57 N. Sayed, P. Tambe, P. Kumar, S. Jadhav, K. M. Paknikar and V. Gajbhiye, *Nanomedicine*, 2020, **15**, 163–181.
58 H. Liang, W. Chang, K. Lin and H. Sung, *J. Biomed. Mater. Res., Part A*, 2003, **65A**, 271–282.
59 Y. Yu, S. Xu, S. Yu, J. Li, G. Tan, S. Li and W. Pan, *ACS Biomater. Sci. Eng.*, 2020, **6**, 1543–1552.
60 X. Song, K. Lan, Q.-Y. Lv, H. Liu and H.-F. Cui, *J. Drug Delivery Sci. Technol.*, 2021, **61**, 102161.
61 M. F. Butler, Y. F. Ng and P. D. A. Pudney, *J. Polym. Sci., Part A: Polym. Chem.*, 2003, **41**, 3941–3953.



© 2024 The Author(s). Published by the Royal Society of Chemistry

Open Access Article. Published on 19 July 2024. Downloaded on 5/15/2025 12:59:42 PM.
This article is licensed under a Creative Commons Attribution 3.0 Unported Licence.

62 J. Qiu, J. Li, G. Wang, L. Zheng, N. Ren, H. Liu, W. Tang, H. Jiang and Y. Wang, *ACS Appl. Mater. Interfaces*, 2013, **5**, 344–350.
63 S. Matcham and K. Novakovic, *Polymers*, 2016, **8**, 1–10.
64 Y. Gao, J. Y. Huang, J. O'Keeffe Ahern, L. Cutlar, D. Zhou, F. H. Lin and W. Wang, *Biomacromolecules*, 2016, **17**, 3640–3647.
65 W. Wang, D. Zhou, L. Cutlar, Y. Gao, W. Wang, J. O'Keeffe-Ahern, S. McMahon, B. Duarte, F. Larcher, B. J. Rodriguez and U. Greiser, *Sci. Adv.*, 2016, **2**, 1–15.
66 J. He, S. Xu and A. James Mixson, *Pharmaceutics*, 2020, **12**, 1–31.
67 J. Nguyen and F. C. Szoka, *Acc. Chem. Res.*, 2012, **45**, 1153–1162.
68 I. Honoré, S. Grosse, N. Frison, F. Favatier, M. Monsigny and I. Fajac, *J. Controlled Release*, 2005, **107**, 537–546.
69 H. Lv, S. Zhang, B. Wang, S. Cui and J. Yan, *J. Controlled Release*, 2006, **114**, 100–109.
70 K. Kim, H. S. Hwang, M. S. Shim, Y. Y. Cho, J. Y. Lee, H. S. Lee and H. C. Kang, *Colloids Surf., B*, 2019, **184**, 110497.
71 Y. Yue, F. Jin, R. Deng, J. Cai, Z. Dai, M. C. M. Lin, H. F. Kung, M. A. Mattebjerg, T. L. Andresen and C. Wu, *J. Controlled Release*, 2011, **152**, 143–151.
72 B. Winkeljann, D. C. Keul and O. M. Merkel, *J. Controlled Release*, 2023, **353**, 518–534.
73 A. Fus-Kujawa, P. Prus, K. Bajdak-Rusinek, P. Teper, K. Gawron, A. Kowalczuk and A. L. Sieron, *Front. Bioeng. Biotechnol.*, 2021, **9**, 701031.
74 Y. Qin, A. A. Walters, N. Rouatbi, J. T. W. Wang, H. M. Abdel-Bar and K. T. Al-Jamal, *Biomaterials*, 2023, **299**, 122158.
75 L. Mott, C. Akers and D. W. Pack, *J. Drug Delivery Sci. Technol.*, 2023, **84**, 104465.
76 J. Rejman, V. Oberle, I. S. Zuhorn and D. Hoekstra, *Biochem. J.*, 2004, **377**, 159–169.
77 M. A. Jackson, T. A. Werfel, E. J. Curvino, F. Yu, T. E. Kavanaugh, S. M. Sarett, M. D. Dockery, K. V. Kilchrist, A. N. Jackson, T. D. Giorgio and C. L. Duvall, *ACS Nano*, 2017, **11**, 5680–5696.
78 C. T. Greco, J. C. Andrechak, T. H. Epps and M. O. Sullivan, *Biomacromolecules*, 2017, **18**, 1814–1824.
79 H. J. Greyner, T. Wiraszka, L. S. Zhang, W. M. Petroll and M. E. Mummert, *Matrix Biol.*, 2010, **29**, 503–510.
80 J. A. Swanson and J. S. King, *Philos. Trans. R. Soc., B*, 2019, DOI: **10.1098/RSTB.2018.0146**.
81 J. V. V. Arafiles, H. Hirose, M. Akishiba, S. Tsuji, M. Imanishi and S. Futaki, *Bioconjugate Chem.*, 2020, **31**, 547–553.
82 E. Grecka, M. Statkiewicz, A. Gorska, M. Biernacka, M. A. Grygorowicz, M. Masnyk, M. Chmielewski, K. Gawarecka, T. Chojnacki, E. Swiezewska and M. Malecki, *PLoS One*, 2016, **11**, 1–25.
83 K. Harpe, P. Kondiah, Y. Choonara, T. Marimuthu, L. Toit and V. Pillay, *Cells*, 2019, **8**, 1–25.

© 2024 The Author(s). Published by the Royal Society of Chemistry

103

# Chapter 6

# Red Blood Cell Membrane Vesicles for siRNA Delivery: A Biocompatible Carrier with Passive Tumor Targeting and Prolonged Plasma Residency

Erythrocytes have long been used as drug carriers for pharmaceutical applications. Their long story began in the Seventies, as elucidated in the Introduction, but reached a halt due to HIV epidemics. Recently, the use of erythrocytes as starting materials for biocompatible carriers has gained new momentum because they have entered into clinical trials of several formulations [331]. Erythrocytes are the most abundant cells in mammals; they have a lifespan of 2--3 months in humans, do not possess any nucleus but only regulatory miRNAs [257], and their membrane shows exciting rheological properties owing to its relative stiffness, lipid raft composition and unique cytoskeleton, which endows them with the typical biconcave shape [332], [333]. The use of erythrocyte membranes for nanodrug applications has been attempted multiple times in the literature [194], and such nanoparticles have been termed nanoerythrosomes. In the present work, we aimed to load nanoerythrosomes, which we termed erythrocyte membrane vesicles (EMVs), with a small-interfering RNA to be passively delivered to solid tumors via the enhanced permeation and retention effect [84] and prolonged plasma residence.

The following conceptualization follows certain hypotheses inherent in red blood cells:

1. The small size of EMVs—100–180 nm—is suitable for extravasating from leaky, newly formed tumor blood vessels and therefore accumulating in the extracellular matrix;
2. CD47, known as the “don’t eat me!” marker of macrophages and is capable of blocking phagocytosis, is retained on the membrane of EMVs;
3. The sialic acid glycocalyx of erythrocytes is also retained and confers the negative zeta potential of parental cells to EMVs;
4. These EMVs have either prolonged cell persistence or fast diffusion toward target organs and escape recognition by the reticuloendothelial system [78].

On this basis, as outlined in **Figure 13**, we followed a conventional protocol to generate erythrocyte ghosts, i.e., empty erythrocytes deprived of hemoglobin, and sonicated and extruded the ghosts in the presence of a siRNA targeting a fluorescent reporter gene, tdTomato. We then developed a density-based ultracentrifugation protocol based on a trisodium citrate cushion, selecting only the most densely packed EMVs and eliminating membrane debris and unencapsulated siRNA. We characterized the ultrastructures of the EMVs via conventional TEM, freeze-fracture EM, cryo-EM and STED confocal microscopy. A well-known murine melanoma cell line, B16F10, which contains the

fluorescent protein tdTomato, was chosen as the transfection model. EMVs could elicit 80% target gene knockdown at a dose of 0.3 nM and showed no signs of cytotoxicity in multiple cell lines. Furthermore, they follow an endosome-independent internalization pathway in the B16F10, NHLF and CT26 cell lines. We also tested EMV activity in vivo in mice challenged with a B16F10-derived tumor in the left flank. At a dose of 2.5 mg/ml, after 48 hours, the tdTomato gene showed a 78% reduction in gene expression after a single injection, while its fluorescence was halved from the beginning of the experiment. Using a stem–loop TaqMan PCR technique, we tracked the lead strand of the siRNA, and we excised and prepared for fluorescence microscopy the tumors, kidneys, lungs, spleen, brain, liver and heart of mice that were intravenously injected with fluorescently labeled siRNAs and EMVs. Surprisingly, EMVs were still present (1% of the injected dose) in the blood at 48 h postadministration but almost completely escaped liver clearance and accumulated in capillaries of the lungs and brain. Indeed, the most important clearance organs were the spleen and the kidney. Finally, 10% of the injected dose was in the tumor, where it passively accumulated in the cells and the ECM. These results show how erythrocytes are suitable starting materials for biocompatible and efficient nanodrugs that can be engineered for precision medicine via the use of patients' own blood. Finally, the supplementary material from this chapter is presented in **Appendix C**.

In this paper, **Hypothesis 1**, **Hypothesis 2**, **Hypothesis 3 were assayed and confirmed.**

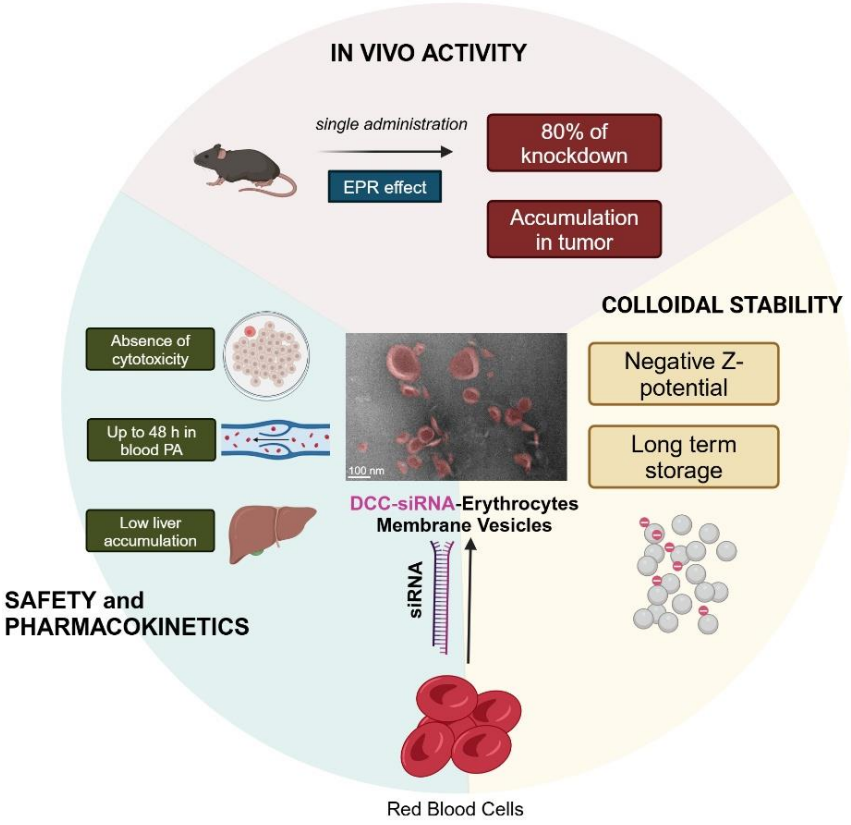



Figure 13 Graphical Abstract of Chapter 6, reprinted with permission from [208].

International Journal of Nanomedicine

Dovepress
Taylor & Francis Group

Open Access Full Text Article

ORIGINAL RESEARCH

# Red Blood Cell Membrane Vesicles for siRNA Delivery: A Biocompatible Carrier With Passive Tumor Targeting and Prolonged Plasma Residency

Giulia Della Pelle[1,2], Bostjan Markelc[3], Tim Bozic[3], Jernej Šribar[4], Igor Krizaj[4], Kristina Zagar Soderznik[1], Samo Hudoklin[5,*], Mateja Erdani Kreft[5,*], Iztok Urbančič[6], Matic Kisovec[7], Marjetka Podobnik[7], Nina Kostevšek[1]

[1]Department for Nanostructured Materials, Jožef Stefan Institute, Ljubljana, 1000, Slovenia; [2]Jožef Stefan International Postgraduate School, Ljubljana, 1000, Slovenia; [3]Department of Experimental Oncology, Institute of Oncology Ljubljana, Ljubljana, 1000, Slovenia; [4]Department of Molecular and Biomedical Sciences, Jožef Stefan Institute, Ljubljana, 1000, Slovenia; [5]Institute of Cell Biology, Faculty of Medicine, University of Ljubljana, Ljubljana, 1000, Slovenia; [6]Laboratory of Biophysics, Condensed Matter Physics Department, Jožef Stefan Institute, Ljubljana, 1000, Slovenia; [7]Department of Molecular Biology and Nanobiotechnology, National Institute of Chemistry, Ljubljana, 1000, Slovenia

*These authors contributed equally to this work

Correspondence: Giulia Della Pelle, Jozef Stefan Institute, Jamova Cesta 39, Ljubljana, 1000, Slovenija, Tel +393356577520, Email giulia.della.pelle@ijs.si

International Journal of Nanomedicine downloaded from https://www.dovepress.com/
For personal use only.

**Background:** Despite many advances in gene therapy, the delivery of small interfering RNAs is still challenging. Erythrocytes are the most abundant cells in the human body, and their membrane possesses unique features. From them, erythrocytes membrane vesicles can be generated, employable as nano drug delivery system with prolonged blood residence and high biocompatibility.

**Methods:** Human erythrocyte ghosts were extruded in the presence of siRNA, and the objects were termed EMVs (erythrocyte membrane vesicles). An ultracentrifugation-based method was applied to select only the densest EMVs, ie, those containing siRNA. We evaluated their activity in vitro in B16F10 cells expressing fluorescent tdTomato and in vivo in B16F10 tumor-bearing mice after a single injection.

**Results:** The EMVs had a negative zeta potential, a particle size of 170 nm and excellent colloidal stability after one month of storage. With 0.3 nM siRNA, more than 75% gene knockdown was achieved in vitro, and 80% was achieved in vivo, at 2 days PI at 2.5 mg/kg. EMVs mostly accumulate around blood vessels in the lungs, brain and tumor. tdTomato fluorescence steadily decreased in tumor areas with higher EMVs concentration, which indicates efficient gene knockdown. Approximately 2% of the initial dose of EMVs was still present in the plasma after 2 days.

**Conclusion:** The entire production process of the purified siRNA-EMVs took approximately 4 hours. The erythrocyte marker CD47 offered protection against macrophage recognition in the spleen and in the blood. The excellent biocompatibility and pharmacokinetic properties of these materials make them promising platforms for future improvements, ie, active targeting and codelivery with conventional chemotherapeutics.

**Keywords:** biomimetic, RNA interference, EPR effect, nanomedicine, melanoma

## Introduction

Red blood cells (RBCs) are the most abundant cells in the human body.[1] From a pharmaceutical point of view, they have been overlooked for a long time, being considered merely hemoglobin carriers, until "nanorevolution" alighted new interest in biomimetic nanocarriers. They can be harvested from the patient's body, suitably treated,[2] and reinjected, thereby obtaining an allergy-free drug carrier that can persist in the blood flow for several weeks. They, and their derivatives, fall within the ever-growing category of biomimetic carriers.[3,4]

As of 2023, the full proteome of red blood cells[5] and their membrane-derived vesicles[6] and full transcriptome[7] have been intensely characterized. Moreover, the RBC membrane, and its underlying cytoskeleton, is a unique scaffold with interesting rheological and biological properties: extreme deformability[8] combined with good mechanical resistance to shear force;[9] the

Received: 4 November 2024
Accepted: 4 February 2025
Published: 15 March 2025



© 2025 Della Pelle et al. This work is published and licensed by Dove Medical Press Limited. The full terms of this license are available at https://www.dovepress.com/terms.php and incorporate the Creative Commons Attribution – Non Commercial (unported, v3.0) License (http://creativecommons.org/licenses/by-nc/3.0/). By accessing the work you hereby accept the Terms. Non-commercial uses of the work are permitted without any further permission from Dove Medical Press Limited, provided the work is properly attributed. For permission for commercial use of this work, please see paragraphs 4.2 and 5 of our Terms (https://www.dovepress.com/terms.php).

RBC membrane also possesses the CD47 marker, colloquially known as the "don't eat me" marker for macrophage recognition,[10] which, in aging RBCs, is instead triggered by phosphatidylserine exposure on the outer leaflet.[11] CD47, which is also present on naturally released extracellular vesicles [10,11], enables RBC-derived carriers to achieve long blood circulation times and systemic activity. RBCs have also rarely been used as therapeutic nucleic acid carriers.[1] Since the discovery of RNA interference,[12] the research and development of therapeutic RNAs have become a new challenge in personalized molecular medicine, despite only a handful of drugs being approved by the European Medicine Agency and the Federal Drug Agency.[13] Indeed, as of 2022, five siRNA drugs have been approved by the US FDA, and, later, by EMA: the already mentioned Patisiran (Onpattro), Givosiran (Givlaari), Lumasiran (Oxlumo), Inclisiran (Leqvio), and Vutrisiran (Amvutta), all directed to the liver. Nanomedicine runs in strict correlation with personalized medicine, with the number of papers concerning small interfering RNA delivery skyrocketing in the last fifteen years and with more than 20,000 papers in 2022 about siRNA delivery (data from[14]). Furthermore, the discovery of extracellular vesicles (EVs)[15] as naturally occurring microinterfering RNA carriers fueled research on lipidic, biomimetic, neutral delivery systems for therapeutic nucleic acids (TNAs) as safe replacements for cationic lipofection. Unfortunately, the route for the clinical translation of EVs as small interfering RNA carriers is challenging and steep because of their difficult recovery, purification, low encapsulation efficiency and presence of off-target miRNAs.[16] On the other hand, red blood cells are a large source of EVs.[17] Therefore, the advantages of using RBC as starting material for a nanocarriers, compared with synthetic alternatives, are numerous: lack of recognition from phagocytic cells due to the presence of CD47 co-receptor; presence, in the membrane proteome, of the protein machinery for membrane fusion/cell uptake typical of EVs, but without the collection and purification hurdles;[6,18] the possibility of using patient's own blood, as it happened for a some approved formulations that uses red blood cells as carriers;[1,19] the presence of an RNAse inhibitor, that allows for long-term storage of ribonucleic TNA;[20,21] the negative surface charge, due to red blood cell sialic acid glycocalyx, reduces the interaction with plasma protein, prolonging circulation time, tuning the composition and abundance of protein corona components.[22,23] For an enhanced targeting and a specific tissue-tropism, red blood cell surface modification has been extensively characterized and successfully achieved, both via "hitchhiking", due to electrostatic interactions in the glycocalyx, and via covalent coupling: the reader can then refer to the following review.[24] Furthermore, they share the advantages of other "neutral" TNA carriers, such as liposomes and micelles: the lack of cationic charges, typical of polymers and dendrimers such as PEI[25] and PAMAM,[26,27] notoriously eliciting apoptotic cascades.[28–30]

In the present work, we used red blood cells as the starting material for a neutral therapeutic nucleic acid (TNA) delivery system, which we named erythrocyte membrane vesicles (EMVs). Our TNA of choice is a siRNA because of its compactness and well-established clinical applications.[27] Nevertheless, siRNA are double-stranded RNA molecules, behaving as PAMPS within macrophages (pathogen-associated molecular pattern), being recognized by toll-like receptor 3.[31] SiRNAs are capable of activating multiple immune system pathways, including interferon 1 cascade, composed of roughly 2000 genes; finally, a mitochondrial apoptosis is initiated via dsRNA dependent caspase-binding domains in important RNA helicases and transducers such as MDA5 and RIG-I.[32] Lastly, siRNA has a very short residency time in plasma, being rapidly cleared away by kidney filtration.[33] For its innate cytotoxicity and brief permanence in blood, encapsulation of siRNAs within nanodrugs is advisable and a thriving field of study.[34]

As a proof-of-concept, we loaded an anti-tdTomato siRNA into EMVs obtained via sonication and extrusion of red blood cell membranes. tdTomato (tandem-dimer Tomato) is an orange-emitting fluorescent protein, derived from coral *Discosoma* sp.[35] Despite being used as a coating material,[36–38] this is the first report of an erythrocyte membrane being used as a liposomal-like formulation, reduced to object of 100–200 nm, for a TNA delivery, that does not involve any other nanoparticle actor ie a core shell structure, where the TNA is embedded within the core and the red blood cell membrane acts as a camouflaging material. We characterized the interactions of the payload and erythrocyte membranes via superresolution fluorescence microscopy and cryo- and freeze-fracture TEM. We greatly optimized the purification strategy, reaching 67% encapsulation efficiency, and were able to select and use only the carriers containing the TNA for transfection, removing the unloaded and unprotected molecules, together with cell debris not shaped into EMVs. Moreover, we optimized a long-term freeze–drying storage strategy. EMVs have been proven to be a successful, inexpensive, and safe delivery system for siRNAs both in vitro and in vivo as demonstrated in a tdTomato-expressing murine melanoma cell line in vitro and in a subcutaneous murine tumor model in vivo, with excellent pharmacokinetic properties. At low doses, they elicited significant knockdown of target genes as early as 24 hours postinjection, whereas EMVs were still present in the blood circulation two days postinjection. Despite relying solely on passive targeting,

more than 15% of the injected dose was present in the tumor tissue at 48 hours postinjection, effectively silencing the target gene in the proximity of major and minor blood vessels. Moreover, the mean circulation time of EMVs exceeds 4–5 times that of a naked, unmodified siRNA,[39,40] and their main clearance route is via renal filtration with low liver accumulation.

## Materials and Methods

### Materials and Chemicals

Red blood cells were obtained from the Blood Transfusion Centre of Slovenia (Ethical approval number 0120–592/2020/7), which belong to two young anonymous males, A RhD+ blood type, supplemented with CPD-SAGM preservative, 70% v/v hematocrit, accounting for $4•10^9$ RBCs/mL, and stored in 1 mL aliquots at −80°C without additional cryopreservatives. For EMVs preparation, we used phosphate-buffered saline tablets obtained from Sigma Aldrich (P4417) in diethyl-pyrocarbonate-treated Milli-Q water. Trisodium citrate dihydrate, RNase A (catalog number 10109142001) and Amicon centrifugal devices (30, 10 and 4 kDa NMWL, EMD Millipore), as well as fluorescent dyes (CM-DiI, C7000, and Vybrant DiO, V22886), were purchased from Sigma Aldrich. For the Stewart assay, ferric chloric hexahydrate (F2877) and ammonium thiocyanate (A7149) were purchased from Sigma Aldrich, whereas the heart lipid extract (171201), which was used as a standard, was obtained from Avanti Polar lipids. The Bradford reagent was prepared according to the traditional recipe[41] (Coomassie Brilliant Blue R-250, B7920, ethanol and phosphoric acid were obtained from Sigma Aldrich), and bovine serum albumin (A9418, Sigma Aldrich) at a stock concentration of 1 mg/mL was used as a standard. The polycarbonate extrusion membranes were 19 mm wide, 800 nm wide (610009), and 200 nm wide (610006), and the support filters (610014) were all purchased from Avanti Polar and installed on an Avanti Polar mini extruder. Anti-TdTomato-siRNA was purchased from Thermo Fisher as a duplex oligo with the following sequence: 5'rGrCrC rArCrC rArCrC rUrGrU rUrCrC rUrGrU rATT- 3′; 3′rUrArC rArGrG rArArC rArGrG rUrGrG rUrGrG rCGG-5′; "r" stands for ribonucleotide to distinguish it from DNA overhangs), whereas Cy-5 siRNA was later obtained from Integrated DNA Technologies (USA). All the labware, including tips and Falcon and Eppendorf tubes, was RNAse/pyrogenase free, and the buffers were DEPC-treated. Advanced Dulbecco's modified MEM (ADMEM), Advanced Roswell Park Memorial Institute 1640 medium (RPMI-1640), and MCDB 131 media were purchased from Gibco (Thermo Fisher Scientific, VA, US), and FGM™-2 Fibroblast Growth Medium-2 BulletKit™ was purchased from Lonza (Basel, CH). All media except FGM™-2 were supplemented with GlutaMAX (100x, Gibco) and penicillin–streptomycin (100x, Sigma–Aldrich, Merck, Darmstadt, Germany). ADMEM and ARPMI were supplemented with 5% fetal bovine serum (FBS; Gibco). MCDB 131 was supplemented with 10% FBS (Gibco), 10 ng/mL epidermal growth factor (EGF; Gibco), 1 µg/mL hydrocortisone (Sigma–Aldrich) and 10 mm glutamine (GlutaMAX; Gibco). The MycoAlertTM PLUS Mycoplasma Detection Kit was purchased from Lonza (Basel, CH). The B16F10 (CRL-6475), CT26 (CRL-2638), 4T1 (CRL-2539), and Hulec-5a (CRL-3244) cell lines were purchased from ATCC (VA, US), the NHLF cell line was purchased from Lonza (Basel, CH), and the B16F10-tdTomato line was a kind gift from Dr. Muriel Golzio (The Institute of Pharmacology and Structural Biology, IPBS-Toulouse). The cells were grown in a humidified 5% $CO_2$ atmosphere at 37°C in a cell culture incubator. The Presto Blue reagent (A13261) and Hoechst 33342 solution (62249) were purchased from Thermo Fisher Scientific, and the MemBrite® Fix 488/515 Cell Surface Staining Kit from Biotium (#30093-T, Fremont, CA, USA) were used.

### Preparation of Erythrocyte Membrane Vesicles

Erythrocytes were depleted of hemoglobin via the hypotonic lysis method.[42] The cells were incubated overnight with 40 mL/each mL of erythrocytes at 4°C, as first established by,[43] and later centrifuged at 11,000 rpm with a benchtop Minispin Eppendorf centrifuge. The pellet was washed four times to allow hemoglobin release. One milliliter of original red blood cell suspension was finally diluted four times in buffer containing siRNA at a suitable concentration, incubated at 37°C under gentle shaking, sonicated with an ultrasonic processor for 10 seconds (Sonics Vibra cell VC-505; pulses: 1 s on, 1 s off; 20% amplitude) for 10s, and subsequently extruded at 37°C with an Avanti Polar mini extruder, which was previously thoroughly rinsed with DEPC water via an 800 nm membrane 5 times and a 200 nm membrane 20 times. The final suspension was stored at 4°C.

#### Protein and Lipid Quantification

A Bradford assay was used to evaluate the protein concentration, with bovine serum albumin used as a standard. The Bradford reagent was prepared according to previous methods,[41] and the assay-to-sample ratio was 30:1 v/v. All

measurements were performed in triplicate. The absorbances at 450 and 595 nm were recorded, and a calibration curve was built from their ratio. A Stewart assay was used to quantify the phospholipid content,[44] with heart lipid extract (Avanti Polar) used as a standard reference.

### Selection of the Best Purification Method

First, for size exclusion chromatography, siRNA-EMVs were loaded into a PD10 G25 Sephadex column (GE Healthcare) as reported elsewhere for similar purposes;[45] the sample was recovered after the addition of 5–6 mL of 1× PBS (Figure 1). Second, Amicon 30 kDa centrifugal units were used: 500 µL of the sample was loaded into a 0.5 mL tube and centrifuged at 13,000 rpm for 5 minutes. Subsequently, the retentate and eluate were redispersed in the original volume and used for RNA quantification. Third, we tested common ultracentrifugation-based purification techniques for siRNA recovery and EMVs integrity (details in the), ie, a sucrose gradient, regular ultracentrifugation, and density-changing centrifugation.[46]

### Density Changing Ultracentrifugation

Density changing centrifugation (DCC) has proven to be the best and easiest method for obtaining high concentrations of siRNA-loaded EMVs, and it is described in detail here. To select only loaded EMVs and to separate correctly shaped ones from protein aggregates and unloaded siRNA, we adapted an easy purification protocol by.[46] Ultracentrifuge tubes

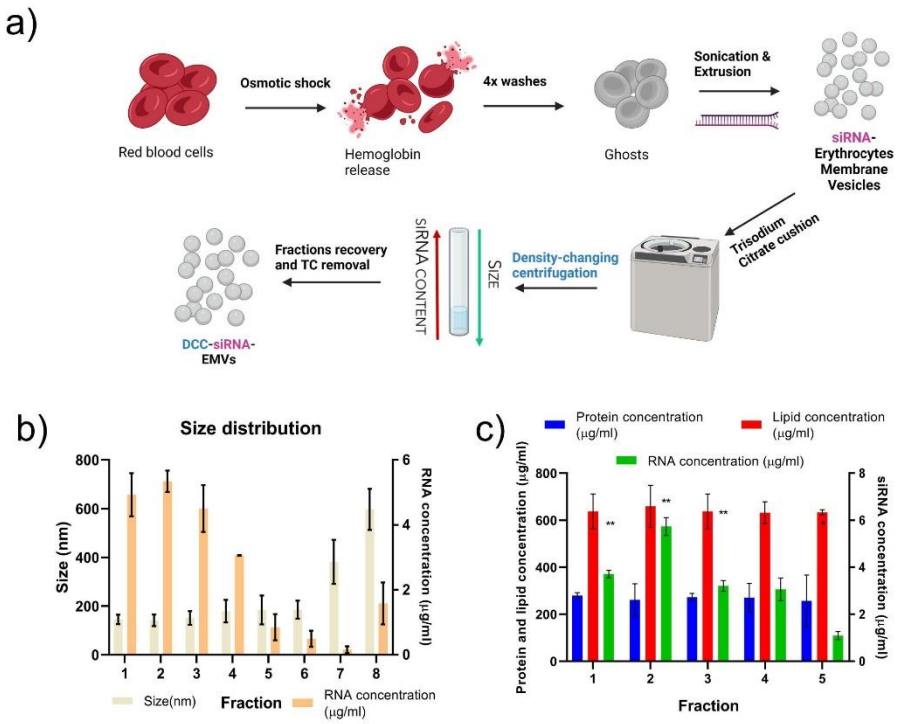



**Figure 1** (**a**) Overview of the protocol used for the preparation of DCC-siRNA-EMVs. (**b**) Size (nm) and RNA concentration (µg/mL) after ultracentrifugation. The data refer to n=3 experiments. The initial concentration of siRNA, before DCC, was 10 µg/mL, resulting in a 67% encapsulation efficiency. (**c**) Concentrations of protein, lipids, and siRNA among the 5 top fractions. $p \leq 0.01$ **.

(3 mL, Beckman Coulter Life Sciences, catalog number 355635) were filled with 2 mL of 10% (m/v) trisodium citrate (TC) dissolved in PBS, and the sample to be separated was gently pipetted on top. This allows selection on the basis of the mixed effects of changed solubility and density rather than time-consuming sucrose gradient ultracentrifugation. Heavier and denser EMVs will be found in the upper layer of the tube with decreasing siRNA concentration while approaching the bottom, where protein and other cellular debris, together with unloaded siRNA, will be pelleted. The tubes were centrifuged in a Beckman Coulter Optima XPN-90 ultracentrifuge equipped with an SW 60 Ti swinging-bucket rotor for 40 minutes at 4°C and 100.000 × g (27.200 rpm). Eight 0.25 mL fractions were then collected and subjected to analysis. The six top fractions were determined to contain siRNA via a Quantifluor RNA assay (see next section). The TC was removed with an Amicon centrifugal device, 10 kDa NMWL (EMD Millipore, UFC8010). Finally, the DCC-siRNA-EMVs were resuspended in PBS and stored at 4°C until further use.

### Encapsulation Efficiency Determination

On the basis of at least three replicates, the siRNA concentration was determined for every collected fraction via the following formula:

$$\mathrm{EE\%} = \frac{(\mu\mathrm{g\ of\ encapsulated\ siRNA})}{\mu\mathrm{g\ of\ added\ siRNA}} \times 100$$

A Quantifluor RNA system (Promega) and a Quantus spectrophotometer were used to evaluate the RNA concentration according to the manufacturer's specifications.

## Particle Size and Zeta Potential Determination

The hydrodynamic diameter, polydispersity index (PDI), and zeta potential of the empty and siRNA-containing EMVs were determined via a zeta potential and particle size analyzer Litesizer (Anton Paar, Austria) equipped with a built-in volume-weighted algorithm in proprietary software (Kalliope). Omega cuvettes were used for both analyses. The backscattering angle (175°) was used for EMVs particle size determination.

## Encapsulation Stability

Amicon 0.5 mL 30 NMWL devices were used to quantify spontaneous RNA leakage from EMVs after siRNA encapsulation. Two hundred microliters of each sample was loaded in the centrifugal device and centrifuged at 13,500 rpm on a Minispin Eppendorf tabletop centrifuge for 10 minutes until it was reduced to a final volume of 60 µL. The eluate was resuspended to the initial volume with PBS and used for RNA quantification. Between measurements, the samples were kept at 4°C.

## RNase A Stability Assay

To evaluate the nuclease resistance of EMVs, three different concentrations of RNAse A (50, 5, and 0.5 µg/mL) were tested on naked RNA, followed by centrifugation of EMVs and ultracentrifugation of EMVs for 24 and 2 hours, with two independent preparations. After incubation at 37°C for the desired amount of time, the samples were run on a 2% agarose gel, and the same amount of siRNA in each well was carefully pipetted to avoid dilution bias. In accordance with the manufacturer's procedures, the gels were subsequently stained with SYBR Gold stain and visualized in a transilluminator.

## Ultrastructure Characterization

### CryoTEM

Four kinds of samples were analyzed:

- Empty EMVs not subjected to density-changing centrifugation (DCC)
- Empty EMVs, DCC
- Loaded EMVs with 10 µg/mL siRNA, not subjected to DCC
- LoadedEMVs with 10 µg/mL siRNA, not subjected to DCC

Two hundred microliters of each typology were used as the starting material, and a 3x concentrated sample of each centrifuged sample was obtained. The samples for cryoTEM were prepared via Vitrobot Mark IV (Thermo Fischer Scientific, Waltham, MA, USA). Quantifoil® R 2/2, 200 mesh holey carbon grids (Quantifoil Micro Tools GmbH, Großlöbichau, Germany) were glow-discharged for 60s at 20 mA and positive polarity in an air atmosphere (GloQube® Plus, Quorum, Laughton, UK). Vitrobot conditions were set to 4°C, 95% relative humidity, a Blot time of 6 s and a Blot force of 2. Three microliters of the suspension were applied to the grid, blotted, and vitrified in liquid ethane. The samples were visualized with a 200 kV Glacios microscope (Thermo Fischer Scientific, Waltham, MA, USA). Micrographs were analyzed for size distribution via ImageJ software and GraphPad 9.0 for statistical analysis. Size analysis was performed on n>6 20.000x micrographs.

### Freeze-Fracturing EM

The same set of samples analyzed with cryoTEM was also used for freeze-fracturing EM. Suspensions of EMVs were mixed 1:1 with 60% glycerol and incubated for 30 minutes at 4°C. Using a pipette, 1.5 µL samples were transferred to gold-stub well-type carriers and frozen in a $LN_2$-cooled freezer. The frozen samples were immediately transferred to a freeze-fracture device (BALZERS, BAF200), fractured (knife temperature of −150°C), shadowed with carbon-platinum (nominal angle of 45°) and further strengthened with carbon (nominal angle of 90°). The obtained replicas were cleaned overnight in a sodium hypochlorite solution, subsequently collected on copper microscopic grids and examined with a CM100 transmission electron microscope (Philips, Netherlands) running at 80 kV.

### Negative Staining Conventional Transmission Electron Microscopy

EMV suspensions were fixed for 30 minutes in 1:1 2.5% glutaraldehyde cacodylate buffer (pH 7.3, 0.008 M) to match the osmolarity of the PBS solution. Briefly, 5 µL of suspension was placed on Formvar-coated copper grids (150 mesh, TEMFCF150CU50, Sigma Aldrich) for 10 minutes, and excess liquid was gently removed with Whatman filter paper. The grids were briefly washed with Milli-Q water by placing them on drops, and the excess liquid was removed. Finally, the grids were placed over a drop of UA-zero negative stain (Alpha Aesar) for 45 seconds and subsequently air-dried. Sample grids were examined with a JEOL JEM-2100 instrument operating at an accelerating voltage of 200 kV. The samples were imaged at 20,000x to 40,000x magnification.

### Superresolution Fluorescence Microscopy

DCC-siRNA-EMVs and siRNA-EMVs were imaged on a superresolution confocal microscope[47] equipped with a STED laser. Glass slides and coverslips were first coated with 0.1% polylysine (P8920, Sigma Aldrich) by gently dipping them in the solution, followed by a brief wash with 1× PBS. Finally, 20–50 µL of CM-DiI-labeled Cy5-siRNA-EMVs were spread on the slide surface with a coverslip and subsequently sealed with nail polish. The slides were imaged a maximum of two hours after mounting. Imaging of the samples was performed on an Olympus IX83 microscope with a 60 × water-immersion objective (NA 1.2), custom-upgraded by Abberior Instruments with 561 nm and 640 nm excitation lasers (120 ps pulse length, 50 µW mean power), a 775 nm STED laser (1.2 ns pulse length, 170 mW mean power), and two avalanche photodiodes for fluorescence detection in the ranges of 580–625 nm and 655–720 nm, as defined by prefilters and a dichroic. All imaging was performed at an 80 MHz frequency with a 1.1 A.U. pinhole. To compare the resolution between confocal and STED microscopy, a field of view of 5 µm × 5 µm was imaged with a 33 nm pixel size. The dwell time was 10 µs for confocal microscopy and 30 µs for STED microscopy, and the pinhole size was 0.6 AU. Other parameters (gating and laser powers) were tuned for each probe separately to achieve the best possible resolution. Superimposition of the Cy-5 and DiI signals was performed via the Colocalization Finder ImageJ plugin.

## In Vitro Assays

### Cytotoxicity Assay

For the in vitro cytotoxicity assay, 1000 cells/well in 100 µL of appropriate cell culture medium for each cell line were seeded in a 96-well plate (VWR, PA, US) and allowed to grow overnight. The next day, the medium was exchanged with medium containing 4.5 µg/mL EMVs protein and incubated for 72 h. Then, 10 µL/well Presto Blue reagent (A13261, Thermo Fisher Scientific) was added to the cells, which were incubated at 37°C for an hour when the emitted

fluorescence was read with a Cytation 1 system (BioTek Instruments, VT, USA). The measured fluorescence intensity was then normalized to that of the control group without the EMVs.

### In Vitro Internalization Assay

The cells were seeded in 12-well chamber slides (#81201, iBidi, Germany) in 100 µL of appropriate cell culture medium for each cell line. The next day, the media was changed to 100 µL of appropriate media for each cell line containing 0.7 nmol of Cy-5 siRNA loaded in DCC-EMVs. At 24, 48 and 72 h after incubation, the cells were washed with 1x HBSS and stained with the MemBrite® Fix 488/515 Cell Surface Staining Kit (Biotium) following the manufacturer's instructions. Briefly, the cells were incubated for 5 min at 37°C in 100 µL/well of presoliding solution, followed by a 10 min incubation at 37°C with 100 µL/well of MemBrite® Fix 488/515 stain. The cells were then washed twice with 1x HBSS and fixed with 4% PFA (#12606, Cell Signaling Technology, Massachusetts, USA) for 15 min at 37°C. Afterwards, the cells were washed twice with PBS for 5 min and stained with 3 µg/mL Hoechst solution (Hoechst 33342, Thermo Fisher Scientific) in PBS for 15 min at RT to label the nuclei. The cells were subsequently washed twice with PBS at RT for 5 min, the silicon wells were removed, and the slides were mounted in Prolong Glass Antifade Mount (Thermo Fisher Scientific) for 24 h at RT and then sealed with nail polish. Imaging was performed with an LSM 800 confocal microscope (Carl Zeiss, Oberkochen, Germany) with a 20× objective (NA 0,8). Hoechst 33342, Alexa Fluor 488, CM-DiI and Cy-5 dyes were excited with lasers with excitation wavelengths of 405, 488, 561 and 640 nm, respectively. The emitted light was collected sequentially with a Gallium Arsenide Phosphide (GaAsP) detector via a variable dichroic and filtered at the following wavelengths: 410–545 nm (Hoechst 33342), 488–545 nm (Alexa Fluor 488), 565–620 nm (CM-DiI), and 645–700 nm (Cy-5).

### Protease Activity Determination

A Pierce colorimetric protease assay (Thermo Scientific, 23263) was used according to the manufacturer's instructions to evaluate the hypothetical protease activity of the RBCs. While the trypsin positive control assay was carried out at pH 8, RBC ghosts and DCC-EMVs were assayed at pH 3 at a known concentration of proteins. The final absorbance was read at 450 nm and normalized to the intrinsic absorbance of the sample. The data were further processed in GraphPad 9.0.

### Evaluation of RNA Interference Ability in Vitro

DCC-siRNA-EMVs were mixed 1:1 with Optimem medium (#31985070, Thermo Fisher Scientific), and the volume corresponding to 30 picomoles of siRNA/well was added to B16F10-TdTomato cells. The empty control volumes used were subjected to density-changing centrifugation as well and calibrated according to protein content to add the same amount of EMVs to the cell culture. The experiment was carried out on a 24-well culture plate, in which 50,000 cells/well were seeded the day before transfection. After 48 hours, total RNA extraction was carried out with a VWR RNA Gold kit, and the relative amount of RNA was quantified with an Agilent Cytation 5 with a Take3 plate for nucleic acid quantification. Retrotranscription (Nippon Genetics, Scriptase II, LS563) was carried out according to the manufacturer's specifications. Tdtomato mRNA silencing was evaluated via RT–PCR (Table 1 for primer sequence), with n = 6 replicates each of a final volume of 20 µL, on Eppendorf Twin Tec 96-well plates. Beta-actin was used as a calibrator. The delta-delta CT method was used to calculate the relative expression of the Tdtomato gene. The GraphPad 9 built-in ROUT algorithm for outlier recognition was used to clean the Ct data.

**Table 1** RT–qPCR Primer Sequences

| Primer | Sequence |
|---|---|
| **Tdtomato- Forward** | 5′-GACAACAACATGGCCGTC-3′ |
| **Tdtomato-Reverse** | 5′-GGTCTGGGTGCCCTCGTA-3′ |
| **β-actin-Forward** | 5′- GAAGTGTGACGTTGACATCC –3′ |
| **β-actin – Reverse** | 5′- ACTCATCGTACTCCTGCTTG –3′ |

## Freeze-Drying Optimization

To optimize long-term storage stability, EMVs were freeze dried in the presence of different cryoprotectants, their RNA retention, particle size, and Z-potential were measured, and their ultrastructures were evaluated via conventional transmission electron microscopy (TEM). To maintain the osmolarity between the inner section of the EMVs and the outer buffer, 0.83X diluted PBS was used when 5% disaccharides (ie, sucrose and trehalose) were present. PVP-40 (polyvinyl-pyrrolidone average molecular weight of 40.000 Da) was also tested as a cryoprotectant at a 2.5% w/v concentration and was not considered to influence the osmolarity balance. For each formulation, at least three replicates were prepared. Lyophilization was carried out in a Martin Christ freeze drier for 24 hours, and the chamber temperature was approximately −20°C. Every replicate sample was weighed, and the samples were stored at room temperature for one month. For comparison, the samples were stored at 4°C without any additives.

## CM-DiI/Vybrant DiO Labeling of EMVs

CM-DiI (550/564 ex/em), a highly lipophilic dye, inserts spontaneously in double layers. It was found to optimally stain erythrocyte ghost membranes at a 1 μM concentration. The ghosts were incubated with the dye according to the manufacturer's recommendations. Briefly, the suspension was first incubated at 37°C under vigorous shaking for 15 minutes and then for another 15 minutes at 4°C. Afterwards, the suspension was pelletized, and the supernatant, containing the excess dye, was removed. The same procedure was applied for Vybrant DiO (483/501 ex/em) labeling.

## In Vivo Experiments

### Injection and Biodistribution of Fluorescently Labeled DCC-siRNA-EMVs

All experiments were approved by the Ministry of Agriculture, Forestry and Food of the Republic of Slovenia (permission no. U34401-35/2020/8). Up to six mice were housed per cage in specific pathogen-free conditions in an IVC rack system (Animal Care Systems Inc., Revere Parkway, USA) with a 12 h light–dark cycle, food and water *ad libitum*, and cage enrichment (VWR). Female 6–8-week-old C57BL/6NCrl mice (Charles River, Lecco, Italy) were used in the experiments. Tumors were induced by subcutaneously injecting $3\times10^5$ B16F10-tdTomato cells in 100 μL of 0.9% NaCl into the right flank of each mouse. The tumor volume was determined by measuring the tumor volume with a digital caliper and calculating the tumor volume via the formula for ellipsoid ($V = a \times b \times c \times \pi/6$, where a, b, and c are perpendicular tumor diameters). Animal weight was monitored three times a week as a sign of well-being. When the tumors reached a volume of 50–60 $mm^3$, Vybrant-DiO-labeled DCC-siRNA-EMVs containing Cy5-labeled anti-tdTomato siRNA were injected via the caudal vein into each mouse. A total of 30 μg of Cy5-siRNA (1.5 mg/kg weight) was administered to each mouse in 100 μL of 1x PBS. The mice were randomly divided into four groups: the control group (n=4), 2 hours after injection (n=5), 24 hours after injection (n=5) and 48 hours after injection (n=5). At 10 min after EMV injection, 100–200 μL of blood was collected from the retro-orbital plexus of the mouse eye, and whole blood was obtained immediately before sacrifice. The plasma was immediately separated from the whole blood via BD Microtainer SST Blood Collection Tubes (Beckton Dickinson). For quantification, the mice were assumed to have 1.65 mL of blood in total on the basis of their weight. The samples were stored at −80°C until further use. At the time of mouse sacrifice, the spleen, lungs, brain, kidneys, tumor, heart and liver were collected and weighed, and one half of each organ was flash frozen and processed for RNA extraction by homogenizing the organ in liquid nitrogen with a mortar and pestle. The resulting powder was collected and stored at −80°C until further use. The other half of each organ/tumor was fixed in 4% paraformaldehyde (PFA, Thermo Fisher Scientific) overnight at 4°C and dehydrated in 30% sucrose overnight at 4°C before being embedded in Tissue-Tek O.C.T. compound (Sakura Finetek, VWR) and stored at −80°C for further use.

### Biodistribution and Pharmacokinetics via stem–loop PCR

RNA extraction was performed with a mirVANA MagMax kit (Thermo Fisher, A27828) from 10–15 mg of fine tissue powder and a total of 100 μL of plasma from each mouse, and a total of 5 ng was used for reverse transcription with a TaqMan MicroRNA Reverse Transcription Kit (Thermo Fisher, 4366596) with custom primers against anti-TdTomato siRNA (TaqMan Small Assay, Applied Biosystems, 4440418). A total of 1.33 μL of cDNA was used in each stem–loop qPCR. Thermal cycling was performed according to the manufacturer's specifications. The amount of anti-TdTomato

siRNA guide strand in plasma and tissues was subsequently quantified via TaqMan real-time PCR with the help of a siRNA calibration curve (the procedure is described below). All samples were run in triplicate, and a nontemplate well was added to every reaction.

For standard curve generation, the following procedure was carried out. Five nanograms of both Cy5-siRNA and unlabeled siRNA were used as templates for reverse transcription from a stock of 1000 ng/mL, and then, serial dilutions of its cDNA were used in qPCR to generate a standard curve. For tissue quantification, values in nanograms obtained from the standard curve were divided for the qPCR, reverse transcription, and RNA extraction dilution factors and multiplied by the original amount of total RNA obtained from RNA extraction.

$$\frac{ng\ of\ duplex}{grams\ of\ processed\ tissue} = ng\ in\ PCR\ reaction \times \frac{RNA\ stock\ concentration}{DF_{cDNA-qPCR} \times DF_{RNAstock-cDNA} \times Elution\ volume \times amount\ of\ processed\ tissue(g)}$$

Noncompartmental analysis of pharmacokinetic parameters relative to those of plasma was performed via PKSolver Excel add-in,[48] with linear uplog down settings. All pharmacokinetic parameters refer to the terminal half-life of the siRNA.

### Tissue Sample Preparation for Fluorescence Microscopy

From OCT-embedded tissues, 14 µm thick sections were cut on a Leica CM1850 cryostat and collected on SuperFrost Plus slides (Epredia, Netherlands, J7800AMNZ), with a final n=3 sections on each slide. The slides were stored at −20°C until further use. Later, the nuclei were stained with 3 µg/mL Hoechst 33342 nuclear stain, the sections were mounted with ProLong Glass Antifade Mountant (Thermo Fisher, P36982), and the cover slip (#1.5) was sealed with transparent nail polish. The slides were subsequently imaged on an Axio Observer 7 equipped with a Colibri 7 LED light source (UV (385 nm), Violet (430 nm), Blue (475 nm), Green (555 nm), Yellow (590 nm), Red (630 nm), Far Red (735 nm) and a Hamamatsu Orca Flash 4.0 V3 camera. Emitted light was imaged through the following filters: Filter set 38 hE eGFP shift free (Zeiss), Filter set 43 hE Cy 3 shift free (Zeiss), Filter set 50 Cy 5 shift free (Zeiss) and Filter Set 112 hE LED (Zeiss).

### Evaluation of RNA Interference Ability in Vivo

For the in vivo silencing experiment, B16F10 tumor-bearing mice were divided into three experimental groups and injected with 1) 100 µL of PBS; 2) 100 µL of naked anti-TdTomato siRNA, for a total of 2.5 mg/kg body weight; or 3) 100 µL of DCC-siRNA-EMVs, for a total of 2.5 mg/kg body weight, as indicated by the siRNA content. After 48 hours, the mice were sacrificed, and the tumors were excised, flash-frozen in liquid nitrogen and ground to a fine powder with a mortar and pestle. RNA extraction was carried out with a mirVANA MagMax kit (Thermo Fisher) from 10–15 mg of fine tissue powder. TdTomato gene knockdown was quantified similarly to that in vitro, and the presence of the guide strand of anti-TdTomato siRNA was assayed as described in the previous sections. Images of tdTomato-fluorescent B16F10 tumors were taken at the beginning of the experiment (t=0), at 24 hours and at 48 hours with a SteREO Lumar. A V12 fluorescence microscope (ZEISS, Jena, Germany) was used. The mean fluorescence intensity of the tdTomato protein in tumors was quantified with ImageJ, the appropriate region of interest (ROI) area was selected, and the Yen threshold algorithm[49] was used to minimize disturbance by mouse hair. For tdTomato MFI quantification in frozen sections, with n = 5 for each mouse, images of the tdTomato channel were taken with a 20x objective. Images were subjected to the above-described process via the Huang thresholding algorithm.

### Ex Vivo Red Blood Cell and DCC-siRNA-EMV Incubation With Inverted Confocal Microscopy

DCC-EMVs were prepared as previously described, with DiO-labeled ghosts, and their final protein concentration was 0.54 mg/mL. The mice were anesthetized via isoflurane inhalation, and blood was collected via cardiac puncture in 3.2% sodium citrate, after which the mice were sacrificed. The collected blood was then centrifuged at 100 × g for 10 min at RT and washed twice in 1x PBS. The washed red blood cells (RBCs) were counted via a CytoSMART cell counter (AXION Biosystems) and resuspended in RPMI medium containing GlutaMAX (Gibco, Thermo Fisher Scientific, VA, US) and penicillin/streptomycin at a concentration of 1×106 RBCs/mL. The cell culture medium did not contain fetal

bovine serum. The erythrocytes were labeled with Vybrant-DiD according to the manufacturer's instructions with a final dye concentration of 5 μM (Invitrogen, Thermo Fisher Scientific, VA, US). Subsequently, 100 μL of the prepared RBCs were transferred to 96-well plates (96-well plates μCLEAR®, BLACK, Greiner), mixed with 10 μL of DCC-EMVs and incubated at 37°C in a humidified incubator at 5% CO2 for 24 or 48 h. The interaction between mouse RBCs and EMVs was observed via inverted confocal laser scanning microscopy (CLSM, Axio Observer Z1 LSM 710, ZEISS, Germany) with a Plan-Apochromat 63x/1.40 Oil DIC M27 objective. The two dyes CM-DiO and Vybrant-DiD were excited simultaneously with argon (488 nm) and helium–neon (633 nm) lasers, and the emitted light was collected through emission bandpass filters set.

### Statistical Analysis

All the statistical analyses were performed via GraphPad 9, with $p \leq 0.05$ *$p \leq 0.01$ **$p \leq 0.001$ ***$p \leq 0.0001$ ****. For cryo-TEM EMV size, postfreeze drying siRNA retention and EV size, qRT–PCR fold changes (in vitro and in vitro), and in vivo tumor tdTomato MFI variation, a normality test was carried out. A parametric (two- or one-way ANOVA) or nonparametric (Kruskal–Wallis) test was chosen to test the statistical significance of the results. In instances where multiple comparisons testing was needed, the Tukey's test for multiple comparisons was utilized. Where present), the data were log10 transformed to highlight the differences.

## Results

### Comparison of Different Techniques for Removing Unencapsulated siRNA

EMVs were prepared via the hypotonic lysis method[42] and then loaded with siRNA via incubation, sonication and extrusion steps. Before any purification, the vesicles had a median particle size of 192 nm (Table 2). To establish actual encapsulation efficiency and remove unloaded siRNA, five different methods were tested (Supplementary Material for protocols), ie, sucrose gradient, regular ultracentrifugation, and density-changing centrifugation.[46] The final apparent encapsulation efficiency, an estimate of the required time and most significant drawbacks are shown in Table 3.

**Table 2** Particle Size Distributions of Different Preparations of EMVs After Freeze Drying and Cryoprotectant Removal. In Light Gray, Empty EMVs; in White and Dark Gray, Noncentrifuged siRNA-EMVs and DCC-siRNA-EMVs, Respectively

| | Sample | Median Particle Size (nm) | PDI | Significance Against Initial Sample |
|---|---|---|---|---|
| Empty | Before FD | 173 ± 5 | 0.253 ± 0.013 | |
| | Sucrose 50 mm | 190 ± 10 | 0.277 ± 0.007 | ns |
| | Trehalose 50 mm | 163 ± 8 | 0.259 ± 0.010 | ns |
| | PVP40 Sucrose | 281 ± 45 | 0.340 ± 0.004 | *** |
| | PVP40 Trehalose | 265 ± 2 | 0.363 ± 0.004 | *** |
| siRNA-EMVs | Before FD | 192 ± 7 | 0.245 ± 0.012 | |
| | Sucrose 50 mm | 200 ± 4 | 0.253 ± 0.014 | ns |
| | Trehalose 50 mm | 205 ± 3 | 0.216 ± 0.010 | ns |
| | PVP40 Sucrose | 278 ± 27 | 0.355 ± 0.013 | *** |
| | PVP40 Trehalose | 264 ± 6 | 0.280 ± 0.018 | *** |
| DCC-siRNA-EMVs | Before FD | 185 ± 7 | 0.192 ± 0.015 | |
| | Sucrose 50 mm | 202 ± 15 | 0.169 ± 0.017 | ns |
| | Trehalose 50 mm | 193 ± 7 | 0.157 ± 0.013 | ns |
| | PVP40 Sucrose | 308 ± 5 | 0.357 ± 0.023 | *** |
| | PVP40 Trehalose | 324 ± 19 | 0.368 ± 0.014 | *** |

**Notes**: The data refer to average subpopulations of EMVs in the colloidal suspension and are calculated via a volume-weighted algorithm. Statistical analysis against the initial sample size was performed via one-way ANOVA. $p \leq 0.001$ ***.

**Table 3** Efficiency of the Encapsulation of siRNAs Into EMVs via Different Techniques

| Technique | siRNA Apparent EE% ± SE, n=3 | Time Required | Drawbacks | Advantages |
|---|---|---|---|---|
| Size exclusion purification (PD10 columns) | 95 ± 2.5 | 5–10 minutes | Inefficient separation between siRNA-EMVs and unloaded siRNA/weakly complexed with RBC debris | Fast, repeatable, cost-effective |
| 30 kDa centrifugal units | 80 ± 4.5 | 10–15 minutes | Sterility issues and inefficient removal of RBC debris | Fast, repeatable, cost-effective |
| Sucrose gradient centrifugation | 53 ± 7.5 | >2 hours | Technically laborious, requires sucrose removal | Extremely precise, repeatable |
| Density Changing centrifugation (DCC) | 68 ± 3.5 | 50 minutes | Requires one step of salt removal | Technically easy and undemanding |
| Regular ultracentrifugation | 42 ± 5% | 40 minutes | Does not distinguish between EMVs and RBC debris | Technically easy and undemanding |

The use of PD10 desalting columns led to interesting results: the encapsulation efficiency, that is, multiple recoveries of EMVs and siRNA, reached 90%, suggesting an interaction between the two (Figure S1). The siRNA-EMVs were recovered after the addition of 4/5 mL, and no other amount of siRNA was detected after complete elution of the column (~20 mL). While unbound siRNA is supposed to be eluted later than EMVs, this was not the case since, after the addition of 6 mL of recovery, the total initial dose of siRNA was almost complete, with only 0.3–0.5% of the initial siRNA amount being eluted after EMV recovery. EMVs recovery was confirmed by DLS analysis and RNA quantification with a Quantifluor kit.

Both size exclusion purification and the use of Amicon centrifugal units pose the problem of maintaining sterility. Both can allow the recovery of weakly externally complexed siRNA and imperfectly shaped EMVs. Moreover, while the preparation of sucrose gradient columns is laborious and time consuming, regular ultracentrifugation does not discriminate among EMVs of different densities. We then decided on density changing centrifugation (DCC), with 10% w/v trisodium citrate dissolved in PBS, since it was proven to be the most repeatable and reliable technique and capable of ensuring the isolation of siRNA internally loaded with EMVs.[46]

## DCC-siRNA-EMV Characterization

EMVs were loaded with different amounts of siRNA (2.5–12 μg/mL) and subjected to purification via density-changing ultracentrifugation, as schematically shown in Figure 1a. Eight fractions of equal volume from the centrifugation tubes were collected, the TC was replaced with 1× PBS, and the RNA concentration was evaluated with a Quantifluor RNA kit. The average encapsulation efficiency was 67.21 ± 3.36% in six fractions (as a result of 6 independent experiments), with a particle size ranging from 170–190 nm and a PDI ranging from 0.01–0.02. The size was found to increase from the top to the bottom, and vice versa for RNA quantity (Figure 1b), indicating that the method is effective in selecting EMVs on the basis of their density alone. The last fraction arose from the resuspension of the pellet, consisting of membrane remnants not shaped into vesicles and unloaded siRNA. Notably, RBC ghosts, prior to coextrusion with siRNA and subsequent postprocessing, were free from endogenous miRNAs and other RBC-related RNAs.[50,51]

The overall phospholipid concentration in the original sample not subjected to ultracentrifugation was found to be 0.240 ± 0.09 mg/mL via the Stewart assay, whereas the protein concentration was 0.46 mg/mL ± 0.097 (determined via the Bradford assay), which is in line with the literature for erythrocyte membranes, where 40% of the dry weight is composed of lipids, including 40% cholesterol, and approximately 60% is composed of proteins and sugars. Starting from one mL of a solution of 70% v/v erythrocyte ghosts diluted in 4 mL of PBS, the dry mass (protein, lipid and salt) obtained was 10.63 mg ±0.9. To further prove the solidity of this purification method for EMVs, we evaluated the phospholipid and protein concentrations in the five top fractions (See *Protein and lipid quantification*) in a separate experiment, ie, those with the highest concentration of RNA (Figure 1b and c), with 1--5 fractions.

The mixed effect analysis revealed ($p < 0.01$) that the siRNA content was the only source of variation among the different fractions (Figure 1c), decreasing from top to bottom, whereas the lipid and protein concentrations remained

constant. The lipid/protein ratio slightly increased after DCC, from approximately 0.5, as in extruded ghosts, to 0.8, indicating a loss of protein net content. The zeta potential was also measured for every fraction and was found to be constant throughout the sample, accounting for −11.2 ± 0.2 mV in the presence of 10% TC at pH = 7.4. In line with the literature,[46] the zeta potential was re-established to precentrifugation values after 10% TC removal, which was −17.7 ± 3.4 mV, confirming that the DCC-siRNA-EMVs were right-side out.[42] We then decided to save the top six fractions for further experiments, combining them, eventually concentrating the EMV suspension, which was needed for further analysis. The particle size of all the siRNA-containing fractions combined was slightly lower than 200, with a value of 185.4 ± 6.7 and a PDI of 0.192 ± 0.015. DCC-siRNA-EMVs also shared a similar protein profile with parental erythrocyte ghosts and with the pellet resulting from DCC, as established with SDS–PAGE (s, Figure S2).

## Microscopic Characterization of siRNA-EMVs: CryoTEM, Freeze-Fracture TEM and STED Microscopy

DCC-siRNA-EMVs resulting from ultracentrifugation were imaged via cryo-electron microscopy to determine whether ultracentrifugation was effective at reducing the amount of unloaded EMVs and membrane debris, which could harm the stability of the colloidal suspension. Both empty and loaded (siRNA concentration before DCC was 12 μg/mL) EMVs were assayed before and after ultracentrifugation. Compared with extruded EMVs, cryoTEM imaging (Figure 2a) has indeed proven our premises to be true, showing centrifuged samples as clearer from membrane debris, which are not correctly rearranged into EMVs, when compared to only extruded EMVs. Many rod-shaped objects were also present, which is consistent with literature.[52,53] Such objects are most likely EMVs sitting on their side, being EMVs biconcave as confirmed by conventional TEM (Figures 3 and 5, yellow arrows). Therefore, EMVs can be assumed to be relatively flat (1–10 nm thick), discoidal nanoparticles, as already reported for similar objects.[53] Image analysis via ImageJ (Figure 2b) revealed that loaded and centrifuged EMVs were significantly larger than empty EMVs were (one-way ANOVA, $p < 0.001$), confirming that their internal content was the only selection factor in DCC. All four size distributions followed

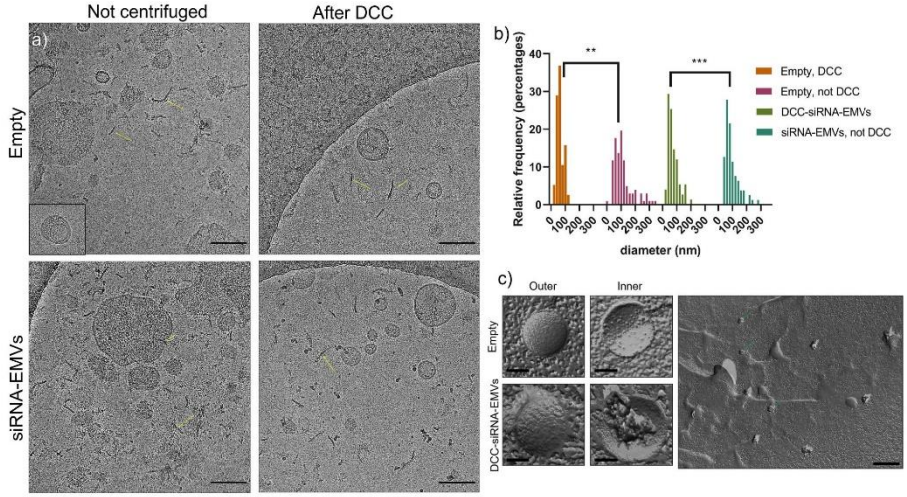



**Figure 2** (**a**) CryoTEM micrographs of EMVs. The scale bar is 200 nm, and it refers to the insert too. Yellow arrows are pointing at EMVs sitting on the side, appearing as rod-like objects. (**b**) Relative frequencies of the diameters in the analyzed cryoTEM micrographs. Measurements were carried out on 10 micrographies for each category, for a total of n > 200 measurements per typology. One-way ANOVA was performed to assess the statistical significance of the distributions. p≤0.01 **, p ≤ 0.001 *** (**c**) Freeze fracture TEM micrograph of empty and DCC-siRNA EMVs. For higher magnification images (left), the scale bar is 50 nm. In the right image, a wider field of DCC-siRNA-EMVs is shown (scale bar = 500 nm). The internal content is recognizable as aggregate material (green arrows).

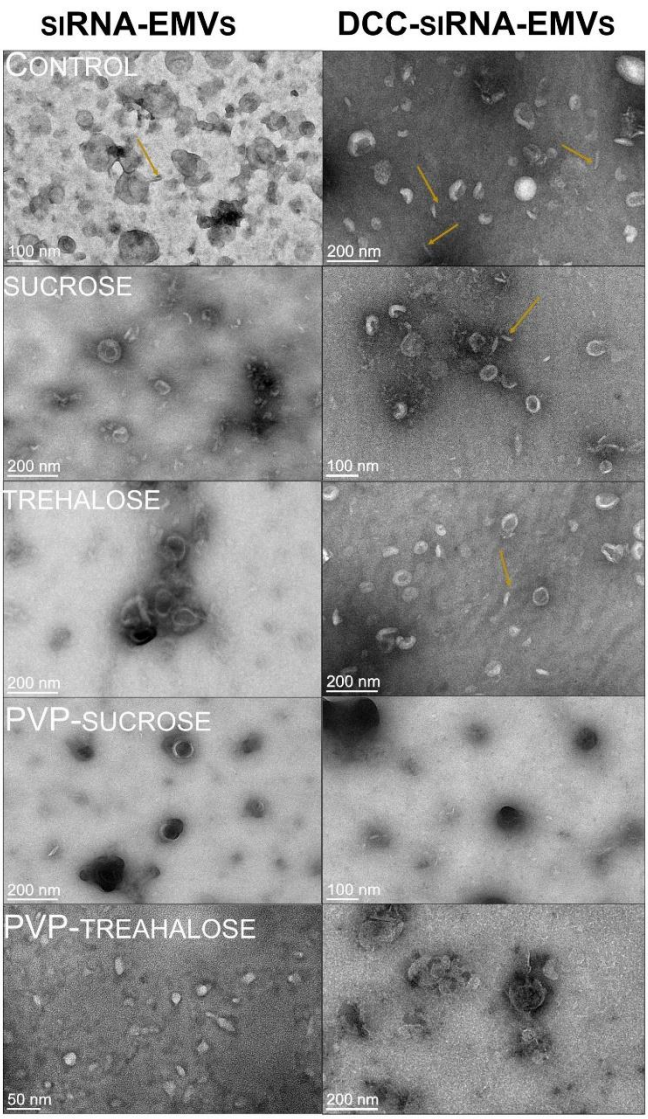



**Figure 3** TEM micrographs of freeze-dried, noncentrifuged samples negatively stained with UA Zero. EMVs appear as discoidal, flat objects. Yellow arrows are pointing at EMVs sitting on the side.


https://doi.org/10.2147/IJN.S504644

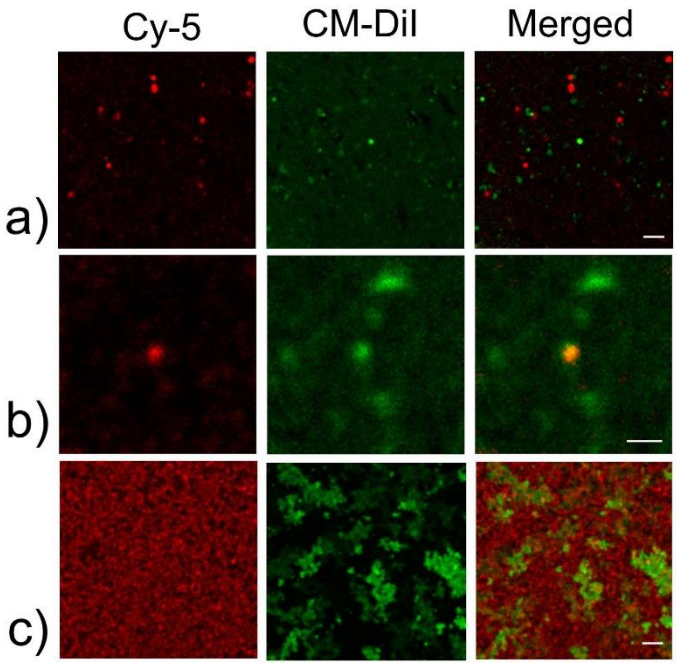



**Figure 4** Fluorescence superresolution microscope images of siRNA-EMVs. (**a**) Wide-field image of DCC-siRNA-EMVs; scale bar = 1 μm. (**b**) Close-up image of an EMV, Cy-5 and CM-DiI signals colocalized, scale bar = 250 nm; (**c**) non-DCC-siRNA-EMVs, scale bar = 1 μm.

a lognormal distribution ($p < 0.001$, Figure 2b) according to the Kolmogorov–Smirnov and Anderson–Darling tests. Multilamellar EMVs are extremely rare and hard to spot (Figure 2a, inset).

To investigate the internal side of EMVs and DCC-siRNA-EMVs and better appreciate their surface structure, we also conducted freeze-fracturing electron microscopy on the same set of samples (Figure 2c). The surface structure was consistent with that of EMVs obtained via a similar technique[54] and with red blood cell extracellular vesicles,[55] being rough and wrinkled but overall circular and regular. When DCC-siRNA-EMVs were imaged, a clot of solid material was found in most of the fractured vesicles (Figure 2c, inner). While aggregation has already been reported[56] in the case of sonicated siRNA loaded inside extracellular vesicles, this is the first time, to our knowledge, that such clots can be visualized via electron microscopy techniques.

To verify the identity of such clots, we conducted several tests on a confocal microscope equipped with a STED laser,[47] which labels EMV membranes with CM-DiI dye and loads them with Cy-5-conjugated siRNA. The average size, as measured by CM-DiI fluorescence signals, was consistent with previously reported data (<200 nm, Figure S3). Furthermore, Cy-5 is prone to create nonfluorescent H-aggregates[57] and self-quench its fluorescence when it is found at high concentrations, as occurs in the lumen of 100–150 nm DCC-siRNA-EMVs. Indeed, the DiI and Cy-5 signals were hardly perfectly superimposed (Pearson Rr parameter = −0.00075, over the average of 10,200x200 pixels/20x20 μm images). EMVs, in which the two signals overlap (Figure 4b), are extremely difficult to spot. CLSM also confirmed the efficient removal of RBC membrane debris in the DCC-siRNA-EMV sample (Figure 4a), considering the lack of CM-DiI-labeled aggregates, which are present in noncentrifuged samples (Figure 4c). This finding further supports the observation via cryoTEM (Figure 2a) of a cleaner,

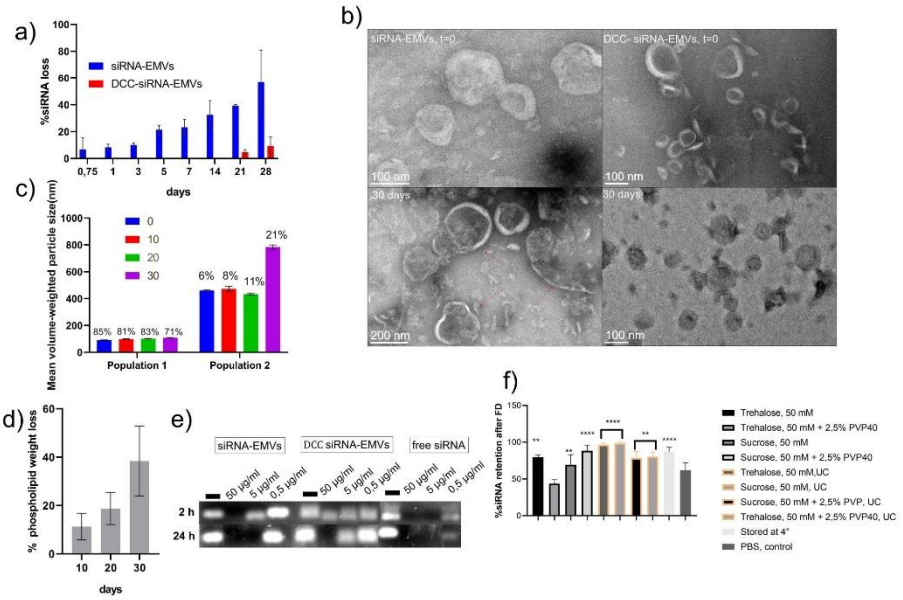



**Figure 5** (**a**) Percentage of siRNA payload loss over the course of four weeks for DCC and siRNA-EMVs. Data are reported over n=3 replicates. (**b**) Ultrastructural evolution of negatively stained siRNA-EMVs (left) and DCC-siRNA-EMVs (right). REd arrows indicate pancake-shaped EMVs, which appear as rods via cryo-EM. (**c**) Size evolution of siRNA-EMVs stored at 4 °C. Above the bars, the percentage of recorded events belonging to a specific population is shown. (**d**) Percentage of phospholipid weight loss in siRNA-EMVs, stored at 4 °C. (**e**) Agarose gel (2 % w/v) for free siRNA, DCC-siRNA-EMVs, and non-ultracentrifuged siRNA-EMVs exposed to different concentrations of RNAse A. (**f**) siRNA retention in siRNA-EMVs after freeze drying. The marked results are significant compared with those of the PBS control for the siRNA concentration. $p \leq 0.05$ * $p \leq 0.01$ ** $p \leq 0.001$ *** $p \leq 0.0001$ ****.

monodisperse colloidal suspension. Finally, the Cy-5 siRNA signal seemed to be concentrated only within EMVs in samples subjected to DCC (Figure 4a and c), confirming the total removal of unencapsulated siRNA molecules.

## Encapsulation Stability Over Time and Effects on the Storage of EMVs

To assess the eventual spontaneous release of cargo by EMVs upon long-term storage at 4°C, two identical sets of samples were evaluated (initial siRNA concentration of 10 μg/mL). One was subjected to DCC, while the other was not. To remove unencapsulated siRNA, the noncentrifuged set of samples was ultrafiltered immediately after extrusion at 30 kDa via Amicon devices. At fixed intervals, 100 μL ($n$=3 for each time point) of each replicate of both sets of samples were subsequently loaded into an Amicon 30 kDa centrifugal filter device. The eluate and retentate were resuspended to the original volume, and the siRNA concentration was evaluated with a Quantus RNA fluorometric assay over one month of storage at 4°C. The payload loss was much greater for nonultracentrifuged EMVs (57% after 4 weeks, Figure 5a), suggesting continuous leakage of the payload from EMVs or slow decomplexation of siRNA from RBC debris. However, in the case of the DCC-siRNA-EMVs, leakage started to be noticeable after only one month (Figure 3a), accounting for 10% of the initial amount by the end of the experiment. Noncentrifuged EMVs were also assayed for phospholipid loss (Figure 5d): a consistent amount of phospholipid was found in the eluate of Amicon 15 NMWL centrifugal devices, which increased with increasing incubation time. EMVs and DCC-siRNA-EMVs were also evaluated via TEM (Figures 5b and S5 for uranyl acetate comparison), whereas for DCC-siRNA-EMVs, no morphological or ultrastructural changes were noticeable; for non-DCC-EMVs, the increase in size was evident in the TEM micrographs, with the appearance of "pancake-like" objects (red arrows, in Figure

5b) and a general loss of a stable structure and the appearance of smaller EMVs, probably due to further vesiculation. The size evolution of the siRNA-EMVs was also assayed via DLS (Figure 5c). Even if quite stable, the volume-weighted diameter of the EMVs increased over time, causing a slight increase both in size and in the population abundance of objects larger than 400 nm. Nonetheless, after one month, the regular-sized EMV population (less than 120 nm) still represented the majority of the objects, accounting for 71% of the measured events. We therefore speculated that an already reported protease activity present in the red blood cell membrane is responsible for self-digestion, loss of structure and, finally, spontaneous budding of the membrane in the absence of ATP.[58,59] The digestion of integral membrane proteins such as Band 3 proteins is indeed involved in aging, which includes aspecific vesiculation due to disassembly of the cytoskeleton.[60,61] The presence of such proteases, which are active both in self-digestion and toward cascin, was confirmed via a Pierce protease assay on EMVs but was not detectable or extremely faint on DCC-siRNA-EMVs (s, Figure S4), likely being less represented in the population of objects selected via density-changing centrifugation.

Density-changing centrifugation again effectively removed the cellular debris and stabilized the overall colloidal suspension: no significant changes in terms of the hydrodynamic radius or fusion or fragmentation of EMVs were observed, confirming what was previously observed for siRNA retention.

### RNase A Protection Assay

To test the RNA accessibility of siRNA-loaded EMVs, we carried out an RNase A resistance assay. Briefly, we incubated a known amount of siRNA-EMVs with 0.5, 5, or 50 μg/mL RNAse A for 2 hours or 24 hours at 37°C and then run the appropriate volume of each sample on a 2% agarose electrophoresis gel. The volumes to be loaded were carefully calculated to run the same initial amount of siRNA-EMVs. The starting concentrations of siRNA were 10, 8.5 and 10 μg/mL for naked siRNA, DCC-siRNA EMVs, and siRNA-EMVs, respectively. For DCC-siRNA-EMVs, ie, siRNA-EMVs subjected to density-changing centrifugation, bands were present even after 24 hours (Figure 5e), in the presence of 5 μg/mL bovine pancreatic RNase A and after two hours at 50 μg/mL. Surprisingly, the noncentrifuged siRNA-EMVs also presented a band at 5 μg/mL after two hours of incubation, while the corresponding free siRNA band was absent.

## Freeze-Drying and Storage Optimization

To establish a long-term optimal storage procedure, DCC-siRNA-EMVs, siRNA-EMVs and empty EMVs were freeze dried in the presence of different common cryo-/lyoprotectants: sucrose, trehalose and PVP40. In the case of the siRNA-EMVs, the DCC and noncentrifuged samples were equally freeze-dried and characterized. Disaccharides were added to a diluted PBS solution at a 50 mm concentration, while PVP40 was used at 2.5 w/v %.[62] The same volume of PBS was used as a negative control. After one month of storage at room temperature, the freeze-dried samples ($n$=6 for each type) were rehydrated to the original volume, and the cryoprotectant was removed via Amicon device ultrafiltration (4 kDa). Particle size, zeta potential (Table 2, Table 4), and siRNA retention (Figure 5f) were assessed, and their ultrastructures were evaluated via conventional TEM preparations with a UA-Zero negative stain (Figure 3). Upon rehydration, all the samples were immediately dissolved in DEPC water except for the negative control, which contained numerous insoluble clots and a foggy appearance. Indeed, PBS is not the most suitable buffer for freeze drying both exosomes and extracellular vesicles since it is subjected to changes in pH during drying and after rehydration;[63] after rehydration, the pH also shifted from 7.4 to 6.5. Nonetheless, when freeze-dried with only disaccharides, all the samples retained their original size, zeta potential, and siRNA cargo (Table 2, Figure 5f). The presence of cryo-lyoprotectant increased siRNA retention in DCC-siRNA-EMVs dried, only, in the presence of the same volume of PBS 1x, with almost 100% of recovery in presence of disaccharides, ie trehalose and sucrose. Indeed, payload retention reached 99%, for DCC samples in the presence of disaccharides, indicating excellent colloidal stability. PVP40 is another well-known and widely used not-penetrative cryo/lyoprotectant,[62,64] whose mechanism relies on the modification of the collapse temperature of the structure[65] by increasing the glass transition temperature of the colloidal suspension and water sequestration properties.[66] We therefore chose to test this nontoxic and well-known polymer to extend the shelf-life of freeze-dried EMVs. Counterintuitively, before cryoprotectant removal, samples freeze-dried in the presence of PVP40 presented a much lower zeta potential (−23.5 ± 3.1 mV and −23.3 ± 3.8 mV for trehalose + PVP40 and sucrose + PVP40, respectively) and lower siRNA payload retention after rehydration than samples freeze-dried in the presence of disaccharides (even if overall higher than that of the negative control, ie, PBS). After centrifugal dialysis and PVP40 removal, the zeta potential of both sets of samples returned to their original values (Table 4),

**Table 4** Z-Potentials of Freeze-Dried DCC-siRNA-EMVs After Cryo-Lyoprotectant Removal

| Sample | Zeta Potential (mV) |
|---|---|
| Before freeze drying | −16.7 ± 5.8 |
| Sucrose 50 mm | −17.0 ± 2.5 |
| Trehalose 50 mm | −17.7 ± 2.5 |
| Sucrose 50 mm + 2.5% PVP | −17.7 ± 4.1 |
| Trehalose 50 mm + 2.5% PVP | −16.2 ± 6.4 |
| PBS only | −18.0 ± 1.9 |
| Stored at 4° for one month | −16.4 ± 3.4 |

despite the particle size still being significantly larger ($p < 0.001$ in all cases). This finding is consistent with what has already been reported for extracellular vesicles and exosomes,[62,63] ie, a reduction in the number of nanoparticles, possibly originating from their fusion with each other, and the substantial impossibility of complete polymer removal; therefore, the unsuitability of PVP40 as a cryoprotective for this type of object is assessed. On the other hand, trehalose or sucrose alone did not significantly affect the size of any type of EMVs sample (Table 2).

Given that siRNA was retained after freeze drying, the best-performing cryo-lyoprotectant was sucrose at a 50 mm concentration. Moreover, we used TEM to assess the suitability of the above-said cryo-lyoprotectant with TEM, observing the ultrastructures of EMVs. The samples (DCC and not DCC) were negatively stained with UA-zero (Figure 3 and S6 for freeze-drying only in the presence of PBS). Exceptionally interesting were also the ultrastructure differences highlighted by the staining: UA-zero complexation with membranes was lower in the presence of PVP40, and where trehalose was present, both for DCC and not samples, an organic and soft shield around the vesicles can be observed. This feature was not highlighted in previous reports on cell-derived vesicles freeze-dried in the presence of PVP polymers[62] negatively stained with uranyl acetate, although a similar electron-dense area was observed around organic objects. Owing to their safety and cost-effectiveness, disaccharides have been proven to be the best cryo-/lyoprotectant for RBC membrane-derived vesicles.

## In Vitro Activity of DCC-siRNA EMVs

### Cytotoxicity and Internalization of siRNA-EMVs by Different Cell Lines

We investigated whether DCC-siRNA-EMVs at a final concentration of 4.5 μg/mL EMV protein (1:66 dilution), corresponding to 30 nM siRNA, had any toxic effects on multiple cell lines: NHLF human lung fibroblasts, Hulec 5a human lung microvascular cells, CT26 murine colorectal carcinoma, B16F10 murine melanoma, and 4T1 murine mammary carcinoma. These conditions were chosen to mimic an in vitro knockdown experiment. No signs of cytotoxicity were detected in any of the tested cell lines (Figure 7a). To determine whether the DCC-siRNA-EMVs internalized B16F10, CT26 and NHLF cells were incubated with them (Figure 6). The vesicles were loaded with Cy-5-labeled siRNA, and a total of 0.7 nM/well of Cy-5 siRNA/well was incubated with the cells. Additionally, the EMV membranes were marked with CM-DiI. After 48 hours of coincubation, the CM-DiI signal was present in both the plasma and inner membranes of the cells, suggesting membrane fusion between the cells and EMVs, together with the presence of Cy-5 in the cytoplasm. Overall, these findings indicate that EMVs are actively internalized by normal and tumor cells rather than just adhering to the cell surface. As a proof of concept for our carriers, we chose B16F10 cells, a well-characterized murine melanoma cell line that showed robust membrane fusion with CM-DiI-labeled EMVs, as a model for further experiments.

### In Vitro Knockdown Effect of siRNA-EMVs

The tdTomato-expressing B16F10 murine melanoma cell line was selected to evaluate the ability of the siRNAs to silence the tdTomato fluorescent protein expression. To prove the robustness of our storage protocol, we also tested sucrose-freeze-dried

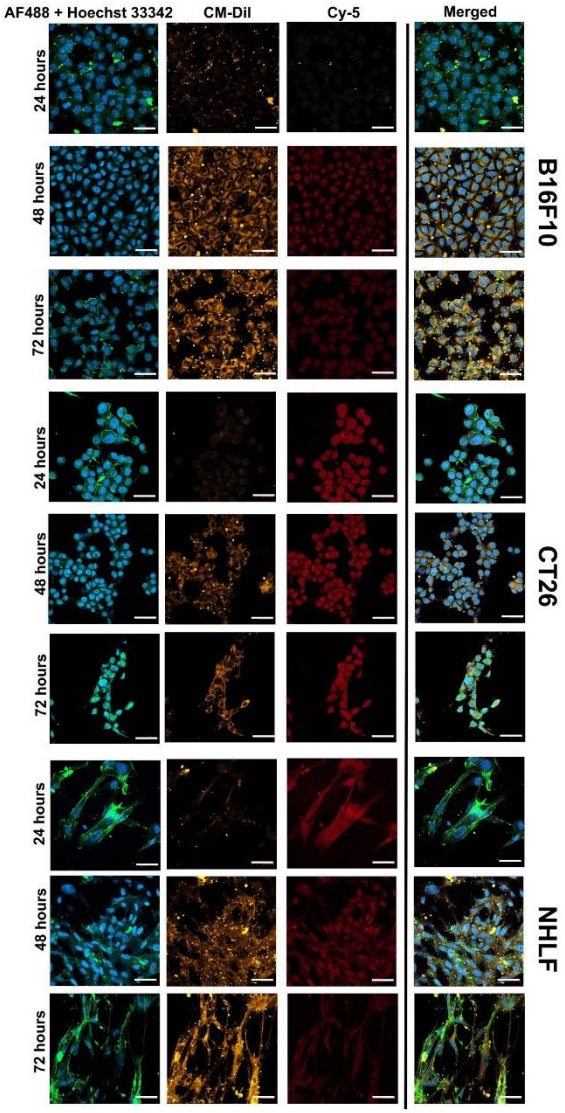



**Figure 6** Internalization of DCC-siRNA-EMVs by B16F10, CT26 and NHLF cells over three days. The cell nuclei were labeled with Hoechst 33342 (blue), and the membranes were labeled with MemBrite® Fix 488/515 stain (green). The membranes of EMVs were stained with CM-DiI (Orange), while they were loaded with Cy-5-labeled siRNA (red). The scale bar is 50 μm.

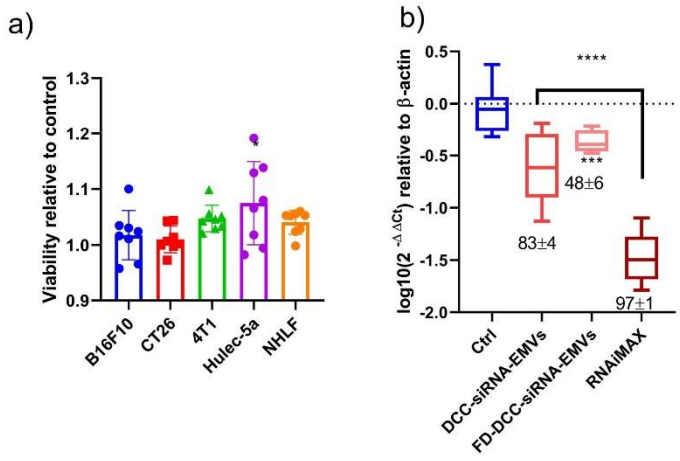



**Figure 7** (**a**) Viability of various cell lines treated with 4.5 μg/mL DCC-siRNA-EMVs; (**b**) log10 of in vitro tdTomato (fold change) at a final concentration of 0.3 nanomolar. The data are expressed as the means ± SDs. The percentage of knockdowns ± SDs is reported below the graph. $p \leq 0.001$ ***, $p \leq 0.0001$ ****.

DCC-siRNA-EMVs. The silencing efficiency was compared with that of RNAiMAX, the most efficient nonviral transfection agent on the market, and the same final amount of anti-tdTomato siRNA was added to the cells, corresponding to 30 picomoles/well (for a final siRNA concentration of 30 nM in each well). Total RNA extraction was performed after 48 hours. Real-time PCR revealed circa 80% knockdown efficacy in the case of the DCC-siRNA-EMVs (Figure 7b), whereas the FD samples retained approximately 50% of their activity. Transfection with EMVs did not impact β-actin expression, since none of the samples shown were significantly different from the control Ct (Figure S7). The reduced activity of sucrose freeze-dried DCC-siRNA-EMVs can be attributed to the eventual loss of the right-sidedness of EMVs, protein unfolding, lipid loss upon rehydration, and early cargo release. In contrast, RNAiMAX caused almost complete knockdown of the target gene at the same dose.

## In Vivo Experiments: Biodistribution, Pharmacokinetic and Knockdown Effects

### Biodistribution and Pharmacokinetics of DCC-siRNA-EMVs

To determine the biodistribution of DCC-siRNA-EMVs in mice, we coupled stem–loop PCR of the siRNA guide strand with fluorescence microscopy of thin tissue sections. For this purpose, we subcutaneously induced tdTomato-B16F10 tumors in C57BL/6 mice. When the tumors reached 50–60 $mm^3$, we intravenously injected 100 μL of DCC-siRNA EMVs, whose membranes were labeled with Vybrant-DiO and loaded with Cy-5-labeled passenger strand siRNA (Figure S8 for the TaqMan calibration curve). We first determined the pharmacokinetic parameters relative to those of the DCC-siRNA-EMVs (Table 5). Upon caudal vein injection, siRNA-EMVs were rapidly distributed among body compartments, with 40% of the total injected dose (ID) per mL of blood remaining in circulation after 10 minutes (Figure 8a). After two days, approximately 1.5% ID/mL was still present. The mean residence time[67] was 18 hours, where a commonly reported value for a free siRNA is 2–4 hours;[40,68] distribution in the tissue phase was extremely fast, with an apparent volume of distribution ($V_z$) of 20 mL (or 1000 L/kg of mouse weight). This behavior can be attributed to the low affinity of EMVs for plasma proteins, leading to faster tissue distribution, as observed in other nanoparticle-assembled siRNA treatments.[69,70] Overall, the distribution half-life was comparable to that of other stealth, neutral siRNA delivery systems,[36,40] confirming the potential of our delivery system.

We then proceeded to determine the presence of the siRNA lead strand in various organs. At an injected dose of 1.5 mg/kg of weight of anti-tdTomato siRNA (30 μg/mouse), the earliest clearance organ for DCC-siRNA-EMVs

**Table 5** Basic Pharmacokinetic Parameters Relative to siRNA-EMVs Administered at 1.5 mg/kg, Calculated With the PK Solver 2.0 Excel Add-in

| Parameter | Value |
|---|---|
| Cl, Total Body Clearance | 0,0143 mL/min |
| $\lambda_z$ (elimination rate constant) | 7,3 $10^{-4}$ $min^{-1}$ |
| $C_{max}$ | 12733 ng/mL |
| MRT (Mean residence time) | 1107 min (18 h) |
| $V_z$, Apparent volume distribution (48 hours) | 20 mL |
| $T_{1/2}$, plasma terminal half life | 944 min (15,7 h) |
| Terminal AUC $_{0-\infty}$ | 2088806 (min ng/mL) |
| Total injected dose (ID) | 30000 ng |

appeared to be the spleen (Figure 8b). Similar to Liang et al,[71] the lungs were shown to be one of the main accumulation sites for EMVs, although after administration (ie, 24 hours), the presence of the lead strand of anti-tdTomato siRNA in the kidneys was already substantially lower than that of free siRNA.[33] While the concentration of the lead strand of anti-tdTomato siRNA remained constant in the liver, it increased over two days in tumors, reaching 4000 ng/g ± 335 of siRNA/g tumor tissue. Therefore, the DCC-siRNA-EMVs appeared to have eluded accumulation in the main reticuloendothelial site organ, ie, the liver: at 48 hours, the ratio of the tumor siRNA/liver siRNA was 1.83. Such behavior can be ascribed to the presence of CD47 on EMVs, masking effect on phagocytic SIRPα + Kupffer cells, as observed elsewhere[72,73]. While the occurrence of high accumulation in heavily perfused organs such as the heart and lungs was predictable, we were surprised by the abundance of siRNAs in the brain.

To investigate this phenomenon, we analyzed the distribution in organs in detail by tracking Cy-5 (conjugated at the 5′ end of the anti-tdTomato passenger strand) and DiO fluorescence, which was used to label EMV membranes. Taken together, these findings confirmed the molecular data and strongly suggested that EMVs rapidly entered the blood circulation and promptly accumulated in tissues. As early as 2 h, the accumulation of the Cy-5 and DiO signals was greater in proximity to the blood vessels and more abundant in highly perfused organs, such as the lungs (Figure 9), brain (Figure 14)) and heart (Figure S10). In the lungs, after 24 hours, the Cy-5 signal had a homogenous distribution, suggesting deeper tissue penetration from blood vessels over time (Figure 9), reflecting the molecular data. In the kidneys (Figure 10), the main filtration organs for the nanoparticles, Cy-5 and DiO fluorescence, appeared to be homogenously distributed, without any greater accumulation in either the glomeruli or tubules. No preference for any lobe can be noted in the liver, despite the Cy-5 signal being mostly concentrated in the proximity of sinusoids (Figure S9) and around larger blood vessels. Within 24 hours, the Cy-5 signal is present around small arteriolae in the brain but not in tissues, as EMVs are likely unable to cross

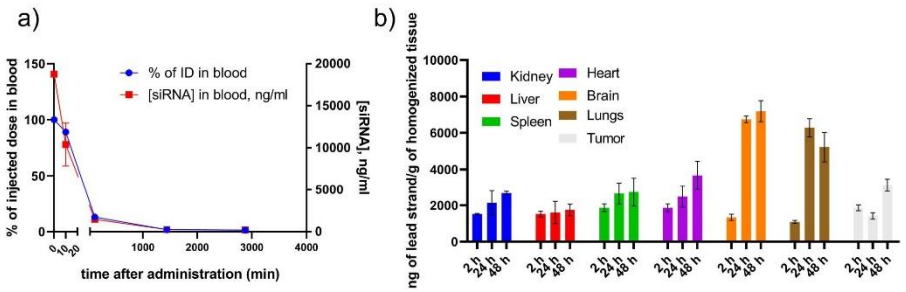



**Figure 8** (**a**) Plasma concentration of the anti-tdTomato siRNA lead strand. For calculation of the injected dose (ID), the mice were assumed to have 1.6 mL of blood. (**b**) Nanograms of anti-tdTomato siRNA lead strand for each gram of organ, as obtained via interpolation of stem–loop qPCR data from tissues with a calibration curve (Figure S8).

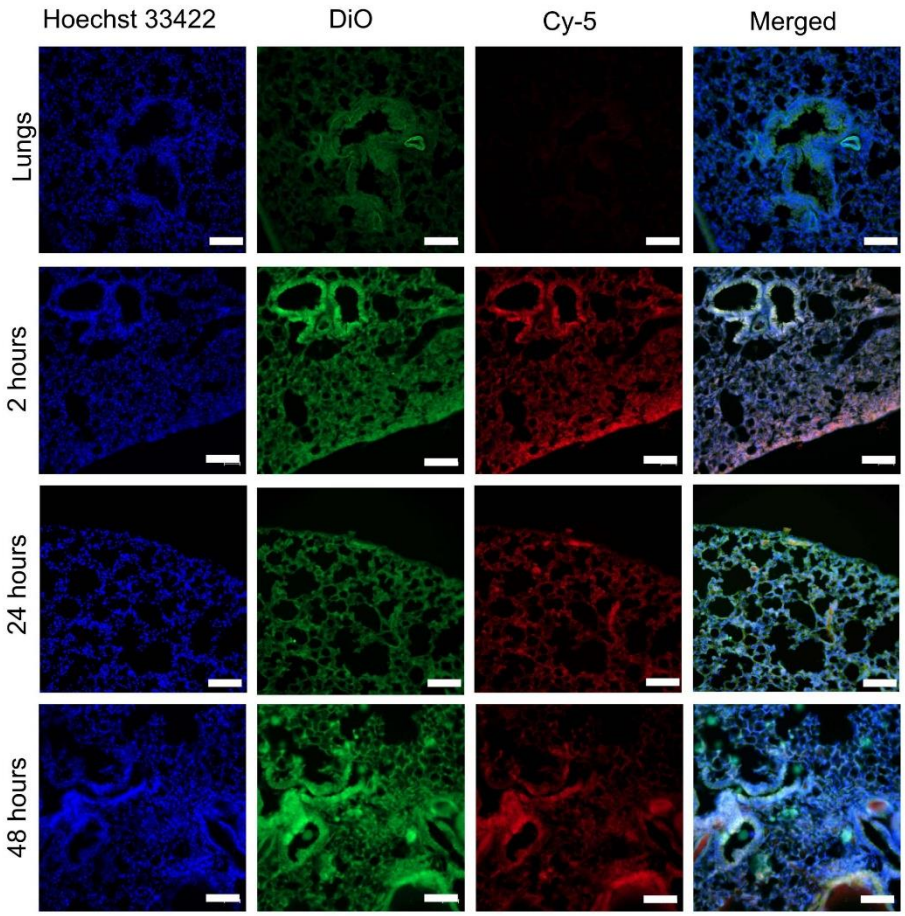



**Figure 9** Distribution of Cy-5/DiO DCC-siRNA-EMVs at different time points in frozen sections of mouse lungs via siRNA-Cy-5 (red) and DiO (green) signals in frozen sections of lungs. Nuclei were labeled with Hoechst 33342 (blue). The scale bar is 100 μm.

the tight endothelium of the blood–brain barrier; the high density of brain capillaries[74] (Figure 8 and 14), therefore, explains the strong accumulation determined via qRT–PCR. The absence of the Cy-5 signal can be noted in the spleen white pulp (Figure 11) and in the marginal zone, while strong accumulation can be observed in the red pulp, which is devoted to recycling old erythrocytes;[75] EMVs, therefore, eluded capture by the lymphoid tissue of white pulp, which is composed of T and B lymphocytes and macrophages.[75] On the other hand, the B16F10 tdTomato-treated tumors presented a disorganized and chaotic structure, with moderate autofluorescence in the green channel around blood vessels and in connective tissue and heterogeneously distributed blood vessels. In the controls, a vast majority of the cells presented fluorescence in the tdTomato channel (Figure 12 and 13).


https://doi.org/10.2147/IJN.S504644

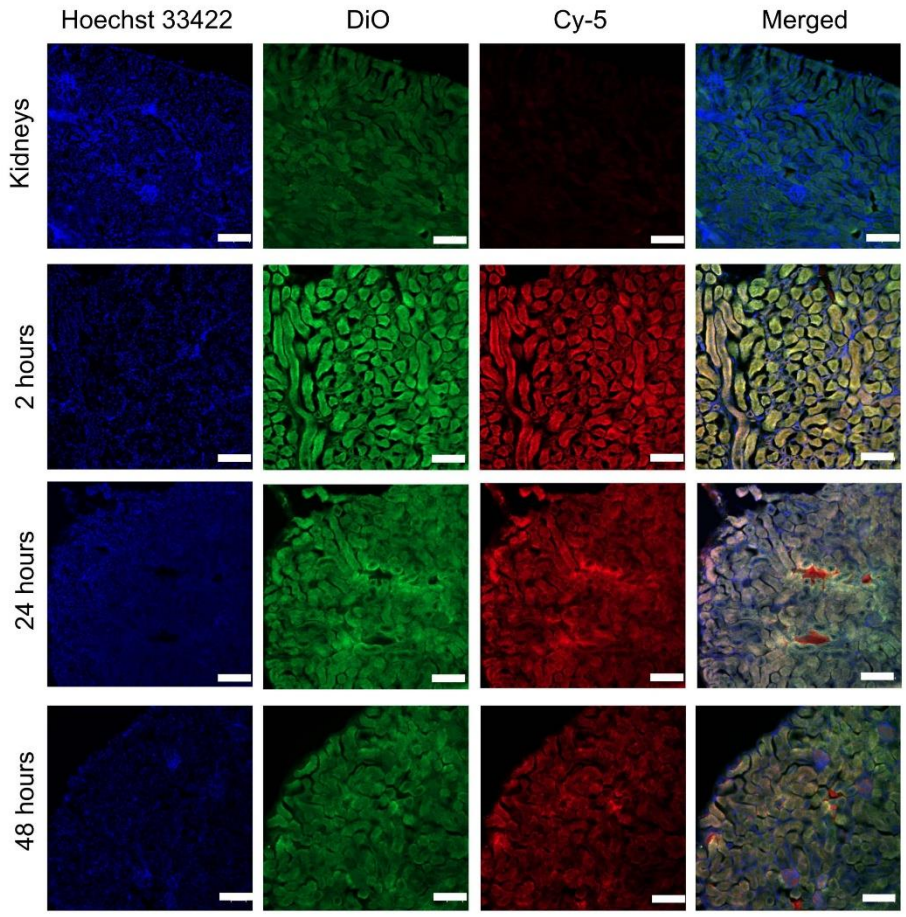



**Figure 10** Distribution of Cy-5/DiO DCC-siRNA-EMVs at different time points in frozen sections of mouse kidneys via siRNA-Cy-5 (red) and DiO (green) signals. Nuclei were labeled with Hoechst 33342 (blue). The scale bar is 100 μm.

In tumors, despite being not the main accumulation site, the Cy-5 signal is greater in the tumor rim and within a layer of 9–10 cells from the closest capillary, which is consistent with the enhanced permeation and retention theory,[76] and it slowly diffuses farther from blood vessels over 48 hours. Indeed, while EMV tissue penetration is limited to 3–4 cells from the closest blood vessel at the 2-hour time point, the Cy-5 signal distribution appears to be much more homogenous at 48 hours (Figure 12). Overall, as indicated by the qRT–PCR data, the Cy-5 and DiO signals continued to increase over time (Figures 13 and 12). Interestingly, extravasated erythrocytes, which occur in solid melanomas due to defective blood vessels,[77] are widespread in tumor tissue and are fluorescent in the Cy-5 channel (Figure 13) as early as 2 h post-administration but are positive but fainter in the FITC channel.

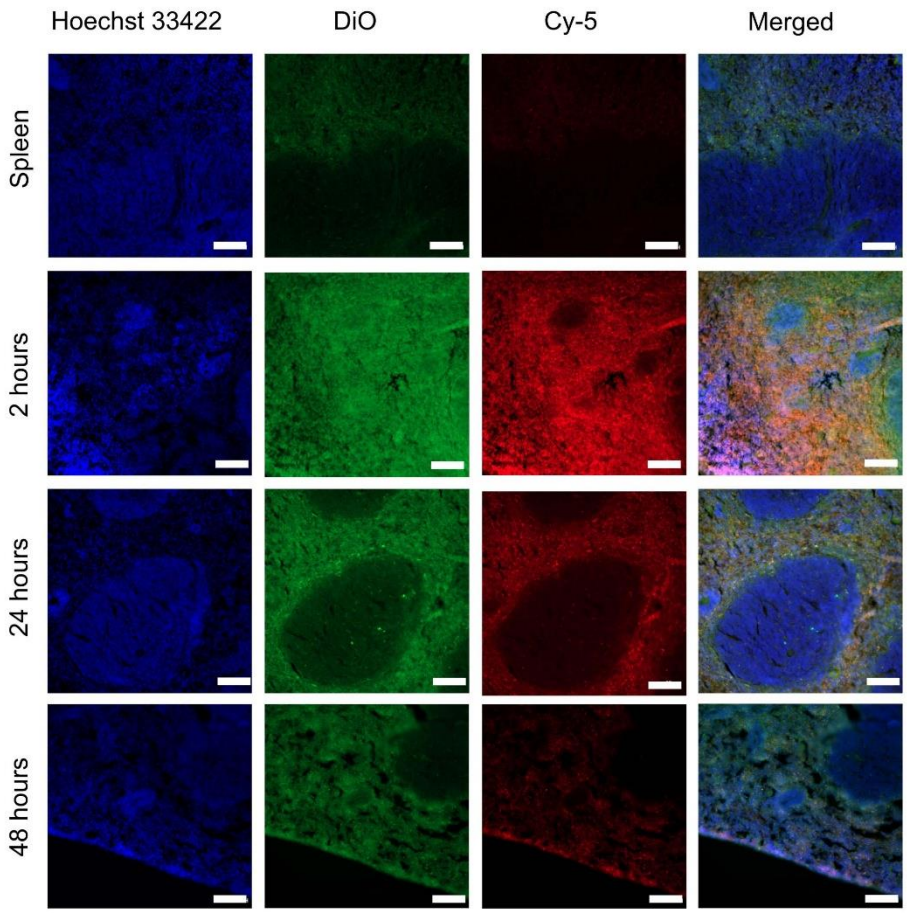



**Figure 11** Distribution of Cy-5/DiO DCC-siRNA-EMVs at different time points in frozen sections of the mouse spleen via siRNA-Cy-5 (red) and DiO (green) signals. Nuclei were labeled with Hoechst 33342 (blue). The scale bar is 100 μm.

From 24 hours onward, the circulating erythrocytes in the blood vessels in the kidneys (Figure 10), heart, brain, lungs and liver showed the same behavior. The Cy-5/DiO erythrocytes were absent in every organ in the control group. In tumors, areas of extravasated erythrocytes 20–40 μm in diameter were completely labeled with Cy-5 48 hours after administration and were weaker in the DiO channel. Although red fluorescence of erythrocytes has been previously reported [78] and hemoglobin fluorescence has been evaluated by fluorescence microscopy with two-photon excitation, [79] the phenomenon we observed appears to be different. We therefore performed a small-scale ex vivo experiment in which we incubated mouse erythrocytes with DiO-labeled DCC-EMVs to detect any membrane fusion and payload transfer under physiological conditions. After 24 and 48 hours of coincubation, several erythrocytes acquired DiO fluorescence (Figure S11c), indicating membrane fusion, as the diffusion rate of such a lipophilic tracker in lipid bilayers is low [80] In


https://doi.org/10.2147/IJN.S504644

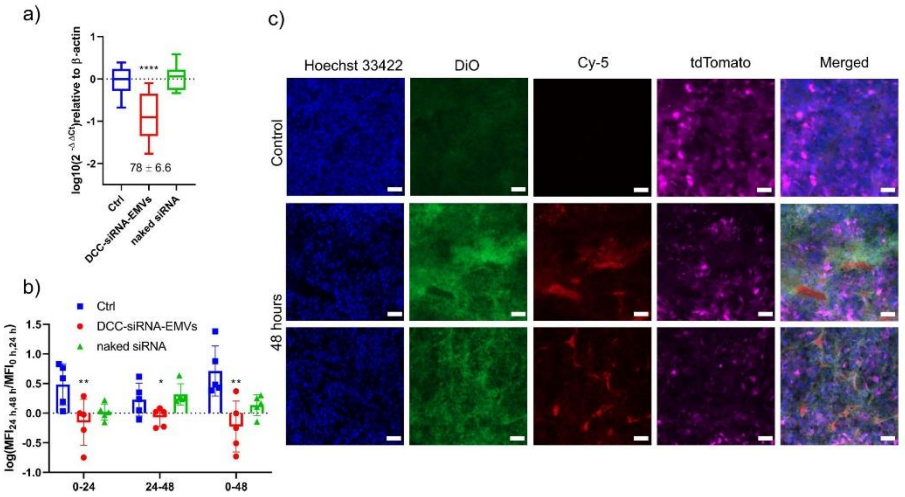



**Figure 12** Summary of the knockdown activity of systemically delivered DCC-siRNA-EMVs. (**a**) Log10 of the tdTomato fold change in vivo at the 2.5 mg/kg dose compared with the basal expression of the gene in control tumors, as analyzed with the Kruskal–Wallis nonparametric t-test. $p \leq 0.0001$ **** (**b**) Log10 of the tdTomato median fluorescence intensity variation at 0–48 hours and 24–48 hours in control, DCC-siRNA-EMV-, and naked siRNA-treated mice. $p \leq 0.05$ *, $p \leq 0.01$ ** (**c**) Tumor tissue sections with blood vessel details at 0 and 48 hours. Red blood cells were unanimously positive in the Cy-5 channel at 48 hours and fainter in the DiO channel. The scale bar is 50 μm.

the absence or presence of EMVs, many erythrocytes take the form of echinocytes [81] while the addition of RPMI medium caused the aggregation of DCC-EMVs, which was confirmed by DLS analysis (Figure S11b and); agglomerates of 2–5 μm were indeed absent in the DCC-EMVs dispersed in PBS (Figure S11a).

## Successful in Vivo Delivery of siRNA-EMVs to Tumors and Knockdown of tdTomato Expression After Systemic Administration of DCC-siRNA-EMVs

Having confirmed the strong in vitro knockdown ability and successful delivery of EMVs to B16F10-tdTomato tumors, we aimed to ascertain whether the DCC-siRNA-EMVs had the ability to elicit gene knockdown in vivo. For this purpose, we again subcutaneously induced B16F10-tdTomato tumors in C57BL/6 mice, and when the tumors reached 50–60 $mm^3$, we intravenously injected 100 μL of naked siRNA (2.5 mg/kg in 0.9% NaCl, n = 4), unlabeled DCC-siRNA-EMVs (2.5 mg/kg in 0.9% NaCl, corresponding to 50 μg for each mouse, n = 5), and, finally, 100 μL of saline (0.9% NaCl, n=4, due to the passing out of one mouse during the experiment). At this dose, the DCC-siRNA-EMVs caused 79% ± 4.38% (SEM, n=5) tdTomato gene knockdown at 48 hours post injection (Figure 12a). The relative expression of the tdTomato gene in the naked siRNA-injected group (n=5) did not significantly differ from that in the control group because of the previously reported[13] quick clearance and rapid degradation of dsRNAs. The mean fluorescence intensity of whole tumors (Figures 12b and S12), on the other hand, suggested that tdTomato protein elimination is a much slower process: indeed, 48 hours post-administration, the reduction in MFI was 48 ± 10% SEM, whereas the variation from 24–48 hours was, compared with the control group, 14 ± 7% (Table 6). Unsurprisingly, the MFI of the B16F10-tdTomato tumors continued to increase throughout the experiment in both the naked siRNA and control groups. We also assessed whether there was any knockdown in the biodistribution mouse group injected with a 1.5 mg/kg dose (30 μg/mouse). We monitored tdTomato gene expression at 24 and 48 hours via qRT–PCR and then measured the MFI of its protein product in thin sections. The presence of Cy-5 on the 5′ end of the passenger strand did not jeopardize the RNA interference process. The knockdown effect on tdTomato gene expression appears to be a relatively early phenomenon because most of the gene silencing occurred within the first 24 hours post-injection (Table 6),

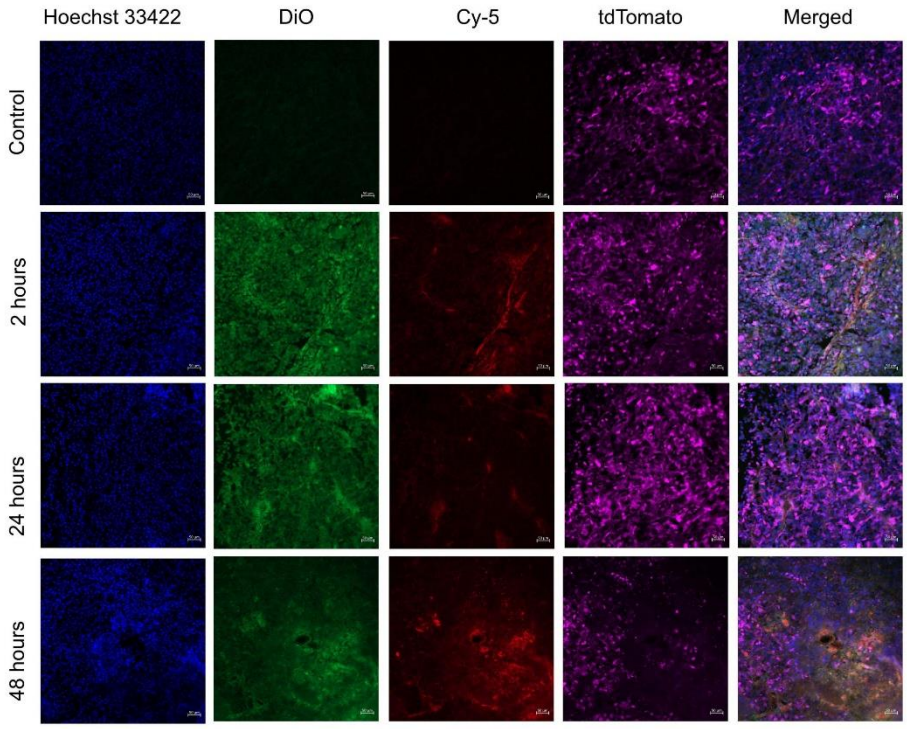



**Figure 13** Distribution of Cy-5/DiO DCC-siRNA-EMVs within B16F10-tdTomato tumors via frozen sections of B16F10-tdTomato tumors at different time points after the injection of DCC-siRNA-EMVs with nuclei labeled with Hoechst 33342 (blue), Vybrant DiO (green), Cy-5 siRNA (red) and tdTomato expression (magenta). The scale bar is 100 μm.

with 47% ± 10 (SEM, n = 5) total tdTomato gene silencing, reaching 69% ± 5.4% (SEM, n=5) at 48 hours. In frozen tissue sections, after 48 hours, the fluorescent signal of the target gene, tdTomato, was indeed lower or absent in the proximity of capillaries (Figures 12c and 13), indicating successful internalization of EMVs and gene knockdown. Logically, the Cy-5 and tdTomato signals hardly ever superimpose at 48 hours within 5–6 cells from the closest capillary. Overall, as shown in Table 6, the total MFI of tdTomato was 48 ± 15% greater than that of the control at 48 hours after injection (Figure S13).

## Discussion

The RBC membrane has already been used as a coating material for polycationic nanoparticles in siRNA delivery[37] to take advantage of endocytosis and, subsequently, endosomal escape; Wang et al failed to address the stability of their co-assemblies. Our platform is RBC-based as well, but we consciously decided to avoid the involvement of any polyplexes in the development of a siRNA carrier and to rely, for cell uptake, only on membrane properties to minimize toxicity and ensure biocompatibility. When small nucleic acids are loaded into neutral, lipid-based, and naturally occurring nano-carriers, such as extracellular vesicles and exosomes,[78,82] available techniques—electroporation, sonication and lipofection—are laborious and work intensive[79] or can lead to RNA degradation.[56,82] Furthermore, the removal of unloaded cargo can pose another problem: naturally occurring EVs are already tightly packed with miRNAs and other small RNAs,


https://doi.org/10.2147/IJN.S504644

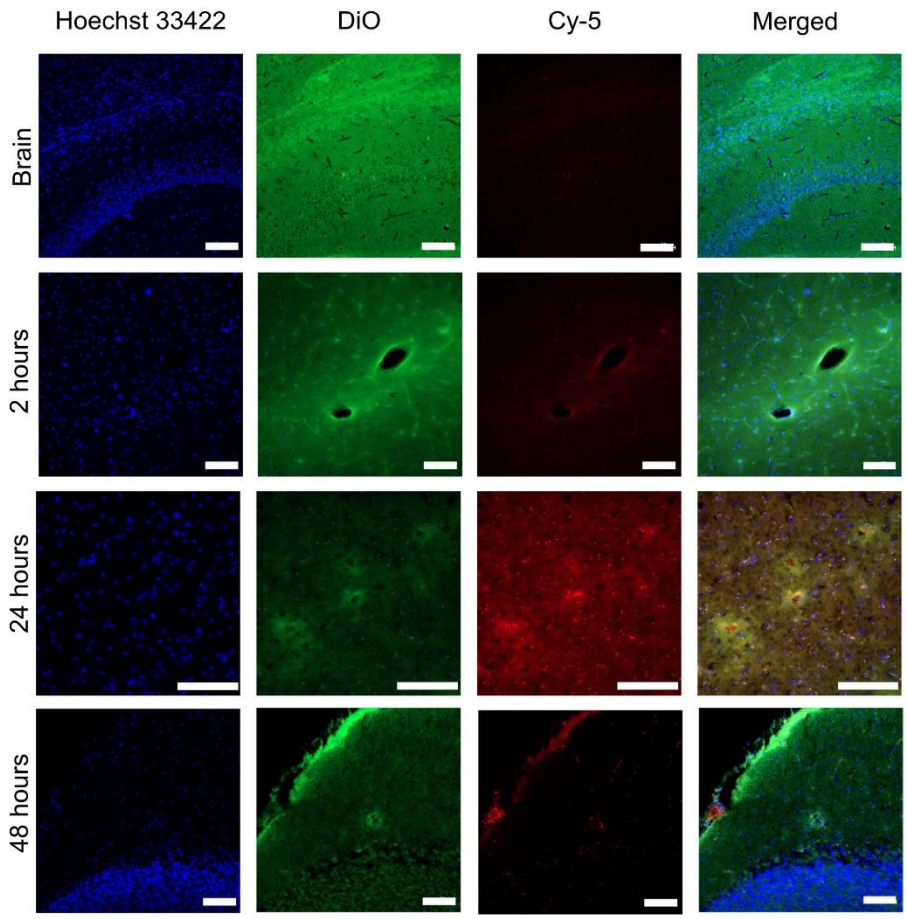



**Figure 14** Distribution of Cy-5/DiO DCC-siRNA-EMVs at different time points in frozen sections of the mouse brain via siRNA-Cy-5 (red) and DiO (green) signals. Nuclei were labeled with Hoechst 33342 (blue). The scale bar is 100 μm.

and the systemic administration of such contents may lead to unwanted off-target effects and hinder the loading efficiency of exogenous nucleic acids.[80]

In contrast, the whole process of production and purification of DCC-siRNA-EMVs requires approximately four hours. We tested different methods for the removal of unloaded siRNA and cell debris: simple ultracentrifugation, with pelletization of loaded EMVs, sucrose gradient ultracentrifugation, density-changing centrifugation, and size exclusion chromatography with G25–PD10 Sephadex packed columns, which are commonly used for liposome purification.[45,83] Density-changing centrifugation was proven to be the technically least demanding, most repeatable separation method among those tested: a solution of 10% trisodium citrate could select EMVs according to their RNA content in precise and well-defined layers (Figure 1).

**Table 6** TdTomato Gene Knockdown and Relative MFI Decrease at Two Different Doses of Anti-tdTomato siRNA

| Dose (mg/kg) | Time point (h) | % of mRNA Knockdown (± SEM) | % of tdTomato MFI Variation (± SEM) |
|---|---|---|---|
| 1.5 | 0–24 | 47% ± 10 | 20 ± 6 |
| | 24–48 | 31% ± 6 | 21 ± 5 |
| | 0–48 | 69% ± 5 | 37 ± 4 |
| 2.5 | 0–24 | | 34 ± 12 |
| | 24–48 | | 14 ± 7 |
| | 0–48 | 79% ± 4 | 48 ± 15 |

While successful loading of siRNAs into a single EV seems to be the limiting step for their ability as silencing carriers,[84] we confirmed that loading of siRNAs in our EMVs via freeze-fracture TEM (Figure 2) and a STED laser equipped with a confocal microscope (Figure 4) effectively visualized the siRNAs within the lumen of the vesicles. Loading resulted in a final encapsulation efficiency of 67%. Freeze fracturing of EMVs has already been successfully used in,[54] and despite being a widely exploited technique in liposome and nanocapsule characterization,[85,86] our results are the first, to our knowledge, to show RNA aggregates in the lumen of lipid/protein objects. Notably, despite appearing as amorph aggregates, the integrity and ability of the loaded siRNA to elicit RNA interference were maintained both in vitro and in vivo. Moreover, as it is a valuable tool for the in-depth characterization of such elusive objects, an ever-growing number of studies have investigated the characterization of extracellular vesicles/exosomes/liposomes via fluorescence microscopy.[87–90] We used this technique to characterize the density of packing of DCC-siRNA-EMVs, and we confirmed the efficient removal of unencapsulated siRNA and of membrane debris not shaped into EMVs. Furthermore, owing to the high STED resolution, we confirmed that this technique is reliable for size characterization. The rare superimposition of Cy-5 and CM-DiI signals hints at a high density of packing of siRNA inside the EMVs, enough for Cy-5 to self-quench, as already reported for a similar system.[91]

Membrane-derived vesicles have already been exploited for nucleic acid delivery,[92,93] but red blood cell-derived vesicles have never been fully characterized as TNA delivery systems. The Lejeune group extensively described these objects – termed them "nanoerythrosomes" – in a series of follow-up papers.[94–96] When P3881 cells were loaded with daunorubicin, the internalization pathway was remarkably similar to that we observed (Figure 6), with initial accumulation of DCC-siRNA-EMVs around the plasma membrane followed by robust internalization of the payload. The migration of the CM-DiI signal inside the cytoplasm indicates EMV–cell membrane fusion and subsequent translocation of the dye in the internal membrane system, as reported elsewhere.[97] Naturally occurring EVs are highly likely to follow some endosomal escape pathways to expose their RNA payload to the cytosol without rupturing the endosomal membrane, as happens in cationic gene delivery, but through a simple fusion event,[98] whose minute molecular mechanism has yet to be elucidated. RBCs express flotillin 1 and 2 on their lipid rafts,[18] a protein pair known to elicit a caveolae/clathrin-independent endocytosis process.[99,100] Therefore, siRNAs are either directly translocated into the cytoplasm by direct membrane fusion or released from endosomes and are ready to be complexed with Ago2. BCAM1 might also play a role in membrane fusion, as it is present both in the RBC proteome and in naturally released EVs.[5,18] Similarly, even if they are of minor importance in the native RBC membrane,[5] typical exosome markers such as TSG101 and ALIX have also been reported. This nonspecific uptake mechanism seems to be shared among the cell lines we evaluated (CT26, B16F10 and NHLF) with no preferred target. Finally, the in vitro ability of DCC-siRNA-EMVs to silence B16F10 expression on tdTomato mRNA was found to be approximately 80% at a final well concentration of 30 nM, a result comparable to that reported for RBC-derived EVs.[17] Notably, compared with HEK293-derived EVs, DCC-siRNA-EMVs elicited RNA interference at a markedly lower dose,[56] Sk-hep1-derived DPPC hybrid EVs,[87] and Neuro2a-EVs loaded with lipidic siRNA.[101]

Our DCC-siRNA-EMVs showed promising results for future clinical translation. In vivo, in melanoma-bearing mice, at 2.5 mg/kg body weight, upon systemic administration via the caudal vein, DCC-siRNA-EMVs were capable of causing 80% tdTomato gene silencing, whereas intact EMVs containing the anti-tdTomato siRNA were still present in the blood after

48 h of administration. The early occurrence of gene knockdown is consistent with siRNA activity models,[102] which favor early mRNA degradation rather than GW182 translation blockage. In similar experiments (ie single injection, systemic administration of siRNA-loaded nanoparticles towards B16F10 derived tumors and metastasis), DCC-siRNA-EMVs outperformed untargeted PEGylated cationic lipid nanoparticles in terms of knock-down[103] and transferrin-based nanoparticles.[104] Remarkably, similar knock-down levels are reached after multiple administrations.[105,106]

The accumulation of EMVs in the tumor directly confirms the enhanced permeation and retention effect (EPR effect), as established for rodents,[107,108] for the passive accumulation of 100–200 nm nanoparticles in tumor tissues. B16F10 tumors are known to have a leaky vasculature and lower recruitment of CD8+ cells,[109] suggesting that melanoma-related metastasis is a possible target of EMVs. Furthermore, the lack of uptake by white pulp macrophages in the spleen (Figure 11) confirms the masking activity of the CD47 marker on EMVs. EMVs also managed to elude clearance by Kupffer cells in the liver, with the siRNA concentration in tumors being twice that in the liver after 48 hours. The high apparent volume of distribution $V_d$ of DCC-siRNA-EMVs allowed precocious delivery of siRNA to tumors, leading to 50% gene knockdown (at 1.5 mg/kg weight) as early as 24 hours after administration. As the EPR effect is known to fail in vivo in humans due to the higher blood flow rate,[108,110] increased washout to achieve a longer circulation time and lower clearance by RES is of utmost importance, together with active targeting of the tissue of interest.

Interestingly, with respect to the tissue penetration of our carriers, 48 hours postinjection, DCC-siRNA-EMVs exhibited a knockdown ability within a layer of 5--6 cells from the closest blood vessel, thereby successfully crossing the endothelium but, unfortunately, extremely slow diffusion within the extracellular matrix (ECM) of B16F10 tumors. Nevertheless, we observed increased homogenization of the Cy-5 signal, which was conjugated with the siRNA passenger strand in EMVs, in tumor tissue over the course of the experiment. This finding indicated that despite being extremely hindered by collagen and hyaluronic acids and interstitial fluid pressure,[111] our carriers diffuse from the endothelium within the interstitial space. Liposomes and other spherical nanoparticles larger than 60 nm have been shown not to be able to diffuse into the ECM and interstitial tissue,[112] but such a phenomenon appears to be heavily dependent on the physical characteristics of the nanoparticle,[113,114] such as its size. The ECM indeed behaves like a hydrogel matrix: the penetration of nanoparticles is more efficient when collagen fibers are aligned in an ordered, isotropic architecture. As elucidated by cryo-EM, EMVs are flat objects overall, with a pronounced discoidal/ellipsoidal shape. In the literature, a vast majority of papers report differential diffusion efficiency within solid tumors for hard nanoparticles, such as Au nanorods, nanodisks or nanospheres,[114,115] but many fewer reports are available for soft matter, such as polymeric nanoparticles,[116] or plant-derived virus-like particles,[117] and to our knowledge, soft-matter, hydrophilic nanodisk solid–tumor diffusion depths have never been reported.

The fusion or attachment/hitchhiking event between EMVs and circulating erythrocytes, which has already occurred 2 hours post-administration, is highly important for the advancement and optimization of biodistribution techniques. A common method used to determine the presence of fluorescently labeled siRNA in mice is monitoring the remaining fluorescence of the labeled carrier in the mouse whole body at fixed time points via equipment such as the IVIS.[118,119] This technique, even if fast, does not focus on the tissue level. Murine and human red blood cells are prone to membrane fusion with synthetic liposomes,[120,121] but fusion with EVs, exosomes, or membrane-derived artificial vesicles has never been reported. Moreover, red blood cells are known to adsorb, on their outer layers, a variety of artificial nanoparticles in the absence of plasma proteins;[122,123] unfortunately, investigations of putative hitchhiking or membrane fusion of EMVs with red blood cells are outside the scope of this paper.

We also characterized the best storage option of our DCC-siRNA-EMVs to evaluate the most cost/effective storage option for long-term potential treatment. We concluded that disaccharides—sucrose and trehalose—are our system's best cryolyoprotectant, leading to minimal payload loss upon rehydration. Sucrose FD-DCC-siRNA-EMVs retained the ability to induce RNA interference (Figure 6). Upon storage at 4°C, the EMVs caused phospholipid loss over time and a significant increase in size. Such storage lesions have already been reported for whole red blood cells and are connected to oxidative stress and subsequent EVs release.[124] As reported in,[125] larger extracellular vesicles may arise from the fusion of smaller protein/lipid complexes released during the early stages of storage. These data, taken together with the findings of siRNA leakage upon storage, lead us to speculate that a budding mechanism, similar to that observed for whole RBCs, is maintained in EMVs. An inner membrane-bound proteasome has been previously reported[59,126] and confirmed in[5] and,[127] and despite being the main

target of hemoglobin, it can also digest Band 3 and glycophorin A proteins, thus explaining the colloidal instability of stored EMVs and the presence of storage lesions. However, whether this protease activity might play a role in transfection efficiency and tumor ECM diffusion has yet to be elucidated.

## Conclusion

Red blood cells are the ideal starting material for a biomimetic and biocompatible nanodelivery system with low immunogenicity and prolonged circulation time. Additionally, the intriguing mechanical properties of their cytoskeleton lead to interesting soft-matter stiff nanoparticles. We developed an easy and repeatable procedure that allowed us to obtain a high encapsulation efficiency of a therapeutic nucleic acid, siRNA, in a relatively short amount of time. Despite relying only on passive targeting, our erythrocyte membrane vesicles, in vivo, had a remarkable circulation time and safely delivered their payload to tumors. The passive high accumulation of these objects in the lungs may lead to the development of new therapies for lung cancer. We were therefore able to develop a simple, cost-effective, therapeutic nucleic acid carrier that is also prone to easy scaling-up. Most importantly, the patient's own blood might be used, avoiding immune reactions, for actual personalized medicine. As of 2024, many nanoparticle-siRNA formulations (such as CALAA-01, ARC-520) fail in clinical translation due to off-site accumulation and knock-down of off-target mRNAs, insufficient gene knock-down in target tissue, and hepatic or kidney toxicity. Therefore, for a successful drug approval, not only the TNA sequence must be carefully tailored and chemically modified (incorporation of locked-nucleic acids, methylation of the guide strand in position 2)[128] to avoid unwanted knockdown, but also carrier tropism needs careful tuning to ensure the lowest possible effective dose without significant side effects. Future developments for these carriers will include active targeting tumor sites, to avoid healthy cells accumulation, and simultaneous loading to a reporter agent to obtain an all-in-one theranostic agent. Furthermore, we aim to quantitatively investigate the correlation between soft-matter nanoparticle shapes and their tissue penetration.

## Ethical Approvals

Red blood cells were obtained from the Blood Transfusion Centre of Slovenia (Ethical approval number 0120-592/2020/7), which belong to two young anonymous males, A RhD+ blood type. The blood donors provided informed consent, in accordance with the Declaration of Helsinki. All in vivo experiments were approved by the Ministry of Agriculture, Forestry and Food of the Republic of Slovenia (permission no. U34401-35/2020/8). All the procedures involving animals were conducted in concordance with the EU directive 2010/63/EU, the NC3Rs ARRIVE guidelines and complied with Slovenian legislation.

## Acknowledgments

We thank Rok Zupanc for his contribution to thin section preparation. We also thank Dr Simona Kranjc Brezar for her precious help during in vivo experiments.

## Funding

The study was supported by the Slovenian Research and Innovation Agency ARIS (program numbers P1-0207, P2-0084, P3-0003, P3-0108, project numbers PR-10482, J3-14531 and J4-50150). CryoTEM was performed at the National Institute of Chemistry CryoEM Facility, supported by the Slovenian Research Agency Infrastructure Programme IO-0003.

## Disclosure

The author(s) report no conflicts of interest in this work.

## References

1. Della Pelle G, Kostevšek N. Nucleic acid delivery with red-blood-cell-based carriers. *Int J mol Sci*. 2021;22(10):5264. doi:10.3390/ijms22105264
2. Rossi L, Pierigè F, Aliano MP, Magnani M. Ongoing developments and clinical progress in drug-loaded red blood cell technologies. *BioDrugs*. 2020;34(3):265–272. doi:10.1007/s40259-020-00415-0

3. Fondaj D, Arduino I, Lopedota AA, Denora N, Iacobazzi RM. Exploring the microfluidic production of biomimetic hybrid nanoparticles and their pharmaceutical applications. *Pharmaceutics*. 2023;15(7):1953. doi:10.3390/pharmaceutics15071953
4. Fang RH, Jiang Y, Fang JC, Zhang L. Cell membrane-derived nanomaterials for biomedical applications. *Biomaterials*. 2017;128:69–83. doi:10.1016/j.biomaterials.2017.02.041
5. Bryk AH, Wiśniewski JR. Quantitative analysis of human red blood cell proteome. *J Proteome Res*. 2017;16(8):2752–2761. doi:10.1021/acs.jproteome.7b00025
6. Bosman GJCGM, Lasonder E, Groenen-Döpp YAM, Willekens FLA, Werre JM. The proteome of erythrocyte-derived microparticles from plasma: new clues for erythrocyte aging and vesiculation. *J Proteomics*. 2012;76(286):203–210. doi:10.1016/j.jprot.2012.05.031
7. Jain V, Yang WH, Wu J, Roback JD, Gregory SG, Chi JT. Single cell RNA-seq analysis of human red cells. *Front Physiol*. 2022;13:1–9. doi:10.3389/fphys.2022.828700
8. Shiga T, Maeda N, Kon K. Erythrocyte rheology. *Crit Rev Oncol Hematol*. 1990;10(1):9–48. doi:10.1016/1040-8428(90)90020-S
9. Dao M, Lim CT, Suresh S. Mechanics of the human red blood cell deformed by optical tweezers. *J Mech Phys Solids*. 2003;51(11–12):2259–-2280. doi:10.1016/j.jmps.2003.09.019
10. Oldenborg PA, Zheleznyak A, Fang YF, Lagenaur CF, Gresham HD, Lindberg FP. Role of CD47 as a marker of self on red blood cells. *Science*. 2000;288(5473):2051–2054. doi:10.1126/science.288.5473.2051
11. Vahedi A, Bigdelou P, Farnoud AM. Quantitative analysis of red blood cell membrane phospholipids and modulation of cell-macrophage interactions using cyclodextrins. *Sci Rep*. 2020;10(1):1–13. doi:10.1038/s41598-020-72176-3
12. Sioud M. RNA interference: challenges and therapeutic opportunities. *RNA Interf Challenges Ther Oppor*. 2014;1218:1–489. doi:10.1007/978-1-4939-1538-5
13. Friedrich M, Aigner A. Therapeutic siRNA: state-of-the-art and future perspectives. *BioDrugs*. 2022;36(5):549–571. doi:10.1007/S40259-022-00549-3
14. Digital Science. *Dimensions [Software]*. 2018. Available from: https://app.dimensions.ai. Accessed March 05, 2025.
15. Harisa GI, Badran MM, Alanazi FK. Erythrocyte nanovesicles: biogenesis, biological roles and therapeutic approach: erythrocyte nanovesicles. *Saudi Pharm J*. 2017;25(1):8–17. doi:10.1016/j.jsps.2015.06.010
16. Song J, Song B, Yuan L, Yang G. Multiplexed strategies toward clinical translation of extracellular vesicles. *Theranostics*. 2022;12(15):6741–6761. doi:10.7150/thno.75899
17. Usman WM, Pham TC, Kwok YY, et al. Efficient RNA drug delivery using red blood cell extracellular vesicles. *Nat Commun*. 2018;9(1):1–15. doi:10.1038/s41467-018-04791-8
18. Prudent M, Delobel J, Hübner A, Benay C, Lion N, Tissot J-D-D. Proteomics of stored red blood cell membrane and storage-induced microvesicles reveals the association of flotillin-2 with band 3 complexes. *Front Physiol*. 2018;9:1–11. doi:10.3389/fphys.2018.00421
19. Yona S, Gordon S, Van Nostrand EL, et al. Co-development of diagnostic vectors to support targeted therapies and theranostics: essential tools in personalized cancer therapy. *Front Oncol*. 2017;11(1):1–12. doi:10.1002/marc.200500777
20. Moenner M, Vosoghi M, Ryazantsev S, Glitz DG. Ribonuclease inhibitor protein of human erythrocytes: characterization, loss of activity in response to oxidative stress, and association with Heinz bodies. *Blood Cells, mol Dis*. 1998;24(2):149–164. doi:10.1006/bcmd.1998.0182
21. Ohashi A, Murata A, Cho Y, et al. The expression and localization of RNase and RNase inhibitor in blood cells and vascular endothelial cells in homeostasis of the vascular system. *PLoS One*. 2017;12(3):e0174237. doi:10.1371/journal.pone.0174237
22. Blanco E, Shen H, Ferrari M, Blanco HSMF E. Principles of nanoparticle design for overcoming biological barriers to drug delivery. *Nature Biotechnology*. 2015;33(9):941–951. doi:10.1038/nbt.3330
23. Partikel K, Korte R, Stein NC, et al. Effect of nanoparticle size and PEGylation on the protein corona of PLGA nanoparticles. *Eur J Pharm Biopharm*. 2019;141:70–80. doi:10.1016/j.ejpb.2019.05.006
24. Chen M, Leng Y, He C, et al. Red blood cells: a potential delivery system. *J Nanobiotechnology*. 2023;21(1):1–19. doi:10.1186/s12951-023-02060-5
25. Mao S, Neu M, Germershaus O, et al. Influence of polyethylene glycol chain length on the physicochemical and biological properties of poly (ethylene imine)-graft-poly(ethylene glycol) block copolymer/SiRNA polyplexes. *Bioconjug Chem*. 2006;17(5):1209–1218. doi:10.1021/bc060129j
26. Janaszewska A, Lazniewska J, Trzepiński P, Marcinkowska M, Klajnert-Maculewicz B. Cytotoxicity of dendrimers. *Biomolecules*. 2019;9(8):330. doi:10.3390/biom9080330
27. Abedi-Gaballu F, Dehghan G, Ghaffari M, et al. PAMAM dendrimers as efficient drug and gene delivery nanosystems for cancer therapy. *Appl Mater Today*. 2018;12(3):177–190. doi:10.1016/j.apmt.2018.05.002
28. Correia JS, Mirón-Barroso S, Hutchings C, et al. How does the polymer architecture and position of cationic charges affect cell viability? *Polym Chem*. 2022;14(3):303–317. doi:10.1039/d2py01012g
29. Della Pelle G, Bozic T, Vukomanović M, Sersa G, Markelc B, Kostevšek N. Efficient siRNA delivery to murine melanoma cells via a novel genipin-based nano-polymer. *Nanoscale Adv*. 2024;6(18):4704–4723. doi:10.1039/d4na00363b
30. Beddoes CM, Case CP, Briscoe WH. Understanding nanoparticle cellular entry: a physicochemical perspective. *Adv Colloid Interface Sci*. 2015;218:48–68. doi:10.1016/j.cis.2015.01.007
31. Franchi L, Eigenbrod T, Muñoz-Planillo R, et al. Cytosolic double-stranded RNA activates the NLRP3 inflammasome via MAVS-induced membrane permeabilization and K+ Efflux. *J Immunol*. 2014;193(8):4214–4222. doi:10.4049/jimmunol.1400582
32. Wang W, Wang WH, Azadzoi KM, et al. Activation of innate antiviral immune response via double-stranded RNA-dependent RLR receptor-mediated necroptosis. *Sci Rep*. 2016;6:1–14. doi:10.1038/srep22550
33. Gao S, Dagnaes-Hansen F, Nielsen EJB, et al. The effect of chemical modification and nanoparticle formulation on stability and biodistribution of siRNA in mice. *Mol Ther*. 2009;17(7):1225–1233. doi:10.1038/mt.2009.91
34. Pérez-Carrión MD, Posadas I, Ceña V. Nanoparticles and siRNA: a new era in therapeutics? *Pharmacol Res*. 2024;201:107102. doi:10.1016/j.phrs.2024.107102
35. Shaner NC, Campbell RE, Steinbach PA, Giepmans BNG, Palmer AE, Tsien RY. Improved monomeric red, orange and yellow fluorescent proteins derived from discosoma sp. red fluorescent protein. *Nat Biotechnol*. 2004;22(12):1567–1572. doi:10.1038/nbt1037
36. Hu CMJ, Zhang L, Aryal S, Cheung C, Fang RH, Zhang L. Erythrocyte membrane-camouflaged polymeric nanoparticles as a biomimetic delivery platform. *Proc Natl Acad Sci U S A*. 2011;108(27):10980–10985. doi:10.1073/pnas.1106634108

37. Wang Y, Ji X, Ruan M, et al. Worm-like biomimetic nanoerythrocyte carrying siRNA for melanoma gene therapy. *Small*. 2018;14(47):1–13. doi:10.1002/smll.201803002
38. Yang L, Wang T, Zhang D, et al. Black phosphorus nanosheets assist nanoerythrosomes for efficient mRNA vaccine delivery and immune activation. *Adv Healthc Mater*. 2023;12(26):1–12. doi:10.1002/adhm.202300935
39. Huang Y, Hong J, Zheng S, et al. Elimination pathways of systemically delivered siRNA. *Mol Ther*. 2011;19(2):381–385. doi:10.1038/mt.2010.266
40. Perepelyuk M, Thangavel C, Liu Y, et al. Biodistribution and pharmacokinetics study of siRNA-loaded anti-NTSR1-mAb-functionalized novel hybrid nanoparticles in a metastatic orthotopic murine lung cancer model. *mol Ther - Nucleic Acids*. 2016;5:e282. doi:10.1038/mtna.2015.56
41. Bradford MM. A rapid and sensitive method for the quantitation of microgram quantities of protein utilizing the principle of protein-dye binding. *Anal Biochem*. 1976;72(1–2):248–254. doi:10.1006/ABIO.1976.9999
42. Della Pelle G, Delgado López A, Salord Fiol M, Kostevšek N. Cyanine dyes for photo-thermal therapy: a comparison of synthetic liposomes and natural erythrocyte-based carriers. *Int J mol Sci*. 2021;22(13):6914. doi:10.3390/ijms22136914
43. Steck TL. Preparation of impermeable inside-out and right-side-out vesicles from erythrocyte membranes. In: *Methods in Membrane Biology. Vol 255*. Springer US; 1974:245–281. doi:10.1007/978-1-4615-8960-0_4
44. Stewart JCM, JC S. Colorimetric determination of phospholipids with ammonium ferrothiocyanate. *Anal Biochem*. 1980;104(1):10–14. doi:10.1016/0003-2697(80)90269-9
45. Resnier P, Lepeltier E, Emina AL, et al. Model affitin and PEG modifications onto siRNA lipid nanocapsules: cell uptake and in vivo biodistribution improvements. *RSC Adv*. 2019;9(47):27264–27278. doi:10.1039/C9RA03668G
46. Han L, Zhan H, Sun X, Zhang Z-R-R, Deng L. A density-changing centrifugation method for efficient separation of free drugs from drug-loaded particulate delivery systems. *AAPS J*. 2019;21(3):1–11. doi:10.1208/s12248-019-0306-1
47. Sezgin E, Schneider F, Galiani S, et al. Measuring nanoscale diffusion dynamics in cellular membranes with super-resolution STED–FCS. *Nat Protoc*. 2019;44:1–51. doi:10.1038/s41596-019-0127-9
48. Zhang Y, Huo M, Zhou J, Xie S. PKSolver: an add-in program for pharmacokinetic and pharmacodynamic data analysis in Microsoft Excel. *Comput Methods Programs Biomed*. 2010;99(3):306–314. doi:10.1016/j.cmpb.2010.01.007
49. Yen J-C, Chang F-J, Chang S. A new criterion for automatic multilevel thresholding. *IEEE Trans Image Process*. 1995;4(3):370–378. doi:10.1109/83.366472
50. Kabanova S, Kleinbongard P, Volkmer J, Andrée B, Kelm M, Jax TW. Gene expression analysis of human red blood cells. *Int J Med Sci*. 2009;6(4):156–159. doi:10.7150/ijms.6.156
51. Sun L, Yu Y, Niu B, Wang D, Lamont SJ. Red blood cells as potential repositories of microRNAs in the circulatory system. *Front Genet*. 2020;11:11. doi:10.3389/FGENE.2020.00442
52. Deák R, Mihály J, Szigyártó IC, Wacha A, Lelkes G, Bóta A. Physicochemical characterization of artificial nanoerythrosomes derived from erythrocyte ghost membranes. *Colloids Surfaces B Biointerfaces*. 2015;135:225–234. doi:10.1016/j.colsurfb.2015.07.066
53. Kuo YC, Wu HC, Hoang D, Bentley WE, D'Souza WD, Raghavan SR. Colloidal properties of nanoerythrosomes derived from bovine red blood cells. *Langmuir*. 2016;32(1):171–179. doi:10.1021/acs.langmuir.5b03014
54. Deák R, Mihály J, Szigyártó IC, et al. Nanoerythrosomes tailoring: lipid induced protein scaffolding in ghost membrane derived vesicles. *Mater Sci Eng C*. 2020;109:110428. doi:10.1016/j.msec.2019.110428
55. Singh P, Szigyártó IC, Ricci M, et al. Membrane active peptides remove surface adsorbed protein corona from extracellular vesicles of red blood cells. *Front Chem*. 2020:8(August):1–10. doi:10.3389/fchem.2020.00703
56. Lamichhane TN, Jeyaram A, Patel DB, et al. Oncogene knockdown via active loading of small RNAS into extracellular vesicles by sonication. *Cell Mol Bioeng*. 2016;9(3):315–324. doi:10.1007/s12195-016-0457-4
57. Kang J, Kaczmarek O, Liebscher J, Dähne L. Prevention of H-aggregates formation in Cy5 labeled macromolecules. *Int J Polym Sci*. 2010;2010:1–7. doi:10.1155/2010/264781
58. Fagan JM, Waxman L. Purification of a protease in red blood cells that degrades oxidatively damaged haemoglobin. *Biochem J*. 1991;277(3):779–786. doi:10.1042/bj2770779
59. Murakami T, Suzuki Y, Murachi T. An acid protease in human erythrocytes and its localization in the inner membrane. *Eur J Biochem*. 1979;96(2):221–227. doi:10.1111/j.1432-1033.1979.tb13032.x
60. Bosman GJCGM, Stappers M, Novotný VRMJ. Changes in band 3 structure as determinants of erythrocyte integrity during storage and survival after transfusion. *Blood Transfus*. 2010;8(SUPPL. 3):48–52. doi:10.2450/2010.008S
61. Tarone G, Hamasaki N, Fukuda M, Marchesi VT. Proteolytic degradation of human erythrocyte band 3 by membrane-associated protease activity. *J Membr Biol*. 1979;48(1):1–12. doi:10.1007/BF01869253
62. El Baradie KBY, Nouh M, O'Brien F, et al. Freeze-dried extracellular vesicles from adipose-derived stem cells prevent hypoxia-induced muscle cell injury. *Front Cell Dev Biol*. 2020;8:181. doi:10.3389/FCELL.2020.00181/BIBTEX
63. Trenkenschuh E, Richter M, Heinrich E, Koch M, Fuhrmann G, Friess W. Enhancing the stabilization potential of lyophilization for extracellular vesicles. *Adv Healthc Mater*. 2021;11:2100538. doi:10.1002/ADHM.202100538
64. Takahashi T, Hirsh A, Erbe E, Williams RJ. Mechanism of cryoprotection by extracellular polymeric solutes. *Biophys J*. 1988;54(3):509–518. doi:10.1016/S0006-3495(88)82983-7
65. Abdelwahed W, Degobert G, Fessi H. Investigation of nanocapsules stabilization by amorphous excipients during freeze-drying and storage. *Eur J Pharm Biopharm*. 2006;63(2):87–94. doi:10.1016/j.ejpb.2006.01.015
66. Buera MDP, Levi G, Karel M. Glass transition in poly(vinylpyrrolidone): effect of molecular weight and diluents. *Biotechnol Prog*. 1992;8(2):144–148. doi:10.1021/bp00014a008
67. Berezhkovskiy LM. Determination of mean residence time of drug in plasma and the influence of the initial drug elimination and distribution on the calculation of pharmacokinetic parameters. *J Pharm Sci*. 2009;98(2):748–762. doi:10.1002/jps.21440
68. Sun CY, Shen S, Xu CF, et al. Tumor acidity-sensitive polymeric vector for active targeted siRNA delivery. *J Am Chem Soc*. 2015;137(48):15217–15224. doi:10.1021/jacs.5b09602
69. Khaja F, Jayawardena D, Kuzmis A, Önyüksel H. Targeted sterically stabilized phospholipid siRNA nanomedicine for hepatic and renal fibrosis. *Nanomaterials*. 2016;6(1):8. doi:10.3390/nano6010008

70. Li SD, Chen YC, Hackett MJ, Huang L. Tumor-targeted delivery of siRNA by self-assembled nanoparticles. *Mol Ther*. 2008;16(1):163–169. doi:10.1038/sj.mt.6300323
71. Liang X, Ye X, Wang C, et al. Photothermal cancer immunotherapy by erythrocyte membrane-coated black phosphorus formulation. *J Control Release*. 2019;296:150–161. doi:10.1016/J.JCONREL.2019.01.027
72. Sosale NG, Ivanovska II, Tsai RK, et al. "Marker of Self" CD47 on lentiviral vectors decreases macrophage-mediated clearance and increases delivery to SIRPA-expressing lung carcinoma tumors. *mol Ther Methods Clin Dev*. 2016;3:16080. doi:10.1038/mtm.2016.80
73. Jalil AAR, Tobin MP, Discher DE. Suppressing or enhancing macrophage engulfment through the use of CD47 and related peptides. *Bioconjug Chem*. 2022;33(11):1989–1995. doi:10.1021/acs.bioconjchem.2c00019
74. Cipolla MJ. The Cerebral Circulation. *Colloq Ser Integr Syst Physiol From mol to Funct*. 2009;1(1):1–59. doi:10.4199/C00005ED1V01Y200912ISP002
75. Cataldi M, Vigliotti C, Mosca T, Cammarota MR, Capone D. Emerging role of the spleen in the pharmacokinetics of monoclonal antibodies, nanoparticles and exosomes. *Int J mol Sci*. 2017;18(6):1249. doi:10.3390/ijms18061249
76. Hoffman AS. The origins and evolution of "controlled" drug delivery systems. *J Control Release*. 2008;132(3):153–163. doi:10.1016/j.jconrel.2008.08.012
77. Hashizume H, Baluk P, Morikawa S, et al. Openings between defective endothelial cells explain tumor vessel leakiness. *Am J Pathol*. 2000;156(4):1363–1380. doi:10.1016/S0002-9440(10)65006-7
78. O'Brien K, Breyne K, Ughetto S, Laurent LC, Breakefield XO. RNA delivery by extracellular vesicles in mammalian cells and its applications. *Nat Rev mol Cell Biol*. 2020;21(10):585–606. doi:10.1038/s41580-020-0251-y
79. Roerig J, Mitrach F, Schmid M, et al. Synergistic siRNA loading of extracellular vesicles enables functional delivery into cells. *Small Method*. 2022;6(12). doi:10.1002/smtd.202201001
80. Faruqu FN, Xu L, Al-Jamal KT. Preparation of exosomes for siRNA delivery to cancer cells. *JoVE*. 2018;2018(142):e58814. doi:10.3791/58814
81. Reinhart WH, Chien S. Red cell rheology in stomatocyte-echinocyte transformation: roles of cell geometry and cell shape. *Blood*. 1986;67(4):1110–1118. doi:10.1182/blood.v67.4.1110.1110
82. Kooijmans SAA, Stremersch S, Braeckmans K, et al. Electroporation-induced siRNA precipitation obscures the efficiency of siRNA loading into extracellular vesicles. *J Control Release*. 2013;172(1):229–238. doi:10.1016/j.jconrel.2013.08.014
83. Li C, Wang J, Wang Y, et al. Recent progress in drug delivery. *Acta Pharm Sin B*. 2019;9(6):1145–1162. doi:10.1016/j.apsb.2019.08.003
84. Murphy DE, de Jong OG, Evers MJW, Nurazizah M, Schiffelers RM, Vader P. Natural or synthetic RNA delivery: a stoichiometric comparison of extracellular vesicles and synthetic nanoparticles. *Nano Lett*. 2021;21(4):1888–1895. doi:10.1021/acs.nanolett.1c00094
85. Kuvichkin VV. Investigation of ternary complexes: DNA-phosphatidylcholine liposomes-mg2+ by freeze-fracture method and their role in the formation of some cell structures. *J Membr Biol*. 2009;231(1):29–34. doi:10.1007/S00232-009-9201-5/FIGURES/5
86. Toub N, Maksimenko A, Maccario J, Malvy C, Fattal E, Couvreur P. Efficacy of siRNA nanocapsules targeted against the EWS-Fli1 oncogene in Ewing sarcoma efficacy of siRNA nanocapsules targeted against the EWS – fli1 oncogene in Ewing sarcoma. *Pharm Res*. 2006;23:892–900. doi:10.1007/s11095-006-9901-9
87. Zhou X, Miao Y, Wang Y, et al. Tumour-derived extracellular vesicle membrane hybrid lipid nanovesicles enhance siRNA delivery by tumour-homing and intracellular freeway transportation. *J Extracell Vesicles*. 2022;11(3). doi:10.1002/jev2.12198
88. Szatanek R, Baj-Krzyworzeka M, Zimoch J, Lekka M, Siedlar M, Baran J. The methods of choice for extracellular vesicles (EVs) characterization. *Int J mol Sci*. 2017;18(6):1153. doi:10.3390/ijms18061153
89. Chen C, Zong S, Wang Z, et al. Imaging and intracellular tracking of cancer-derived exosomes using single-molecule localization-based super-resolution microscope. *ACS Appl Mater Interfaces*. 2016;8(39):25825–25833. doi:10.1021/acsami.6b09442
90. Ter-Ovanesyan D, Kowal EJK, Regev A, Church GM, Cocucci E. Imaging of isolated extracellular vesicles using fluorescence microscopy. In: *Buchwald's Atlas of Metabolic & Bariatric Surgical Techniques and Procedures. Vol 1660*. Elsevier; 2017:233–241. doi:10.1007/978-1-4939-7253-1_19
91. Blau R, Epshtein Y, Pisarevsky E, et al. Image-guided surgery using near-infrared Turn-ON fluorescent nanoprobes for precise detection of tumor margins. *Theranostics*. 2018;8(13):3437–3460. doi:10.7150/thno.23853
92. Phua KKL, Boczkowski D, Dannull J, Pruitt S, Leong KW, Nair SK. Whole blood cells loaded with messenger RNA as an anti-tumor vaccine. *Adv Healthc Mater*. 2014;3(6):837–842. doi:10.1002/adhm.201300512
93. Xu C, Ju D, Zhang X. Cell membrane-derived vesicle: a novel vehicle for cancer immunotherapy. *Front Immunol*. 2022;13:3573. doi:10.3389/FIMMU.2022.923598/BIBTEX
94. Lejeune A, Moorjani M, Gicquaud C, Lacroix J, Poyet P, Gaudreault CR. Nanocerythrosome, a new derivative of erythrocyte ghost: preparation and antineoplastic potential as drug carrier for daunorubicin. *Anticancer Res*. 1994;14(3 A):915–919.
95. Lejeune A, Poyet P, C.-Gaudreault R, Gicquaud C. Nanoerythrosomes, a new derivative of erythrocyte ghost: III. Is phagocytosis involved in the mechanism of action? *Anticancer Res*. 1997;17(5 A):3599–3603.
96. Moorjani M, Lejeune A, Gicquaud C, Lacroix J, Poyet P, Gaudreault RC. Nanocerythrosomes, a new derivative of erythrocyte ghost II: identification of the mechanism of action. *Anticancer Res*. 1996;16(5A):2831–2836.
97. Lassailly F, Griessinger E, Bonnet D. "Microenvironmental contaminations" induced by fluorescent lipophilic dyes used for noninvasive in vitro and in vivo cell tracking. *Blood*. 2010;115(26):5347–5354. doi:10.1182/BLOOD-2009-05-224030
98. Joshi BS, de Beer MA, Giepmans BNG, Zuhorn IS. Endocytosis of extracellular vesicles and release of their cargo from endosomes. *ACS Nano*. 2020;14(4):4444–4455. doi:10.1021/acsnano.9b10033
99. Ciana A, Achilli C, Gaur A, Minetti G. Membrane remodelling and vesicle formation during ageing of human red blood cells. *Cell Physiol Biochem*. 2017;42(3):1127–1138. doi:10.1159/000478768
100. Frick M, Bright NA, Riento K, Bray A, Merrified C, Nichols BJ. Coassembly of flotillins induces formation of membrane microdomains, membrane curvature, and vesicle budding. *Curr Biol*. 2007;17(13):1151–1156. doi:10.1016/j.cub.2007.05.078
101. O'Loughlin AJ, Mäger I, de Jong OG, et al. Functional delivery of lipid-conjugated siRNA by extracellular vesicles. *Mol Ther*. 2017;25(7):1580–1587. doi:10.1016/j.ymthe.2017.03.021
102. Zeng Y, Yi R, Cullen BR. MicroRNAs and small interfering RNAs can inhibit mRNA expression by similar mechanisms. *Proc Natl Acad Sci U S A*. 2003;100(17):9779–9784. doi:10.1073/pnas.1630797100

103. Li S-D, Chono S, Huang L. Efficient gene silencing in metastatic tumor by siRNA formulated in surface-modified nanoparticles. *J Control Release*. 2008;126(1):77–84. doi:10.1016/j.jconrel.2007.11.002
104. Yhee JY, Lee SJ, Lee S, et al. Tumor-targeting transferrin nanoparticles for systemic polymerized siRNA delivery in tumor-bearing mice. *Bioconjug Chem*. 2013;24(11):1850–1860. doi:10.1021/bc400226b
105. Reddy TL, Garikapati KR, Reddy SG, et al. Simultaneous delivery of Paclitaxel and Bcl-2 siRNA via pH-Sensitive liposomal nanocarrier for the synergistic treatment of melanoma. *Sci Rep*. 2016;6(1):35223. doi:10.1038/srep35223
106. Ehexige E, Bao M, Bazarjav P, et al. Silencing of STAT3 via peptidomimetic LNP-mediated systemic delivery of RNAi downregulates PD-L1 and inhibits melanoma growth. *Biomolecules*. 2020;10(2):1–13. doi:10.3390/biom10020285
107. Maeda H. Toward a full understanding of the EPR effect in primary and metastatic tumors as well as issues related to its heterogeneity. *Adv Drug Deliv Rev*. 2015;91:3–6. doi:10.1016/j.addr.2015.01.002
108. Danhier F. To exploit the tumor microenvironment: since the EPR effect fails in the clinic, what is the future of nanomedicine? *J Control Release*. 2016;244:108–121. doi:10.1016/j.jconrel.2016.11.015
109. Zang G, Gustafsson K, Jamalpour M, Hong JW, Genové G, Welsh M. Vascular dysfunction and increased metastasis of B16F10 melanomas in Shb deficient mice as compared with their wild type counterparts. *BMC Cancer*. 2015;15(1):1–11. doi:10.1186/s12885-015-1269-y
110. Leporatti S. Thinking about Enhanced Permeability and Retention Effect (EPR). *J Pers Med*. 2022;12(8):12–14. doi:10.3390/jpm12081259
111. Hofmann M, Guschel M, Bernd A, et al. Lowering of tumor interstitial fluid pressure reduces tumor cell proliferation in a xenograft tumor model. *Neoplasia*. 2006;8(2):89–95. doi:10.1593/neo.05469
112. Alexandrakis G, Brown EB, Tong RT, et al. Two-photon fluorescence correlation microscopy reveals the two-phase nature of transport in tumors. *Nat Med*. 2004;10(2):203–207. doi:10.1038/nm981
113. Munir MU. Nanomedicine penetration to tumor: challenges, and advanced strategies to tackle this issue. *Cancers*. 2022;14(12):2904. doi:10.3390/cancers14122904
114. Black KCL, Wang Y, Luehmann HP, et al. Radioactive 198 au-doped nanostructures with different shapes for in vivo analyses of their biodistribution, tumor uptake, and intratumoral distribution. *ACS Nano*. 2014;8(5):4385–4394. doi:10.1021/nn406258m
115. Zhang YR, Lin R, Li HJ, ling HW, Du JZ, Wang J. Strategies to improve tumor penetration of nanomedicines through nanoparticle design. *Wiley Interdiscip Rev Nanomed Nanobiotech*. 2019;11(1):1–12. doi:10.1002/wnan.1519
116. Cabral H, Matsumoto Y, Mizuno K, et al. Accumulation of sub-100 nm polymeric micelles in poorly permeable tumours depends on size. *Nat Nanotechnol*. 2011;6(12):815–823. doi:10.1038/nnano.2011.166
117. Shukla S, Eber FJ, Nagarajan AS, et al. The impact of aspect ratio on the biodistribution and tumor homing of rigid soft-matter nanorods. *Adv Healthc Mater*. 2015;4(6):874–882. doi:10.1002/adhm.201400641
118. Wen Y, Bai H, Zhu J, Song X, Tang G, Li J. A supramolecular platform for controlling and optimizing molecular architectures of siRNA targeted delivery vehicles. *Sci Adv*. 2020;6(31). doi:10.1126/sciadv.abc2148
119. Jiang T, Qiao Y, Ruan W, et al. Cation-free siRNA micelles as effective drug delivery platform and potent RNAi nanomedicines for glioblastoma therapy. *Adv Mater*. 2021;33(45):1–10. doi:10.1002/adma.202104779
120. Constantinescu I, Levin E, Gyongyossy-Issa M. Liposomes and blood cells: a flow cytometric study. *Artif Cells, Blood Substitutes, Biotechnol*. 2003;31(4):395–424. doi:10.1081/BIO-120025410
121. Zhu K, Xu Y, Zhong R, et al. Hybrid liposome–erythrocyte drug delivery system for tumor therapy with enhanced targeting and blood circulation. *Regen Biomater*. 2023:10. doi:10.1093/rb/rbad045
122. Pan DC, Myerson JW, Brenner JS, et al. nanoparticle properties modulate their attachment and effect on carrier red blood cells. *Sci Rep*. 2018;8(1):1–12. doi:10.1038/s41598-018-19897-8
123. Lenders V, Escudero R, Koutsoumpou X, et al. Modularity of RBC hitchhiking with polymeric nanoparticles: testing the limits of non-covalent adsorption. *J Nanobiotechnology*. 2022;20(1):1–12. doi:10.1186/s12951-022-01544-0
124. Chaudhary R, Katharia R. Oxidative injury as contributory factor for red cells storage lesion during twenty eight days of storage. *Blood Transfus*. 2012;10(1):59–62. doi:10.2450/2011.0107-10
125. Bebesi T, Kitka D, Gaál A, et al. Storage conditions determine the characteristics of red blood cell derived extracellular vesicles. *Sci Rep*. 2022;12(1):1–13. doi:10.1038/s41598-022-04915-7
126. Ballas S, Burka E. Protease activity in the human erythrocyte: localization to the cell membrane. *Blood*. 1979;53(5):875–882. doi:10.1182/blood.V53.5.875.875
127. Sae-Lee W, McCafferty CL, Verbeke EJ, et al. The protein organization of a red blood cell. *Cell Rep*. 2022;40(3):111103. doi:10.1016/J.CELREP.2022.111103
128. Ranjbar S, Zhong X, Manautou J, Lu X. A holistic analysis of the intrinsic and delivery-mediated toxicity of siRNA therapeutics. *Adv Drug Deliv Rev*. 2023;201:1–38. doi:10.1016/j.addr.2023.115052

**International Journal of Nanomedicine**

**Dovepress**
Taylor & Francis Group

**Publish your work in this journal**

The International Journal of Nanomedicine is an international, peer-reviewed journal focusing on the application of nanotechnology in diagnostics, therapeutics, and drug delivery systems throughout the biomedical field. This journal is indexed on PubMed Central, MedLine, CAS, SciSearch®, Current Contents®/Clinical Medicine, Journal Citation Reports/Science Edition, EMBase, Scopus and the Elsevier Bibliographic databases. The manuscript management system is completely online and includes a very quick and fair peer-review system, which is all easy to use. Visit http://www.dovepress.com/testimonials.php to read real quotes from published authors.

**Submit your manuscript here:** https://www.dovepress.com/international-journal-of-nanomedicine-journal

# Chapter 7

# Novel Vector for Efficient siRNA Delivery to Lymphoblasts and Melanoma based on Genipin-Spermine Nanocarriers Protected with Hybrid Erythrocyte Membrane Coating

In this work, on the basis of the findings of Chapters 5 and 6, we aimed to develop EMV-camouflaged genipin-spermine-glycine polymers for siRNA delivery. As camouflaging is a widely used approach to improve the efficiency of nanoparticles and confer interesting properties [293], erythrocyte membranes are among the most desirable coating agents because of their stealth ability (due to the presence of CD47), unique mechanical properties and easy isolation [294]. From the results of Chapter 5, we selected the best performing polymer from the developed set, whose initial molar fraction in the reaction batch was genipin-spermine-glycine = 1:5:10, which was termed G10S5. The process is outlined in **Figure 14**. We therefore aimed to further improve its transfection efficiency by camouflaging the nanoparticles with erythrocyte membranes. This proved to be difficult because of the mechanical properties of the two materials. As siRNA complexation was confirmed to be a prerequisite for successful coating, owing to the electrostatic repulsion between the erythrocyte glycocalyx and the negatively charged polyplex, doping erythrocyte membranes with DPPC/DSPE-PEG2000 (9:1 ratio) proved to be instrumental in conferring the resulting membrane with suitable properties for camouflaging G10S5. Hybrid membranes, i.e., erythrocytes doped with 10% DPPC/DSPE-PEG2000 phospholipids, were characterized via conventional TEM, cryo-TEM and AFM, and the fusion of the two parental membranes was confirmed via Forster Resonance Energy Transfer and confocal fluorescence microscopy. The successful camouflaging of G10S5-siRNA polyplexes was confirmed via the solvatochromic effect: the intrinsic fluorescence of G10S5 was used to evaluate the best phosphate-to-nitrogen ratio (and, therefore, the zeta potential) with the highest hypsochromic potential and a blueshift in the fluorescence peak emission, i.e., the most complete coating. Furthermore, the resulting nanoparticles, termed hybrid-G10S5-siRNAs, were characterized via cryo-TEM and AFM and appeared to be widely dispersed in terms of size and core–shell structure. Moreover, the self-fluorescence of G10S5 was used to investigate the uptake efficiency and mechanism in the b16F10 murine melanoma cell line in the presence of the endocytosis inhibitors genistein, imipramine and chlorpromazine. While naked G10S5 appears to follow clathrine-mediated endocytosis, hybrid-G10S5 preferentially follows pinocytosis and direct-membrane fusion mechanisms, similar to parental erythrocyte–membrane vesicles [208]. Moreover, we tested the capability of successfully delivering and silencing a model gene that we previously used,

tdTomato, which encodes a fluorescent orange protein at doses of 5 and 10 picomoles/50,000 cells. In murine melanoma cells expressing tdTomato, hybrid-G10S5-siRNA outperformed naked G10S5 at 5 and 10 picomoles in terms of protein knockdown, as indicated by fluorescence assisted cell sorting (FACS), and had comparable results to a commercial cationic polymer (interferin). Interestingly, the q-RT–PCR results for tdTomato mRNA expression revealed a different story at 5 picomoles, i.e., that, at extremely low concentrations of siRNA, in B16F10 cells, translation repression is preferred over RISC-driven silencing. Finally, we assessed the ability of hybrid-G10S5-siRNA to deliver the payload to lymphoblastoid cells, which are known to be extremely difficult to transfect with commercial agents [307], [334], [335]. Our target was FARS-A, the A-subunit (and the catalytic subunit) of FARS, an aminoacyl tRNA synthetase, and a potential therapeutic target for genetic diseases[336]. Surprisingly, hybrid-G10S5-siRNA almost completely knocked down FARS-A at a dose of 20 picomoles/200,000 cells, greatly outperforming naked G10S5.

Taken together, these data show how camouflaging with a biomimetic agent dramatically improves the properties of a polymeric nanoparticle, combining the advantages of both models.

In this paper, **Hypothesis 6 and Hypothesis 7 were assayed and confirmed.**

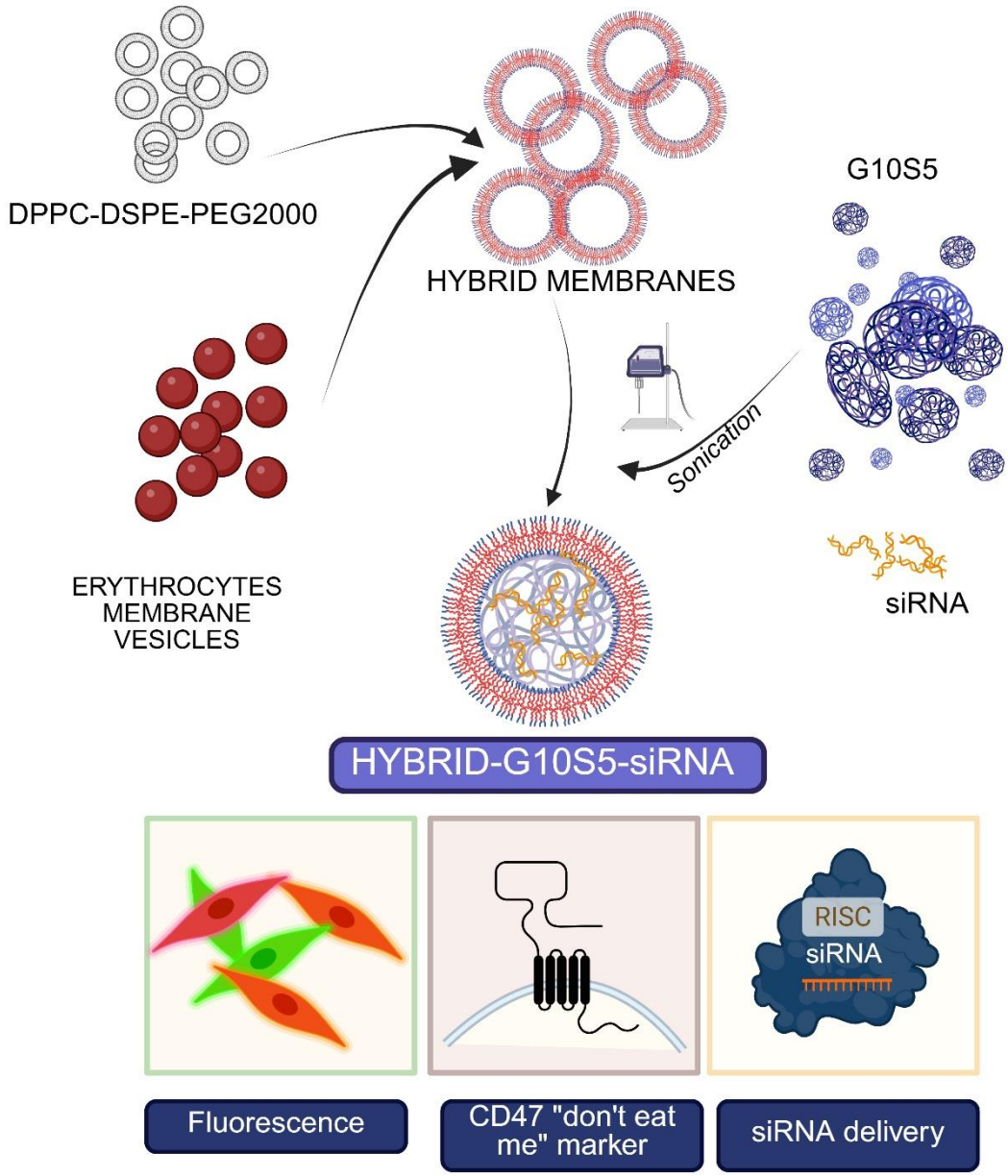



Figure 14 Graphical Abstract of Chapter 7.

Biomaterials Advances 180 (2026) 214537

Contents lists available at ScienceDirect

Biomaterials Advances

journal homepage: www.journals.elsevier.com/materials-science-and-engineering-c

# Novel vector for efficient siRNA delivery to lymphoblasts and melanoma based on genipin-spermine nanocarriers protected with hybrid erythrocyte membrane coating

Giulia Della Pelle [a,b], Boštjan Markelc [c], Urša Čerček [d], Urška Živič [b], Mia Coupard [e], Jernej Šribar [f], Igor Križaj [f], Muhammad Shahid Arshad [a], Tim Božič [c], Lea Gazvoda [g], Boris Rogelj [d], Nina Kostevšek [a,b,*]

[a] Department for Nanostructured Materials, Jožef Stefan Institute, 1000, Ljubljana, Slovenia
[b] Jožef Stefan International Postgraduate School, 1000, Ljubljana, Slovenia
[c] Department of Experimental Oncology, Institute of Oncology Ljubljana, 1000, Ljubljana, Slovenia
[d] Department of Biotechnology, Jožef Stefan Institute, 1000, Ljubljana, Slovenia
[e] Faculty of Health, Medicine and Life Sciences (FHML), Maastricht University, 6211, LH, Maastricht, Netherlands
[f] Department of Molecular and Biomedical Sciences, Jožef Stefan Institute, 1000, Ljubljana, Slovenia
[g] Advanced Materials Department, Jožef Stefan Institute, 1000, Ljubljana, Slovenia

ARTICLE INFO

*Keywords:*
RNAi
Biomimetic
Camouflaging
Genipin
Erythrocytes

ABSTRACT

Efficient delivery of small interfering RNA (siRNA) remains a significant challenge in gene therapy because of the instability, poor cellular uptake, and immunogenicity of the carriers. In this study, we developed a hybrid delivery system combining genipin-spermine-glycine nanoparticles (G10S5) with erythrocyte membrane vesicles (EMVs) doped with DPPC and DSPE-PEG2000. G10S5 nanoparticles offer robust siRNA complexation and biocompatibility but may suffer from rapid clearance and immune detection. By camouflaging G10S5-siRNA polyplexes with hybrid EMVs, we aimed to increase their cell uptake and delivery efficiency. Physicochemical characterization via DLS, FTIR, TEM, cryo-EM, and AFM confirmed successful coating and favorable nanoscale morphology. Solvatochromic fluorescence analysis via the fluorescence of G10S5 indicated efficient coating. The optimized formulations at a phosphate-to-nitrogen (P/N) ratio of 1:12 exhibited excellent RNase A resistance, strong siRNA binding, and storage stability. Compared with uncoated controls, in vitro assays demonstrated significantly enhanced cellular uptake of hybrid-coated G10S5-siRNA, with distinct internalization mechanisms. Gene silencing efficiency was validated by targeting tdTomato in tdTomato-expressing B16F10 cells, which showed effective knockdown with minimal cytotoxicity. Further validation was achieved in lymphoblastoid cell lines by targeting FARSA that has recently been implicated in C9orf72 mutation mechanism in lymphoblastoid lines. Our findings establish hybrid membrane-camouflaged G10S5 nanoparticles as promising siRNA delivery platforms, addressing the limitations of conventional carriers by leveraging their natural membrane properties and polymeric versatility. This strategy opens new avenues for the development of biomimetic, nonviral nucleic acid therapeutics.

## 1. Introduction

Gene silencing therapy has emerged as a promising approach for the treatment of various genetic disorders. The successful application of this technique depends on the effective delivery of therapeutic nucleic acids, such as small interfering RNA (siRNA), to target cells. However, the delivery of naked siRNA presents several challenges due to its susceptibility to degradation by serum nucleases, rapid renal clearance, and poor cellular uptake due to its large size and negative charge [1]. Furthermore, small interfering RNA (siRNA) molecules, such as double-stranded RNA, can trigger immune responses, leading to the production of proinflammatory cytokines, such as type I interferons (IFN-α and IFN-β) and interleukin-6 (IL-6) [2]. Additionally, siRNAs are large, lipid-insoluble molecules that rarely diffuse spontaneously within double

* Corresponding author at: Department for Nanostructured Materials, Jožef Stefan Institute, 1000, Ljubljana, Slovenia.
*E-mail address:* nina.kostevsek@ijs.si (N. Kostevšek).

https://doi.org/10.1016/j.bioadv.2025.214537
Received 7 August 2025; Received in revised form 23 September 2025; Accepted 29 September 2025
Available online 3 October 2025
2772-9508/© 2025 The Author(s). Published by Elsevier B.V. This is an open access article under the CC BY-NC-ND license (http://creativecommons.org/licenses/by-nc-nd/4.0/).

layers; humans lack the well-characterized dsRNA transported, SID I, which is present in *Caenorhabditis elegans*, the model animal for RNA interference characterization [3]. On the other hand, in mammals and human tissues, RNAs are present in every niche, rapidly cleaving dsRNA [4]. Hence, the development of effective delivery systems is crucial for enhancing the stability, targeting ability, and biocompatibility of siRNA-based therapies.

Several siRNA delivery platforms have been developed, including synthetic nanoparticles (NPs) and viral vectors. While viral vectors demonstrate high and stable transfection efficiency, their clinical application is limited by high costs and the risk of insertional mutagenesis, which may lead to unpredictable genetic alterations [5]. As alternatives, nonviral systems such as lipid-based nanoparticles (LNPs), polymer-based nanoparticles (PNPs), inorganic nanoparticles (INPs), cell-penetrating peptides (CPPs), liposomes, carbon nanotubes (CNTs), and mesoporous silica nanoparticles have been explored [6–8]. Among these, cationic polymer nanoparticles are widely used for siRNA delivery because of their strong ability to complex with negatively charged nucleic acids.

Genipin-based cationic polymer nanoparticles (G10S5 NPs) were developed as a safe and efficient siRNA delivery system [9]. These nanoparticles were synthesized via the use of spermine, a polyamine that acts as a stabilizer, and genipin, a natural crosslinker derived from the fruit of *Gardenia jasminoides*. Glycine was incorporated to control crosslinking, yielding the optimized nanoparticle formulation. Within the set that we prepared, the genipin-spermine-glycine combination that yielded the best nanoparticle, in terms of biocompatibility and transfection efficiency, was genipin:1:spermine:5:glycine:10, termed "G10S5". This formulation was previously found to generate optimal NPs in terms of size, ionizability at acidic pH and zeta potential. G10S5 NPs offer several advantages, including easy and undemanding synthesis under mild conditions, with little batch-to-batch variation, their natural origin, self-fluorescence in a wide wavelength range, strong nucleic acid complexation ability, and favorable biocompatibility.

In this study, we sought to improve the biocompatibility and stability of G10S5 NPs by camouflaging them with red blood cell (erythrocyte) membranes doped with dipalmitoylphosphatidylcholine (DPPC)/1,2-distearoyl-sn-glycero-3-phosphorylethanolamine (DSPE)-PEG2000. Indeed, camouflaging nanoparticles with a biomimetic agent, which is usually generated from the membrane of cells, has become a thriving field of research [10], and red blood cells, owing to their abundance, easy processing and interesting membrane properties, are among the most common coating agents [11].

Erythrocyte membranes have been used extensively as coatings to enhance the biocompatibility of various nanoparticles by cloaking them and conferring interesting properties [12,13], such as prolonged circulation time, immune system masking effects, and stable encapsulation. In some cases, the addition of external phospholipids might be needed to appropriately tune the membrane properties. The feasibility of doping their membrane composition by incorporating external phospholipids has already been demonstrated [14]. In addition to being used to coat solid, metallic or mesoporous silica nanoparticles [12,15], erythrocyte membranes have also been used in the literature in preparations involving poly(lactic-*co*-glycolycolic acid) (PLGA) [16], a Food and Drug Administration (FDA)-approved block copolymer. For example, to coat PLGA/Arsenic Trioxide nanoparticles via sonication to force the membrane to rearrange around the nanoparticles [17], a similar approach was applied when PLGA was complexed with curcumin [18]. Furthermore, erythrocyte membranes have also been used to coat gelatin microcapsules for antibiotic target release purposes, confirming again a lower clearance from phagocytic cells and prolonged circulation time [19].

The elasticity of the nanoparticles affects membrane wrapping, and vice versa [20]; overall, the interplay of the mechanical properties of the camouflaging material and the material to be camouflaged has been poorly investigated [21]. To date, successful camouflaging has been limited to relatively rigid nanoparticles, such as mesoporous silica [22] and metallic nanoparticles, or block copolymers. The rigidity of PLGA nanoparticles, despite being highly variable depending on the ratio of lactic acid to glycolic acid and the molecular weight of the units, appears to be relatively high compared to that of other nanoparticle systems used for drug delivery, i.e., liposomes. For example, a value for the Young modulus of 2.0 ± 0.43 GPa was reported in [23]; a similar value, measured via atomic force microscopy (2.8 ± 0.4 G Pa), was reported in [24]. Conversely, the Young's modulus of a common liposomal formulation, with a great degree of variation with respect to unsaturation, the head-to-tail ratio in phospholipids, and the presence of cholesterol, is on the order of MPa, which is many times lower than that of the material it will cloak [25,26]. However, the size of the analyzed system, whether if the bilayer is deposited on a solid surface (supported) or not, the liposome size, the AFM substrate used, and, in the same technique, the indentation depth of the measurement greatly influence the measured value for the Young modulus, leading to extremely unreliable and variable values—from 110 MPa for mica-deposited liposomes [27] to 1.1 for kPA for hyaluronic acid-loaded DPPC liposomes [28] to approximately 300 kPa for cholesterol-doped DPPC liposomes [29]. Within the realm of phospholipids, an important effect on the mechanical properties also comes from the presence of polyethylene glycol (PEG), which is conjugated with 1,2-distearoyl-sn-glycero-3-phosphorylanolamine (DSPE-PEG2000), whereas data regarding the Young's modulus are not available; to the best of our knowledge, for a system containing DPPC and DSPE-PEG2000, some information can be inferred from the bending modulus of giant unilamellar vesicles [30]. Indeed, when the molar ratio of DSPE-PEG increases (regardless of the molecular weight of the latter), the bending modulus increases as well, as reported elsewhere [31]. According to fluorophore release studies, the addition of DSPE-PEG to DPPC membranes slightly slows the leakage of calcein and carboxyfluorescein [32,33], indicating increased membrane instability.

The erythrocyte membrane is also less rigid than that of PLGA: it lies within the range of kPa, with a great degree of variation according to the technique (AFM-force indentation, micropipette aspiration, optical tweezers), sample preparation (i.e., greater or lower loss of proteins influencing the Young's modulus), and surface geometry (affected by nanoparticle size, i.e., if the measurement is carried out on nano-erythrosomes or on the whole ghost). The reliable value for erythrocyte ghosts, as shown by [34], is 2.5–10 kPa [34,35], whereas for whole erythrocytes, which still contain hemoglobin and an intact cytoskeleton, it is 2.54 ± 0.6 mPa [36].

To the best of our knowledge, an erythrocyte membrane coating has not yet been successfully applied to soft, genipin-based polymer nanoparticles. Therefore, this study explores the feasibility of using DPPC-doped EMV coatings for G10S5 NP-based siRNA delivery. By integrating G10S5 NPs with erythrocyte membrane coatings, we aim to achieve a synergistic effect, combining the structural advantages of G10S5 NPs with the immune evasion properties of EMVs.

To evaluate the effectiveness of this hybrid system, we performed a series of comparative analyses, including physicochemical characterization, morphology investigations via four different microscopic techniques, stability studies, cytotoxicity assays, internalization pathway determination and in vitro gene silencing assays. These experiments aimed to assess whether the hybrid system provides superior siRNA protection, cellular uptake, and gene silencing efficiency compared with standalone G10S5 NPs.

Gene silencing efficiency was validated on two different cell lines; a) fluorescent protein tdTomato-expressing murine melanoma B16F10 cells to prove successful therapeutic potential in cancer treatment and b) lymphoblastoid cell lines by targeting FARSA, which has recently been implicated in C9orf72 mutation mechanism in lymphoblastoid lines and is the main genetic cause of amyotrophic lateral sclerosis and frontotemporal dementia. Importantly, lymphoblastoid cells, derived from Eipstein–Barr immortalized lymphocytes, are known to be difficult to transfect via nonviral carriers, similar to parental lymphocytes, which

are widely used for CAR-T-cell therapy [37,38]. They are suspension cells with poorly active endocytic pathways and a low affinity for polycations, such as PEI and Lipofectamine, due to the lack of proteoglycans in their outer shell [39,40]; the same can be said of all hematopoietic cell lines and leukemia-like immortalized cells [41]. While electroporation has some success and is prone to degree of optimization in terms of buffer composition, it still affects viability [42]. To the best of our knowledge, successful siRNA transfection via chemical, polymeric and nanoparticle methods has rarely been achieved in lymphocyte-like cells [43]. Therefore, the development of an efficient and safe transfection system for these "difficult to transfect" cells would be of great importance for the advancement of current state-of-the-art protocols.

Overall, this study presents a novel approach to siRNA delivery by combining genipin-based polymer nanoparticles with DPPC-doped erythrocyte membrane coatings. By addressing the limitations of existing delivery systems, this hybrid approach holds promise for enhanced nucleic acid delivery and gene silencing efficacy.

## 2. Materials and methods

### 2.1. Chemicals and materials

All the chemicals (glycine, genipin, and spermine-HCl) used to prepare the G10S5 polymer were purchased from Sigma Aldrich, as were the PBS tablets. The latter were dissolved in DEPC (di-ethyl-pyrocarbonate) Milli-Q water at a final concentration of 10 mM phosphate buffer, 137 mM sodium chloride, and 2.7 mM potassium chloride (from now on, 1× PBS). Potassium bromide for FTIR analysis was obtained from Honeywell Fluka. Anti-tdTomato siRNA was purchased from IDT Genomics from Custom Silencer™ ThermoFisher design (the sequence has already been published elsewhere [44]), whereas anti-FARSA siRNA was purchased from a predesigned ThermoFisher sequence (assay number S5029; catalog number 4392421) and was subsequently purchased from IDT Genomics. Scramble siRNA, a validated design from the Mission® series, is a universal negative control purchased from Merck. Erythrocytes were obtained from the Ljubljana Transfusion Center (see the Ethical Approval section). Dipalmytoil-phosphatidylcholine (DPPC) and 1,2-distearoyl-sn-glycero-3-phosphoethanolamine-N-[amino(polyethylene glycol)-2000] (DSPE-PEG-2000) were purchased from Avanti Polar (USA) as a 25 mg/ml chloroform suspension and as a powder from Lipoid Kosmetic (Switzerland) and stored at -20 °C. Endocytosis inhibitors (chlorpromazine, imipramine and genistein) were purchased from Sigma Aldrich, dissolved in DMSO at a final concentration of 30 mg/ml and stored at 4 °C.

### 2.2. Genipin-polyamine nanoparticle (GP NP) preparation

The preparation of the genipin-spermine-glycine nanosized polymer followed the same procedure as in [9]. Briefly, glycine, spermine and genistein were added to PBS buffer, pH 7.4, to a final molar ratio of 10 and 5, respectively, with respect to genipin. The final molar concentration of genipin was 0.5 M in a total of 300 µl. The reaction was carried out in excess of oxygen for a total of 36 h at 25 °C under gentle shaking. Afterwards, the unreacted spermine and glycine were removed from the suspension via size-exclusion chromatography (Sephadex G50 elution columns, Cytiva), and 1 ml was eluted with DEPC water; the nanoparticle suspension was subsequently collected as fractions 6 and 7. Finally, the samples were subjected to freeze drying with a Martin Christ table-top freeze dryer and stored at room temperature. Before use, the powder was resuspended in PBS, pH 7.4.

### 2.3. Complexation of G10S5 with siRNA

TdTomato or FARSA siRNA was mixed at various phosphate-to-nitrogen molar ratios with G10S5 NPs, vortexed for 10 s, and incubated for at least half an hour at room temperature in sterile, filtered, autoclaved DEPC-PBS (pH 7.4). The total nitrogen amine content was determined via a ninhydrin assay, as described previously [9]. The free siRNA content was measured via an RNA QuantiFluor kit (Promega E3310) according to the manufacturer's specifications.

### 2.4. Preparation of coatings

#### 2.4.1. Liposome preparation

The liposome suspension was prepared via the thin film hydration method, as described in [45]. Briefly, a lipid suspension composed of DPPC/DSPE-PEG2000 at a 9:1 M ratio was dissolved in an excess of chloroform and then dried in a Rotavapor instrument (R-100 equipped with a heating bath, Interface I-100, and vacuum pump V-100; Bunchi, Switzerland) with a water bath temperature of 40 °C for one hour. The stock concentrations were 25 mg/ml for DPPC and 10 mg/ml for DSPE-PEG2000, both in chloroform. Afterwards, the lipid film was rehydrated (60 °C in a water bath for one hour under constant rotation) to a final concentration of 3.8 mg/ml in 1× PBS and stored at 4 °C until further use. For liposome preparation, a diluted stock of 0.24 mg/ml in PBS was briefly sonicated with a Sonics Vibra Cell sonicating finger (10 s) and then extruded via an 800 nm filter on an Avanti Polar Mini Extruder 15 times. Before use, the liposomes were incubated at RT for at least one hour.

#### 2.4.2. Erythrocyte membrane vesicles (EMV) preparation

Frozen human erythrocytes were deprived of hemoglobin via hypotonic shock and incubated with 1 ml of 0.1× PBS in 40 ml of PBS overnight. The suspension was subsequently centrifuged, and the pellet was subsequently resuspended in 4 ml of 1× PBS and further washed 3 times until the supernatant was clear. The suspension was subsequently sonicated for 10 s (Sonics Vibra cell VC-505; pulses: 1 s on, 1 s off; 20 % amplitude) and extruded via an 800 nm filter on an Avanti Polar Mini Extruder 15 times. Before use, the suspension was incubated at RT for at least one hour. The final phospholipid concentration in the EMVs was 0.24 ± 0.01 mg/ml, while the protein concentration was 0.47 ± 0.08 mg/ml.

#### 2.4.3. Hybrid liposomes-EMVs

To generate hybrid membranes that are used for coating G10S5 nanoparticles, the EMV suspension and liposomes are mixed so that the final quantity of external phospholipids is 10 % by mass, i.e., a final concentration of 0.024 mg/ml of DPPC/DSPE-PEG 2000 in EMVs, up to a final volume of 1 ml. The final colloidal suspension was named "doped EMVs". After mixing, the sample was incubated at 37 °C under vigorous shaking for one hour and then extruded via an 800 nm filter.

### 2.5. Coating of G10S5 NPs with liposomes and EMVs

A total of 0.5 mg/ml of nanoparticles, relative to G10S5, was sonicated with a Vibra cell sonicator for 45 s in the presence of 0.25 mg/ml of liposomes or the corresponding amount of EMVs (0.24 mg/ml in phospholipids, 0.45 mg/ml in proteins) and allowed to rest at RT for at least one hour before any use.

### 2.6. Coating of G10S5 NPs with hybrid liposomes-EMVs

To allow a homogenous coating of G10S5-siRNA polyplexes, the latter were dispersed in an undiluted suspension of EV-liposome hybrids up to a final concentration of 0.5 mg/ml and sonicated for 45 s in a Sonics Vibra cell sonicator. The resulting sample was stored at 4 °C until further use.

### 2.7. Labeling with lipid trackers

For labeling purposes, three lipid trackers were used: Vybrant-DiO (ThermoScientific, catalog number V22886), Vybrant-DiD

(ThermoScientific, catalog number V22887), and CM-DiI (V22888). For labeling the liposomes, the dye was added to the suspension directly after rehydration of the thin film (at 1 μM), and the erythrocyte ghosts were incubated with the label of choice for 15 min at 37 °C and 15 min at 4 °C. Afterwards, the excess dye was removed via centrifugation. To study the interaction between liposomes and erythrocyte ghost membranes, the first were labeled with DiI, and the latter was labeled with DiO; on the other hand, for confocal microscopy, DiD was used to label liposomes, and DiO was used to label erythrocyte ghosts.

### 2.8. Characterization

#### 2.8.1. Zeta potential and particle size determination

All dynamic light scattering (DLS) measurements were carried out on an Anton Paar Litesizer equipped with Kallyope built-in software. An Omega cuvette with a volume of 1000–650 μl was used for all the measurements. The final data are reported as the number-weighted data for the polyplexes and the volume-weighted data for the EMVs and hybrid membranes.

#### 2.8.2. Lipid and protein content determination

A Bradford assay was used to evaluate the protein concentration, with bovine serum albumin used as a standard. The Bradford reagent was prepared according to previous methods [46], and the assay-to-sample ratio was 30:1 *v*/v. All measurements were performed in triplicate. The absorbances at 450 and 595 nm were recorded, and a calibration curve was built from their ratio. A Stewart assay was used to quantify the phospholipid content [47] with heart lipid extract (Avanti Polar) used as a standard reference.

#### 2.8.3. Absorbance and fluorescence spectra acquisition

All spectra (Vis-UV and fluorescence) were acquired on a Greiner Bio-One UV-Star™ 96-well Microplates, on a Synergy Microplate (Biotek) reader, or on a Tecan Infinite M1000. For the DiO-DiI FRET effect, the same bandwidths for excitation and emission (8 nm) were used for both dyes. Parameters such as the fluorescence yield and read height were adjusted according to the experimental conditions. DiO-liposomes were prepared by incubating, according to the manufacturer's specifications, 1 μM dye solution for 15 min at 4 °C with 3.8 mg/ml unextruded phospholipid suspension after vigorous vortexing. The phospholipid suspension was subsequently centrifuged, the supernatant containing the unbound dye was removed, and the suspension was processed as described above. Similarly, for DiD-EMVs, 1 ml of 0.24 mg/ml, in terms of phospholipids, of the ghost suspension was incubated with DiD dye and centrifuged, and the excess dye was removed from the supernatant.

#### 2.8.4. Fourier Transform Infrared Spectroscopy (FTIR)

FTIR spectra were recorded using a PerkinElmer Spectrum 400 series to confirm chemical structure of prepared samples and to evaluate the modifications. For all compositions 2 % mixture of samples with KBr was prepared for measurements in powder form. The integration of 20 spectra were recorded from 4000 to 450 $cm^{-1}$ range with a spectral resolution of 4 $cm^{-1}$. Automatic baseline correction was performed using Spectra measurement program, provided by the supplier.

#### 2.8.5. Intercalating dye assay and resistance against RNase A digestion

To assess the stability of the complexation of the polymers with tdTomato siRNA, G10S5/siRNA, at a 1:12 P/N ratio, coated with hybrid membranes and uncoated, were loaded in a 2.5 % agarose gel, pre-stained with Midori Green (Nippon Genetics), and allowed to run for 20 min at 70 V in TAE buffer 1× (pH 8.5, Tris 40 mM, acetic acid 20 mM, and EDTA sodium salt 1 mM). A similar procedure was followed after the incubation of coated and uncoated G10S5 at 1:12 P/N and 1:5 P/N for 4 and 24 h in the presence of 50 μg/ml RNase A; the polyplexes were decomplexed with exposure to 2 mg/ml heparin. The DNA ruler used was a 50 bp DNA ladder (Thermo Fisher Scientific, Waltham, MA, USA).

#### 2.8.6. Conventional transmission electron microscopy

To visualize the ultrastructures of G10S5, EMVs and hybrid membranes via conventional transmission electron microscopy (TEM), a negative stain protocol was used. Briefly, 10 μl of nanoparticle suspension was applied to a copper grid, formvar-coated (Emsdiasum, USA, catalog number FF200-Cu-25), for at least 15 min. Subsequently, the "drop technique" was applied. The grids were washed once on a Milli-Q water drop, gently tapped with filter paper, air dried, and later applied to a drop of UA-Zero (Agar Scientific, United Kingdom) for 45 s. The grids were allowed to air dry for at least two hours before imaging. The samples were subsequently visualized via a JEOL JEM-2100 instrument operating at an accelerating voltage of 200 kV. The samples were imaged at 20,000× to 40,000× magnification.

#### 2.8.7. Cryoelectron microscopy

To prepare the samples for cryoTEM, a Vitrobot Mark IV (Thermo Fisher Scientific, Waltham, MA, USA) was used. Quantifoil® R 2/2 grids (200 mesh, holey carbon; Quantifoil Micro Tools GmbH, Großlöbichau, Germany) were treated with glow discharge for 60 s at 20 mA and positive polarity in an air atmosphere (GloQube® Plus, Quorum, Laughton, UK). The Vitrobot settings were adjusted to 4 °C and 95 % relative humidity, with a 6-s blot time and a blot force of 2. Then, 3 μl of the suspension was added to the grid, blotted, and quickly vitrified in liquid ethane. Finally, we visualized the samples via a 200 kV Glacios microscope (Thermo Fisher Scientific, Waltham, MA, USA).

#### 2.8.8. Atomic Force Microscopy

AFM imaging was performed via a Digital Instruments Dimension 3100 microscope operated in contact mode to characterize the surface morphology of the EMVs, empty hybrid nanoparticles, empty DPPC-DSPE-PEG2000 liposomes, naked G10S5, and G10S5-siRNA complexes (1:12 P/N-coated hybrids). A gold-coated beam-shaped cantilever (ContGD-G-10, Budget Sensors; spring constant: 0.2 N/m, resonance frequency: 13 kHz) was employed for all the scans. Approximately 20 μL of each sample was gently pipetted onto polylysine-coated glass slides (Sigma–Aldrich, P0425), carefully spread using a coverslip, and allowed to adhere at room temperature for 30 min. Prior to AFM scanning, the slides were gently rinsed with Milli-Q water to remove residual PBS salts, which could interfere with image quality. The samples were scanned within two hours after preparation to maintain structural integrity. The raw AFM data were exported and contrast-adjusted via Gwyddion software, whereas the particle heights were quantified via WSxM software.

### 2.9. Cell-based experiments

#### 2.9.1. Red blood cells

Red blood cells were obtained from the Transfusion Center of Ljubljana (ethical approval number 0120-592/2020/7) and belonged to two young anonymous males, a RhD+ blood type, supplemented with CPD-SAGM preservative, 70 % *v*/v hematocrit, accounting for 4 × $10^9$ RBCs per ml.

#### 2.9.2. Cell culture conditions

Murine melanoma cells (B16F10), human colon carcinoma CT26 cell lines were purchased from ATCC (VA, US), the NHLF cell line was purchased from Lonza (Basel, CH), and the B16F10-tdTomato line was a kind gift from Dr. Muriel Golzio (The Institute of Pharmacology and Structural Biology, IPBS-Toulouse). The cells were grown in a humidified 5 % CO2 atmosphere at 37 °C in a cell culture incubator. The Presto Blue reagent (A13261) and Hoechst 33342 solution (62249) were purchased from Thermo Fisher Scientific. NHLF (normal human lung fibroblast) and B16F10 (murine melanoma cell line) cells were cultured as previously reported [9,44]. All the cells were maintained in a humidified atmosphere containing 5 % $CO_2$ at 37 °C. All the labware, including tips and Falcon and Eppendorf tubes, was RNAse/pyrogenase

free, and the buffers were DEPC-treated. Advanced Dulbecco's modified MEM (ADMEM), Advanced Roswell Park Memorial Institute 1640 medium (RPMI-1640), and MCDB 131 media were purchased from Gibco (Thermo Fisher Scientific, VA, US), and FGM™-2 fibroblast growth medium-2 BulletKit™ was purchased from Lonza (Basel, CH). All media were supplemented with GlutaMAX (100×, Gibco) and penicillin–streptomycin (100×, Sigma–Aldrich, Merck, Darmstadt, Germany).

Normal lymphoblastoid cells without a mutation were prepared from patients with segregating C9orf72 mutations as previously described [48]. The cells were cultured in RPMI 1640 (Gibco, Thermo Fisher Scientific, Waltham, Massachusetts, USA) supplemented with 15 % FBS and 100 U/mL penicillin/streptomycin.

#### 2.9.3. Cytotoxicity

The cytotoxicity of camouflaged G10S5 was evaluated in the B16F10 and NHLF cell lines in 96-well plates (VWR). A total of 500 (B16F10) or 1500 (NHLF) cells were seeded and allowed to grow overnight. Increasing concentrations of G10S5, 1:12 P/N with anti-tdTomato siRNA, were added to the cells, with 6 replicates for each condition. The cell survival was subsequently evaluated via a Presto Blue assay 72 h later (A13261), with 10 % *v*/v in each well, and the cells were incubated for 1 h at 37 °C. Finally, the emitted fluorescence was read with a Cytation 1 system (BioTek Instruments, VT, USA). With respect to lymphoblastoid cells, cytotoxicity was established via the Trypan blue assay. Briefly, 200,000 cells were seeded onto 24-well plates. The next day, the polymers were diluted to 1.25 mg/mL in PBS and 0.625 mg/mL with OptiMem (Thermo Fisher Scientific). Polymers were added to the cells at the desired concentrations (6.25, 12.5, 25, 40 and 80 μg/mL) and incubated for 24 or 48 h. After incubation, 0.4 % trypan blue in water was added to the cells, and viability was determined via a Countess 3 automated cell counter. The same settings (focus = 65 and light = 37) were used to estimate the percentage of dead cells. The experiment was repeated three times with two technical replicates. [49].

#### 2.9.4. Cellular uptake of G10S5-siRNA polyplexes and Hybrid-G10S5-siRNA

The uptake of naked and hybrid membrane-camouflaged G10S5, which was complexed 1:12 with scrambled siRNA, was evaluated via fluorescence microscopy, taking advantage of the fluorescence of the polymers in the green and orange channels. A total of 2000 B16F10 cells were seeded in each well of an iBidi removable 12-chamber slide (catalog number 81201) and allowed to grow overnight in standard cell culture conditions. The following day, the cells were preincubated for 20 min in the presence of endocytosis inhibitors (chlorpromazine 20 μM, genistein 100 μM, imipramine 3 μM); afterwards, the cell culture medium was replaced with fresh medium containing a total of 20 picomoles of siRNA, i.e., both naked and camouflaged G10S5, with a final G10S5 concentration of 3.5 μg/ml in 100 μl of medium. The cells were allowed to incubate in the presence of naked medium and camouflaged with G10S5 for 2 h prior to fixation with 4 % paraformaldehyde (15 min at room temperature), after which the nuclei were stained with Hoechst 33342 (3 μg/ml, Thermo Fisher Scientific) and mounted with ProLong Glass Antifade Mountant (Thermo Fisher, P36982); the cover slip (#1.5) was sealed with transparent nail polish. Images were then acquired with an Axio Observer 7 equipped with a Colibri 7 LED light source (UV (385 nm), violet (430 nm), blue (475 nm), green (555 nm), yellow (590 nm), red (630 nm), Far Red (735 nm) and a Hamamatsu Orca Flash 4.0 V3 camera. Emitted light was imaged through the following filters: Filter set 38 HE eGFP shift free (Zeiss), Filter set 43 HE Cy 3 shift free (Zeiss), Filter set 50 Cy 5 shift free (Zeiss) and Filter Set 112 HE LED (Zeiss). Image analysis was carried out with ImageJ for a total of 100 measurements/typology in the green (493/517) and orange (548/561) channels, and the background was subtracted from each image to obtain the corrected total fluorescence (CTCF). The results from the green and orange channels were averaged and used for quantification. The final CTCF values were analyzed via two-way ANOVA on GraphPad 9.0.

#### 2.9.5. siRNA-induced knockdown in murine melanoma

To evaluate the extent of RNA interference elicited by anti-tdTomato siRNA carried out by camouflaged G10S5, we transfected B16F10-TdTomato-positive cells with 5 and 10 picomole doses, corresponding to final concentrations of G10S5 of 0.0005 mg/ml and 0.001 mg/ml, respectively. tdTomato gene expression was assessed via qRT–PCR as previously reported [9]; briefly, total RNA was extracted after 48 h of coincubation (VWR PeqGold total RNA) and quantified with a Take3 plate installed on a Cytation 1 (BioTek Instruments, VT, USA). A Scriptase II kit (Nippon Genetics, LS53) was used to synthesize cDNA at a final concentration of 50 ng/μl. Negative controls for both naked and camouflaged G10S5 contained a scrambled siRNA. q-PCR was carried out on a Quantstudio 3 and 4 system. Power SYBR Green master mix (Applied Biosystems, 4367659) was used for qPCR. The classical 2ddCT method was used for quantification, and 4 technical replicates were used for CT quantification. β-Actin was the calibrator gene of choice. The sequences of primers used were previously reported elsewhere [9]. Additionally, tdTomato fluorescence was evaluated via flow cytometry, for a total of 6 replicates of each experimental condition, using a BD FACSymphony™ A3 Cell Analyzer. The cells were incubated with naked G10S5 (1:5 P/N and 1:12 P/N) or hybrid membrane-coated G10S5 (similarly, 1:5 P/N and 1:12 P/N), while Interferin (Polyplus, Sartorius) was used as a positive control. Furthermore, naked and coated G10S5 cells were also prepared with a scrambled siRNA to function as a negative control for baseline fluorescence caused by the polymer itself. The trypsinized and washed murine melanoma cells were subsequently resuspended in phenol-free DMEM and incubated with 3 μg/ml DAPI to label dead cells. From the live cell population, the percentage of fluorescent cells (i.e., tdTomato fluorescent) and their median fluorescence intensity (MFI) were determined. The MFI was then normalized to that of the negative controls for each analytical group. FlowJo software (BD Biosciences) was used for data analysis.

#### 2.9.6. siRNA-induced knockdown in lymphoblasts

Additionally, to assess gene knockdown in different cell lines, a lymphoblastoid cell line was used; an anti-FARSA (phenylalanyl-tRNA synthetase alpha chain, UniProt Q9Y285) small interfering RNA (siRNA) was used, followed by an ongoing characterization of this cell line [48]. Protein knockdown was assessed via Western blot analysis of the FARSA product after 72 h of incubation with the carriers (20 and 30 picomoles of siRNA). Protein lysates were prepared via RIPA buffer (50 mM Tris-HCl, pH 8.0; 150 mM NaCl; 0.5 mM sodium deoxycholate; 0.1 % SDS; and 1 % Triton X-100) supplemented with protease inhibitors. The samples were mixed with 2× SDS loading buffer containing 200 mM dithiothreitol (DTT) and incubated at 95 °C for 5 min. Equal amounts of protein were separated on 12 % stain-free gels (Bio-Rad, Hercules, CA, USA) at 125 V. Following electrophoresis, the proteins were transferred to nitrocellulose membranes (GE Healthcare, Chicago, IL, USA) via semidry transfer (Bio-Rad). After semidry transfer, the membranes were imaged via the GelDoc System and ImageLab software (Bio-Rad) to obtain the total protein load. The membranes were blocked for 1 h at room temperature with 5 % (*w*/*v*) skim milk in TBS. Primary (FARSA antibody was obtained from Proteintech, USA) and fluorescent secondary (anti-rabbit, StarBright 520) antibody incubations were performed according to the manufacturers' instructions overnight at 4 °C at a 1:1000 dilution for the primary antibody and for two hours at 4 °C for the secondary antibody. Imaging of the fluorescent signal was conducted via the GelDoc System and ImageLab software (Bio-Rad), and densitometric analysis was performed via ImageJ (NIH, Bethesda, MD, USA). The level of FARSA protein was normalized to the whole protein level for each loaded lane, which was obtained via stain-free imaging, as shown in the Supplementary Material (Fig. 10S).

## 3. Results and discussion

### 3.1. Preparation and characterization of the starting material: G10S5 NPs and camouflaging membranes

Genipin, glycine and spermine were allowed to react, as in genipin: spermine:glycine = 1:5:10, for 36 h in excess of oxygen, in PBS 1 × at pH 7.4, and unincorporated molecules were removed via column filtration in water elution. The final suspension, which was freeze-dried, was resuspended at 20 mg/ml, corresponding to 0.181 M R-NHx, as determined by a ninhydrin assay. As a camouflaging material for G10S5 NPs, we chose a) erythrocyte membrane vesicles (EMVs), a biomimetic carrier that we previously used [44,45,50], b) liposomes made of DPPC: DSPE-PEG-2000 at a molar ratio of 9:1 and c) hybrid vesicles made of EMVs doped with 10 % phospholipid weight from liposomes, the two parental membrane suspensions of which were cosonicated to allow complete mixing. The latter's characterization and preparation are reported in greater depth in the following paragraphs.

The particle sizes of the G10S5 NPS, EMVs, liposomes and hybrid vesicles are reported in Table 1, with the zeta potentials measured. The G10S5 NPs have a bimodal size distribution, with a first peak at 120 nm and a second peak at approximately 1 μm. Owing to the presence of ionized amino groups, G10S5 NPs at pH 7.4 have a positive surface charge of +13 mV. For liposomes, EMVs and hybrid vesicles, the zeta potential values are mildly negative, which is consistent with the literature [33,45], whereas the DLS-measured particle sizes range from 130 to 145 nm.

We also evaluated the ultrastructures of all the starting materials for the final formulation (G10S5 NPs, EMVs, liposomes and their hybrids) via a) conventional transmission electron microscopy, with contrast-enhancing negative stain, and b) cryo-EM. Both techniques have well-known drawbacks and advantages: in the case of conventional TEM, the dehydration of a sample relies on hydration for its shape, deforms the material and causes artifacts, together with the heavy-metal salts used in negative stain [51]. Conversely, cryo-EM, while retaining the hydration shell of the sample owing to vitrification, tends to underestimate the size of the particles due to the inherent sample preparation required for this technique [52]. Therefore, conventional TEM and cryo-EM are both complementary to DLS. We previously [9] demonstrated that in the case of genipin-based nanosized polymers, DLS tends to greatly overestimate the abundance of micron-sized aggregates and to measure a greater diameter of smaller particles of approximately 30 % with respect to TEM. We also conducted cryo-EM imaging of G10S5 NPs alone (Fig. 1a). Indeed, consistent with the literature for similar objects, the suspension of G10S5 NPs, visualized as a vitrified sample, appears to be composed of extremely tiny particles (Fig. 1a and Table 1), with high variability in terms of size. Interestingly, smaller particles tended to accumulate within grid holes, i.e., where the vitrification of ice occurs, while most of the NPs remained on the surface; the size distribution of the latter was similar to that observed with conventional TEM.

Conventional TEM and cryo-TEM images of EMVs and liposomes (Fig. 1b and Fig. 1c, respectively) reveal the expected morphology for such structures [44,50]. EMVs retain a biconcave shape, similar to that of parent erythrocytes, whereas liposomes are spherical, even with structures. Interestingly, hybrid vesicles (Fig. 1d) have a morphology similar to that of EMVs, meaning that low addition of phospholipids (10 % w/w in our case) does not affect morphology in a way that can be noted via this technique and does not significantly affect size. Cryo-EM of hybrid membranes revealed the presence of "rod-like" structures already noted in [44], i.e., most likely EMVs sitting on the side. A comparison of the vesicle sizes obtained via all 3 characterization techniques (Table 1) revealed that, as expected, the particle sizes obtained via DLS were slightly larger than those measured via conventional transmission electron microscopy (TEM) and even lower than those measured via cryo-EM.

Since electron microscopy does not distinguish between liposomes and EMVs in hybrid vesicles, we performed a fluorescence spectroscopy study. We therefore took advantage of the Förster resonance energy transfer (FRET) of two fluorescent dyes. DiO and DiI are capable of FRET when in close proximity, i.e., in this case, they are colocalized in the bilayer. For this purpose, liposomes were labeled with FRET dye (DiO), and EMVs were labeled with acceptor dye (DiI). First, the excitation (Fig. 2a) and emission fluorescence spectra (Fig. 2b) were recorded for DiI-EMVs, liposome-doped EMVs with various phospholipid mass ratios between EMVs and liposome lipids; second, DiO-liposome spectra at the same concentrations as those in the doped EMVs were recorded as background. Interestingly, the fluorescence intensity of DiI-EMVs was dramatically lower than that of liposomes at the same phospholipid concentration (EMV:liposome mass ratio of 1:0,85–1,7): such an effect can be attributed to the composition of the two carriers. Indeed, as demonstrated for Sp-DiO [53], cyanine-based dyes, with 18-carbon aliphatic chains, do not incorporate well into POPC bilayers; the latter is indeed the main component of the erythrocyte membrane [54]. Therefore, the less efficient incorporation also leads to a lower total fluorescence intensity. Furthermore, in our experimental set-up, DiI was added to preformed erythrocyte ghosts, whereas for liposomes, DiO was added at the rehydrated thin-film stage; a steric hindrance effect, impairing the insertion of the dye within the double layer, cannot be ruled out. Finally, a liquid disordered phase might influence the DiO/DiI insertion efficiency. Indeed, a liquid crystalline phase is present in the erythrocyte membrane due to the high concentration of cholesterol (up to 46 % in mass) [54,55], which has been demonstrated to impair the fluorescence intensity due to a shortened lifetime [53]. When excited at the DiO excitation maximum (487 nm), a FRET peak appeared in the DiI emission region (Fig. 2c), indicating energy transfer. A Forster resonance effect (FRET) is evident in hybrids, suggesting the mixing of the two parental membranes and the close spatial proximity of the two dyes. Indeed, the Forster radius $R_0$ for the DiO-DiI couple is reported to be generally less than 10 nm, but the overall FRET efficiency is heavily dependent on the chemical environment [56], the nature of the bilayers affecting the quantum yield of the fluorophores, and the real distance between the two dyes [57]. Indeed, a more pronounced fluorescence intensity is reported for, logically, higher DiO-liposome ratios in the final hybrid carriers but also in the case of cosonicated membranes: extrusion itself via an 800 nm membrane led to minimal mixing of the two parental carriers. Therefore, we concluded that cosonication and high shear stress are instrumental for obtaining effective hybrid carriers.

Then, we used confocal fluorescence microscopy to characterize the

**Table 1**
Particle sizes were measured along the long axis of the G10S5 nanoparticles and camouflaging material. Data arise from measurements, via ImageJ, of 300 objects over 5 micrographs.

| Sample | DLS particle size, nm ± SD | PDI (%) | TEM size, nm ± SEM | Cryo-EM size, nm ± SEM | Zeta potential, mV ± SD |
|---|---|---|---|---|---|
| G10S5 | 120 ± 11; 998 ± 23 | 39 | 98 ± 29; 576 ± 73 | 42 ± 29 (within holes); 78 ± 45 (throughout the grid) | + 13.2 ± 0.5 |
| Liposomes (DPPC+DSPE-PEG 2000) | 131 ± 16 | 32 | 121 ± 5 | 87 ± 5 | -6.2 ± 0.7 |
| EMVs | 144 ± 16 | 20 | 112 ± 3.5 | 93 ± 10 | -13.0 ± 1.0 |
| Hybrids (EMVs+10 % liposomes) | 134 ± 16 | 27 | 140 ± 4 | 107 ± 7 | -12.9 ± 0.6 |

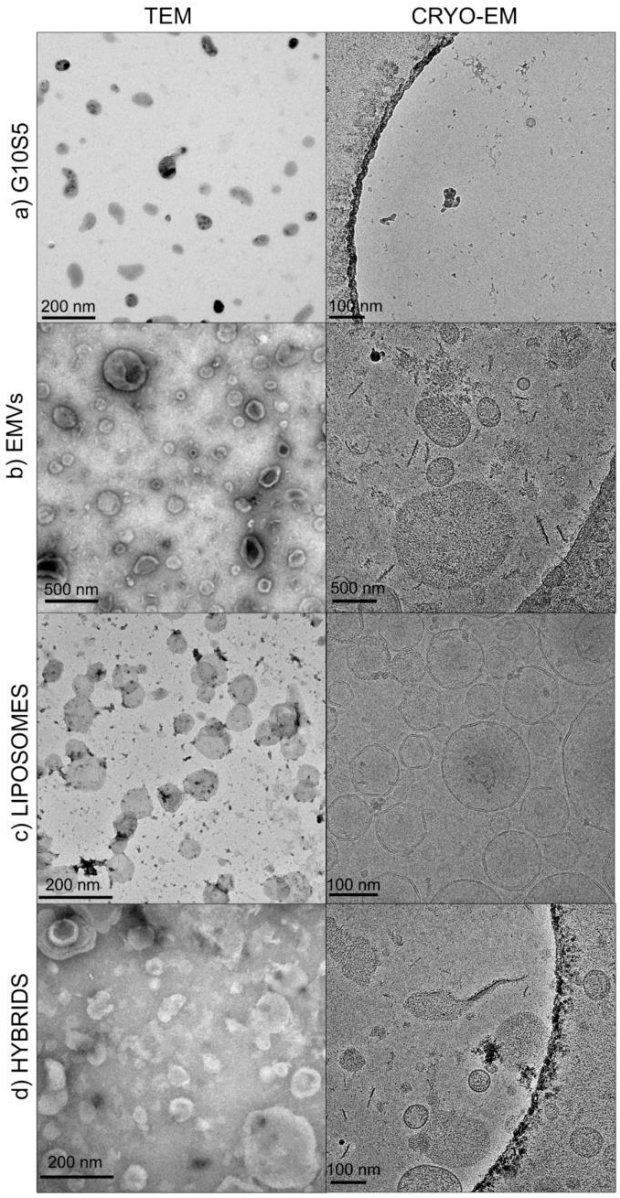



**Fig. 1.** Comparison between conventional negative-staining TEM and cryo-TEM for all the single components of G10S5-hybrids. Scale bar values are reported for clarity due to different magnifications.

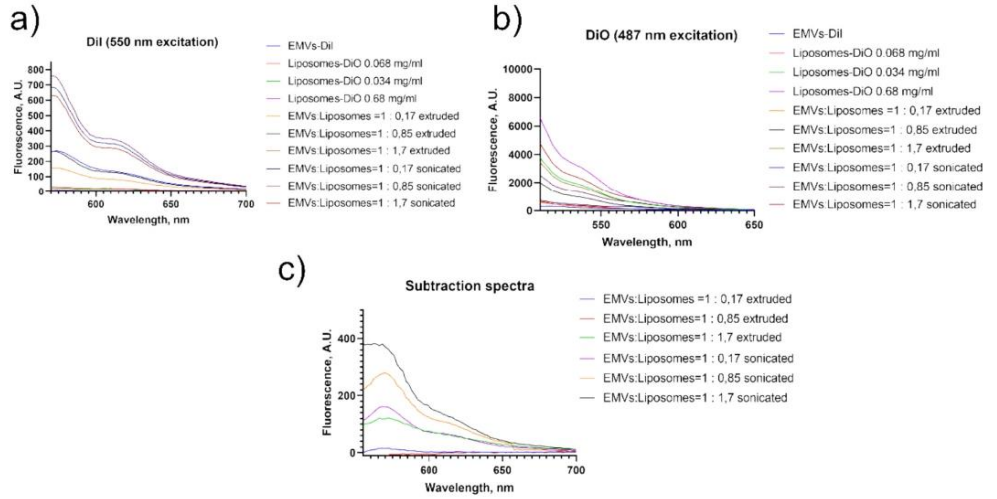



**Fig. 2.** a) DiI emission spectrum (excitation at 550 nm) of 0.17–1.7 mass ratio, cosonicated or coextruded, of liposome-doped EMVs. DiI-EMVs and DiO-liposomes, the latter at the same concentration as doped-EMVs, were added for comparison. 2) DiO emission spectra (excitation at 487 nm) of the same suspensions. c) Spectra resulting from subtraction from each DiI hybrid fluorescence spectrum (liposome-doped EMVs), the respective DiO background that might arise from a bleed-through signal. This approach is used to highlight the FRET effect between DiI (acceptor) and DiO (donor), which is necessary because of the dramatically higher DiO-liposome quantum yield.

mixing of the two parental carriers, i.e., EMVs and liposomes, further. For this purpose, we avoided any possible FRET effect; therefore, liposomes were labeled with a DiD lipophilic tracker, a dye that has a less than 10 % J spectral overlap with DiO. We then aimed to assay the colocalization ratio of DiO and DiD events. Hybrid vesicles were prepared with 10 % mass liposomes (relative to the EMP phospholipid content) in three different ways: a) sonication, b) sonication and extrusion through 800 nm pore sizes and c) sonication and extrusion through 800 and 200 nm pore sizes. The fluorescence confocal microscopy images are shown in Fig. 3a–c, respectively. Owing to the limited resolution of the confocal microscope and small vesicle size, EMVs and liposomes are shown as green and red dots, respectively (Fig. 3d). The pictures (7 for each type) were analyzed via the colocalization finder plugin in ImageJ, and the outcome (termed the *overlap value*) was compared via one-way ANOVA (Fig. 3e). Sonication (Fig. 3c) and extrusion at 200 nm (Fig. 3b) led to similar results, which were not significantly different, with high colocalization values (close to 1). These results, especially those for sonication, are in good agreement with those observed with fluorescence spectroscopy. Notably, Di-X lipophilic trackers have a low rate of intermembrane migration, i.e., once incorporated, they diffuse only within the same bilayer in a thermodynamically driven manner; a "dye hopping" between two differently stained objects is reported only for long coincubation times, typically for cocultured cells exchanging exosomes and other phagocytable elements [58,59].

In conclusion, extrusion via a small-pore filter and sonication lead to incorporation within double layers and to effective mixing of EMVs and doped liposomes. As expected, the suspension appeared cleaner upon extrusion through the 200 nm pore size (Fig. 3b), whereas the sonicated samples contained more debris (Fig. 3c).

### 3.2. Complexation of G10S5 NPs with siRNA

In our previous work on genipin-based polymers, we evaluated the siRNA binding profile to GxS5 NPs; the nature of this interaction, as it is for cationic polymers in general, is electrostatic [60], where siRNA phosphate groups interact with amino groups. For the current work, we aimed to choose a phosphate-to-nitrogen (P/N) ratio that would yield stable, negatively charged polyplexes to make camouflage possible with surface-negatively charged erythrocyte membranes. For this purpose, we evaluated various P/N ratios, ranging from 1 to 25, to determine the size and zeta potential evolution, upon increasing the number of phosphate groups (from siRNA) in the system. This approach was carried out for both naked and camouflaged polyplexes via sonication. The naked G10S5 particle size, in the absence of nucleic acids, follows a bimodal distribution, with a more abundant population composed of small nanoparticles (50–200 nm in diameter) and a less abundant population composed of larger particles (500–1 μm) (Fig. 4a, Table 1). Upon siRNA binding, following the trend previously observed for the G10S5 NPs, the smaller population, due to internal rearrangements and electrostatic repulsion, overtakes the micron-sized population, leading to uniform, 100 nm-sized nanoparticles (Fig. 4a, uncoated). The zeta potential decreases accordingly, becoming increasingly negative with increasing ratios of siRNA phosphate groups (Fig. 4b, uncoated). Then, via a dye exclusion assay, we characterized the percentage of siRNA duplexes accessible to an intercalating dye, which, as expected, steadily decreased with increasing P/N ratio (Fig. 4c), as previously reported [9]. Owing to their promising zeta potential and small, relatively monodisperse particle size, two P/N ratios were selected for the G10S5 P/N polyplexes: 1:12 and 1:5. Both offered excellent RNase A protection (Fig. 4d) when incubated with the enzyme at 25 μg/ml for 24 h.

### 3.3. Characterization of camouflaged G10S5-siRNAs: liposomes, EMVs and hybrids of the two

As a starting point, we attempted to coat G10S5, complexed with siRNA or not, with DPPC-DSPE-PEG2000 (9:1) liposomes; the weight ratio of G10S5 to phospholipids was 2 (0.5 mg/ml of G10S5 coated with

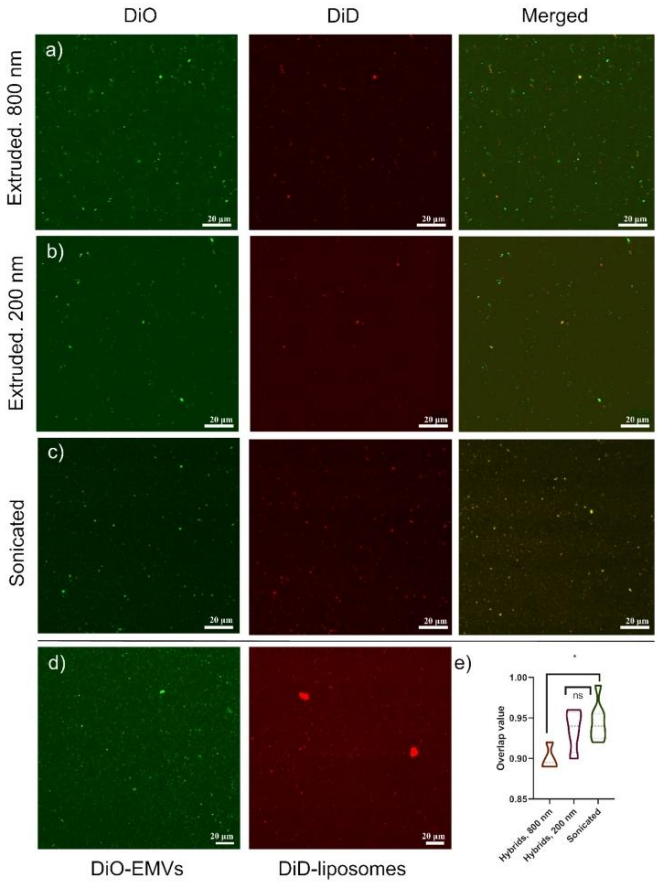



**Fig. 3.** Confocal images of hybrids extruded via a) 800 nm only, b) 800 and c) 200 nm and sonicated only acquired both DiO and DiD channels. Pictures of parental carriers were added for comparison (d). Finally, one-way ANOVA was performed on the overlap values obtained with the colocalization finder ImageJ plugin over 7 pictures per group.

0.25 mg/ml of phospholipids). The attempt yielded a clear core–shell structure that was electron-dense and monodisperse, with a slightly negative *Z*-potential (Fig. 1S and Table 1S, supplementary materials), which is in line with the literature [21]. During this preliminary experiment, extrusion was detrimental to G10S5 NPs (elongated, deformed nanostructures were produced, Fig. 2S, Supplementary Material), and subsequently, we decided to apply sonication to coat G10S5-siRNA NPs with liposomes, similar to [61]. In light of this success, we aimed to use erythrocyte–membrane vesicles (EMVs) via the same approach: failure. Attempts to coat G10S5-siRNA NPs with pure EMVs were not successful (Fig. 3S, Supplementary Material): rather than erythrocyte membranes surrounding G10S5-siRNA polyplexes, EMVs appeared to gather around aggregates of amorphous G10S5, creating objects with particle sizes greater than 600 nm. This is likely due to the stiff nature of EMVs, which made the encapsulation of G10S5 difficult: indeed, for erythrocytes, the elastic (or Young) modulus is reported to be between 2.5 and 10 kPa [34,35,62,63] when measured with AFM, whereas the values for the bending module (i.e., the resistance of a double layer to bending, an important parameter during shear stress treatments [64] range greatly when the cytoskeleton is taken into consideration during the measurement (up to 250 kBT, [65]). The bending module value decreases to a moderate value of 4-6 kbT when the protein contribution from the measurement range is removed [66]. Conversely, for a DPPC double layer, at standard temperatures, the bending modulus is approximately 12 kBT [67], whereas the Young's modulus, for a situation superimposable to ours (i.e., PBS-filled liposomes), is 0.47 kPa [28].

We therefore aimed to investigate the performance of hybrid membranes (EMVs doped with 10 % *w*/w DPPC-DSPE-PEG2000) to ensure full coating of the G10S5-siRNA polyplexes. This was achieved by sonicating the hybrid membranes in the presence of G10S5-siRNA polyplexes, since, as shown in Section 3.1, full mixing of the two parental membranes is also achieved via only sonication.

First, we applied Fourier Transform Infrared Spectroscopy (FTIR),

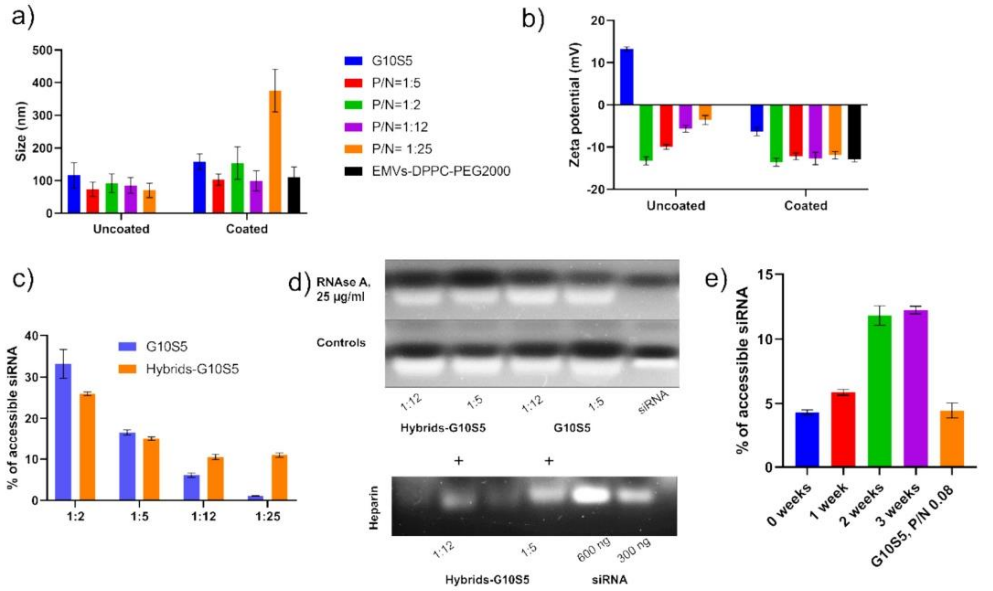



**Fig. 4.** a) Size comparison and b) zeta potential at different P/N ratios between hybrid-coated and uncoated G10S5 polyplexes. Empty hybrids are added for clarity. c) Percentage, where 100 % is free siRNA (therefore, completely accessible to the intercalating dye), of accessible siRNA for naked and coated polyplexes. The data are reported as percentages of the fluorescence of the free siRNA. d) Agarose gels prestained with Midori Green for (above) RNAse A protection assay, for 1:5 and 1:12 P/N, naked and coated polyplexes; below, the results of the heparin exclusion assay, i.e., the capacity of heparin to disassociate the polyplex, are reported. e) Percentage of accessible siRNA for 1:12-coated polyplexes over the course of three weeks. The value relative to the naked polyplex (G10S5 P/N 0.08 or 1:12) at 0 weeks is reported for comparison.

which can offer additional evidence for successful coating and interfacial interactions. FTIR spectra of freeze-dried samples (liposomes, EMVs, hybrids, G10S5 NPs, G10S5-liposomes and G10S5-hybrids) are shown in Fig. 4S with a zoom in of the fingerprint region. We have identified characteristic peaks that belong to phospholipids in liposomes, cell membranes and G10S5 NPs and are described in the Supplementary information file. Importantly, all peaks that appear in liposomes or hybrids, also appear in G10S5-coated NPs. However, this is not proof for itself that the coating is successful, but it shows that all components are present in the sample. Therefore, we searched for the appearance/disappearance/shift of peaks after coating. Only the peak that is found in G10S5 NPs and not in other samples is the peak at ~880 $cm^{-1}$, which could be a marker of genipin–amine crosslinking, related to the cyclic structures formed during NP assembly. The disappearance of the ~880 $cm^{-1}$ band after coating is consistent with a coating, but it is not definitive proof by itself. It can be caused by several different mechanisms (physical masking, spectral overlap, chemical reaction, or measurement artifacts). We also have a tiny peak in G10S5 NPs at 1574 $cm^{-1}$ that is not present in other samples, including coated samples. However, the disappearance of this peak can be related to physical masking/overlap by the coating. Therefore, despite some subtle hardly appreciable differences among the spectra, FTIR doesn't have enough resolution to provide clear evidence for successful coating and interfacial interactions. Therefore, we applied complementary methods to further characterize coatings.

*3.3.1. Size and zeta potential of hybrid-coated G10S5-siRNA at various P/N ratios*

We then took advantage of the dynamic light scattering technique to characterize the coating effect on G10S5-siRNA polyplexes at various P/N ratios. The presence of the hybrid coating around the G10S5-siRNA NPs increased the particle size relative to that of the naked G10S5-siRNA NPs at all P/N ratios (Fig. 4a, coated), with the particle size accounting for approximately 150 nm up to 1:25 P/N; from this point on, micron-sized aggregates started to appear because of the lack of electrostatic repulsion between the EV/PEG outer layer and the G10S5-siRNA polyplex at 1:25 P/N. Indeed, the latter shows only a mildly negative zeta potential, making an effective coating unlikely. In addition, all the coated samples possessed equal zeta potentials to those of the hybrid vesicles alone (Fig. 4b, coated). The disrupted equilibrium between G10S5 and siRNA, in terms of electrostatic interactions, at 1:25 P/N, in the presence of camouflaging, is also proven by the percentage of accessible siRNA to the intercalating dye (Fig. 4c, hybrids-G10S5), which does not equate to that offered by naked G10S5 at the same ratio. For the sake of coating, as stated, a negatively charged polyplex is needed; the complex should also sequester the nucleic acid strongly enough to exclude the access of intercalating dyes. At a 1:2 P/N ratio, more than 30 % of the siRNA was accessible from the solvent due to saturation of the binding sites, despite a low zeta potential (~ -13 mV). We therefore decided to use 1:5 and 1:12 P/N ratios to evaluate the RNAse A resistance of the polyplexes, camouflaged and naked (Fig. 4d): after 24 h of incubation with 25 µg/ml of the enzyme, both naked and not, at both P/N ratios offered excellent protection to the cargo. We also tested the strength of the polyplex (naked and not) interactions via a heparin-displacement assay (Fig. 4d). As already noted from the dye exclusion assay, at a 1:12 P/N ratio, there was almost no binding of Midori Green to the siRNA in the absence of heparin; at a 1:5 P/N ratio, a moderately intense band appeared. At 2 mg/ml heparin, the 1:12 P/N

band, both for the camouflaged and naked polyplexes, did not equate in intensity with the corresponding amount of free siRNA, suggesting a very strong and stable interaction. Finally, we tested the stability of the 1:12 P/N ratio over the course of one month (Fig. 4e), repeating a fluorescent dye intercalating assay once a week: the interaction was extremely stable, with just 5 % more siRNA accessible to the fluorescent dye after one month of storage at 4 °C. Finally, we decided to perform further characterization of camouflaged polyplexes with a 1:12 P/N ratio due to the a) negative zeta potential and monodisperse nanoparticle sizes; b) protection against RNase A degradation; and c) good siRNA sequestration, with only 10 % of the nucleic acid binding sites accessible to the fluorescent dye (Fig. 4c), even in camouflaged form.

### 3.3.2. *Ultrastructure characterization: cryo-TEM and AFM imaging*

We then visualized G10S5 coated and uncoated, complexed with siRNA (1:12 P/N ratio) or free, via cryo-TEM (Fig. 5). Importantly, the preparation of hybrid-coated G10S5-siRNA NPs is rather difficult for the following reasons. In conventional TEM, vesicles cannot be visualized without the use of negative stain and/or fixation due to the absence of heavy atoms for contrast. They decompose due to exposure to high vacuum and electron beams. However, the negative stain was detrimental to G10S5 NPs (which undergo dissolution due to the presence of ethanol, as in the UA Zero stain, and acid, Fig. 5S, Supplementary Material). In addition, cryo-TEM is an excellent method for visualizing vesicles, but G10S5 nanoparticles exhibit an unexpected trend of distribution inside and outside the grid holes (Paragraph 3.1). While G10S5 nanoparticles are reported in Fig. 1, here, we focus on the morphological aspects of the coated nanoparticles in the presence and absence of siRNA. As shown in Table 1, G10S5 has a positive zeta potential at pH 7.4, which decreases to a mildly negative value when it is complexed with a nucleic acid. On the other hand, the sialic acid moieties present on the erythrocyte's ghost surface confer a moderately negative zeta potential; therefore, to respect the right-sidedness of the membrane, the nanoparticle to be coated must electrostatically repel the erythrocyte surface [68]. Indeed, eliminating precomplexation, prior to coating G10S5 nanoparticles with siRNA, led to clutters of doped EMVs aggregating around G10S5 nanoparticles (Fig. 5), as seen in the cryo-TEM images, with occasional solitary vesicles. On the other hand, the hybrid-G10S5 PN 1:12 suspension looked much cleaner, with a majority of well-dispersed, round-shaped vesicles. The rod-like structures still appear to be present, together with membrane debris. Interestingly, the cryo-TEM particle size for hybrid-G10S5-siRNA is consistent with what is observed via DLS (Fig. 4a).

Furthermore, we applied an alternative technique in which no stain is needed and the NPs can also be visualized in 3D mode, i.e., atomic force microscopy (AFM). Fig. 6 shows 2D and 3D AFM images of our samples. The G10S5 NPs have a well-defined, spherical morphology and good separation between the individual particles (Fig. 6), which is consistent with the TEM observations. The size ranges between 100 and 200 nm, which is in good agreement with the values determined via DLS and TEM. Their average height is 34 ± 14 nm (Fig. 7a, b). On the other hand, EMVs appear as stiff, relatively tall objects, which is consistent with the observation of erythrocyte ghosts via AFM under similar conditions, despite the extremely high variability in terms of preparation

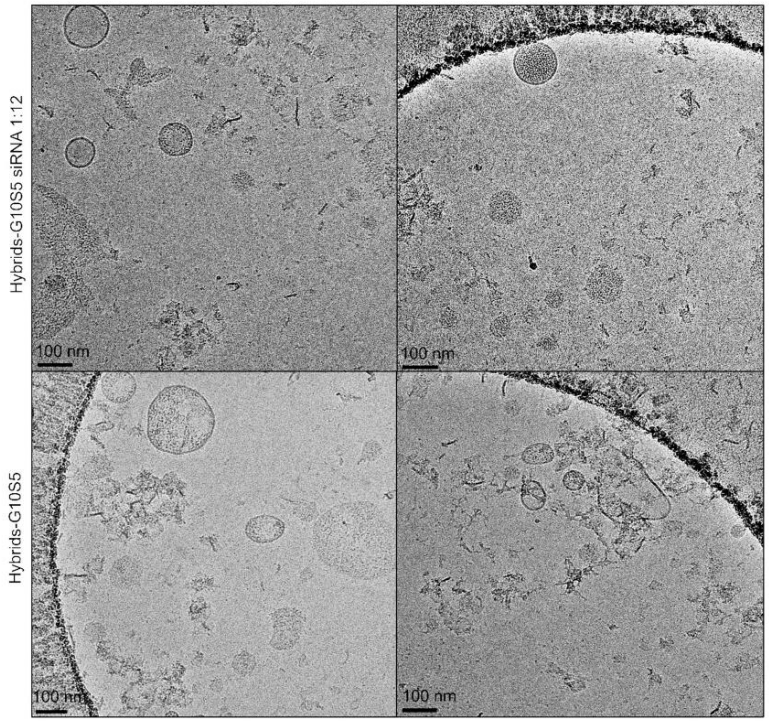



**Fig. 5.** Hybrids-G10S5 precomplexed with or without siRNA prior to coating via cryo-TEM.

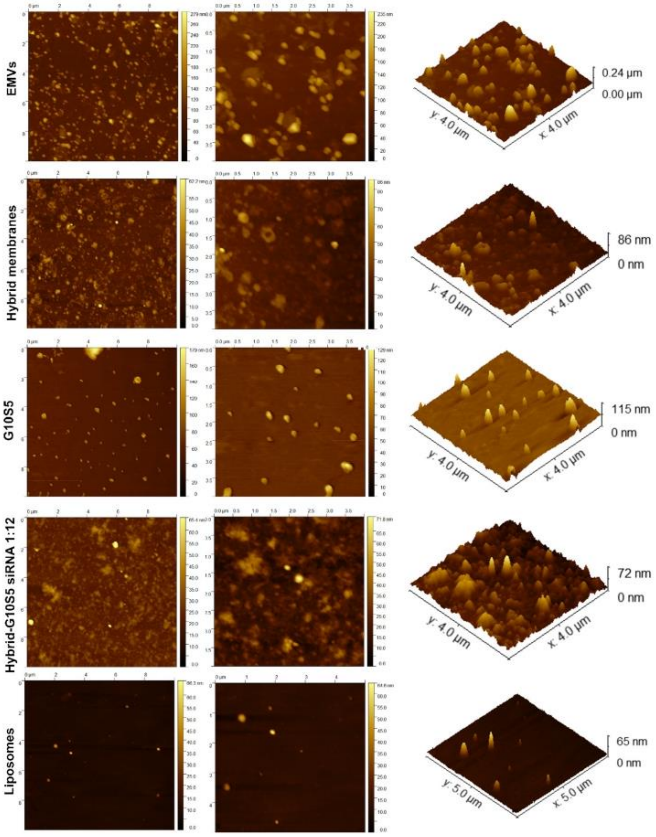



**Fig. 6.** AFM images of the NPs immobilized on the polylysine-modified glass surface at 10 and 4 µm image sizes; a 3D view of the 4 µm image is also shown. The colour scale was adjusted case by case to increase the contrast of the nanoparticles.

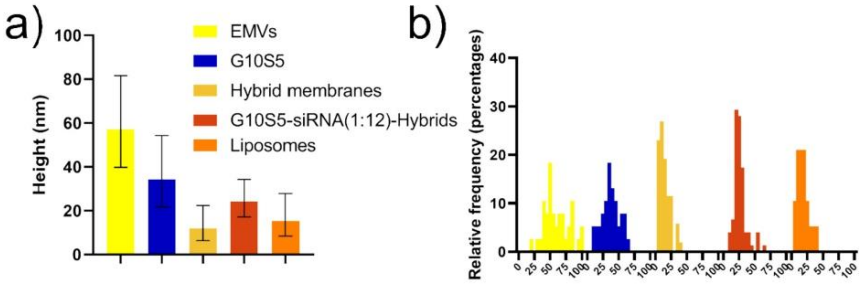



**Fig. 7.** Height analysis of the nanoparticles via AFM. a) Geometric mean with SD, reported for $n = 100$ height measurements on 10-by10 µm acquired images. b) Frequency distribution of the same data.

and hydration: when dehydrated, ghosts occur at a height of approximately 80 nm [69,70] at the rim. Indeed, EMVs (Fig. 7a) appear to have an average height of approximately 60 nm, and the frequency distribution follows a normal trend (Anderson/Darling test, $p < 0.01$). The reason behind the apparent rigidity of the EMV cytoskeleton during dehydration falls outside the scope of this paper, but it is to be tracked back to the interaction with the polylysine-coated substrate and the glycocalyx and the increased surface tension of EMVs due to their small size. On the other hand, the hybrid vesicles resembled a cup-shaped morphology, as observed in the TEM images (Fig. 1d and Fig. 6), and appeared to be flatter than the parental EMVs. Since hybrid vesicles are flatter than G10S5 NPs are, the background signal is greater in this case. The average height of hybrid vesicles is approximately 15 nm, which is dramatically lower than that of parental EMVs (Fig. 7a); their frequency distribution (Fig. 7b) follows a lognormal trend (Anderson-Darling test, $p \leq 0.0001$). However, a significant number of spherical, biconcave vesicles in different orientations can be observed, confirming that the addition of 10 % phospholipids to EMVs does not impact the vesicle formation process but rather influences the ultrastructure, which cannot be detected via electron microscopy, enhancing the biconcave shape even in nanosized objects. The size of the hybrid vesicles was approximately 200 nm, as determined by DLS and TEM measurements. Finally, images obtained with coated G10S5 NPs revealed no visible cup shape-like vesicles and had a greater height profile than did those obtained with empty hybrid vesicles, indicating that solid G10S5 NPs are coated with vesicles surrounded by some residues, which is most likely due to the excess vesicles compared with those of the G10S5 material. Indeed, the average height of the coated G10S5 nanoparticles is 26 ± 9 nm (Fig. 7a, b), which is intermediate between those of naked G10S5 and empty hybrid vesicles: highly dispersed, and, again, follows a lognormal trend (Anderson Darling test, $p \leq 0.0001$). Last, empty DPPC-DSPE-PEG2000 liposomes appear to have little to no residue on the substrate, as a very clean and well monodisperse particle distribution; again, they are extremely flat objects, with an average height of 20 ± 2 nm (Fig. 7a, b), and, again, their height profile follows a lognormal trend (Anderson Darling test, $p \leq 0.0001$).

### 3.3.3. *Self-fluorescence properties of G10S5 NPs: solvatochromism effect to investigate coating efficiency*

We further investigated the success of camouflaging via the fluorescence of G10S5. As previously reported [71–73], genipin-crosslinking products exhibit fluorescence. This effect arises from the long, π-conjugated double bonds in the crosslinked matrix, and it is highly dependent on the reaction conditions. Genipin products exhibit continuous fluorescence from green to far red, depending on the length of the aliphatic chain of the amine donor and the enantiomer of genipin used for the reaction[1,2]. As we used the 1S,2R,6S stereoisomer of genipin, our polymers show strong emission in the green region, with an excitation peak of 375 nm and emission peak of 460 nm (Fig. 8a), whereas a fainter peak is present in the red/orange area, with an excitation peak of 560 nm and emission peak at 615 nm (Fig. 8b) [9]. All the genipin products are characterized by an absorbance peak at approximately 600 nm, again depending on the nature and length of the amine donor [9,74,75], and in the presence of spermine as a substituent, the absorbance peak of our polymers is at 580 nm. While the absorbance spectra of the naked and camouflaged polyplexes did not show any remarkable features, in addition to the contribution of traces of hemoglobin appearing at 415 nm (Fig. 6S, Supplementary Materials), the fluorescence spectra provided insight into the chemical surroundings of the fluorescent probe. Therefore, the shifts in the fluorescence spectra can be used as indirect indicators of the coating efficiency in relation to the surface charge of the polyplex (siRNA + cationic G10S5) and, finally, their electrostatic interaction. As a proof of concept, we also prepared a colloidal suspension containing G10S5 NPs, which were not in complex with siRNA and whose cationic charges would not be masked by the phosphate groups, sonicated in the presence of hybrid membranes, similarly, to camouflaged the polyplexes. We then prepared various polyplexes, from 1:5 to 1:25 P/N, coated them with hybrid membranes, and recorded their fluorescence spectra (375 and 560 nm of excitation) in the green and orange/red regions (Fig. 8a, b). Proving our theory to be correct, a hypochromic shift and a blueshift of 5 nm appeared when highly negatively charged polyplexes were coated with hybrid membranes, with a fluorescence yield of G10S5 doubling in the green region with 1:5

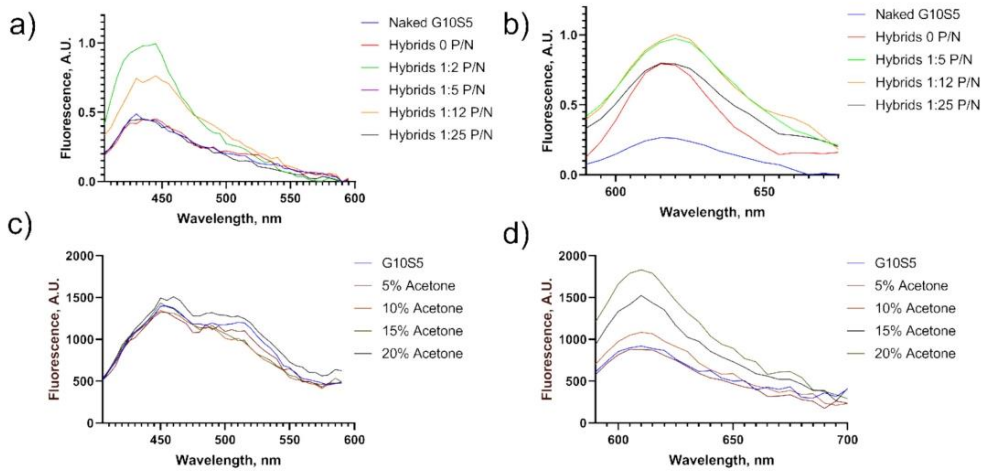



**Fig. 8.** Fluorescence analysis of naked G10S5 and various (1:2 to 1:25 P/N ratios) hybrid membrane-coated formulations. In a) and b), respectively, the spectra for the green emitting region (375 nm ex) and the red emitting region (460 nm ex) are plotted. To confirm the hypsochromic and blueshifts of the maxima peak observed for coated G10S5, the latter's fluorescence spectra were recorded in the presence of increasing v/v % acetone, where c) the excitation wavelength was 375 nm and d) the excitation wavelength was 460 nm.

and 1:12 P/N-camouflaged polyplexes. A hydrophobic environment can affect the fluorescence spectrum of a fluorophore [76,77] by reducing the solvent interaction (water) with the fluorophore and reducing the contribution of nonradiative decay phenomena upon excitation, effectively increasing the quantum yield [78,79]. While the exact fluorescence lifetime and nonradiative decay constants of G10S5 are not known, we previously demonstrated that, in plasma, its quantum yield (Φf) slightly increases [9]. Moreover, information can be inferred from the outcome of the abovementioned experiment: upon increasing the shielding (i.e., siRNA ratio) on G10S5 cationic charges, the fluorescence spectrum maximum shifts toward shorter, more energetic wavelengths and increases in yield. Similar behavior is known to occur in commonly used fluorescent, polarity-sensitive dyes, such as those that are coumarin-based or based on 7-nitro-2-1,3-benzoxadiazol4-yl (NBD) or, alternatively, 4-sulfamonyl-7-aminobenzoxadiazole (SBD) [79]. To confirm this speculation, we also conducted a small-scale solvatochromic experiment by exposing naked G10S5 to increasing amounts of acetone dissolved in water (Fig. 8c, d) and recording their spectra in the red and green regions (excitation at 375 and 460 nm, respectively). The results confirmed what was already observed, with a significant increase in fluorescence intensity in the presence of more than 10 % *v*/v acetone in PBS; despite still being a polar solvent, acetone is a proxy that can form hydrogen bonds between its carbonyl group and water hydrogens but requires a hydrogen bond donor to interact with other solvates. For example, the surface polarity of serum albumin was reported to be similar to that of acetone, making it a suitable simplified model for investigating the solvatochromism of fluorophores [80]. For BODIPY-520 derivatives, acetone appears to increase the quantum yield, although not as dramatically as methanol does [81]. Similarly, for the azo dye 4-(2,3,5,6-tetrafluoro-pyridin-4-yl azo)-phenol, the fluorescence band maximum in acetone was slightly greater than that in water [82].

Taken together, the above data provide insights into the coating efficiency over G10S5/siRNA polyplexes: the more negative the surface *Z*-potential is due to the presence of the siRNA phosphate groups (Fig. 4b), the better the coating with hybrid membranes. Thus, the coating efficiency strongly depends on electrostatic interactions between the coating material and the nanoparticle.

### 3.4. Cytotoxicity of G10S5-siRNA-hybrids

The toxicity of the coated and noncoated G10S5-siRNA NPs was tested in two different cell lines, normal human lung fibroblasts (NHLFs) and a murine melanoma cell line (B16F10), at concentrations ranging from 0 to 0.032 mg/mL with respect to the G10S5 mass, which equals 0, 10, 50 and 100 nanomolar siRNA (i.e., 1, 5, and 10 picomoles in 100 μl). In both cell lines, empty vesicles (EMVs or liposomes) had no toxic effect in the tested concentration range (Fig. 9). To replicate real-case data, anti-tdTomato siRNA was included in the experiment. These results contrast with those of our previous study [9], where G10S5 had little to no toxicity (up to 0.08 mg/ml) after 72 h on B16F10 cells; subsequently, to investigate this discrepancy, we used ultracentrifugation-purified-EMVs, loaded with siRNA or empty, to test how the addition of a targeted siRNA—capable of activating the RNAi machinery—impacts cytotoxicity. We chose such a control since these carriers were developed in our lab, already assayed in vivo and have a well-known uptake mechanism and kinetics. Indeed, as shown in Fig. 7S in the Supplementary Materials, at a comparable concentration of siRNA to that tested with G10S5, even DCC-siRNA-EMVs proved to be cytotoxic after 72 h, thus confirming that RISC activation, without exerting an effect due to the absence of the target mRNA, has a cytotoxic effect, as already widely reported [83,84]. However, for transfection purposes, a starting concentration of 0.0005 mg/ml G10S5 was used, which was 100× lower than the concentration tested for cytotoxicity.

### 3.5. Internalization study in B16F10 cells

To evaluate the internalization pathways of both coated and uncoated G10S5-siRNA NPs, we applied different endocytosis inhibitors, namely, genistein, chlorpromazine and imipramine, during the incubation of murine melanoma cells. The self-fluorescence of G10S5 was used to follow the internalization of naked and coated G10S5 at a final well concentration of 3.5 μg/ml (Fig. 10 and Fig. 11, respectively). Despite having the same final concentration, the overall MFI of hybrids, in the absence of endocytosis inhibitors, appeared to be significantly greater (Fig. 12a); however, such an effect can both indicate a slightly greater quantum yield of G10S5 when coated (Fig. 8) or, in fact, more efficient uptake. Moreover, as shown in Fig. 12b, the percentage of internalized nanoparticles normalized to that of the inhibitor-free controls is reported; G10S5 self-fluorescence was used to quantify the number of positive cells. Genistein appeared to have a strong inhibitory effect on the uptake of naked G10S5 ($p \leq 0.0001$ compared with the control): it acts by causing local disruption of the actin network, blocking the recruitment of dynamin II, which is related to caveolae-mediated endocytosis [85,86]. Moreover, incubation with genistein had an effect on the uptake of coated G10S5, but the effect was not as dramatic (50 % reduction compared with the control). Interestingly, chlorpromazine also appeared to significantly impair naked G10S5 uptake, while it had no effect on coated G10S5. This phenomenon strongly suggests that G10S5 naked nanoparticles may follow a clathrin-dependent mechanism of internalization, since chlorpromazine is believed to prevent clathrin assembly and disassembly in endosomes [87]. Like other phenotiazine-derived drugs, it appears to block the downstream

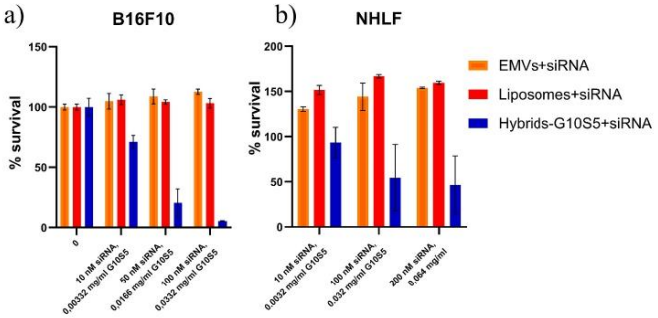



**Fig. 9.** Cytotoxicity, measured with the PrestoBlue assay after 72 h, for a) B16F10 murine melanoma and b) normal human lung fibroblasts (NHLFs). The data are reported over 6 replicates ± sd. The concentrations of siRNA and G10S5/well are shown below the plot.

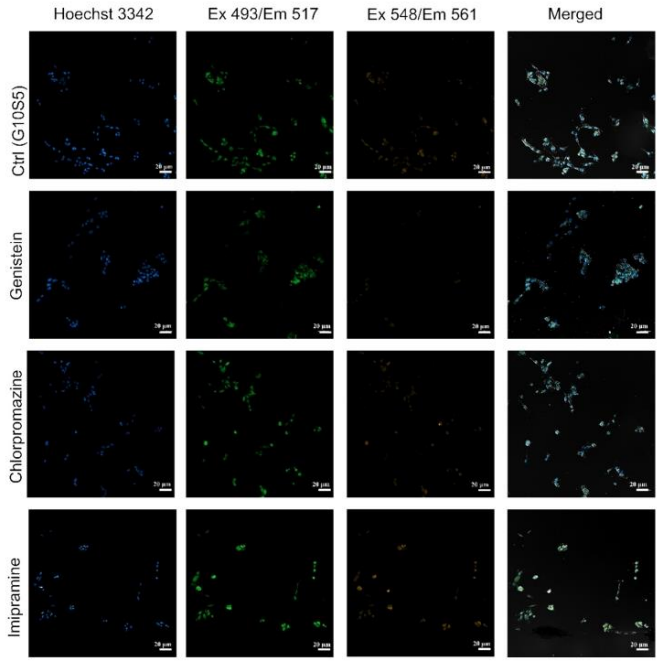



**Fig. 10.** G10S5 self-fluorescence in the green and orange channels. Nuclei were stained with DAPI.

recycling of clathrin-coated vesicles (CCVs) by interacting with dynamin, which is involved in the budding of CCVs toward the inner side of the plasma membrane [88]. Finally, imipramine has a low but significant effect on the uptake efficiency of naked G10S5 (Fig. 12) but impairs hybrid nanoparticle internalization to a greater degree: imipramine inhibits macropynocytosis [89,90] and the endocytic pathway involving membrane ruffling, typically in cancerous cells, to internalize large volumes of external medium [91]. Overall, coating with hybrid membranes significantly enhances uptake by murine melanoma cells and can be key to reducing the effective dose needed to achieve significant siRNA-driven knockdown.

### *3.6. Gene knockdown efficacy in murine melanoma and lymphoblastoid cells: decreasing the effective dose*

G10S5 NPs, which were complexed with siRNA at two different P/N ratios (1:5 and 1:12), both coated and uncoated with hybrid vesicles, were tested for their ability to deliver siRNA against the fluorescent protein tdTomato to tdTomato-expressing B16F10 cells and to silence that target gene. The total amount of siRNA used for transfection was 5 or 10 pmol/well, corresponding to 5 and 10 nanomolar. Interferin, a commercially available transfection agent, was used as a positive control. The G10S5 concentrations used were far below the cytotoxicity threshold: indeed, the final well concentration, both for naked and coated nanoparticles, was 0.0005 mg/ml for the 5 picomole dose and 0.001 mg/ml for the 10 picomole dose.

The median fluorescence intensity (MFI) of TdTomato was significantly reduced by 30 % by hybrid-G10S5 (1:12) at a dose of 5 picomoles (Table 2, Fig. 13a), whereas the uncoated counterpart had little to no effect; this result strongly confirms what has already been inferred from uptake mechanism studies, with the internalization route being the key for effective knockdown. A similar situation is observed for hybrid-G10S5 (1:5). Interestingly, a higher siRNA dose (10 picomoles) did not lead to a significantly greater signal reduction (Table 2, Fig. 13a). The best result was obtained with hybrid-G10S5 (1:12) at a 10 pmol siRNA concentration (31 % reduction in MFI), which was comparable to that obtained with the 10 picomole dose of the siRNA-interferin complex (34 %). Nevertheless, for Interferin, an MFI reduction of 43 % was observed at 5 picomoles. Since the tdTomato emission peak overlaps with the G10S5 emission peak, the MFI analysis was normalized for signals generated by B16F10 cells transfected with similar polyplexes, coated with hybrid membranes or not, complexed with a scramble siRNA. To further investigate these observations, we used qRT–PCR to determine the efficacy of tdTomato silencing (Fig. 13b) in an independent, replicate experiment in which total RNA was collected 48 h after transfection. Overall, the mRNA fold change (Table 3) did not align with the FACS results, as the knockdown effect was significant only at the 10 picomole dose—that, in terms of MFI reduction, yielded little to no difference from the lower dose; the presence of protein knockdown indicated translation blockage as a preferred pathway at low concentrations of siRNA [92,93] for the B16F10 cell line.

Furthermore, we aimed to test the efficacy of G10S5, coated and uncoated, on lymphoblastoid cells (where G10S5 had already shown little-to-no toxicity after 48 h, Fig. 8S in the Supplementary Materials); therefore, suspension-growing cells and whose nanoparticle internalization mechanism is inherently different from that of murine melanoma - a lower area exposed to the medium but an interaction driven more by random collisions rather than gravity [94,95]. For the ongoing characterization of this cell line (details in Section 2.8.3), we transfected 20,000 cells with 20 and 30 picomoles of anti-FARSA siRNA, complexed

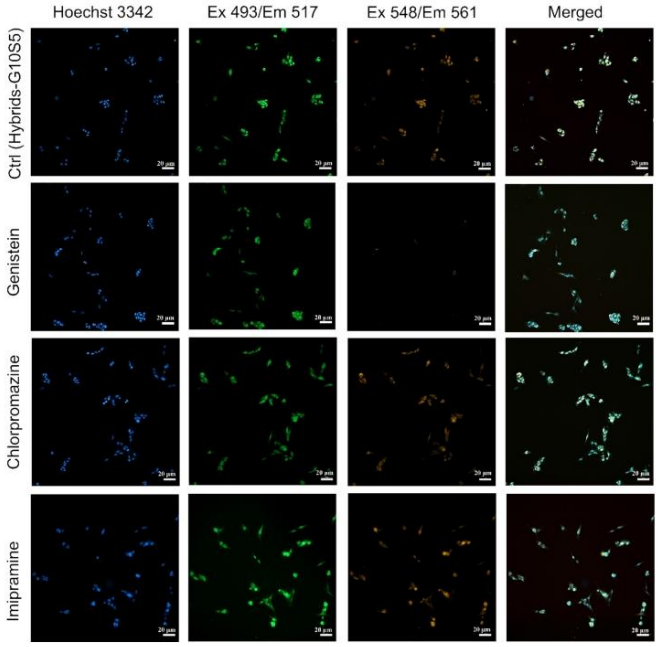



**Fig. 11.** G10S5-hybrids self-fluorescence in the green and orange channels. Nuclei were stained with DAPI.

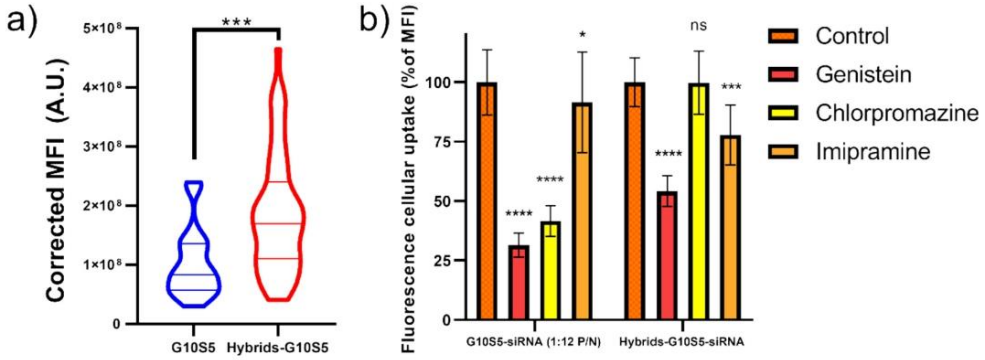



**Fig. 12.** Quantification of the uptake efficiency of naked G10S5 and hybrid membranes coated in the absence of endocytosis inhibitors. a) Comparison of corrected MFIs for positive control cells (in the absence of endocytosis inhibitors). b) Quantification, over the % of the positive control cells (100 %), of the G10S5 MFI, following uptake, in the presence of endocytosis inhibitors, for both naked and coated nanoparticles. $p \leq 0.05$ *, $p \leq 0.01$ **, $p \leq 0.001$ ***, $p \leq 0.0001$ ****.

with either naked or coated G10S5, at a ratio of 1:12 P/N. The final concentrations of G10S5 (naked or hybrid) were 0.004 mg/ml and 0.006 mg/ml for the 20 and 30 picomole doses, respectively. FARSA expression was quantified via Western blotting (Fig. 14). Stain-free gels of FARSA knockdown in lymphoblastoid cell line are shown in Fig. 10S. Moreover, hybrid-G10S5 outperformed naked nanoparticles, with almost total knockdown at 20 picomoles (Table 4). At a higher dose, both G10S5 cytotoxicity and FARSA knockdown led to cell death and unreliable results in terms of quantification, since FARSA, encoding phenylalanyl-tRNA synthetase, is a vital factor for protein translation, and its repression triggers an apoptotic cascade in most cell lines [48,93].

These data indicate how strong the internalization efficiency is in determining the effectiveness of the treatment: by coating G10S5 with

**Table 2**
Knockdown results shown as the decrease in the median fluorescence intensity of the tdTomato gene product. Data are reported as the median over six technical replicates.

| Sample | % MFI decrease ± SEM | *P* value | Dose |
|---|---|---|---|
| G10S5 1:12 | 3.7 ± 1.3 | 0.68 | 5 picomoles |
| Hybrids-G10S5 1:12 | 29.9 ± 3.75 | 0.02 | |
| G10S5 1:5 | 6.8 ± 2.2 | 0.21 | |
| Hybrids-G10S5 1:5 | 24.5 ± 3.7 | 0.027 | |
| Interferin | 43.6 ± 8.3 | 0.051 | |
| G10S5 1:12 | 10.2 ± 4.4 | 0.043 | 10 picomoles |
| Hybrids-G10S5 1:12 | 30.9 ± 3.4 | 0.0001 | |
| G10S5 1:5 | 0 ± 4.1 | 0.28 | |
| Hybrids-G10S5 1:5 | 25.5 ± 3.3 | 0.012 | |
| Interferin | 36.4 ± 5.0 | 0.005 | |

DPPC/DSPE-2000/EMV hybrid membranes, we managed to reduce the dose capable of exerting a 6-fold knockdown effect (30 picomoles in [9] vs 5 picomoles in Fig. 13 and Table 2).

## 4. Discussion

It was previously demonstrated how genipin, spermine and glycine are suitable building blocks for a novel class of short RNA transfection agents, with moderate cytotoxicity and high tunability [9]. In this study, we aimed to demonstrate how coating with a biomimetic agent can reduce the effective dose for a small interfering RNA, which is directed at two model cell lines: B16F10 murine melanoma and human lymphoblastoid cells.

The success in camouflaging the G10S5-siRNA polyplex was not immediate. Indeed, the generation of hybrid membranes, originating from erythrocyte membrane vesicles doped with DPPC-DSPE-PEG2000, at a 10 % weight ratio in phospholipids was needed. The fusion of the two membranes was stable but required high shear stress (such as in 200 nm extrusion and sonication at 20 Hz, Fig. 2 and Fig. 3) and generated vesicles with a negative zeta potential of -13 mV (Table 1).

The keys to effective camouflaging of a nanoparticle with a phospholipid-based coating material are tracking down to two macro areas: 1) electrostatic interactions on the exposed surfaces of the two materials and 2) the mechanical properties of the two materials. For extrusion to be effective, the size of the coating material must be larger than the diameter of the extrusion membrane pores to generate enough shear stress to break the vesicles formed by the coating material [96]; the elastic/Young's modulus and bending modulus are the main mechanical properties at play. Moreover, overall membrane fluidity is the final actor that causes the rearranging of phospholipids around the nanoparticle and the closure of partially coated, "patchy", areas [96]. The coating of G10S5-siRNA polyplexes with DPPC-DSPE-PEG2000 liposomes via sonication was successfully achieved at RT (25 °C, Fig. 1S), a temperature at which the double layer is in a solid-ordered phase [97], but the ultrasounds themselves cause the temperature to increase by several degrees. It cannot be ruled out that, despite the short time of sonication (30 s, 1 off and 1 on, for a total of 15 pulses at 20 mHz), a local increase in temperature led to the transition of the bilayer to the liquid–crystalline phase, a higher fluidity, and an energetically convenient reorganization of the bilayer around the polyplexes [98]. On the other hand, the same approach failed when the camouflaging material was composed of pure erythrocyte membranes (Fig. 3S). The transition temperature for cell membranes varies greatly due to the presence of cholesterol and proteins in the scaffold and the presence of hemoglobin cargo [99]; at RT (>20 °C), the erythrocyte ghost membrane switches to the liquid crystalline phase in cholesterol-deficient domains, whereas rafts tend to remain in the liquid-ordered state [100]. Overall, the stiffness and rigidity of the erythrocyte membrane appear to be lower than those of a DPPC-DSPE-PEG2000 double layer, whereas the fluidity and elasticity (i.e., the Young's modulus) appear to be greater: the failure of coating G10S5-siRNA polyplexes with erythrocyte membrane ghosts therefore leads to an apparent contradiction. This dilemma could be solved by taking into account the contributions of integral proteins, cholesterol and the cytoskeleton, which are often overlooked in the literature. We already demonstrated that EMVs retain the same SDS–PAGE protein profile of parental ghosts [44], therefore retaining

**Table 3**
The knockdown results shown as the expression of the tdTomato mRNA. The data are reported as the geometric means of six technical replicates.

| Sample | % mRNA decrease (with regards of scramble controls) ± SEM | P value | Dose |
|---|---|---|---|
| G10S5 1:12 | 15.9 ± 11.9 | 0.60 | 5 |
| Hybrids-G10S5 1:12 | 0 ± 4.8 | 0.98 | picomoles |
| G10S5 1:5 | 0 ± 8.5 | 0.84 | |
| Hybrids-G10S5 1:5 | 6.7 ± 4.2 | 0.24 | |
| Interferin | 0 ± 7.5 | 0.99 | |
| G10S5 1:12 | 32.3 ± 6.3 | 0.15 | 10 |
| Hybrids-G10S5 1:12 | 48.5 ± 1.5 | 0.0023 | picomoles |
| G10S5 1:5 | 32.8 ± 2.8 | 0.014 | |
| Hybrids-G10S5 1:5 | 33.4 ± 3.9 | 0.016 | |
| Interferin | 25.9 ± 3.7 | 0.017 | |

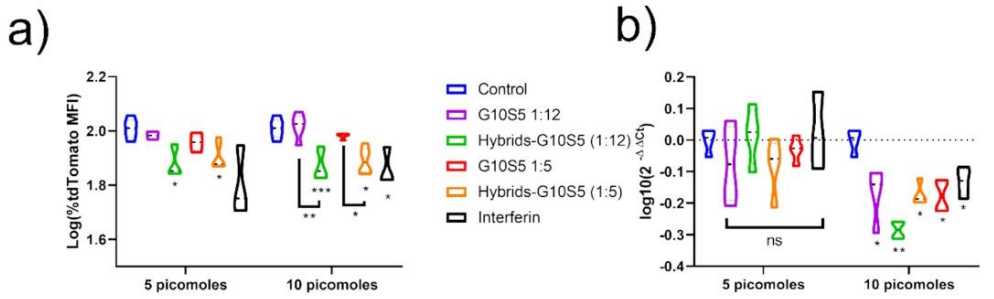



**Fig. 13.** Knockdown of the tdTomato a) protein product, as measured from its median fluorescence intensity (MFI). The significance symbols immediately after the violin plot for each treatment refer to mixed-effect analysis against the control; otherwise, the significance comparison between naked and coated G10S5 is reported. b) Gene expression. In a), only significant comparisons are reported. The line in the violin plot refers to the median for a) and to the geometric mean for b). The data are reported as log10 values for both cases. $p \leq 0.05$ *, $p \leq 0.01$ **, $p \leq 0.001$ ***, $p \leq 0.0001$ ****.

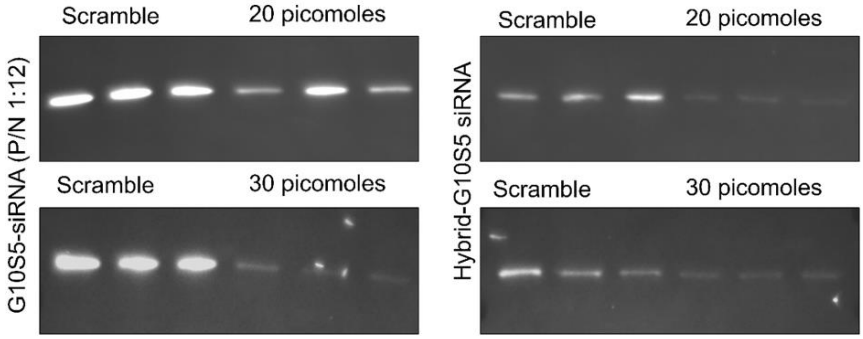



**Fig. 14.** Western blot gels of FARSA protein from three replicates of lymphoblastoid cells transfected with 20 and 30 picomoles of anti-FARSA siRNA complexed with naked and hybrid-coated G10S5 at 1:12 P/N.

**Table 4**
Knockdown of FARSA protein from Fig. 14 band quantification via ImageJ and ImageLab.

| Sample | % of remaining FARSA expression ± SEM | P value | Dose |
|---|---|---|---|
| G10S5 1:12 | 36.55 ± 2.50 | 0.148 | 20 |
| Hybrids-G10S5 1:12 | 17.13 ± 1.15 | 0.012 | picomoles |
| G10S5 1:12 | 17.49 ± 1.36 | <0.001 | 30 |
| Hybrids-G10S5 1:12 | 25.69 ± 3.70 | 0.028 | picomoles |

the 80 nm-mesh actin-ankyrin-spectrin cytoskeleton, which underlies the membrane, as well. This structure has a very low bending modulus (0.024–0.24 kbT [101]) but contributes to in-plane shear elasticity and resistance to compression, allowing erythrocytes to withstand deformation without rupturing, which is key for the extreme deformability within the micron-sized capillaries [102]. However, it is predictable that the behavior of the membrane and cytoskeleton structure would be different at smaller scales, i.e., a few hundred nanometers, as in our case. Indeed, high rigidity of the cytoskeleton, marked by a relatively elevated height of EMVs, was noted via AFM (Fig. 6), despite the polylysine coating of the glass slides, which was supposed to flatten the EMVs owing to electrostatic interactions with the negatively charged glycocalyx. The explanation for the apparent greater stiffness of EMVs and their inability to rear around the G10S5-siRNA polyplex could reside in the increased membrane tension at small scales due to the greater membrane curvature: the elevated surface tension induced by the shear stress would overcome the rupture tension of the vesicle membrane, making it less likely, and more energy-consuming, that a small (200–300 nm) vesicle buds and breaks than a larger giant-unilamellar vesicle (a good approximation of a cell) [103,104]. Doping with DPPC-DSPE-PEG2000 (with a final *w*/w ratio relative to DSPE-PEG2000, of 1 %) modifies this interplay between membrane fluidity, cytoskeleton bending and compression resistance, and surface tension at a small scale, clearly leading to flatter, more flaccid structures, even allowing EMVs to regain the parental donut shape (Fig. 6), the latter caused by the interaction of the cytoskeleton and the membrane and its integral proteins [105]. While the greater flattening in the AFM images can be explained by the extra anionic charges provided by PEG, which is capable of interacting with the polylysine substrate, the regain of the donut shape must have another cause. Indeed, 10 % (as in our hybrid membranes) DPPC in nanoerythrosomes/EMVs caused an increase in the transition temperature to 40.1 °C, similar to that of pure DPPC, and led to a generally greater degree of order in the nanoparticle lipid arrangement [106]. The literature data appear to contradict our findings: indeed, the addition of exogenous lipids such as DPPC should increase the bending modulus and Young's modulus but could also affect the surface tension of the resulting vesicles [107] by increasing it. In [106], no insights into the mechanical properties of doped EMVs were given, but interesting scaffolding, in pentagons and hexagons—and therefore, reorganization of the cytoskeleton and membrane interactions—was later noted on the surfaces of EMVs [14].

In our case, DPPC and DSPE-PEG2000 must play a role in actually making the EMV membrane more fluid, which, when mixed, gives rise to hybrid membranes that regain the donut shape and are capable of fully coating G10S5-siRNA polyplexes. We can summarize the explanations as follows: 1) DPPC itself, as a fully saturated lipid, preferentially inserts in cholesterol-rich domains[108], therefore disrupting erythrocyte membrane rafts [109], and can contribute to overall fluidity and reduce the shear stress resistance of the hybrids; 2) DSPE-PEG2000 polymer heads, already known to cause a shape transition from liposomes to flat discoidal [110], despite being only 1 % phospholipid weight in our model, concur in imposing a certain tension on the underlying bilayer, where DSPE is strongly inserted (Fig. 2 and Fig. 3), reducing the packing density of phospholipids [111]. This would occur via electrostatic repulsion between the PEG polymer heads themselves and with the EMV glycocalix, which is negatively charged (Table 1). To further confirm this model, we conducted a small-scale statistical analysis of cryo-TEM images (Fig. 9S). In hydrated conditions, such as vitrified cryo-TEM (in contrast to AFM observations, where the polylysine substrate and dehydration conditions distort the image), EMVs are considered relatively flat objects [44] (Fig. 1) because of the appearance of rod-like objects, which are simply EMVs sitting on the side. These objects are much less abundant (Student's *t*-test, $p = 0.0001$, over 137 objects in EMVs and 134 in hybrid vesicles, present in 10 images each) in hybrid vesicles than in native EMVs, which is consistent with a diminished effect of cholesterol due to the insertion of DPPC on the flat, discoidal shape of the objects [111]. Therefore, the doping of EMVs was instrumental in obtaining vesicles with mechanical properties suitable for efficiently coating G10S5-siRNA polyplexes.

Electrostatic balance is also instrumental in achieving a fully coated material. Indeed, our data also confirmed how electrostatic repulsion is necessary to achieve good camouflaging efficiency, as demonstrated previously for erythrocytes [112]. Using the self-fluorescence of G10S5, we confirmed via solvatochromic fluorescence experiments that the more negative the polyplexes are, the greater the solvatochromic effect, and thus, the better the coating efficiency (Fig. 8). The hybrids are negatively charged, whereas G10S5 is naturally slightly positive (+12

mV): in the absence of siRNA, this would lead to simple aggregation of the hybrids on top of the G10S5 particles, as shown in Fig. 5. Stable and efficient camouflaging also protected the siRNA payload from RNase A (Fig. 4d). At an insufficiently low zeta potential (at a G10S5-siRNA 25:1 N/P ratio), which is capable of electrostatic repulsion with EMVs/PEG negatively charged moieties, large aggregates appear (Fig. 4a), suggesting that coating is not only unsuccessful but also that overall instability of the polyplex occurs.

The success of camouflage also has a distinct effect on cell experiments. Indeed, the coating with hybrid membranes completely changed the uptake profile of B16F10 murine melanoma cells (Fig. 10 and Fig. 11). Compared with naked G10S5, genistein and imipramine significantly reduced hybrid-G10S5-siRNA internalization, although to a lower degree. While genistein inhibits caveolae-mediated endocytosis, imipramine interferes with membrane ruffle-mediated endocytosis [113]. From this profile, it appears that hybrid nanoparticles follow a mixture of caveolae-mediated endocytosis and phenocytosis mechanisms, whereas naked G10S5 relies on clathrin-mediated endocytosis. Indeed, as we previously reported [44], EMVs appear to overcome endosomes and directly fuse with the membrane or use a nondestructive pathway; such multicaveolar clusters appear to exist since the latter's interaction with lysosomes is still a matter of debate [114]. However, chlorpromazine does not hinder hybrid-G10S5-siRNA uptake, ruling out that the main internalization mechanism involves clathrin-coated pits. In addition to caveole-mediated endocytosis, hybrid-G10S5-siRNA uptake can also be mediated by clathrin-independent/dynamin-independent endocytosis (CLIC/GEEC), which is present in mammalian cells [115], or by flotillin 2-mediated endocytosis, a fusogenic protein highly abundant in the erythrocyte proteome [116]. While changes in internalization pathway induced by the hybrid coating were clearly observed (Fig. 12) and functional gene-silencing activity was retained (Fig. 13), these functional readouts conflate uptake, trafficking, and cytosolic release. However, we cannot exclude the possibility that the coating alters the efficiency or mechanism of endosomal escape. Addressing this point will require targeted experiment assays (for example, cytosol-specific activation reporters and high-resolution microscopy), which we plan to pursue to define how the uptake route and escape efficiency are coupled for this system.

The camouflaging allowed the use of a much lower effective dose than the original G10S5 (Fig. 13). Indeed, with our model, tdTomato-expressing B16F10, we previously observed a knockdown effect at a 5 picomole dose, whereas we previously observed this effect at only 30 picomoles under similar experimental conditions. Interestingly, the expression of the mRNA encoding the gene of interest did not significantly decrease at 5 picomole, but it had a distinct effect on protein expression: this characteristic mimics the typical behavior of an encoded miRNA [117,118]. Instead, the siRNA we generated had perfect compatibility with the tdTomato transgene; therefore, a slight mismatch between the effector and substrate, which is typical of miRNAs and favors translation blockage, can be ruled out [119]. At the higher dose (10 picomoles), a more typical scenario was observed: greater gene knockdown, followed by a more moderate decrease in protein abundance (Fig. 13). At a dose of 5 picomole, corresponding to 5 nanomolar in wells, it can be speculated that only a small fraction of available RISC complexes contain the targeted siRNA, while most of the other complexes are involved in physiological functions. Interestingly, the same effect was also observed for the positive control, Interferin. Moreover, it is possible that, at low concentrations and under physiological conditions, in B16F10 cells, siRNA is preferentially loaded in Ago1 rather than in Ago2, the latter of which has nuclease activity, where Ago1 preferentially acts via adenylation and translational repression [120].

To the best of our knowledge, this is the first report of favored translation blockade rather than mRNA cleavage in B16F10 cells at low siRNA doses, and further studies are needed to elucidate the molecular mechanism of this phenomenon.

Finally, we demonstrated how G10S5 has excellent biocompatibility with lymphoblastoid cells (Fig. 8S), an emerging model for amyotrophic lateral sclerosis (ALS) and frontotemporal dementia (FTD) [48,121]. We successfully knocked down expression of FARSA subunit of phenylalanine aminoacyl-tRNA synthetase (FARS) (Fig. 14 and Table 4), which we have recently shown to be involved in the mechanism of C9orf72 mutation, a dominant genetic cause of ALS and FTD [42]. Furthermore, its mutation has been linked to a number of morbidities, despite the poor characterization of genetic variants, caused by the inherent lethality in the malfunction of the protein [122,123]. It is, therefore, together with all aminoacyl-tRNA synthetases, an interesting target for mitigating the symptoms of multiple genetic conditions (including cancer [124]) in combination with functional protein replacement therapy [125].

In our study, hybrid-G10S5-siRNA appears to overpower commercial transfection agents such as Accell (Horizon Discovery) and Nucleofection (Amaxa Nucofector Kit V, Lonza), [126,127] where the common final well concentration of the siRNA is in the micromolar range [128]; indeed, in our case, a dose of 20 picomoles (i.e., 40 nanomolar) already led to more than 70 % target protein knockdown (Table 4). Indeed, while cytotoxicity was negligible in the case of naked G10S5, the knockdown effect on FARSA, a phenylalanine-tRNA synthetase, subunit A, was more than double for hybrids than for naked G10S5 (Fig. 14), again confirming that the coating is an effective tool for reducing the dose. On the other hand, more advanced approaches for siRNA delivery to lymphocyte-like cells often employ a lipid nanoparticle-conjugated targeting agent, such as an antibody [129] or an aptamer [130]. As we confirmed, for transfecting siRNA into lymphocyte-like cells, the development of an agent with amphiphilic and zwitterionic properties (similar to G10S5) is instrumental [131]. Erythrocyte/DPPC-DSPE-PEG2000-coated G10S5 nanoparticles represent a new staple for siRNA transfection in suspension cells. While in vivo studies are beyond the current scope, based on the well-established properties of erythrocyte membranes in prolonging systemic circulation [44] and PEGylation in reducing immune recognition, we anticipate that our system would demonstrate extended blood retention and enhanced stability in vivo compared to naked G10S5 (they are positively charged and are expected to be rapidly eliminated). With coating, G10S5's good complexation ability is retained and high tumour accumulation is expected due to the coating, but with even enhanced siRNA delivery as in the case of siRNA-EMVs only.

## 5. Conclusions and future perspectives

Over the past few years, we have developed a set of genipin-spermine-glycine-based, zwitterionic, nanosized particles. Among these, the one with the best transfection efficiency and biocompatibility was G10S5, the name referring to the molar ratio, relative to genipin, of glycine (G) and spermine (S). We therefore aimed to further improve its characteristics by camouflaging it with a biomimetic membrane, conferring novel properties. We attempted to do this with pure erythrocyte membranes, a carrier already deeply characterized within our lab [44], but the mechanical and electrostatic properties appeared not to be suitable for the scope; therefore, we doped the EMVs with a common liposomal formulation, DPPC-DSPE-PEG 2000 (9:1 M ratio), at 10 % weight relative to EMP phospholipids. This second attempt was successful: we then examined the ultrastructures of the resulting camouflaged nanoparticles via conventional TEM, cryoTEM and AFM; we investigated their properties in terms of size and zeta potential; their cytotoxicity; the internalization pathway; and, finally, their ability to deliver a small-interfering RNA targeted toward a reference gene in an adherent and a suspension cell line. The results revealed how camouflaging improved the international rate and greatly reduced the effective dose to achieve good knockdown compared with that of the »naked« nanoparticles. Given these results, we look forward to in vivo experiments. Furthermore, we aimed to validate actively targeted nanoparticles to achieve even more efficient in situ delivery and knockdown.

### CRediT authorship contribution statement

**Giulia Della Pelle:** Writing – review & editing, Writing – original draft, Investigation, Formal analysis, Data curation, Conceptualization. **Boštjan Markelc:** Supervision, Methodology, Investigation, Formal analysis. **Urša Čerček:** Methodology, Formal analysis, Data curation. **Urška Živic:** Investigation, Data curation. **Mia Coupard:** Investigation, Data curation. **Jernej Šribar:** Supervision, Methodology, Investigation, Funding acquisition, Formal analysis. **Igor Križaj:** Resources, Funding acquisition. **Muhammad Shahid Arshad:** Methodology, Data curation. **Tim Božic:** Methodology, Formal analysis, Data curation. **Lea Gazvoda:** Formal analysis, Investigation. **Boris Rogelj:** Resources, Methodology, Funding acquisition. **Nina Kostevšek:** Writing – review & editing, Writing – original draft, Supervision, Resources, Project administration, Methodology, Funding acquisition.

### Declaration of competing interest

The authors declare no competing financial interests.

### Acknowledgements

The study was supported by the Slovenian Research and Innovation Agency ARIS (program numbers P1-0207, P2-0084, P2-0091, P3-0003, P3-0108, P4-0127, project numbers PR-10482, J3-4503, J3-3065, J3-60057, J7-60125, J1-50026, J2-60047 and J4-50150). CryoTEM was performed by Dr. Matic Kisovec at the National Institute of Chemistry CryoEM Facility, supported by the Slovenian Research Agency Infrastructure Programme IO-0003.

### Appendix A. Supplementary data

Supplementary data to this article can be found online at https://doi.org/10.1016/j.bioadv.2025.214537.

### Data availability

Data will be made available on request.

### References

[1] B. Hu, et al., Therapeutic siRNA: State of the art, Signal Transduct. Target. Ther. 5 (1) (2020), https://doi.org/10.1038/s41392-020-0207-x.
[2] S. Ranjbar, X. Bo Zhong, J. Manautou, X. Lu, A holistic analysis of the intrinsic and delivery-mediated toxicity of siRNA therapeutics, Adv. Drug Deliv. Rev. 201 (2023) 1–38, https://doi.org/10.1016/j.addr.2023.115052.
[3] J.D. Shih, C.P. Hunter, SID-1 is a dsRNA-selective dsRNA-gated Channel, 2011, pp. 1057–1065, https://doi.org/10.1261/rna.2596511.genetic.
[4] S. Sorrentino, The eight human 'canonical' ribonucleases: molecular diversity, catalytic properties, and special biological actions of the enzyme proteins, FEBS Lett. 584 (11) (Jun. 2010) 2194–2200, https://doi.org/10.1016/J.FEBSLET.2010.04.018.
[5] C.E. Thomas, A. Ehrhardt, M.A. Kay, Progress and problems with the use of viral vectors for gene therapy, Nat. Rev. Genet. 4 (5) (May 2003) 346–358, https://doi.org/10.1038/nrg1066.
[6] K. Paunovska, D. Loughrey, J.E. Dahlman, Drug delivery systems for RNA therapeutics, Nat. Rev. Genet. 23 (5) (May 2022) 265–280, https://doi.org/10.1038/s41576-021-00439-4.
[7] M.J. Byun, et al., Advances in nanoparticles for effective delivery of RNA therapeutics, Biochip J. 16 (2) (Jun. 2022) 128–145, https://doi.org/10.1007/s13206-022-00052-5.
[8] J.D. Torres-Vanegas, J.C. Cruz, L.H. Reyes, Delivery systems for nucleic acids and proteins: barriers, cell capture pathways and nanocarriers, Pharmaceutics 13 (3) (Mar. 2021) 428, https://doi.org/10.3390/pharmaceutics13030428.
[9] G. Della Pelle, T. Bozic, M. Vukomanović, G. Sersa, B. Markelc, N. Kostevšek, Efficient siRNA delivery to murine melanoma cells via a novel genipin-based nano-polymer, Nanoscale Adv. (2024), https://doi.org/10.1039/d4na00363b.
[10] V. Vijayan, S. Uthaman, I.K. Park, Cell membrane-camouflaged nanoparticles: a promising biomimetic strategy for cancer theragnostics, Polymers 10 (9) (2018) 983, https://doi.org/10.3390/POLYM10090983.
[11] P. Wang, et al., Bioinspired red blood cell membrane-encapsulated biomimetic nanoconstructs for synergistic and efficacious chemo-photothermal therapy, Colloids Surf. B: Biointerfaces 189 (May 2020) 110842, https://doi.org/10.1016/J.COLSURFB.2020.110842.
[12] A. Vincy, S. Mazumder, I. Banerjee Amrita, K.C. Hwang, R. Vankayala, Recent progress in red blood cells-derived particles as novel bioinspired drug delivery systems: challenges and strategies for clinical translation, Front. Chem. 10 (Apr. 2022) 905256, https://doi.org/10.3389/FCHEM.2022.905256/BIBTEX.
[13] Y. Wang, et al., Worm-like biomimetic nanoerythrocyte carrying siRNA for melanoma gene therapy, Small 14 (47) (Nov. 2018) 1803002, https://doi.org/10.1002/SMLL.201803002;PAGE:STRING:ARTICLE/CHAPTER.
[14] R. Deák, et al., Nanoerythrosomes tailoring: lipid induced protein scaffolding in ghost membrane derived vesicles, Mater. Sci. Eng. C 109 (2020) 110428, https://doi.org/10.1016/j.msec.2019.110428.
[15] C.F. Rodrigues, I.J. Correia, A.F. Moreira, Red blood cell membrane-camouflaged gold-core silica shell nanorods for cancer drug delivery and photothermal therapy, Int. J. Pharm. 655 (Apr. 2024) 124007, https://doi.org/10.1016/J.IJPHARM.2024.124007.
[16] C.M.J. Hu, L. Zhang, S. Aryal, C. Cheung, R.H. Fang, L. Zhang, Erythrocyte membrane-camouflaged polymeric nanoparticles as a biomimetic delivery platform, Proc. Natl. Acad. Sci. USA 108 (27) (Jul. 2011) 10980–10985, https://doi.org/10.1073/PNAS.1106634108/SUPPL_FILE/PNAS.1106634108_SI.PDF.
[17] J. Su, et al., Preparation and characterization of erythrocyte membrane cloaked PLGA/arsenic trioxide nanoparticles and evaluation of their in vitro anti-tumor effect, RSC Adv. 8 (36) (May 2018) 20068–20076, https://doi.org/10.1039/C8RA01417E.
[18] X. Xie, et al., Erythrocyte membrane cloaked curcumin-loaded nanoparticles for enhanced chemotherapy, Pharmaceutics 11 (9) (2019) 429, https://doi.org/10.3390/PHARMACEUTICS11090429.
[19] L.L. Li, J.H. Xu, G. Bin Qi, X. Zhao, F. Yu, H. Wang, Core-shell supramolecular gelatin nanoparticles for adaptive and 'on-demand' antibiotic delivery, ACS Nano 8 (5) (May 2014) 4975–4983, https://doi.org/10.1021/NN501040H/SUPPL_FILE/NN501040H_SI_001.PDF.
[20] D. Zou, et al., Nanoparticle elasticity regulates the formation of cell membrane-coated nanoparticles and their nano-bio interactions, Proc. Natl. Acad. Sci. USA 120 (1) (Jan. 2023) e2214757120, https://doi.org/10.1073/PNAS.2214757120/SUPPL_FILE/PNAS.2214757120.SAPP.PDF.
[21] L. Liu, et al., Systematic design of cell membrane coating to improve tumor targeting of nanoparticles, Nat. Commun. 13 (1) (Oct. 2022) 1–15, https://doi.org/10.1038/s41467-022-33889-3.
[22] R. Mizuta, F. Inoue, Y. Sasaki, S. Ichi Sawada, K. Akiyoshi, A facile method to coat nanoparticles with lipid bilayer membrane: hybrid silica nanoparticles disguised as biomembrane vesicles by particle penetration of concentrated lipid layers, Small 19 (12) (Mar. 2023), https://doi.org/10.1002/SMLL.202206153.
[23] M. Pannuzzo, B.A.C. Horta, C. La Rosa, P. Decuzzi, Predicting the miscibility and rigidity of poly(lactic- co-glycolic acid)/polyethylene glycol blends via molecular dynamics simulations, Macromolecules 53 (10) (May 2020) 3643–3654, https://doi.org/10.1021/ACS.MACROMOL.0C00110/ASSET/IMAGES/LARGE/MA0C00110_0006.JPEG.
[24] B. Sarrazin, N. Tsapis, L. Mousnier, N. Taulier, W. Urbach, P. Guenoun, AFM investigation of liquid-filled polymer microcapsules elasticity, Langmuir 32 (18) (2016) 4610–4618, https://doi.org/10.1021/acs.langmuir.6b00431.
[25] J. Xu, V. Karra, D.E. Large, D.T. Auguste, F.R. Hung, Understanding the mechanical properties of ultradeformable liposomes using molecular dynamics simulations, J. Phys. Chem. B 127 (44) (Nov. 2023) 9496–9512, https://doi.org/10.1021/ACS.JPCB.3C04386/ASSET/IMAGES/LARGE/JP3C04386_0010.JPEG.
[26] N. Benne, et al., Atomic force microscopy measurements of anionic liposomes reveal the effect of liposomal rigidity on antigen-specific regulatory T cell responses, J. Control. Release 318 (Feb. 2020) 246–255, https://doi.org/10.1016/J.JCONREL.2019.12.003.
[27] X. Liang, G. Mao, K.Y.S. Ng, Mechanical properties and stability measurement of cholesterol-containing liposome on mica by atomic force microscopy, J. Colloid Interface Sci. 278 (1) (Oct. 2004) 53–62, https://doi.org/10.1016/j.jcis.2004.05.042.
[28] K. Mendová, M. Otáhal, M. Drab, M. Daniel, Size matters: rethinking hertz model interpretation for cell mechanics using AFM, Int. J. Mol. Sci. 25 (13) (2024), https://doi.org/10.3390/ijms25137186.
[29] C. Corbo, et al., Unveiling the in vivo protein corona of circulating leukocyte-like carriers, ACS Nano 11 (3) (2017) 3262–3273, https://doi.org/10.1021/acsnano.7b00376.
[30] A. Mahendra, H.P. James, S. Jadhav, PEG-grafted phospholipids in vesicles: Effect of PEG chain length and concentration on mechanical properties, Chem. Phys. Lipids 218 (2019) 47–56, https://doi.org/10.1016/j.chemphyslip.2018.12.001.
[31] E. Evans, W. Rawicz, Elasticity of 'fuzzy' biomembranes, Phys. Rev. Lett. 79 (12) (1997) 2379–2382, https://doi.org/10.1103/PhysRevLett.79.2379.
[32] M. Silvander, M. Johnsson, K. Edwards, Effects of PEG-lipids on permeability of phosphatidylcholine/cholesterol liposomes in buffer and in human serum, Chem. Phys. Lipids 97 (1) (Dec. 1998) 15–26, https://doi.org/10.1016/S0009-3084(98)00088-7.
[33] M. Kowalska, M. Broniatowski, M. Mach, Ł. Płachta, P. Wydro, The effect of the polyethylene glycol chain length of a lipopolymer (DSPE-PEGn) on the properties of DPPC monolayers and bilayers, J. Mol. Liq. 335 (Aug. 2021) 116529, https://doi.org/10.1016/J.MOLLIQ.2021.116529.
[34] K. Wang, Z. Li, O. Egini, R. Wadgaonkar, X.C. Jiang, Y. Chen, Atomic force microscopy reveals involvement of the cell envelope in biomechanical properties of sickle erythrocytes, BMC Biol. 21 (1) (Dec. 2023) 31, https://doi.org/10.1186/S12915-023-01523-3.

[35] V. Sergunova, et al., Investigation of red blood cells by atomic force microscopy, Sensors (Basel) 22 (5) (Mar. 2022) 2055, https://doi.org/10.3390/S22052055.
[36] A. Langari, et al., Morphometric and nanomechanical features of erythrocytes characteristic of early pregnancy loss, Int. J. Mol. Sci. 23 (9) (2022), https://doi.org/10.3390/ijms23094512.
[37] A.J. Ewunkem, K. Agee, Optimization of transfection methods for human lymphoblast TK6 cell line, Gene Prot. Dis. 2 (2) (May 2023) 0353, https://doi.org/10.36922/gpd.0353.
[38] I. Rahimmanesh, M. Totonchi, H. Khanahmad, The challenging nature of primary T lymphocytes for transfection: Effect of protamine sulfate on the transfection efficiency of chemical transfection reagents, Res. Pharm. Sci. 15 (5) (Oct. 2020) 437–446, https://doi.org/10.4103/1735-5362.297846.
[39] B. Fadnes, et al., The proteoglycan repertoire of lymphoid cells, Glycoconj. J. 29 (7) (Oct. 2012) 513, https://doi.org/10.1007/S10719-012-9427-9.
[40] G.T. Hess, W.H. Humphries IV, N.C. Fay, C.K. Payne, Cellular binding, motion, and internalization of synthetic gene delivery polymers, Biochim. Biophys. Acta, Mol. Cell Res. 1773 (10) (2007) 1583–1588, https://doi.org/10.1016/j.bbamcr.2007.07.009.
[41] S.A.B. Riedl, P. Kaiser, A. Raup, C.V. Synatschke, V. Jérôme, R. Freitag, Non-viral transfection of human T lymphocytes, Processes 6 (10) (2018) 188, https://doi.org/10.3390/PR6100188.
[42] J. An, et al., Enhancement of the viability of T cells electroporated with DNA via osmotic dampening of the DNA-sensing cGAS–STING pathway, Nat. Biomed. Eng. 8 (2) (Jul. 2023) 149–164, https://doi.org/10.1038/s41551-023-01073-7.
[43] S. Mizrahy, I. Hazan-Halevy, N. Dammes, D. Landesman-Milo, D. Peer, Current progress in non-viral RNAi-based delivery strategies to lymphocytes, Mol. Ther. 25 (7) (Jul. 2017) 1491, https://doi.org/10.1016/J.YMTHE.2017.03.001.
[44] G. Della Pelle, et al., Red blood cell membrane vesicles for siRNA delivery: a biocompatible carrier with passive tumor targeting and prolonged plasma residency, Int. J. Nanomedicine 20 (Mar. 2025) 3269–3301, https://doi.org/10.2147/IJN.S504644.
[45] G. Della Pelle, A. Delgado López, M. Salord Fiol, N. Kostevšek, Cyanine dyes for photo-thermal therapy: a comparison of synthetic liposomes and natural erythrocyte-based carriers, Int. J. Mol. Sci. 22 (13) (2021), https://doi.org/10.3390/ijms22136914.
[46] S. Friedenauer, H.H. Berlet, Sensitivity and variability of the Bradford protein assay in the presence of detergents, Anal. Biochem. 178 (2) (1989) 263–268, https://doi.org/10.1016/0003-2697(89)90636-2.
[47] J. S.-A. biochemistry and U, Colorimetric determination of phospholipids with ammonium ferrothiocyanate, Anal. Biochem. 104 (1) (1980) 10–14, https://doi.org/10.1016/0003-2697(80)90269-9.
[48] M. Malnar Črnigoj, et al., Phenylalanine-tRNA aminoacylation is compromised by ALS/FTD-associated C9orf72 C4G2 repeat RNA, Nat. Commun. 14 (1) (2023) 1–15, https://doi.org/10.1038/s41467-023-41511-3.
[49] W. Strober, Trypan blue exclusion test of cell viability, Curr. Protoc. Immunol. 111 (1) (Nov. 2015), https://doi.org/10.1002/0471142735.ima03bs111.
[50] N. Kostevšek, P. Miklavc, M. Kisovec, M. Podobnik, W. Al-Jamal, I. Serša, Magneto-erythrocyte membrane vesicles' superior t2 mri contrast agents to magneto-liposomes, Magnetochemistry 7 (4) (Apr. 2021) 51, https://doi.org/10.3390/magnetochemistry7040051.
[51] T. Li, C.J. Nowell, D. Cipolla, T. Rades, B.J. Boyd, Direct comparison of standard transmission electron microscopy and cryogenic-TEM in imaging nanocrystals inside liposomes, Mol. Pharm. 16 (4) (2019) 1775–1781, https://doi.org/10.1021/acs.molpharmaceut.8b01308.
[52] V. Mittal, N.B. Matsko, Analytical imaging techniques for soft matter characterization, in: Engineering Materials vol. 11, no. 1, Springer Berlin Heidelberg, Berlin, Heidelberg, 2012, https://doi.org/10.1007/978-3-642-30400-2.
[53] Q. Lubart, et al., Lipid vesicle composition influences the incorporation and fluorescence properties of the lipophilic sulphonated carbocyanine dye SP-DiO, Phys. Chem. Chem. Phys. 22 (16) (2020) 8781–8790, https://doi.org/10.1039/c9cp04158c.
[54] W. Rodgers, M. Glaser, Characterization of lipid domains in erythrocyte membranes, Proc. Natl. Acad. Sci. USA 88 (4) (1991) 1364–1368, https://doi.org/10.1073/pnas.88.4.1364.
[55] G. Bianchetti, et al., Spatial reorganization of liquid crystalline domains of red blood cells in type 2 diabetic patients with peripheral artery disease, Int. J. Mol. Sci. 23 (19) (2022), https://doi.org/10.3390/ijms231911126.
[56] S.L. Yefimova, T.N. Tkacheva, I.Y. Kurilchenko, A.V. Sorokin, Y.V. Malyukin, Spectroscopic Study of Interactions Between Dye Molecules in Micelle and Liposome Nanovolumes 79, 2013, pp. 914–921, https://doi.org/10.1007/s10812-013-9694-7.
[57] G. Yang, Y. Liu, J. Teng, C.X. Zhao, FRET ratiometric nanoprobes for nanoparticle monitoring, Biosensors (Basel) 11 (12) (2021), https://doi.org/10.3390/bios1120505.
[58] T.P. Lehmann, et al., Quantification of the asymmetric migration of the lipophilic dyes, DiO and DiD, in homotypic co-cultures of chondrosarcoma SW-1353 cells, Mol. Med. Rep. 14 (5) (2016) 4529–4536, https://doi.org/10.3892/mmr.2016.5793.
[59] F. Lassailly, E. Griessinger, D. Bonnet, 'Microenvironmental contaminations' induced by fluorescent lipophilic dyes used for noninvasive in vitro and in vivo cell tracking, Blood 115 (26) (2010) 5347–5354, https://doi.org/10.1182/blood-2009-05-224030.
[60] R. Rai, S. Alwani, I. Badea, Polymeric nanoparticles in gene therapy: New avenues of design and optimization for delivery applications, Polymers (Basel) 11 (4) (2019), https://doi.org/10.3390/polym11040745.
[61] F. Yang, M.H. Cabe, S.D. Ogle, V. Sanchez, K.A. Langert, Optimization of critical parameters for coating of polymeric nanoparticles with plasma membrane vesicles by sonication, Sci. Rep. 0123456789 (2021) 1–13, https://doi.org/10.1038/s41598-021-03422-5.
[62] M. Lekka, et al., Erythrocyte stiffness probed using atomic force microscope, Biorheology 42 (4) (Jul. 2005) 307–317, https://doi.org/10.1177/0006355X2005042004004.
[63] S. Barns, M.A. Balanant, E. Sauret, R. Flower, S. Saha, Y.T. Gu, Investigation of red blood cell mechanical properties using AFM indentation and coarse-grained particle method, Biomed. Eng. Online 16 (1) (Dec. 2017) 140, https://doi.org/10.1186/S12938-017-0429-5.
[64] J. Eid, H. Razmazma, A. Jraij, A. Ebrahimi, L. Monticelli, On calculating the bending modulus of lipid bilayer membranes from buckling simulations, J. Phys. Chem. B 124 (29) (2020) 6299–6311, https://doi.org/10.1021/acs.jpcb.0c04253.
[65] J. Tapia, et al., Correlated flickering of erythrocytes membrane observed with dual time resolved membrane fluctuation spectroscopy under different d-glucose concentrations, Sci. Rep. 11 (1) (2021) 1–12, https://doi.org/10.1038/s41598-021-82018-5.
[66] S. Himbert, et al., The bending rigidity of the red blood cell cytoplasmic membrane, PLoS One 17 (8 August) (2022) 1–20, https://doi.org/10.1371/journal.pone.0269619.
[67] D. Drabik, G. Chodaczek, S. Kraszewski, M. Langner, Mechanical properties determination of DMPC, DPPC, DSPC, and HSPC solid-ordered bilayers, Langmuir 36 (14) (Apr. 2020) 3826–3835, https://doi.org/10.1021/acs.langmuir.0c00475.
[68] Q. Xia, Y. Zhang, Z. Li, X. Hou, N. Feng, Red blood cell membrane-camouflaged nanoparticles: a novel drug delivery system for antitumor application, Acta Pharm. Sin. B 9 (4) (2019) 675–689, https://doi.org/10.1016/j.apsb.2019.01.011.
[69] M. Takeuchi, H. Miyamoto, Y. Sako, H. Komizu, A. Kusumi, Structure of the erythrocyte membrane skeleton as observed by atomic force microscopy, Biophys. J. 74 (5) (1998) 2171–2183, https://doi.org/10.1016/S0006-3495(98)77926-3.
[70] V. Sergunova, et al., Investigation of red blood cells by atomic force microscopy, Sensors 22 (5) (2022) 1–13, https://doi.org/10.3390/s22052055.
[71] K.M. Schakowski, J. Linders, K.B. Ferenz, M. Kirsch, Synthesis and characterisation of aqueous haemoglobin-based microcapsules coated by genipin-cross-linked albumin, J. Microencapsul. 37 (3) (2020) 193–204, https://doi.org/10.1080/02652048.2020.1715498.
[72] D. Vukajlovic, et al., Mathematical modelling of genipin-bovine serum albumin interaction using fluorescence intensity measurements, Int. J. Biol. Macromol. 276 (P1) (2024) 133850, https://doi.org/10.1016/j.ijbiomac.2024.133850.
[73] S. Matcham, K. Novakovic, Fluorescence imaging in genipin crosslinked chitosan-poly(vinyl pyrrolidone) hydrogels, Polymers (Basel) 8 (11) (2016) 1–10, https://doi.org/10.3390/polym8110385.
[74] C. Pizzolitto, et al., On the mechanism of genipin binding to primary amines in lactose-modified chitosan at neutral pH, Int. J. Mol. Sci. 21 (18) (2020) 1–17, https://doi.org/10.3390/ijms21186831.
[75] N.M. Bonanno, et al., Substituent effects of amines on genipin dye formation – Insights into dye origin, Dyes Pigments 220 (Dec. 2023) 111681, https://doi.org/10.1016/j.dyepig.2023.111681.
[76] F. Buonocore, et al., Fish-derived antimicrobial peptides: activity of a chionodracine mutant against bacterial models and human bacterial pathogens, Dev. Comp. Immunol. 96 (December 2018) (2019) 9–17, https://doi.org/10.1016/j.dci.2019.02.012.
[77] L.D. Hughes, R.J. Rawle, S.G. Boxer, Choose your label wisely: water-soluble fluorophores often interact with lipid bilayers, PLoS One 9 (2) (Feb. 2014), https://doi.org/10.1371/journal.pone.0087649.
[78] M. Homocianu, Exploring solvatochromism: a comprehensive analysis of research data, Microchem. J. 198 (Mar. 2024) 110166, https://doi.org/10.1016/j.microc.2024.110166.
[79] X. Qin, X. Yang, L. Du, M. Li, Polarity-based Fluorescence Probes: Properties and Applications, Royal Society of Chemistry, Nov. 01, 2021, https://doi.org/10.1039/d1md00170a.
[80] H. Sunahara, Y. Urano, H. Kojima, T. Nagano, Design and synthesis of a library of BODIPY-based environmental polarity sensors utilizing photoinduced electron-transfer-controlled fluorescence ON/OFF switching, J. Am. Chem. Soc. 129 (17) (May 2007) 5597–5604, https://doi.org/10.1021/ja068551y.
[81] B. Kamel, M. Sayem El-Daher, W. Bachir, A. Ibrahim, S. Aljalali, Effect of solvents on the fluorescent spectroscopy of BODIPY-520 derivative, J. Spectrosc. 2022 (2022), https://doi.org/10.1155/2022/1172183.
[82] S.T. Abdel-Halim, Effect of solvent on absorption and fluorescence spectra of a typical fluorinated azo dye for its acidic and basic structures, Spectrochim. Acta A Mol. Biomol. Spectrosc. 82 (1) (Nov. 2011) 253–259, https://doi.org/10.1016/j.saa.2011.07.045.
[83] R. Yi, Y. Qin, I.G. Macara, B.R. Cullen, Exportin-5 mediates the nuclear export of pre-microRNAs and short hairpin RNAs, Genes Dev. 17 (24) (Dec. 2003) 3011–3016, https://doi.org/10.1101/gad.1158803.
[84] D. Grimm, The Dose Can Make the Poison: Lessons Learned From Adverse In vivo Toxicities Caused by RNAi Overexpression, Aug. 26, 2011, https://doi.org/10.1186/1758-907X-2-8.
[85] F. Chen, et al., Clathrin-mediated endocytosis is a candidate entry sorting mechanism for Bombyx mori cypovirus, Sci. Rep. 8 (1) (May 2018) 7268, https://doi.org/10.1083/jcb.123.5.1107.
[86] I.R. Nabi, P.U. Le, Caveolae/Raft-dependent Endocytosis, May 26, 2003, https://doi.org/10.1083/jcb.200302028.

[87] L.H. Wang, K.G. Rothberg, R.G. Anderson, Mis-assembly of clathrin lattices on endosomes reveals a regulatory switch for coated pit formation, J. Cell Biol. 123 (5) (Dec. 1993) 1107–1117, https://doi.org/10.1083/jcb.123.5.1107.
[88] J.A. Daniel, et al., Phenothiazine-derived antipsychotic drugs inhibit dynamin and clathrin-mediated endocytosis, Traffic 16 (6) (Jun. 2015) 635–654, https://doi.org/10.1111/tra.12272.
[89] H.P. Lin, et al., Identification of novel macropinocytosis inhibitors using a rational screen of Food and Drug Administration-approved drugs, Br. J. Pharmacol. 175 (18) (Sep. 2018) 3640–3655, https://doi.org/10.1111/bph.14429.
[90] R. Biswas, K.L. Trout, F. Jessop, J.R. Harkema, A. Holian, Imipramine blocks acute silicosis in a mouse model, Part. Fibre Toxicol. 14 (1) (Sep. 2017), https://doi.org/10.1186/s12989-017-0217-1.
[91] R.R. Kay, Macropinocytosis: Biology and Mechanisms, Elsevier B.V., Dec. 01, 2021, https://doi.org/10.1016/j.cdev.2021.203713.
[92] S. Niaz, M.U. Hussain, Role of GW182 protein in the cell, Int. J. Biochem. Cell Biol. 101 (2018) 29–38, https://doi.org/10.1016/j.biocel.2018.05.009.
[93] M. Feng, K. Yang, J. Wang, G. Li, H. Zhang, First report of FARSA in the regulation of cell cycle and survival in mantle cell lymphoma cells via PI3K-AKT and FOXO1-RAG1 axes, Int. J. Mol. Sci. 24 (2) (2023), https://doi.org/10.3390/ijms24021608.
[94] H.J. Shin, M. Kwak, S. Joo, J.Y. Lee, Quantifying fluorescent nanoparticle uptake in mammalian cells using a plate reader, Sci. Rep. 12 (1) (Dec. 2022), https://doi.org/10.1038/s41598-022-24480-3.
[95] T.G. Iversen, T. Skotland, K. Sandvig, Endocytosis and Intracellular Transport of Nanoparticles: Present Knowledge and Need for Future Studies, Apr. 2011, https://doi.org/10.1016/j.nantod.2011.02.003.
[96] Z. Shen, H. Ye, X. Yi, Y. Li, Membrane wrapping efficiency of elastic nanoparticles during endocytosis: size and shape matter, ACS Nano 13 (1) (2019) 215–228, https://doi.org/10.1021/acsnano.8b05340.
[97] W. Chen, F. Duša, J. Witos, S.K. Ruokonen, S.K. Wiedmer, Determination of the main phase transition temperature of phospholipids by nanoplasmonic sensing, Sci. Rep. 8 (1) (Oct. 2018) 1–11, https://doi.org/10.1038/s41598-018-33107-5.
[98] M.D. Rieth, A. Lozano, Preparation of DPPC liposomes using probe-tip sonication: Investigating intrinsic factors affecting temperature phase transitions, Biochem. Biophys. Rep. 22 (Jul. 2020) 100764, https://doi.org/10.1016/J.BBREP.2020.100764.
[99] G.M. Artmann, C. Kelemen, D. Porst, G. Buldt, S. Chien, Temperature transitions of protein properties in human red blood cells, Biophys. J. 75 (6) (Dec. 1998) 3179–3183, https://doi.org/10.1016/S0006-3495(98)77759-8.
[100] R. Cullis, Hydrocarbon phase transitions, heterogeneous lipid distributions and lipid-protein interactions in erythrocyte membranes, FEBS Lett. 68 (2) (1976) 173–176, https://doi.org/10.1016/0014-5793(76)80430-9.
[101] H. Li, G. Lykotrafitis, Erythrocyte membrane model with explicit description of the lipid bilayer and the spectrin network, Biophys. J. 107 (3) (2014) 642–653, https://doi.org/10.1016/j.bpj.2014.06.031.
[102] S. Himbert, M.C. Rheinstädter, Structural and mechanical properties of the red blood cell's cytoplasmic membrane seen through the lens of biophysics, Front. Physiol. 13 (Sep. 2022) 953257, https://doi.org/10.3389/FPHYS.2022.953257/XML/NLM.
[103] P.J. Patty, B.J. Frisken, The pressure-dependence of the size of extruded vesicles, Biophys. J. 85 (2) (Aug. 2003) 996–1004, https://doi.org/10.1016/S0006-3495(03)74538-X.
[104] M. Traïkia, D.E. Warschawski, O. Lambert, J.L. Rigaud, P.F. Devaux, Asymmetrical membranes and surface tension, Biophys. J. 83 (3) (Sep. 2002) 1443–1454, https://doi.org/10.1016/S0006-3495(02)73915-5.
[105] K. Zeman, H. Engelhard, E. Sackmann, Bending undulations and elasticity of the erythrocyte membrane: effects of cell shape and membrane organization, Eur. Biophys. J. 18 (4) (1990) 203–219, https://doi.org/10.1007/BF00183373.
[106] R. Deák, J. Mihály, I.C. Szigyártó, A. Wacha, G. Lelkes, A. Bóta, Physicochemical characterization of artificial nanoerythrosomes derived from erythrocyte ghost membranes, Colloids Surf. B: Biointerfaces 135 (2015) 225–234, https://doi.org/10.1016/j.colsurfb.2015.07.066.
[107] E. Evans, W. Rawicz, Entropy-driven tension and bending elasticity in condensed-fluid membranes, Phys. Rev. Lett. 64 (17) (Apr. 1990) 2094, https://doi.org/10.1103/PhysRevLett.64.2094.
[108] S.H. Yu, F. Possmayer, Dipalmitoylphosphatidylcholine and cholesterol in monolayers spread from adsorbed films of pulmonary surfactant, J. Lipid Res. 42 (9) (Sep. 2001) 1421–1429, https://doi.org/10.1016/S0022-2275(20)30274-1.
[109] A. Ciana, C. Achilli, G. Minetti, Membrane rafts of the human red blood cell, Mol. Membr. Biol. 31 (2–3) (2014) 47–57, https://doi.org/10.3109/09687688.2014.896485.
[110] K. Edwards, M. Johnsson, G. Karlsson, M. Silvander, Effect of polyethyleneglycol-phospholipids on aggregate structure in preparations of small unilamellar liposomes, Biophys. J. 73 (1) (1997) 258–266, https://doi.org/10.1016/S0006-3495(97)78066-4.
[111] W. Zhang, et al., The effect of DSPE-PEG2000, cholesterol and drug incorporated in bilayer on the formation of discoidal micelles, Eur. J. Pharm. Sci. 125 (2018) 74–85, https://doi.org/10.1016/j.ejps.2018.09.013.
[112] B.T. Luk, et al., Interfacial interactions between natural RBC membranes and synthetic polymeric nanoparticles, Nanoscale 6 (5) (2014) 2730–2737, https://doi.org/10.1039/c3nr06371b.
[113] H.P. Lin, et al., Identification of novel macropinocytosis inhibitors using a rational screen of Food and Drug Administration-approved drugs, Br. J. Pharmacol. 175 (18) (Sep. 2018) 3640–3655, https://doi.org/10.1111/BPH.14429;WGROUP:STRING:PUBLICATION.
[114] A.L. Kiss, E. Botos, Endocytosis via caveolae: Alternative pathway with distinct cellular compartments to avoid lysosomal degradation? J. Cell. Mol. Med. 13 (7) (Jul. 2009) 1228, https://doi.org/10.1111/J.1582-4934.2009.00754.X.
[115] M. Shafaq-Zadah, E. Dransart, L. Johannes, Clathrin-independent endocytosis, retrograde trafficking, and cell polarity, Curr. Opin. Cell Biol. 65 (Aug. 2020) 112, https://doi.org/10.1016/J.CEB.2020.05.009.
[116] M. Prudent, J. Delobel, A. Hübner, C. Benay, N. Lion, J.D. Tissot, Proteomics of stored red blood cell membrane and storage-induced microvesicles reveals the association of flotillin-2 with band 3 complexes, Front. Physiol. 9 (MAY) (May 2018) 318559, https://doi.org/10.3389/FPHYS.2018.00421/BIBTEX.
[117] R. Singhania, et al., Short interfering RNA induced generation and translation of stable 5′ mRNA cleavage intermediates, Biochim. Biophys. Acta Gene Regul. Mech. 1859 (8) (Aug. 2016) 1034–1042, https://doi.org/10.1016/j.bbagrm.2016.06.005.
[118] Y. Zeng, R. Yi, B.R. Cullen, MicroRNAs and small interfering RNAs can inhibit mRNA expression by similar mechanisms, Proc. Natl. Acad. Sci. USA 100 (17) (2003) 9779–9784, https://doi.org/10.1073/pnas.1630797100.
[119] B. Yao, S. Li, E.K.L. Chan, Function of GW182 and GW bodies in siRNA and miRNA pathways, Adv. Exp. Med. Biol. 768 (2013) 71–96, https://doi.org/10.1007/978-1-4614-5107-5_6.
[120] A. van den Berg, J. Mols, J. Han, RISC-target interaction: cleavage and translational suppression, Biochim. Biophys. Acta 1779 (11) (Nov. 2008) 668, https://doi.org/10.1016/J.BBAGRM.2008.07.005.
[121] O. Pansarasa, et al., Lymphoblastoid cell lines as a model to understand amyotrophic lateral sclerosis disease mechanisms, Dis. Model. Mech. 11 (3) (Mar. 2018) dmm031625, https://doi.org/10.1242/DMM.031625.
[122] K. Krenke, et al., FARSA mutations mimic phenylalanyl-tRNA synthetase deficiency caused by FARSB defects, Clin. Genet. 96 (5) (Nov. 2019) 468–472, https://doi.org/10.1111/CGE.13614.
[123] S.Y. Kim, et al., Fatal systemic disorder caused by biallelic variants in FARSA, Orphanet J. Rare Dis. 17 (1) (Dec. 2022) 1–10, https://doi.org/10.1186/S13023-022-02457-9/FIGURES/4.
[124] Y. Sung, I. Yoon, J.M. Han, S. Kim, Functional and pathologic association of aminoacyl-tRNA synthetases with cancer, Exp. Mol. Med. 54 (5) (May 2022) 553–566, https://doi.org/10.1038/s12276-022-00765-5.
[125] N.H. Kwon, P.L. Fox, S. Kim, Aminoacyl-tRNA synthetases as therapeutic targets, Nat. Publ. Group (Aug. 01, 2019), https://doi.org/10.1038/s41573-019-0026-3.
[126] H.Ø. Larsen, A.S. Roug, K. Nielsen, C.S. Søndergaard, P. Hokland, Nonviral transfection of leukemic primary cells and cells lines by siRNA—a direct comparison between Nucleofection and Accell delivery, Exp. Hematol. 39 (11) (Nov. 2011) 1081–1089, https://doi.org/10.1016/J.EXPHEM.2011.08.003.
[127] T. Shih, S. De, B.J. Barnes, RNAi transfection optimized in primary naive B cells for the targeted analysis of human plasma cell differentiation, Front. Immunol. 10 (2019) 1652, https://doi.org/10.3389/FIMMU.2019.01652/FULL.
[128] J. Yin, Z. Ma, N. Selliah, D.K. Shivers, R.Q. Cron, T.H. Finkel, Effective gene suppression using small interfering RNA in hard-to-transfect human T cells, J. Immunol. Methods 312 (1–2) (May 2006) 1–11, https://doi.org/10.1016/j.jim.2006.01.023.
[129] S. Weinstein, et al., Harnessing RNAi-based nanomedicines for therapeutic gene silencing in B-cell malignancies, Proc. Natl. Acad. Sci. USA 113 (1) (Jan. 2016) E16–E22, https://doi.org/10.1073/PNAS.1519273113/SUPPL_FILE/PNAS.201519273SI.PDF.
[130] L.A. Wheeler, et al., Inhibition of HIV transmission in human cervicovaginal explants and humanized mice using CD4 aptamer-siRNA chimeras, J. Clin. Invest. 121 (6) (Jun. 2011) 2401, https://doi.org/10.1172/JCI45876.
[131] J. Chen, et al., Synthesis and use of an amphiphilic dendrimer for siRNA delivery into primary immune cells, Nat. Protoc. 16 (1) (Jan. 2020) 327, https://doi.org/10.1038/S41596-020-00418-9.

# Conclusions

RNA interference is a powerful yet temporary phenomenon with considerable therapeutic potential. At the same time, nanotechnology can be the key to the translation of unconventional theranostic medicine: diagnosis/reporting agents and biotech therapeutics, all in one formulation. Small interfering RNAs (siRNAs) are artificial molecules that mimic naturally occurring miRNAs and exert a knockdown effect. In this study, two kinds of carriers for small-interfering RNA were used: erythrocyte membrane vesicles (EMVs), also known as nanoerythrosomes, and genipin-spermine-glycine crosslinked nanopolymers. While the first one was thoroughly optimized in terms of process, encapsulation efficiency, unloaded siRNA removal, and ultrastructure characterization, the second represents a de novo model for a naturally fluorescent, easy-to-synthesize, scalable and repeatable transfection agent. The low cost, both in terms of labor and reagents, of GXS5 makes it suitable for translation to other laboratories as an *in-house* transfection agent. Moreover, the effectiveness of EMVs in encapsulating indocyanine green, a well-known cyanine dye used in blood vessel-related diagnostics that is capable of photothermal effects when irradiated by infrared light but also prone to fast degradation, was tested. Interestingly, EMVs significantly reduced the degradation of ICG, paving the way for theranostic agent development.

The ability of EMVs to deliver the payload siRNA to the target organ in rodents (i.e., a melanoma-derived solid tumor) was also tested in vivo; the final efficiency was extremely satisfactory for a pilot-scale nanocarrier, with more than 80% gene knockdown two days after intravenous injection. Given these interesting premises, we decided to investigate the possibility of using erythrocyte membranes to cloak the best-performing GXS5 (G10S5). Indeed, while doping with external phospholipids was needed to achieve full camouflaging, the coated-G10S5 outperformed the naked polymer in terms of its knockdown efficiency in murine melanoma, and its success in transfecting lymphoblasts—which is known to be very difficult in that sense—paves the way for further applications.

In conclusion, in this study, the feasibility of tumor delivery via erythrocyte-derived carriers was finally established; the biocompatibility of genipin as a crosslinking agent established a new class of zwitterionic transfecting agents, which are also suitable for being coated with doped-erythrocyte membranes, yielding an agent with the advantages of both systems. In future work, active targeting via conjugation with peptides, antibodies, and aptamers will be attempted on EMVs to further increase their delivery efficiency to the site.

Lastly, it hereby follows a table summarizing the confirmation or rejection or partial rejection of hypotheses explained in **Chapter 2**.

Table 5: Summary Table with the rejection, acceptance of partial acceptance of the formulated hypotheses.

| Hypothesis | Paper reference | Chapter in this Thesis | Conclusion |
|---|---|---|---|
| **To prolong the nanodrug circulation time thanks to the presence of "don't eat me" CD47 marker.** | [208] | Chapter 6 | Acceptance: circulation time prolonged by circa 10 hours than for naked siRNAs |
| **The internalization efficiency and the cargo release of the nanodrug can be increased by the presence of extracellular vesicle machinery on erythrocytes membrane.** | [208] | Chapter 6 | Acceptance: Confocal Fluorescence studies show that the carrier is internalized and releases the payload in the cytoplasm without endosomal sequestration |
| **Exploiting the enhanced permeation and retention effect (EPR) for tumor tissue penetration.** | [208] | Chapter 6 | Acceptance: the passive accumulation in solid tumor (10% of Injected Dose) occurred solely due to EPR effect. However, this effect has a lesser importance in humans. |
| **Stabilizing cyanine dye monomeric forms to reduce light-induced degradation and improve the photothermal properties** | [54] | Chapter 4 | Acceptance: the photo-induced degradation of ICG loaded in EMVs was significantly lower than for soluble ICG |
| **Improving endosomal escape and biocompatibility via tailoring the cationic charge of transfecting agents toward a zwitterionic character** | [330] | Chapter 5 | Partial acceptance: the cytotoxicity of GXS5 based polymers is significantly lower than similar cationic delivery agents. The knockdown effect was present but lower than well-established transfecting agents (i.e. RNAiMAX) at the same dose. This opened the need for further optimization, carried out in Chapter 7. |
| **Camouflaging the genipin-polyamine nanoparticles with erythrocyte-derived membranes to generate a novel vector with properties of both** | [253] | Chapter 7 | Acceptance: the novel vector arising from genipin-based polymers and coated with DPPC-PEG/erythrocytes hybrid membrane retained the lower cytotoxicity of the first and the internalization mechanism of the latter. Its knockdown efficiency overperformed naked polymers. |
| **The self-fluorescence, both green and red, of GxS5 polymers makes it possible to follow their** | [330] | Chapter 5, Chapter 7 | Acceptance: Genipin-polyamines products are self-fluorescent in a broad spectrum, and despite the low quantum yield, it is possible to assay their internalization efficiency and internalization route via fluorescence |

| | | | |
|---|---|---|---|
| **internalization route in real time** | | | assisted cell sorting and fluroescence microscopy. |

# Appendix A

## TdTomato sequence , small interfering RNA position and primers

**Tdtomato cDNA**

ATGGTGAGCAAGGGCGAGGAGGTCATCAAAGAGTTCATGCGCTTCAAGGT
GCGCATGGAGGGCTCCATGAACGGCCACGAGTTCGAGATCGAGGGCGAGGGC
GAGGGCCGCCCCTACGAGGGCACCCAGACCGCCAAGCTGAAGGTGACCAAGG
GCGGCCCCCTGCCCTTCGCCTGGGACATCCTGTCCCCCCAGTTCATGTACGGC
TCCAAGGCGTACGTGAAGCACCCCGCCGACATCCCCGATTACAAGAAGCTGTC
CTTCCCCGAGGGCTTCAAGTGGGAGCGCGTGATGAACTTCGAGGACGGCGGT
CTGGTGACCGTGACCCAGGACTCCTCCCTGCAGGACGGCACGCTGATCTACAA
GGTGAAGATGCGCGGCACCAACTTCCCCCCCGACGGCCCCGTAATGCAGAAG
AAGACCATGGGCTGGGAGGCCTCCACCGAGCGCCTGTACCCCCGCGACGGCG
TGCTGAAGGGCGAGATCCACCAGGCCCTGAAGCTGAAGGACGGCGGCCACTA
CCTGGTGGAGTTCAAGACCATCTACATGGCCAAGAAGCCCGTGCAACTGCCC
GGCTACTACTACGTGGACACCAAGCTGGACATCACCTCCCACAACGAGGACTA
CACCATCGTGGAACAGTACGAGCGCTCCGAGGGCCGCCACCACCTGTTCCTG
GGGCATGGCACCGGCAGCACCGGCAGCGGCAGCTCCGGCACCGCCTCCTCCG
AGGACAACAACATGGCCGTCATCAAAGAGTTCATGCGCTTCAAGGTGCGCAT
GGAGGGCTCCATGAACGGCCACGAGTTCGAGATCGAGGGCGAGGGCGAGGGC
CGCCCCTACGAGGGCACCCAGACCGCCAAGCTGAAGGTGACCAAGGGCG
GCCCCCTGCCCTTCGCCTGGGACATCCTGTCCCCCCAGTTCATGTACGGCTCC
AAGGCGTACGTGAAGCACCCCGCCGACATCCCCGATTACAAGAAGCTGTCCTT
CCCCGAGGGCTTCAAGTGGGAGCGCGTGATGAACTTCGAGGACGGCGGTCTG
GTGACCGTGACCCAGGACTCCTCCCTGCAGGACGGCACGCTGATCTACAAGG
TGAAGATGCGCGGCACCAACTTCCCCCCCGACGGCCCCGTAATGCAGAAGAA
GACCATGGGCTGGGAGGCCTCCACCGAGCGCCTGTACCCCCGCGACGGCGTG
CTGAAGGGCGAGATCCACCAGGCCCTGAAGCTGAAGGACGGCGGCCACTACC
TGGTGGAGTTCAAGACCATCTACATGGCCAAGAAGCCCGTGCAACTGCCCGG
CTACTACTACGTGGACACCAAGCTGGACATCACCTCCCACAACGAGGACTACA
CCATCGTGGAACAGTACGAGCGCTCCGAGGGCCGCCACCACCTGTTCCTGTAC
GGCATGGACGAGCTGTACAAGTAG

**Forward primer**: GACAACAACATGGCCGTC

**Reverse primer**: GGTCTGGGTGCCCTCGTA, whose reverse complement is: **TACGAGGGCACCCAGACC**.

**siRNA sequence** for the passenger strand (complementary with lead strand, that targets this sequence within RISC): GCCACCACCTGTTCCTGT

# Appendix B

## Supplementary Material from Chapter 5

Electronic Supplementary Material (ESI) for Nanoscale Advances.
This journal is © The Royal Society of Chemistry 2024

## Supplementary materials

# Efficient siRNA delivery to murine melanoma cells via a novel genipin -based nano-polymer

Giulia Della Pelle [1,2], Tim Bozic [3], Marija Vukomanović [4], Gregor Sersa [3, 5], Bostjan Markelc [3], Nina Kostevšek [1,2]

[1] Department for Nanostructured Materials, Jožef Stefan Institute, 1000 Ljubljana, Slovenia
[2] Jožef Stefan International Postgraduate School, 1000 Ljubljana, Slovenia
[3] Department of Experimental Oncology, Institute of Oncology Ljubljana, 1000 Ljubljana, Slovenia
[4] Advanced Materials Department, Jožef Stefan Institute, 1000 Ljubljana, Slovenia
[5] Faculty of Health Sciences, University of Ljubljana, Zdravstvena pot 5, SI-1000 Ljubljana, Slovenia

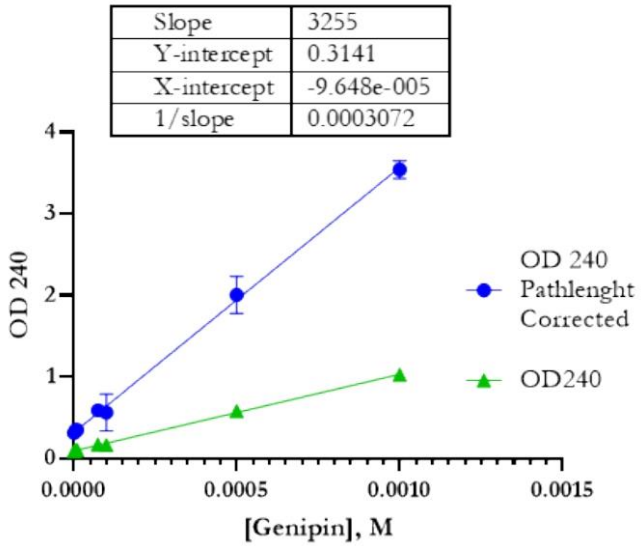



*Figure S1: Calibration curve of genipin in 300 µl as in "Kinetic evaluation of genipin reaction with two naturally occurring polyamines" and corrected for a virtual 1-cm pathlength cuvette with equation (14).*

| **[Genipin], M** | **υ (M/h), 240 nm** | $a_1$ |
|---|---|---|
| 0.000168 | -0.0000557 | 1.57 ± 0.25 |

| | |
|---|---|
| 0.000252 | -0.000133 |
| 0.000335 | -0.000309 |
| 0.000504 | -0.000546 |

*Table S1. Initial reaction speed monitored at 240 nm versus different initial genipin concentrations, i.e., spermine was the isolated reactant. Reaction order $a_1$ was derived by equation (3) and averaged for all reactions. Spermine concentration is 0.00083 M in all cases.*

| **Primary amine groups donor** | **[R-NH2], M** | **υ (M/h), 240 nm** | **$b_1$** |
|---|---|---|---|
| **Spermine** | 0.000166667 | 9.197E-07 | 1.16 ± 0.32 |
| **Spermidine** | 0.000166667 | 0.000003554 | |
| **Mix 1:1 m/m** | 0.000166667 | 0.000009269 | |
| **Spermine** | 0.000833333 | 0.000004941 | |
| **Spermidine** | 0.000833333 | 0.0000154 | |
| **Mix 1:1 m/m** | 0.000833333 | 0.00002301 | |
| **Spermine** | 0.001666667 | 0.00001137 | |
| **Spermidine** | 0.001666667 | 0.00002944 | |
| **Mix 1:1 m/m** | 0.001666667 | 0.00004428 | |

*Table S2. Initial reaction speed monitored at 240 nm versus different amine donor initial concentrations, i.e. genipin was the isolated reactant, with a concentration of 0.00083 M. Amine groups sources are in brackets. Reaction order $b_1$ was derived by equation (4) and averaged for all reactions.*

| **[Genipin], M** | **υ (M/h), 580 nm** | ***$a_2$*** |
|---|---|---|
| 0.000168 | 0.03176 | 1.51 ± 0.8 |
| 0.000252 | 0.05277 | |
| 0.000336 | 0.1003 | |
| 0.000504 | 0,3216 | |

*Table S3. Initial reaction speed monitored at 580 nm versus different genipin initial concentrations, i.e. spermine being the isolated reactant. Reaction order $a_2$ was derived by equation (3) and averaged for all reactions.*

| Primary amine groups donor | [R-$NH_2$], M | υ (M/h), 580 nm | $b_2$ |
|---|---|---|---|
| **Spermine** | 0.000166667 | 0.000662 | 0.53 ± 0.17 |
| **Spermidine** | 0.000166667 | 0.000818 | |
| **Mix 1:1 m/m** | 0.000166667 | 0.001391 | |
| **Spermine** | 0.000833333 | 0.001278 | |
| **Spermidine** | 0.000833333 | 0.001669 | |
| **Mix 1:1 m/m** | 0.000833333 | 0.002188 | |
| **Spermine** | 0.001666667 | 0.001307 | |
| **Spermidine** | 0.001666667 | 0.001052 | |
| **Mix 1:1 m/m** | 0.001666667 | 0.00274 | |

*Table S4. Initial reaction speed monitored at 580 nm versus different amine donor initial concentrations, i.e., genipin being the isolated reactant. Amine groups sources are in brackets. Reaction order $a_2$ was derived by equation (4) and averaged for all reactions.*

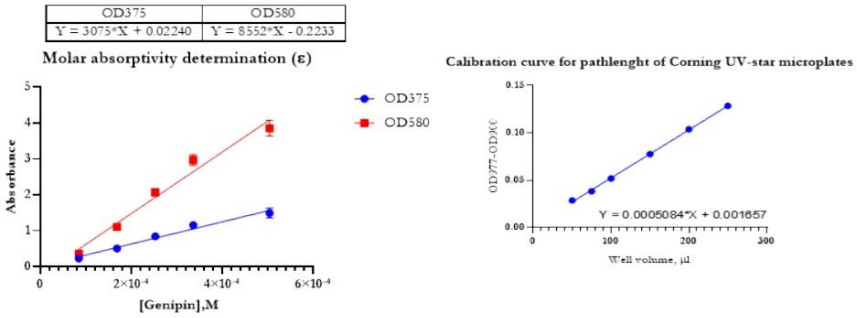



*Figure S2: a) Plot genipin vs plateau OD375 nm and OD580 value. ε is represented by the slope, as for Lambert and Beer law; b) Calibration curve for pathlength correction used to determine molar absorptivity of GxS5 products.*

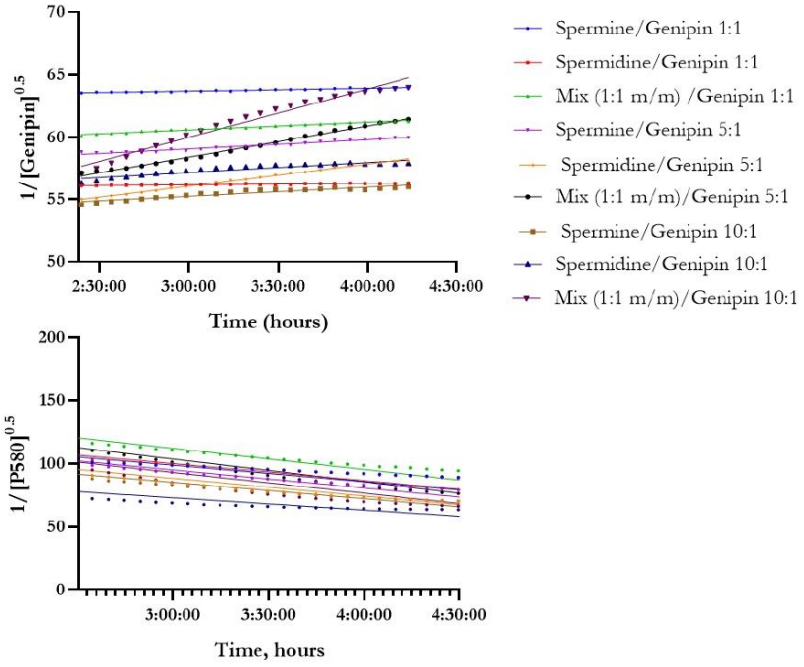
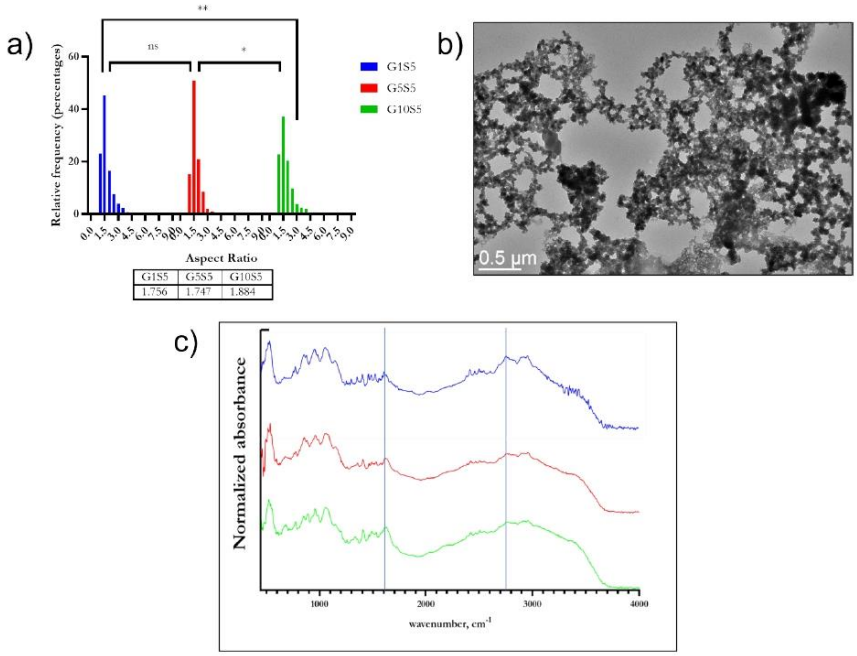



*Figure S3. Above, graph for genipin consumption monitored at 240 nm corresponding to a reaction order of 3/2, reworked according to [1] as of equation (8). In legend, amine groups source and molar ratio with genipin. Below, graph for P580 formation, corresponding to experimental reaction order ½. Slope is k.obs/2, as of equation (9). Colours refer to the same sample for both graphs.*

| **Molar ratio with Genipin** | **ζ potential, mV** |
|---|---|
| **Spermine, 1:1** | 14.78 ± 3.18 |
| **Spermidine, 1:1** | 3.4 ± 1.23 |
| **Mix 1:1, 1:1** | 10.67 ± 2.33 |
| **Spermidine, 1:5** | 5.68 ± 1.59 |
| **Mix 1:1, 1:5** | 7.68 ± 1.68 |
| **Spermine, 1:5** | 18.96 ± 0.95 |

| | |
|---|---|
| **Spermidine, 1:10** | 12.46 ± 2.05 |
| **Mix 1:1, 1:10** | 18.94 ± 0.65 |

*Table S5. ζ potentials of polymeric suspensions resulting from reaction of genipin with multiple combinations of spermine and spermidine.*




| G1S5 | G5S5 | G10S5 |
|---|---|---|
| 1.756 | 1.747 | 1.884 |

*Figure S4 a)Aspect ratio frequency distribution of GXS5 nanoparticles from TEM micrographies. The datasets included 10 micrographies at 6000x magnification for each polymer while measured nanoparticles were, 1213, 1149 and 1187 respectively for G1S5, G5S5, G10S5. Aspect ratio was derived from ImageJ software built-in functionality. The harmonic mean of aspect ratios is reported below the plot. b) TEM micrograph of G0S5 polymer. No monodisperse, well-defined particle suspension was detectable.c)FT-IR spectra of, from top to bottom, G1S5, G5S5 and G10S5.*

**Fourier-Transform Infrared (FT-IR) Spectroscopy**

The Fourier-transform infrared spectroscopy (FTIR) data are presented in Figure S4c. The spectra are consistent with those already present in the literature for genipin/spermine amine crosslinking [2,3]. Although the spectra of GxS5 did not differ dramatically, a few differences should be highlighted. The peaks corresponding to primary and aliphatic amines (3500–3100 $cm^{-1}$) are much more pronounced in G1S5, but minimal in G10S5. The intramolecular C–H stretch signal at 2700 $cm^{-1}$ appears to be stronger for the lower glycine molar fraction. In all three samples, the alcoholic function stretching of the genipin monomer is present as a small hump at 3500 $cm^{-1}$, while the O–H bending peaks around 1345 $cm^{-1}$ are equally intense. At

shorter wavenumbers, the carboxylic group stretching at 1700 $cm^{-1}$, on the contrary, appeared to be stronger for a higher glycine molar fraction. A peak corresponding to lactone heterocycle, belonging to the amide moiety of reacted iridoid ring of genipin, is present at 1645 $cm^{-1}$ in all three samples [3]. Regions between 1600 $cm^{-1}$ and 500 $cm^{-1}$ are challenging to interpret. Whereas the N-H amine bending signal at 1615 $cm^{-1}$ increases from G10S5 to G1S5, C–O stretching, carboxylic acid C–H bending, and C–N cyclic stretching are heavily superimposed in the 1300 $cm^{-1}$ and 1200 $cm^{-1}$ region. However, the carboxylic C–H at 1415 $cm^{-1}$ appears neater in the G10S5 due to presence of a glycine-carboxylic-free moiety. Lastly, no appreciable differences are evident in the C=C and C–H bending region from 1100 $cm^{-1}$ onwards. Due to the overlapping signals in the range 1250–1300 $cm^{-1}$, it was not possible to distinguish those arising only from tertiary amines, i.e., amines derived from the nucleophilic attack of genipin on spermine, the substitution of the oxygen at position 2 and the final crosslinking with another genipin moiety. Therefore, despite some subtle differences among the three spectra, FT-IR does not have sufficient resolution to investigate our polymers' fine structure thoroughly, and further analysis will be needed.

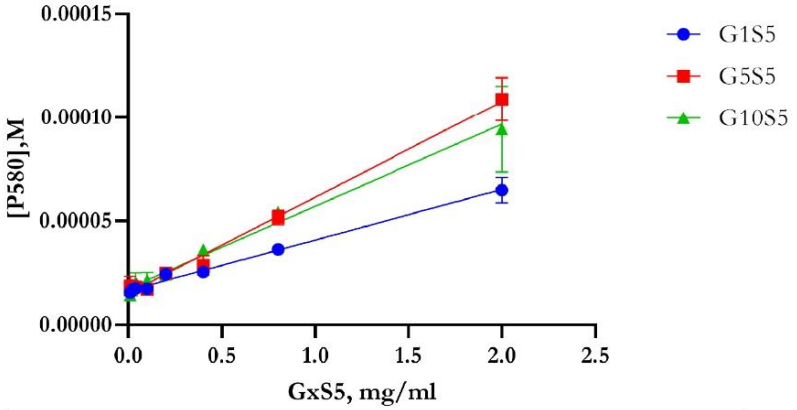
1 S. K. Upadhyay, *Chem. Kinet. React. Dyn.*, 2006, 1–256.

2 M. F. Butler, Y. F. Ng and P. D. A. Pudney, *J. Polym. Sci. Part A Polym. Chem.*, 2003, **41**, 3941–3953.

3 F.-L. Mi, H.-W. Sung and S.-S. Shyu, *J. Polym. Sci. Part A Polym. Chem.*, 2000, **38**, 2804–2814.

**Quantification of mass concentration of GxS5 polymers using OD at 580 nm**

After assessing the repeatability of our synthesis and purification protocol, we aimed to establish a correlation between the molar concentration of P580 and the weight. After elution in water with Sephadex G50 PD10 columns (Materials and Methods), polymers were freeze-dried for a maximum of 48 hours and subsequently rehydrated in PBS 1× at 20 mg/ml. With a series of serial dilutions, absorbance at 580 nm was recorded. A linear relation for molar concentration of P580 vs weight concentration was generated (Figure 5Sa) and used for all P580 quantifications in subsequent experiments. [P580] (Figure 2s) was obtained from absorbance using Lambert & Beer relation, being $\varepsilon = 8.5\ 103\ mol^{-1}\ l^{-1}$, similar to the reported molar absorptivity of genipin reacted with lysine [23], and it is used for all the further calculations whereas molar concentration was needed.




| G1S5 | G5S5 | G10S5 |
|---|---|---|
| Y = 2.436e-005*X + 1.647e-005 | Y = 4.621e-005*X + 1.526e-005 | Y = 3.953e-005*X + 1.759e-005 |

*Figure S5. Relation between weight concentration (in mg/ml) of rehydrated GxS5 polymers, and P580 molar concentration. R2 was found to be, for G1S5, G5S5, G10S5, 0.97, 0.97 and 0.98, respectively.*

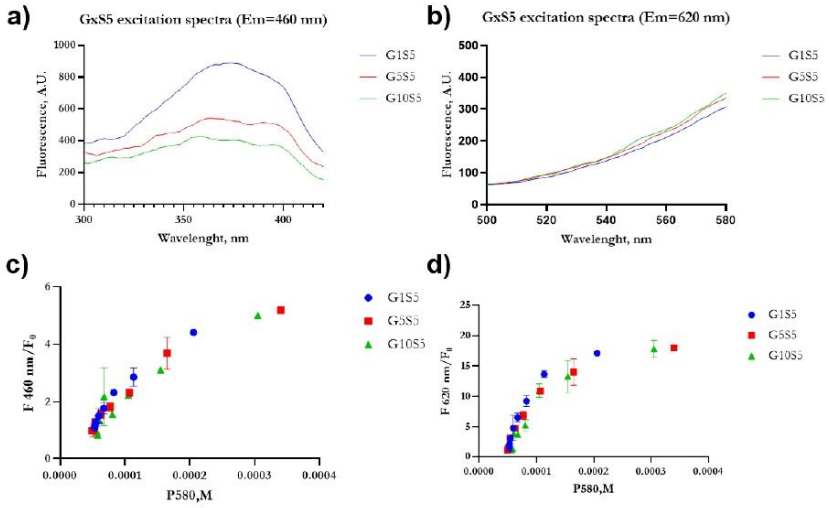



*Figure S6. Fluorescence excitation spectra, with fixed emission at 460 nm (a), and 620 nm (b). Fluorescence emission respectively a) at 460 nm ; b) at 620 nm versus [P580],M.*

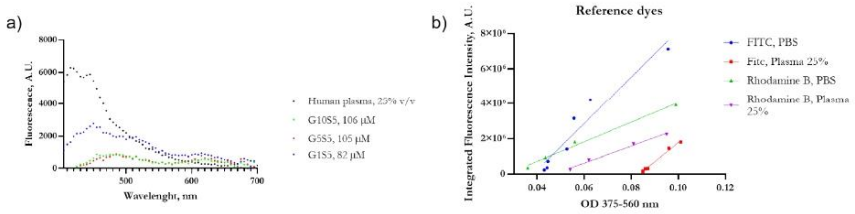



*Figure S7. a) Baseline-removed emission spectra of GXS5 (excitation at 375 nm) in 25% v/v of human plasma compared to baseline. b) Slopes of fluorescence reference dyes, FITC and Rhodamine B.*

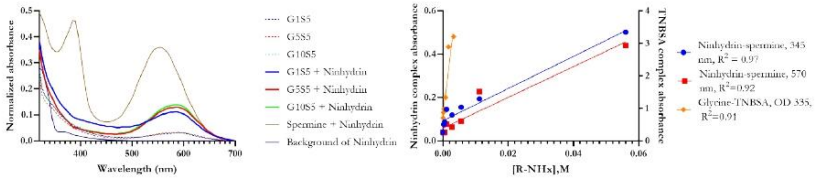



*Figure S8. a) Absorbance spectra of polymers alone and complexed with ninhydrin. b) Calibration curves of spermine at 345 nm and 570 nm with ninhydrin, and relative to glycine in presence of TNBS.*

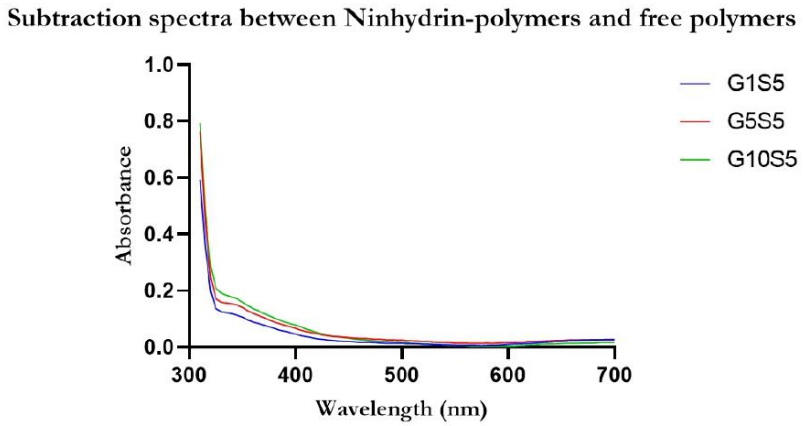


*Figure 9S. Subtraction spectra resulting from GxS5 absorbance and their spectra after complexing with ninhydrin. The faint hump at 340–350 nm was used for quantification via spermine-generated standard curve.*

| | **Fold variation in P1/P2 ratio from pH 7.4 to pH 5** | **Fold size increase in P1** | **Volume increase in P1** |
|---|---|---|---|
| **G1S5** | 1,93 | 1,92 | 5,64 |
| **G5S5** | 1,51 | 1,95 | 9,45 |
| **G10S5** | 1,15 | 2,24 | 11,29 |

*Table S6. Fold variation of relative abundancies of P1 and P2, increase in terms of diameter of particles from pH 7.4 to 5, and relative increase in volume.*

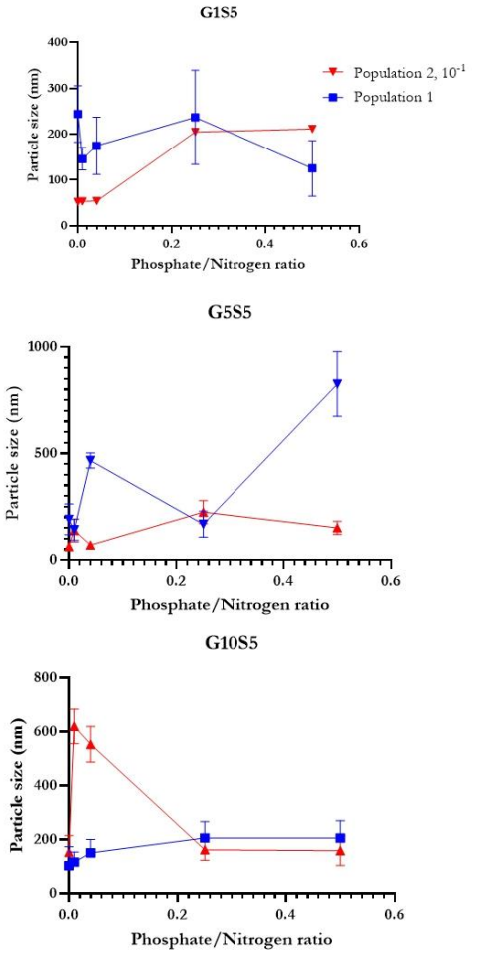



*Figure S10. Evolution of particle size of GxS5 polymers, each divided in two different nanoparticle populations, according to P/N ratio.*

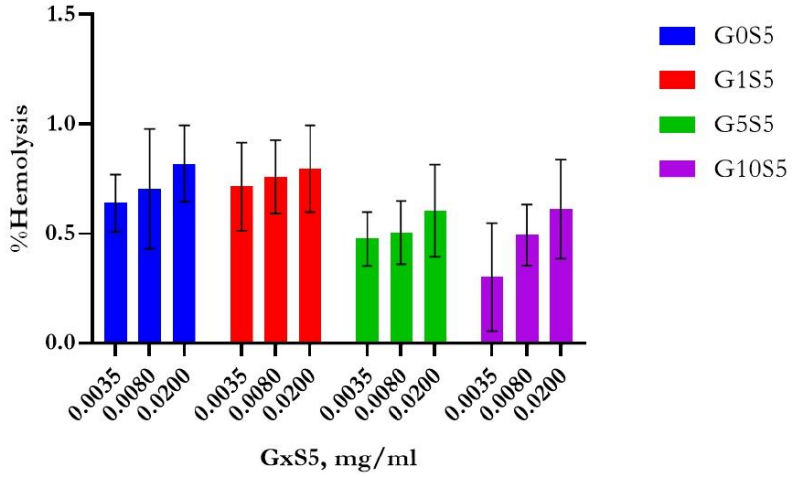



*Fig S11.Percentage of hemolysis of GxS5 polymers.*

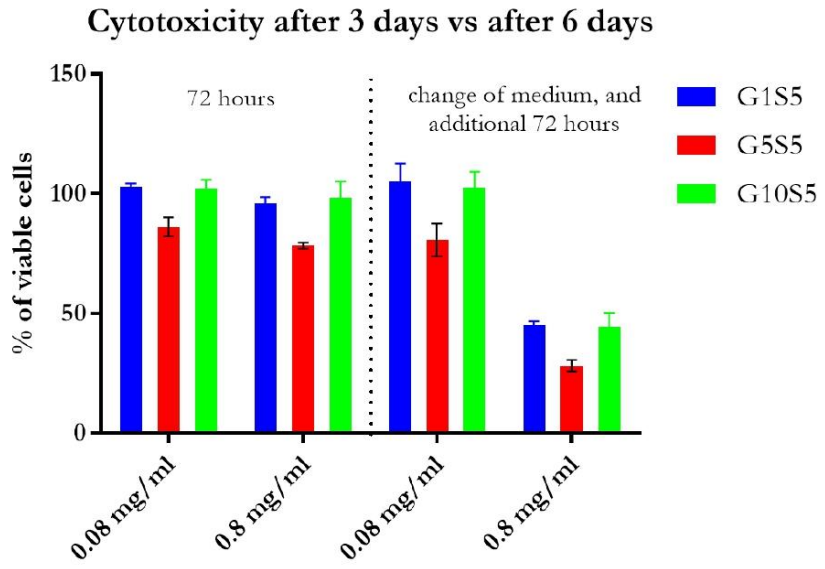



*Fig S12. Cytotoxicity on HaCaT cells.*

| Ratio with siRNA phosphates | Polymer | Concentration in wells (mg/ml) |
|---|---|---|
| | G1S5 | 0.0033 |
| | G5S5 | 0.0032 |
| 1:2 P/N | G10S5 | 0.0027 |
| | G1S5 | 0.0357 |
| | G5S5 | 0.0310 |
| 1:25 P/N | G10S5 | 0.0264 |
| | G1S5 | 0.0868 |
| | G5S5 | 0.0774 |
| 1:50 P/N | G10S5 | 0.0682 |

*Table S7. Final concentrations of GxS5 used for B16F10 transfection, in a 24 well-plate, each filled with 1 ml of culture medium.*

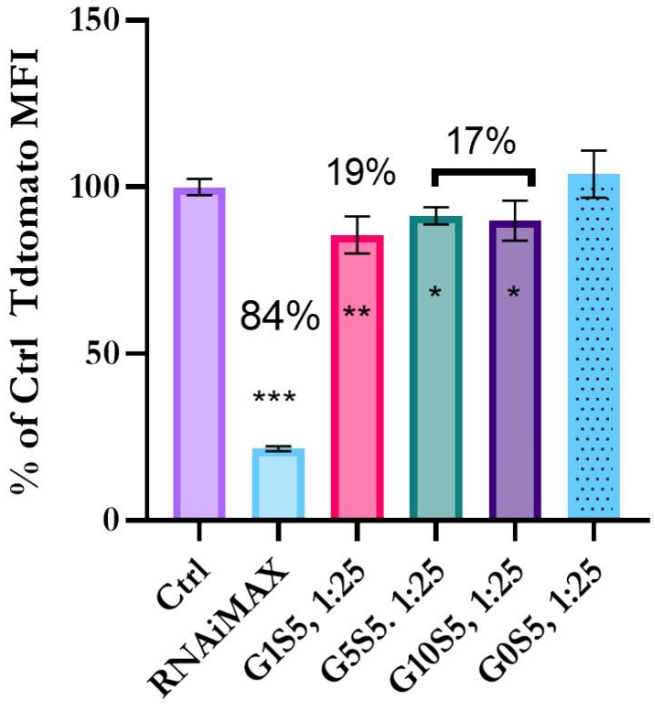



*Figure S13. Remaining MFI of tdTomato, normalized for the control, for GxS5 polymers complexed with siRNA at 1:25 P/N. The final siRNA amount used to transfect cells was 10 picomoles.*

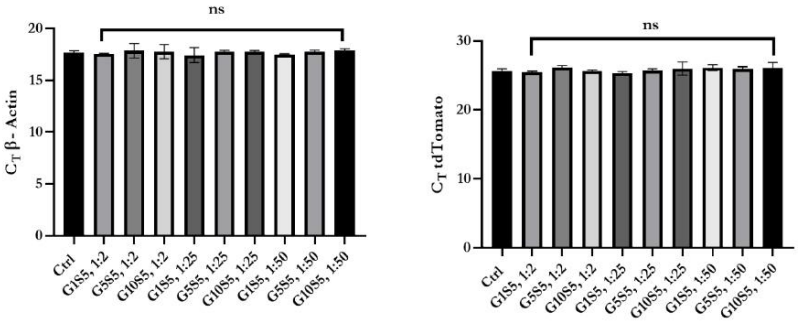



*Figure S14. Average β-actin for siRNA/GxS5 complexes and tdTomato $C_T$ at various GXS5 concentrations (as per Table S7) un-complexed with siRNA, used as negative control.*

# Appendix C

# Supplementary Material from Chapter 6

## Supplementary materials

### Selection of best-unloaded siRNA removal method

*Density gradient centrifugation*. Various stocks of sucrose (from 90 to 10% w/v) were freshly prepared and layered in a thin-walled polypropylene tube (5 ml nominal volume, Beckman Coulter Life Sciences, catalog number 342194) with increasing concentrations from bottom to top. 2 ml of siRNA-EMVs were then placed on sucrose cushion, and centrifuged for 40 minutes at 100.000 g (27.200 rpm) on a Beckman Coulter Optima-Xe 90 ultracentrifuge, equipped with an SW 60-Ti swinging rotor. The presence of EMVs was confirmed via DLS and Quantifluor RNA assay.

*Conventional ultracentrifugation*. 2 ml of siRNA-EMVs in PBS were loaded in a thin-walled polypropylene tube and subjected to ultracentrifugation in the same conditions as above. SiRNA-EMVs were collected as a pellet.

*Amicon Ultrafiltration filter*. 0.5 ml of siRNA-EMVs in PBS were loaded in a pre-activated Amicon ultrafiltration device (EMD Millipore, catalogue number, UFC503008) and centrifuged on a tabletop Eppendorf Minispin centrifuge (model number Model 5415R) for 5 minutes at maximum speed, up to a final volume of 50 µl. The sample was then resuspended with PBS back at original volume and the siRNA concentration was analysed via Quantifluor RNA assay. Subsequently, retentate and eluate were re-dispersed in original volume and used for RNA quantification.

*Size exclusion column chromatography*. 1 ml of siRNA-EMVs was applied to a PD10 G25 Sephadex column (GE Healthcare), and, upon subsequent addition of 1 ml PBS aliquotes, 12 fractions were collected. EMVs and siRNA presences were respectively confirmed via DLS and Quantifluor RNA assay. EMVs and siRNA were recovered as in Figure 1, Supplementary Materials.

### SDS-page on erythrocytes ghosts, DCC-siRNA-EMVs, and DCC-pellet

RBC ghosts, DCC-siRNA-EMVs and DCC-pellet protein concentration were obtained via Bradford assay. RBC membrane (i.e. ghosts) and EMV proteins were solubilized for 2 hours at 4°C under continuous shaking in 10 mM Tris-HCl, 150 mM NaCl, pH 7.4, containing 1% (m/v) Triton X-100. After solubilization, the samples were centrifuged at 16.100 × g for half an hour, and the supernatant was stored for further use. Aliquots of samples were loaded (15 µg/lane) on a 10% (m/v) SDS-PAGE gel and the proteins were stained with colloidal silver. Gels were imaged on a ChemiDoc MP System gel imager (Bio-Rad, Hercules, CA, USA). PageRuler™ Plus Prestained Protein Ladder was from Thermo Fisher Scientific (catalogue number 26619).

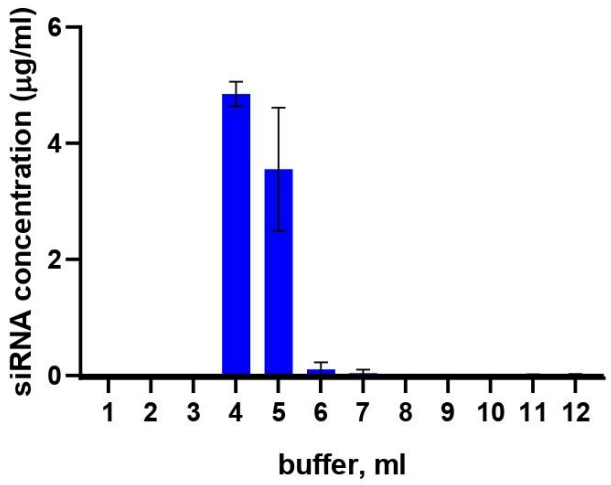



*Figure S1. Recovery of siRNA from Sephadex PD10 column loaded with siRNA-EMVs and eluted with 1 ml of each fraction of PBS. The presence of EMVs was confirmed via DLS.*

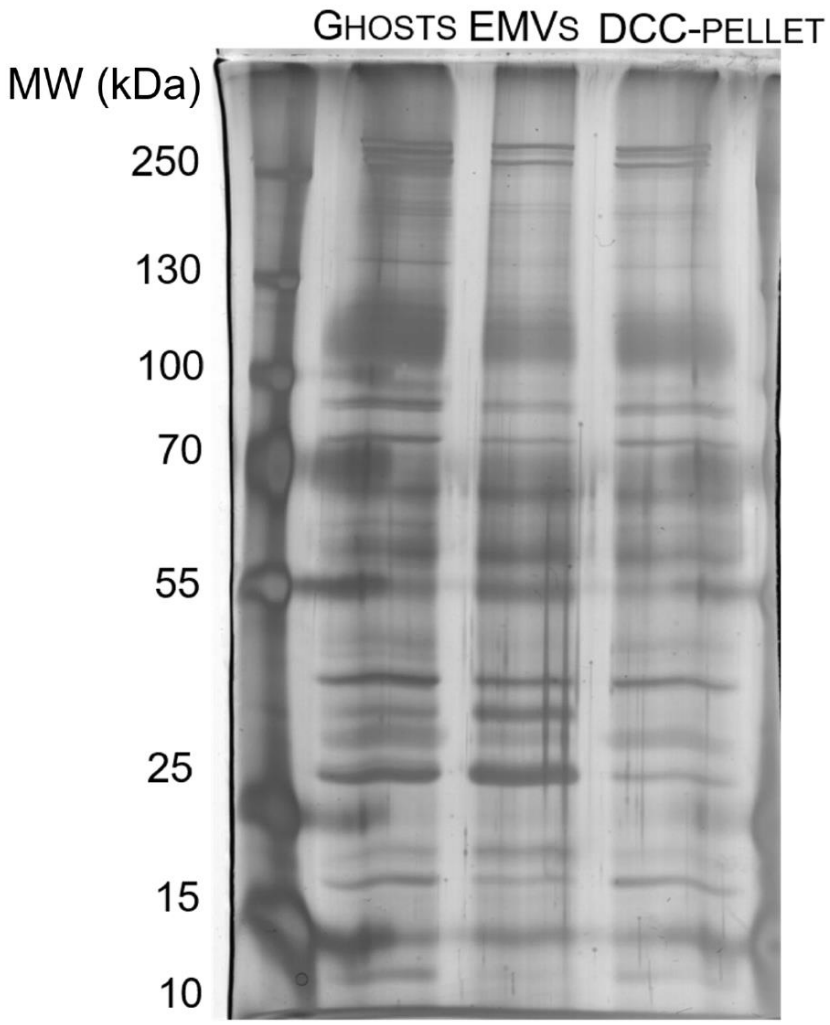



*Figure S2 SDS-page of red blood cell ghosts, DCC-siRNA-EMVs, and the pellet resulting from density changing centrifugation.*

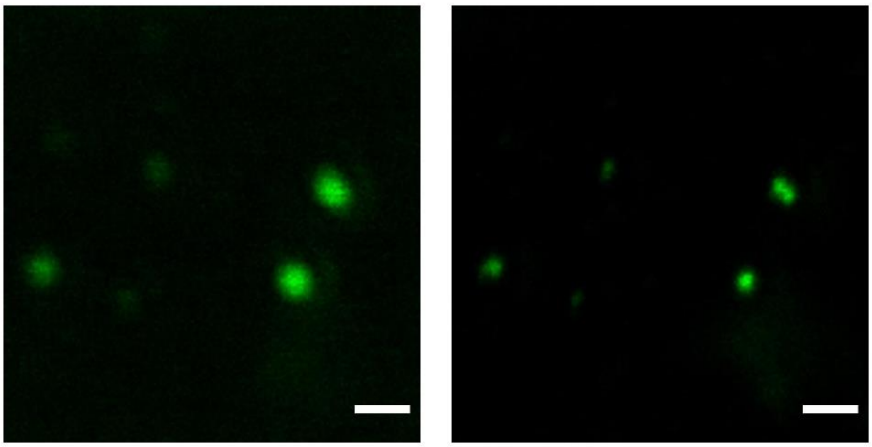


*Figure 3 Comparison between confocal (left) and STED imaging on CM-DiI labeled EMVs. Scale bar is 1 µm.*

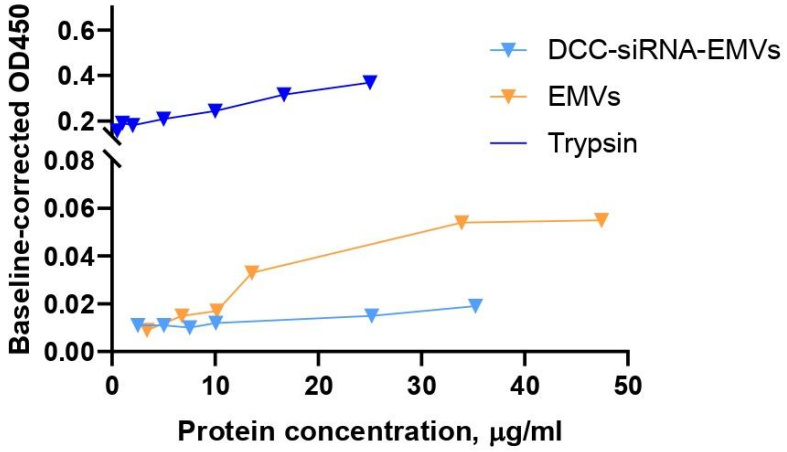



*Figure S4 Self-digestion protease assay on DCC-siRNA-EMVs and extruded EMVs, not subjected to ultracentrifugation, compared with Trypsin.*

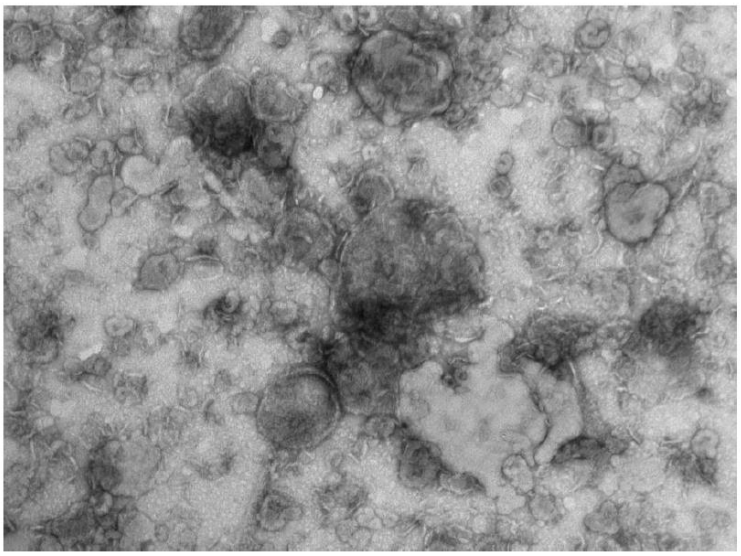


*Figure S5 DCC-siRNA-EMVs as negatively stained with uranyl acetate 0,5 w/v.*

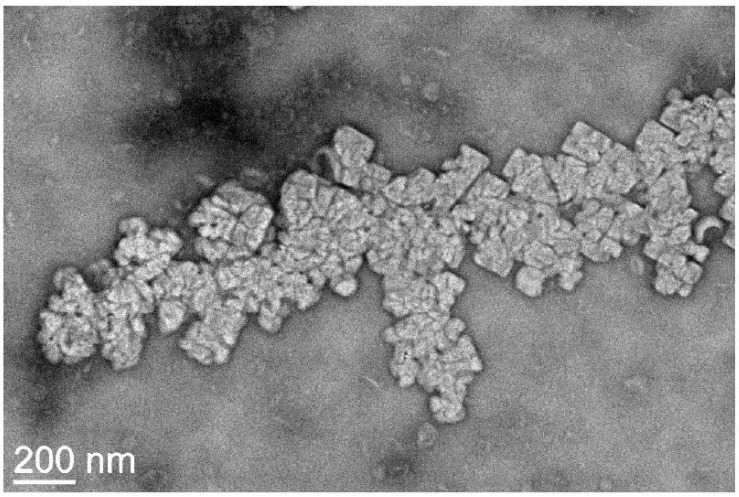



*Figure S6 DCC-siRNA-EMVs freeze-dried only in the presence of PBS and subsequently stained with UA-zero. A slight change in pH due to freeze-drying caused the deposition of heavy metal crystals on the grid.*

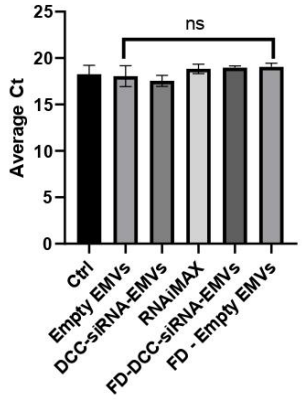



*Figure S7 Average β-actin threshold cycle for untreated cells (ctrl), and those transfected with empty EMVs, DCC-siRNA-EMVs (FD and not) and RNAiMAX. ANOVA one way was carried out (Graphpad 9) in order to ascertain whether transfection significantly affects β-actin basal levels.*

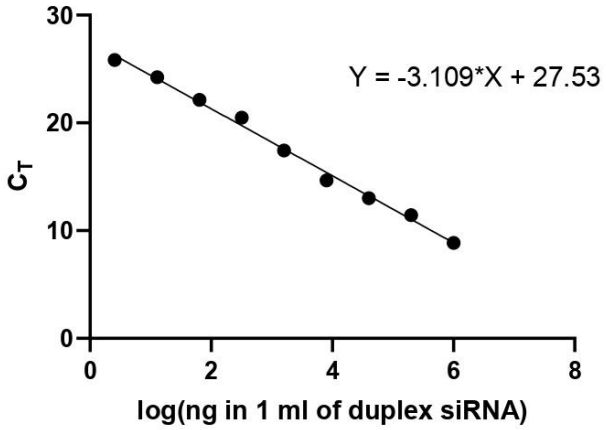



*Figure S8 Standard curve used for Taqman quantification of lead-strand siRNA in tissues and plasma of mice. To generate the standard curve, serial dilutions of Cy5-siRNA cDNA were used as a template for real-time PCR, while reverse transcription followed the same procedure already described in Materials and Methods.*

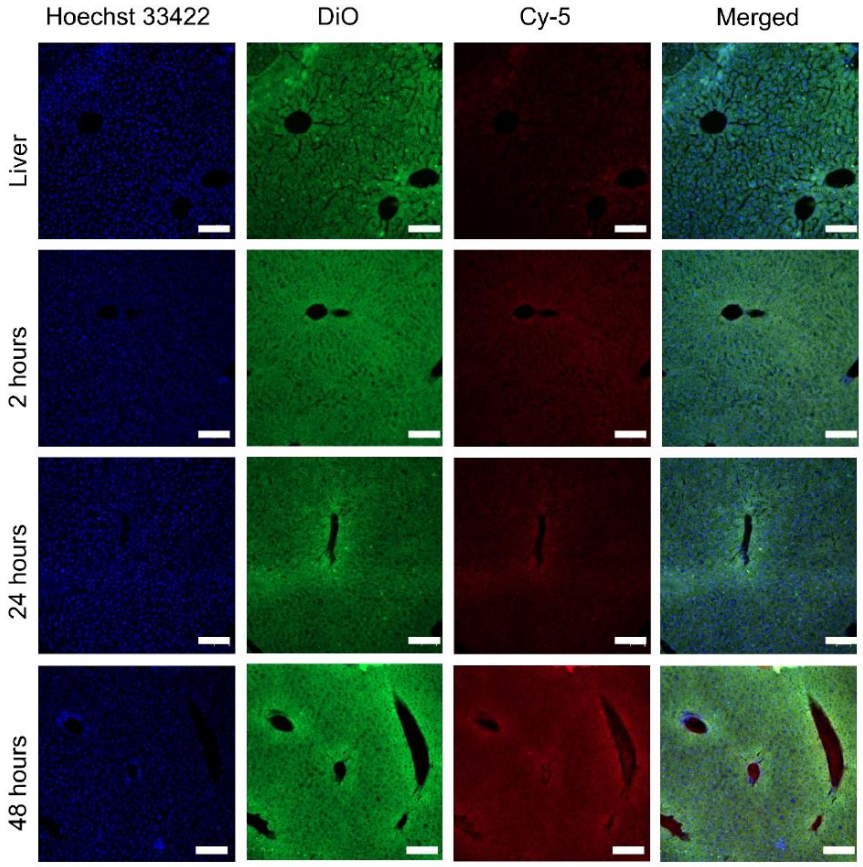



*Figure S9 Distribution of Cy-5/DiO DCC-siRNA-EMVs at different timepoints in frozen section of mouse liver via siRNA-Cy-5 (red) and DiO (green) signals. Nuclei were labelled with Hoechst 33342 (blue). The scalebar is 100 µm.*

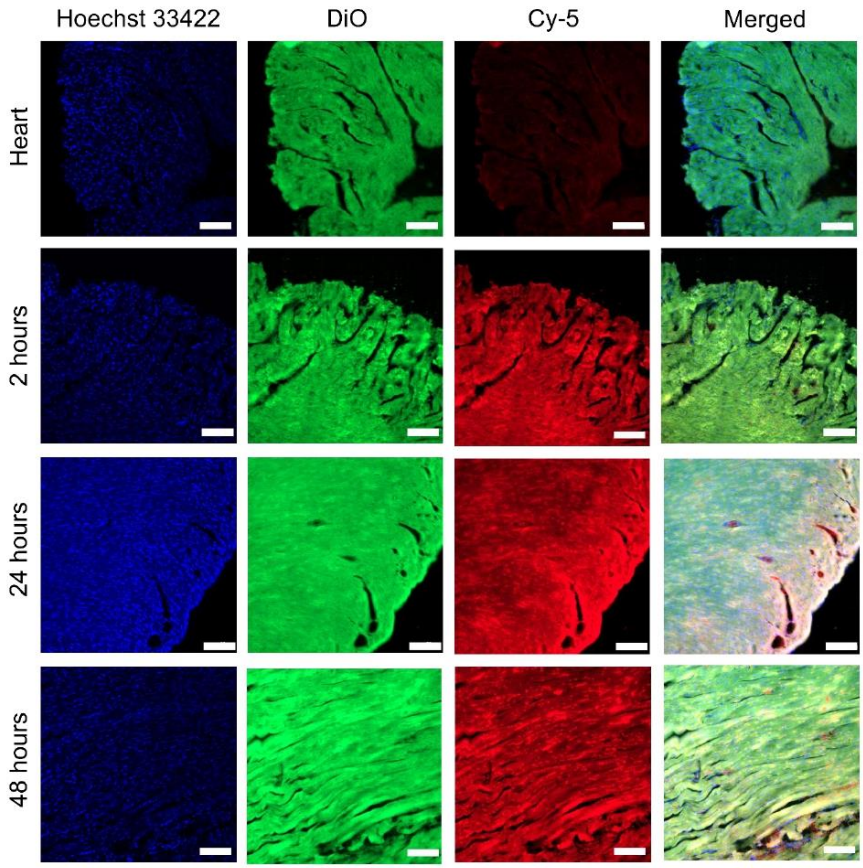



*Figure S10 Distribution of Cy-5/DiO DCC-siRNA-EMVs at different time points in frozen section of mouse heart via siRNA-Cy-5 (red) and DiO (green) signals. Nuclei were labeled with Hoechst 33342 (blue). The scalebar is 100 μm.*

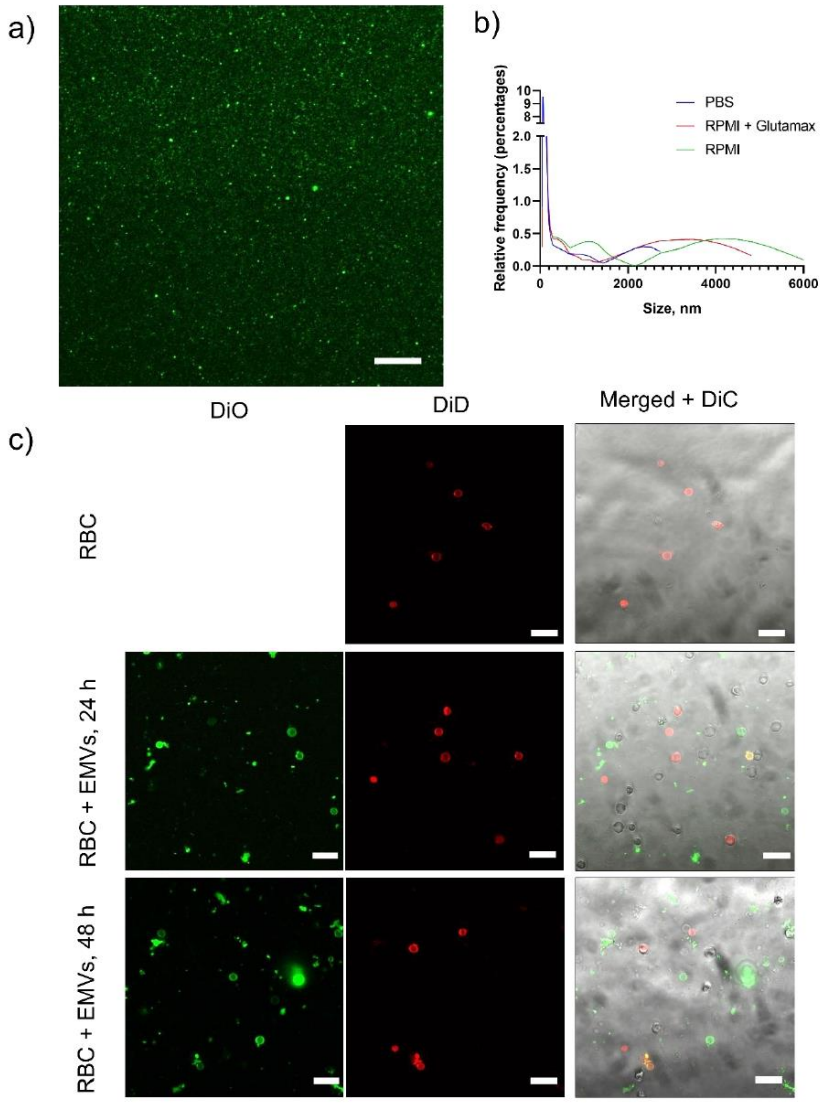



*Figure S11 a) DCC-EMVs, DiO labeled, in PBS, imaged via CLSM . b)Volume-weighted DLS particle size frequency distribution for DCC-EMVs incubated with PBS, RPMI medium, and RPMI medium addition with Glutamax; c) CLSM imaging of DiD-RBC, ex vivo incubated with DiO-EMVs. The scalebar is 10 µm.*

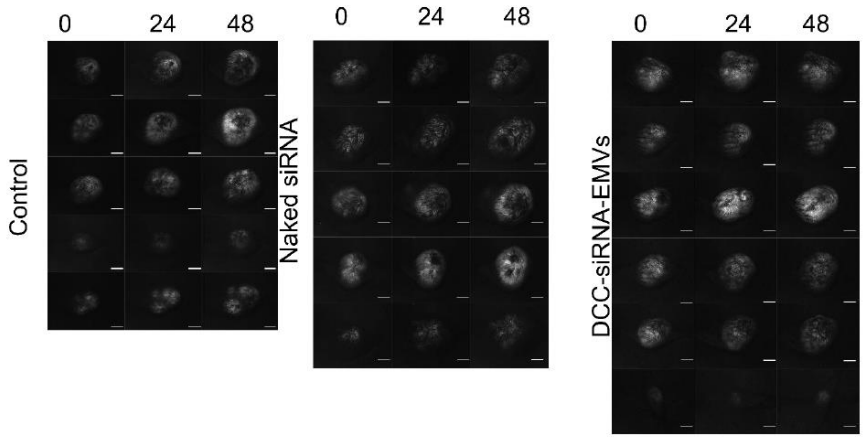



*Figure S12. Fluorescence-weighted mosaic pictures of tdTomato+ B16F10 induce tumors in mice. The scalebar is 5 mm.*

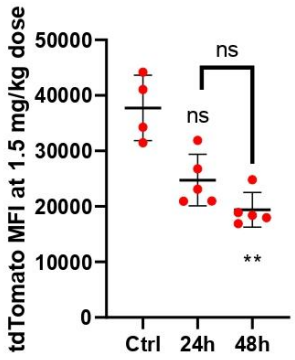



*Figure S13 Mean fluorescence intensity of tdTomato protein in control tumors (mice number = 4, 5 measurements each mouse), 24 (mice number = 5), and 48h (mice number = 5) DCC-EMVs-siRNA treated mice. p≤0.01 ***

# Appendix D

# Supplementary Material from Chapter 7

# Supplementary Material

## Novel vector for efficient siRNA delivery to lymphoblasts and melanoma based on genipin-spermine nanocarriers protected with hybrid erythrocyte membrane coating

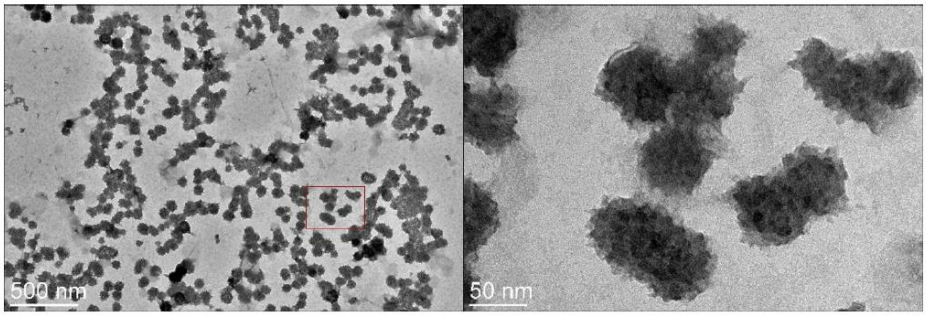



**Figure 1S**. G10S5-siRNA coated with DPPC-DSPE-PEG2000 membranes via sonication.

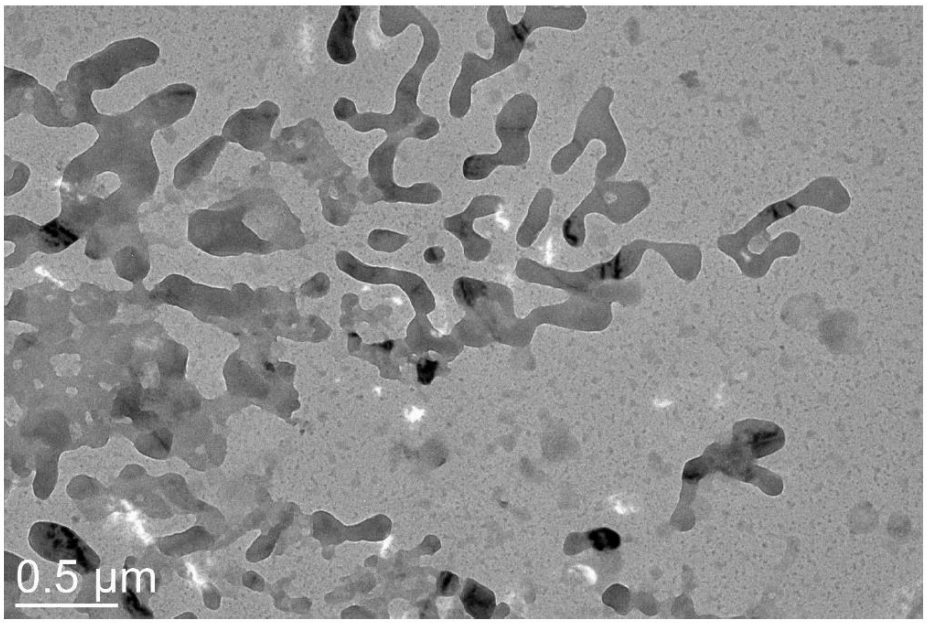



**Figure 2S**. G10S5 nanoparticles as seen via conventional TEM after extrusion via 200 nm filter.

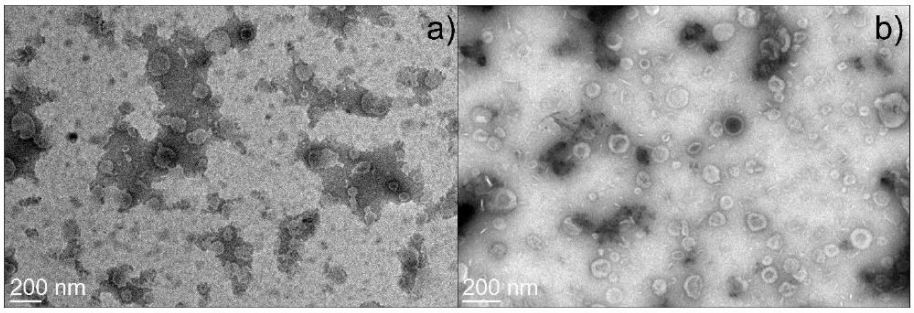



**Figure 3S**. EMVs-coated G10S5-siRNA (1:12), sonicated for 30 seconds. a) Native sample; b) Negative-stained.

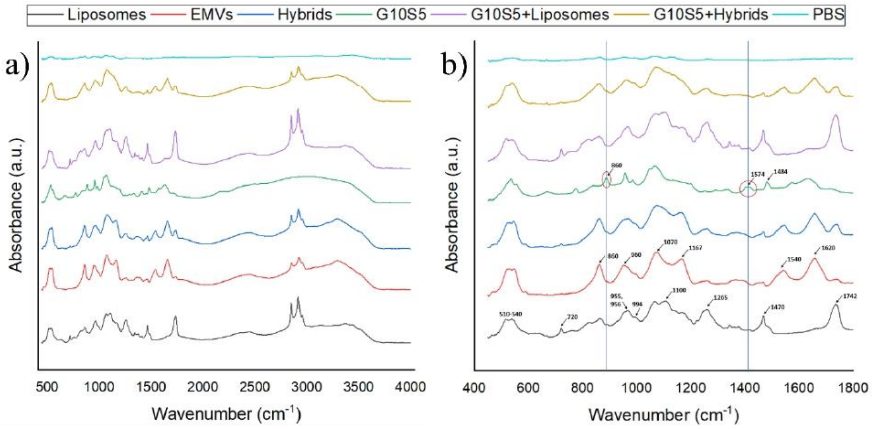



**Figure 4S**. a) Whole-region FTIR spectra of freeze-dried samples with b) zoom-in of the fingerprint region. Identified peaks are described in the text. Two peaks found in G10S5 NPs and not in other samples are shown with red circles and blue lines.

In FTIR spectra in Figure 4Sb, we have identified the most important peaks listed from higher towards lower wavenumbers. We marked two peaks that are present in G10S5 NPs and are not visible in coatings alone or coated samples.

- Triple peaks at 2848, 2922, 2960 $cm^{-1}$ peaks = aliphatic C–H stretches, strongly suggesting lipid chains that are expectedly strongly present in all liposomes and EMVs-containing samples.
- Small and broad humb between 2300–2450 $cm^{-1}$, it's almost certainly $CO_2$ artifact.
- In liposomes, a sharp band at ~**1742 $cm^{-1}$** is characteristic of C=O stretching vibration of the ester groups in the glycerol backbone of phospholipids.
- At **1650 $cm^{-1}$**, amide I in proteins is clearly seen in EMVs, but not in liposomes.
- Amide II band from proteins is located at ~**1540 $cm^{-1}$** and is present in EMVs, hybrids and hybrid-coated G10S5 NPs.
- **1470 $cm^{-1}$**, $CH_2$ scissoring (bending) vibration comes from the acyl chains of phospholipids. In G10S5 is this peak is shifted to **1484 $cm^{-1}$**.
- Weak peaks at **1440 $cm^{-1}$** in G10S5 can be attributed to the $–CH_2$ scissoring from spermine / glycine, $COO^-$ symmetric stretch, weak C–N/N–H bending and ring vibrations from genipin.
- In the fingerprint region, we have two peaks significant for liposomes at **1265 $cm^{-1}$** and **720 $cm^{-1}$** that are less pronounced in EMVs. So 1265 $cm^{-1}$ is the phosphate asymmetric stretch in phospholipids and 720 $cm^{-1}$ is the methylene rocking of lipid tails.
- In EMVs, we have significant peaks at **1167 $cm^{-1}$** = ester C–O–C stretch (lipids) ± glycosidic C–O stretches and **1070 $cm^{-1}$** = phosphate symmetric stretch (with possible carbohydrate contributions).
- Several weak peaks around **1100 $cm^{-1}$** in liposomes are a superposition of ester (DPPC) and ether (PEG) C–O–C stretches, along with phosphate symmetric stretching.
- Peaks in **950–1000 $cm^{-1}$** at in liposomes and EMVs correspond to O–P–O and P–O–C skeletal vibrations of phospholipids. In EMVs could be also C–O–C stretching in glycosidic bonds (glycolipids, glycoproteins).
- At **860 $cm^{-1}$** we have a high-intensity peak in EMVs, which is less pronounced in liposomes, and is very likely attributed to the choline headgroup vibrations. In cell membranes, the peak can be

intensified by tighter packing or interactions with cholesterol/proteins, making it more pronounced than in simple liposomes.

- Peak that is found in G10S5 NPs and not in other samples is peak at **880 cm⁻¹** , which could be a marker of genipin–amine crosslinking, related to the cyclic structures formed during nanoparticle assembly. The disappearance of the ~880 $cm^{-1}$ band after coating is consistent with a coating, but it is not definitive proof by itself. It can be caused by several different mechanisms (physical masking, spectral overlap, chemical reaction, or measurement artefacts).
- We also have a low-intensity peak in G10S5 NPs at **1574** $cm^{-1}$ that is not present in other samples, including coated samples and can be ssigned to Amide II–like vibration (N–H bend / C–N stretch). However, the disappearance of this peak after coating can be simply due to the physical masking/overlap by the coating.
- Bands in **510–540 cm⁻¹** range can be found in all samples are assigned to the phosphate backbone vibrations and also also present in PBS.

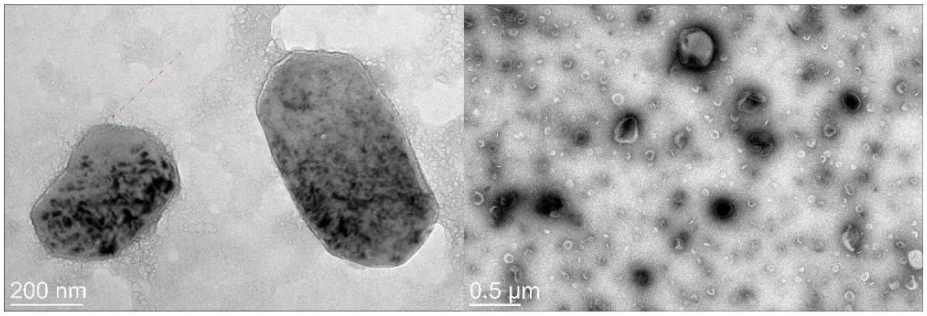



**Figure 5S.** Dissolution of G10S5 nanoparticles in presence of ethanol-containing negative stain for electron microscopy (UA-Zero). Here, the same sample of hybrids-G10S5 siRNA (1:12) was negative stained (right) or not. Indeed, on the image on the left it is possible to note a decomposed organic layer around G10S5 nanoparticles, while on the image on the right (negative stained) it is impossible to distinguish between empty vesicles and those coating G10S5-siRNA polyplexes.

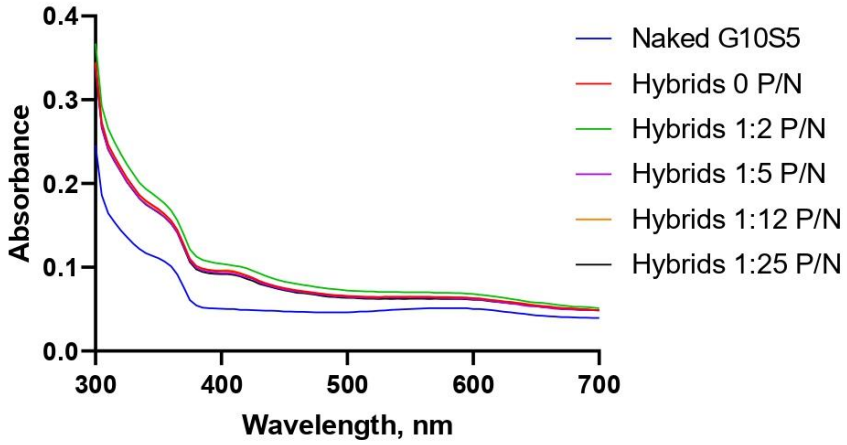



**Figure 6S**. Absorbance spectrum of hybrids-G10S5-siRNA.

**Table 1S**. Particle size and zeta potential of G10S5 (complexed with siRNA or not), coated with DPPC-DSPE-PEG2000 membranes.

| Sample | Particle size (nm) | Zeta potential (mV) |
|---|---|---|
| G10S5-siRNA (1:12)-liposomes | 413 ± 5 nm (PDI 0.392) | -5.1 ± 4.4 mV |
| G10S5-liposomes | 387 ± 36 (PDI = 0.369) | -10.7 ± 3.7 mV |

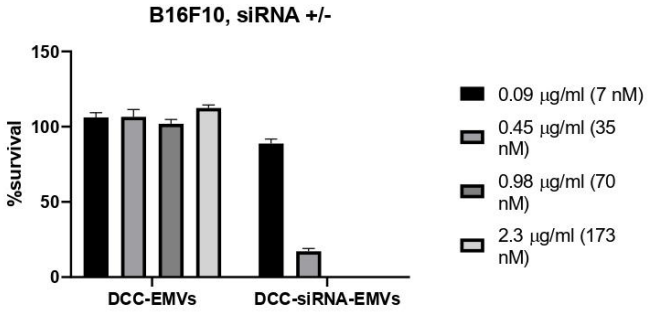



**Figure 7S**. Cytotoxicity of DCC-EMVs and DCC-siRNA-EMVs on B16F10, via Presto Blue assay. Reported is also the EMVs protein concentration with the concentration of anti-TdTomato siRNA.

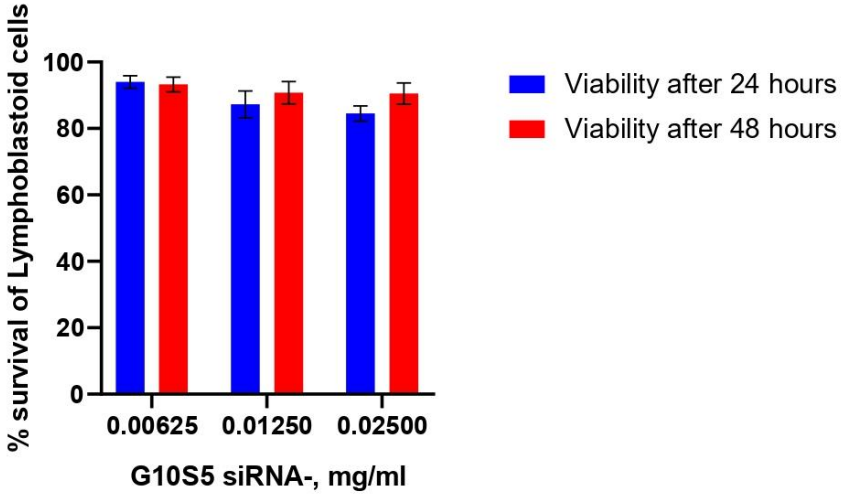



**Figure 8S**. Cytoxicity of naked G10S5 on lymphoblastoid cells, via Trypan Blue assay.

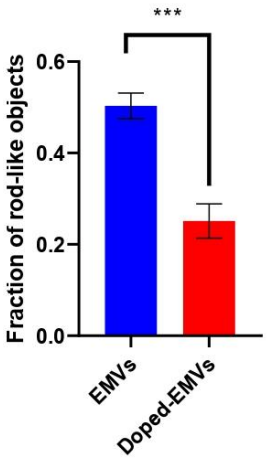



**Figure 9S**. Fraction of rod-like objects in cryo-TEM images of EMVs and DPPC-DSPE-PEG2000 doped EMVs. $p < 0.001$, over 137 objects in EMVs and 134 in hybrid vesicles, distributed over 10 images each.

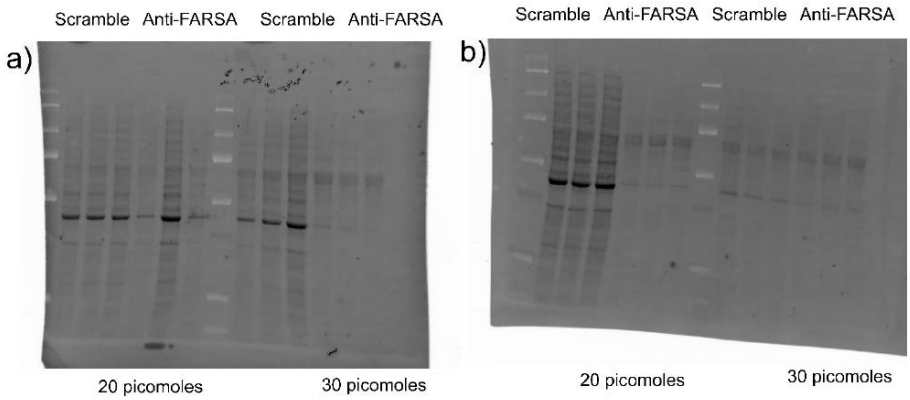



**Figure 10S.** Stain-free gels of FARSA knockdown in lymphoblastoid cell line. Experiments performed in triplicate using a) G10S5 or b) Hybrids-G10S5 for transfection. The volume of the bands (measured via ImageLab built-in analysis) was used for quantification of FARS-A knockdown elicited by transfection.

# References


[1] W. J. Cho, A. Jeremic, and B. P. Jena, "Size of supramolecular SNARE complex: Membrane-directed self-assembly," *J Am Chem Soc*, vol. 127, no. 29, pp. 10156–10157, Jul. 2005, doi: 10.1021/ja052442m.

[2] A. Jurczak-Kurek *et al.*, "Biodiversity of bacteriophages: Morphological and biological properties of a large group of phages isolated from urban sewage," *Sci Rep*, vol. 6, no. 1, pp. 1–17, Oct. 2016, doi: 10.1038/srep34338.

[3] K. G. Andersen, A. Rambaut, W. I. Lipkin, E. C. Holmes, and R. F. Garry, "The proximal origin of SARS-CoV-2," *Nat Med*, vol. 26, no. 4, pp. 450–452, 2020, doi: 10.1038/s41591-020-0820-9.

[4] K. W. Witwer and J. Wolfram, "Extracellular vesicles versus synthetic nanoparticles for drug delivery," *Nat Rev Mater*, vol. 6, no. February, pp. 103–106, 2021, doi: 10.1038/s41578-020-00277-6.

[5] R. P. Feyman, "There's Plenty of Room at the Bottom," *Journal of Microelectricalmechanical systems*, vol. 1, no. 1, pp. 60–66, 1992, doi: 10.1023/B:NACO.0000027752.95792.a9.

[6] S. Norton, "A Brief History of Potable Gold," *Mol Interv*, vol. 8, no. 3, pp. 120–123, Jun. 2008, doi: 10.1124/mi.8.3.1.

[7] B. R. J. Xiaoling Li, *Design of Controlled Release Drug Delivery Systems*. McGraw-Hill, 1387. doi: 10.1036/0071417591.

[8] J. KREUTER, "Nanoparticles—a historical perspective," *Int J Pharm*, vol. 331, no. 1, pp. 1–10, Feb. 2007, doi: 10.1016/j.ijpharm.2006.10.021.

[9] U. Scheffel, T. K. Natarajan, J. Wagner, and H. N, "Albumin for Study of the Reticuloendothelial System.," *Journal of Nuclear Medicine*, vol. 13, no. 7, pp. 498–503, 1972.

[10] A. D. Bangham and R. W. Horne, "Negative staining of phospholipids and their structural modification by surface-active agents as observed in the electron microscope," *J Mol Biol*, vol. 8, no. 5, pp. 660-IN10, Jan. 1964, doi: 10.1016/S0022-2836(64)80115-7.

[11] G. Gregoriadis, "Drug entrapment in liposomes," *FEBS Lett*, vol. 36, no. 3, pp. 292–296, Nov. 1973, doi: 10.1016/0014-5793(73)80394-1.

[12] F. Farjadian, A. Ghasemi, O. Gohari, A. Roointan, M. Karimi, and M. R. Hamblin, "Nanopharmaceuticals and nanomedicines currently on the market: Challenges and opportunities," Jan. 01, 2019, *Future Medicine Ltd.* doi: 10.2217/nnm-2018-0120.

[13] K. Boussery, F. M. Belpaire, and J. Van de Voorde, *Physiological Aspects Determining the Pharmacokinetic Properties of Drugs*. Elsevier Ltd, 2008. doi: 10.1016/B978-0-12-417205-0.00023-7.

[14] T. Lima, K. Bernfur, M. Vilanova, and T. Cedervall, "Understanding the Lipid and Protein Corona Formation on Different Sized Polymeric Nanoparticles," *Sci Rep*, vol. 10, no. 1, p. 1129, Dec. 2020, doi: 10.1038/s41598-020-57943-6.

[15] S. Onoue, S. Yamada, and H. K. Chan, "Nanodrugs: pharmacokinetics and safety," *Int J Nanomedicine*, vol. 9, no. 1, p. 1025, Feb. 2014, doi: 10.2147/IJN.S38378.

[16] F. Alexis, E. Pridgen, L. K. Molnar, and O. C. Farokhzad, "Factors affecting the clearance and biodistribution of polymeric nanoparticles," *Mol Pharm*, vol. 5, no. 4, pp. 505–515, 2008, doi: 10.1021/mp800051m.

[17] D. J. Cutler, "Definition of mean residence times in pharmacokinetics," *Biopharm Drug Dispos*, vol. 8, no. 1, pp. 87–97, Jan. 1987, doi: 10.1002/bdd.2510080110.

[18] H. Frei, *Cancer Medicine*. 2000.

[19] R. A. Petros and J. M. Desimone, "Strategies in the design of nanoparticles for therapeutic applications," *Nat Rev Drug Discov*, vol. 9, no. 8, pp. 615–627, 2010, doi: 10.1038/nrd2591.

[20] S. M. Moghimi, H. Hedeman, I. S. Muir, L. Illum, and S. S. Davis, "An investigation of the filtration capacity and the fate of large filtered sterically-stabilized microspheres in rat spleen," *BBA - General Subjects*, vol. 1157, no. 2, pp. 233–240, Jun. 1993, doi: 10.1016/0304-4165(93)90105-H.

[21] F. Haghiralsadat *et al.*, "A comprehensive mathematical model of drug release kinetics from nano-liposomes, derived from optimization studies of cationic PEGylated liposomal doxorubicin formulations for drug-gene delivery," *Artif Cells Nanomed Biotechnol*, vol. 46, no. 1, pp. 169–177, 2018, doi: 10.1080/21691401.2017.1304403.

[22] L. Chen *et al.*, "Inflammatory responses and inflammation-associated diseases in organs," *Oncotarget*, vol. 9, no. 6, pp. 7204–7218, Jan. 2018, doi: 10.18632/oncotarget.23208.

[23] H. Reza Rezaie, M. Esnaashary, A. Aref arjmand, A. Öchsner, H. R. Rezaie, and M. Esnaashary, "A Review of Biomaterials and Their Applications in Drug Delivery," pp. 27–30, 2018, doi: 10.1007/978-981-10-0503-9.

[24] N. Kostevšek *et al.*, "Magneto-liposomes as MRI contrast agents: A systematic study of different liposomal formulations," *Nanomaterials*, vol. 10, no. 5, p. 889, May 2020, doi: 10.3390/nano10050889.

[25] J. Huang, X. Zhong, L. Wang, L. Yang, and H. Mao, "Improving the magnetic resonance imaging contrast and detection methods with engineered magnetic nanoparticles," 2012, *Ivyspring International Publisher*. doi: 10.7150/thno.4006.

[26] T. Lajunen *et al.*, "The effect of light sensitizer localization on the stability of indocyanine green liposomes," *Journal of Controlled Release*, vol. 284, no. June, pp. 213–223, Aug. 2018, doi: 10.1016/j.jconrel.2018.06.029.

[27] F. Danhier, "To exploit the tumor microenvironment: Since the EPR effect fails in the clinic, what is the future of nanomedicine?," *Journal of Controlled Release*, vol. 244, pp. 108–121, 2016, doi: 10.1016/j.jconrel.2016.11.015.

[28] C. L. Ventola, "Progress in nanomedicine: Approved and investigational nanodrugs," *P and T*, vol. 42, no. 12, pp. 742–755, Dec. 2017.

[29] S. T. Khan, J. Musarrat, and A. A. Al-Khedhairy, "Countering drug resistance, infectious diseases, and sepsis using metal and metal oxides nanoparticles: Current status," *Colloids Surf B Biointerfaces*, vol. 146, pp. 70–83, 2016, doi: 10.1016/j.colsurfb.2016.05.046.

[30] O. B. Koper, J. S. Klabunde, G. L. Marchin, K. J. Klabunde, P. Stoimenov, and L. Bohra, "Nanoscale powders and formulations with biocidal activity toward spores and vegetative cells of Bacillus species, viruses, and toxins," *Curr Microbiol*, vol. 44, no. 1, pp. 49–55, Jan. 2002, doi: 10.1007/s00284-001-0073-x.

[31] T. Nakamura, F. Sugihara, H. Matsushita, Y. Yoshioka, S. Mizukami, and K. Kikuchi, "Mesoporous silica nanoparticles for 19F magnetic resonance imaging, fluorescence imaging, and drug delivery," *Chem Sci*, vol. 6, no. 3, pp. 1986–1990, Mar. 2015, doi: 10.1039/c4sc03549f.

[32] Z. Chen, W. Wu, and Y. Lu, "What is the future for nanocrystal-based drug-delivery systems?," *Ther Deliv*, vol. 11, no. 4, pp. 225–229, 2020, doi: 10.4155/tde-2020-0016.

[33] E. V. Tazina, K. V. Kostin, and N. A. Oborotova, "Specific features of drug encapsulation in liposomes (A review)," Oct. 02, 2011, *Springer*. doi: 10.1007/s11094-011-0661-4.

[34] D. Lombardo, M. A. Kiselev, and M. T. Caccamo, "Smart Nanoparticles for Drug Delivery Application: Development of Versatile Nanocarrier Platforms in Biotechnology and Nanomedicine," *J Nanomater*, vol. 2019, 2019, doi: 10.1155/2019/3702518.

[35] C. Zylberberg and S. Matosevic, "Pharmaceutical liposomal drug delivery: a review of new delivery systems and a look at the regulatory landscape," *Drug Deliv*, vol. 23, no. 9, pp. 3319–3329, Nov. 2016, doi: 10.1080/10717544.2016.1177136.

[36] I. Franiak-Pietryga, B. Ziemba, B. Messmer, and D. Skowronska-Krawczyk, "Dendrimers as Drug Nanocarriers: The Future of Gene Therapy and Targeted Therapies in Cancer," in *Dendrimers - Fundamentals and Applications*, InTech, 2018. doi: 10.5772/intechopen.75774.

[37] G. Bonacucina, M. Cespi, M. Misici-Falzi, and G. F. Palmieri, "Colloidal soft matter as drug delivery system," Jan. 01, 2009, *John Wiley and Sons Inc.* doi: 10.1002/jps.21423.

[38] S. Y. Lee *et al.*, "A theranostic micelleplex co-delivering SN-38 and VEGF siRNA for colorectal cancer therapy," *Biomaterials*, vol. 86, pp. 92–105, Apr. 2016, doi: 10.1016/j.biomaterials.2016.01.068.

[39] S. B. van Witteloostuijn, S. L. Pedersen, and K. J. Jensen, "Half-Life Extension of Biopharmaceuticals using Chemical Methods: Alternatives to PEGylation,"

*ChemMedChem*, vol. 11, no. 22, pp. 2474–2495, Nov. 2016, doi: 10.1002/cmdc.201600374.

[40] J. Kousalová and T. Etrych, "Polymeric nanogels as drug delivery systems," 2018, *Czech Academy of Sciences*. doi: 10.33549/physiolres.933979.

[41] M. Sushnitha, M. Evangelopoulos, E. Tasciotti, and F. Taraballi, "Cell Membrane-Based Biomimetic Nanoparticles and the Immune System: Immunomodulatory Interactions to Therapeutic Applications," Jun. 17, 2020, *Frontiers Media S.A.* doi: 10.3389/fbioe.2020.00627.

[42] J. E. Riviere, "Pharmacokinetics of nanomaterials: an overview of carbon nanotubes, fullerenes and quantum dots," *Wiley Interdiscip Rev Nanomed Nanobiotechnol*, vol. 1, no. 1, pp. 26–34, Jan. 2009, doi: 10.1002/wnan.24.

[43] A. C. Tripathi, S. A. Saraf, and S. K. Saraf, "Carbon Nanotropes: A Contemporary Paradigm in Drug Delivery," *Materials*, vol. 8, pp. 3068–3100, 2015, doi: 10.3390/ma8063068.

[44] R. Shrestha *et al.*, "Hierarchically Assembled Theranostic Nanostructures for siRNA Delivery and Imaging Applications," 2012, doi: 10.1021/ja306616n.

[45] X. (Shawn) Chen, " Introducing Theranostics Journal - From the Editor-in-Chief ," *Theranostics*, vol. 1, pp. 1–2, Jan. 2012, doi: 10.7150/thno/v01p0001.

[46] Z. Chen, B. Krishnamachary, J. Pachecho-Torres, M. F. Penet, and Z. M. Bhujwalla, "Theranostic small interfering RNA nanoparticles in cancer precision nanomedicine," *Wiley Interdiscip Rev Nanomed Nanobiotechnol*, vol. 12, no. 2, pp. 1–22, 2020, doi: 10.1002/wnan.1595.

[47] Y. Jeong, H. S. Hwang, and K. Na, "Theranostics and contrast agents for magnetic resonance imaging," Jul. 27, 2018, *BioMed Central Ltd.* doi: 10.1186/s40824-018-0130-1.

[48] B. M. Vickerman, C. P. O'banion, X. Tan, and D. S. Lawrence, "Light-Controlled Release of Therapeutic Proteins from Red Blood Cells," *ACS Cent Sci*, 2020, doi: 10.1021/acscentsci.0c01151.

[49] H. Ke *et al.*, "Gold nanoshelled liquid perfluorocarbon magnetic nanocapsules: A nanotheranostic platform for bimodal ultrasound/magnetic resonance imaging guided photothermal tumor ablation," *Theranostics*, vol. 4, no. 1, pp. 12–23, 2014, doi: 10.7150/thno.7275.

[50] L. Ren *et al.*, "'all-in-One' Theranostic Agent with Seven Functions Based on Bi-Doped Metal Chalcogenide Nanoflowers," *ACS Appl Mater Interfaces*, vol. 11, no. 49, pp. 45467–45478, 2019, doi: 10.1021/acsami.9b16962.

[51] K. Herrmann, S. M. Larson, and W. A. Weber, "Theranostic concepts: More than just a fashion trend-introduction and overview," Sep. 01, 2017, *Society of Nuclear Medicine Inc.* doi: 10.2967/jnumed.117.199570.

[52] I. Texier *et al.*, "Cyanine-loaded lipid nanoparticles for improved in vivo fluorescence imaging," *J Biomed Opt*, vol. 14, no. 5, p. 054005, 2009, doi: 10.1117/1.3213606.

[53] N. Kostevšek *et al.*, "Magneto-liposomes as MRI contrast agents: A systematic study of different liposomal formulations," *Nanomaterials*, vol. 10, no. 5, p. 889, May 2020, doi: 10.3390/nano10050889.

[54] G. Della Pelle, A. Delgado López, M. Salord Fiol, and N. Kostevšek, "Cyanine dyes for photo-thermal therapy: A comparison of synthetic liposomes and natural erythrocyte-based carriers," *Int J Mol Sci*, vol. 22, no. 13, 2021, doi: 10.3390/ijms22136914.

[55] S. M. Janib, A. S. Moses, and J. A. MacKay, "Imaging and drug delivery using theranostic nanoparticles," Aug. 30, 2010, *NIH Public Access*. doi: 10.1016/j.addr.2010.08.004.

[56] N. C. Nicolaides, D. J. O'Shannessy, E. Albone, and L. Grasso, "Co-development of diagnostic vectors to support targeted therapies and theranostics: Essential tools in personalized cancer therapy," *Front Oncol*, vol. 4 JUN, no. June, 2014, doi: 10.3389/fonc.2014.00141.

[57] N. D. Thorat, H. E. Townley, R. M. Patil, S. A. M. Tofail, and J. Bauer, "Comprehensive approach of hybrid nanoplatforms in drug delivery and theranostics to combat cancer," *Drug Discov Today*, vol. 25, no. 7, pp. 1245–1252, 2020, doi: 10.1016/j.drudis.2020.04.018.

[58] H. Kang, S. Mintri, A. V. Menon, H. Y. Lee, H. S. Choi, and J. Kim, "Pharmacokinetics, pharmacodynamics and toxicology of theranostic nanoparticles," *Nanoscale*, vol. 7, no. 45, pp. 18848–18862, 2015, doi: 10.1039/C5NR05264E.

[59] G. Cao, *Nanostructures and Nanomaterials*. PUBLISHED BY IMPERIAL COLLEGE PRESS AND DISTRIBUTED BY WORLD SCIENTIFIC PUBLISHING CO., 2004. doi: 10.1142/p305.

[60] A. Tsuda and N. V. Konduru, "The role of natural processes and surface energy of inhaled engineered nanoparticles on aggregation and corona formation," Apr. 01, 2016, *Elsevier B.V.* doi: 10.1016/j.impact.2016.06.002.

[61] S. Nejati, E. Mohseni Vadeghani, S. Khorshidi, and A. Karkhaneh, "Role of particle shape on efficient and organ-based drug delivery," *Eur Polym J*, vol. 122, p. 109353, 2020, doi: 10.1016/j.eurpolymj.2019.109353.

[62] Z. Chu *et al.*, "Unambiguous observation of shape effects on cellular fate of nanoparticles," *Sci Rep*, vol. 4, no. 1, pp. 1–9, Mar. 2014, doi: 10.1038/srep04495.

[63] E. Boldyreva, "Mechanochemistry of inorganic and organic systems: What is similar, what is different?," *Chem Soc Rev*, vol. 42, no. 18, pp. 7719–7738, 2013, doi: 10.1039/c3cs60052a.

[64] H. Palmelund, J. B. Eriksen, A. Bauer-Brandl, J. Rantanen, and K. Löbmann, "Enabling formulations of aprepitant: in vitro and in vivo comparison of nanocrystalline, amorphous and deep eutectic solvent based formulations," *Int J Pharm X*, vol. 3, no. May, 2021, doi: 10.1016/j.ijpx.2021.100083.

[65] M. H. U. Bhuiyan, R. Saidur, M. A. Amalina, R. M. Mostafizur, and A. K. M. S. Islam, "Effect of nanoparticles concentration and their sizes on surface tension of

nanofluids," *Procedia Eng*, vol. 105, no. Icte 2014, pp. 431–437, 2015, doi: 10.1016/j.proeng.2015.05.030.

[66] J. Lazarovits, Y. Y. Chen, E. A. Sykes, and W. C. W. Chan, "Nanoparticle-blood interactions: The implications on solid tumour targeting," *Chemical Communications*, vol. 51, no. 14, pp. 2756–2767, 2015, doi: 10.1039/c4cc07644c.

[67] S. M. Moghimi, A. C. Hunter, and T. L. Andresen, "Factors controlling nanoparticle pharmacokinetics: An integrated analysis and perspective," *Annu Rev Pharmacol Toxicol*, vol. 52, pp. 481–503, 2012, doi: 10.1146/annurev-pharmtox-010611-134623.

[68] A. E. Nel *et al.*, "Understanding biophysicochemical interactions at the nano-bio interface," *Nat Mater*, vol. 8, no. 7, pp. 543–557, 2009, doi: 10.1038/nmat2442.

[69] M. Cataldi, C. Vigliotti, T. Mosca, M. R. Cammarota, and D. Capone, "Emerging role of the spleen in the pharmacokinetics of monoclonal antibodies, nanoparticles and exosomes," Jun. 10, 2017, *MDPI AG*. doi: 10.3390/ijms18061249.

[70] M. Longmire, P. L. Choyke, and H. Kobayashi, "Clearance properties of nano-sized particles and molecules as imaging agents: considerations and caveats," *Nanomedicine*, vol. 3, no. 5, pp. 703–717, Oct. 2008, doi: 10.2217/17435889.3.5.703.

[71] T. Ishida, H. Harashima, and H. Kiwada, "Liposome Clearance," *Biosci Rep*, vol. 22, no. 2, pp. 197–224, Apr. 2002, doi: 10.1023/A:1020134521778.

[72] M. B. Pedersen *et al.*, "Curvature of Synthetic and Natural Surfaces Is an Important Target Feature in Classical Pathway Complement Activation," *The Journal of Immunology*, vol. 184, no. 4, pp. 1931–1945, Feb. 2010, doi: 10.4049/jimmunol.0902214.

[73] M. Mohamed *et al.*, "PEGylated liposomes: immunological responses," *Sci Technol Adv Mater*, vol. 20, no. 1, pp. 710–724, Dec. 2019, doi: 10.1080/14686996.2019.1627174.

[74] D. Westmeier, R. H. Stauber, and D. Docter, "The concept of bio-corona in modulating the toxicity of engineered nanomaterials (ENM)," *Toxicol Appl Pharmacol*, vol. 299, pp. 53–57, 2016, doi: 10.1016/j.taap.2015.11.008.

[75] O. K. Kari *et al.*, "In situ analysis of liposome hard and soft protein corona structure and composition in a single label-free workflow," *Nanoscale*, vol. 12, no. 3, pp. 1728–1741, Jan. 2020, doi: 10.1039/C9NR08186K.

[76] L. Vroman, "Effect of adsorbed proteins on the wettability of hydrophilic and hydrophobic solids," *Nature*, vol. 196, no. 4853, pp. 476–477, 1962, doi: 10.1038/196476a0.

[77] S. Y. Fam, C. F. Chee, C. Y. Yong, K. L. Ho, A. R. Mariatulqabtiah, and W. S. Tan, "Stealth coating of Nanoparticles in drug-delivery systems," *Nanomaterials*, vol. 10, no. 4, pp. 1–18, 2020, doi: 10.3390/nano10040787.

[78] S. Yona and S. Gordon, "From the Reticuloendothelial to Mononuclear Phagocyte System – The Unaccounted Years," *Front Immunol*, vol. 6, no. JUL, Jul. 2015, doi: 10.3389/fimmu.2015.00328.

[79] T. Gjetting, T. L. Andresen, C. L. Christensen, F. Cramer, T. T. Poulsen, and H. S. Poulsen, "A simple protocol for preparation of a liposomal vesicle with encapsulated plasmid DNA that mediate high accumulation and reporter gene activity in tumor tissue," 2011, doi: 10.1016/j.rinphs.2011.08.001.

[80] S. Schöttler *et al.*, "Protein adsorption is required for stealth effect of poly(ethylene glycol)- and poly(phosphoester)-coated nanocarriers," *Nature Nanotechnology 2016 11:4*, vol. 11, no. 4, pp. 372–377, Feb. 2016, doi: 10.1038/nnano.2015.330.

[81] D. Shi *et al.*, "To PEGylate or not to PEGylate: Immunological properties of nanomedicine's most popular component, polyethylene glycol and its alternatives," *Adv Drug Deliv Rev*, vol. 180, p. 114079, Jan. 2022, doi: 10.1016/j.addr.2021.114079.

[82] C. Lubich *et al.*, "The Mystery of Antibodies Against Polyethylene Glycol (PEG) - What do we Know?," *Pharm Res*, vol. 33, no. 9, pp. 2239–2249, 2016, doi: 10.1007/s11095-016-1961-x.

[83] D. Needham, *Reverse engineering of the low temperature-sensitive liposome (LTSL) for treating cancer*. Woodhead Publishing Limited, 2013. doi: 10.1533/9780857096760.3.270.

[84] Y. Barenholz, "Doxil® - The first FDA-approved nano-drug: Lessons learned," Jun. 10, 2012, *J Control Release*. doi: 10.1016/j.jconrel.2012.03.020.

[85] Y. Xia, J. Tian, and X. Chen, "Effect of surface properties on liposomal siRNA delivery," *Biomaterials*, vol. 79, pp. 56–68, 2016, doi: 10.1016/j.biomaterials.2015.11.056.

[86] D. Shi *et al.*, "To PEGylate or not to PEGylate: Immunological properties of nanomedicine's most popular component, polyethylene glycol and its alternatives," *Adv Drug Deliv Rev*, vol. 180, p. 114079, Jan. 2022, doi: 10.1016/j.addr.2021.114079.

[87] M. Jafari, W. Xu, R. Pan, C. M. Sweeting, D. N. Karunaratne, and P. Chen, "Serum stability and physicochemical characterization of a novel amphipathic peptide C6M1 for siRNA delivery," *PLoS One*, vol. 9, no. 5, p. e97797, May 2014, doi: 10.1371/journal.pone.0097797.

[88] T. T. Hoang Thi, E. H. Pilkington, D. H. Nguyen, J. S. Lee, K. D. Park, and N. P. Truong, "The Importance of Poly(ethylene glycol) Alternatives for Overcoming PEG Immunogenicity in Drug Delivery and Bioconjugation," *Polymers (Basel)*, vol. 12, no. 2, p. 298, Feb. 2020, doi: 10.3390/polym12020298.

[89] S. N. Cohen, "DNA cloning: A personal view after 40 years," *Proc Natl Acad Sci U S A*, vol. 110, no. 39, pp. 15521–15529, 2013, doi: 10.1073/pnas.1313397110.

[90] Siddhartha Mukherjee, *The Gene: An Intimate History*. 2016.

[91] X. Du *et al.*, "Advanced physical techniques for gene delivery based on membrane perforation," *Drug Deliv*, vol. 25, no. 1, pp. 1516–1525, Jan. 2018, doi: 10.1080/10717544.2018.1480674.

[92] P. J. Chen and D. R. Liu, "Prime editing for precise and highly versatile genome manipulation," *Nat Rev Genet*, vol. 24, no. 3, pp. 161–177, 2023, doi: 10.1038/s41576-022-00541-1.

[93] F. Sinclair, A. A. Begum, C. C. Dai, I. Toth, and P. M. Moyle, "Recent advances in the delivery and applications of nonviral CRISPR/Cas9 gene editing," *Drug Deliv Transl Res*, vol. 13, no. 5, pp. 1500–1519, 2023, doi: 10.1007/s13346-023-01320-z.

[94] I. Ahn, C. S. Kang, and J. Han, "Where should siRNAs go: applicable organs for siRNA drugs," *Exp Mol Med*, vol. 55, no. 7, pp. 1283–1292, 2023, doi: 10.1038/s12276-023-00998-y.

[95] D. Collotta, I. Bertocchi, E. Chiapello, and M. Collino, "Antisense oligonucleotides: a novel Frontier in pharmacological strategy," *Front Pharmacol*, vol. 14, no. November, pp. 1–18, 2023, doi: 10.3389/fphar.2023.1304342.

[96] X. Huang, Z. Chen, and Y. Liu, "RNAi-mediated control of CRISPR functions," *Theranostics*, vol. 10, no. 15, pp. 6661–6673, 2020, doi: 10.7150/thno.44880.

[97] G. Ruvkun, "Glimpses of a Tiny RNA World," *Science (1979)*, vol. 294, no. 5543, pp. 797–799, Oct. 2001, doi: 10.1126/science.1066315.

[98] C. Gareri, A. Polimeni, S. Giordano, L. Tammè, A. Curcio, and C. Indolfi, "Antisense Oligonucleotides and Small Interfering RNA for the Treatment of Dyslipidemias," *J Clin Med*, vol. 11, no. 13, p. 3884, Jul. 2022, doi: 10.3390/jcm11133884.

[99] H. oki Iwakawa and Y. Tomari, "Life of RISC: Formation, action, and degradation of RNA-induced silencing complex," *Mol Cell*, vol. 82, no. 1, pp. 30–43, 2022, doi: 10.1016/j.molcel.2021.11.026.

[100] D. C. Swarts *et al.*, "The evolutionary journey of Argonaute proteins," *Nat Struct Mol Biol*, vol. 21, no. 9, pp. 743–753, 2014, doi: 10.1038/nsmb.2879.

[101] K. Nakanishi, "Anatomy of RISC: how do small RNAs and chaperones activate Argonaute proteins?," *Wiley Interdiscip Rev RNA*, vol. 7, no. 5, pp. 637–660, 2016, doi: 10.1002/wrna.1356.

[102] B. Yao, S. Li, and E. K. L. Chan, "Function of GW182 and GW bodies in siRNA and miRNA pathways," *Adv Exp Med Biol*, vol. 768, pp. 71–96, 2013, doi: 10.1007/978-1-4614-5107-5_6.

[103] R. J. Golden *et al.*, "An Argonaute phosphorylation cycle promotes microRNA-mediated silencing," *Nature*, vol. 542, no. 7640, pp. 197–202, Feb. 2017, doi: 10.1038/nature21025.

[104] H. oki Iwakawa and Y. Tomari, "The Functions of MicroRNAs: mRNA Decay and Translational Repression," *Trends Cell Biol*, vol. 25, no. 11, pp. 651–665, 2015, doi: 10.1016/j.tcb.2015.07.011.

[105] Y. Zeng, R. Yi, and B. R. Cullen, "MicroRNAs and small interfering RNAs can inhibit mRNA expression by similar mechanisms," *Proc Natl Acad Sci U S A*, vol. 100, no. 17, pp. 9779–9784, 2003, doi: 10.1073/pnas.1630797100.

[106] A. Branscheid *et al.*, "SKI2 mediates degradation of RISC 5′-cleavage fragments and prevents secondary siRNA production from miRNA targets in Arabidopsis," *Nucleic Acids Res*, vol. 43, no. 22, pp. 10975–10988, Dec. 2015, doi: 10.1093/nar/gkv1014.

[107] R. Singhania *et al.*, "Short interfering RNA induced generation and translation of stable 5′ mRNA cleavage intermediates," *Biochimica et Biophysica Acta (BBA) - Gene Regulatory Mechanisms*, vol. 1859, no. 8, pp. 1034–1042, Aug. 2016, doi: 10.1016/j.bbagrm.2016.06.005.

[108] M. P. Gantier and B. R. G. Williams, "The response of mammalian cells to double-stranded RNA," *Cytokine Growth Factor Rev*, vol. 18, no. 5–6, pp. 363–371, Oct. 2007, doi: 10.1016/j.cytogfr.2007.06.016.

[109] W. Wang *et al.*, "Activation of innate antiviral immune response via double-stranded RNA-dependent RLR receptor-mediated necroptosis," *Sci Rep*, vol. 6, no. October 2015, pp. 1–14, 2016, doi: 10.1038/srep22550.

[110] L. Franchi *et al.*, "Cytosolic Double-Stranded RNA Activates the NLRP3 Inflammasome via MAVS-Induced Membrane Permeabilization and K+ Efflux," *The Journal of Immunology*, vol. 193, no. 8, pp. 4214–4222, Oct. 2014, doi: 10.4049/jimmunol.1400582.

[111] J. D. Shih and C. P. Hunter, "SID-1 is a dsRNA-selective dsRNA-gated channel," *RNA*, vol. 17, no. 6, p. 1057, Jun. 2011, doi: 10.1261/RNA.2596511.

[112] T. B. Rodrigues and J. S. Petrick, "Safety Considerations for Humans and Other Vertebrates Regarding Agricultural Uses of Externally Applied RNA Molecules," *Front Plant Sci*, vol. 11, no. April, pp. 1–12, 2020, doi: 10.3389/fpls.2020.00407.

[113] S. F. Dowdy, "Overcoming cellular barriers for RNA therapeutics," *Nature Biotechnology 2017 35:3*, vol. 35, no. 3, pp. 222–229, Feb. 2017, doi: 10.1038/nbt.3802.

[114] S. Sorrentino, "The eight human 'canonical' ribonucleases: Molecular diversity, catalytic properties, and special biological actions of the enzyme proteins," Jun. 03, 2010, *No longer published by Elsevier*. doi: 10.1016/j.febslet.2010.04.018.

[115] L. A. Mulcahy, R. C. Pink, D. Raul, F. Carter, D. David, and R. F. Carter, "Routes and mechanisms of extracellular vesicle uptake", doi: 10.3402/jev.v3.24641.

[116] R. R. Nikam and K. R. Gore, "Journey of siRNA: Clinical Developments and Targeted Delivery," *Nucleic Acid Ther*, vol. 28, no. 4, pp. 209–224, Aug. 2018, doi: 10.1089/nat.2017.0715.

[117] M. Friedrich and A. Aigner, "Therapeutic siRNA: State-of-the-Art and Future Perspectives," *BioDrugs 2022 36:5*, vol. 36, no. 5, pp. 549–571, Aug. 2022, doi: 10.1007/S40259-022-00549-3.

[118] T. Friedmann and R. Roblin, "Gene therapy for human genetic disease?," *Science (1979)*, vol. 178, no. 4061, pp. 648–649, 1972, doi: 10.1126/science.178.4061.648.

[119] C. C. Ma, Z. L. Wang, T. Xu, Z. Y. He, and Y. Q. Wei, "The approved gene therapy drugs worldwide: from 1998 to 2019," *Biotechnol Adv*, vol. 40, no. December 2019, p. 107502, 2020, doi: 10.1016/j.biotechadv.2019.107502.

[120] J. P. Gillet and M. M. Gottesman, "Mechanisms of multidrug resistance in cancer.," *Methods Mol Biol*, vol. 596, pp. 47–76, 2010, doi: 10.1007/978-1-60761-416-6_4.

[121] Y. Ishino, M. Krupovic, and P. Forterre, "History of CRISPR-Cas from encounter with a mysterious repeated sequence to genome editing technology," *J Bacteriol*, vol. 200, no. 7, Apr. 2018, doi: 10.1128/JB.00580-17.

[122] A. L. Cooney *et al.*, "Lentiviral-mediated phenotypic correction of cystic fibrosis pigs," *JCI Insight*, vol. 1, no. 14, Sep. 2016, doi: 10.1172/jci.insight.88730.

[123] E. A. Taha, J. Lee, and A. Hotta, "Delivery of CRISPR-Cas tools for in vivo genome editing therapy: Trends and challenges," *Journal of Controlled Release*, vol. 342, no. November 2021, pp. 345–361, 2022, doi: 10.1016/j.jconrel.2022.01.013.

[124] C. L. Hardee, L. M. Arévalo-Soliz, B. D. Hornstein, and L. Zechiedrich, "Advances in non-viral DNA vectors for gene therapy," Feb. 01, 2017, *MDPI AG*. doi: 10.3390/genes8020065.

[125] N. Raval, H. Jogi, P. Gondaliya, K. Kalia, and R. K. Tekade, "Method and its Composition for encapsulation, stabilization, and delivery of siRNA in Anionic polymeric nanoplex: An In vitro- In vivo Assessment," *Sci Rep*, vol. 9, no. 1, pp. 1–19, 2019, doi: 10.1038/s41598-019-52390-4.

[126] R. Goswami *et al.*, "Gene therapy leaves a vicious cycle," *Front Oncol*, vol. 9, no. APR, pp. 1–25, 2019, doi: 10.3389/fonc.2019.00297.

[127] A. Gupta, K. N. Kafetzis, A. D. Tagalakis, and C. Yu-Wai-Man, "RNA therapeutics in ophthalmology - translation to clinical trials," *Exp Eye Res*, vol. 205, p. 108482, Apr. 2021, doi: 10.1016/j.exer.2021.108482.

[128] J. Bruniaux, S. Ben Djemaa, K. Hervé-Aubert, H. Marchais, I. Chourpa, and S. David, "Stealth magnetic nanocarriers of siRNA as platform for breast cancer theranostics," *Int J Pharm*, vol. 532, no. 2, pp. 660–668, 2017, doi: 10.1016/j.ijpharm.2017.05.022.

[129] Z. Wang, J. Wang, and G. Liu, *Theranostic Magnetic Nanoparticles as Molecular Imaging Agents for siRNA Delivery*. Elsevier Inc., 2018. doi: 10.1016/B978-0-12-813339-2.00019-0.

[130] M. Woo Kim *et al.*, "Anti-EGF Receptor Aptamer-Guided Co-Delivery of Anti-Cancer siRNAs and Quantum Dots for Theranostics of Triple-Negative Breast Cancer," *Theranostics*, vol. 9, p. 3, 2019, doi: 10.7150/thno.30228.

[131] A. Antonelli, C. Sfara, E. Manuali, I. J. Bruce, and M. Magnani, "Encapsulation of superparamagnetic nanoparticles into red blood cells as new carriers of MRI contrast agents," *Nanomedicine*, vol. 6, no. 2, pp. 211–223, Feb. 2011, doi: 10.2217/nnm.10.163.

[132] B. Bahmani, D. Bacon, and B. Anvari, "Erythrocyte-derived photo-theranostic agents: hybrid nano-vesicles containing indocyanine green for near infrared imaging and therapeutic applications," *Sci Rep*, vol. 3, no. 1, p. 2180, Dec. 2013, doi: 10.1038/srep02180.

[133] S. Ahn, S. Y. Jung, E. Seo, and S. J. Lee, "Gold nanoparticle-incorporated human red blood cells (RBCs) for X-ray dynamic imaging," *Biomaterials*, vol. 32, no. 29, pp. 7191–7199, Oct. 2011, doi: 10.1016/j.biomaterials.2011.05.023.

[134] R. Huschka, A. Barhoumi, Q. Liu, J. A. Roth, L. Ji, and N. J. Halas, "Gene Silencing by Gold Nanoshell-Mediated Delivery and Laser-Triggered Release of Antisense Oligonucleotide and siRNA NIH Public Access," *ACS Nano*, vol. 6, no. 9, pp. 7681–7691, 2012, doi: 10.1021/nn301135w.

[135] D. Grimm, "The dose can make the poison: Lessons learned from adverse in vivo toxicities caused by RNAi overexpression," Aug. 26, 2011. doi: 10.1186/1758-907X-2-8.

[136] D. Grimm *et al.*, "Fatality in mice due to oversaturation of cellular microRNA/short hairpin RNA pathways," *Nature*, vol. 441, no. 7092, pp. 537–541, May 2006, doi: 10.1038/nature04791.

[137] R. Yi, Y. Qin, I. G. Macara, and B. R. Cullen, "Exportin-5 mediates the nuclear export of pre-microRNAs and short hairpin RNAs," *Genes Dev*, vol. 17, no. 24, pp. 3011–3016, Dec. 2003, doi: 10.1101/gad.1158803.

[138] J. Neumeier and G. Meister, "siRNA Specificity: RNAi Mechanisms and Strategies to Reduce Off-Target Effects," Jan. 28, 2021, *Frontiers Media S.A.* doi: 10.3389/fpls.2020.526455.

[139] B. Hu *et al.*, "Therapeutic siRNA: state of the art," *Signal Transduct Target Ther*, vol. 5, no. 1, 2020, doi: 10.1038/s41392-020-0207-x.

[140] J. Zhou, M. S. Song, A. M. Jacobi, M. A. Behlke, X. Wu, and J. J. Rossi, "Deep sequencing analyses of DsiRNAs reveal the influence of 3' terminal overhangs on dicing polarity, strand selectivity, and RNA editing of siRNAs," *Mol Ther Nucleic Acids*, vol. 1, no. 4, p. e17, Jan. 2012, doi: 10.1038/mtna.2012.6.

[141] M. Egli and M. Manoharan, "Chemistry, structure and function of approved oligonucleotide therapeutics," *Nucleic Acids Res*, vol. 51, no. 6, pp. 2529–2573, Apr. 2023, doi: 10.1093/nar/gkad067.

[142] R. Singhania *et al.*, "Short interfering RNA induced generation and translation of stable 5′ mRNA cleavage intermediates," *Biochim Biophys Acta Gene Regul Mech*, vol. 1859, no. 8, pp. 1034–1042, Aug. 2016, doi: 10.1016/j.bbagrm.2016.06.005.

[143] A. K. Pearce and R. K. O'Reilly, "Insights into Active Targeting of Nanoparticles in Drug Delivery: Advances in Clinical Studies and Design Considerations for Cancer Nanomedicine," *Bioconjug Chem*, vol. 30, no. 9, pp. 2300–2311, Sep. 2019, doi: 10.1021/acs.bioconjchem.9b00456.

[144] B. Ozpolat, A. K. Sood, and G. Lopez-Berestein, "Liposomal siRNA nanocarriers for cancer therapy," *Adv Drug Deliv Rev*, vol. 66, pp. 110–116, Feb. 2014, doi: 10.1016/j.addr.2013.12.008.

[145] F. Borel and C. Mueller, "Design of AAV vectors for delivery of RNAi," *Methods in Molecular Biology*, vol. 1950, pp. 3–18, 2019, doi: 10.1007/978-1-4939-9139-6_1.

[146] B. S. Joshi, M. A. de Beer, B. N. G. Giepmans, and I. S. Zuhorn, "Endocytosis of Extracellular Vesicles and Release of Their Cargo from Endosomes," *ACS Nano*, vol. 14, no. 4, pp. 4444–4455, Apr. 2020, doi: 10.1021/acsnano.9b10033.

[147] S. El Andaloussi, I. Mäger, X. O. Breakefield, and M. J. A. Wood, "Extracellular vesicles: Biology and emerging therapeutic opportunities," *Nat Rev Drug Discov*, vol. 12, no. 5, pp. 347–357, 2013, doi: 10.1038/nrd3978.

[148] V. Syromiatnikova, A. Prokopeva, and M. Gomzikova, "Methods of the Large-Scale Production of Extracellular Vesicles," Sep. 01, 2022, *MDPI*. doi: 10.3390/ijms231810522.

[149] C. T. Pham, X. Zhang, A. Lam, and M. T. N. Le, "Red blood cell extracellular vesicles as robust carriers of RNA-based therapeutics," *Cell Stress*, vol. 2, no. 9, pp. 239–241, 2018, doi: 10.15698/cst2018.09.155.

[150] W. M. Usman *et al.*, "Efficient RNA drug delivery using red blood cell extracellular vesicles," *Nat Commun*, vol. 9, no. 1, 2018, doi: 10.1038/s41467-018-04791-8.

[151] T. N. Lamichhane *et al.*, "Oncogene Knockdown via Active Loading of Small RNAs into Extracellular Vesicles by Sonication," *Cell Mol Bioeng*, vol. 9, no. 3, pp. 315–324, 2016, doi: 10.1007/s12195-016-0457-4.

[152] Y.-L. Chen, C.-J. Bao, J.-L. Duan, Y. Xie, and W.-L. Lu, "Overcoming biological barriers by virus-like drug particles for drug delivery," *Adv Drug Deliv Rev*, vol. 203, p. 115134, Dec. 2023, doi: 10.1016/j.addr.2023.115134.

[153] M. Kheirvari, H. Liu, and E. Tumban, "Virus-like Particle Vaccines and Platforms for Vaccine Development," *Viruses*, vol. 15, no. 5, p. 1109, May 2023, doi: 10.3390/v15051109.

[154] R. D. Cadena-Nava, M. Comas-Garcia, R. F. Garmann, A. L. N. Rao, C. M. Knobler, and W. M. Gelbart, "Self-Assembly of Viral Capsid Protein and RNA Molecules of Different Sizes: Requirement for a Specific High Protein/RNA Mass Ratio," *J Virol*, vol. 86, no. 6, pp. 3318–3326, Mar. 2012, doi: 10.1128/JVI.06566-11.

[155] S. Nooraei *et al.*, "Virus-like particles: preparation, immunogenicity and their roles as nanovaccines and drug nanocarriers," *J Nanobiotechnology*, vol. 19, no. 1, pp. 1–27, 2021, doi: 10.1186/s12951-021-00806-7.

[156] C. Qian *et al.*, "Recent Progress on the Versatility of Virus-Like Particles," *Vaccines (Basel)*, vol. 8, no. 1, p. 139, Mar. 2020, doi: 10.3390/vaccines8010139.

[157] P. Lam and N. F. Steinmetz, "Delivery of siRNA therapeutics using cowpea chlorotic mottle virus-like particles," *Biomater Sci*, vol. 7, no. 8, pp. 3138–3142, Aug. 2019, doi: 10.1039/c9bm00785g.

[158] A. Nuñez-Rivera, P. G. J. Fournier, D. L. Arellano, A. G. Rodriguez-Hernandez, R. Vazquez-Duhalt, and R. D. Cadena-Nava, "Brome mosaic virus-like particles as siRNA nanocarriers for biomedical purposes," *Beilstein Journal of Nanotechnology*, vol. 11, pp. 372–382, Feb. 2020, doi: 10.3762/bjnano.11.28.

[159] C. Xu, D. Ju, and X. Zhang, "Cell Membrane-Derived Vesicle: A Novel Vehicle for Cancer Immunotherapy," *Front Immunol*, vol. 13, p. 3573, Jul. 2022, doi: 10.3389/FIMMU.2022.923598/BIBTEX.

[160] L. Liu *et al.*, "Cell membrane coating integrity affects the internalization mechanism of biomimetic nanoparticles," *Nat Commun*, vol. 12, no. 1, pp. 1–12, 2021, doi: 10.1038/s41467-021-26052-x.

[161] G. M. Ihler, R. H. Glew, and F. W. Schnure, "Enzyme loading of erythrocytes," *Proc Natl Acad Sci U S A*, vol. 70, no. 9, pp. 2663–2666, Sep. 1973, doi: 10.1073/pnas.70.9.2663.

[162] B. E. Bax *et al.*, "Clinical Medicine Erythrocyte Encapsulated Thymidine Phosphorylase for the Treatment of Patients with Mitochondrial Neurogastrointestinal Encephalomyopathy: Study Protocol for a Multi-Centre, Multiple Dose, Open Label Trial," *J. Clin. Med*, vol. 8, p. 1096, 2019, doi: 10.3390/jcm8081096.

[163] G. Mambrini *et al.*, "Ex vivo encapsulation of dexamethasone sodium phosphate into human autologous erythrocytes using fully automated biomedical equipment," *Int J Pharm*, vol. 517, no. 1–2, pp. 175–184, Jan. 2017, doi: 10.1016/j.ijpharm.2016.12.011.

[164] D. W. Stuckey and K. Shah, "Stem cell-based therapies for cancer treatment: Separating hope from hype," Jan. 01, 2014, *Nature Publishing Group*. doi: 10.1038/nrc3798.

[165] M. Munerati, R. Cortesi, D. Ferrari, F. Di Virgilio, and C. Nastruzzi, "Macrophages loaded with doxorubicin by ATP-mediated permeabilization: Potential carriers for antitumor therapy," *BBA - Molecular Cell Research*, vol. 1224, no. 2, pp. 269–276, Nov. 1994, doi: 10.1016/0167-4889(94)90200-3.

[166] B. Dalzon *et al.*, "Utility of macrophages in an antitumor strategy based on the vectorization of iron oxide nanoparticles," *Nanoscale*, vol. 11, no. 19, pp. 9341–9352, May 2019, doi: 10.1039/c8nr03364a.

[167] J. Gao, D. Chu, and Z. Wang, "Cell membrane-formed nanovesicles for disease-targeted delivery," *Journal of Controlled Release*, vol. 224, pp. 208–216, Feb. 2016, doi: 10.1016/j.jconrel.2016.01.024.

[168] G. Della Pelle and N. Kostevšek, "Nucleic acid delivery with red-blood-cell-based carriers," *Int J Mol Sci*, vol. 22, no. 10, 2021, doi: 10.3390/ijms22105264.

[169] A. D'Alessandro, M. Dzieciatkowska, T. Nemkov, and K. C. Hansen, "Red blood cell proteomics update: Is there more to discover?," *Blood Transfusion*, vol. 15, no. 2, pp. 182–187, Mar. 2017, doi: 10.2450/2017.0293-16.

[170] E. M. Pasini, M. Kirkegaard, P. Mortensen, H. U. Lutz, A. W. Thomas, and M. Mann, "In-depth analysis of the membrane and cytosolic proteome of red blood cells," *Blood*, vol. 108, no. 3, pp. 791–801, Aug. 2006, doi: 10.1182/blood-2005-11-007799.

[171] A. Ohashi *et al.*, "The expression and localization of RNase and RNase inhibitor in blood cells and vascular endothelial cells in homeostasis of the vascular system," *PLoS One*, vol. 12, no. 3, p. e0174237, Mar. 2017, doi: 10.1371/journal.pone.0174237.

[172] A. A. Gabizon, Y. Barenholz, and M. Bialer, "Prolongation of the Circulation Time of Doxorubicin Encapsulated in Liposomes Containing a Polyethylene

Glycol-Derivatized Phospholipid: Pharmacokinetic Studies in Rodents and Dogs," *Pharmaceutical Research: An Official Journal of the American Association of Pharmaceutical Scientists*, vol. 10, no. 5, pp. 703–708, 1993, doi: 10.1023/A:1018907715905.

[173] A. Gabizon *et al.*, "Prolonged Circulation Time and Enhanced Accumulation in Malignant Exudates of Doxorubicin Encapsulated in Polyethylene-glycol Coated Liposomes," *Cancer Res*, vol. 54, no. 4, 1994.

[174] L. Koleva, E. Bovt, F. Ataullakhanov, and E. Sinauridze, *Erythrocytes as carriers: From drug delivery to biosensors*, vol. 12, no. 3. MDPI AG, 2020. doi: 10.3390/pharmaceutics12030276.

[175] L. Rossi *et al.*, "Red Blood Cell Membrane Processing for Biomedical Applications," vol. 10, p. 1070, Aug. 2019, doi: 10.3389/fphys.2019.01070.

[176] Q. Xia, Y. Zhang, Z. Li, X. Hou, and N. Feng, "Red blood cell membrane-camouflaged nanoparticles: a novel drug delivery system for antitumor application," Jul. 01, 2019, *Chinese Academy of Medical Sciences*. doi: 10.1016/j.apsb.2019.01.011.

[177] J. G. Piao, L. Wang, F. Gao, Y. Z. You, Y. Xiong, and L. Yang, "Erythrocyte membrane is an alternative coating to polyethylene glycol for prolonging the circulation lifetime of gold nanocages for photothermal therapy," *ACS Nano*, vol. 8, no. 10, pp. 10414–10425, 2014, doi: 10.1021/nn503779d.

[178] M. Demoy, J. P. Andreux, C. Weingarten, B. Gouritin, V. Guilloux, and P. Couvreur, "In vitro evaluation of nanoparticles spleen capture," *Life Sci*, vol. 64, no. 15, pp. 1329–1337, 1999, doi: 10.1016/S0024-3205(99)00068-5.

[179] A. Vahedi, P. Bigdelou, and A. M. Farnoud, "Quantitative analysis of red blood cell membrane phospholipids and modulation of cell-macrophage interactions using cyclodextrins," *Sci Rep*, vol. 10, no. 1, pp. 1–13, Dec. 2020, doi: 10.1038/s41598-020-72176-3.

[180] L. Burnier, P. Fontana, B. R. Kwak, and A. S. Anne, "Cell-derived microparticles in haemostasis and vascular medicine," Mar. 24, 2009, *Schattauer GmbH*. doi: 10.1160/TH08-08-0521.

[181] D. L. Daleke, "Regulation of phospholipid asymmetry in the erythrocyte membrane," *Curr Opin Hematol*, vol. 15, no. 3, pp. 191–195, 2008, doi: 10.1097/MOH.0b013e3282f97af7.

[182] R. O. Bua, A. Messina, L. Sturiale, R. Barone, D. Garozzo, and A. Palmigiano, "N-Glycomics of Human Erythrocytes," *International Journal of Molecular Sciences 2021, Vol. 22, Page 8063*, vol. 22, no. 15, p. 8063, Jul. 2021, doi: 10.3390/IJMS22158063.

[183] D. L, *Blood Groups and Red Cell Antigens*.

[184] Y. Zhao *et al.*, "Surface-anchored framework for generating RhD-epitope stealth red blood cells," *Sci Adv*, vol. 6, no. 12, pp. 1–12, 2020, doi: 10.1126/sciadv.aaw9679.

[185] M. M. Kay, "Localization of senescent cell antigen on band 3.," *Proceedings of the National Academy of Sciences*, vol. 81, no. 18, pp. 5753–5757, Sep. 1984, doi: 10.1073/pnas.81.18.5753.

[186] M. Prudent, J. Delobel, A. Hübner, C. Benay, N. Lion, and J.-D. D. Tissot, "Proteomics of stored red blood cell membrane and storage-induced microvesicles reveals the association of flotillin-2 with band 3 complexes," *Front Physiol*, vol. 9, no. MAY, pp. 1–11, May 2018, doi: 10.3389/fphys.2018.00421.

[187] W. Sae-Lee *et al.*, "The protein organization of a red blood cell," *Cell Rep*, vol. 40, no. 3, p. 111103, Jul. 2022, doi: 10.1016/J.CELREP.2022.111103.

[188] V. Pretini *et al.*, "Red blood cells: Chasing interactions," Jul. 31, 2019, *Frontiers Media S.A.* doi: 10.3389/fphys.2019.00945.

[189] D. Z. de Back, E. B. Kostova, M. van Kraaij, T. K. van den Berg, and R. van Bruggen, "Of macrophages and red blood cells; a complex love story," *Front Physiol*, vol. 5, p. 9, Jan. 2014, doi: 10.3389/fphys.2014.00009.

[190] C. Peetla, A. Stine, and V. Labhasetwar, "Biophysical Interactions with Model Lipid Membranes: Applications in Drug Discovery and Drug Delivery," 2008, doi: 10.1021/mp9000662.

[191] A. I. Bunea, S. Harloff-Helleberg, R. Taboryski, and H. M. Nielsen, "Membrane interactions in drug delivery: Model cell membranes and orthogonal techniques," Jul. 01, 2020, *Elsevier B.V.* doi: 10.1016/j.cis.2020.102177.

[192] M. Kepczyński, K. Nawalany, M. Kumorek, A. Kobierska, B. Jachimska, and M. Nowakowska, "Which physical and structural factors of liposome carriers control their drug-loading efficiency?," *Chem Phys Lipids*, vol. 155, no. 1, pp. 7–15, Sep. 2008, doi: 10.1016/j.chemphyslip.2008.05.174.

[193] W. E. Moerner, "New directions in single-molecule imaging and analysis," 2007.

[194] A. Lejeune, M. Moorjani, C. Gicquaud, J. Lacroix, P. Poyet, and C. R. Gaudreault, "Nanoerythrosome, a new derivative of erythrocyte ghost: Preparation and antineoplastic potential as drug carrier for daunorubicin," *Anticancer Res*, vol. 14, no. 3 A, pp. 915–919, 1994.

[195] R. Deák *et al.*, "Nanoerythrosomes tailoring: Lipid induced protein scaffolding in ghost membrane derived vesicles," *Materials Science and Engineering C*, vol. 109, p. 110428, 2020, doi: 10.1016/j.msec.2019.110428.

[196] R. Deák, J. Mihály, I. C. Szigyártó, A. Wacha, G. Lelkes, and A. Bóta, "Physicochemical characterization of artificial nanoerythrosomes derived from erythrocyte ghost membranes," *Colloids Surf B Biointerfaces*, vol. 135, pp. 225–234, 2015, doi: 10.1016/j.colsurfb.2015.07.066.

[197] V. Heinrich, K. Ritchie, N. Mohandas, and E. Evans, "Elastic thickness compressibilty of the red cell membrane," *Biophys J*, vol. 81, no. 3, pp. 1452–1463, Sep. 2001, doi: 10.1016/S0006-3495(01)75800-6.

[198] T. Lu, J. T. Mac, R. Tweini, K. Tran, R. Vankayala, and B. Anvari, "Mechanical characterization of erythrocyte-derived optical microparticles by quantitative phase imaging and optical tweezers," in *Quantitative Phase Imaging V*, G. Popescu and Y. Park, Eds., SPIE, Mar. 2019, p. 42. doi: 10.1117/12.2507943.

[199] A. Lejeune, M. Moorjani, C. Gicquaud, J. Lacroix, P. Poyet, and C. R. Gaudreault, "Nanoerythrosome, a new derivative of erythrocyte ghost: Preparation and antineoplastic potential as drug carrier for daunorubicin," *Anticancer Res*, vol. 14, no. 3 A, pp. 915–919, 1994.

[200] A. Lejeune, M. Moorjani, C. Gicquaud, J. Lacroix, P. Poyet, and C. R. Gaudreault, "Nanoerythrosome, a new derivative of erythrocyte ghost: Preparation and antineoplastic potential as drug carrier for daunorubicin," *Anticancer Res*, vol. 14, no. 3 A, pp. 915–919, 1994.

[201] N. Buss, O. Yasa, Y. Alapan, M. B. Akolpoglu, and M. Sitti, "Nanoerythrosome-functionalized biohybrid microswimmers," *APL Bioeng*, vol. 4, no. 2, pp. 1–9, 2020, doi: 10.1063/1.5130670.

[202] A. Lejeune, P. Poyet, R. C.-Gaudreault, and C. Gicquaud, "Nanoerythrosomes, a new derivative of erythrocyte ghost: III. Is phagocytosis involved in the mechanism of action?," *Anticancer Res*, vol. 17, no. 5 A, pp. 3599–3603, 1997.

[203] N. Buss, O. Yasa, Y. Alapan, M. B. Akolpoglu, and M. Sitti, "Nanoerythrosome-functionalized biohybrid microswimmers," vol. 4, p. 26103, 2020, doi: 10.1063/1.5130670.

[204] X. Han *et al.*, "Red blood cell-derived nanoerythrosome for antigen delivery with enhanced cancer immunotherapy," *Sci Adv*, vol. 5, no. 10, pp. 1–10, 2019, doi: 10.1126/sciadv.aaw6870.

[205] A. Lejeune, P. Poyet, R. C.-Gaudreault, and C. Gicquaud, "Nanoerythrosomes, a new derivative of erythrocyte ghost: III. Is phagocytosis involved in the mechanism of action?," *Anticancer Res*, vol. 17, no. 5 A, pp. 3599–3603, 1997.

[206] N. Gupta, B. Patel, and F. Ahsan, "Nano-engineered erythrocyte ghosts as inhalational carriers for delivery of fasudil: Preparation and characterization," *Pharm Res*, vol. 31, no. 6, pp. 1553–1565, 2014, doi: 10.1007/s11095-013-1261-7.

[207] G. Della Pelle, A. Delgado López, M. Salord Fiol, and N. Kostevšek, "Cyanine Dyes for Photo-Thermal Therapy: A Comparison of Synthetic Liposomes and Natural Erythrocyte-Based Carriers," *Int J Mol Sci*, vol. 22, no. 13, p. 6914, Jun. 2021, doi: 10.3390/ijms22136914.

[208] G. Della Pelle *et al.*, "Red Blood Cell Membrane Vesicles for siRNA Delivery: A Biocompatible Carrier With Passive Tumor Targeting and Prolonged Plasma Residency," *Int J Nanomedicine*, vol. Volume 20, pp. 3269–3301, Mar. 2025, doi: 10.2147/IJN.S504644.

[209] N. Kostevšek, P. Miklavc, M. Kisovec, M. Podobnik, W. Al-Jamal, and I. Serša, "Magneto-erythrocyte membrane vesicles' superior t2 mri contrast agents to magneto-liposomes," *Magnetochemistry*, vol. 7, no. 4, p. 51, Apr. 2021, doi: 10.3390/magnetochemistry7040051.

[210] P. B. Canham, "The minimum energy of bending as a possible explanation of the biconcave shape of the human red blood cell," *J Theor Biol*, vol. 26, no. 1, pp. 61–81, Jan. 1970, doi: 10.1016/S0022-5193(70)80032-7.

[211] M. H. Antonelou, A. G. Kriebardis, and I. S. Papassideri, "Aging and death signalling in mature red cells: from basic science to transfusion practice," *Blood Transfusion*, vol. 8, no. Suppl 3, p. s39, 2010, doi: 10.2450/2010.007S.

[212] J. Han, Q. Wang, Z. Zhang, T. Gong, and X. Sun, "Cationic bovine serum albumin based self-assembled nanoparticles as siRNA delivery vector for treating lung metastatic cancer," *Small*, vol. 10, no. 3, pp. 524–535, 2014, doi: 10.1002/smll.201301992.

[213] W. Ma *et al.*, "Biomimetic Nanoerythrosome-Coated Aptamer–DNA Tetrahedron/Maytansine Conjugates: pH-Responsive and Targeted Cytotoxicity for HER2-Positive Breast Cancer," *Advanced Materials*, vol. 34, no. 46, Nov. 2022, doi: 10.1002/adma.202109609.

[214] Y. Guo *et al.*, "Erythrocyte Membrane-Enveloped Polymeric Nanoparticles as Nanovaccine for Induction of Antitumor Immunity against Melanoma," *ACS Nano*, vol. 9, no. 7, pp. 6918–6933, Jul. 2015, doi: 10.1021/acsnano.5b01042.

[215] R. Rai, S. Alwani, and I. Badea, "Polymeric Nanoparticles in Gene Therapy: New Avenues of Design and Optimization for Delivery Applications," *Polymers (Basel)*, vol. 11, no. 4, p. 745, Apr. 2019, doi: 10.3390/polym11040745.

[216] L. Duan *et al.*, "Nanoparticle Delivery of CRISPR/Cas9 for Genome Editing," *Front Genet*, vol. 12, no. May, 2021, doi: 10.3389/fgene.2021.673286.

[217] B. Winkeljann, D. C. Keul, and O. M. Merkel, "Engineering poly- and micelleplexes for nucleic acid delivery – A reflection on their endosomal escape," *Journal of Controlled Release*, vol. 353, no. October 2022, pp. 518–534, 2023, doi: 10.1016/j.jconrel.2022.12.008.

[218] M. A. Jackson *et al.*, "Zwitterionic Nanocarrier Surface Chemistry Improves siRNA Tumor Delivery and Silencing Activity Relative to Polyethylene Glycol," *ACS Nano*, vol. 11, no. 6, pp. 5680–5696, 2017, doi: 10.1021/acsnano.7b01110.

[219] B. Mandal *et al.*, "Core-shell-type lipid-polymer hybrid nanoparticles as a drug delivery platform," May 01, 2013, *Elsevier*. doi: 10.1016/j.nano.2012.11.010.

[220] A. M. Ramos-de-la-Peña, C. M. G. C. Renard, J. Montañez, M. de la Luz Reyes-Vega, and J. C. Contreras-Esquivel, "A review through recovery, purification and identification of genipin," *Phytochemistry Reviews*, vol. 15, no. 1, pp. 37–49, Feb. 2016, doi: 10.1007/S11101-014-9383-Z/TABLES/2.

[221] V. G. Tacias-Pascacio *et al.*, "Genipin as an emergent tool in the design of biocatalysts: Mechanism of reaction and applications," *Catalysts*, vol. 9, no. 12, pp. 1–18, 2019, doi: 10.3390/catal9121035.

[222] G. Della Pelle, T. Bozic, M. Vukomanović, G. Sersa, B. Markelc, and N. Kostevšek, "Efficient siRNA delivery to murine melanoma cells via a novel genipin-based nano-polymer," *Nanoscale Adv*, 2024, doi: 10.1039/d4na00363b.

[223] M. F. Butler, Y. F. Ng, and P. D. A. Pudney, "Mechanism and kinetics of the crosslinking reaction between biopolymers containing primary amine groups and genipin," *J Polym Sci A Polym Chem*, vol. 41, no. 24, pp. 3941–3953, 2003, doi: 10.1002/pola.10960.

[224] F. Jeeva and C. Caputo, "Substituent Effects of Amines on Genipin Dye Formation – Insights into Dye Origins," 2021.

[225] C. Ninh, A. Iftikhar, M. Cramer, and C. J. Bettinger, "Diffusion-reaction models of genipin incorporation into fibrin networks," *J Mater Chem B*, vol. 3, no. 22, pp. 4607–4615, 2015, doi: 10.1039/c4tb02025a.

[226] J. Qiu *et al.*, "In vitro investigation on the biodegradability and biocompatibility of genipin cross-linked porcine acellular dermal matrix with intrinsic fluorescence," *ACS Appl Mater Interfaces*, vol. 5, no. 2, pp. 344–350, 2013, doi: 10.1021/am302272k.

[227] S. L. Reay, E. L. Jackson, A. M. Ferreira, C. M. U. Hilkens, and K. Novakovic, "In vitro evaluation of the biodegradability of chitosan-genipin hydrogels," *Mater Adv*, vol. 3, no. 21, pp. 7946–7959, Aug. 2022, doi: 10.1039/D2MA00536K.

[228] G. Kaufmann, M. P. Klein, M. I. Goettert, and T. A. S. Aguirre, "Development and cytotoxicity evaluation of a cylindrical pH-responsive chitosan-genipin hydrogel for the oral delivery of diclofenac sodium," *Eur Polym J*, vol. 181, p. 111649, Dec. 2022, doi: 10.1016/j.eurpolymj.2022.111649.

[229] A. Moon, "Genipin, a constituent of Gardenia jasminoides Ellis, induces apoptosis and inhibits invasion in MDA-MB-231 breast cancer cells," *Oncol Rep*, Oct. 2011, doi: 10.3892/or.2011.1508.

[230] B. R. Kim *et al.*, "Genipin suppresses colorectal cancer cells by inhibiting the Sonic Hedgehog pathway," *Oncotarget*, vol. 8, no. 60, pp. 101952–101964, 2017, doi: 10.18632/oncotarget.21882.

[231] H.-J. Koo *et al.*, "Antiinflammatory effects of genipin, an active principle of gardenia," *Eur J Pharmacol*, vol. 495, no. 2–3, pp. 201–208, Jul. 2004, doi: 10.1016/j.ejphar.2004.05.031.

[232] L. Riacci, A. Sorriento, and L. Ricotti, "Genipin-based crosslinking of jellyfish collagen 3d hydrogels," *Gels*, vol. 7, no. 4, Dec. 2021, doi: 10.3390/gels7040238.

[233] X. Zhou *et al.*, "Genipin-cross-linked type II collagen scaffold promotes the differentiation of adipose-derived stem cells into nucleus pulposus-like cells," *J Biomed Mater Res A*, vol. 106, no. 5, pp. 1258–1268, May 2018, doi: 10.1002/jbm.a.36325.

[234] R. A. A. Muzzarelli, M. El Mehtedi, C. Bottegoni, A. Aquili, and A. Gigante, "Genipin-crosslinked chitosan gels and scaffolds for tissue engineering and regeneration of cartilage and bone," Dec. 01, 2015, *MDPI AG.* doi: 10.3390/md13127068.

[235] J. Andrade del Olmo *et al.*, "Wound healing and antibacterial chitosan-genipin hydrogels with controlled drug delivery for synergistic anti-inflammatory activity," *Int J Biol Macromol*, vol. 203, pp. 679–694, Apr. 2022, doi: 10.1016/J.IJBIOMAC.2022.01.193.

[236] H. Ragelle, K. Vanvarenberg, G. Vandermeulen, and V. Préat, "Chitosan Nanoparticles for SiRNA Delivery In Vitro," 2016, pp. 143–150. doi: 10.1007/978-1-4939-3112-5_12.

[237] A. Ghasemi, M. Mohtashami, S. S. Sheijani, and K. Aliakbari, "Chitosan-genipin nanohydrogel as a vehicle for sustained delivery of alpha-1 antitrypsin," 2015.

[238] K. Výborný *et al.*, "Genipin and EDC crosslinking of extracellular matrix hydrogel derived from human umbilical cord for neural tissue repair," *Sci Rep*, vol. 9, no. 1, p. 10674, Jul. 2019, doi: 10.1038/s41598-019-47059-x.

[239] H. C. Ha, N. S. Sirisoma, P. Kuppusamy, J. L. Zweier, P. M. Woster, and R. A. Casero, "The natural polyamine spermine functions directly as a free radical scavenger," *Proc Natl Acad Sci U S A*, vol. 95, no. 19, pp. 11140–11145, Sep. 1998, doi: 10.1073/PNAS.95.19.11140,.

[240] S. Mandal, A. Mandal, H. E. Johansson, A. V. Orjalo, and M. H. Park, "Depletion of cellular polyamines, spermidine and spermine, causes a total arrest in translation and growth in mammalian cells," *Proc Natl Acad Sci U S A*, vol. 110, no. 6, pp. 2169–2174, Feb. 2013, doi: 10.1073/PNAS.1219002110/SUPPL_FILE/PNAS.201219002SI.PDF.

[241] K. Igarashi and K. Kashiwagi, "Modulation of cellular function by polyamines," Jan. 2010. doi: 10.1016/j.biocel.2009.07.009.

[242] H. L. Lightfoot and J. Hall, "Endogenous polyamine function—the RNA perspective," *Nucleic Acids Res*, vol. 42, no. 18, p. 11275, Oct. 2014, doi: 10.1093/NAR/GKU837.

[243] T. Eisenberg *et al.*, "Induction of autophagy by spermidine promotes longevity," *Nat Cell Biol*, vol. 11, no. 11, pp. 1305–1314, Oct. 2009, doi: 10.1038/NCB1975;KWRD=LIFE+SCIENCES.

[244] A. E. Pegg, "Mammalian polyamine metabolism and function," *IUBMB Life*, vol. 61, no. 9, pp. 880–894, Sep. 2009, doi: 10.1002/IUB.230.

[245] A. M. Katz, I. S. Tolokh, S. A. Pabit, N. Baker, A. V. Onufriev, and L. Pollack, "Spermine Condenses DNA, but Not RNA Duplexes," *Biophys J*, vol. 112, no. 1, p. 22, Jan. 2017, doi: 10.1016/J.BPJ.2016.11.018.

[246] H. P. Til, H. E. Falke, M. K. Prinsen, and M. I. Willems, "Acute and subacute toxicity of tyramine, spermidine, spermine, putrescine and cadaverine in rats," *Food and Chemical Toxicology*, vol. 35, no. 3–4, pp. 337–348, 1997, doi: 10.1016/S0278-6915(97)00121-X.

[247] Y. Lv, J. Xue, P. Cui, and L. Qiu, "Spermine Significantly Increases the Transfection Efficiency of Cationic Polymeric Gene Vectors," *Pharmaceutics*, vol. 17, no. 1, p. 131, Jan. 2025, doi: 10.3390/PHARMACEUTICS17010131/S1.

[248] Z. Du, M. Chen, Q. He, Y. Zhou, and T. Jin, "Polymerized spermine as a novel polycationic nucleic acid carrier system," *Int J Pharm*, vol. 434, no. 1–2, pp. 437–443, Sep. 2012, doi: 10.1016/J.IJPHARM.2012.05.065.

[249] Y. Jin, F. Adams, L. Isert, D. Baldassi, and O. M. Merkel, "Spermine-based poly(β-amino ester)s for siRNA delivery against mutated KRAS in lung cancer," *Mol Pharm*, vol. 20, no. 9, p. 4505, Sep. 2023, doi: 10.1021/ACS.MOLPHARMACEUT.3C00206.

[250] G. Della Rosa *et al.*, "Tailoring of silica-based nanoporous pod by spermidine multi-activity," *Sci Rep*, vol. 10, no. 1, pp. 1–15, Dec. 2020, doi: 10.1038/S41598-

020-77957-4;SUBJMETA=152,2295,301,54,638,639,92,990;KWRD=BIOMATERIALS+.

[251] I. Mallov, F. Jeeva, and C. B. Caputo, "An edible genipin-based sensor for biogenic amine detection," *Journal of Chemical Technology & Biotechnology*, vol. 97, no. 4, pp. 830–836, Apr. 2022, doi: 10.1002/JCTB.6556.

[252] G. Della Pelle, T. Bozic, M. Vukomanović, G. Sersa, B. Markelc, and N. Kostevšek, "Efficient siRNA delivery to murine melanoma cells via a novel genipin-based nano-polymer," *Nanoscale Adv*, 2024, doi: 10.1039/d4na00363b.

[253] G. Della Pelle *et al.*, "Novel vector for efficient siRNA delivery to lymphoblasts and melanoma based on genipin-spermine nanocarriers protected with hybrid erythrocyte membrane coating," *Biomaterials Advances*, p. 214537, Mar. 2025, doi: 10.1016/j.bioadv.2025.214537.

[254] N. G. Sosale *et al.*, "'Marker of Self' CD47 on lentiviral vectors decreases macrophage-mediated clearance and increases delivery to SIRPA-expressing lung carcinoma tumors," *Mol Ther Methods Clin Dev*, vol. 3, no. October, p. 16080, 2016, doi: 10.1038/mtm.2016.80.

[255] D. Hatherley, S. C. Graham, J. Turner, K. Harlos, D. I. Stuart, and A. N. Barclay, "Paired Receptor Specificity Explained by Structures of Signal Regulatory Proteins Alone and Complexed with CD47," *Mol Cell*, vol. 31, no. 2, pp. 266–277, Jul. 2008, doi: 10.1016/j.molcel.2008.05.026.

[256] K. Thangaraju, S. N. Neerukonda, U. Katneni, and P. W. Buehler, "Extracellular Vesicles from Red Blood Cells and Their Evolving Roles in Health, Coagulopathy and Therapy," *Int J Mol Sci*, vol. 22, no. 1, pp. 1–25, Jan. 2021, doi: 10.3390/IJMS22010153.

[257] L. Sun, Y. Yu, B. Niu, and D. Wang, "Red Blood Cells as Potential Repositories of MicroRNAs in the Circulatory System," *Front Genet*, vol. 11, Jun. 2020, doi: 10.3389/FGENE.2020.00442.

[258] A. H. Bryk and J. R. Wiśniewski, "Quantitative Analysis of Human Red Blood Cell Proteome," *J Proteome Res*, vol. 16, no. 8, pp. 2752–2761, Aug. 2017, doi: 10.1021/acs.jproteome.7b00025.

[259] C. M. Termini and J. M. Gillette, "Tetraspanins function as regulators of cellular signaling," *Front Cell Dev Biol*, vol. 5, no. APR, pp. 1–14, 2017, doi: 10.3389/fcell.2017.00034.

[260] T. M. Leisner, T. C. Freeman, J. L. Black, and L. V. Parise, "CIB1: a small protein with big ambitions," *The FASEB Journal*, vol. 30, no. 8, pp. 2640–2650, Aug. 2016, doi: 10.1096/fj.201500073R.

[261] K. O'Brien, K. Breyne, S. Ughetto, L. C. Laurent, and X. O. Breakefield, "RNA delivery by extracellular vesicles in mammalian cells and its applications," *Nat Rev Mol Cell Biol*, vol. 21, no. 10, pp. 585–606, Oct. 2020, doi: 10.1038/s41580-020-0251-y.

[262] M. Frick, N. A. Bright, K. Riento, A. Bray, C. Merrified, and B. J. Nichols, "Coassembly of Flotillins Induces Formation of Membrane Microdomains,

Membrane Curvature, and Vesicle Budding," *Current Biology*, vol. 17, no. 13, pp. 1151–1156, 2007, doi: 10.1016/j.cub.2007.05.078.

[263] H. Maeda, "Toward a full understanding of the EPR effect in primary and metastatic tumors as well as issues related to its heterogeneity," *Adv. Drug Deliv. Rev.*, vol. 91, pp. 3–6, 2015.

[264] Y. R. Zhang, R. Lin, H. J. Li, W. ling He, J. Z. Du, and J. Wang, "Strategies to improve tumor penetration of nanomedicines through nanoparticle design," *Wiley Interdiscip Rev Nanomed Nanobiotechnol*, vol. 11, no. 1, pp. 1–12, 2019, doi: 10.1002/wnan.1519.

[265] T. Ji *et al.*, "Designing Liposomes to Suppress Extracellular Matrix Expression to Enhance Drug Penetration and Pancreatic Tumor Therapy," *ACS Nano*, vol. 11, no. 9, pp. 8668–8678, 2017, doi: 10.1021/acsnano.7b01026.

[266] S. Leporatti, "Thinking about Enhanced Permeability and Retention Effect (EPR)," *J Pers Med*, vol. 12, no. 8, pp. 12–14, 2022, doi: 10.3390/jpm12081259.

[267] J. Wu, "The enhanced permeability and retention (Epr) effect: The significance of the concept and methods to enhance its application," *J Pers Med*, vol. 11, no. 8, 2021, doi: 10.3390/jpm11080771.

[268] A. Y. Rwei, W. Wang, and D. S. Kohane, "Photoresponsive nanoparticles for drug delivery," *Nano Today*, vol. 10, no. 4, pp. 451–467, Aug. 2015, doi: 10.1016/j.nantod.2015.06.004.

[269] J. Wu, "The enhanced permeability and retention (Epr) effect: The significance of the concept and methods to enhance its application," *J Pers Med*, vol. 11, no. 8, 2021, doi: 10.3390/jpm11080771.

[270] S. Mindt, I. Karampinis, M. John, M. Neumaier, and K. Nowak, "Stability and degradation of indocyanine green in plasma, aqueous solution and whole blood," *Photochemical and Photobiological Sciences*, vol. 17, no. 9, pp. 1189–1196, 2018, doi: 10.1039/c8pp00064f.

[271] E. Engel *et al.*, "Light-induced decomposition of indocyanine green," *Invest Ophthalmol Vis Sci*, vol. 49, no. 5, pp. 1777–1783, 2008, doi: 10.1167/iovs.07-0911.

[272] V. Saxena, M. Sadoqi, and J. Shao, "Degradation Kinetics of Indocyanine Green in Aqueous Solution," *J Pharm Sci*, vol. 92, no. 10, pp. 2090–2097, Oct. 2003, doi: 10.1002/jps.10470.

[273] B. Bahmani, D. Bacon, and B. Anvari, "Erythrocyte-derived photo-theranostic agents: Hybrid nano-vesicles containing indocyanine green for near infrared imaging and therapeutic applications," *Sci Rep*, vol. 3, pp. 1–7, 2013, doi: 10.1038/srep02180.

[274] H. S. Han and K. Y. Choi, "Advances in nanomaterial-mediated photothermal cancer therapies: Toward clinical applications," *Biomedicines*, vol. 9, no. 3, pp. 1–15, 2021, doi: 10.3390/biomedicines9030305.

[275] W. Bäumler *et al.*, "Photo-oxidative killing of human colonic cancer cells using indocyanine green and infrared light," *Br J Cancer*, vol. 80, no. 3–4, pp. 360–363, 1999, doi: 10.1038/sj.bjc.6690363.

[276] J. C. Kraft and R. J. Y. Ho, "Interactions of indocyanine green and lipid in enhancing near-infrared fluorescence properties: The basis for near-infrared imaging in vivo," *Biochemistry*, vol. 53, no. 8, pp. 1275–1283, 2014, doi: 10.1021/bi500021j.

[277] R. Weigand, F. Rotermund, and A. Penzkofer, "Aggregation dependent absorption reduction of indocyanine green," *Journal of Physical Chemistry A*, vol. 101, no. 42, pp. 7729–7734, 1997, doi: 10.1021/jp9700894.

[278] W. Holzer *et al.*, "Photostability and thermal stability of indocyanine green," *J Photochem Photobiol B*, vol. 47, no. 2–3, pp. 155–164, 1998, doi: 10.1016/S1011-1344(98)00216-4.

[279] H. Gratz, A. Penzkofer, C. Abels, R. M. Szeimies, M. Landthaler, and W. Bäumler, "Photo-isomerisation, triplet formation, and photo-degradation dynamics of indocyanine green solutions," *J Photochem Photobiol A Chem*, vol. 128, no. 1–3, pp. 101–109, 1999, doi: 10.1016/S1010-6030(99)00174-4.

[280] F. Rotermund, R. Weigand, W. Holzer, M. Wittmann, and A. Penzkofer, "Fluorescence spectroscopic analysis of indocyanine green J aggregates in water," *J Photochem Photobiol A Chem*, vol. 110, no. 1, pp. 75–78, Oct. 1997, doi: 10.1016/S1010-6030(97)00167-6.

[281] C. Abels *et al.*, "Indocyanine green (ICG) and laser irradiation induce photooxidation," *Arch Dermatol Res*, vol. 292, no. 8, pp. 404–411, 2000, doi: 10.1007/s004030000147.

[282] K. Zhang *et al.*, "Novel peptide-directed liposomes for targeted combination therapy of breast tumors," *Mater Adv*, vol. 1, no. 9, pp. 3483–3495, 2020, doi: 10.1039/D0MA00536C.

[283] V. B. Rodriguez, S. M. Henry, A. S. Hoffman, P. S. Stayton, X. Li, and S. H. Pun, "Encapsulation and stabilization of indocyanine green within poly(styrene-alt-maleic anhydride) block-poly(styrene) micelles for near-infrared imaging," *J Biomed Opt*, vol. 13, no. 1, p. 014025, 2008, doi: 10.1117/1.2834296.

[284] S. Srinivasan, R. Manchanda, A. Fernandez-Fernandez, T. Lei, and A. J. Mcgoron, "Near-infrared fluorescing IR820-chitosan conjugate for multifunctional cancer theranostic applications," *J Photochem Photobiol B*, vol. 119, pp. 52–59, Feb. 2013, doi: 10.1016/j.jphotobiol.2012.12.008.

[285] B. Du *et al.*, "An IR820 Dye–Protein Complex for Second Near-Infrared Window and Photoacoustic Imaging," *Adv Opt Mater*, vol. 8, no. 4, p. 1901471, Feb. 2020, doi: 10.1002/adom.201901471.

[286] T. Wang, L. M. Larcher, L. Ma, and R. N. Veedu, "Systematic Screening of Commonly Used Commercial Transfection Reagents towards Efficient Transfection of Single-Stranded Oligonucleotides," *Molecules*, vol. 23, no. 10, p. 2564, Oct. 2018, doi: 10.3390/molecules23102564.

[287] Y. Li, R. Liu, Y. Shi, Z. Zhang, and X. Zhang, "Zwitterionic poly(carboxybetaine)-based cationic liposomes for effective delivery of small interfering RNA therapeutics without accelerated blood clearance phenomenon," *Theranostics*, vol. 5, no. 6, pp. 583–596, 2015, doi: 10.7150/thno.11234.

[288] S. F. Dowdy, "Endosomal escape of RNA therapeutics: How do we solve this rate-limiting problem?," *RNA*, vol. 29, no. 4, p. 396, Apr. 2023, doi: 10.1261/RNA.079507.122.

[289] C. M. Beddoes, C. P. Case, and W. H. Briscoe, "Understanding nanoparticle cellular entry: A physicochemical perspective," *Adv Colloid Interface Sci*, vol. 218, pp. 48–68, 2015, doi: 10.1016/j.cis.2015.01.007.

[290] Q. Yang *et al.*, "pH-Sensitive Polycations for siRNA Delivery: Effect of Asymmetric Structures of Tertiary Amine Groups," *Macromol Biosci*, vol. 21, no. 5, pp. 1–12, 2021, doi: 10.1002/mabi.202100025.

[291] C. Qiu *et al.*, "Advanced Strategies for Overcoming Endosomal/Lysosomal Barrier in Nanodrug Delivery," *Research*, vol. 6, Jan. 2023, doi: 10.34133/research.0148.

[292] Y. Q. Zhang *et al.*, "Ionizable drug delivery systems for efficient and selective gene therapy," *Mil Med Res*, vol. 10, no. 1, pp. 1–29, 2023, doi: 10.1186/s40779-023-00445-z.

[293] V. Vijayan, S. Uthaman, and I. K. Park, "Cell Membrane-Camouflaged Nanoparticles: A Promising Biomimetic Strategy for Cancer Theragnostics," *Polymers 2018, Vol. 10, Page 983*, vol. 10, no. 9, p. 983, Sep. 2018, doi: 10.3390/POLYM10090983.

[294] C. M. J. Hu, L. Zhang, S. Aryal, C. Cheung, R. H. Fang, and L. Zhang, "Erythrocyte membrane-camouflaged polymeric nanoparticles as a biomimetic delivery platform," *Proc Natl Acad Sci U S A*, vol. 108, no. 27, pp. 10980–10985, Jul. 2011, doi: 10.1073/PNAS.1106634108/SUPPL_FILE/PNAS.1106634108_SI.PDF.

[295] P. Wang *et al.*, "Bioinspired red blood cell membrane-encapsulated biomimetic nanoconstructs for synergistic and efficacious chemo-photothermal therapy," *Colloids Surf B Biointerfaces*, vol. 189, p. 110842, May 2020, doi: 10.1016/J.COLSURFB.2020.110842.

[296] W. Wang and K. Park, "Biomimetic Polymers for In Vivo Drug Delivery," *Wiley Blackwell 6*, vol. 9783527334, no. i, pp. 109–148, 2015, doi: 10.1002/9783527672752.ch5.

[297] C. F. Rodrigues, I. J. Correia, and A. F. Moreira, "Red blood cell membrane-camouflaged gold-core silica shell nanorods for cancer drug delivery and photothermal therapy," *Int J Pharm*, vol. 655, p. 124007, Apr. 2024, doi: 10.1016/J.IJPHARM.2024.124007.

[298] R. Mizuta, F. Inoue, Y. Sasaki, S. ichi Sawada, and K. Akiyoshi, "A Facile Method to Coat Nanoparticles with Lipid Bilayer Membrane: Hybrid Silica Nanoparticles Disguised as Biomembrane Vesicles by Particle Penetration of Concentrated Lipid Layers," *Small*, vol. 19, no. 12, Mar. 2023, doi: 10.1002/SMLL.202206153,.

[299] K. M. Schakowski, J. Linders, K. B. Ferenz, and M. Kirsch, "Synthesis and characterisation of aqueous haemoglobin-based microcapsules coated by genipin-cross-linked albumin," *J Microencapsul*, vol. 37, no. 3, pp. 193–204, 2020, doi: 10.1080/02652048.2020.1715498.

[300] D. Vukajlovic *et al.*, "Mathematical modelling of genipin-bovine serum albumin interaction using fluorescence intensity measurements," *Int J Biol Macromol*, vol. 276, no. P1, p. 133850, 2024, doi: 10.1016/j.ijbiomac.2024.133850.

[301] S. Matcham and K. Novakovic, "Fluorescence imaging in genipin crosslinked chitosan-poly(vinyl pyrrolidone) hydrogels," *Polymers (Basel)*, vol. 8, no. 11, pp. 1–10, 2016, doi: 10.3390/polym8110385.

[302] J. Qiu *et al.*, "In vitro investigation on the biodegradability and biocompatibility of genipin cross-linked porcine acellular dermal matrix with intrinsic fluorescence," *ACS Appl Mater Interfaces*, vol. 5, no. 2, pp. 344–350, 2013, doi: 10.1021/am302272k.

[303] H. G. Sundararaghavan, G. A. Monteiro, N. A. Lapin, Y. J. Chabal, J. R. Miksan, and D. I. Shreiber, "Genipin-induced changes in collagen gels: Correlation of mechanical properties to fluorescence," *J Biomed Mater Res A*, vol. 87, no. 2, pp. 308–320, 2008, doi: 10.1002/jbm.a.31715.

[304] Y. Zhang, L. Mao, J. Liu, and T. Liu, "Self-fluorescent drug delivery vector based on genipin-crosslinked polyethylenimine conjugated globin nanoparticle," *Materials Science and Engineering C*, vol. 71, pp. 17–24, 2017, doi: 10.1016/j.msec.2016.09.059.

[305] S. Mazumdar, D. Chitkara, and A. Mittal, "Exploration and insights into the cellular internalization and intracellular fate of amphiphilic polymeric nanocarriers," *Acta Pharm Sin B*, vol. 11, no. 4, pp. 903–924, Apr. 2021, doi: 10.1016/J.APSB.2021.02.019.

[306] K. Murugan, Y. E. Choonara, P. Kumar, D. Bijukumar, L. C. du Toit, and V. Pillay, "Parameters and characteristics governing cellular internalization and trans-barrier trafficking of nanostructures," *Int J Nanomedicine*, vol. 10, p. 2191, Mar. 2015, doi: 10.2147/IJN.S75615.

[307] M. Malnar Črnigoj *et al.*, "Phenylalanine-tRNA aminoacylation is compromised by ALS/FTD-associated C9orf72 C4G2 repeat RNA," *Nat Commun*, vol. 14, no. 1, pp. 1–15, 2023, doi: 10.1038/s41467-023-41511-3.

[308] M. Arias, J. C. Quijano, V. Haridas, J. U. Gutterman, and V. V. Lemeshko, "Red blood cell permeabilization by hypotonic treatments, saponin, and anticancer avicins," *Biochim Biophys Acta Biomembr*, vol. 1798, no. 6, pp. 1189–1196, Jun. 2010, doi: 10.1016/j.bbamem.2010.03.018.

[309] J. Doskocz *et al.*, "The Elucidation of the Molecular Mechanism of the Extrusion Process," *Materials*, vol. 14, no. 15, p. 4278, Jul. 2021, doi: 10.3390/ma14154278.

[310] L. Han, H. Zhan, X. Sun, Z. R. Zhang, and L. Deng, "A Density-Changing Centrifugation Method for Efficient Separation of Free Drugs from Drug-Loaded Particulate Delivery Systems," *AAPS Journal*, vol. 21, no. 3, pp. 1–11, 2019, doi: 10.1208/s12248-019-0306-1.

[311] J. K. Mills and D. Needham, "Lysolipid incorporation in dipalmitoylphosphatidylcholine bilayer membranes enhances the ion permeability and drug release rates at the membrane phase transition," *Biochim Biophys Acta Biomembr*, vol. 1716, no. 2, pp. 77–96, 2005, doi: 10.1016/j.bbamem.2005.08.007.

[312] M. F. Butler, Y. F. Ng, and P. D. A. Pudney, "Mechanism and kinetics of the crosslinking reaction between biopolymers containing primary amine groups and genipin," *J Polym Sci A Polym Chem*, vol. 41, no. 24, pp. 3941–3953, 2003, doi: 10.1002/pola.10960.

[313] A. O. Nwokeoji, P. M. Kilby, D. E. Portwood, and M. J. Dickman, "Accurate Quantification of Nucleic Acids Using Hypochromicity Measurements in Conjunction with UV Spectrophotometry," *Anal Chem*, vol. 89, no. 24, pp. 13567–13574, 2017, doi: 10.1021/acs.analchem.7b04000.

[314] R. Galindo-Murillo and T. E. Cheatham, "Ethidium bromide interactions with DNA: an exploration of a classic DNA–ligand complex with unbiased molecular dynamics simulations," *Nucleic Acids Res*, vol. 49, no. 7, pp. 3735–3747, Apr. 2021, doi: 10.1093/nar/gkab143.

[315] M. M. Bradford, "A rapid and sensitive method for the quantitation of microgram quantities of protein utilizing the principle of protein-dye binding," *Anal Biochem*, vol. 72, no. 1–2, pp. 248–254, May 1976, doi: 10.1016/0003-2697(76)90527-3.

[316] J. C. M. Stewart, "Colorimetric determination of phospholipids with ammonium ferrothiocyanate," *Anal Biochem*, vol. 104, no. 1, pp. 10–14, May 1980, doi: 10.1016/0003-2697(80)90269-9.

[317] C. B. Bottom, S. S. Hanna, and D. J. Siehr, "Mechanism of the ninhydrin reaction," *Biochem Educ*, vol. 6, no. 1, pp. 4–5, 1978, doi: 10.1016/0307-4412(78)90153-X.

[318] A. Fernandez-Fernandez *et al.*, "Comparative study of the optical and heat generation properties of IR820 and indocyanine green," *Mol Imaging*, vol. 11, no. 2, pp. 99–113, 2012, doi: 10.2310/7290.2011.00031.

[319] W. Strober, "Trypan Blue Exclusion Test of Cell Viability," *Curr Protoc Immunol*, vol. 111, no. 1, Nov. 2015, doi: 10.1002/0471142735.ima03bs111.

[320] N. C. Shaner, R. E. Campbell, P. A. Steinbach, B. N. G. Giepmans, A. E. Palmer, and R. Y. Tsien, "Improved monomeric red, orange and yellow fluorescent proteins derived from Discosoma sp. red fluorescent protein," *Nat Biotechnol*, vol. 22, no. 12, pp. 1567–1572, Dec. 2004, doi: 10.1038/nbt1037.

[321] Y. Zhang, M. Huo, J. Zhou, and S. Xie, "PKSolver: An add-in program for pharmacokinetic and pharmacodynamic data analysis in Microsoft Excel," *Comput Methods Programs Biomed*, vol. 99, no. 3, pp. 306–314, Sep. 2010, doi: 10.1016/j.cmpb.2010.01.007.

[322] M. F. Kramer, "Stem-loop RT-qPCR for miRNAs," *Curr Protoc Mol Biol*, no. SUPPL. 95, pp. 1–22, 2011, doi: 10.1002/0471142727.mb1510s95.

[323] J. Zhou, F. Yang, G. Jiang, and J. Wang, "Applications of indocyanine green based near-infrared fluorescence imaging in thoracic surgery," 2016, *AME Publishing Company*. doi: 10.21037/jtd.2016.09.49.

[324] M. Saboktakin, "Polymeric Nanoencapsulation of Indocyanine green for Photodynamic Therapy Technique," *Am J Biomed Sci Res*, vol. 3, no. 1, pp. 35–48, 2019, doi: 10.34297/ajbsr.2019.03.000630.

[325] E. Engel *et al.*, "Light-induced decomposition of indocyanine green," *Invest Ophthalmol Vis Sci*, vol. 49, no. 5, pp. 1777–1783, Apr. 2008, doi: 10.1167/iovs.07-0911.

[326] M. Overchuk, R. A. Weersink, B. C. Wilson, and G. Zheng, "Photodynamic and Photothermal Therapies: Synergy Opportunities for Nanomedicine," *ACS Nano*, vol. 17, no. 9, pp. 7979–8003, 2023, doi: 10.1021/acsnano.3c00891.

[327] D. S. Conceiç ão, D. P. Ferreira, and L. F. Vieira Ferreira, "Photochemistry and Cytotoxicity Evaluation of Heptamethinecyanine Near Infrared (NIR) Dyes," *OPEN ACCESS Int. J. Mol. Sci*, vol. 14, p. 14, 2013, doi: 10.3390/ijms140918557.

[328] G. Yeroslavsky *et al.*, "Photostabilization of indocyanine green dye by energy transfer in phospholipid-peg micelles," *Journal of Photopolymer Science and Technology*, vol. 32, no. 1, pp. 115–121, 2019, doi: 10.2494/photopolymer.32.115.

[329] K. Igarashi and K. Kashiwagi, "Modulation of cellular function by polyamines," *Int J Biochem Cell Biol*, vol. 42, no. 1, pp. 39–51, Jan. 2010, doi: 10.1016/J.BIOCEL.2009.07.009.

[330] G. Della Pelle, T. Bozic, M. Vukomanović, G. Sersa, B. Markelc, and N. Kostevšek, "Efficient siRNA delivery to murine melanoma cells via a novel genipin-based nano-polymer," *Nanoscale Adv*, 2024, doi: 10.1039/d4na00363b.

[331] A. Vincy, S. Mazumder, Amrita, I. Banerjee, K. C. Hwang, and R. Vankayala, "Recent Progress in Red Blood Cells-Derived Particles as Novel Bioinspired Drug Delivery Systems: Challenges and Strategies for Clinical Translation," *Front Chem*, vol. 10, p. 905256, Apr. 2022, doi: 10.3389/FCHEM.2022.905256/BIBTEX.

[332] H. Li and G. Lykotrafitis, "Erythrocyte membrane model with explicit description of the lipid bilayer and the spectrin network," *Biophys J*, vol. 107, no. 3, pp. 642–653, Aug. 2014, doi: 10.1016/j.bpj.2014.06.031.

[333] A. Ciana, C. Achilli, and G. Minetti, "Membrane rafts of the human red blood cell," 2014, *Informa Healthcare*. doi: 87.

[334] S. Mizrahy, I. Hazan-Halevy, N. Dammes, D. Landesman-Milo, and D. Peer, "Current Progress in Non-viral RNAi-Based Delivery Strategies to Lymphocytes," *Molecular Therapy*, vol. 25, no. 7, p. 1491, Jul. 2017, doi: 10.1016/J.YMTHE.2017.03.001.

[335] B. Fadnes *et al.*, "The proteoglycan repertoire of lymphoid cells," *Glycoconj J*, vol. 29, no. 7, p. 513, Oct. 2012, doi: 10.1007/S10719-012-9427-9.

[336] N. H. Kwon, P. L. Fox, and S. Kim, "Aminoacyl-tRNA synthetases as therapeutic targets," Aug. 01, 2019, *Nature Publishing Group*. doi: 10.1038/s41573-019-0026-3.

# Bibliography

## Publications Related to the Thesis

### Journal Articles

DELLA PELLE, Giulia, MARKELC, Boštjan, CERCEK, Urša, ZIVIC, Urška, COUPARD Mia, ARSHAD Shahid Muhammad, BOŽIČ, Tim, GAZVODA Lea, ROGELJ Boris, KOSTEVŠEK, Nina. Novel vector for efficient siRNA delivery to lymphoblasts and melanoma based on genipin-spermine nanocarriers protected with hybrid erythrocyte membrane coating. *Biomaterials Advances*, Volume 180, 2026, 214537, ISSN 2772-9508, DOI: 1016/j.bioadv.2025.214537

DELLA PELLE, Giulia, MARKELC, Boštjan, BOŽIČ, Tim, ŠRIBAR, Jernej, KRIŽAJ, Igor, ŽAGAR, Kristina, HUDOKLIN, Samo, ERDANI-KREFT, Mateja, URBANČIČ, Iztok, KISOVEC, Matic, PODOBNIK, Marjetka, KOSTEVŠEK, Nina. Red blood cell membrane vesicles for siRNA delivery : a biocompatible carrier with passive tumor targeting and prolonged plasma residency. *International journal of nanomedicine*. [Online ed.]. 15 Mar. 2025, vol. 20, str. 3269-3301, ilustr. ISSN 1178-2013. , DOI: 10.2147/IJN.S504644

DELLA PELLE, Giulia, BOŽIČ, Tim, VUKOMANOVIĆ, Marija, SERŠA, Gregor, MARKELC, Boštjan, KOSTEVŠEK, Nina. Efficient siRNA delivery to murine melanoma cells via a novel genipin-based nano-polymer. *Nanoscale advances*. Sep. 2024, vol. 6, iss. 18, str. 4704-4723, ilustr. DOI: 10.1039/D4NA00363B.

DELLA PELLE, Giulia, KOSTEVŠEK, Nina. Nucleic acid delivery with red-blood-cell-based carriers. *International journal of molecular sciences*. 2021, vol. 22, no. 10, str. 5264-1-5264-25. ISSN 1422-0067. DOI: 10.3390/ijms22105264.

DELLA PELLE, Giulia, DELGADO LÓPEZ, Andrea, SALORD FIOL, Marina, KOSTEVŠEK, Nina. Cyanine dyes for photo-thermal therapy : a comparison of synthetic liposomes and natural erythrocyte-based carriers. International journal of molecular sciences. 2021, vol. 22, no. 13, str. 6914-1- 6914-16. ISSN 1422-0067. DOI: 10.3390/ijms22136914.

### Conference Abstracts

- DELLA PELLE, Giulia, KOSTEVŠEK, Nina. Erythrocytes based carriers for therapy and diagnostic. V: NanoMed 2021, joint Hybrid Conferences 2021, 20-22 Oct. 2021, Milan, Italy[COBISS.SI-ID 96289539]
- DELLA PELLE, Giulia, KOSTEVŠEK, Nina. Red blood cell derived vesicles for gene therapy and theranostics. *14th Jožef Stefan Institute: Jožef Stefan International Postgraduate School*, 2022. COBISS.SI-ID 139147779]
- DELLA PELLE, Giulia, BOŽIČ, Tim, MARKELC, Boštjan, VUKOMANOVIĆ, Marija, ČEMAŽAR, Maja, KOSTEVŠEK, Nina. siRNA delivery with genipin-polyamines based polymers : characterization, safety, and efficacy. *15th Jožef Stefan International Postgraduate School Students' Conference* [COBISS.SI-ID 156816899]

- DELLA PELLE, Giulia. Biodistribution and in vivo knock-down ability of erythrocytes membrane vesicles : Mini symposium "Development of biomimetic carriers for gene therapy for cancer treatment", 26.3.2024, IJS. [COBISS.SI-ID 190871811]
- DELLA PELLE, Giulia, MARKELC, Boštjan, BOŽIČ, Tim, KOSTEVŠEK, Nina. Small-interfering RNA delivery via erythrocytes-membrane vesicles : GenE-HumDi Cyprus Meeting, 8-10 April 2024, Cyprus. [COBISS.SI-ID 202577411]

## Contributions to Conference Abstracts

- KOSTEVŠEK, Nina, DELLA PELLE, Giulia, BOŽIČ, Tim, ŠRIBAR, Jernej, MARKELC, Boštjan. Erythrocyte membrane-derived vesicles for safe and efficient siRNA delivery in gene silencing therapy. V: ORTIZ DE LA MORENA, Rodrigo (ur.), MERC, Vesna (ur.). *CTGCT Days 2025 : abstract book*. Ljubljana: Centre for the Technologies of Gene and Cell Therapy, National Institute of Chemistry, 2025. Str. 69. ISBN 978-961-7238-13-6. https://ctgct.si/wp-content/uploads/2025/09/Abstract-book-CTGCT-Days-2025-F-1.pdf. [COBISS.SI-ID 250639875]
- BELEC, Blaž, KOSTEVŠEK, Nina, DELLA PELLE, Giulia, GARDONIO, Sandra, FANETTI, Mattia, VALANT, Matija. Topological insulator nanoparticles: material with prospect for photo-thermal applications. V: ICPPP21 [also] International Conference on Photoacoustic and Photothermal Phenomena : [COBISS.SI-ID 112827395]
- KOSTEVŠEK, Nina, DELLA PELLE, Giulia, MARKELC, Boštjan, BOŽIČ, Tim, ČEMAŽAR, Maja, SERŠA, Igor. Erythrocyte-based vesicle as a biomimetic platform for drug delivery. 29th Annual Meeting of the Slovenian Chemical Society Portorose, Slovenija. Ljubljana: ISBN 978-961-95922-2-9. [COBISS.SI-ID 164811011]
- KOSTEVŠEK, Nina, SERŠA, Igor, MIKLAVC, Patricija, DELLA PELLE, Giulia. Erythrocyte-membrane vesicles as drug carriers. Molecular oncology, EACR 2023: Innovative Cancer Science, 12-15 June 2023, Torino. Jun. 2023 [COBISS.SI-ID 158635779]
- PLAVEC, Tina Vida, ŽAGAR, Kristina, DELLA PELLE, Giulia, KOSTEVŠEK, Nina, VIDMAR, Robert, BERLEC, Aleš. Isolation and analysis of extracellular vesicles from recombinant Lactococcus lactis. al. Small New World 2.0 : 4-5 September 2023, Graz :[COBISS.SI-ID 163483651]
- KOSTEVŠEK, Nina, DELLA PELLE, Giulia, BOŽIČ, Tim, MARKELC, Boštjan. Erythrocyte membrane-based vesicles as siRNA carriers for safe and efficient gene silencing therapy. V: 2nd MOVE Symposium : 8-11 October 2024, Belgrade, Serbia [COBISS.SI-ID 211418371]
- KOSTEVŠEK, Nina, DELLA PELLE, Giulia, MARKELC, Boštjan, ŠRIBAR, Jernej, ČEMAŽAR, Maja, BOŽIČ, Tim. Red blood cell-derived vesicles for safe and efficient siRNA delivery. V: EACR 2024 congress, 10 - 13 June 2024, Rotterdam : Abstracts. New York: Wiley, 2024. Str. 79. Molecular oncology, Vol. 18, Suppl. 1. ISSN 1878-0261. [COBISS.SI-ID 229541635]

## Other Publications

Belec, B., Kostevšek, N., Pelle, G. Della, Nemec, S., Kralj, S., Bergant Marušič, M., Gardonio, S., Fanetti, M., & Valant, M. (2023). Silica Coated Bi2Se3 Topological Insulator Nanoparticles: An Alternative Route to Retain Their Optical Properties and Make Them Biocompatible. *Nanomaterials*, *13*(5). https://doi.org/10.3390/NANO13050809

Plavec, T. V., Žagar Soderžnik, K., Della Pelle, G., Zupančič, Š., Vidmar, R., & Berlec, A. (2025). Incorporation of recombinant proteins into extracellular vesicles by Lactococcus cremoris. *Scientific Reports*, *15*(1), 1768. https://doi.org/10.1038/S41598-025-86492-Z

. . .

# Biography

The author of this thesis, Giulia Della Pelle, was born in Bracciano (nearby Rome, Italy), on the 24$^{th}$ of November of 1992. She graduated from High School in 2011, and enrolled at Biotechnology program at Tuscia University, Viterbo, Italy, graduating in 2015. Her BSc thesis focused on the theoretical background of the mechanism of action of antimicrobial peptides, under the supervision of Professor Fernando Porcelli. She graduated in 2015, and enrolled in the Master of Science program, Biotechnology for Agriculture, Environment, Health, graduating in 2018 with a thesis entitled "Mechanism of Action of a Chionodracine Mutant", Later, she joined Professor Boudinot group for Erasmus Traineeship, at Jouy-en-Josas INRA, Paris cedex (France). For the next two years, she worked at DIBAF department at Tuscia University as research assistant, again in the field of bioactive molecules discovery and early characterization. From 2020 on, she joined the Jožef Stefan International Postgraduate school (Ljubljana, Slovenija), program Nanoscience and Nanotechnologies, under the supervision of Assist. Professor Nina Kostevšek. After being employed at Novartis Slovenija as Product Steward, she started as Senior Scientist at Lek|Sandoz in Biosimilars development.